Underground Power Transmission

UNDERGROUND POWER TRANSMISSION

The Science, Technology, and Economics of High Voltage Cables

Peter Graneau

Underground Power Corporation and
Massachusetts Institute of Technology

A Wiley-Interscience Publication

JOHN WILEY & SONS
New York • Chichester • Brisbane • Toronto

Library of Congress Cataloging in Publication Data:

Graneau, Peter.
Underground power transmission.

"A Wiley-Interscience publication."
Bibliography: p.
Includes indexes.
1. Electric cables. Electric lines—Underground.
3. Electric power transmission. I. Title.

TK3351.G675 621.219'23 79-15746
ISBN 0-471-05757-6

Printed in the United States of America
10 9 8 7 6 5 4 3 2 1

To Brigitte and Neal

PREFACE

Despite the mounting social pressure for the preservation of landscape aesthetics, and despite the fear of biological hazards caused by electric fields in the vicinity of overhead lines, progress in underground and underwater electric power transmission has been painfully slow. One reason for this is the very small number of engineers and scientists who are taught about high voltage cables in our colleges and universities. The energy-conscious applied science community knows much about the pros and cons of nuclear power generation, the world reserves of fossile fuels, and how to use solar energy for domestic purposes. Yet it has remained largely unaware of the dramatic change in the economics of power transmission set in motion by the 1973 oil embargo. They do not realize that, for years to come, a new conductor metal may conserve as much energy as solar home heating.

I hope this book will make it easier to design courses of study in which underground power lines rank with the widely taught subject of overhead lines. The subject matter is broad enough to institute specialized graduate courses in high voltage cable technology. Its teachers should not fear crossing the borders between physics, chemistry, metallurgy, and engineering. The development, installation, and operation of power cables, their interaction with electricity supply systems, and their economic implications form a multidisciplinary field which both requires and furnishes a broad educational foundation for engineers who plan to enter the utility industry or to join manufacturers, consultants, and contractors who serve the utilities.

In many years of research and consulting I have grown tired of roaming through an accumulation of fraying papers, loose-leaf tables, little manufacturer's handbooks, and so on. This collection defies a rational system of indexing, yet is essential for day-to-day evaluation, design and operation of underground power lines. If this reference volume achieves nothing else, in its self-supporting stance on the shelf, it will at least save the reader hours and days of searching and give him or her the satisfaction of winning one skirmish in the paper war.

Some will maintain that too much has been said about sodium conductors at a time when they are unavailable for purchase. I make no apology, for I firmly believe that the low cost of this metal and the good service performance of existing sodium cables will make them the power cable of the twenty-first century. Sodium cables have the potential of sweeping away the wire cobwebs of the first hundred years of our electrical age and of making visible more blue sky. Blue is the color of hope!

PETER GRANEAU

Concord, Massachusetts
October 1979

CONTENTS

Part I
Power Conductors 1

1.1 Free Electron Model and Wiedemann-Franz Law 1
1.2 The Nature of Electrical Resistance and Mathiessen's Rule 5
1.3 Size Effect and Magnetoresistance 11
1.4 Electron Band Structure and the Fermi Surface 14
1.5 Type I Superconductivity 19
1.6 The Cause of Superconductivity 25
1.7 Type II Superconductivity 28
1.8 Skin Effect 31
1.9 Finite-Element Method for Noncircular Conductors 42
1.10 Proximity Effect in Go-and-Return Circuit 47
1.11 The Mutual Inductance between Parallel Linear Conductors 50
1.12 Single Conductor in a Metallic Pipe and Crossbonding 58
1.13 Circulating-Current Sheath Loss in Non-Cross-bonded Systems as a Function of Geometrical Factors and Conductivity 69
1.14 Eddy Current Sheath Losses in Single-Core Cables of Three-Phase Circuits 75
1.15 The Application of the Finite Element Method to Three-Conductor Cables 79
1.16 Electromechanical Forces between Conductors and Metallic Pipes 90
1.17 The AC Performance of Stranded Conductors 97
1.18 Joule Heating and Magnetic Hysteresis Losses in Pipe-Type Cables 107
1.19 Cable Inductance and Voltage Drop 112
1.20 Copper 125

1.21 Aluminum 130
1.22 Sodium 136
1.23 Beryllium 141
1.24 Niobium and its Superconducting Alloys 145
1.25 Conductor Economics and Kelvin's Law 148

Part II
High Voltage Insulation 157

2.1 Reliability of Transmission Lines 157
2.2 The Trend to Ever Increasing Transmission Voltages 160
2.3 Dielectric Breakdown of Gases 167
2.4 Dielectric Breakdown of Liquids 192
2.5 Dielectric Breakdown of Solids 200
2.6 Breakdown of Vacuum Insulation 245
2.7 Polarization, Cable Capacitance, and Dielectric Loss 259

Part III
Cable Technology and Economics 276

3.1 Historical Evolution of High Voltage Cables 276
3.2 Self-contained Oil-Paper Insulated AC and DC Cables 284
3.3 Oil-Paper Insulated Pipe-Type Cables 347
3.4 Gas Pressure Assisted Paper Insulated Cables 401
3.5 Solid Dielectric Cables 401
3.6 Gas Insulated Cables 441
3.7 The Prospect of Resistive and Superconducting Cryocables 468

References 488

Author Index 503

Subject Index 507

Underground Power Transmission

Part I
POWER CONDUCTORS

1.1 FREE ELECTRON MODEL AND THE WIEDEMANN-FRANZ LAW

Electrical power transmission, as we know it today, would not be possible without the easy motion of electrons through the metal lattice. The theory of metallic conduction, voluminous though it is, has not reached the stage where the charge transport phenomena may be calculated with sufficient accuracy for designing electrical cables. At the same time the concepts of this theory are guiding the evolution of cable technology and should therefore be understood by serious students of the subject.

At the dawn of the electrical age, electricity was believed to be a fluid, or even two fluids, one positive and the other negative, contained by metals more or less like water in a pipe. Our present understanding nucleated at the turn of the century with the free-electron model. It was noticed that the best conductors were the noble metals silver, copper, and gold, which, according to the periodic table of elements, have only one electron in the outermost electronic shell surrounding the atomic nucleus. This lone electron is apparently free to roam through the metallic lattice. The same state of affairs prevails in the monovalent alkali metals, which include sodium. Exceptions to the monovalency rule are the very important conductor metal aluminum with three electrons in the incomplete outer electron shell, and the potentially important beryllium with two valency electrons. Figure 1.1 lists the electrical conductivity of all metals at ambient temperature in the form of a periodic table. It is clear from the table that other factors than the electronic structure influence charge transfer processes. They have to do with the collisions a free conduction electron suffers as it moves through the host metal.

In the free-electron model of a monovalent metal it is assumed that the loosely bound outer electron is detached from the atom, leaving behind a

Li 1.07	Be 3.08											B	C	N	O	F	Ne
Na 2.11	Mg 2.33											Al 3.65	Si	P	S	Cl	Ar
K 1.39	Ca 2.78	Sc 0.21	Ti 0.23	V 0.50	Cr 0.78	Mn 0.07	Fe 1.02	Co 1.72	Ni 1.43	Cu 5.88	Zn 1.69	Ga 0.67	Ge	As	Se	Br	Kr
Rb 0.80	Sr 0.47	Y 0.17	Zr 0.24	Nb 0.69	Mo 1.89	Tc 0.70	Ru 1.35	Rh 2.08	Pd 0.95	Ag 6.21	Cd 1.38	In 1.14	Sn 0.91	Sb 0.24	Te	I	Xe
Cs 0.50	Ba 0.26	La 0.13	Hf 0.33	Ta 0.76	W 1.89	Re 0.54	Os 1.10	Ir 1.96	Pt 0.96	Au 4.55	Hg 0.10	Tl 0.61	Pb 0.48	Bi 0.09	Po 0.22	At	Rn
Fr	Ra	Ac															

Ce 0.12	Pr 0.15	Nd 0.17	Pm	Sm 0.10	Eu 0.11	Gd 0.07	Tb 0.09	Dy 0.11	Ho 0.13	Er 0.12	Tm 0.16	Yb 0.38	Lu 0.19
Th 0.66	Pa	U 0.39	Np 0.09	Pu 0.07	Am	Cm	Bk	Cf	Es	Fm	Md	No	Lw

Figure 1.1 Electrical conductivity at ambient temperature of the metals of the periodic table in units of $10^5(\Omega \cdot \text{cm})^{-1}$.

positive ion frozen to its lattice position. Under these conditions the free-electron density is equal to the number of atoms per unit volume. Each electron with charge $-e$ moves with a randomly directed velocity v depending on temperature. If m is the mass of the electron, then its thermal velocity is related to the absolute temperature T by the Boltzmann constant k according to

$$\tfrac{1}{2}mv^2 = \tfrac{3}{2}kT \tag{1.1}$$

The particle velocity of (1.1) is the average molecular velocity of a classical gas obeying the Maxwell-Boltzmann distribution of velocities. This explains why the free-electron model is often called an electron gas. An electric field E applied to the metal will accelerate the conduction electrons in the direction opposite to the field until they collide with the lattice ions. On the average the free electron will aquire a drift velocity v_d given by the change in momentum $(m \cdot v_d)$ that is being produced by the force $(-e \cdot E)$ acting for a time interval τ. Therefore

$$v_d = -\left(\frac{e}{m}\right) \cdot E \cdot \tau \tag{1.2}$$

The average time τ between electron scattering events is related to the mean free path of the electron by

$$l = v_d \cdot \tau \tag{1.3}$$

The charge transport, or current density J, in the electron gas may be expressed as

$$J = -n \cdot e \cdot v_d \tag{1.4}$$

with n being the number of electrons (or atoms) per unit volume. Ohm's law is obtained by combining (1.2) and (1.4)

$$J = \frac{n \cdot e^2 \cdot \tau}{m} \cdot E \tag{1.5}$$

This shows that the free-electron model is compatible with the empirically observed proportionality of current density to applied electric field strength. Equation (1.5) defines the electrical conductivity σ as

$$\sigma = \frac{n \cdot e^2 \cdot \tau}{m} \tag{1.6}$$

The kinetic theory of gases gives the thermal conductivity of the assembly of particles as

$$\kappa = \tfrac{2}{3} n \cdot c_v \cdot v \cdot l \tag{1.7}$$

with the specific heat at constant volume being defined by

$$c_v = \tfrac{3}{2} \cdot k \tag{1.8}$$

If the mean free path l between thermal collisions is related to the average thermal velocity v by a collision time τ as in (1.3), the thermal conductivity may be written

$$\kappa = \frac{3n}{2m} \cdot \sigma \cdot k^2 \cdot T \tag{1.9}$$

Therefore the ratio of thermal to electrical conductivity of the free-electron gas becomes

$$\frac{\kappa}{\sigma} = 3 \cdot \left(\frac{k}{e}\right)^2 \cdot T^2 \tag{1.10}$$

Equation (1.10) is an expression of the Wiedemann-Franz law, which states that the ratio of thermal to electrical conductivity is independent of the material and proportional to absolute temperature. In the temperature range 0 to 100°C it is a fairly good approximation to the experimental facts and therefore has important practical consequences in cable design. In a cable that is being cooled by its environment, the heat generated in the conductor has to flow through the electrical insulation. Therefore the insulation should at the same time be a good thermal conductor. No solid materials exist that satisfy this condition. The difficulty can be overcome by internal conductor cooling or the use of fluid insulation systems that permit heat transport by convection and radiation and are not subject to the Wiedemann-Franz law. A further consequence of this law is that all the important electrical conductors are also good thermal conductors, which keep the temperature distributions over the conductor cross-sections constant. Furthermore, hot spots arising along a cable route for a variety of reasons are to some extent smoothed out by the excellent heat-transport properties of the conductors.

In spite of the success of the Wiedemann-Franz law, the simple free-electron model had to be modified because it overestimated the contribution made to the specific heat of metals by the conduction electrons and it also predicted erroneous relationships between electrical resistivity and temperature. Major adjustments had to be made to the number of available

conduction electrons and the mean free path. Fortunately, these two quantities did not enter (1.10), which remains the basis of the Wiedemann-Franz law.

1.2 THE NATURE OF ELECTRICAL RESISTANCE AND MATHIESSEN'S RULE

The initial success of the free-electron model was due mainly to the qualitative explanations it provided for the firmly rooted experimental facts underlying the laws of Ohm and Wiedemann-Franz. It failed to give any insight in the mechanism by which the electric current heats the conductor and how temperature influences the electrical resistivity. That the electrical resistance of a wire increases approximately in proportion to the absolute temperature was well known to Mathiessen, who in 1860 found that alloying a conductor metal with a small amount of another metal always increases the electrical resistivity. Furthermore, he determined that this increase, ρ_0, was fixed and independent of the temperature of the conductor. From these findings he formulated the rule

$$\rho = \rho_0 + \rho_i \tag{1.11}$$

The temperature-dependent part ρ_i of the resistivity ρ is often called the ideal resistivity. It should vanish as the temperature approaches absolute zero, leaving only the residual resistivity ρ_0.

A practical consequence of Mathiessen's rule is that all good electrical conductors are pure metals. It saved the search for a "wonder-alloy" in an infinite number of possible alloys. Mathiessen's rule does not hold for superconductors, the best of which are actually alloys. This exception opened the door to the modern alchemist's dream of finding an alloy or compound of zero resistivity, preferably at ambient temperature.

Today it is known that the residual resistivity is due not only to impurity atoms but also to elastic strain, lattice defects, and grain boundaries. It so happens that the metal specimen that have the largest grains (crystals), contain the fewest lattice defects, and support the least elastic strain. Metal refining therefore has become the most important operation in the production of good electrical conductors. The resistivity of the common conductor metals is also decreased by annealing and similar heat treatments. They cause recrystallization and the formation of larger grains with fewer lattice imperfections. Annealing relaxes strain that has previously been frozen into the conductor metal.

The residual resistivity is readily measured by immersing the specimen in a bath of boiling liquid helium (4.2°K). At this very low temperature the ideal resistivity is negligibly small. It has become customary to check the

quality of a conductor specimen by determining its resistance ratio at ambient and liquid-helium temperature. Taking account of thermal contraction, this measurement also gives the resistivity ratio. With Mathiessen's rule it may be expressed as

$$\frac{\rho_{293°K}}{\rho_{4.2°K}} = \frac{\rho_{i,293°K} + \rho_0}{\rho_0} = 1 + \frac{\rho_{i,293°K}}{\rho_0} \tag{1.12}$$

The most widely used material for high-voltage cable conductors is electrolytically refined tough-pitch copper. Depending on the degree of work hardening and subsequent heat treatments, this material has resistance ratios varying from 50 to 500. In contrast with this, a ratio as high as 45,000 was measured in the National Bureau of Standards on an aluminum specimen with an impurity content as low as 0.2 parts per million. The wide spread in resistance ratios makes this parameter a sensitive indicator of the metallurgical condition of the conductor material.

At ordinary temperatures the electrical resistance of a metal specimen is dominated by the ideal resistivity. It is thought to be caused by the amplitude of the thermal vibrations of the lattice atoms or ions. The larger this amplitude, the greater is the probability that conduction electrons will collide with the atoms. The thermal energy stored in the vibrating lattice atom increases both its frequency and amplitude and provides a plausible explanation of the temperature dependence of the electrical resistivity as well as the Joule heating of the metal by an electric current. This model assumes that the negative conduction electrons are not attracted by the Coulomb action of the positive lattice ions. The best way of understanding this unexpected behavior of charged particles is to think of the electron as a wave of electromagnetic energy. The electric field governing the propagation of the electron wave consists of two components. One of them is the applied electric field caused by the voltage between the ends of the conductor. The other is due to the Coulomb force of the lattice ions. The latter varies with a spatial periodicity determined by the crystal structure of the conductor. It is known from X-ray transmission and diffraction studies that electromagnetic waves of certain frequencies can travel unimpeded through the periodic potential of the metal lattice. With this knowledge it seems reasonable to believe that the same is true for waves representing the electron. The propagation of the electron wave will however be impeded by any irregularity in the periodic potential of the ion lattice. All the factors contributing to the residual and ideal resistivities constitute deviations from the perfectly periodic lattice potential.

The measured ideal resistivity of most metals is in quite good agreement with the Bloch-Grueneisen equation

$$\rho_i = \frac{A}{M\Theta_D}\left(\frac{T}{\Theta_D}\right)^5 \int_0^{\Theta_D/T} \frac{z^5\,dz}{(e^z-1)(1-e^{-z})} \tag{1.13}$$

where

M = atomic weight of the lattice ion
Θ_D = Debye temperature (°K)
T = absolute temperature (°K)
A = constant
z = integration parameter

This is a semiempirical equation involving the characteristic Debye temperature, which is related to the heat content of the lattice by

$$k\Theta_D = h\upsilon_m \tag{1.14}$$

where υ_m is the maximum frequency of the thermal lattice vibrations and h is Planck's constant.

Every chemical element is associated with a characteristic Debye temperature. The magnitude of this temperature defines the highest vibration frequency the lattice atoms can assume. A large Debye temperature therefore implies a high vibration frequency and a correspondingly small amplitude for a given lattice temperature. The Debye temperature is also a measure of the lattice specific heat. Given the same temperature and abundance of conduction electrons, elements with large Debye temperatures should have low ideal resistivity. The atomic mass M helps to keep the thermal vibration amplitude small. This is the reason why it appears in the denominator of (1.13).

The Bloch-Grüneisen equation (1.13) has been evaluated in the form

$$\rho_i = \frac{A}{4M}\,\frac{T}{\Theta^2}\,G\left(\frac{\Theta}{T}\right) \tag{1.15}$$

$G(\Theta_D/T)$ is known as the Grüneisen function, and it is plotted in Fig. 1.2 and tabulated in Table 1.1. The Grüneisen function is seen to be approximately equal to unity for temperatures close to and greater than the Debye temperature. This leads to the following high-temperature approximation of

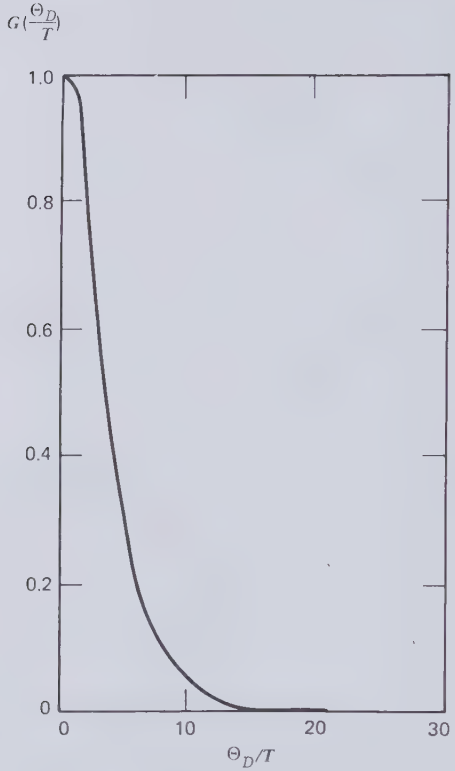

Figure 1.2 Plot of the Grüneisen function.

the Bloch-Grüneisen equation

$$\text{when } T \geqslant \Theta_D \qquad \rho_i \simeq \frac{AT}{4M\Theta_D^2} \tag{1.16}$$

which agrees with the experimentally well-confirmed proportionality of the ideal resistivity of the common conductor metals to absolute temperature. At low temperatures ($T < 0.1\Theta_D$) the Grüneisen function tends to the limit $497.6(T/\Theta_D)^4$. This can be checked with the aid of Table 1.1. Therefore the low temperature approximation of the Bloch-Grüneisen equation becomes

$$\text{when } T \leqslant 0.1\Theta \qquad \rho_i \simeq \frac{124.4AT^5}{M\Theta^6} \tag{1.17}$$

The fifth-power low-temperature law, as approximation (1.17) is sometimes

Table 1.1 The Grüneisen Function $G(\Theta/T)$, Defined by (1.15), Tabulated in Terms of Θ/T

Θ/T	$G(\Theta/T)$	ΘT	$G(\Theta/T)$	Θ/T	$G(\Theta/T)$	Θ/T	$G(\Theta/T)$
0	1.0000	4.5	0.3867	9.0	0.06740	14.0	0.01289
0.1	0.9994	4.6	0.3729	9.1	0.06490	14.2	0.012185
0.2	0.9978	4.7	0.3595	9.2	0.06250	14.4	0.011528
0.3	0.9950	4.8	0.3466	9.3	0.06021	14.6	0.010915
0.4	0.9912	4.9	0.3340	9.4	0.05800	14.8	0.010344
0.5	0.9862	5.0	0.3217	9.5	0.05589	15.0	0.0_29805
0.6	0.9803	5.1	0.3098	9.6	0.05386	15.2	0.0_29302
0.7	0.9733	5.2	0.2983	9.7	0.05192	15.4	0.0_28831
0.8	0.9653	5.3	0.2871	9.8	0.05005	15.6	0.0_28389
0.9	0.9563	5.4	0.2763	9.9	0.04826	15.8	0.0_27974
1.0	0.9465	5.5	0.2658	10.0	0.04655	16.0	0.0_27584
1.1	0.9357	5.6	0.2557	10.1	0.04490	16.2	0.0_27218
1.2	0.9241	5.7	0.2460	10.2	0.04332	16.4	0.0_26873
1.3	0.9118	5.8	0.2366	10.3	0.04181	16.6	0.0_26549
1.4	0.8986	5.9	0.2275	10.4	0.04035	16.8	0.0_26243
1.5	0.8848	6.0	0.2187	10.5	0.03896	17.0	0.0_25955
1.6	0.8704	6.1	0.2103	10.6	0.03762	17.2	0.0_25683
1.7	0.8554	6.2	0.2021	10.7	0.03633	17.7	0.0_25427
1.8	0.8398	6.3	0.1942_5	10.8	0.03509	17.6	0.0_25185
1.9	0.8238	6.4	0.1867	10.9	0.03390	17.8	0.0_24956
2.0	0.8073	6.5	0.1795	11.0	0.03276	18.0	0.0_24740
2.1	0.7905	6.6	0.1725	11.1	0.03167	19.0	0.0_23819
2.2	0.7733	6.7	0.1658	11.2	0.03061	20.0	0.0_23111
2.3	0.7559	6.8	0.1593	11.3	0.02960	22	0.0_22125
2.4	0.7383	6.9	0.1531	11.4	0.02863	24	0.0_21500
2.5	0.7205	7.0	0.1471_5	11.5	0.02769	26	0.0_21089
2.6	0.7026	7.1	0.1414	11.6	0.02680	28	0.0_38097
2.7	0.6846	7.2	0.1359	11.7	0.02593	30	0.0_36145
2.8	0.6666	7.3	0.1306	11.8	0.02510	32	0.0_34747
2.9	0.6486	7.4	0.1255_5	11.9	0.02430	34	0.0_33724
3.0	0.6307	7.5	0.1206_7	12.0	0.02353	36	0.0_32963
3.1	0.6128	7.6	0.11599	12.1	0.02279	38	0.0_32387
3.2	0.5950	7.7	0.11150	12.2	0.02208	40	0.0_31944
3.3	0.5775	7.8	0.10719	12.3	0.02139	44	0.0_31328
3.4	0.5600	7.9	0.10306	12.4	0.02073	48	0.0_49375
3.5	0.5428	8.0	0.09909	12.5	0.02009	50	0.0_47964
3.6	0.5259	8.1	0.09529	12.6	0.01948	52	0.0_46806
3.7	0.5091	8.2	0.09165	12.7	0.01889	56	0.0_45061
3.8	0.4927	8.3	0.08816	12.8	0.01832	60	0.0_43841
3.9	0.4766	8.4	0.08480	12.9	0.01777	64	0.0_42967
4.0	0.4608	8.5	0.08159	13.0	0.01725	68	0.0_42328
4.1	0.4453	8.6	0.07851	13.2	0.01624	70	0.0_42073
4.2	0.4301	8.7	0.07555	13.4	0.01531	72	0.0_41852
4.3	0.4153	8.8	0.07272	13.6	0.01445	76	0.0_41492
4.4	0.4008	8.9	0.07000	13.8	0.01364	80	0.0_41215

Source: Reprinted by permission of Plenum Press from G. T. Meaden, *Electrical Resistance of Metals*, New York, 1965.

called, has been observed to hold for a variety of metals of widely different crystal structure, among them tin, lead, and titanium. Agreement with experiment is not so good for copper and aluminum.

Of particular interest in the development of cryogenically cooled cables is the ratio of ideal resistivities at room temperature ($\rho_{i,295}$) and at low temperature ($\rho_{i,1}$). The high and low temperature approximations of the Bloch-Grüneisen equation define this ratio as

$$\frac{\rho_{i,295}}{\rho_{i,1}} = \frac{0.593\Theta^4}{T_1^5} \tag{1.18}$$

In the form of (1.18) the ideal resistivity ratio is seen to be independent of the atomic weight M and the constant A. Substituting values for the ideal room temperature resistivity from Table 1.2 into (1.18), the low-temperature ideal resistivity has been calculated for copper, aluminum, beryllium, and sodium. The results are plotted in Fig. 1.3. They clearly show the importance of the Debye temperature for cryogenically cooled conductors. A typical figure for the residual resistivity ρ_0 due to all lattice imperfections is 10^{-9} $\Omega \cdot$cm. The ideal resistivity of beryllium is reduced to this value by cooling to approximately 60°K. The same result could be obtained for sodium by cooling to 10°K. Copper and aluminum lie close together on Fig. 1.3. Their resistivity would be reduced to 10^{-9} $\Omega \cdot$cm just above 20°K. The Bloch-Grüneisen theory therefore predicts that beryllium is the best low-temperature conductor in the sense that it requires the least cooling. There is little to choose between copper and aluminum. Both approach their residual resistivities at liquid-hydrogen temperatures (15 to 25°K). However, to reduce the ideal resistivity of sodium to negligible proportions, this metal has to be cooled with helium (3 to 12°K). The only conductor material that comes close to residual resistivity at liquid-nitrogen temperatures (65 to 120°K) is beryllium.

Table 1.2 Debye Temperature, Atomic Weight, and Ideal Resistivity at Room Temperature of Conductor Metals

Metal		Debye Temp. (°K)	Atomic Weight (M)	Ideal Resistivity 295°K ($\mu\Omega \cdot$cm)
Copper	Cu	343	63.54	1.70
Aluminum	Al	428	26.98	2.74
Sodium	Na	158	22.99	4.75
Silver	Ag	225	107.87	1.61
Lead	Pb	105	195.09	21.0
Beryllium	Be	1440	9.01	3.25

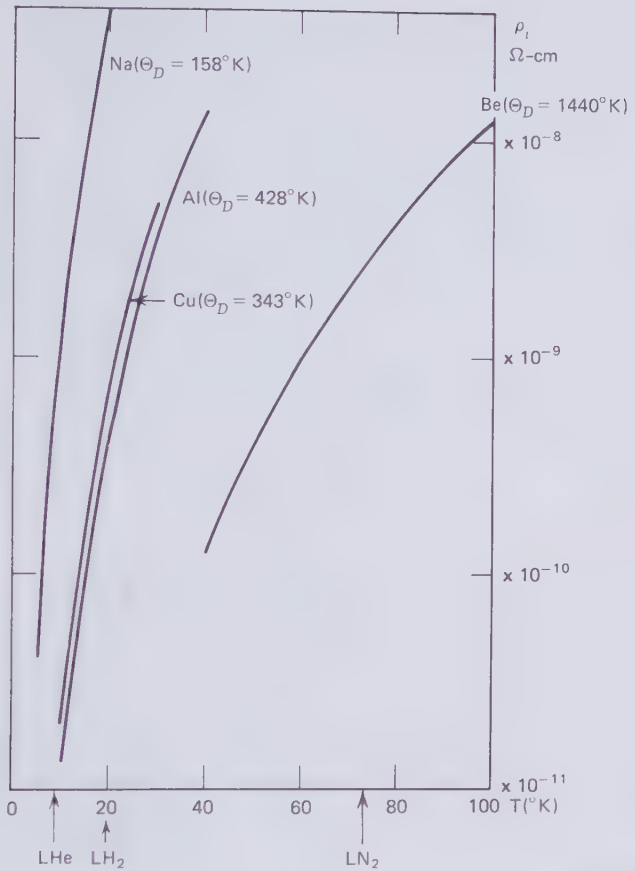

Figure 1.3 Ideal low temperature resistivity of copper, aluminum, sodium and beryllium.

1.3 SIZE EFFECT AND MAGNETORESISTANCE

At room temperature the mean free path of conduction electrons is of the order of 10^{-6} to 10^{-5} cm. Cryogenic cooling may increase it by a factor of 1000 or more. The free path then becomes comparable with the cross-sectional dimension of thin wires and tapes. Under these conditions a significant fraction of all electron collisions may occur at the conductor surface. The resistivity increase produced by electron-surface collisions is called the "size effect." In fact, measurements of this effect provide the best experimental information about the electron mean free path.

In the theory derived from the free-electron model relationships (1.3 and 1.6), the bulk resistivity of a metal specimen may be expressed by

$$\rho_b = \frac{mv}{ne^2 l} \tag{1.19}$$

This equation shows the bulk resistivity to be inversely proportional to the electron mean free path l. In a thin wire of diameter d, the size effect contribution ρ_s to the resistivity is then expected to be

$$\rho_s = \frac{mv}{ne^2 d} \tag{1.20}$$

The total resistivity may be expressed as

$$\rho = \rho_b + \rho_s = \frac{mv}{ne^2}\left(\frac{1}{l} + \frac{1}{d}\right) \tag{1.21}$$

and the ratio of total to bulk resistivity becomes

$$\frac{\rho}{\rho_b} = 1 + \frac{l}{d} \tag{1.22}$$

Equation (1.22) is not rigorously supported by experimental facts but provides a guideline. It suggests that the size effect doubles the wire resistivity when the diameter becomes comparable with the electron mean free path. It is normally assumed that the size effect is not temperature dependent and forms part of the residual resistivity. When the resistance ratio method is used to determine the purity of a specimen, it is important to choose a wire of large enough diameter so as not to obscure the electron scattering of lattice defects by surface scattering. The size effect has to be taken in consideration in the design of superconducting cables where it is proposed to stabilize superconductors by bonding them to high-purity normal conductor materials. One function of the normal backing material is to take over the load current transfer when the superconductor is accidentally driven into the normal conducting mode. The resistivity of the backing material will determine how much heat has to be absorbed by the helium coolant during the brief period of malfunction of the superconductor. In an ac cable, conductor stabilization has to meet the conflicting requirements of thin subdivided conductor filaments to keep the ac resistance low and large enough filaments to avoid size effect difficulties.

Electrons traveling in a magnetic field are acted upon by the Lorentz force in a direction perpendicular to both the velocity and the magnetic

field. This deflects electrons from a path that would otherwise be parallel to the applied electric field and results in additional electron collisions with the thermally vibrating lattice ions and all lattice imperfections, giving rise to *magnetoresistance*. Magnetic fields in electric cables are usually due to the flow of load current and possibly parallel induced currents in shields and enclosures. Therefore the magnetic field is perpendicular to the cable currents, a condition that causes *transverse* magnetoresistance. *Longitudinal* magnetoresistance could be produced by superimposing an externally generated axial magnetic field on the cable currents. For the same magnitudes of current and magnetic field, the transverse magnetoresistance is generally larger than the longitudinal magnetoresistance.

Kohler discovered that for most metals the increase in resistivity $\Delta\rho$ due to the magnetic field strength H divided by the zero-field resistivity ρ is a single-valued function of the quantity H/ρ, or

$$\frac{\Delta\rho}{\rho} = f\left(\frac{H}{\rho}\right) \tag{1.23}$$

Figure 1.4 is a reduced Kohler diagram of the transverse magnetoresistance of copper, aluminum, beryllium, and sodium. In this diagram the resistivity used in the function parameter is in fact reduced to a fraction of the resistivity at the Debye temperature. The magnetic field strength in power cables is commonly a few hundred gauss and rarely reaches 1000 G. As can be seen from Fig. 1.4, the 1 percent level of magnetoresistance ($\Delta\rho/\rho = 0.01$) is not being exceeded unless the resistivity ratio ρ_Θ/ρ_t is at least 100. This immediately suggests that magnetoresistance will only be significant at cryogenic temperatures.

Of the metals to which Fig. 1.4 refers, beryllium has the highest magnetoresistance. In a sufficiently pure beryllium specimen at liquid-nitrogen temperature, the ratio ρ_Θ/ρ_t could conceivably be as high as 1000. This would result in a magnetoresistance increment $\Delta\rho/\rho$ ranging from 10 to 100 percent, depending on the current density that is responsible for the magnetic field strength. Magnetoresistance would, therefore, be an important factor in a cryocable containing beryllium conductors. Aluminum and copper are less affected in the liquid-nitrogen temperature range. But this can change when these materials are used for thermally stabilizing superconductors. High-purity aluminum with a resistance ratio of 10,000 might have to work in a field strength of 1000 G. According to Fig. 1.4 this combination of parameters would result in a magnetoresistance increment of 100 percent, thereby eliminating some of the advantage of the high-purity material. On the basis of magnetoresistance alone, sodium would be the best backing material for superconductors. However, the data for aluminum in Fig. 1.4

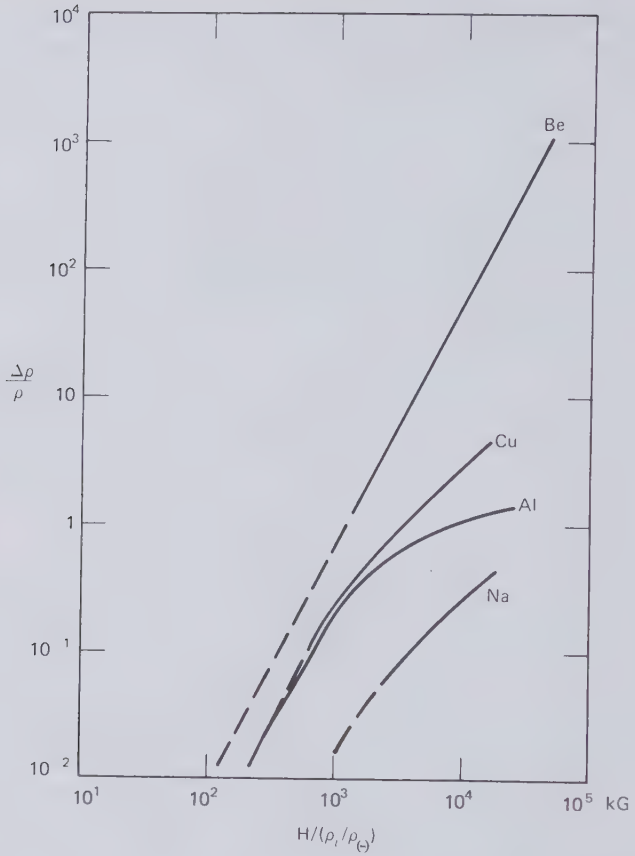

Figure 1.4 Kohler plot of transverse magnetoresistance of copper, aluminum, sodium, and beryllium.

may be too pessimistic. More recent measurements [1.1] of the magnetoresistance of this metal indicate that it does not obey Kohler's rule of a single-valued dependence on H/ρ.

1.4 ELECTRON BAND STRUCTURE AND THE FERMI SURFACE OF METALS

The wave motion of electrons through the regular crystal lattice leads to the Bragg reflection of certain frequencies that cannot partake in the conduction process. Swarms of electrons drifting through a conductor under the influence of an externally applied field will therefore be devoid of the

frequencies corresponding to the reflected waves. Taking the particle view of the electron, the same idea may be expressed by saying that the conduction electrons move in energy bands separated by forbidden energy gaps. The energy of an electron may be given, interchangeably, in terms of its velocity, frequency, or wave number (number of wavelengths in 1 cm). Quantum theory demands that within each band there exist a discrete number of energy levels or states, each capable of accepting only two electrons of opposite spin per primitive cell of the lattice. This elementary volume cell encloses a single lattice ion. The energy imparted by an external field to the electron is usually much smaller than the gap between bands. For this reason, only electrons in a partially filled band can be accelerated by the external field and contribute to charge transport. Most of the electrons of the solid will be prevented from being accelerated by the unavailability of unoccupied energy states in their reach or by the presence of forbidden energy gaps. This explains why a metal may be a poor conductor even though it has no lattice imperfections and the lattice vibration amplitude is kept small by cryogenic cooling. The high resistivity is then due to the lack of charge carriers and not the density of electron-scattering centers.

A crystalline material in which individual energy bands are either completely filled or empty is an insulator because the energy imparted by electric fields of normal strength to the electron would be insufficient to propel it across the energy gap dividing the last filled band from the first empty band. Now since the highest filled energy level in the highest filled band must contain two electrons of opposite spin, monovalent elements have to have a partially filled energy band and therefore must be conductors. This is the case with the alkali and the noble metals. Crystals with an even number of valency electrons may be insulators or conductors. To be conductors they must have two partly filled energy bands that overlap, with one of the valence electrons in each band. Examples of the latter type of conductor are the alkaline earth metals. Diamond, silicon, and germanium, on the other hand, have an even number of valence electrons and no overlapping energy bands. This makes them insulators at absolute zero temperature.

At ordinary temperatures both silicon and germanium are semiconductors because the energy gap between the uppermost filled band and the next empty band is small enough for a limited number of thermally excited electrons to be able to jump across it. These few electrons then find themselves in an unfilled band where they can respond to externally applied electric fields. Charge transport in semiconductors may be further aided by the presence of impurity atoms with energy levels in the critical band gap of the host lattice. Quite modest thermal activation may then lift some of the impurity electrons into the unfilled band of the semiconductor, further

reducing its resistivity. The electronic band structure of crystalline matter in this way explains the existence of conductors, semiconductors, and insulators.

To determine the electrical resistivity of a metal from first principles it is necessary to know, first, the electron mean free path between scattering centers, and, second, the number of electrons per unit volume that are permitted to contribute to charge transport. The latter quantity is significantly smaller than the number of valence electrons per unit volume. It is instructive to examine a little further how quantum theory deals with this aspect. The classical electron gas model that led to an equation for the electrical conductivity (1.6) was modeled on the gas laws involving equipartition of energy between all participating particles. In this classical model the distribution of particle velocities is governed by a law due to Maxwell and Boltzman, as shown in Fig. 1.5a. The area under the distribution curve is proportional to the total number of particles in the gas. It is important to note that a certain fraction of the particles have velocities that are much greater than the average near the peak of the distribution curve. An increase in gas temperature shifts the maximum in the Maxwell-Boltzman distribution to a higher velocity and generally broadens the velocity spectrum. The most relevant factor of the classical distribution law is that a change in temperature or energy will change the velocity of almost all particles.

A gas subject to quantum restrictions is called a Fermi gas, and its particle velocities will obey the Fermi-Dirac distribution law depicted in Fig. 1.5b. A feature of the Fermi gas is that all electrons have to be placed in a discrete number of energy states (velocities) with no more than two of opposite spin occupying the same level or velocity. This restriction is known as the Pauli exclusion principle. A second quantum condition to be obeyed by the Fermi gas is that at absolute zero temperature the assembly of particles settles down to the lowest possible total energy consistent with the Pauli exclusion principle. This requires the filling of all discrete energy states from zero up to a maximum level defined as the Fermi energy E_F. These two quantum restrictions result in the Fermi-Dirac distribution of an electron gas shown in Fig. 1.5b. An important new feature of this distribution is that a large fraction of the particles are associated with the highest velocities. They are said to reside in the vicinity of the Fermi level.

In heating an electron from absolute zero to room temperature it aquires kinetic energy equal to kT, which is generally small compared with E_F. Nevertheless, a small number of the electrons already residing near the Fermi level will gain sufficient velocity to be transferred from region A to region B of the distribution graph Fig. 1.5b. The area under this graph is proportional to the total number of electrons in the Fermi gas. Therefore only a fraction of the electrons equal to kT/E_F will contribute to the specific heat of the conductor. This eliminates the serious difficulty of the classical

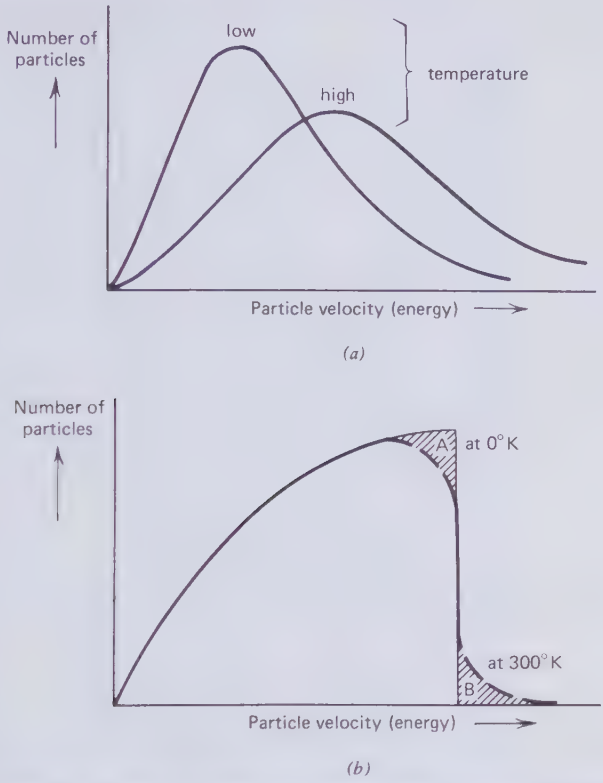

Figure 1.5 Classical and quantum mechanical velocity distribution laws. (a) Maxwell-Boltzmann distribution. (b) Fermi-Dirac distribution.

electron gas which attributed far too much heat capacity to the body of electrons.

Like an increase in temperature, the application of an external electric field will also accelerate a fraction of the electrons across the Fermi level. But unlike heat, the electric field produces a unidirectional effect, which creates a net charge transport. Here it is important to recognize that, with a Fermi-Dirac distribution, the number of electrons that will be lifted across the Fermi level by a given energy increment ΔE depends on the magnitude of E_F itself. Therefore, all other factors being equal, the metal with the largest Fermi energy should also exhibit the largest electrical conductivity. The Fermi energies of free-electron gases in various metals have been calculated and the results are presented in Fig. 1.6. From this it is clear that the Fermi level of the free-electron gas alone does not give the correct ranking of the best electrical conductors. One factor contributing to the

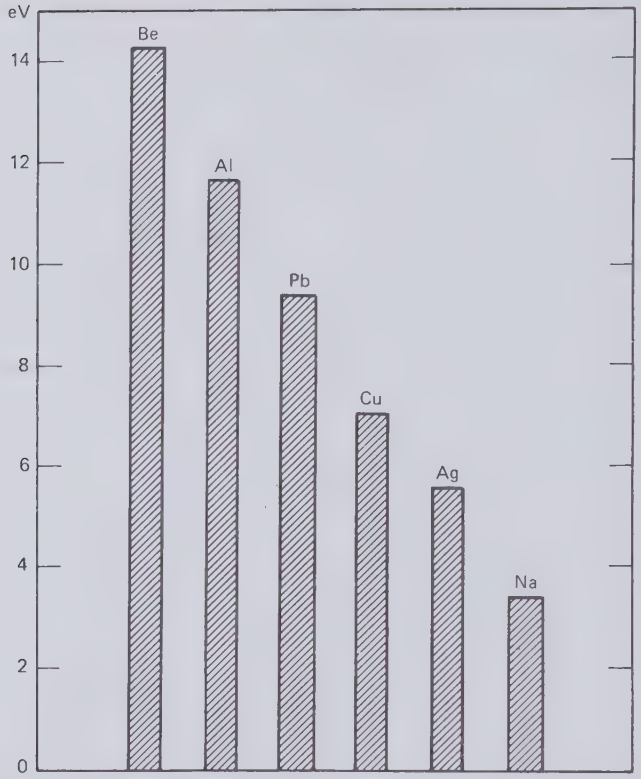

Figure 1.6 Fermi energies of the Fermi electron gas in conductor metals.

discrepancy is the presence of the periodic lattice in the conductor metals that is ignored in a free-electron gas. The effect the lattice has on electrical charge transport is best discussed with the aid of "Fermi surfaces."

The *Fermi surface* of a metal is probably one of the more difficult mathematical abstractions of modern science. Basically it represents nothing more than a diagram of the Fermi level in three dimensions. The one-dimensional counterpart is the Fermi-Dirac distribution of Fig. 1.5b. The Fermi surface separates filled from empty energy states in the vector space of electron velocity centered on an atom in the crystal lattice. For a Fermi gas of free electrons, the Fermi surface lies on a sphere having the Fermi energy E_F as radius. Each point inside the Fermi surface represents a pair of electrons with opposite spin. The periodic potential of the crystal lattice changes the shape of the otherwise spherical Fermi surface because the energy of electrostatic interaction of the traveling electron with lattice ions is greater in some directions than others. Where the Fermi surface bulges outward,

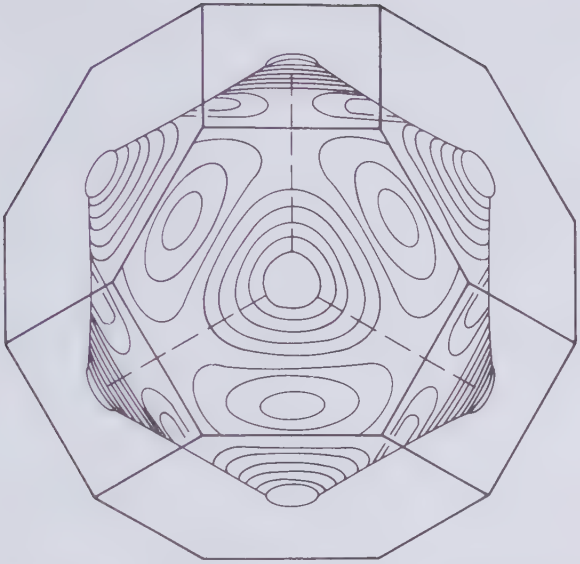

Figure 1.7 The Fermi surface of copper according to Pippard. [*Phil. Trans.* Vol. A 250, 325 (1957)].

there are more electrons available to take part in charge transport than in other areas where it may contract inward. This explains the unisotropy of electrical resistivity in single crystals. The effect is averaged out in the multicrystalline structure of practical conductors but it generally means a reduction in conductivity compared to the free-electron Fermi gas with a spherical Fermi surface. A knowledge of the topology of Fermi surfaces not only helps to recognize good electrical conductors but it provides one of the most unifying concepts of solid state physics interrelating electrical, magnetic, thermodynamic, elastic, optical, and acoustic properties of the metal.

Pippard was the first to carry out a detailed survey of a Fermi surface. He chose copper and the Fermi surface of this metal is shown in Fig. 1.7. From among the conductor metals, sodium is believed to have the most spherical Fermi surface, whereas that of higher valency conductors, such as aluminum, is extremely complicated.

1.5 TYPE I SUPERCONDUCTIVITY

After Kamerlingh-Onnes had been successful in liquifying helium in 1908, he turned his attention to the properties of materials in the new range of low

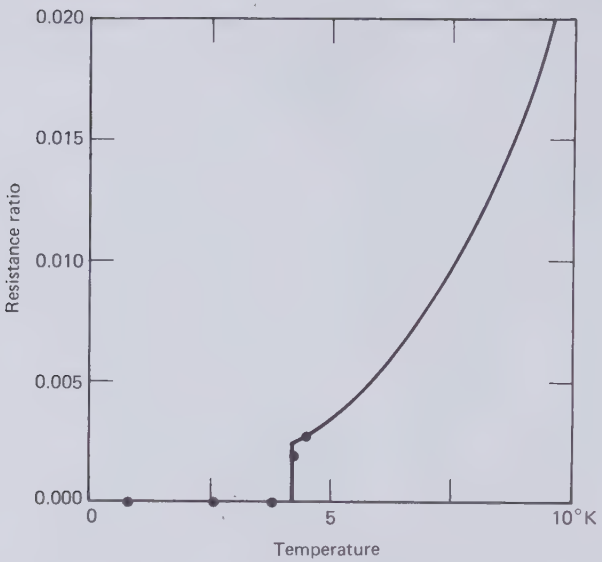

Figure 1.8 Low- to high-temperature resistance ratio of mercury according to Kamerlingh-Onnes [1.2].

temperatures that he could then reach. It was already known that the electrical resistivity of metals could be greatly reduced by cryogenic cooling. Below 10°K the resistivity of gold and platinum was found to assume a constant nonvanishing value. Kamerlingh-Onnes attributed the residual resistance to impurity atoms and hoped that he could refine mercury to so high a degree that its resistance would disappear. When he came to do the measurements, he obtained the results reproduced in Fig. 1.8. The resistivity of mercury did indeed fall to zero, but not in the anticipated manner. Instead of decreasing gradually as the temperature is lowered, it fell abruptly to zero at 4.2°K. By coincidence this critical temperature T_c was also the atmospheric boiling point of liquid helium. In the words of the discoverer: "Thus the mercury at 4.2°K has entered a new state, which owing to its particular electrical properties, can be called the state of superconductivity." This new word led to great expectations, many of which have not come true.

In his Nobel lecture in 1913 [1.2], Kamerlingh-Onnes raised the question:

> ... as to whether the absence of Joule heat makes feasible the production of strong magnetic fields using coils without iron, for a current of very great density can be sent through very fine, closely wound wire spirals?

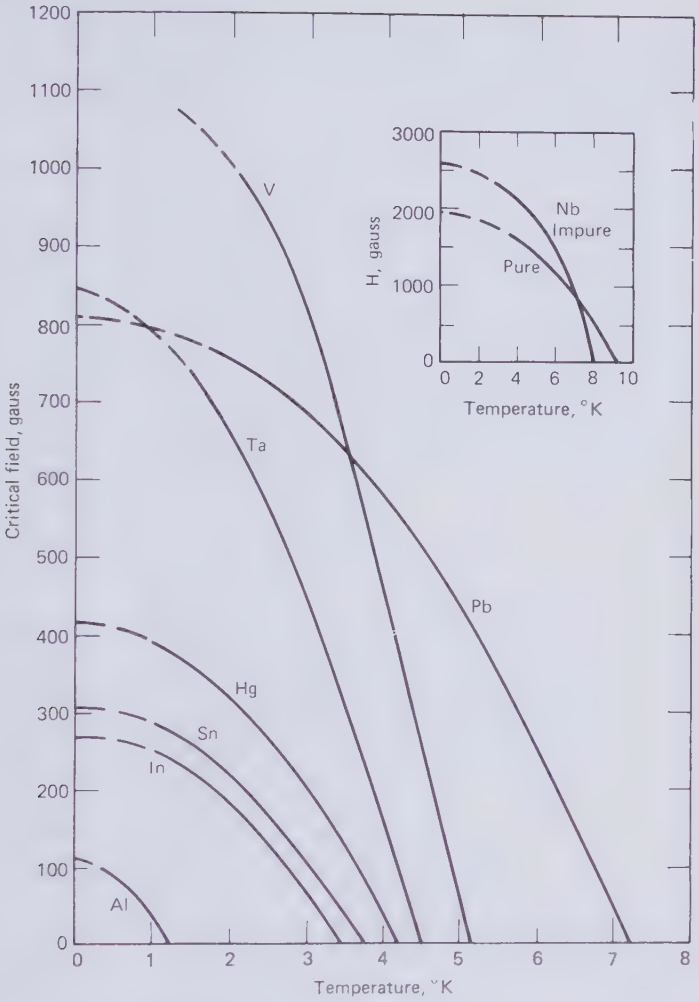

Figure 1.9 Critical field of superconductors [1.73]. (By permission of Dr. V. L. Newhouse).

By the time the lecture was printed he felt compelled to add a disappointed footnote saying:

The experiments then planned were carried out after this lecture was given and produced surprising results. In fields below a threshold value (for lead at the boiling point of helium 600 gauss), which was not reached during the experiment with the small coil mentioned in the text, there is no magnetic resistance at all. In fields above this threshold value a relatively large resistance arises at once, and grows considerably with the field.

The threshold field is now called the critical field H_c. For the best known superconducting metals, it varies with temperature as plotted in Fig. 1.9. These curves also explain why niobium is used in most technological applications of superconductivity. The only other metal that has at times been given serious consideration for superconducting power transmission lines is lead.

Concurrently with the discovery of the critical magnetic field it was also found that there exists a critical current limit beyond which the superconductor will show ohmic resistance. Silsbee [1.3] then formulated the hypothesis that the critical current is that at which the magnetic field due to the current itself is equal to the critical magnetic field. By analyzing the then available experimental data, he showed that typical superconducting elements such as mercury, tin, and lead obey the rule approximately. At any rate he deduced from measurements with various conductor cross-sectional areas that the critical magnetic field was more of a material constant than either the critical current or the critical current density. The Silsbee hypothesis tended to establish the magnetic field as the parameter controlling superconductivity. Quantum theory of superconductivity suggests that current is the controlling factor.

In the first 20 years after the discovery of superconductivity there was some doubt about how the supercurrent distributes itself over the cross section of a superconducting wire. In normal conductors this distribution is governed by Ohm's law and electromagnetic induction. The behavior of superconductors indicated that they cannot sustain internal electric fields associated with resistive voltage drop or electromagnetic induction. Therefore the laws determining the current distribution in normal conductors are inapplicable to superconductors. At the time it was believed superconductors could contain 'frozen-in' magnetic flux. Therefore it seemed possible that steady direct currents might distribute themselves uniformly over the cross section of a superconducting wire so long as H_c was not exceeded at the surface.

In 1933 Meissner and Ochsenfeld [1.4] proved conclusively by experiment that superconductors expell all magnetic flux from their interior regions, as they are cooled through the transition temperature. However shielding currents flow in a thin skin of the superconductor, which also retains some magnetic flux. As the shielding currents were induced without time variation of the external magnetic field, it seemed certain that they were of thermodynamic origin. Another way of looking at the same problem is to think of the normal-to-superconducting transition as a second-order phase transformation, not involving a heat of transformation, which changes the metal to a perfect diamagnetic material. The externally observed magnetic effects of

current loops and diamagnetism are indistinguishable. For this reason the shielding currents are sometimes called diamagnetic currents.

If wire made of superconducting material carries a normal current while it is being cooled through the critical temperature T_c, thermodynamic actions associated with the phase transformation will suddenly expell the magnetic flux due to the normal current and set up diamagnetic surface currents that cannot be distinguished from lossless transport currents. The discovery of the Meissner effect therefore provided the broad answer to the question how supercurrents are distributed over the wire section.

A quantitative treatment of the superconducting penetration depth was furnished by H. and F. London [1.5]. They in effect realized that the dc skin effect in superconductors could be handled with the same vector field equations that are being used for the ac skin effect in normal conductors. The magnetic field H inside a conductor in which displacement currents are negligible can with the aid of Maxwell's equations be expressed by

$$\nabla^2 H = \frac{1}{\lambda^2} H \tag{1.24}$$

With different materials constants λ, this holds for normal conductors placed into an ac field and superconductors in a stationary (dc) field. The solution of (1.24) obtained for normal conductors in terms of the current density j, the electric field strength in the conductor E, the magnetic vector potential A, the electrical conductivity σ, and the radian frequency of the alternating electromagnetic field ω is

$$j = \sigma E = -\sigma \frac{dA}{dt} = -\sqrt{-1}\ \sigma \omega A \tag{1.25}$$

Equation (1.25) is expressed in electromagnetic units. The corresponding London equation for superconductors then is

$$j = -\frac{1}{\lambda^2} A \tag{1.26}$$

A most useful result is obtained if (1.26) is applied to infinite half-space filled with a superconductor carrying a surface current density j_0. The current density at a depth z below the surface is then given by

$$j = j_0 e^{-z/\lambda} \tag{1.27}$$

Therefore, corresponding to the ac skin depth in normal conductors, there

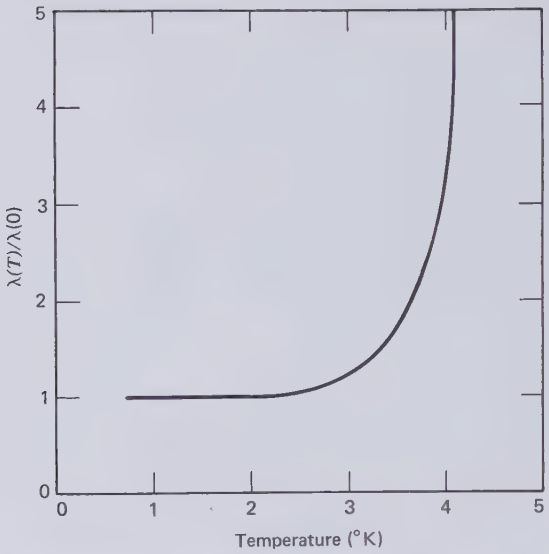

Figure 1.10 Supercurrent penetration depth in mercury according to Shoenberg [*Proc. Roy. Soc.*, A 175, 49 (1940)].

exists a dc skin depth λ in superconductors that is a function of the material and the absolute temperature. If $\lambda(0)$ is the penetration depth at absolute zero, the skin depth at temperature T is given by

$$\lambda(T)=\lambda(0)\left[1-\left(\frac{T}{T_c}\right)^4\right]^{-1/2} \tag{1.28}$$

The skin depth equation (1.28) has been derived from thermodynamic considerations of the second-order phase transformation and is in reasonable agreement with experimental results.

The exact solution of (1.26) for an infinitely long straight wire involves Bessel functions. However, when the wire radius is large compared to λ, (1.27) still represents an adequate approximation to the decay of the supercurrent density from the wire surface inward.

In summary, the phenomenological London theory provided an adequate answer to the question of how the supercurrent distributes itself over a wire section. The concept that emerged was one of a second-order phase transformation that results in perfect diamagnetism and thereby expels magnetic flux from the interior of the superconducting body. Currents and magnetic fields were allowed to coexist in a thin skin, which thereby became the least perfect part of the superconductor. Well below the critical temperature, the

penetration depth was found to be typically 1 to 5×10^{-6} cm. The penetration depth in mercury as a function of temperature is shown in Fig. 1.10. It is seen to tend to infinity as T_c is approached from below, in agreement with (1.28). Even though there exists a finite magnetic field in the skin of the superconductor, the London theory assumes the skin resistance to be identically zero.

The experimental proof of zero resistance rests on the very slow decay of persistent currents. Such currents may be induced in a superconducting ring or wire loop cooled in a magnetic field with a component that is perpendicular to the plane of the ring. If the external field is later switched off while the ring remains superconducting, the magnetic flux linking the ring is trapped by a supercurrent in the ring which continues to flow for years apparently without supply of energy. The magnitude of the persistent current can be checked from time to time by measuring the magnetic moment of the superconducting ring.

1.6 THE CAUSE OF SUPERCONDUCTIVITY

Early in the 1950s it was known that Joule heating would occur in superconductors placed in a high-frequency alternating magnetic field [1.6]. Pippard who measured this phenomenon also introduced the concept of superconducting coherence. By this he implied that the superconducting current density was not determined solely by the local magnetic vector potential according to the London (1.26), but by the average of the vector potential over a region defined by the superconducting coherence length. Another important experimental fact discovered before that time was the sharp increase in heat capacity of the superconducting body as it was cooled through the transition temperature T_c. This empirical knowledge suggested that some of the conduction electrons of the metal condensed to a superconducting phase while others remained in the normal state. This two-fluid model, as it became known, had difficulties in explaining yet another experimental discovery: the isotope effect [1.7]. This descriptive name was given to a small shift in the superconducting transition temperature in going from one isotope to another of the same element. It provided conclusive proof that not only electrons but also the ions of the metal lattice were involved in the phenomenon of superconductivity.

The condensation of a gas is coupled to the creation of forces of attraction between the particles and a corresponding binding energy. In the electron gas which is subject to the Pauli exclusion principle, it seemed natural that two electrons of opposite spin should combine so that at zero temperature they should have zero momenta of linear, angular, and spin motion. But how could two electrons of like electrostatic charge attract each other? The

answer to this question was given by Cooper, Bardeen, and Schrieffer in what is now known as the CBS theory. These physicists argued that at the very low temperatures at which superconductivity is found, the thermal lattice vibrations are so weak that an individual electron moving past an ion can, by Coulomb attraction, slightly distort the lattice by bringing the neighboring positive ions a little closer to the electron. This slight concentration of positive charge will show a small time lag due to the greater mass of the ions, and in turn it will attract a trailing electron following the leading one at a distance of 10^{-4} to 10^{-5} cm. The two electrons, separated by thousands of atoms, form a Cooper pair of a binding energy 2Δ and are communicating with each other in the coherence volume. The forces of interaction involve the lattice ions and in the language of quantum mechanics they are called virtual phonon exchanges.

Well below the transition temperature, most of the conduction electrons constituting the electron gas are paired. A small number remains unpaired and they are responsible for the ohmic resistance at high frequencies. In a steady magnetic field the current is carried entirely by Cooper pairs in the lossless mode. The fact that impurity atoms and lattice defects do not inelastically scatter Cooper electron pairs is explained by energy quantization. The binding energy of the electron pair 2Δ forms an energy gap at the Fermi surface. Unless the electron-lattice collision involves an energy greater than 2Δ the pair bond cannot be broken and no energy is exchanged with the lattice. This is equivalent to saying that no Joule heat can be generated in the metal, or in other words the resistance to current flow is zero. At some critical current density the Cooper pairs will travel with sufficient velocity for collisions with impurity atoms and lattice defects to break the pair bond and this is the cause of the destruction of superconductivity by current flow. When superconductivity is quenched by a magnetic field it is because the shielding currents exceed the critical current density at which Cooper pair bonds are broken. Therefore, unlike the Silsbee hypothesis, the CBS theory ascribes the superconducting to normal transition to electron transport rather than the magnetic field strength.

As a superconductor is allowed to warm up from absolute zero temperature, the energy gap decreases and disappears at the transition temperature. Therefore the number of electrons than can be accelerated across the gap into the normal state grows as the transition temperature is approached from below. This type of behavior accords with the high-frequency resistance measurements carried out on superconductors, of which Fig. 1.11 is typical. The CBS theory also explains the temperature dependence of the electronic specific heat near the superconducting transition temperature shown in Fig. 1.12. It is the absorption of pair binding energy on cooling through the transition temperature that accounts for the sudden jump of the specific

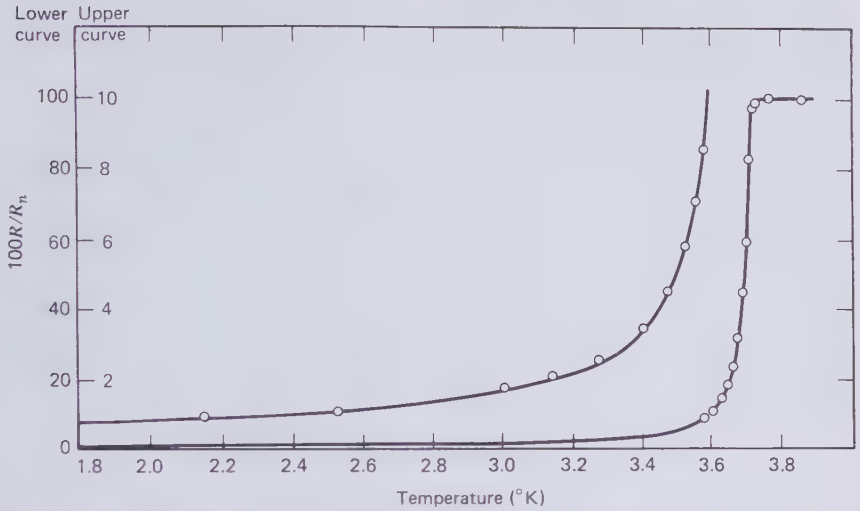

Figure 1.11 Resistivity of superconducting tin at 1200 MHz according to Pippard [1.6]. The upper curve is drawn on ten times the vertical scale of the lower curve.

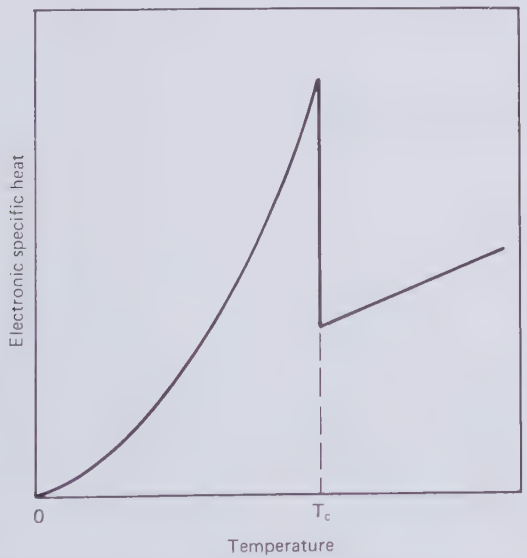

Figure 1.12 Temperature dependence of the electronic specific heat near the superconducting transition temperature.

heat. The change in binding energy (or the energy gap) is responsible for the exponential decay of the specific heat of the electrons as absolute zero temperature is approached.

This very brief nonmathematical description of the CBS theory has accounted in a qualitative way for both the zero resistance in stationary magnetic fields and finite resistance in high-frequency fields. It has explained the specific heat behavior of superconductors and the isotope effect. The CBS theory has been less successful in establishing the cause of the Meissner effect on the electron-ion level, but it is entirely consistent with the local and nonlocal London equations that describe the effect in uniform and nonuniform magnetic fields. Others have criticized the CBS theory for not giving any indication in which metals and alloys superconductivity should be found and what mechanism determines the transition temperature.

1.7 TYPE II SUPERCONDUCTIVITY

Soon after the discovery of the Meissner effect which characterizes ideal superconductors, other materials were found that apparently had zero resistance but allowed magnetic flux to penetrate deep into the metal. Even more interesting was that the final magnetic quench in these unusual materials occurred at much higher field strengths than the critical field of ideal superconductors. It lead to the revival of Kamerlingh-Onnes' dream of creating very strong magnets that did not dissipate energy. Efforts in this direction produced two successful superconducting alloys of niobium with tin and titanium that can withstand magnetic fields in excess of 100 kG. Superconductors that permit magnetic flux to penetrate through the bulk of the material have become known as type II superconductors.

They are believed to contain a mixture of normal and superconducting regions. Type I or ideal superconductors can be converted to type II by adding impurity atoms or producing lattice defects through cold working. Lattice irregularities are responsible for the hardness and brittleness of type II materials that, for this reason, are sometimes called hard superconductors. Another consequence of the lattice imperfections is the reduction of the mean free path l of normal conduction electrons. The electron mean free path, the London penetration depth λ, and the Pippard coherence length ξ are related to each other as indicated in Fig. 1.13. From this it will be seen that as l is reduced, the coherence length can be shorter than the penetration depth, which is believed to be the dividing criterion between type I and type II superconductivity. If $\xi < \lambda$, the surface energy of the superconductor in a magnetic field becomes negative. From an energy point of view, this favors the formation of many internal interfaces between normal and supercon-

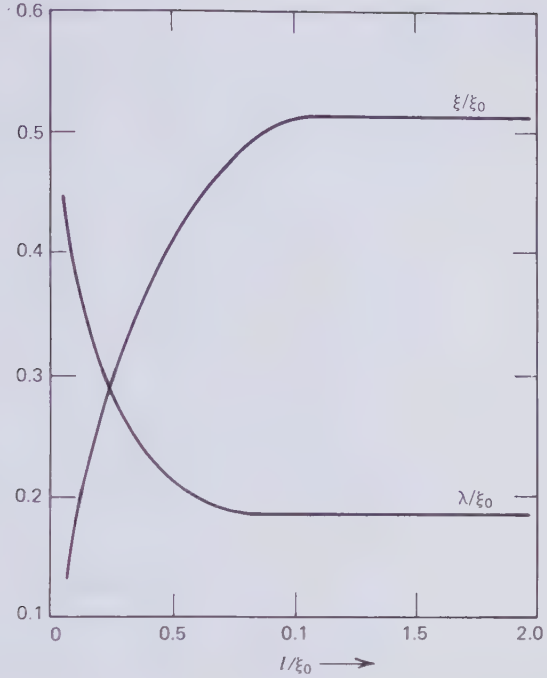

Figure 1.13 Relationship between normal electron mean free path l, London penetration depth λ and Pippard coherence length ξ [3.18]. (By permission of Wiley). Note: ξ—coherence length of impure materials; ξ_0—intrinsic coherence length of pure materials.

ducting zones. The minimum energy concept provides at least a partial explanation of the magnetic behavior of type II superconductors. The important features of this behavior are best explained with the help of the magnetization curves of Fig. 1.14. Defect-free superconducting type II alloys have a reversible magnetization curve like A. Type I behavior prevails between $H=0$ and $H=H_{c1}$ (the first critical field). Beyond H_{c1} some magnetic flux penetrates into the superconductor. At the second critical field H_{c2} the transition to the normal state takes place in the bulk of the superconductor. Cold-worked type II superconductors exhibit magnetic hysteresis in accordance with curve B. The result is the retention of some magnetic moment after the removal of the external field. In alternating fields the magnetic hysteresis of superconductors will give rise to energy losses proportional to frequency. Curve C indicates how prominent magnetic hysteresis may become in a severely cold-worked superconductor.

With the advent of research on superconducting power transmission, it became apparent that virtually all superconductors dissipate energy, while

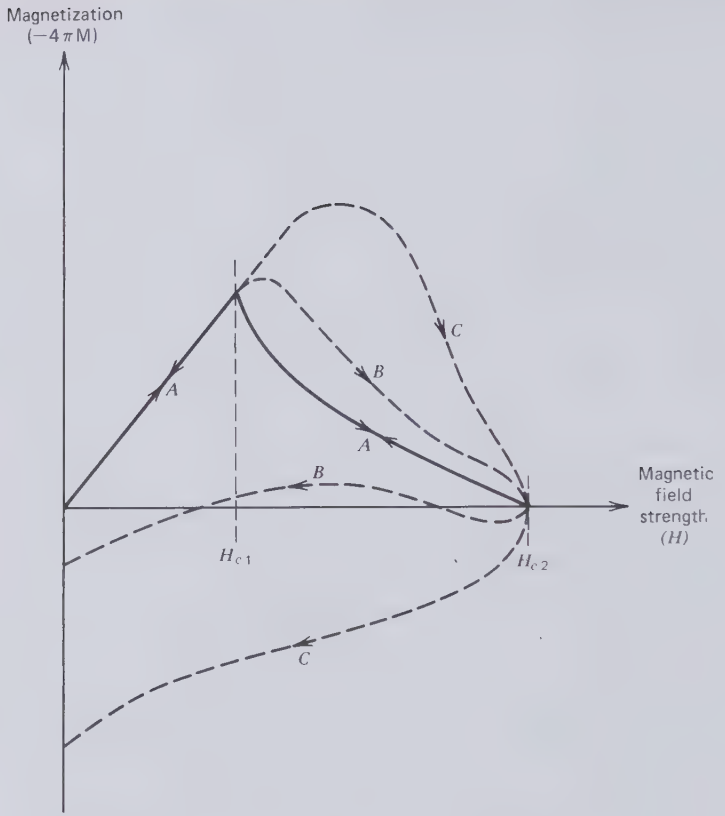

Figure 1.14 Magnetization curves of type II superconductors.

supporting 50 or 60 Hz transport currents. Near the phase transition to the normal state, this loss appears to be approximately proportional to frequency, suggesting the cause to be magnetic hysteresis. However the ac losses do not disappear completely at low-current densities when the superconductor should operate along the reversible portion of the magnetization curve. Furthermore, experiments have shown that the loss depends on the surface finish of the superconductor and not only the bulk properties. In some cases surface supercurrents have been found to exist well beyond the second critical field H_{c2}. To aid the confusion, some very careful measurements with dc transport currents by Reich and Renucci [1.9] well below the critical current have provided the results reproduced in Fig. 1.15. The material used by Reich and Renucci was ultra-pure tin obtained with 27 passes of zone refining. The implication of these careful measurements is that even type I superconductivity may not be completely lossfree and that the magnitude of the extremely small loss affects the transition temperature.

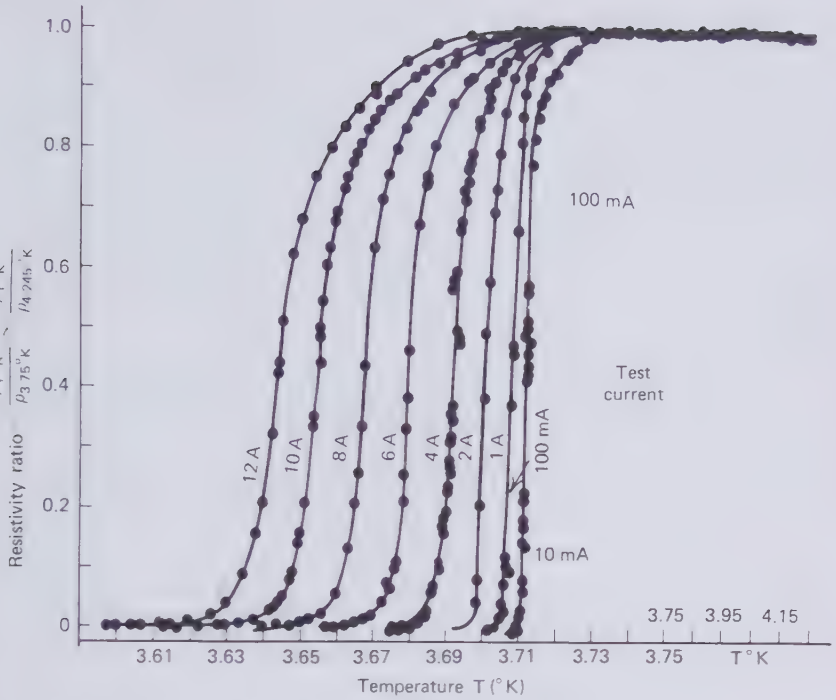

Figure 1.15 Resistance ratio of ultrapure tin according to Reich and Renucci [1.9] for wire sample currents from 10 mA to 12 A.

1.8 SKIN EFFECT

Of the whole complex of electromagnetic theory dealing with the accumulation and transport of charge in matter, that which is concerned with the metallic components in electrical cables may be termed the electrodynamics of linear conductors. No significant accumulation of charge takes place in conductors transporting power frequency currents. This topic, therefore, covers only induced effects caused by forced alternating current flow and it ignores the flow of charging current to the high-voltage insulation.

Important engineering parameters to be calculated with the aid of this branch of electromagnetic theory are the current distribution and the related ac resistance and Joule heating distribution. From the current distribution it is possible to derive the stored magnetic energy responsible for the circuit self-inductance. The current distribution further determines the electromagnetic forces acting between the metallic components of a cable. It is one of the most difficult branches of cable science. In many instances calculations have to be carried out with approximations of unknown limits of error.

Prudence dictates that, whenever possible, a few spot-check measurements should be carried out for comparison with theoretical results.

It is well known that in a conducting object placed into an alternating magnetic field, the induced currents will tend to concentrate near the surface of the conductor. This so-called skin effect is all the stronger, the higher the electrical conductivity and the energizing frequency. In linear cable conductors the current first creates the alternating magnetic field and then, in a self-consistent way, the field produces the skin effect. It has three practical consequences which, in falling order of importance, are (1) additional Joule heating, (2) a decrease in self-inductance, and (3) changes in the electromagnetic force distribution.

The uniform distribution of a given current over the cross section of a homogeneous conductor results in the lowest ohmic loss that this amount of total current may generate at a given resistivity. Any departure from uniform current distribution, as for example caused by the skin effect, will increase the loss and reduce the conductor efficiency. The loss minimum for uniform current distribution may be proved as follows: Let the cross section of a homogeneous conductor be subdivided in a number of equal material filaments, as shown in Fig. 1.16. Let the total number of equal filaments be g. Then the dc resistance of the conductor is given by the resistance of one filament R_f divided by the total number of filaments, or

$$R_{dc} = \frac{R_f}{g} \tag{1.29}$$

The instantaneous filament current i may be thought of as the sum of the

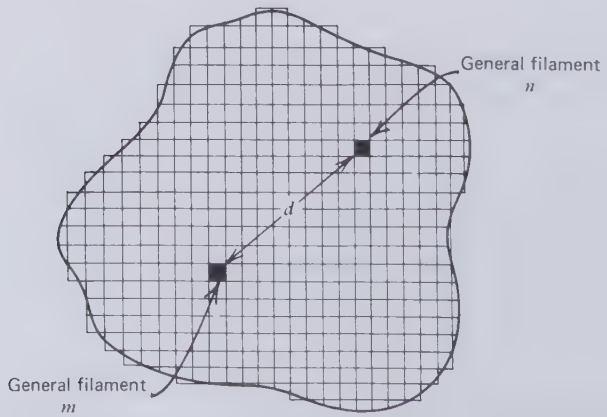

Figure 1.16 Conductor subdivision into g filaments of equal cross-sectional area and filament resistance R_f.

average filament current i_f and the deviation from this average Δi, so that

$$i = i_f + \Delta i \tag{1.30}$$

By the ac resistance of a linear conductor is meant the resistance obtained by dividing the total ohmic loss by the square of the total current, or

$$R_{ac} = \frac{\sum_g \left[R_f (i_f + \Delta i)^2 \right]}{(g i_f)^2} \tag{1.31}$$

Dividing (1.31) by (1.29) gives the ac-dc resistance ratio

$$\frac{R_{ac}}{R_{dc}} = \frac{\sum_g (i_f + \Delta i)^2}{g i_f^2}$$

$$\frac{R_{ac}}{R_{dc}} = \sum_g \frac{1}{g} + \frac{2}{(g i_f)} \sum_g \Delta i + \frac{1}{g i_f^2} \sum_g \Delta i^2 \tag{1.32}$$

We note that the first term of (1.32) is equal to one. The second term is zero because, by definition, the sum of the current deviations from the average must be zero. This leaves

$$\frac{R_{ac}}{R_{dc}} = 1 + \frac{1}{g i_f^2} \sum_g \Delta i^2 \tag{1.33}$$

Now Δi may be positive or negative, but Δi^2 is always positive. Therefore, unless Δi is zero in every filament (uniform current distribution), the ac-dc resistance ratio will be greater than one. Equation (1.33) proves that the Joule loss is a minimum for uniform current distribution.

That the skin effect also changes the self-inductance of a linear conductor is best explained by the "mean geometric distance concept" first mentioned by Maxwell [1.15]. This recognizes that the self-inductance of a homogeneous linear conductor carrying a uniformly distributed current is equal to the mutual inductance of two thin wires separated by the mean geometric distance of the conductor cross section. Neumann's formula for the mutual inductance of a pair of thin filaments m and n is

$$M_{m,n} = \int_m \int_n (\cos\theta / r)\, dm\, dn \tag{1.34}$$

where dm and dn are length elements of the two respective filaments, r is the distance between the elements, and θ is the angle of inclination between the elements. A solution of this double integral for two straight, parallel filaments of length L and spacing d was provided by Sommerfeld [1.16] in the form

$$M_{m,n} = 2\left(L \ln \frac{L + \sqrt{L^2 + d^2}}{d} - \sqrt{L^2 + d^2} + d\right) \tag{1.35}$$

When $L \gg d$, (1.35) simplifies to the approximation

$$\frac{M_{m,n}}{2L} \simeq -1 + \ln 2L - \ln d$$

or

$$M_{m,n}/L \simeq \ln \frac{2L}{ed} \tag{1.36}$$

where e is the base of natural logarithms. With d being the independent variable, the mutual inductance between a pair of straight and parallel filaments therefore varies as the logarithm of the distance of separation. If a cable conductor is subdivided in filaments, as in Fig. 1.16, its self-inductance is equal to the mutual inductance of a pair of filaments separated by a distance d' such that $\ln d'$ is the average of $\ln d$ for all possible filament pairs in the conductor. For g filaments there will be $g/2$ pairs, and the average of the logarithms may be written

$$\frac{2}{g} \sum_{g/2} \ln d = \ln d' \tag{1.37}$$

This is the definition of the mean geometric distance d' of the conductor area.

The following analysis provides a formal proof of Maxwell's theorem connecting the self-inductance of a conductor with the mutual inductance between a pair of filaments. It is a curious fact that to obtain this proof it has to be assumed that the infinitely thin filament does not interact with itself, but only with its neighbors [1.17].

If an electromotive force E drives a current i along a linear conductor of self-inductance L and resistance R, then these quantities obey the equation

$$iR = E - \frac{d(Li)}{dt} \tag{1.38}$$

Let us now look at two general filaments m and n of the conductor cross section (Fig. 1.16). They are imagined to be as thin as the atomic constitution of matter permits. The current i_m flowing in the filament m, the resistance of which is R_m, can be calculated from

$$i_m R_m = E - \frac{d}{dt} \sum_n M_{m,n} i_n \tag{1.39}$$

where i_n is the current in the general filament n, $M_{m,n}$ the mutual inductance between the two filaments and the solution covers all possible positions n in the conductor cross-section. Bearing in mind that

$$\frac{1}{R} = \sum_m \frac{1}{R_m} = \sum_n \frac{1}{R_n} \tag{1.40}$$

$$i = \sum_m i_m = \sum_n i_n \tag{1.41}$$

(1.39) can be solved for i_m, and summing for all filament currents in accordance with (1.41) gives

$$i = E \sum_m \frac{1}{R_m} - \frac{d}{dt} \left(\sum_m \frac{1}{R_m} \sum_n M_{m,n} i_n \right) \tag{1.42}$$

Substituting (1.40) into the first term of (1.42) and multiplying throughout by R results in

$$iR = E - \frac{d}{dt} \left(\sum_m \frac{R}{R_m} \sum_n M_{m,n} i_n \right) \tag{1.43}$$

A comparison of (1.38) with (1.43) defines the self-inductance as

$$L = \sum_m \frac{R}{R_m} \sum_n M_{m,n} \frac{i_n}{i} \tag{1.44}$$

So far it has not been necessary to restrict the analysis with respect to conductor homogeneity and current distribution. Provided the current and conductivity distributions are known, (1.44) may be applied to composite conductors consisting, for example, of layers of different materials.

The expression for the self-inductance can be simplified when all filaments have the same resistance and carry the same current (uniform current

distribution) so that for a total of g filaments

$$\frac{1}{g} = \frac{R}{R_m} = \frac{R}{R_n} = \frac{i_m}{i} = \frac{i_n}{i} \tag{1.45}$$

With (1.45) the self-inductance formula (1.44) reduces to

$$L = \frac{1}{g^2} \sum_m \sum_n M_{m,n} \tag{1.46}$$

In this form L is seen to be the mean of all possible mutual inductance combinations in agreement with the method of mean geometric distances exemplified by (1.36) and (1.37).

The mutual electromagnetic force $F_{m,n}$ acting between a pair of current carrying filaments is

$$F_{m,n} = i_m i_n \frac{dM_{m,n}}{dz} \tag{1.47}$$

with dz being a displacement between the filaments. As the skin effect is changing the current distribution, and therefore the relative values of i_m and i_n, it is clear that this also brings about changes in the force distribution.

Rayleigh [1.10] laid the foundation to a skin and proximity effect theory that is still widely used. Significant extensions and contributions to this theory were made by Butterworth [1.11], Cockroft [1.12], Dwight [1.13] and Arnold [1.14], to mention but the most fruitful researches. All these authors found solutions to differential equations that arose from the application of Maxwell's equations to metallic conductors. These equations can be solved for straight conductors of circular cross section. For noncircular conductors the analytical approach has to be abandoned in favor of numerical finite element techniques, which are all based on Neumann's formula (1.34) for mutual inductance.

For the analysis of the skin effect in round wires and rods consider a long straight conductor of circular cross section and radius a. Let E be the electric field, $B = \mu H$ the magnetic field, i the current density, which is related to the electrical conductivity σ by Ohm's law

$$i = \sigma E \tag{1.48}$$

In the asbsence of displacement currents, Maxwell's equations for the conductor reduce to

$$\text{curl } E = -\frac{dB}{dt} \tag{1.49}$$

$$\text{curl } H = i \tag{1.50}$$

With ac exitation $f=\omega/2\pi$, the field equations combine in the cylindrical coordinate system of the conductor to the "diffusion equation"

$$\frac{\partial^2 i}{\partial r^2}+\frac{1}{r}\frac{\partial i}{\partial r}+k^2 i=0 \tag{1.51}$$

where r is the radial distance from the z axis of the conductor and the constant k (wave number) is given in various forms by

$$k=\sqrt{-j\sigma\mu\omega}=(j-1)\sqrt{\frac{\sigma\mu\omega}{2}}=\frac{j-1}{\delta} \tag{1.52}$$

where $j=\sqrt{-1}$ and δ is the skin depth to be defined later. The diffusion equation (1.51) is the zero-order Bessel equation having the known solution [1.18]

$$\frac{i}{i_0}=\frac{J_0(kr)}{J_0(ka)} \tag{1.53}$$

with $J_0(x)$ being the available tabulated Bessel function of the first kind and zero order. The current density at the conductor surface is i_0.

According to Smythe [1.18], the corresponding Bessel function solution for tubes of outer radius a and inner radius b is

$$\frac{i}{i_0}=CJ_0(kr)+DK_0(kr) \tag{1.54}$$

$K_0(x)$ is the modified Bessel function of zero order and the constants C and D are

$$C=\frac{K_1(kb)}{J_0(ka)K_1(kb)+J_1(kb)K_0(ka)}$$

$$D=\frac{J_1(kb)}{J_0(ka)K_1(kb)+J_1(kb)K_0(ka)}$$

Equations (1.53) and (1.54) make it possible to compute the Joule heating rate per unit length of conductor with unit current flowing through it. The calculations are very tedious and the results have, therefore, been published in tables and graphs. For this purpose it has been found convenient to give the ac-dc resistance ratio as a function of

$$\sqrt{\frac{f}{R_{dc}}}=a\sqrt{\frac{\sigma\omega}{2}}=\frac{ka}{\sqrt{2}} \qquad \mu=1$$

This quantity is proportional to the skin depth parameter δ.

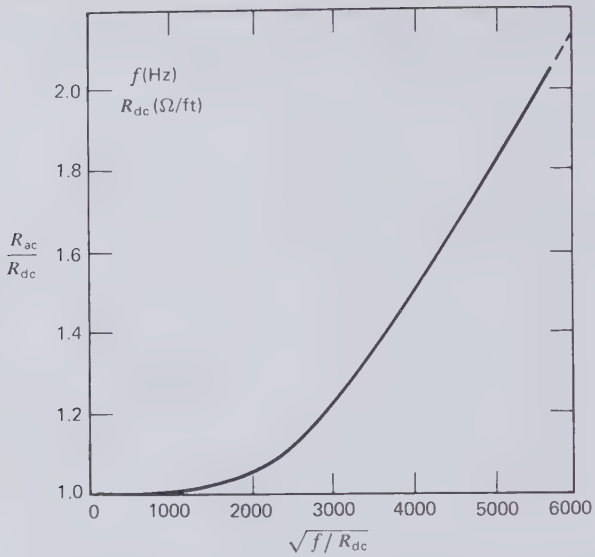

Figure 1.17 Skin effect in round rods [1.13, 1.19].

The ac-dc resistance ratio of round wires and rods due to the skin effect may be taken directly from Fig. 1.17, which has been plotted using tabulated data given by Neher and McGrath [1.19]. For the same purpose Goldenberg [1.20] derived three approximations that lie within 1 percent of the exact solution of the Bessel equation. For

$$x = 8.75 \times 10^{-4} \sqrt{f/R_{dc}} \qquad \text{(c.g.s. units)}$$

they are

$$0 < x \leqslant 2.8 \qquad \frac{R_{ac}}{R_{dc}} \simeq \frac{192 + 1.8x^4}{192 + 0.8x^4} \tag{1.55}$$

$$2.8 < x \leqslant 3.8 \qquad \frac{R_{ac}}{R_{dc}} \simeq 0.864 - 0.0177x + 0.0563x^2 \tag{1.56}$$

$$x > 3.8 \qquad \frac{R_{ac}}{R_{dc}} \simeq 0.267 + 0.354x \tag{1.57}$$

The ac-dc resistance ratio of round tubes has been calculated by Dwight [1.21] according to (1.54). His results are plotted in Fig. 1.18 for a variety of values of the ratio of wall thickness to overall diameter.

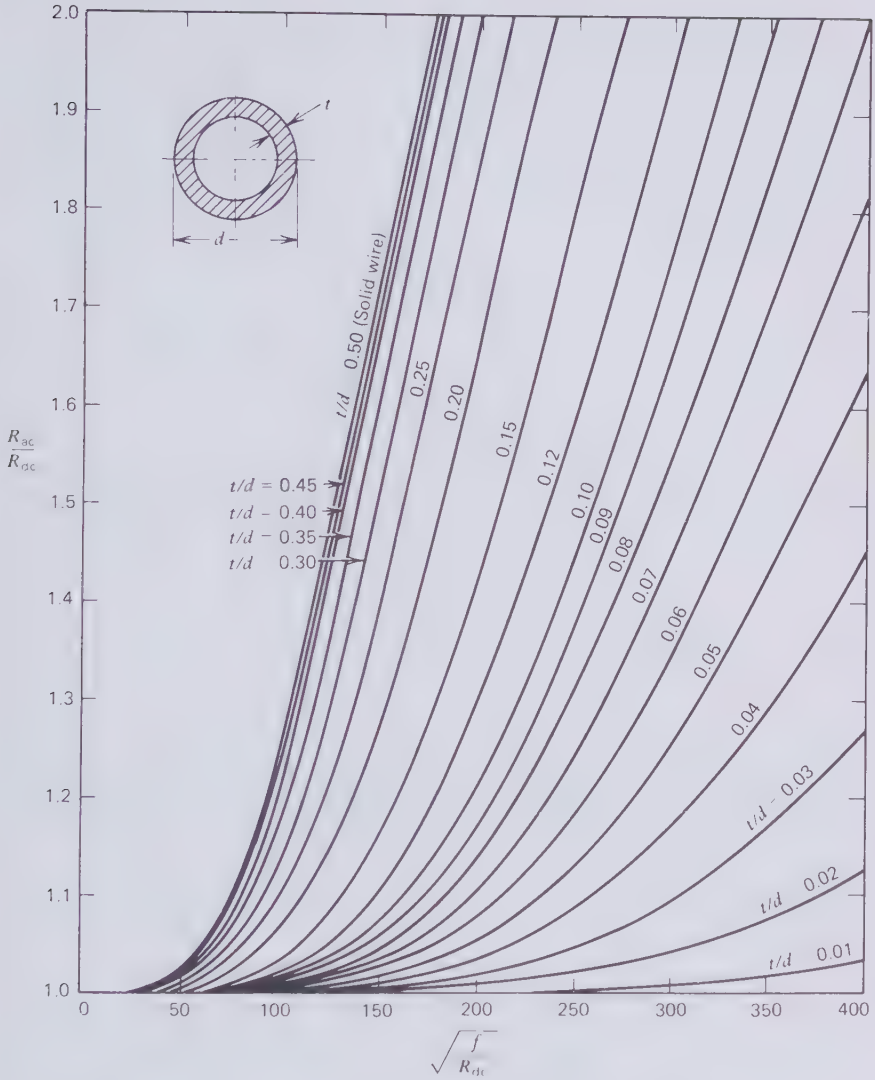

Figure 1.18 Skin effect in round tubes [1.21]. f (Hz); R_{dc} (Ω/1000 ft).

At high conductivities or high frequencies the skin effect may be so pronounced that the current flowing in the core of the conductor is almost zero. We may then speak of a skin or penetration depth. To analyze this case we have to consider a flat conductor filling infinite half-space with the current flowing parallel to the surface. In a Cartesian coordinate system in which z is the depth below the surface, the diffusion equation corresponding to (1.51) becomes

$$\frac{\partial^2 i}{\partial z^2} + k^2 i = 0 \tag{1.58}$$

The solution of (1.58) is

$$i = i_0 e^{j(kz \pm \omega t)} \tag{1.59}$$

where i_0 is the surface current density and t is the time. Substituting for the wave number k from (1.52), the current density distribution becomes

$$i = i_0 e^{-z/\delta} e^{j(z/\delta \pm \omega t)} \tag{1.60}$$

In the resolved phasor notation this is equivalent to

$$i = i_0 e^{-z/\delta} \cos(z/\delta \pm \omega t) \tag{1.61}$$

The last equation shows that the current density decreases exponentially with depth z below the surface and the phase angle also changes with z. At a depth δ the current density amplitude reaches the value i_0/e, as shown in Fig. 1.19.

The ohmic heating rate is proportional to the integral of the square of the current density, given by

$$\begin{aligned} \int_0^\infty i^2 \, dz &= i_0^2 \int_0^\infty e^{-2z/\delta} \cos^2(z/\delta \pm \omega t) \, dz \\ &= i_0^2 \int_0^\infty e^{-2z/\delta} 0.5 \left[1 + \cos 2(z/\delta \pm \omega t) \right] dz \end{aligned} \tag{1.62}$$

The cosine part of this integral vanishes because of the zero time-average, so that

$$\int_0^\infty i^2 \, dz = \left(\frac{i_0}{2} \right)^2 \delta \tag{1.63}$$

An examination of Fig. 1.19 and (1.63) reveals that the ohmic heating rate may also be calculated by assuming that the current density is constant

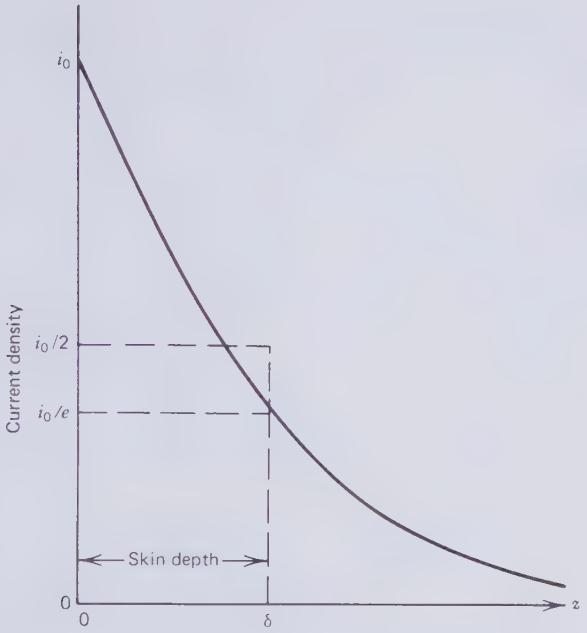

Figure 1.19 Current density decrease below conductor surface.

at $i_0/2$ to a depth δ below the surface and then falls abruptly to zero.

Equation (1.52) presents the skin depth in terms of the electrical conductivity σ, the magnetic permeability μ, and the radian frequency ω as

$$\delta = \sqrt{\frac{2}{\sigma\mu\omega}} \tag{1.64}$$

In Fig. 1.20 the skin depth parameter δ has been plotted as a function of resistivity $(1/\sigma)$ from 0–5 $\mu\Omega \cdot$cm for the two common power frequencies of 50 and 60 Hz. It will be seen that at liquid-nitrogen temperatures (80°K) the skin depth of both copper and aluminum is approximately 0.3 cm, whereas at room temperature it is of the order of 1 cm. Sodium at 85°C and 50 Hz has a skin depth of 1.8 cm. In general the skin depth of common conductor materials and sizes is not very small compared with the major cross-sectional conductor dimension. Therefore ac resistance calculations with (1.64) will only give qualitative guidance. Figure 1.20 further illustrates that the higher power frequency in the *United States* represents a not insignificant penalty as far as conductor losses are concerned.

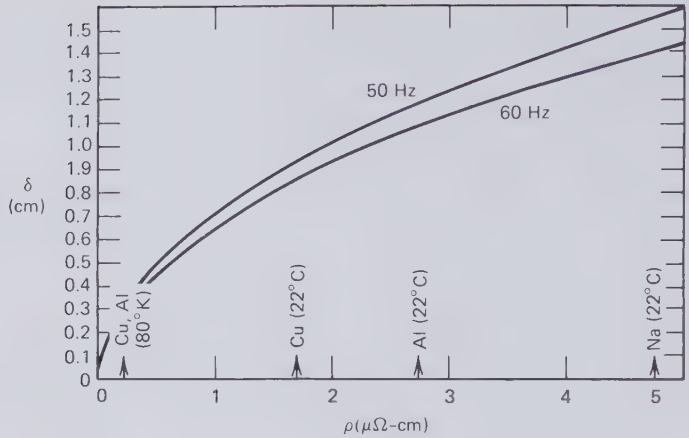

Figure 1.20 Skin depth as a function of resistivity at power frequencies.

1.9 FINITE-ELEMENT METHOD FOR NONCIRCULAR CONDUCTORS

No analytical techniques are available for calculating the current distribution in square, rectangular, and sector-shaped conductors. The computation can, however, be accomplished by dividing the conductors in a finite number of material filaments and then applying Neumann's mutual inductance formula to filament pairs. The finer the subdivision, the greater will be the accuracy with which the current distribution can be determined. On the other hand, the amount of computation increases steeply with the number of filaments. Not until high-speed computers became available did it seem feasible to marshal the arithmetical operations of the solution process. Soon after the advent of giant calculating machines Silvester [1.22, 1.23], Graneau [1.24, 1.25] and others developed the finite-element method.

Although the technique may be used on nonhomogeneous conductors that are not straight, we start by considering the more ideal case shown in Fig. 1.16 in which a straight conductor of uniform electrical conductivity has been subdivided in g equal filaments each having a resistance R_f. In the general case every filament will carry a different current. Let the currents in two general filaments labeled m and n be i_m and i_n, respectively. The mutual inductance $M_{m,n}$ may be computed with the help of Neumann's formula (1.34). Its solution for straight parallel filaments is (1.35). When the filaments are very much longer than their distance of separation, the approximation (1.36) will be found useful. Now the instantaneous potential difference between the end faces of the conductor, and hence the extremes of each conductor filament, is denoted by e. In the filament m, the driving electromotive force e_m is opposed by a back electromotive force $e_{b,m}$ due to

the mutual coupling to all other filaments and also the self-coupling to filament m. The difference between the two electromotive forces, or voltages, drives the current i_m through the resistance R_f

$$e_m = i_m R_f + e_{b,m} \tag{1.65}$$

The problem facing us is to find the back e.m.f. which, in turn, depends on all the other filament currents that are also governed by an equation like (1.65). If we denote the self-inductance of filament m by L_m, the set of simultaneous equations corresponding to (1.65) will be structured as

$$\begin{aligned}
e_1 &= \left[R_f i_1 + L_1 i_1'\right] + M_{2,1} i_2' + M_{3,1} i_3' + \cdots + M_{g,1} i_g' \\
e_2 &= M_{1,2} i_1' + \left[R_f i_2 + L_2 i_2'\right] + M_{3,2} i_3' + \cdots + M_{g,2} i_g' \\
e_3 &= M_{1;3} i_1' + M_{2,3} i_2' + \left[R_f i_3 + L_3 i_3'\right] + \cdots + M_{g,3} i_g' \\
&\vdots \\
e_g &= M_{1,g} i_1' + M_{2,g} i_2' + M_{3,g} i_3' + \cdots + \left[R_f i_g + L_g i_g'\right]
\end{aligned} \tag{1.66}$$

In (1.66) i_m' stands for the time derivative of i_m.

We immediately consider the most important practical case in which the driving voltage, and therefore all the currents, are sinusoidal of radian frequency ω, so that

$$M_{m,n} i_n' = j\omega M_{m,n} = Z_{m,n} i_n \tag{1.67}$$

$$R_f i_m + L_m i_m' = (R_f + j\omega L_m) i_m = Z_{m,m} i_m \tag{1.68}$$

where $Z_{m,n}$, and $Z_{m,m}$ are now mutual and self-impedances, respectively, replacing the back electromotive forces of (1.65).

With the impedance notation, the array of simultaneous equations (1.66) may be abbreviated in matrix form.

$$\{e\} = [Z]\{i\} \tag{1.69}$$

where $\{e\}$ and $\{i\}$ are column vectors. The impedance matrix is square, symmetrical, and of order g.

$$[Z] = \begin{bmatrix}
Z_{1,1} Z_{1,2} Z_{1,3} \cdots Z_{1,g} \\
Z_{2,1} Z_{2,2} Z_{2,3} \cdots Z_{2,g} \\
Z_{3,1} Z_{3,2} Z_{3,3} \cdots Z_{3,g} \\
\vdots \\
Z_{g,1} Z_{g,2} Z_{g,3} \cdots Z_{g,g}
\end{bmatrix} \tag{1.70}$$

The solution of (1.69) is

$$\{i\} = [Z]^{-1}\{e\} \tag{1.71}$$

It requires the inversion of the impedance matrix (1.70), which is a tedious undertaking involving the determinant $|Z|$ of the impedance matrix. In full the solution (1.71) may be written

$$\begin{Bmatrix} i_1 \\ i_2 \\ i_3 \\ \vdots \\ i_g \end{Bmatrix} = \frac{1}{|Z|} \begin{bmatrix} |Z_{1,1}||Z_{1,2}||Z_{1,3}|\cdots|Z_{1,g}| \\ |Z_{2,1}||Z_{2,2}||Z_{2,3}|\cdots|Z_{2,g}| \\ |Z_{3,1}||Z_{3,2}||Z_{3,3}|\cdots|Z_{3,g}| \\ \vdots \\ |Z_{g,1}||Z_{g,2}||Z_{g,3}|\cdots|Z_{g,g}| \end{bmatrix} \begin{Bmatrix} e_1 \\ e_2 \\ e_3 \\ \vdots \\ e_g \end{Bmatrix} \tag{1.72}$$

Silvester [26] has shown that the computational work can be reduced by employing the modal network theory for solving (1.69). The impedance matrix is square and symmetrical. Therefore it possesses a set of orthogonal eigenvectors which may be written

$$[I] = \begin{bmatrix} I_{1,1} I_{1,2} \ldots I_{1,g} \\ I_{2,1} I_{2,2} \ldots I_{2,g} \\ \vdots \\ I_{g,1} I_{g,2} \ldots I_{g,g} \end{bmatrix} \tag{1.73}$$

Each element of the eigenvector matrix stands for a current component. If $[I]$ is normalized (multiplied by a constant) in such a way that the sum of all elements is equal to the total conductor current, it turns out that the column sums of (1.73) are the mode currents flowing through the conductor of Fig. 1.16 as a whole. Each mode current oscillates at a different frequency. In dynamical systems the mode frequencies would be resonance frequencies. The sum of all the mode currents makes up the total conductor current that oscillates at frequency ω. The mode currents are of no practical interest for power transmission. However, the row sums of (1.73) represent all the mode currents flowing in the individual filaments. Each row is associated with only one filament and the row sum of (1.73) gives the total current at frequency ω flowing in that filament. This is the result required for the determination of the current distribution. It is obtained in four steps:

1. Set up the mutual and self-inductance matrix (1.70).

2. Replace the symbols by their numerical values that depend on R_f, L_m, $M_{m,n}$ and $j\omega$.
3. Derive the eigenvector matrix with the help of available computer algorithms.
4. Form the row sums of the eigenvector matrix which are the required filament currents.

It is not necessary to be familiar with matrix algebra to determine the current distribution in noncircular conductors. Those interested in this branch of mathematics will have no difficulty in finding a number of suitable books. Hlawiczka [1.27] wrote one that deals specifically with the application of matrix algebra to electrical circuits. It gives a full account of the eigenvalue problem and eigenvalue methods of solution. The elements of the mutual impedance matrix and the eigenvector matrix involve the complex operator $j = \sqrt{-1}$. Therefore each filament current will have its own particular phase angle with respect to the driving voltage. The phase relationships are illustrated in Fig. 1.21. It is the vector sum of all the filament currents that makes up the total conductor current I when expressed as an rms amplitude. This total current lags the driving voltage E by the phase angle ϕ. Normally it will not be known what the driving voltage is in a power transmission line. This adjusts itself in accordance with the load and line impedances. Fortunately, it is sufficient to know the value of I that will be driven through the line to compute the ac resistance of the conductor. The method is illustrated in (1.29) to (1.33). These equations are valid not only for instantaneous currents but also for rms amplitudes of sinusoidal currents. In the latter case we have to define the average rms filament current by

$$I_f = \frac{I}{g} \tag{1.74}$$

and the actual filament currents by

$$I_m = I_f + \Delta I_m \tag{1.75}$$

Remembering also that the ac resistance R_{ac} is the total Joule loss divided by the square of the total rms conductor current, we may write

$$I^2 R_{ac} = \sum_{m=1}^{g} (I_f + \Delta I_m)^2 R_f \tag{1.76}$$

The algebraic steps involved in going from (1.29) to (1.33) will transform

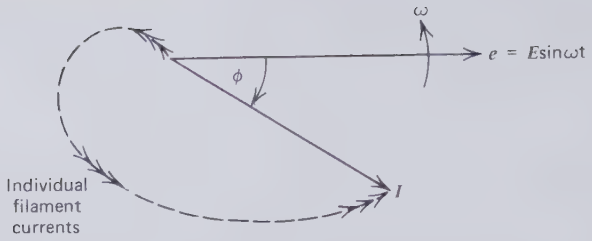

Figure 1.21 Phasor diagram of filament currents.

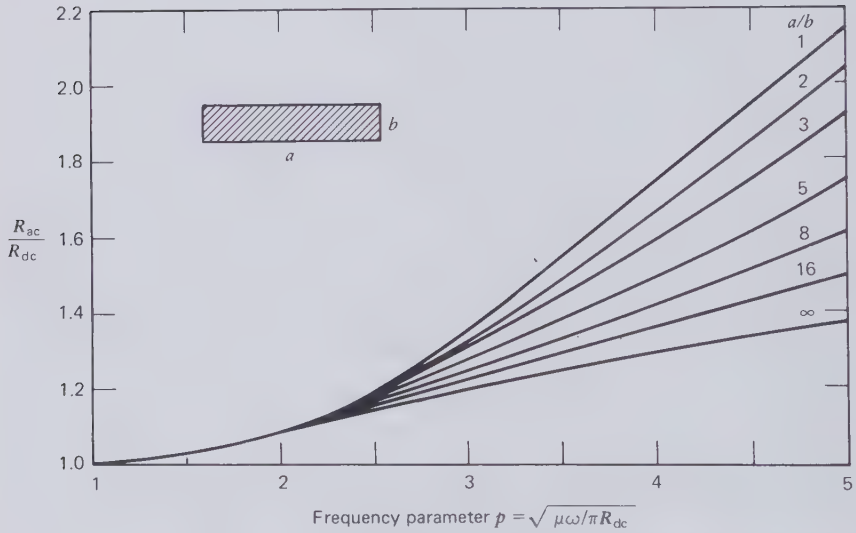

Figure 1.22 AC-DC resistance ratio of isolated rectangular conductors according to Silvester [1.22]. (By permission of Institute of Electrical and Electronics Engineers).

(1.76) to

$$\frac{R_{ac}}{R_{dc}} = 1 + \left(1/gI_f^2\right) \sum_{m=1}^{g} \Delta I_m^2 \tag{1.77}$$

This gives the ac resistance of the conductor in terms of known quantities. Furthermore, by referring to the phasor diagram of Fig. 1.21, it will be recognized that the conductor inductance is given by

$$\frac{\omega L}{R_{ac}} = \tan\phi \tag{1.78}$$

The finite element method, therefore, not only gives the current distribution

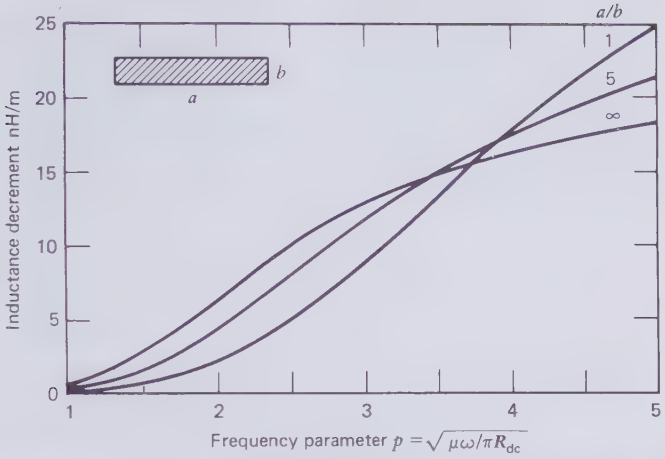

Figure 1.23 Decrease in self-inductance of isolated rectangular conductors due to skin effect according to Silvester [1.22]. (By permission of Institute of Electrical and Electronics Engineers).

and ac resistance, but also the inductance for computing voltage drops and reactive power requirements.

Silvester [1.22] has used this method to compute the ac resistance and inductance decrement of isolated rectangular conductors. Side ratios of the rectangles ranged from 1 to ∞. His results are reproduced in Figs. 1.22 and 1.23 in terms of the generalized frequency parameter

$$p = \sqrt{\frac{\mu\omega}{\pi R_{dc}}} \tag{1.79}$$

up to $p = 5$.

1.10 PROXIMITY EFFECT IN GO-AND-RETURN CIRCUIT

The ac current distribution over the cross section of a conductor depends not only on the magnetic self-field but also the field generated by currents in adjacent conductors. The additional field component of neighboring currents in most cases increases the ac resistance. One exception to this rule is a pair of flat strips. If they are brought close together facing each other, the current distribution becomes more uniform and the ac resistance is decreased. The change in ac resistance due to currents in other conductors is called the "proximity effect". We take account of this effect with a multiplication factor P that has to be applied to the ac resistance of the isolated conductor.

Consider the case of a single-phase circuit consisting of parallel and straight go-and-return conductors. Each of the identical conductors has a radius a and the center lines of them are separated by a distance s. The current distribution in the pair of conductors will be governed by a partial differential equation of the form of (1.51). Its solution involves Bessel functions and in particular the ratio

$$\frac{J_{n+1}(ka\sqrt{j})}{J_{n-1}(ka\sqrt{j})} = \phi_n + j\psi_n \tag{1.80}$$

where k is given by (1.52). $J_n(x)$ is the Bessel function of the first kind of order n and having the argument x and the operator $j = \sqrt{-1}$. Arnold [1.28] has shown that the solution for the ac/dc resistance ratio in the presence of the proximity effect may be written

$$R_{ac}/R_{dc} = f_0(x) + \sum_{n=1}^{\infty} \left(\frac{2a}{s}\right)^{2n} f_n(x) \tag{1.81}$$

where

$$f_0(x) = 1 + \left(\tfrac{1}{8}\right)x^2\psi_2$$

$$f_1(x) = \left(\tfrac{1}{8}\right)x^2\psi_1$$

$$f_2(x) = \left(\tfrac{1}{64}\right)x^2(\psi_2 + 4\phi_1\psi_1)$$

$$f_3(x) = \left(\tfrac{1}{384}\right)x^2(\psi_3 + 6\phi_1\psi_2 + 9\phi_1^2\psi_1 - 3\psi_1^3 + 6\phi_2\psi_1)$$

etc.

The series in (1.81) is converging very slowly. Arnold transformed it to give the proximity factor as

$$P = \frac{R_{ac}/R_{dc}}{f_0(x)} = 1 + \sum_{n=1}^{\infty} \left(\frac{2a}{s}\right)^{2n} \left[\frac{f_n(x)}{f_0(x)}\right] \tag{1.82}$$

It should be noted that $f_0(x)$ is the ac/dc resistance ratio of the isolated conductor. An evaluation of (1.82) gives the results plotted on Fig. 1.24, which were published by Dwight [1.29]. From this it is seen that the proximity effect falls off rapidly as the conductors are separated.

Dwight [1.29] also presented curves of the proximity effect for parallel tubular conductors with a wall thickness equal to $\frac{1}{8}$th of the tube outside diameter. They are reproduced in Fig. 1.25.

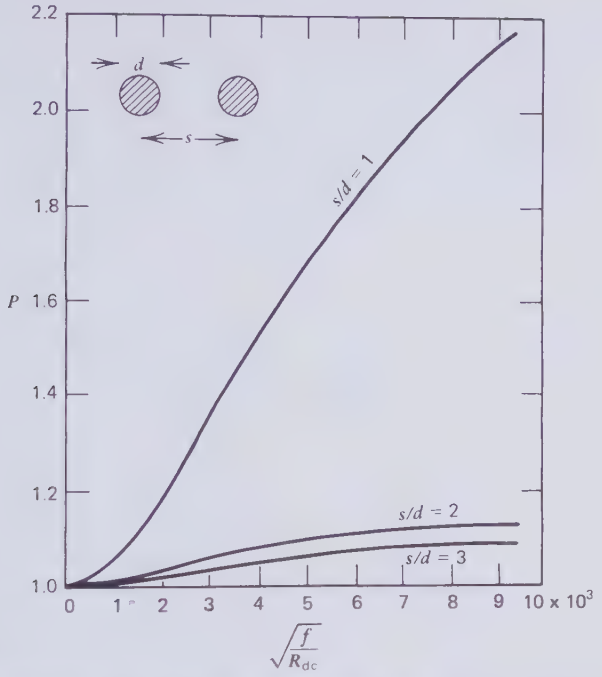

Figure 1.24 Proximity effect of solid round conductors [1.29]. R_{dc} (Ω/ft); f (Hz). (By permission of McGraw-Hill).

For noncircular conductors it is necessary to use the finite-element method for determining not only the skin effect but also the proximity effect. To accomplish this the impedance matrix for the combination of both conductors has to be set up. Considering the matrix (1.72) it will be recognized that the driving voltages e for the filaments of one conductor are all positive and for the other negative. As a result of this the eigenvector matrix, (1.73) will contain positive and negative current components and the algebraic sum of the rows will again give the individual filament currents. Having determined the current distribution, (1.77) may be used to compute the ac/dc resistance ratio, which takes account of skin and proximity effects.

In closing this section it should be stressed that the proximity of a return-conductor does not always increase the ac resistance of the go-conductor. One well-known exception occurs when two flat conductor strips face each other broad side on. When they are widely separated, the proximity effect will indeed increase the ac resistance. However, as they come close together this trend reverses and the ac resistance actually decreases as the distance of separation is further reduced. This flat strip behavior was

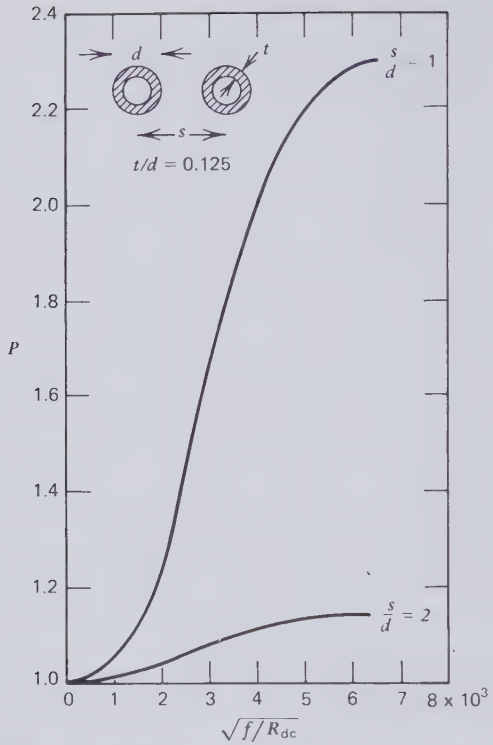

Figure 1.25 Proximity effect of tubular round conductors [1.29]. R_{dc} (Ω/ft); f (Hz). (By permission of McGraw-Hill).

discovered more than 60 years ago by Kennelly et al. [1.41], who pointed out that the magnetic field distribution in and around the closely spaced flat strip conductors becomes more uniform as they are brought in contact with each other with a layer of insulation between them. This is never the case with the round conductors normally employed in high-voltage cables. Knowing the behavior of flat strips, it cannot be taken for granted that sector-shaped conductors will show the same proximity effect behavior as round conductors.

1.11 THE MUTUAL INDUCTANCE BETWEEN PARALLEL LINEAR CONDUCTORS

To determine the interaction of current-carrying linear conductors with metallic pipes and sheaths situated in the magnetic field of the current, it becomes necessary to choose a formula for the mutual inductance acting

between parallel straight conductors of finite length. That there should be a choice of fundamentally different formulas immediately points to a dilemma that has not been resolved by controlled experiments.

The classical concept of mutual inductance between two closed curves was first suggested by F. E. Neumann [1.30, 1.31] in 1845 before the publication of Maxwell's field theory. It is embodied in Neumann's well known law

$$M_{m,n} = \int_m \int_n \frac{\cos\theta}{r}\, dm\, dn$$

which was first mentioned in connection with skin effect calculations (1.34). The symbols m and n stand for two closed curves, with dm being a short element of m and dn a short element of n. The distance between these two elements is denoted by r, and θ is the angle of inclination between the elements.

Neumann's formula may be applied to two rectangular loops $ABCD$ and $EFGH$ lying in perpendicular planes, as shown in Fig. 1.26. In this arrangement the loops are closed by DC and GH located infinitely far away from the closely spaced lines AB and EF of finite length L. For line elements dm and dn on AB and EF, the integrand of Neumann's formula has a finite magnitude. However, the integrand vanishes for line element combinations of any other pair of sides for the reasons listed in Table 1.3. This proves that in this case the mutual inductance acting between parallel straight lines may be calculated by Neumann's formula without regard to the return circuits. As mentioned previously, the difficult integration of Neumann's formula for the particular case of two parallel straight lines was carried out by Sommerfeld [1.16] with the aid of a diagram like Fig. 1.27. Applied to a pair of

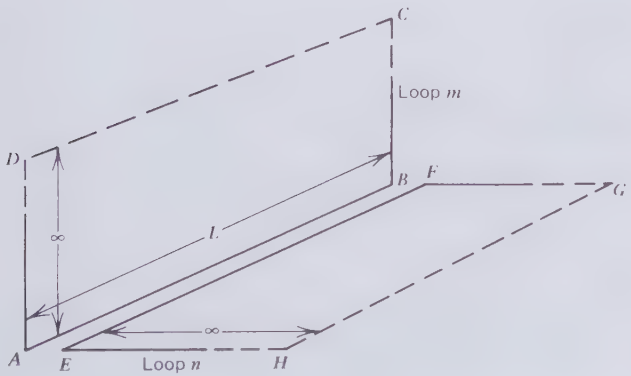

Figure 1.26 Rectangular current loops in perpendicular planes.

Table 1.3 Magnitude of Integrand in Neumann's Formula When This is Applied to the Loops of Fig. 1.26.

Elements of Side Pair	$1/r$	$\cos\theta$	$\cos\theta/r$
AB-EF	finite	finite	finite
AB-FG	finite	0	0
AB-GH	0	finite	0
AB-HE	finite	0	0
BC-EF	finite	0	0
BC-FG	finite	0	0
BC-GH	0	0	0
BC-HE	finite	0	0
CD-EF	0	finite	0
CD-FG	0	0	0
CD-GH	0	finite	0
CD-HE	0	0	0
DA-EF	finite	0	0
DA-FG	finite	0	0
DA-GH	0	0	0
DA-HE	finite	0	0

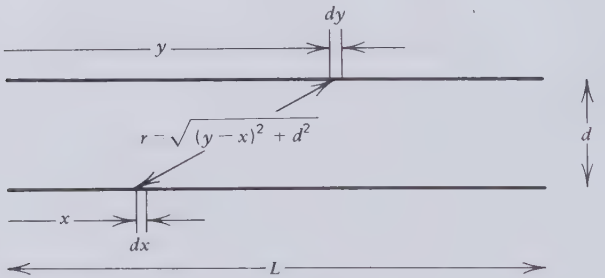

Figure 1.27 Diagram to aid the integration of Neumann's formula.

straight and parallel wires, Neumann's formula reduces to

$$M_{x,y} = \int_0^L \int_0^L \frac{dx\,dy}{\sqrt{(y-x)^2 + d^2}} \quad dx\,dy \tag{1.83}$$

Sommerfeld's solution of this double integration is (1.35). This is an exact expression of the mutual inductance of a pair of parallel straight lines separated by a distance d and of length L. According to this solution, the mutual inductance is not proportional to length.

When L is very much greater than d, (1.35) reduces to the approximation

$$M_{x,y} \simeq 2L\left(-1+\ln\frac{2L}{d}\right) \tag{1.84}$$

Practical conductors are not thin lines but metallic objects having a finite cross-sectional area A. To deal with this situation Maxwell [1.15] developed the geometric mean distance (GMD) method. This will now be explained with the help of Fig. 1.28, which shows two conductor cross sections A_1 and A_2 with the centers of area separated by distance d. Each conductor area is subdivided by a graticule to outline, say, g_1 filaments of conductor material in A_1 and g_2 filaments in A_2. The subdivision must be fine enough to ensure that the side of a square filament is very small compared to d. The mutual inductance of a pair of filaments, such as m and n, may then be equated to that of a pair of lines running along the axes of the two filaments. Maxwell then made the assumption that the mutual inductance between conductors A_1 and A_2 is the mean of all filament mutual inductances $M_{m,n}$. There exist a total of $g_1 \times g_2$ filament pairs with one filament in each conductor and the average mutual inductance is given by

$$M_{A1,A2} = \frac{1}{g_1 g_2} \sum_{A_1} \sum_{A_2} M_{m,n} \tag{1.85}$$

The GMD between A_1 and A_2, $d'_{m,n}$, is now defined as the distance that makes $\ln d'_{m,n}$ equal to the average value of $\ln d_{m,n}$. From this definition and (1.84) it follows that

$$M_{A1,A2} = 2L\left(-1+\ln\frac{2L}{d'_{m,n}}\right) \tag{1.86}$$

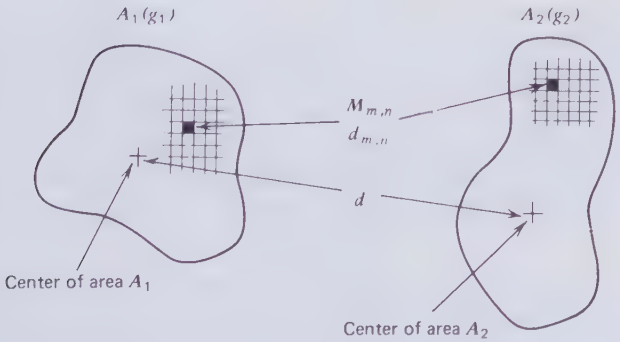

Figure 1.28 Geometric mean distance computation.

In general it will be found that the GMD is smaller than the distance between the centers of area. In some cases it will be equal to that distance.

The important practical conductor arrangements for which sheath voltages, currents, and losses have to be computed are shown in Fig. 1.29. According to Maxwell [1.15], the GMD of any plane area from a ring bounded by two concentric circles of outer and inner radii r_0 and r_i is equal to its GMD from the center of the ring, if it lies entirely outside the ring; but if it lies entirely within the ring the GMD is given by

$$\ln d' = \frac{r_0^2 \ln r_0 - r_i^2 \ln r_i}{r_0^2 - r_i^2} - \frac{1}{2} \tag{1.87}$$

The GMD d' of this last equation is independent of the shape of the enclosed figure and also the position of its center. It therefore applies to the conductor arrangements (a) and (b) of Fig. 1.29.

When the conductor is located outside the tube or ring (Fig. 1.29c), we have to find the GMD of a circular conductor area from a point at a distance d from the center of the area. This requires another of Maxwell's results, which states that the GMD of a point from a circular line is equal to the distance between the point and the center of the circle. Now the circular area may be divided into a series of thin concentric rings. The GMD between the point and every ring is equal to the point to center spacing d and therefore the GMD between a circular conductor and a pipe (Fig. 1.29c) is also equal to d. The same argument applies to the two parallel tubes of Fig. 1.29d.

It should be noted that on the basis of Neumann's law, mutual inductance is a property of lines, and in emu it has the dimension of length. To convert to practical units of inductance, it is necessary to use the identity

$$1 \text{ Henry} = 10^{-7} \text{ meter} \tag{1.88}$$

Although the mutual inductance formulas based on Neumann's law and Maxwell's geometric mean distance are listed in handbooks, for example Ref. [1.32], they do not seem to have found their way into the cable literature. Standard cable reference works [1.19, 1.33, 1.34] quote the following formula for the mutual inductance between a tubular sheath and a conductor located outside the tube (Fig. 1.29c):

$$M = 2L \ln \frac{d}{r_s} \cdot 10^{-7} \text{ Henry} \tag{1.89}$$

where L is the length in meters, d the axial spacing, and r_s the mean sheath

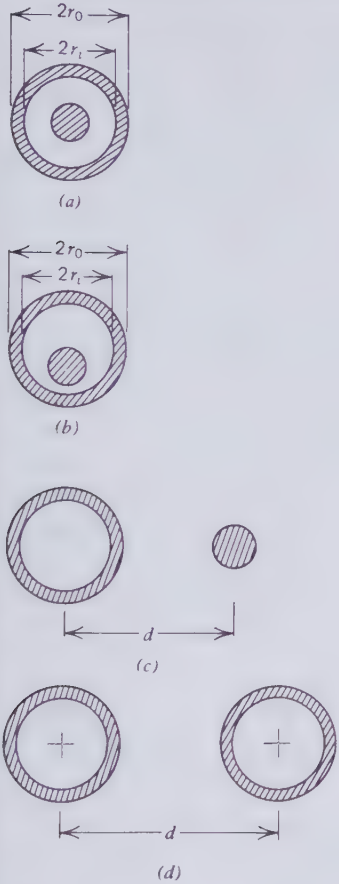

Figure 1.29 GMD of parallel conductors. (a) Concentric conductors, *GMD* given by (1.87). (b) Eccentric conductor in tube, *GMD* given by (1.87). (c) Conductor outside tube, $GMD = d$. (d) Parallel tubes, $GMD = d$.

radius. This formula predicts very different numerical results for long conductors than (1.86) and it does not show the logarithmic length dependence. For example for a 1000-m-long line with $d = 20$ cm, $r_0 = 5$ cm, $r_t = 4$ cm we find

from (1.86)	$M = 1.64$ mH	$(d' = d)$
from (1.89)	$M = 0.31$ mH	

The two formulas are in better agreement for short samples that can be laid out in a laboratory, which may have hidden the discrepancy. It turns out that (1.89) is identical to the formula for the self-inductance of a loop of two parallel straight wires of long length joined at the ends, except that the wire

radius is substituted for the mean sheath radius. No argument appears to have been put forward that would indicate the equality of the two quantities when the wire radius is equal to the mean sheath radius.

There exist two ways of defining mutual inductance. One is based on Neumann's law and the other on the flux linkage $\Phi_{m,n}$ between two closed circuits m and n. The flux linkage definition may be expressed as

$$M_{m,n} = \frac{\Phi_{m,n}}{i_m} \tag{1.90}$$

where i_m is the current flowing in circuit m. Figure 1.30 is a field plot for the conductor and sheath arrangement. The flux that links both conductors is approximately

$$\Phi_{m,n} = L \int_d^\infty \frac{2i_m}{r}\, dr$$

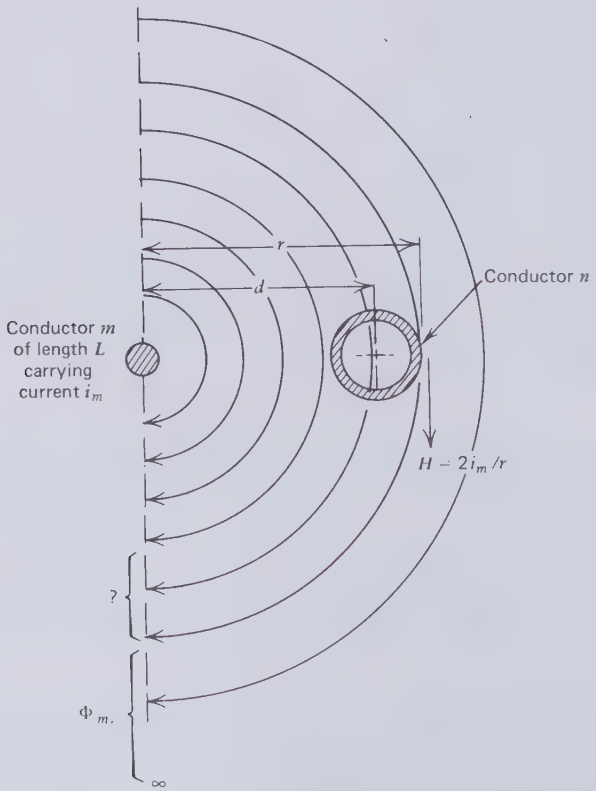

Figure 1.30 Magnetic flux linkage between a straight conductor and a parallel pipe.

With (1.90) this leads to

$$M_{m,n} = 2L(\ln \infty - \ln d)$$

a result that shows that (1.89) is not derived from the flux linkage definition of mutual inductance.

Two further points should be mentioned, which throw doubt on sheath loss computations with (1.89). First, it seems to be common practice to ignore the voltage induced in the sheath by the enclosed conductor current, which would require a formula for the coaxial conductor geometry (Fig. 1.29a). Second, (1.89) finds little use in the calculation of enclosure losses in isolated phase bus installations [1.35, 1.36, 1.37].

For these various reasons, the mutual inductance formulas based on Neumann's law and Maxwell's GMD will be employed in the following section. That Neumann's formula is compatible with the electromagnetic field and flux linkage concepts may be proved as follows. Consider an infinitely long straight wire m, carrying a current i_m, and a line n running parallel to m, as indicated in Fig. 1.31. Anywhere along n the magnetic vector potential is parallel to the line. The vector potential between the ends of the short line element dn and due to the current in the line element dm is $(i_m/r)dn$, where r is the distance between the two line elements. Now the

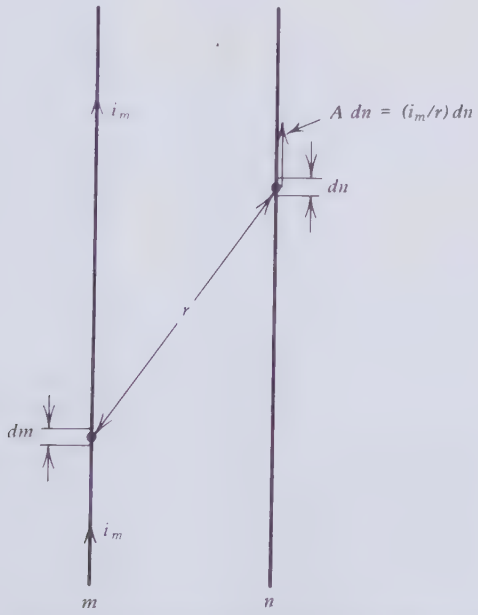

Figure 1.31 Magnetic vector potential A along a line parallel to a current i_m.

vector potential integrated over the total length of n and for all current elements $i_m\,dm$ is

$$\int_m\int_n A\,dn\,dm = i_m\int_m\int_n \frac{1}{r}\,dn\,dm \tag{1.91}$$

The double integral on the right-hand side of (1.91) is Neumann's mutual inductance for parallel straight lines.

1.12 SINGLE CONDUCTOR IN A METALLIC PIPE AND CROSSBONDING

Most high-voltage cable insulations, except polyethylene and similar plastic materials, require a moisture barrier in the form of a metallic pipe, tube, or sheath. Lead or aluminum sheaths are commonly used for single-conductor cables. These pipes are situated in the magnetic field of the conductor currents and therefore will experience induced voltages that may, and normally do, give rise to the flow of induced currents accompanied by Joule losses. If the pipe is made of magnetic steel, then it will also be subject to magnetization and hysteresis loss. In the strong field of a single core cable the hysteresis loss is unacceptably large. However steel pipes are employed to enclose three-phase circuits.

Before examining the more complex case of three-phase circuits, it will be found a helpful introduction to study a single conductor located in a metal tube as shown in Fig. 1.32. In this example it is assumed that the conductor current i_c is returned to the generator by a second conductor so far removed from the metal tube that its magnetic field may be ignored.

The current flowing in the central conductor will induce a longitudinal emf e_p in the pipe wall. The magnitude of e_p is a maximum on the inside surface and a minimum on the outside surface of the wall. The difference between the maximum and minimum emf's will drive a current down the inner portion of the pipe wall and up in the outer parts of it (Fig. 1.32). The energy loss associated with this current is customarily described as an eddy current loss.

Another more serious pipe loss may arise from circulating currents through a ground loop. Such loops exist if the pipe is grounded at more than one point along its length. Normally the cable sheath is grounded at both terminations, which would be equivalent to closing switches A and B in Fig. 1.32. The average induced emf e_p then drives a circulating current i_p along the pipe, which is returned through the ground circuit. In general the circulating currents are much larger than the eddy currents. It should be

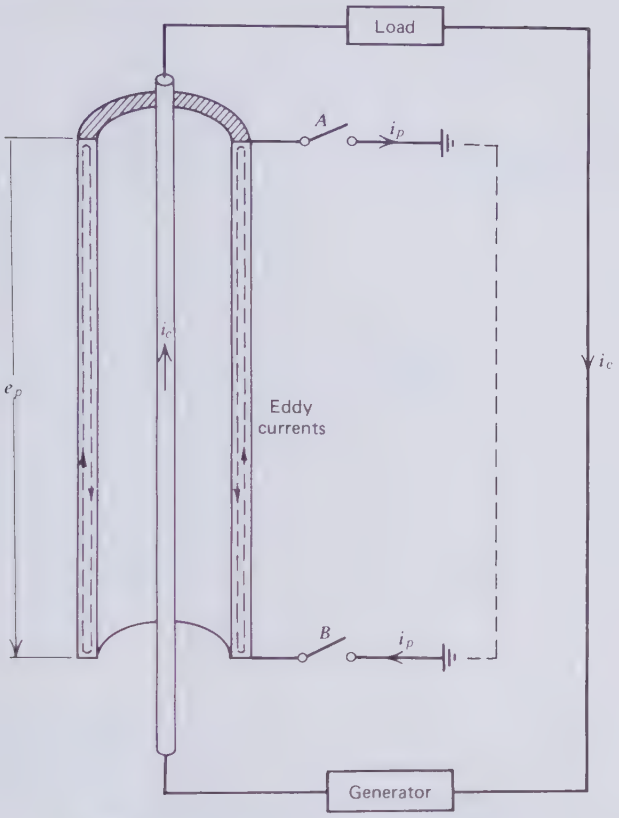

Figure 1.32 Single conductor in a metallic pipe.

noted that the addition of a third and more grounding points between the cable terminations will not vary the magnitude of the circulating current in the pipe wall so long as the metal enclosure is of uniform conductance.

For an accurate determination of the induced current losses, the finite element method should be used, because the current distributions in the conductor and in the pipe wall will in most practical cases be nonuniform. It should further be understood that the tube currents will modify the current distribution in the central conductor and thereby change the skin-effect resistance. The pipe currents tend to concentrate on the inside of the wall.

An approximate estimate of the induced circulating current loss may be made for the idealized case of uniform current distribution over both the conductor and pipe cross sections. The longitudinally induced emf in the

pipe is given by

$$e_p = -M_{c,p}\frac{di_c}{dt} \tag{1.92}$$

$M_{c,p}$ is the mutual inductance between the conductor and the pipe. The GMD of this arrangement is given by (1.87), which for thin wall tubes reduces to

$$d'_{c,p} \simeq \frac{r_o + r_i}{2} \tag{1.93}$$

Approximation (1.93) will underestimate the GMD by less than 2 percent provided $r_i > 2$ and $r_i/r_o > 0.5$. Substituting (1.93) into (1.86) gives the required mutual inductance.

$$M_{c,p}/2L = -1 + \ln 2L - \ln\frac{r_o + r_i}{2} \tag{1.94}$$

To determine i_p, the circulating current that will be driven along the pipe, we have to calculate the pipe impedance

$$|Z_p| = \sqrt{R_p^2 + (\omega L_p)^2} \tag{1.95}$$

where R_p is the dc resistance and L_p is the self-inductance of the pipe. On the assumption of uniform current distribution, L_p is equal to the mutual inductance of a pair of filaments separated by the GMD d'_p of the pipe cross section. This also has been computed by Maxwell [1.15]

$$\ln d'_p = \ln r_o - \frac{r_i^4}{(r_o^2 - r_i^2)^2}\ln\frac{r_o}{r_i} + \frac{3r_o^2 - r_i^2}{4(r_o^2 - r_i^2)} \tag{1.96}$$

Dwight [1.13, p. 134] evaluated (1.96) as a function of r_i/r_o, the ratio of inside to outside radius of the pipe. Figure 1.33 presents his results in graphic form. The appropriate value of the GMD must then be substituted into

$$\frac{L_p}{2L} = -1 + \ln 2L - \ln d'_p \tag{1.97}$$

These equations suffice to calculate the maximum possible pipe circulating current when both ends of the pipe are grounded. For this purpose consider

a coaxial line of the following dimensions and materials:

Conductor:	Solid aluminum rod of 2 cm diam, 1000 m long, 2.7 $\mu\Omega\cdot$cm resistivity, carrying a 60 Hz current of 100 A.
Pipe:	Solid aluminum pipe, 1000 m long, 2.7 $\mu\Omega\cdot$cm resistivity, inside diameter 10 cm, outside diameter 11 cm.
From (1.93)	$d'_{c,p} = 5.25$ cm
From (1.94)	$M_{c,p} = 1.91 \times 10^6$ cm $= 1.91$ mH
From (1.92)	$e_p = -72$ V $R_p = 0.0164\ \Omega$
From Fig. 1.33	$d'_p = 5.335$ cm
From (1.97)	$L_p = 1.91 \times 10^6$ cm $= 1.91$ mH $\omega L_p = 0.72\ \Omega$
From (1.95)	$Z_p = 0.72\ \Omega$

The maximum circulating current that could possibly flow in the pipe would arise in the hypothetical case of zero ground impedance. It would then be given by

$$i_{p,c} = -\frac{e_p}{Z_p} = 100 \text{ A}$$

and it is therefore equal to the conductor current. The 1 : 1 current transformation ratio applies to situations where the mutual inductance between conductor and pipe is equal to the self-inductance of the pipe and the resistance of the pipe is negligibly small compared to the pipe reactance. This is not always the case and then the pipe circulating current will be smaller than the conductor current. When the pipe current is nearly equal to the conductor current, the metal enclosure acts as an almost perfect magnetic shield suppressing the external field. The return conductor or other pipes may then be moved close to the forward conductor without suffering significant additional induced losses.

From this example it is clear that large circulating currents will flow in three adequately grounded single-core cables that form a three-phase circuit, unless special precautions are taken. The method that has been developed for the suppression of sheath circulating currents in three-phase systems is known as crossbonding. It is illustrated by Figs. 1.34 and 1.35. For the sake of clarity, these diagrams do not show the central conductors, which would not normally be transposed at the crossbonding station. Figure 1.34 refers to a trefoil arrangement of the three cables A, B, and C.

Let $e_{A,A}$ be the phasor voltage induced in the sheath of A by the current flowing in the conductor of A. If crossbonding eliminates the flow of

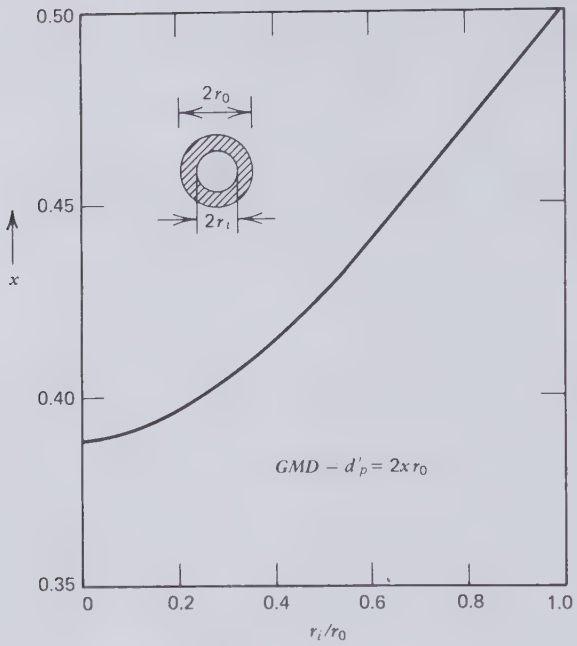

Figure 1.33 GMD of round tube section.

circulating current, then the sheaths will not behave like magnetic shields and the voltage induced in the sheath of A will also contain components due to the conductor currents in B and C. These components will be denoted by $e_{A,B}$ and $e_{A,C}$. The phasor relationship of these three induced components in the sheath of cable A is also indicated in Fig. 1.34. The resultant emf e_A acts in phase with $e_{A,A}$, but it is smaller in magnitude. In fact the resultant can be reduced to a minimum by bringing the three cables in contact with each other. Thermal considerations may make this impractical.

Crossbonding requires the cable sheaths to be insulated from ground and interrupted at regularly spaced intervals. A layer of polyethylene or other plastic insulation is normally extruded over the sheaths to isolate them from ground. Figure 1.34 shows two sheath interruptions between the cable terminations. At the terminations the sheaths are short-circuited and grounded. The crossbonding distance a must be one-third of the distance between ground connections. It will be seen that sheath section 1–2 of cable A is bonded to sheath section 2–3 of cable B and then to sheath section 3–4 of cable C. The interconnections of the remaining sheath sections are handled in a similar manner. The interconnections at crossbonding stations must also be insulated from ground. The voltage that will appear across the

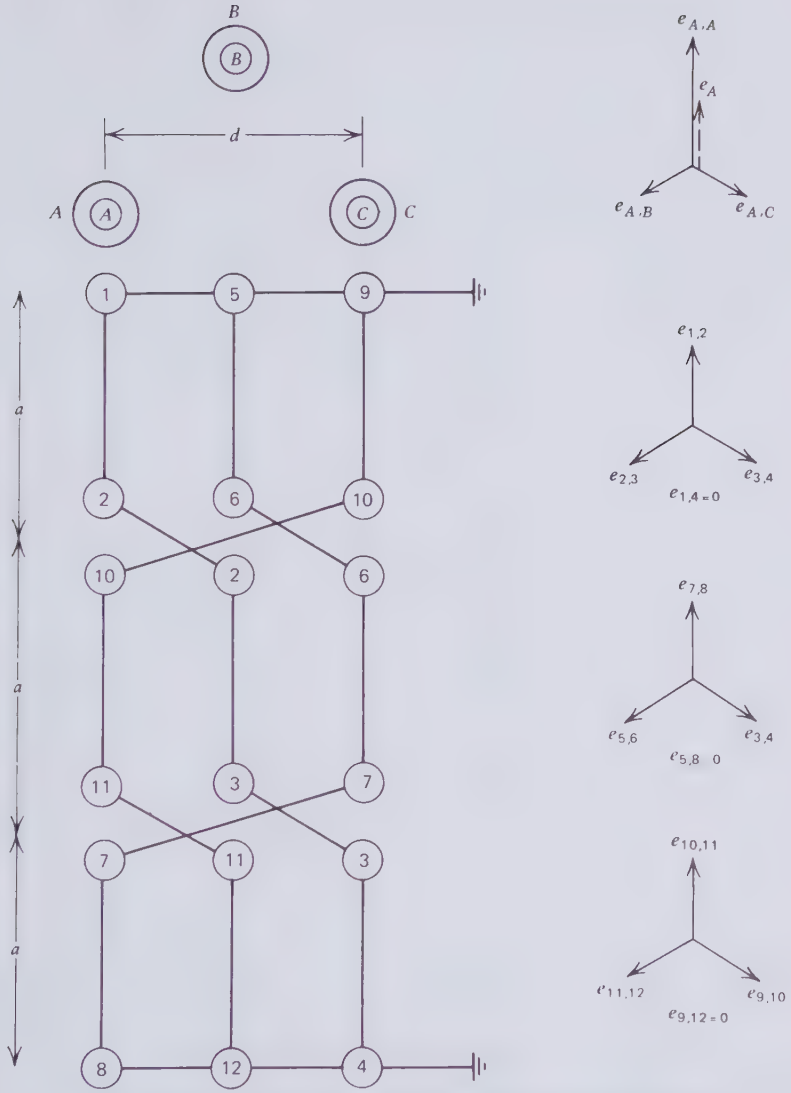

Figure 1.34 Sheath cross-bonding of three-phase circuit in trefoil formation.

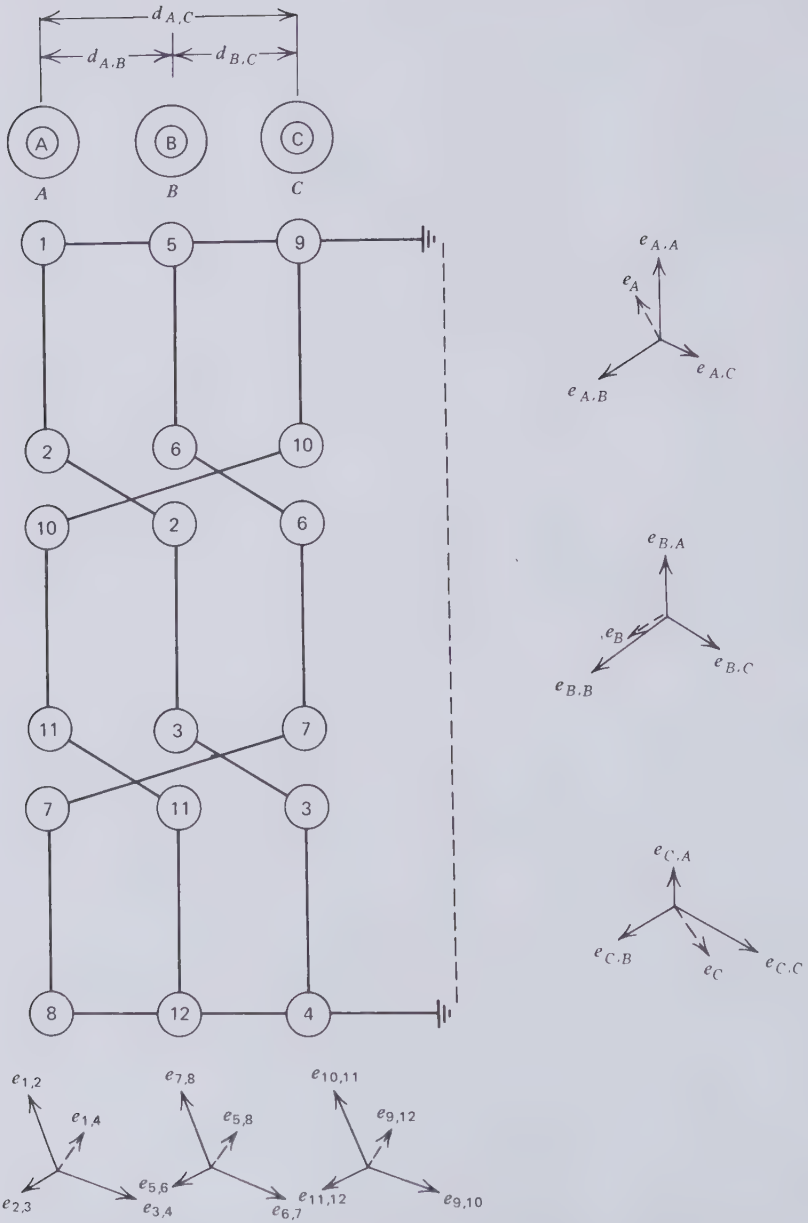

Figure 1.35 Sheath cross-bonding of three-phase circuit in flat formation.

sheath interruptions depends on the crossbonding length a, the conductor currents i_c, and the cable spacing d.

From the phasor diagrams of Fig. 1.34 it will be seen that the voltages between the interconnected sheath terminations are all zero, or $e_{1,4} = e_{5,8} = e_{9,12} = 0$. Consequently there is no driving emf present that could cause circulating current flow along the sheaths or through a ground loop. This represents the ideal operation of a crossbonded ac transmission line.

Crossbonding is usually carried out at cable splices, which ties the crossbonding length to the amount of cable that can be stored on a reel. In a long cable run, the number of cross bonding sections should be a multiple of three. This permits making a ground connection at every third station.

The standing voltage across the sheath gap is equal to the sheath voltage induced within one crossbonding length or $e_A/3 = e_{1,2}$.

$$\begin{aligned} e_A &= \omega i_c M_{A,A} - 2\omega i_c M_{B,A} \cos 60° \\ &= \omega i_c (M_{A,A} - M_{B,A}) \end{aligned} \tag{1.98}$$

where i_c is the balanced phase current, $M_{A,A} = M_{c,p}$ of (1.94) and $M_{B,A}$ is the mutual inductance between the conductor of cable B and the sheath of cable A. $M_{B,A} = M_{C,A}$, and the GMD which has to be used in (1.86) to compute these mutual inductances is equal to the conductor spacing d.

To gauge the magnitude of sheath gap voltages, consider the following example:

Internal sheath diameter = 8 cm
External sheath diameter = 9 cm
$L = 3a = 1000$ m
$d = 20$ cm
$i_c = 500$ A at 60 Hz
From (1.94) $M_{A,A} = 1.95 \times 10^6$ cm = 1.95 mH
From (1.86) $M_{B,A} = 1.64 \times 10^6$ cm = 1.64 mH
From (1.98) $e_A = 58.4$ V
Sheath gap voltage $= e_A/3 = 19.5$ V

This is an acceptably small standing voltage on a cable sheath. It is proportional to the conductor current and may therefore rise to 10 or 20 times this value under through-fault conditions.

It is difficult to install cables in trefoil formation unless they are touching each other and are bound together. In most instances this would be an unsatisfactory solution on account of mutual heating. To satisfy the requirements of easy installation and good ground cooling, self-contained cables are normally installed in flat formation, as illustrated in Fig. 1.35. As a rule the two outer cables are spaced symmetrically about the center cable.

Compared to the trefoil arrangement, the two sheath voltage components that are being induced by neighboring currents may no longer be equal in magnitude, thereby causing a phase shift of e_A, e_B, and e_C relative to $e_{A,A}$, $e_{B,B}$, and $e_{C,C}$. Furthermore the phasor sum is

$$e_{1,4} = e_{1.2} + e_{2,3} + e_{3,4} \neq 0 \tag{1.99}$$

At the same time we find from the phasor diagrams on Fig. 1.35 that

$$e_{1,4} = e_{5,8} = e_{9,12} \tag{1.100}$$

In other words, the resultant sheath voltages are equal in magnitude and phase and may be described as zero sequence components. They are unable to force the flow of circulating current down one sheath and return it in the other two. However, the parallel acting emfs of (1.100) will cause circulating currents to flow through the ground return circuit. This will, of course, be much smaller than the circulating current in a noncrossbonded system. Consider the following example with unequal cable spacing.

Lead sheath	Internal diameter	$= 2r_i = 8$ cm
	External diameter	$= 2r_o = 9$ cm
	Resistivity	$= 22\ \mu\Omega \cdot$ cm
Circuit length	L	$= 1000$ m
Cable spacing	$d_{A,B}$	$= 10$ cm
	$d_{B,C}$	$= 20$ cm
	$d_{A,C}$	$= 30$ cm
Conductor current	i_c	$= 600$ A
From (1.94):	$M_{A,A} = M_{B,B} = M_{C,C} = 1.95 \times 10^6$ cm $= 1.95$ mH	
From (1.86):	$(d'_{m,n} = d_{m,n})$ $M_{A,B} = M_{B,A} = 1.78$ mH	
	$M_{A,C} = M_{C,A} = 1.56$ mH	
	$M_{B,C} = M_{C,B} = 1.64$ mH	
	$\lvert e_{A,A} \rvert = -\omega i_c M_{A,A} = 441.5$ V	
	$\lvert e_{A,B} \rvert = -\omega i_c M_{A,B} = 402.9$ V	
	$\lvert e_{A,C} \rvert = -\omega i_c M_{A,C} = 353.1$ V	
	In-phase component of $e_A = 63.4$ V	
	Quadrature component of $e_A = 43.1$ V	

Therefore

$$|e_A| = 76.7 \text{ V}$$
$$\phi_A = 34.2°$$

Similarly

$$|e_{B,B}| = 441.5 \text{ V}; \qquad |e_{B,C}| = 371.4 \text{ V}; \qquad |e_{B,A}| = 402.9 \text{ V}$$
$$|e_B| = 60.8 \text{ V}; \qquad \phi_B = 26.7°$$
$$|e_{C,C}| = 441.5 \text{ V}; \qquad |e_{C,A}| = 353.1 \text{ V}; \qquad |e_{C,B}| = 371.4 \text{ V}$$
$$|e_C| = 80.6 \text{ V}; \qquad \phi_C = 11.3°$$

Referring to Figs. 1.35 and 1.36, it will be seen that the in-phase component of $e_{1,4}$ with respect to $e_{A,A}$ is given by

$$\frac{e_A}{3}\cos\phi_A + \frac{e_B}{3}\cos(120° - \phi_B) + \frac{e_C}{3}\cos(240° - \phi_C) = 2.25 \text{ V}$$

Similarly, the quadrature component is

$$\frac{e_A}{3}\sin\phi_A + \frac{e_B}{3}\sin(120° - \phi_B) + \frac{e_C}{3}\sin(240° - \phi_C) = 14.42 \text{ V}$$

Combining the two components results in

$$|e_{1,4}| = 14.6 \text{ V} \qquad \phi_{1,4} = 81.1°$$

Figure 1.37 is a graphic representation of these results. As has been pointed out before, $e_{5,8}$ and $e_{9,12}$ are equal to $e_{1,4}$, both in magnitude and phase angle. The three voltages act in parallel and would force a circulating current through the ground return. This current is given by

$$i_s = \frac{e_{1,4}}{\sqrt{R_s^2 + (\omega L_s)^2}}$$

where R_s is the sheath resistance and L_s the sheath self-inductance given by (1.97). The sheath current equation assumes zero ground impedance and it will therefore provide an upper bound of the circulating current. For the given data $\omega L_s = 0.734\ \Omega$ and $R_s = 0.330\ \Omega$. Therefore, the maximum sheath circulating current is 18.1 A resulting in a maximum loss per cable sheath of 108 W. This is negligibly small compared to the Joule loss in the conductor of the cable. The example proves that crossbonding is very effective in reducing sheath losses even for irregularly spaced cables.

For comparison, let us calculate the sheath loss due to circulating currents in a noncrossbonded system in which the terminations of all sheaths are solidly bonded to each other and to ground. The sheath circulating current

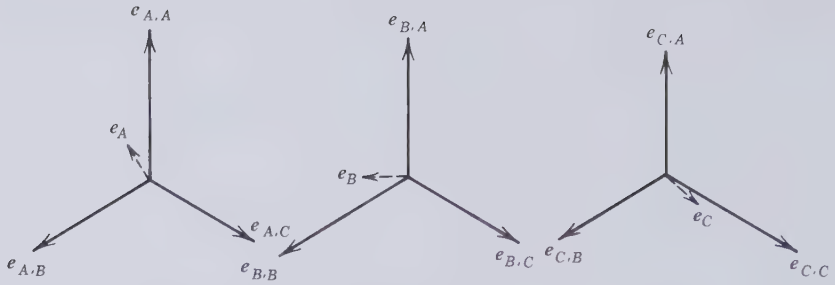

Figure 1.36 Induced sheath voltages of numerical example.

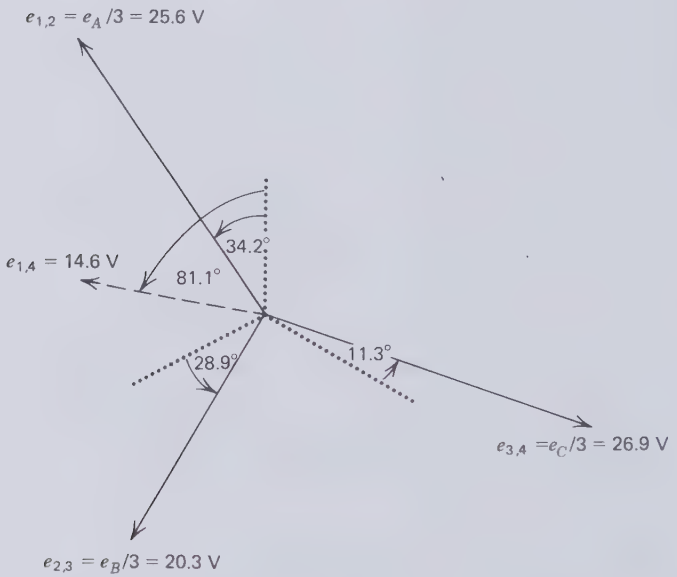

Figure 1.37 Zero sequence voltage $e_{1,4}$ of numerical example.

would then be given by

$$i_s = \frac{e_{A,A}}{\sqrt{R_s^2 + (\omega L_s)^2}} = 548.6 \text{ A}$$

This current is smaller than the conductor current (=600 A) because the resistance of the lead sheath is not negligible compared to the sheath self-inductance.

$$\frac{\text{sheath loss}}{\text{phase}} = i_s^2 R_s = 99.3 \text{ kW}$$

The 600 A of load current in a 1000 kcmil copper conductor would produce approximately 16 kW of conductor loss. This example serves to illustrate just how severe a loss penalty can be incurred in noncrossbonded systems.

Would this loss be smaller if the sheath had been made of a higher conductivity material? Take the case of an aluminum sheath of $\rho = 2.7$ $\mu\Omega \cdot$cm. This gives $R_s = 0.04\ \Omega$. The reactance remains unchanged at $0.734\ \Omega$ and therefore the sheath current becomes equal to the conductor current. For the aluminum sheath the circulating current loss is $600^2 \times 0.04 \times 10^{-3}$ kW $= 14.4$ kW. In this particular case the high-conductivity sheath helps to reduce the loss.

1.13 CIRCULATING-CURRENT SHEATH LOSS IN NONCROSSBONDED SYSTEMS AS A FUNCTION OF GEOMETRICAL FACTORS AND CONDUCTIVITY

Crossbonding of metallic cable enclosures is not always possible. A case in point is the pipe-type cable in which three conductors are enclosed in a single metallic tube. This particular configuration will be studied later. In the present section we consider noncrossbonded three-phase circuits made up of single-core cables. Most underwater ac transmission lines are of this form. Submarine cable cores are usually spaced far apart from each other to avoid accidental crossing of two cables during the laying operation. Even if three cables could be laid simultaneously and held apart by rigid spacers, it would still be difficult to waterproof the insulation over sheath crossbonds. Other examples where crossbonding may not be practical or desirable are short cable runs and isolated phase compressed gas insulated transmission lines. In all these instances it becomes necessary to compute the circulating current sheath loss and determine how it can be kept to a minimum by controlling such design variables as pipe thickness, pipe diameter, and pipe material.

As has already been shown, the circulating sheath current will be almost as great as the enclosed conductor current. This results in good electromagnetic shielding and particularly the elimination of the magnetic field between the cables. In the calculation of the sheath currents, therefore, we have to concern ourselves only with the mutual inductance between the sheath and the enclosed conductor given by (1.94).

It so happens that the self-inductance of a cable sheath or bus enclosure, given by (1.97) and Dwight's function x of Fig. 1.33, is in most practical cases almost the same as the mutual inductance between the enclosed conductor and the sheath. Therefore we may write

$$M_{c,p} \simeq L_s \tag{1.101}$$

The error of this approximation is very small when $r_i / r_0 > 0.85$ and $r_m >$ 4 cm.

No return current need be considered in balanced three-phase circuits. Denoting the power loss per phase by W_s, the induced voltage in the sheath or pipe by e_s, the sheath and conductor currents by i_s and i_c, and the sheath dc resistance by R_s, we have

$$i_s = \frac{e_s}{\sqrt{R_s^2 + (\omega L_s)^2}} = \frac{-i_c \omega M_{c,p}}{\sqrt{R_s^2 + (\omega M_{c,p})^2}} \tag{1.102}$$

$$W_s = i_s^2 R_s = \frac{(\omega M_{c,p})^2 R_s i_c^2}{R_s^2 + (\omega M_{c,p})^2} \tag{1.103}$$

or

$$\frac{W_s}{i_c^2} = \frac{(\omega M_{c,p})^2 R_s}{R_s^2 + (\omega M_{c,p})^2} = R_s' \tag{1.104}$$

Equation (1.104) defines an equivalent sheath resistance that may be added to the conductor resistance. When the sum of the two resistances is multiplied by the square of the conductor current, it gives the total Joule heating loss arising in the cable.

How does R_s', and therefore the sheath loss, vary with the electrical conductivity σ of the sheath material? Equation (1.104) provides the following limits:

$$R_s \gg \omega M_{c,p} \qquad R_s' \propto \frac{1}{R_s} \propto \sigma \tag{1.105}$$

$$R_s \ll \omega M_{c,p} \qquad R_s' \propto R_s \propto \frac{1}{\sigma} \tag{1.106}$$

From this we may expect that the curve representing circulating current sheath loss, or R_s', as a function of σ will leave the origin as a rising straight line, later pass through a maximum, and finally approach the abscissa asymptotically. To find the maximum of this curve we have to differentiate (1.104) with respect to the electrical conductivity, that is

$$\frac{dR_s'}{d\sigma} = \omega^2 M_{c,p}^2 \left\{ -\frac{2R_s^2}{R_s^2 + \omega^2 M_{c,p}^2} + \frac{1}{R_s^2 + \omega^2 M_{c,p}^2} \right\} \frac{dR_s}{d\sigma} \tag{1.107}$$

For the maximum

$$\frac{dR_s'}{d\sigma} = 0 \qquad \text{or} \qquad R_s = \omega M_{c,p} \tag{1.108}$$

Substituting (1.108) into (1.104) results in a maximum equivalent sheath resistance of

$$R'_{s,\max} = 0.5 R_s \tag{1.109}$$

The corresponding maximum sheath loss per phase is

$$W_{s,\max} = 0.5 i_c^2 R_s \tag{1.110}$$

From (1.109) we may determine the value of the conductivity (σ') at which the maximum loss occurs. For this purpose we take the cross-sectional area of the sheath as $2\pi r_m t$ with r_m standing for the mean sheath radius and t the thickness. At the maximum loss we have

$$R_s = \frac{L}{2\pi r_m t \sigma'} = \omega M_{c,p}$$

$$\sigma' = \frac{L}{2\pi r_m t \omega M_{c,p}} \tag{1.111}$$

Since both R_s and $M_{c,p}$ vary with cable length, the maximum value of the loss and the position of the loss peak on the conductivity scale must be functions of circuit length. As the mutual inductance is not a linear function of length, the loss per unit length will itself depend on circuit length. At first sight this appears to be a surprising result, but in most practical situations the sheath loss is approximately proportional to line length, as illustrated by the following example.

Taking the cable that was considered in the last section, that is,

Outside sheath radius	$r_o = 4.5$ cm
Inside sheath radius	$r_i = 4.0$ cm
Therefore	$r_m = 4.25$ cm
	$f = 60$ Hz ($\omega = 377$ sec^{-1})

This data has been used to compute the equivalent sheath resistance from (1.104) for a range of conductivities and the four circuit lengths of 10 m, 100 m, 1000 m, and 10,000 m. The results are plotted on Fig. 1.38 with the ordinate being the equivalent sheath resistance *per unit length*.

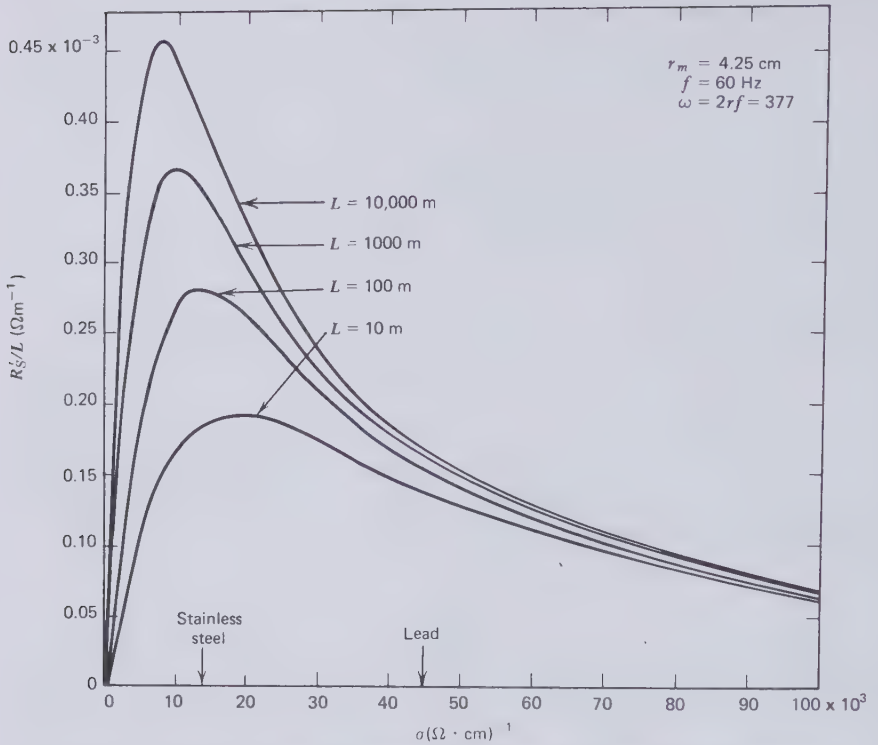

Figure 1.38 Equivalent sheath resistance per unit length as a function of conductivity.

The three curves confirm that the loss per unit length does vary with circuit length, but that this variation is quite small for lead sheaths ($\sigma = 45{,}455\ \Omega^{-1}\text{cm}^{-1}$) provided the cables are more than 100 m long. This length dependence becomes negligibly small for copper and aluminum, which lie beyond the scale of Fig. 1.38, and when $L > 1000$ m. Even a laboratory sample of 10 m length would not show a substantially lower loss per unit length than a long cable, particularly if it consists of aluminum or copper. On the other hand, the equivalent sheath resistance per unit length can show a very marked length dependence for high-resistivity materials such as stainless steels ($\rho \simeq 72\ \mu\Omega \cdot \text{cm}$). From time to time stainless steel has been considered as a sheath material because of its superior mechanical strength and corrosion resistance. At the increased conductivity that would prevail at cryogenic temperatures, this disadvantage of stainless steel will be less important.

In the design of cables it is necessary to know how the circulating current loss changes with sheath thickness. This has been calculated for the present

example and the results are plotted on Fig. 1.39. As would be expected, the thicker sheath presents a lower resistance and thereby reduces the Joule heating of the cable enclosure. On this graph the conductivity scale has been extended to include copper at ambient temperature. It shows very clearly the advantage that aluminum and copper have over lead and stainless steel at a typical sheath thickness of 0.5 cm. However, if a very much thinner sheath can be used, stainless steel moves to the left of the loss maximum. For this reason materials that combine high strength with high resistivity might one day find a use in cable technology.

Finally we consider how the equivalent sheath resistance R_s' is affected by the sheath mean radius r_m. The results for a 1000-m-long circuit with a wall

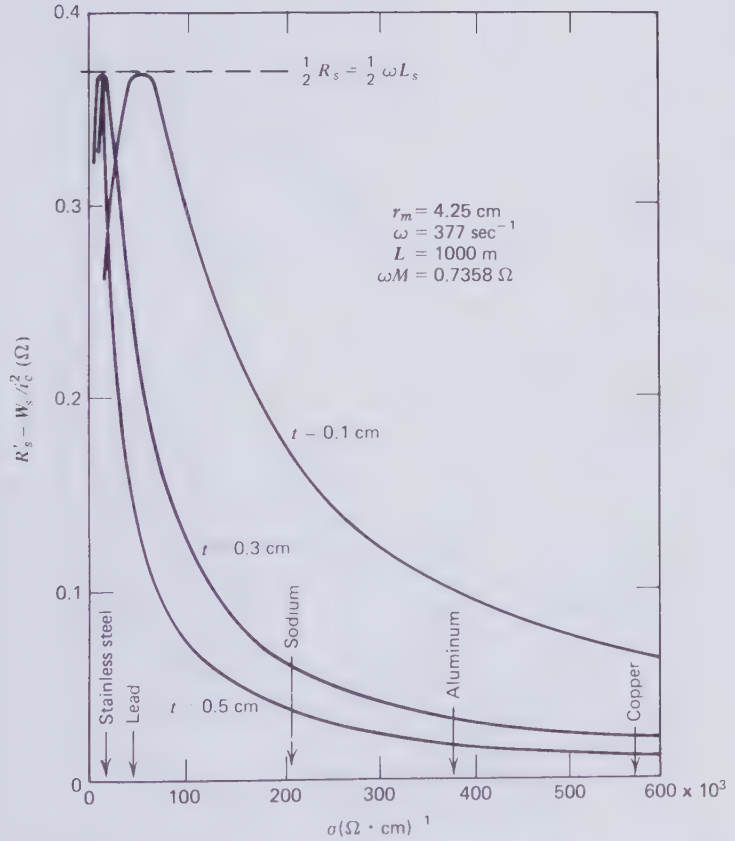

Figure 1.39 Equivalent sheath resistance as a function of conductivity for three sheath thicknesses.

thickness of 0.5 cm are plotted in Fig. 1.40. The larger diameter pipes have a greater conducting cross section and this is one reason for the reduced equivalent resistance. The large pipe diameter also reduces the mutual inductance between the conductor and the enclosure. Both factors taken together bring about a marked lowering of the sheath circulating loss. This is of help to isolated-phase bus systems that are insulated with air or gas and therefore require large tubular enclosures. It will be seen from Fig. 1.40 that a large pipe diameter moves the loss maximum to even lower electrical conductivities, making it virtually impossible to use stainless steel. Isolated-phase bus systems with their large pipe enclosures tend to work in the regime where $R_s \ll \omega M_{c,p}$ and therefore, from (1.104), the equivalent sheath resis-

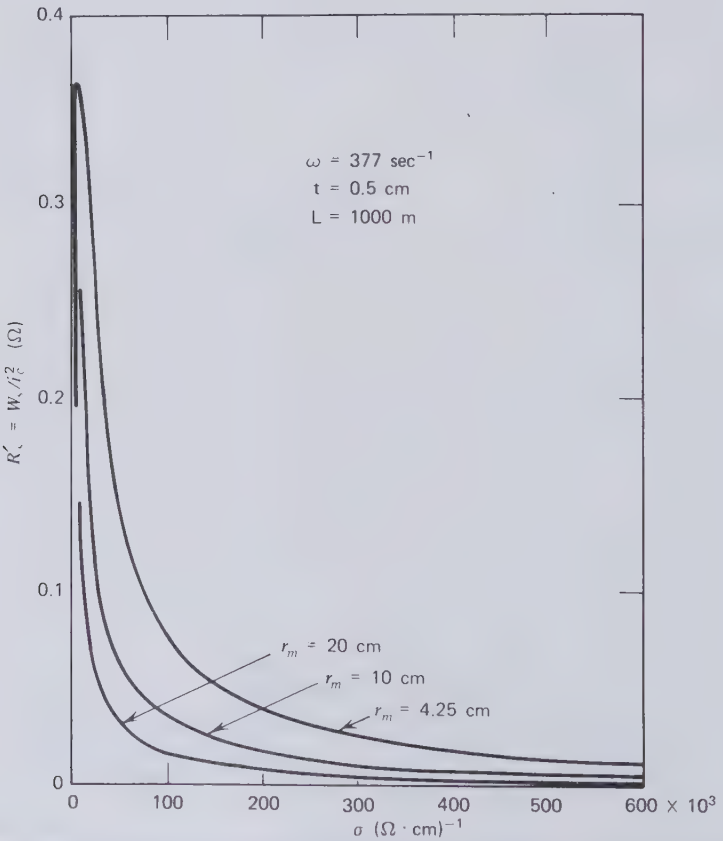

Figure 1.40 Equivalent sheath resistance as a function of conductivity for three mean sheath radii.

tance is nearly equal to the actual sheath resistance. This suggests that the highest possible sheath conductivities should be used and it becomes an important consideration in the development of cryocables.

1.14 EDDY CURRENT SHEATH LOSSES IN SINGLE-CORE CABLES OF THREE-PHASE CIRCUITS

The term *eddy current loss* is often reserved for the difference between measured sheath losses and calculated circulating current losses. It is usually very small compared with all other current-dependent losses of the cable. A rational investigation of the eddy current loss must begin with a determination of the paths that the eddy currents can possibly take. Two such paths are indicated in Fig. 1.41a and b and they are the only paths in a single-core cable sheath that have ever been proposed. Diagram 1.41a shows the eddy currents $i_{s,e1}$ in the enclosure pipe or sheath that are induced by an alternating current i_c carried in a coaxial conductor inside the enclosure. This particular eddy current component arises from the fact that the induced emf in the inside layer of the sheath is greater than the induced emf in the outside layer. Let us describe the difference between these two emfs by Δe_1. Recalling that the GMD between an enclosed conductor and a thin coaxial shell is equal to the radius of the shell, the voltage differential may be derived from the difference in the mutual inductances of the center conductor to the inner and outer shells.

$$\Delta e_1 = -\omega i_c \times 2L \times 10^{-7} \ln\left(\frac{r_0}{r_i}\right) \text{V} \tag{1.112}$$

where the circuit length L is expressed in meters. A significant feature of (1.112) is that in taking the difference between two mutual inductances we have eliminated the logarithmic length dependence. If we assume that the induced currents flow along two shells of equal thickness that divide the pipe wall, it becomes possible to compute the impedance that these currents have to overcome. As before, let r_m stand for the mean sheath radius. The resistance opposing the flow of the eddy current is

$$R_{e,1} = \frac{L}{\sigma\pi\left(\dfrac{1}{r_m^2 - r_i^2} + \dfrac{1}{r_o^2 - r_m^2}\right)} \tag{1.113}$$

where r_o and r_i are the outside and inside radii of the sheath. As before, we will take the GMD of a tube cross section to be equal to the mean radius.

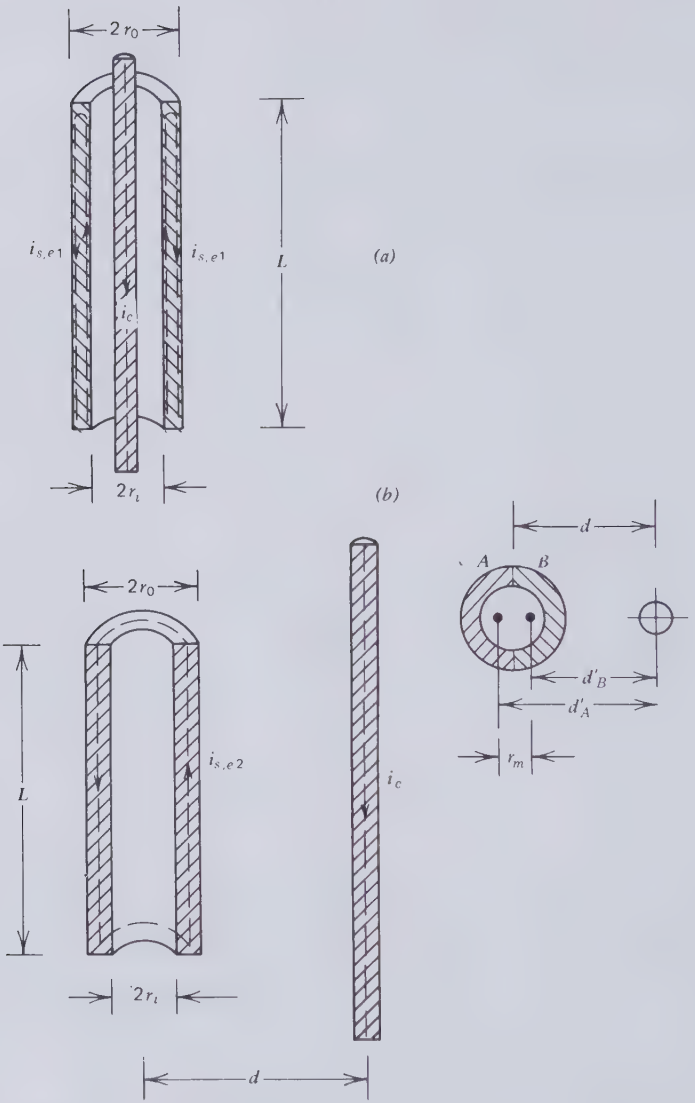

Figure 1.41 Possible paths of eddy currents in single core cable sheaths.

The two self-inductances (sum) that the eddy currents have to overcome are then given by

$$L_{e,1} = 2L\left\{-1+\ln(2L)-\ln\left(\frac{r_o+r_m}{2}\right)-1+\ln(2L)-\ln\left(\frac{r_m+r_i}{2}\right)\right\}$$
$$= 2L\left\{-2+2\ln(8L)-\ln\left[(r_o+r_m)(r_m+r_i)\right]\right\} \qquad (1.114)$$

Equations (1.112), (1.113) and (1.114) are sufficient to determine the magnitude of this kind of eddy current and the associated energy loss.

Let us take once more the example of a lead pipe of $r_o = 4.5$ cm, $r_i = 4.0$ cm, and a length of $L = 1000$ m, a 60 Hz conductor current of 600 A, we find that

$$\Delta e_1 = 5.33 \text{ V}; \qquad R_{e,1} = 0.66\ \Omega; \qquad L_{e,1} = 3.49 \text{ mH}$$
$$\omega L_{e,1} = 1.31\ \Omega; \qquad |Z| = 1.47\ \Omega$$
$$i_{e,1} = \frac{\Delta e_1}{|Z|} = 3.63 \text{ A}$$
$$W_{s,e1} = i_{e,1}^2 R_{e,1} = 8.68 \text{ W} \qquad \frac{W_{s,e1}}{L} = 8.68\times10^{-3} \text{ W/m}$$

Again, if the conductor current is being carried by a 1000 kcmil copper conductor, the Joule loss in the conductor would be 16 W/m. Therefore in this particular case, and probably in most practical situations, the eddy current loss of the first kind is negligibly small.

This small loss will be superimposed on the circulating current loss regardless of whether the sheath is crossbonded or not. It will also exist if the sheath is electrostatically floating or grounded at one point.

Calculating the eddy current flow of the second kind, as indicated in Fig. 1.41b, presents greater difficulties. We do not know the GMDs between the external conductor and the longitudinal portions of the pipe that have to carry the go-and-return currents. But since this loss is also going to be small compared to the conductor loss, we make some simplifying assumptions that permit an approximate estimate to be made. First, we assume that the two current streams occupy the equal areas A and B of the tube cross section, as sketched in Fig. 1.41b. Then the two GMDs of the areas A and B from the exterior conductor will be approximated to

$$d'_B \simeq d - \frac{r_m}{2}$$
$$d'_A \simeq d + \frac{r_m}{2}$$

where r_m is the mean radius of the sheath. With these assumptions, the emf differential in volts between the two halves is given by

$$\Delta e_2 = -i_c \times 2L \times 10^{-7} \ln \frac{2d + r_m}{2d - r_m} \text{ V} \tag{1.115}$$

The circuit length in (1.115) has to be expressed in meters.

The second difficulty arises because we do not know the GMD of half a pipe cross section which is required for self-inductance calculations. Earlier it has been shown that the GMD of a full pipe cross section is equal to the mean radius of the pipe. Now we make use of the fact that, by virtue of the logarithmic definition of GMD, the mean distance between element pairs of an area is always greater than the geometric mean distance. The mean distance of each area A and B will be greater than the mean distance of the total area $A + B$. Therefore the GMD of A or B must be expected to be greater than the GMD of $A + B$. How much greater it will be we do not know. Let us arbitrarily assume that the GMD of A and B is 1.5 times the mean radius of the pipe and the distance R between the go and return conductors is $r_o + r_i$. The self-inductance of the go-and-return current loop taken by the eddy currents of the second kind will then be given by (1.170) to be developed later.

$$L_{e,2} = 4L \ln \frac{2(r_o + r_i)}{1.5(r_o + r_i)} \tag{1.116}$$

Substituting numerical values into (1.116), it is found that

$$\omega L_{e,2} = 0.04\ \Omega$$

The resistance of the eddy current path is readily calculated from

$$R_{e,2} = \frac{4L}{\sigma\pi(r_o^2 - r_i^2)} \tag{1.117}$$

This is all the information required for calculating the eddy current loss of the second kind. With $r_o = 4.5$ cm, $r_i = 4.0$ cm, $d = 20$ cm, $\sigma = 10^6/22$ $(\Omega \cdot \text{cm})^{-1}$ (lead), $L = 1000$ m, $i_c = 600$ A, we find that

$$\Delta e_2 = -9.65 \text{ V}; \quad \omega L_{e,2} = 0.04\ \Omega; \quad R_{e,2} = 0.66\ \Omega; \quad |Z| = 0.66\ \Omega$$

$$i_{e,2} = 14.62 \text{ A}; \quad W_{s,e2} = 141.07 \text{ W}; \quad \frac{W_{s,e2}}{L} = 0.141 \text{ W/m}$$

Therefore the eddy current loss of the second kind per unit length of cable is also negligible compared with the Joule heating rate in the conductor. Furthermore, this loss would not exist at all if the sheath were solidly bonded to each other at the three-phase circuit terminations because the sheath circulating currents would then cancel the external magnetic field.

For an accurate estimate of the eddy current loss of the second kind we would have to take account of the interaction of all three conductors with all three sheaths. The method by which this could be done has been explained in the previous section. Because of the small magnitude of these currents, it does not appear worthwhile here to repeat the lengthy computions.

1.15 THE APPLICATION OF THE FINITE-ELEMENT METHOD TO THREE-CONDUCTOR CABLES

Oil-paper insulated three-conductor cables have been in use for many years for the transmission of relatively small amounts of power. The pipe-type oil-paper insulated cable contains three conductors of much greater transmission capability than flexible three-core cables. Rigid three-core cables using compressed gas insulation, or vacuum insulation in conjunction with cryogenic cooling have been under development since the middle 1960s.

The determination of the current distribution over the conductor and pipe sections of a three-conductor cable is a more complex mathematical operation than has so far been attempted. Knowledge of this current distribution is required for estimating Joule heating losses and interconductor forces. Only in recent years, through the study of cables that carry very large currents, has it become apparent that there exists an electromagnetic torque that tends to twist the conductors inside the metallic enclosure pipe [1.38]. This is due to the longitudinal currents of the pipe, which behaves like the short-circuited rotor of an induction motor. The pipe currents are the equivalent of the circulating currents in a solidly grounded, noncrossbonded three-phase circuit made up of single-core cables.

The current distribution analysis is easiest when the cable does not contain ferromagnetic material and the conductors are spaced symmetrically in trefoil formation. These two conditions are met in liquid-, gas-, and vacuum-insulated cable systems. In the present section it will be shown how the finite-element method can be applied to this class of cables. Pipe-type cables have a magnetic enclosure and their conductors are not spaced symmetrically. They will be studied later.

A full finite-element analysis with the aid of a large digital computer has been carried out for the particular cable geometry shown in Fig. 1.42 [1.38]. It represents a proposal for a 230- and possibly 345-kV vacuum-insulated,

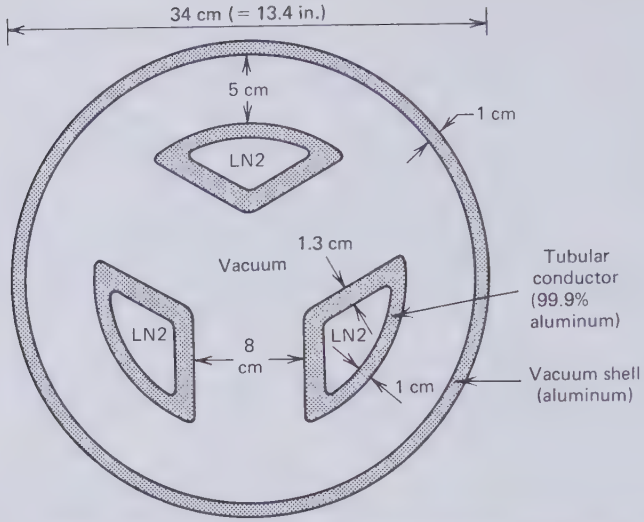

Figure 1.42 Vacuum insulated LN2 cryocable. (By permission of IPC Science and Technology Press).

liquid-nitrogen cooled cryocable. The compact design of the sector-shaped conductors is made possible by the fact that voltage breakdown in vacuum, as opposed to voltage breakdown in gas, is largely independent of the macroscopic electrical stress on the conductor surface. The vacuum enclosure is an aluminum pipe of 34 cm overall diameter. Because of the induced currents, this pipe will operate above ambient temperature. The dimensions of the three conductors and their location in the pipe enclosure are shown in Fig. 1.42. The conductor material is extruded aluminum of 99.9 percent purity. The calculations assume that the outer pipe will run at 45°C and its electrical conductivity will then be 0.322×10^6 $(\Omega \cdot \text{cm})^{-1}$. The conductor temperature of a cryocable varies between coolant inlet and outlet ports. For the purpose of the current distribution analysis, an average conductor temperature of 72°K (−201°C) has been assumed. At this temperature the electrical conductivity of the conductor pipes is 5×10^6 $(\Omega \cdot \text{cm})^{-1}$.

Finite-element computations require the metallic cross-sections of the conductor and pipe system to be subdivided into filaments. In 1968, when these computations were carried out, computer charges were approximately proportional to the third power of the number of filaments. The filaments were therefore made as large as possible without letting the error limits in the computed filament current exceed ±5 percent. For the example of Fig. 1.42, 5×5 mm square filaments were chosen. How the cable cross section

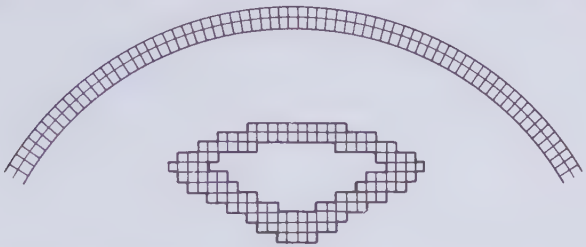

Figure 1.43 Filament subdivision of one-third of the cable cross section. (By permission of IPC Science and Technology Press).

was subdivided into 25-mm^2 filaments is shown in detail in Fig. 1.43. Two layers of filaments were fitted into the vacuum pipe and their sections had to be slightly distorted squares of the same cross-sectional area of the perfectly square conductor filaments. In all cases the filament axis was taken to coincide with the center of area of its cross section. The cable section as a whole contained 768 filaments, of which 256 fell into each of the three symmetrical sectors.

The finite-element method used in Section 1.9 to determine the skin effect in an isolated conductor has to be generalized for multiphase circuits with enclosure pipes. The more complex three-core cable system involves three different impressed voltages and a pipe, which is not subject to any externally applied driving voltage. In addition, the conductors and the pipe may consist of different materials and are likely to operate at different temperatures. This means the electrical conductivity will not be the same throughout the metallic components of the cable. To bring about the required generalization, consider the set of simultaneous equations that govern the current distribution and involve the impressed voltages e, the self- and mutual impedances $R-j\omega L$ and $-j\omega M$, and the resulting filament currents.

$$\begin{aligned}
e_1 &= (R_1 - j\omega L_{1,1})i_1 - j\omega M_{1,2}i_2 \quad - j\omega M_{1,3}i_3 - \ldots - j\omega M_{1,g}i_g \\
e_2 &= -j\omega M_{2,1}i_1 + (R_2 - j\omega L_{2,2})i_2 - j\omega M_{2,3}i_3 - \ldots - j\omega M_{2,g}i_g \\
&\vdots \\
e_g &= -j\omega M_{g,1}i_1 - j\omega M_{g,2}i_2 \quad - j\omega M_{g,3}i_3 - \ldots + (R_g - j\omega L_{g,g})i_g
\end{aligned} \tag{1.118}$$

The mutual impedances of (1.118) can be reduced to dimensionless quantities in electromagnetic units (emu). To achieve this we note that the resistance of a general filament is given by

$$R_m = \frac{L}{\sigma_m \Delta A} \tag{1.119}$$

where L is the circuit length, σ_m the conductivity of the mth filament, $\Delta A = A/g$ the filament cross-sectional area, A the total metal cross section, and g the number of filaments. Furthermore, let a generalized dimensionless radian frequency be defined by

$$\lambda_m = \omega \sigma_m \Delta A \tag{1.120}$$

Finally the self- and mutual inductances must be divided by the circuit length to make them emu dimensionless quantities, that is,

$$\frac{L_{m,m}}{L} = L'_{m,m} \qquad \frac{M_{m,n}}{L} = M'_{m,n} \tag{1.121}$$

With (1.119), (1.120), and (1.121), equation (1.118) can be rewritten as

$$\begin{aligned}
\frac{je_1}{(R_1\lambda_1)} &= (j\lambda_1^{-1} + L'_{1,1})i_1 + M'_{1,2}i_2 + M'_{1,3}i_3 + \ldots + M'_{1,g}i_g \\
\frac{je_2}{(R_2\lambda_2)} &= M'_{2,1}i_1 + (j\lambda_2^{-1} + L'_{2,2})i_2 + M'_{2,3}i_3 + \ldots + M'_{2,g}i_g \\
&\vdots \\
\frac{je_g}{(R_g\lambda_g)} &= M'_{g,1}i_1 + M'_{g,2}i_2 + M'_{g,3}i_3 + \ldots + (j\lambda_g^{-1} + L'_{g,g})i_g
\end{aligned} \tag{1.122}$$

In matrix notation (1.122) can be abbreviated to

$$\left\{ \frac{je_m}{(R_m\lambda_m)} \right\} = [M'_{m,n}]\{i_m\} \tag{1.123}$$

$[M'_{m,n}]$ is a nondimensional, square and symmetric matrix which is associated with a square eigenvector (modal) matrix $[Q_{m,n}]$ and a diagonal eigenvalue (spectral) matrix $[\Lambda_m]$ such that, with the transpose $[Q_{m,n}]^t$, we have

$$[Q_{m,n}]^t [M'_{m,n}][Q_{m,n}] = [\Lambda_m] \tag{1.124}$$

Therefore the column matrix of the unknown currents in (1.123) may be expressed as

$$\{i_m\} = \frac{[Q_{m,n}]^t \{je_m/(R_m\lambda_m)\}[Q_{m,n}]}{[\Lambda_m]} \tag{1.125}$$

The first step of solving (1.125) is to set up the dimensionless mutual inductance matrix $[M'_{m,n}]$, using equation (1.35) or approximation (1.36). The elements along the principal diagonal of this matrix are $(j\lambda_m^{-1} + L'_{m,m})$. $L_{m,m}$ is the self-inductance of the mth filament. Since all filaments are straight and are of the same length and cross-sectional area, they all have the same self-inductance. According to Maxwell [1.15], the GMD of a square of $a \times a$ is $0.44705a$. This GMD has to be substituted into (1.35) or (1.36) to replace the separation d between a pair of filaments.

A convenient way of arranging the dimensionless mutual inductance matrix is shown in Fig. 1.44. Each of the three cable sectors contain $g/3 = s = 256$ filaments labeled in symmetric sequence. Figure 1.44 shows

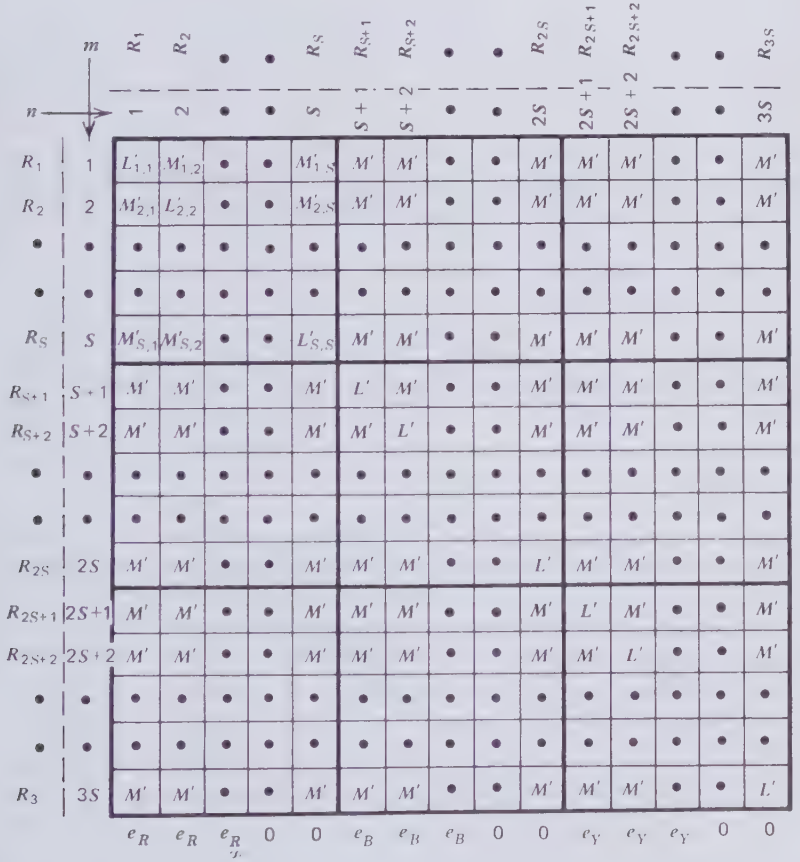

Figure 1.44 Mutual inductance (per unit length) matrix of three-core cable. Note: $L'_{m,m}$ stands for $j\lambda_m^{-1} + L'_{m,m}$.

nine square submatrices with certain symmetry properties. The filament resistances R_m have been written alongside the matrix. They depend on the conductivity σ_m of the filament material. The present example comprises only two different filament resistances; a low one for the cold conductor filaments and a higher one for the pipe filaments. Figure 1.44 also shows the driving voltages e_R, e_B, and e_Y that are externally applied between the ends of the "red," "blue," and "yellow" phase conductors. No external voltage is impressed on the pipe filaments. This accounts for the zeros in the voltage row and column.

In order to save computer time and storage requirements, it is important to fully exploit the matrix symmetry and the partitioning indicated in Fig. 1.44, which can also be expressed as

$$[M'_{m,n}] = \begin{bmatrix} M'_{R,R} & M'_{R,B} & M'_{R,Y} \\ M'_{B,R} & M'_{B,B} & M'_{B,Y} \\ M'_{Y,R} & M'_{Y,B} & M'_{Y,Y} \end{bmatrix} \tag{1.126}$$

The literature on matrix algebra and computer alogarithms [1.39, 1.40] has to be consulted for handling the relatively large matrix in the most economical way.

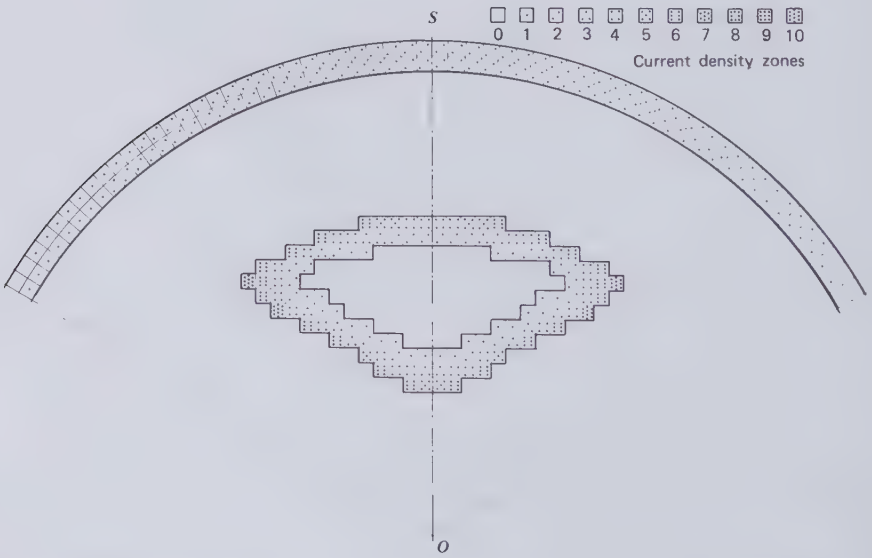

Figure 1.45 Current distribution in the symmetrical three-core cable. (By permission of IPC Science and Technology Press).

The filament currents that have been computed with the aid of (1.125) are, in general, all of different amplitude and phase angle. The process of visualizing this complex current pattern is one of the real difficulties of conductor science. In the absence of any better diagrammatic aids, Fig. 1.45 represents a feeble attempt of depicting the current amplitude distribution over one sector of the cable. The dot density has been made a measure of the current amplitude. Figure 1.45 shows quite clearly that more current is flowing in the outer layer of the conductor than on the inside. The situation is reversed in the enclosure pipe where the current density is greater on the inside. This fact is almost hidden on Fig. 1.45 because of the coarse resolution into 10 density zones. Besides, the pipe skin effect is not well developed in the particular cable design that was chosen for the analysis. A weak skin effect indicates only partial magnetic shielding allowing some of the magnetic field to penetrate to the outside of the cable. Consequently, this particular cable would have some influence on nearby parallel power and communication circuits.

Figure 1.45 also shows that the skin effect of the conductor is not uniform along the conductor perimeter, but that the current concentration is greatest near the three corners of the conductor cross section. The current in the outer arc of the sector-shaped conductor pipes is less dense than in the inner flat sides. Through other computer runs, it was determined that the displacement of current away from the arc is much more pronounced when the conductors are not enclosed in a metal pipe. Although the presence of the outer pipe appears to add to the Joule losses, it tends to distribute the conductor current more uniformly and thereby reduces the conductor loss. This phenomenon is of practical importance in a vacuum-insulated, cryogenically cooled system, where the conductor loss carries a refrigeration penalty while the heat generated in the pipe is dissipated to the surrounding soil without the expenditure of additional energy.

There exists a slight asymmetry in the current amplitude distribution about the bisector *OS* of Fig. 1.45. With the coarse resolution of this diagram it can barely be discerned in the pipe and not at all in the conductor. Nevertheless, the asymmetry is real and it will later be shown to be the cause of a mutual torque between the conductor assembly and the pipe. This current asymmetry becomes very much more pronounced, in both the conductor and the pipe wall, at lower frequencies of less than 20 Hz. This fact has also been established by computer analysis [1.38]. It is obviously due to the presence of the neighboring conductor currents and may therefore be described as a proximity effect. From the definition of the dimensionless radian frequency (1.120), it will be seen that lowering the electrical conductivity has a similar effect as lowering the frequency. Therefore the asymmetry in the current distribution about *OS* of Fig. 1.45 may be expected to

become more important in three-core cables that are not cryogenically cooled, as for example gas insulated systems. These qualitative arguments lead to the conclusion that for low generalized frequencies, the current distribution is dominated by the proximity effect, whereas at higher frequencies it becomes skin effect dominated.

The current distribution asymmetry could lead one to speculate that an asymmetric conductor section would have a greater or lesser Joule loss than a symmetric section, depending on which side of the conductor the current concentration occurs. This speculation has proved to be false. Consider the asymmetric conductor shown in Fig. 1.46. Depending on the direction of phase rotation, the current will be more dense on either the heavy (a) or light (b) side of the conductor. It might be expected, intuitively, that case (a) would cause less Joule heating than case (b). Computer runs have proved, however, that the total conductor loss is identically the same for both the forward and reverse phase rotation. This example illustrates better than any other that the mere knowledge of the current distribution in a given conductor is not sufficient for the design of a better conductor containing the same amount of metal.

A second problem of this nature has remained unresolved. It can be stated by the following question. Given a symmetric but composite conductor such that the conductivity on the left of the bisector *OS* of Fig. 1.45 is greater than the conductivity on the right side, will the total conductor loss be the same for both the forward and reverse phase rotation? Is the Joule loss determined only by the applied voltages and frequencies and the distribution of conducting matter in the cable space or does it also depend on the sense of the imagined rotation of the magnetic field?

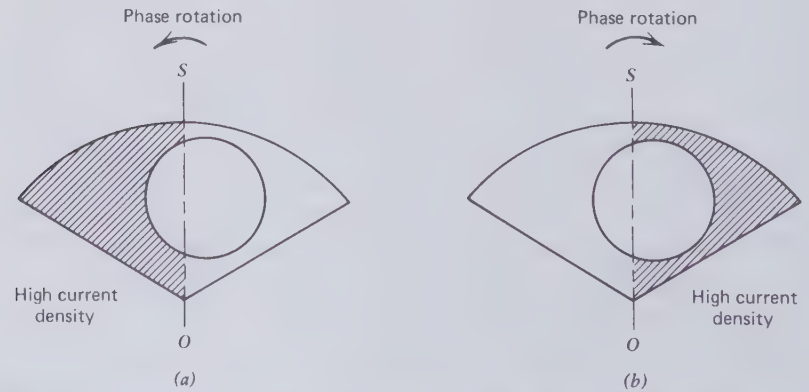

Figure 1.46 Current concentration dependence on phase rotation in asymmetrical conductor section.

It is a curious fact, not normally recognized, that the sum of all filament current amplitudes is greater than the load current that would be indicated by a current meter placed in series with the transmission line. This fact will be more readily understood by examining the phasor diagram of Fig. 1.47. The diagram is for just the red phase conductor R. It shows the load current i_R displaced from the applied voltage by some phase angle ϕ_R. Now all the filament current amplitudes can be sorted such that they lie on a relatively smooth curve, as for example OCD. This sorting process was not carried out for the numerical example. Figure 1.47 just serves as an illustration of the difference between total and measured phase current. Whatever the sorting sequence, it will be realized that the arithmetic sum of the filament current amplitudes is significantly greater than the useful load current OD that would be detected by a current meter. The useful current can be expressed by the following phasor sum.

$$i_r = -OA + AO - jOB + jBO + OD \tag{1.127}$$

The useful filament current components that act in the direction from O to D are not uniformly distributed over the conductor cross section. For this reason alone the ac resistance of the conductor would be greater than its dc resistance, because of the argument developed in Section 1.8 and particularly (1.33). However, this is not the full explanation when the ac loss contribution is very large. There may exist, as in the example of Fig. 1.47, two more sets of closed currents, OA and AO as well as OB and BO, which do not leave the conductor. These sets of internal circulating currents also produce Joule heat as a result of electron scattering which has to be added to the loss power that can be directly attributed to the noncirculating useful load current. The internal circulating currents flow along the conductor in one set of filaments and are returned by the remaining filaments. At the ends of the conductor there must exists transverse currents which connect the

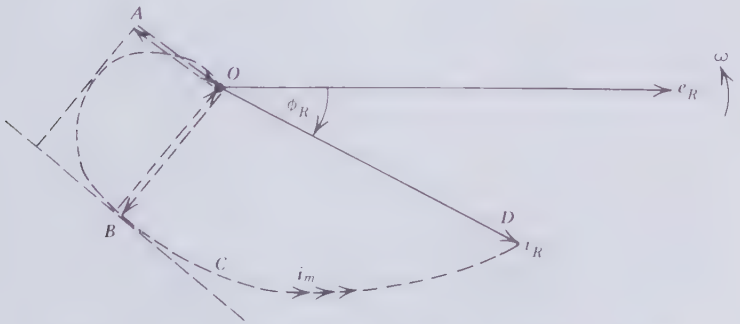

Figure 1.47 Phasor diagram for one conductor of a three-core cable.

go-and-return streams. Of the 116 filaments of each conductor in the cryocable, the innermost 45 were found to carry a negative or reverse load current component. Altogether it amounted to 8.75 percent of the useful forward current.

The Joule heating rate in each filament is given by the product of the filament (dc) resistance and the square of the filament rms current amplitude. Therefore the heat source distribution will be even less uniform than the current amplitude distribution. Most of the conductor heat is actually produced in a relatively small fraction of the metal near the three corners of the conductor, but the excellent heat conductivity at liquid-nitrogen temperatures would prevent the establishment of significant temperature differentials across the conductor area.

The sheath circulating current flowing opposite each conductor was found to be equal to approximately half the conductor current and would, of course, be proportional to the latter whatever the load current value. It has been shown before that in an isolated phase, solidly bonded system, the sheath circulating current would be nearly equal to the conductor current. The lower sheath current in the three-core cable is explained by the partial magnetic field cancellation caused by bringing the conductors of a three-phase circuit close together.

The sheath loss was found to be almost exactly equal to the conductor loss. This equality is believed to be fortuitous and it would probably not prevail in sheaths of different thicknesses and diameters; and also not for different ratios of the sheath to conductor conductivity.

For a 10-km-long cryocable circuit of the given design, the ac resistance that the applied phase voltage would have to overcome was computed to be 53.4 mΩ. Half or 26.7 mΩ of this resistance accounted for the sheath loss. The dc resistance of one conductor at 72°K amounts to only 6.9 mΩ. These figures demonstrate that the ac losses in a cryocable can nullify much of the advantage of the increased electrical conductivity. Substantial sheath losses are probably unavoidable in any three-core cable. Even if they are ignored, the 13.9-fold increase in conductivity due to cooling of the cable of Fig. 1.42 produced only a 3.9-fold gain in ac conductance. From this it may be concluded that there remains much scope for improving the conductor geometry to make the ac penalty smaller.

An important parameter in cable design is the phase inductance. To a large extent this determines the voltage drop between the cable ends. Once the filament currents have been computed by the finite-element method, it is quite easy to derive from them the self-inductance of each conductor, which will be denoted by L_c. For this purpose we consider the energy flow in and out of a single conductor filament. This can be expressed as

$$ei_m = ei_{m,p} - jei_{m,q} \tag{1.128}$$

What before has been referred to as the driving voltage is also the voltage drop along the conductor. In a balanced three-phase transmission line this voltage drop will be the same in each conductor, and in (1.128) it is expressed by the letter e. This equation further assumes that the current i_m flowing in the general conductor filament m has been resolved into components $i_{m,p}$ and $i_{m,q}$ which, respectively, act in phase and in quadrature with the voltage drop e. Both terms of (1.128) are products of voltage and current and they represent power or energy flow. Besides they are sinusoidal quantities that oscillate at twice the energizing frequency (2ω), as can be proved with the following equations. Let

$$e = E\sin\omega t \qquad i_{m,p} = I_m \sin\omega t \qquad i_{m,q} = -I_m \cos\omega t$$

Therefore

$$ei_{m,p} = EI_m \sin^2\omega t = \frac{EI_m(1-\cos 2\omega t)}{2} = \frac{EI_m}{2} - \frac{EI_m \cos 2\omega t}{2} \tag{1.129}$$

$$ei_{m,q} = -I_m \cos\omega t \cdot E\sin\omega t = -\frac{EI_m \sin 2\omega t}{2} \tag{1.130}$$

Now $ei_{m,p}$ has a finite time average, and it represents unidirectional energy flow, which ultimately, when summed over the whole conductor section, must account for the total conductor and sheath losses. Figure 1.47 indicates that some filaments will actually carry a negative in-phase current component, which implies that real power is being regained. The explanation of this fact is that not all the incoming real power from the source of e is immediately converted to heat. Some of it is transferred to the sheath and, by the second stage of induction, back to the conductor, where it helps to defray some of the Joule loss. Even in the absence of the sheath, multistage induction between the conductor filaments provides a similar mechanism for the occurrence of reverse current flow. The negative sign of an in-phase current component ensures that it is not counted a second time as externally supplied loss (real) power.

If a conductor contains c filaments, the energy loss per phase W_r is given by

$$W_r = e\sum_1^c i_{m,p} \tag{1.131}$$

According to the earlier calculations of conductor and sheath losses in one sector of a three-core cable containing s filaments (conductor and sheath) this must also be equal to

$$W_r = \sum_1^s i_m^2 R_m \tag{1.132}$$

The second term of (1.128), which is further defined in (1.130), also represents a pulsation at twice the energizing frequency, but its time average is zero. It stands for imaginary or reactive power associated with the reversible storage in and withdrawal of energy from the transmission line. The total reactive power in one phase is

$$W_i = e \sum_1^c i_{m,q} = ei\omega L_c \tag{1.133}$$

where i is the useful load current flowing in one conductor and L_c the self-inductance of this conductor. The latter quantity may be computed from (1.128) and (1.133) by first noting that

$$i = \sqrt{\left(\sum_1^c i_{m,p}\right)^2 + \left(\sum_1^c i_{n,q}\right)^2} \tag{1.134}$$

and consequently

$$L_c = \frac{1}{\omega i} \sum_1^c i_{m,q} \tag{1.135}$$

1.16 ELECTROMECHANICAL FORCES BETWEEN CONDUCTORS AND METALLIC PIPES

Electromechanical forces set up by the load current and sheath circulating currents are rarely discussed in the literature of high-voltage cables. In the normal operation of the smaller transmission cables, these forces are insignificant. However in the large forced cooled cable systems that have been installed more recently, the electromechanical forces can no longer be ignored, particularly when one or more of the conductors carry fault currents that may be 10 to 20 times as large as the full load current. If gas or vacuum insulated three-core cables become a practical reality, they would be carrying several thousands of ampere of load current and then electromechanical forces would become a major design challenge.

The easiest method of deriving the lateral force between two current-carrying conductors starts with the definition of Neumann's mutual potential $P_{m,n}$ [1.30, 1.31], which for the two currents i_m and i_n and the mutual inductance $M_{m,n}$ is

$$P_{m,n} = -i_m i_n M_{m,n} \tag{1.136}$$

The mutual force acting between the two conductors in an arbitrarily chosen direction z is given by

$$F_{m,n} = -\frac{dP_{m,n}}{dz} = i_m i_n \frac{dM_{m,n}}{dz} \tag{1.137}$$

In the type of cable in which electromechanical forces assume importance, the conductors are so large that it is no longer permissible to assume all the current flows along a line coinciding with the conductor axis. This compels us to subdivide the conductor into filaments and then apply (1.137) to pairs of filaments situated in two conductors. If (1.137) were applied to two filaments in the same conductor, it would reveal internal mechanical stresses with which we are not concerned at this time.

Furthermore, let the discussion from here onwards be limited to straight and parallel conductors. Now consider a pair of filaments m and n situated in go-and-return conductors A and B as shown in Fig. 1.48. The mutual inductance between two straight and parallel filaments is given by (1.35) in terms of the distance of separation d. To convert the variable from d to z, we use the following substitution

$$d = \frac{z}{\cos\theta} = \sqrt{z^2 + h^2} \tag{1.138}$$

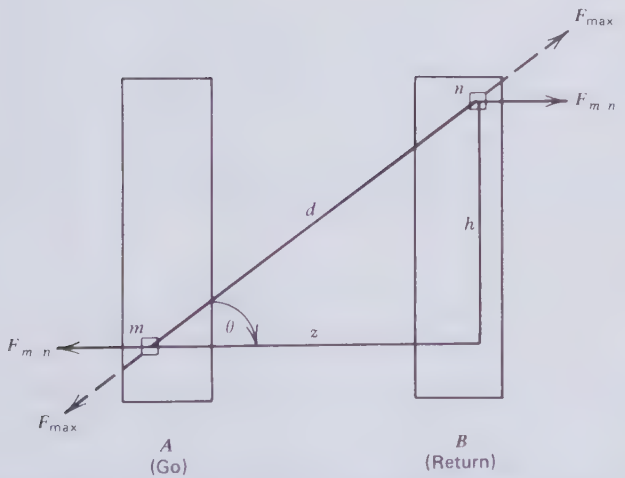

Figure 1.48 Elemental forces in go-and-return circuit [1.25]. (By permission of Taylor & Francis Ltd.).

Substituting (1.138) into (1.35) modifies the mutual inductance formula to

$$M_{m,n} = 2L \ln \frac{L + \sqrt{L^2 + z^2 + h^2}}{\sqrt{z^2 + h^2}} - \sqrt{L^2 + z^2 + h^2} + \sqrt{z^2 + h^2} \quad (1.139)$$

where L is the circuit length. Differentiating (1.139) with respect to z

$$\frac{dM_{m,n}}{dz} = \frac{2z}{z^2 + h^2}\left(\sqrt{z^2 + h^2} - \sqrt{L^2 + z^2 + h^2}\right)$$
$$= \frac{2\cos\theta}{d}\left(d - \sqrt{L^2 + d^2}\right) \quad (1.140)$$

When the circuit length is very much greater than the distance of separation d, which is almost invariably true, (1.140) may be approximated to

$$\frac{dM_{m,n}}{dz} \sim -\frac{2zL}{d^2} \sim -\frac{2L\cos\theta}{d} \quad (1.141)$$

Approximation (1.141) could also have been derived by differentiation of the approximation (1.36). It is useful to remember that in electromagnetic units the mutual inductance is a length and its gradient a dimensionless quantity. The force acting between the filament pair will be greatest in the direction of d (when $\cos\theta = 1$) and it is given by $-2i_m i_n L/d$, which is a well-known formula for line currents. The negative sign stands for attraction and the positive sign for repulsion. In a go-and-return circuit one of the currents would be negative and the conductors repel each other, as indicated in Fig. 1.48.

To go from the instantaneous currents and forces so far considered to the sinusoidal equivalents that will be experienced in an ac cable circuit, we resolve the instantaneous currents as follows

$$i_m = (I_{m,p} - jI_{m,q})\sin\omega t$$
$$i_n = (I_{n,p} - jI_{n,q})\sin\omega t \quad (1.142)$$

The parameters involved in these equations are further defined by the phasor diagram of Fig. 1.49 where the voltage drop, or the driving voltage impressed on both conductors acts in the same direction.

The mutual force $F_{m,n}$ in the z direction may now be expressed as the sum of four contributions arising from the interactions of the in-phase and

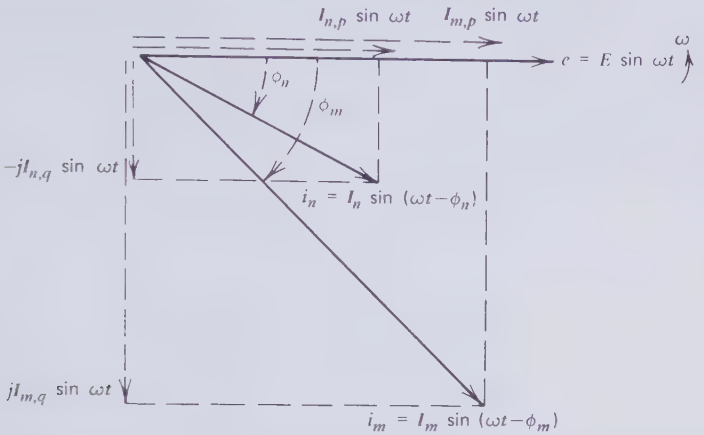

Figure 1.49 Phasor diagram for two general filament currents i_m and i_n [1.25]. (By permission of Taylor & Francis Ltd.).

quadrature components of the two filament currents.

$$F_{m,n} = I_{m,p}I_{n,p}\frac{dM_{m,n}}{dz}\sin^2\omega t + I_{m,p}I_{n,q}\frac{dM_{m,n}}{dz}\sin\omega t(-\cos\omega t) + I_{m,q}I_{n,p}\frac{dM_{m,n}}{dz}(-\cos\omega t)\sin\omega t + I_{m,q}I_{n,q}\left(\frac{dM_{m,n}}{dz}\right)\cos^2\omega t \tag{1.143}$$

It is important to note that the driving voltage e in Fig. 1.49 is in the same direction for both conductors A and B and therefore (1.142) and (1.143) refer to currents flowing in the same direction. The sign of some of the terms in these equations would be changed if the two conductors form a go-and-return loop with opposing driving voltages. Bearing this fact in mind, (1.143) may be reduced to

$$F_{m,n} = \tfrac{1}{2}I_{m,p}I_{n,p}\frac{dM_{m,n}}{dz}(1-\cos 2\omega t) - \tfrac{1}{2}I_{m,p}I_{n,q}\frac{dM_{m,n}}{dz}\sin 2\omega t - \tfrac{1}{2}I_{m,q}I_{n,p}\frac{dM_{m,n}}{dz}\sin 2\omega t + \tfrac{1}{2}I_{m,q}I_{n,q}\frac{dM_{m,n}}{dz}(1+\cos 2\omega t) \tag{1.144}$$

From (1.144) it is readily understood that the mutual force consists of a component that is constant in time and a remainder that pulsates at twice the energizing frequency.

The total interconductor force between A and B is simply the sum of the elemental forces for all filament combinations that involve both conductors. Therefore

$$\begin{aligned} F_{A,B} &= \sum_{mA} \sum_{nB} F_{m,n} \\ &= \tfrac{1}{2} \sum_{mA} \sum_{nB} \frac{dM_{m,n}}{dz} (I_{m,p} I_{n,p} + I_{m,q} I_{n,q}) \\ &\quad + \tfrac{1}{2} \cos 2\omega t \sum_{mA} \sum_{nB} \frac{dM_{m,n}}{dz} (I_{m,q} I_{n,q} - I_{m,p} I_{n,p}) \\ &\quad - \tfrac{1}{2} \sin 2\omega t \sum_{mA} \sum_{nB} \frac{dM_{m,n}}{dz} (I_{m,p} I_{n,q} + I_{m,q} I_{n,p}) \end{aligned} \tag{1.145}$$

The first term of (1.145) gives the steady (nonoscillatory) interconductor force. The other two terms represent pulsating forces, and they could be combined by phasor addition. Maximum and minimum instantaneous forces could then be calculated by taking the sum and difference of the constant term and the resultant phasor amplitude.

For many conductor configurations the choice of the direction z suggests itself, as it did in the example of Fig. 1.48. When the necessary symmetry does not exist, as between sector-shaped conductors or the triangular conductors of Fig. 1.50, two directions z_1 and z_2 at right angles to each other may be chosen to obtain the orthogonal components of the resultant force.

If the filament currents have been computed by the method explained in the previous section, it is possible to determine the interconductor forces for the important case of three-core cables inside large pipes. Each filament of

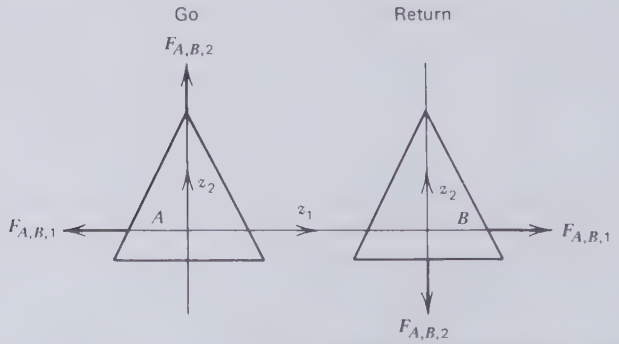

Figure 1.50 Resolution of interconductor forces between asymmetrical conductors [1.25]. (By permission of Taylor & Francis).

such a system will experience a steady lateral force and a 120-Hz pulsating lateral force. As these forces are not subject to the same time variation, they cannot be combined to a single vector. The equal and opposite reactions to this very complex electromechanical force system have to be provided by the metal lattice from which they are transferred to the structural supports. Up to the present no convenient graphic method has been found to depict the multitude of varied interfilamentary forces. Even if we do not consider the forces between filaments of the same conductor or pipe, the remaining forces still set up internal stresses in the conductors. Except for sodium, they are very small in relation to the strength of the conductors. The forces that have to be taken into account during cable design are those that result in conductor support reactions and conductor bending between point supports of vacuum-, gas-, and liquid-insulated systems. Finally, it is necessary to take note of the torque between the set of conductors and the enclosure pipe and check whether the natural frictional drag is sufficient to prevent twisting of the conductors. To obtain an overview of the force pattern, the filament forces should be resolved in the radial and the circumferential (lateral) direction. Sets of parallel components may then be combined to single forces acting through centers of forces, just as distributed gravitational forces are combined to act through the center of gravity. Figure 1.51 shows the combined forces that do exist in three-core cables. Each sector of this diagram indicates a different set of forces that are, of course, present in all three sectors of the cable.

The two combined forces indicated in sector A of Fig. 1.51 have lines of action that pass through the geometrical center of the three-phase circuit. $F_{c,s}$ is the steady outward-directed conductor force that would press against the enclosure pipe or be absorbed by a spacer ring that holds the conductors together in a bundle. $F_{s,s}$ is the steady electromechanical force on the sheath sector A. In reality, both these forces are distributed over the appropriate metal volumes. $F_{s,s}$ is balanced by hoop stress in the enclosure pipe. The fact that $F_{c,s}$ and $F_{s,s}$ do not lie along the same line of action indicates the presence of a steady mutual torque T_m between the conductor bundle and the pipe. This torque is shown graphically in sector B of Fig. 1.51. The combined pulsating forces, $F_{c,p}$ on the conductor and $F_{s,p}$ on the sheath, have been drawn as double vectors in sector C to underline their bidirectional nature and zero time-average. Their x and y components do not oscillate in phase with each other. The large x component of the pulsating conductor force arises from the fact that—unlike the y component—it is not counteracted by opposite-sense sheath currents.

As all filament currents are proportional to the load current, all forces will be proportional to the square of the load current. Using the vacuum-

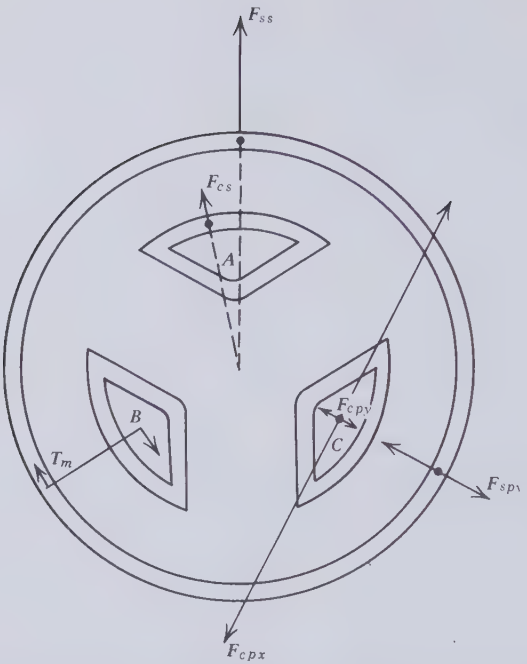

Figure 1.51 Interconductor forces and torque in a symmetrical three-core cable [1.38]. (By permission of IPC Science and Technology Press).

insulated, liquid-nitrogen-cooled cable design outlined in Section 1.15 and the computed filment currents, the force components shown in Fig. 1.51 have been calculated: (1) per unit rms load current, (2) for a full load current of 2 kA, and (3) for a symmetric fault current of 20 kA. The results of these calculations are listed in Table 1.4.

To better appreciate the significance of these forces, they might be compared with the weight of one of the aluminum conductors, which, with its liquid-nitrogen filling, is 9.6 kg/m. The full load electromechanical forces are seen to be small compared to the weight forces. However, when the cable is subject to fault currents, this is no longer true. The steady outward-directed conductor force is then equal to approximately half the conductor weight, and the support insulators have to be capable of dealing with this. The largest force is the transverse vibration force on the conductor of 19.28 kg/m. This oscillates at 120 Hz and therefore reverses direction 240 times /sec. It will be counteracted by the inertia of the conductors and restraining forces at the support insulators. A vibration amplitude up to 1 mm seems possible, but the fault current should not persist longer than a fraction of a second.

Table 1.4 Computed Interconductor Forces and Torque [1.38]

	Per Unit Rms Current (kg/m/A^2)	For Full Load Current of 2 kA (kg/m)	For Fault Current of 20 kA (kg/m)
$F_{c,s}$	1.11×10^{-8}	0.044	4.44
$F_{s,s}$	4.82×10^{-8}	0.193	19.28
$F_{c,p,x}$	18.60×10^{-8}	0.744	74.40
$F_{c,p,y}$	1.29×10^{-8}	0.052	5.16
$F_{s,p,x}$	0.11×10^{-8}	0.004	0.44
$F_{s,p,y}$	4.71×10^{-8}	0.188	18.84
	(kg-m/m/A^2)	(kg-m/m)	(kg-m/m)
T_m	0.081×10^{-8}	0.003	0.32

Source: Reprinted by permission of IPC Science and Technology Press.

The steady torque is quite small and, at any rate up to the full load current, naturally occurring frictional drag should prevent noticeable twisting of the conductors. During symmetric fault conditions, as might be produced by a three-phase short-circuit in the cable itself, the system will experience a rotational jerk, but it is unlikely to last long enough to cause much damage.

1.17 THE AC PERFORMANCE OF STRANDED CONDUCTORS

In the prior discussions of the electrodynamics of linear conductors it has been tacitly assumed that all conductors are solid rods or pipes in which the stream lines of current flow run parallel to the conductor axis. This is not necessarily true for conductors made up of wires twisted together. In the present section we examine the current flow pattern in stranded conductors and the influence this has on the ac resistance and Joule losses.

The primary purpose of the stranded construction is to make the conductor sufficiently flexible for the storage of long lengths of cable on reels. The effect stranding has on the ac resistance of the conductor has been the subject of a long-standing debate. The first series of extensive ac-dc resistance ratio measurements were carried out at the Massachusetts Institute of

Technology early in World War I [1.41, 1.42]. Kennelly and his colleagues at MIT in their first paper [1.41] concluded:

> Stranded copper or aluminum conductors, without twists, appear to have the same skin-effect impedance ratio as their equisectional solid conductors. Twisting and spiraling the strands introduces a change in the ratio, called the spirality-effect. In the very few cases of stranded conductors, thus far tested, the spirality-effect added slightly to the skin-effect.

In the second paper [1.42] it was shown that the skin effect of a seven-strand conductor could be reduced by separating the nonspiralled wires. In fact a case was made for the hyperbolic decrease of the skin-effect resistance increment with the distance of separation between the central and six peripheral wires. Arnold of the British National Physical Laboratory [1.43] reported 27 years later:

> The spirality effect in the core of a cable is an extremely small effect. If the current in a cable follows the strands, a small longitudinal magnetic field is produced, owing to the lay of the strands, and this induces eddy currents. As the layers of a cable are spiralled in opposite directions, the resultant magnetic field is very small. Furthermore, in a well-oiled cable tightly bound with insulation, the contact resistance between (copper) strands is very small, and with alternating current a great part of the current jumps from strand to strand, thus reducing the spirality effect still further. No evidence of appreciable spirality effect could be found in the cables tested, and it is therefore considered that this effect may be neglected.

Another 26 years passed until Ball and Maschio [1.44] published their measurements on large stranded segmental conductors. Their experimental data strongly suggested that, for a given metal cross section, stranding reduces the ac resistance of the conductor. These authors wrote:

> It is clear from these tests that the usefulness of the (stranded) segmental form of the conductor construction, as regards ac resistance, depends upon the elimination (as far as possible) of interwire conduction. The extent to which this is achieved cannot be assessed without tests. A satisfactory and repeatable testing method has been described.

These findings completely reversed the original views on this subject. Today there remains no doubt that in stranded aluminum conductors, the current follows the helical path of individual wires because the tough oxide coating prevents interwire conduction. Much the same seems to be true for copper wires after bending and the thermal expansion and contraction that takes place in service. Good contact points exist in newly stranded and compacted copper conductors which permit some interwire current exchange. As the cables are reeled and unreeled many cold-welded contact points break. This as well as the thermal movement and long-term oxidation apparently ensure that the copper wire surface also becomes a current barrier.

One consequence of the helical current pattern is the lengthening of the current path and the attendant increase in dc resistance. To compute this resistance it is customary to use the actual conductor length, which ignores the helical path extension, and the normal cross-sectional areas of the wires as if they were not laid up in helices, and then multiply the resistance by a stranding factor that depends on lay lengths and therefore the size of the conductor. The most common form of strand construction for high-voltage cables is the concentrically stranded conductor shown in Fig. 1.52. All its wires are of the same diameter. Six wires are twisted around a straight center wire. The next layer contains 12 wires twisted in the opposite sense to the underlying layer. By alternating the sense of twisting from layer to layer, a firm conductor is produced. Figure 1.52 also lists the numbers of wires in consecutive layers. They form an arithmetical progression with a common difference of six. The lay length, that is, the length of one complete helical turn, is usually left to the cable manufacturer's disgression, and in general it increases with every successive layer of wires. The variable lay parameter makes it difficult to give firm figures for the stranding factor. Barnes [1.34] suggests the following values:

No. of wires in conductor	7	19	37	61	91	127	169
Stranding factor	1.145	1.054	1.028	1.017	1.011	1.008	1.006

Typical conductors contain 61, 91, or 127 wires. The stranding factors for these three configurations give dc resistance increases of 1.7, 1.1, and 0.8 percent, respectively.

All that can be said with certainty about the ac resistance of a concentrically stranded conductor is that it will be greater than the dc resistance. The oxide layers on the wire surfaces do not interfere with the skin formation process in the conductor as a whole. The finite element analysis would seem

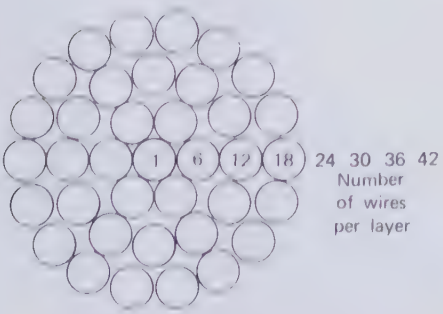

Figure 1.52 Concentric stranding.

ideally suited for computing the ac resistance of stranded conductor, but for the lack of a satisfactory mutual inductance formula for parallel helices. The mutual inductances could be developed from numerical solutions of the double integral in Neumann's formula (1.34). Up to the present time nobody appears to have undertaken this task and therefore the ac resistance of stranded conductors has to be determined by direct measurement on actual conductors. The Neumann electrodynamics permits us to make at least one qualitative statement on this subject. Because of the spaces between wires, many mutual inductances in the finite-element matrix of the stranded conductor will be smaller than the corresponding mutual inductances in the round solid conductor containing the same amount of metal. Reduced mutual induction causes the ac resistance of the stranded conductor to be smaller than the ac resistance of the solid conductor.

It has sometimes been argued [1.43] that concentric stranding and insulation between wires should suppress the proximity effect because an individual wire of the conductor under consideration will in some locations be on the near-side of the return conductor and in others on the far-side. Therefore the magnetic field of the return conductor should not be able to upset the uniform current distribution around any one of the concentric layers of wires. However, experiment contradicted this speculation and Arnold [1.43] interpreted this experimental fact as proof that interwire conduction must take place. When looked upon from the point of view of the finite-element analysis, it is by no means clear whether the proximity of the return conductor will or will not change the ac resistance of the go-conductor.

When very large conductors were first produced for selfcontained oil-paper insulated cables, a more sophisticated method of stranding was introduced, which is depicted in Fig. 1.53. Conductors made in this way are often called Milliken conductors, presumably after the name of the inventor. In the United States conductor cross sections are measured in kilocircular-mils (kcmil). One circular-mil is the cross-sectional area of a wire of 0.001 in. diam. The Milliken construction would be considered for all conductors

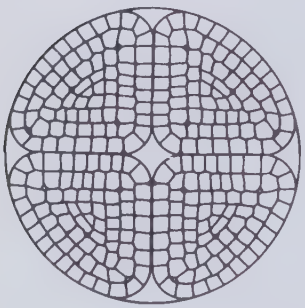

Figure 1.53 Milliken conductor.

that are larger than 2000 kcmil. A comparison of various conductor sizes is listed in Table 1.5.

The Milliken conductor consists of a number of individually stranded segments insulated from each other by a thin layer of paper. Each segment is produced by concentric stranding, followed by compacting and shaping. At the same time the segments are preformed to helices and some are insulated with paper tapes. Alternate insulated and uninsulated segmental helices are cabled together to form the finished Milliken conductor. Not shown in Fig. 1.53 is the oil duct in the center of the conductor that would only be provided for self-contained cables and not for pipe-type cables. It will be realized that a wire in the outside layer of an individual segment will change position along the cable, being sometimes near the periphery and sometimes near the center of the conductor. This transposition counteracts, to some extent, the formation of a current skin in the outer region of the conductor. In a scheme of perfect transposition each wire would for some distance occupy the position of any other wire. So perfect a scheme has the potential of eliminating all nonuniformities of current distribution. Furthermore, the current in each wire would be in phase with the currents of all other wires of the same conductor, so that no internal circulating currents would tend to flow. Machinery for achieving more or less perfect strand transposition has been proposed from time to time, but for reasons of cost it has not been adopted in practice. The Milliken conductor represents a compromise between concentric stranding and perfect strand transposition, which can be produced at reasonable cost.

In the absence of a reliable method of computing the ac resistance of stranded conductors, cable designers depend on measurements carried out on sample conductors. Measurement difficulties have no doubt contributed to the long confusion over the "spirality effect." To keep a reasonable length of a large conductor at uniform temperature is almost impossible, particularly when it carries full load current. Over the range of operating temperatures, the metal conductivity changes by 10 to 20 percent, which is of the same order of magnitude as the expected ac resistance increment. Two

Table 1.5 Comparison of Conductor Sizes

Conductor Area			Approx. Diameter	
kcmil	$in.^2$	mm^2	(in.)	Stranding
1000	0.785	507	1.15	concentric
2000	1.571	1013	1.63	concentric
3000	2.356	1520	2.10	Milliken
4000	3.142	2027	2.40	Milliken
5000	3.927	2534	2.70	Milliken

fundamentally different methods of measuring ac losses and resistances are being used. One is a caloremetric technique in which thermocouples are attached to the conductors and the sheaths. It depends on a good understanding of the operative heat-transfer mechanisms. Although it is a cumbersome method, it has the advantage of separating sheath losses from conductor losses because output heat flow rather than input electrical power is being measured. From the loss separation point of view, an electrical measurement with and without sheath is not a substitute for the calorimetric method, for the presence of sheath currents is likely to change the heat generated in the conductor.

Ball and Maschio [1.44], as well as Castelli et al. [1.45], have made use of the more convenient electrical method of determining the ac resistance of a number of large stranded conductors. Any such method has to relate the voltage drop per unit length in magnitude and phase to the load current (see Fig. 1.47). The current can be measured in two ways, either by a current transformer or by determining the potential difference across a noninductive resistance connected in series with the test conductors. For the voltage drop measurement, potential probes have to be attached to the conductors. Great care has to be taken with the measuring leads to avoid inductive pick-up from the current loop. The phase angle measurement can be accomplished with a phase sensitive voltmeter (phase angle meter) or an ac bridge technique.

Figure 1.54 outlines two different circuits for the measurement of Joule loss W_J and ac resistance R_{ac}. Circuit (a) refers to identical stranded (or nonstranded) go-and-return conductors of a total length L. The two conductors are connected in series with each other and a suitably rated noninductive resistance R_{ni}. The loop is threaded through a toroidal transformer CT and energized at the required power frequency of 50 or 60 Hz to cause the flow of a current i. This current need not necessarily be the full load current of the conductor, but it is desirable to check the proportionality between W_J and i^2 to rule out variability of interwire conduction owing to temperature changes. Furthermore, if the measurements are carried out below the normal cable operating temperatures, the results have to be extrapolated to the higher conductor temperatures. When doing this it should be recalled that the lower metal conductivity at the higher temperatures tend to weaken both the skin and the proximity effects.

By applying Kirchoff's laws to circuit (a), we find

$$e_{AB} + e_{BC} + e_{CD} = e_{AD} \tag{1.146}$$

For reasons of symmetry we can assert that

$$e_{AB} = e_{CD} \tag{1.147}$$

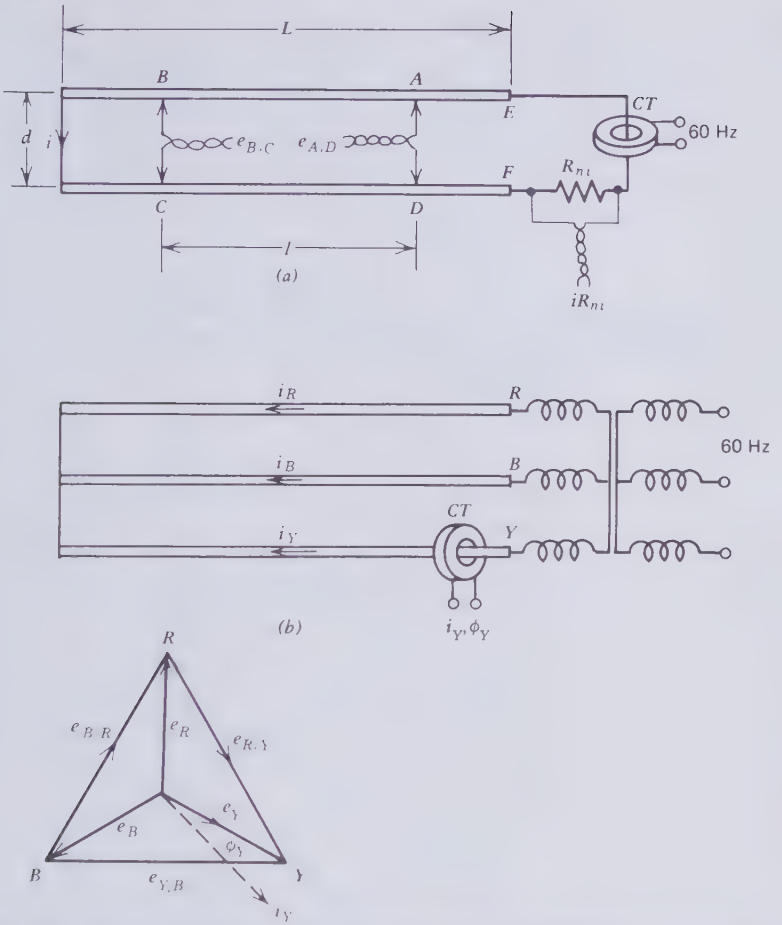

Figure 1.54 Circuits for the measurement of Joule loss and ac resistance [1.44]. (By permission of the Institute of Electrical and Electronics Engineers).

From these two equations it follows that

$$e_{AB} = \tfrac{1}{2}(e_{AD} - e_{BC}) \tag{1.148}$$

Apart from the magnitude of e_{AB} between the potential contacts A and B, we need to know the current i, which is given by the voltage across the noninductive resistance R_{nl} divided by the resistance itself. Alternatively a current transformer may be employed for the current measurement, as indicated in Fig. 1.54b. The phase angle ϕ between e_{AB} and i can be measured with a phase angle meter. For this purpose $e_{AD} - e_{BC}$ has to be

connected to one side of the meter and iR_{ni} to the other. The experimental data may then be used to calculate the Joule loss and ac resistance per unit length. With l being the distance between the potential probes we have

$$\frac{W_J}{l} = \frac{e_{AB}}{l} i \cos\phi \tag{1.149}$$

$$\frac{R_{ac}}{l} = \frac{e_{AB}}{i \cdot l} \cos\phi \tag{1.150}$$

Similar measurements may also be carried out by using just one pair of potential contacts near one end of the loop at E and F. The loss and ac resistance per unit length would then be given by

$$\frac{W_J}{2L} = \frac{e_{EF}}{2L} i \cos\phi \tag{1.151}$$

$$\frac{R_{ac}}{2L} = \frac{e_{EF}}{2L \cdot i} \cos\phi \tag{1.152}$$

The difference between (1.149) and (1.150) on the one hand and (1.151) and (1.152) on the other is that for a relatively short test length L the results calculated from the last two equations would to some extent be falsified by the end effects of the line. Spacing the potential contacts over the shorter distance l produces data which is more representative of a long line. In practice, (1.151) and (1.152) do not lead to serious errors provided L is very much greater than the distance of separation d.

The arrangement of Fig. 1.54a gives the ac resistance of parallel go-and-return conductors, which takes skin and proximity effects into account. The method may also be applied to complete cables inside metallic sheaths with or without sheath bonding. The measured Joule loss will then comprise the sheath loss, and the ac resistance has to account for the total loss.

In practice, the go-and-return circuit is of little interest because most transmission lines consist of three-phase circuits. A measurement setup for three-phase circuits is shown in Fig. 1.54b. In this example it has been assumed that the test length is sufficiently long so that end effects do not significantly diminish the calculated loss per unit length of the line. For shorter cable samples the potential probes may be applied to the middle portion of the sample, much like in Fig. 1.54a. How the measurements of i_Y, ϕ, e_{RB}, e_{BY}, and e_{YR} can be transformed to compute the Joule loss and the ac resistance will be obvious from the phasor diagram of Fig. 1.54b. In this the line voltage triangle encloses the phase voltage star. From a measurement of the phase angle between one of the currents and one of the line voltages, it is possible to compute ϕ_Y and i_Y. In a balanced system this angle is, of course,

the same for all three phases. Again, the measurement on three-phase circuits may be carried out with or without cable sheath enclosures.

One further point should be considered. With the potential points attached to the ends of the conductor it is possible to make certain that each wire in the stranded conductor is subject to the same voltage drop. When the potential probes are applied some distance along the conductor, they will only touch the outer layer of wires. Therefore, if no interwire conduction takes place, the inner wires may be subject to different voltage drops than the outer wires. The error caused by this is unknown.

The results of measurements made by Ball and Maschio on 2764 kcmil Milliken conductors are reproduced in Fig. 1.55. These findings leave no room for doubt about the beneficial effect of a thin layer of insulation on the wire surfaces that positively prevents interwire conduction. Apart from their effective oxide coatings, aluminum conductors of the same geometry as copper conductors should have a lower ac/dc resistance ratio because of the lower conductivity and therefore the smaller generalized frequency defined by (1.120). Ball and Maschio's results also suggest that without interwire conduction, the proximity effect is being completely suppressed. It should at the same time be remembered that the measured results of ac/dc resistance ratios are least reliable when this ratio approaches unity, as with the

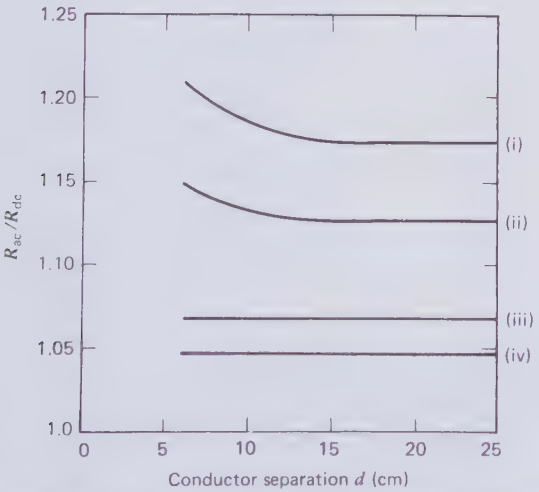

Figure 1.55 AC-DC resistance ratios of 2764 kcmil 4-sector hollow core stranded go-and-return conductors measured by Ball and Maschio [1.44] at working temperature. Curve i—Bare copper wires; contradirectional stranding. Curve ii—Bare copper wires; unidirectional stranding. Curve iii—Insulated copper wires; contradirectional stranding. Curve IV—Aluminum wires (bare); both unidirectional and contradirectional stranding. (By permission of the Institute of Electrical and Electronics Engineers).

well-insulated wire samples of Fig. 1.55. When some interwire conduction is present, the unidirectional stranding appears to be clearly superior to contradirectional stranding. This rather surprising result has not been satisfactorily explained. The interwire mutual inductances would be expected to be greater in the unidirectional cable samples, and this should have led to a reversal of the order of curves (i) and (ii) of Fig. 1.55. On the other hand if both unidirectionally and contradirectionally stranded copper conductors are compacted to the same overall diameter, more plastic deformation would be expected to occur in the contradirectional case, particularly at wire cross-over points, and this is likely to cause additional interwire conduction.

Based mainly on investigations by Wiseman [1.47] and Meyerhoff and Eager [1.48], the Underground Systems Reference Book [1.46] contains guidelines for 60-Hz skin and proximity-effect ratios for stranded copper conductors. They have been used for many years in the design of paper insulated and solid dielectric power cables. The recommended design figures for the skin effect ratio are plotted on Fig. 1.56. The graph refers to concentrically stranded and segmental (four-segments) conductors. The

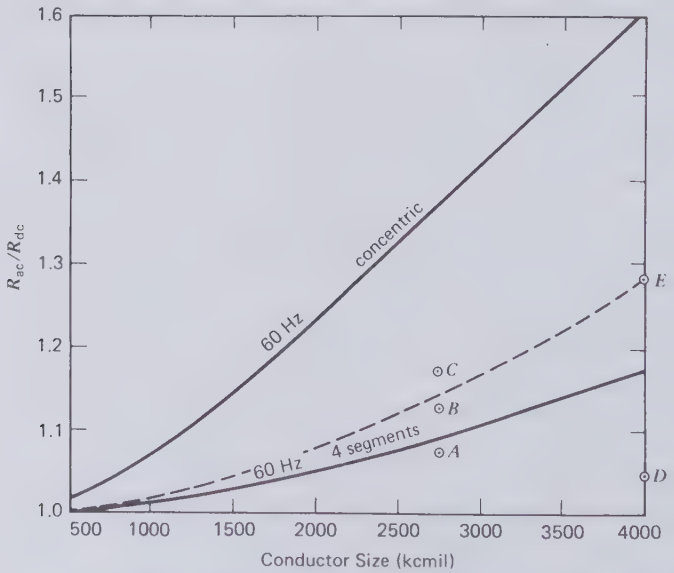

Figure 1.56 Skin effect ratio for stranded copper conductors at 65°C [1.46]. 50 Hz results of Ball and Maschio [1.44] at working temperature for six-segment conductors with oil duct: *A*—insulated wires and contradirectional stranding; *B*—bare wires and unidirectional stranding; *C*—bare wires and contradirectional stranding. 50 Hz results of Castelli et al. [1.45] at 80°C and 15 cm spacing: *D*—insulated wires; *E*—bare wires. The broken curve is recommended for bare wires with contradirectional stranding in 60 Hz pipe-type cables.

points A, B, and C on this graph represent the 50-Hz measurements carried out by Ball and Maschio [1.44] on go-and-return segmental conductors spaced 15 cm apart, when the proximity effect was negligible. Points D and E are measurements made by Castelli et al. [1.45] at 50 Hz, 80°C, and a 15-cm spacing. It would be unreasonable to expect a better agreement between design guidelines and experimental results, because of the absence of a rigorous mathematical treatment, the uncertainties in interwire conduction, and the difficulties encountered in making repeatable measurements.

An empirical formula is available [1.46] to cable designers to calculate the proximity effect in stranded copper conductors. It is based on the assumption that the skin and proximity effects are independent of each other and may, therefore, be superimposed on each other as follows

$$\frac{R_{ac}}{R_{dc}} = 1 + Y_{sk} + Y_{px} \tag{1.153}$$

where Y_{sk} accounts for the skin effect and Y_{px} for the proximity effect. If D is the diameter of the stranded conductors and d their axial separation, the empirical proximity term is given as a function of the skin term by

$$Y_{px} = k\frac{D}{d}Y_{sk} \tag{1.154}$$

Various values have been suggested for the constant k. From [1.46] the preferred values appear to be

Go-and-return circuit	$k = 1.53$
Triangular three-phase circuit	$k = 2.30$

1.18 JOULE HEATING AND MAGNETIC HYSTERESIS LOSSES IN PIPE-TYPE CABLES

In the study of pipe-type oil-paper insulated cables a new electromagnetic problem arises by way of the magnetization of the steel pipe. This magnetization is due to the load current and is therefore considered to be a conductor related problem. As the pipe losses are supplied by the same energy source that drives the current along the conductors, they are often lumped together with all the Joule losses. Much could be gained by using nonmagnetic pipes for the containment of oil pressure and the protection of the cable cores against mechanical damage and the ingress of water. Aluminum and glass-fiber-reinforced synthetic pipes have been proposed for this purpose. However, up to the present, nonmagnetic pipes have not been

adopted in practice because of the advantages steel possesses with regard to strength and cost.

At one time steel armor wires were used quite extensively for reinforcing lead covered self-contained cables, particularly for underwater installations. The high magnetic hysteresis loss has discouraged this practice. Enclosing a single conductor in an iron pipe is out of the question because the hysteresis loss would be much greater than the conductor loss. For example, if a 2500 kcmil copper conductor having an ac resistance of 5.8 $\mu\Omega$/ft would carry 1000 A, the Joule loss in the conductor would be 5.8 W/ft. When the same conductor is surrounded by an $\frac{1}{8}$-in.-thick steel pipe of 2-in. mean radius, the maximum magnetic induction in the steel would be of the order of 10 to 12 kG. An approximate measure of the magnetic hysteresis loss W_h can be obtained from the Steinmetz formula

$$W_h = 0.002 V f B_{\max}^{1.6} \cdot 10^{-7} \text{ W} \tag{1.155}$$

where V is the volume of the magnetic material in cubic centimeters, f is the energizing frequency in hertz, and $B_{\max}$ is the peak value of the magnetic induction in gauss. Taking $B_{\max} = 10$ kG, the hysteresis loss in the steel pipe comes to 9.3 W/ft and is therefore nearly twice as large as the conductor loss. If a layer of steel armor wires surrounds a lead sheath, the hysteresis loss is much less than in a steel pipe because of the reluctance in the magnetic circuit due to air gaps between wires.

The magnetic field surrounding the three conductors of a pipe-type cable is much smaller than that surrounding a single-core cable carrying the same phase current. Nevertheless, the magnetic losses of pipe-type cables are severe. Unfortunately it is virtually impossible to calculate their magnitude, and cable designers have to rely on empirical formulas or measurements. To gain some understanding of the magnetic loss mechanism we consider the three phase currents

$$\begin{aligned} i_R &= I \sin \omega t \\ i_B &= I \sin(\omega t - 120°) \\ i_Y &= I \sin(\omega t - 240°) \end{aligned} \tag{1.156}$$

From this set of balanced currents it follows that

$$i_R + i_B + i_Y = 0 \tag{1.157}$$

and therefore the instantaneous currents must form loops that are closed through the generator and the load. Referring to Fig. 1.57, the instantaneous currents circulate in one or two of the three loops $RR'B'B$, $BB'Y'Y$, and

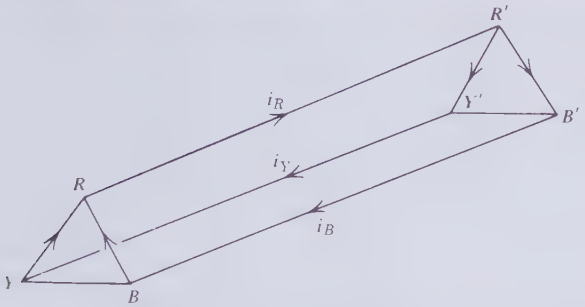

Figure 1.57 Current loops in three-phase circuit of triangular layout.

$YY'R'R$. The loop currents produce magnetic flux vectors proportional to the ampere-turns of the respective loops and perpendicular to the loop planes. Figure 1.57 depicts the particular case in which the current loops are formed by equilateral triangular conductor spacing. It will be realized that only two of the three loops can carry circulating currents at any given time. Table 1.6 lists the instantaneous phase currents for one complete cycle at 30° intervals. At any given instant we can represent the magnetic flux of the three-phase circuit by a vector Φ_{RBY}. Figure 1.58 explains how this resultant flux vector arises at the two instants when $\omega t = 90°$ and $\omega t = 240°$. In the 90° example, conductor R carries current into the plane of the paper and conductors B and Y share the return current equally. This means the active current loops of Fig. 1.57 are $RR'B'B$ and $RR'Y'Y$. They generate flux

Table 1.6 Instantaneous Currents and Ampere-Turns in the Loops of a Triangular Three-Phase Circuit

ωt	$i_R/I = \sin \omega t$	$i_B/I = \sin(\omega t - 120°)$	$i_Y/I = \sin(\omega t - 240°)$	$\Phi_{RBY} \propto AT/A$	$\alpha°$
0°	0	−0.866	+0.866	0.866	270°
30°	+0.500	−1.000	+0.500	0.866	240°
60°	+0.866	−0.866	0	0.866	210°
90°	+1.000	−0.500	−0.500	0.866	180°
120°	+0.866	−0	−0.866	0.866	150°
150°	+0.500	+0.500	−1.000	0.866	120°
180°	0	+0.866	−0.866	0.866	90°
210°	−0.500	+1.000	−0.500	0.866	60°
240°	−0.866	+0.866	0	0.866	30°
270°	−1.000	+0.500	+0.500	0.866	0°
300°	−0.866	0	+0.866	0.866	−30°
330°	−0.500	−0.500	+1.000	0.866	−60°
360°	0	−0.866	+0.866	0.866	−90°

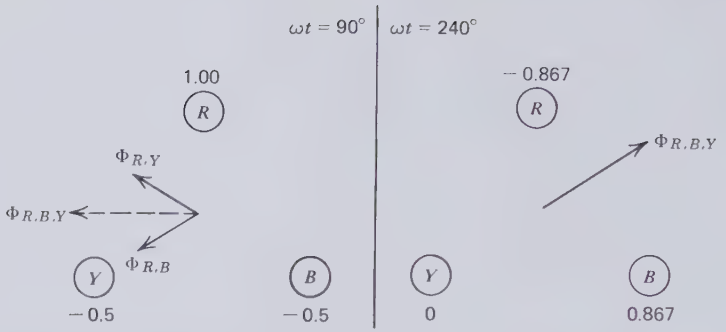

Figure 1.58 Magnetic flux vector of triangular three-phase circuit.

vectors Φ_{RB} and Φ_{RY} perpendicular to the loop planes. These two flux components may then be combined to the resultant flux Φ_{RBY}. Table 1.6 lists the instantaneous phase currents and the ampere-turns per ampere to which the resultant flux vector is proportional. It will be noted that the flux vector rotates at an angular velocity of ω rad/sec in the opposite direction to the phasor current rotation. This is shown more clearly in Fig. 1.59. Therefore the magnetic field exitation sweeps around the pipe wall at 60 rev/sec and it is reinforced by the magnetization of the steel pipe.

At the same time a set of three-phase circulating currents is induced in the pipe wall, which, broadly speaking, flows in the opposite direction of the

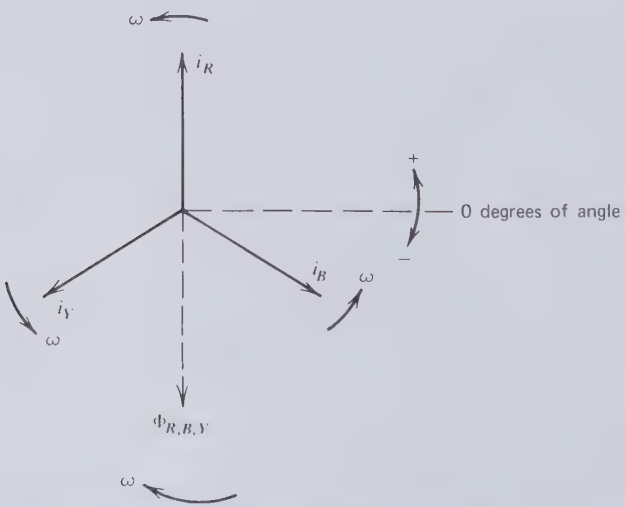

Figure 1.59 Phase rotation of currents and magnetic flux ($\omega t = 0° = 360°$).

conductor currents. The circulating pipe currents will also generate an opposite flux vector, which, but for a phase-lag, will rotate with Φ_{RBY}. The phase lag between the flux vectors results in a mutual torque, analogous to the torque in an ordinary induction motor. However, at normal operating conditions, the cable torque will be quite small and incapable of producing conductor motion against friction and other naturally occurring restraining forces. The difference in the magnitude of the two rotating fluxes gives rise to the hysteresis loss.

The conductor spacing in a pipe-type cable will not coincide with the corners of a centrally located equilateral triangle. The most likely arrangement is the cradled conductor configuration in which the three cores lie at the bottom of the pipe side-by-side. This makes it impossible to derive the hysteresis loss theoretically.

The commonly adopted empirical method of calculating the current-dependent energy loss in the metallic components of a pipe-type cable has been described by Neher and McGrath [1.19]. It is based on the formula

$$\frac{R'_{ac}}{R_{dc}} = 1 + 1.7Y_c + 1.7Y_s + Y_p \tag{1.158}$$

R_{dc} is the dc resistance per unit length of one conductor at the appropriate temperature. As far as (1.158) is concerned R'_{ac} is the effective resistance of the cable, which, when multiplied by the square of the current, accounts for all the current-dependent losses in the pipe-type cable. $Y_c R_{dc} = (Y_{sk} + Y_{px}) R_{dc} = R_{ac}$ is the ac resistance of the conductor alone due to skin and proximity effects and the dc resistance. $R'_s = Y_s R_{dc}$ is a resistance component that stands for the Joule loss in the shield and skid wire assembly. Similarly $R'_p = Y_p R_{dc}$ multiplied by the square of the conductor current gives the pipe magnetic and Joule losses. No justification for the existence nor the magnitude of the 1.7-factor has been provided by Neher and McGrath [1.19]. It seems to have been introduced as a safety factor in case the pipe circulating currents and magnetization further disturb the current distribution in the conductor and the shield.

The finite-element analysis of a three-conductor cable in Section 1.15 actually indicated that an aluminum pipe would reduce Y_c rather than increase it. Furthermore, as has been demonstrated by Ball and Maschio [1.44], the measured value of Y_c varies considerably with interwire conduction. This can be seen on Fig. 1.56. Instead of using the 1.7-factor, therefore, it is here proposed to take Y_c from the broken curve on Fig. 1.56 which holds for 60 Hz segmental conductors of bare wires. This curve will give approximately the same conductor loss as the lower 60-Hz four-segment curve when the latter is multiplied by the 1.7-factor.

For deriving the electrostatic shield and skid wire component Y_s, Neher and McGrath [1.19] compute the mutual inductance between the shield and the enclosed conductor by a formula that involves the axial spacing between the cable cores. In Section 1.12 it has been shown that the correct expression of this mutual inductance per unit length is (1.94). It will result in a value of Y_s that is greater than the one computed by the Neher-McGrath formula and there is then no need for the application of the 1.7-factor.

Hence we may write the effective resistance R'_{ac} per unit length of one conductor of a pipe-type cable as

$$R'_{ac} = R_{ac} + R'_s + R'_p \tag{1.159}$$

$$R_{ac} = (1 + Y_c)R_{dc} = (1 + Y_{sk} + Y_{px})R_{dc} \tag{1.159a}$$

The effective shield resistance may be derived from (1.104), or

$$R'_s = \frac{R_s}{1 + (R_s/\omega M_{c,s})^2} \tag{1.159b}$$

in which R_s is the dc resistance of the shield and skid wire assembly.

Neher and McGrath [1.19] suggest the following empirical formula for the resistance component R'_p which must account for the magnetic and circulating current losses in the steel pipe

$$R'_p = Y_p R_{dc} = (0.34S + 0.175D_p) \times 10^{-6}\ \Omega/\text{ft} \tag{1.159c}$$

where S is the average axial spacing between the cable cores in inches and D_p is the inside diameter of the steel pipe in inches.

1.19 CABLE INDUCTANCE AND VOLTAGE DROP

The inductance of a cable is governed by the design of the conductors and other metallic components, as well as the current distribution over the metallic sections and the magnetization of ferromagnetic materials. The inductance measures the ability of the cable to store the electromagnetic energy associated with current flow. In ac systems this energy is reversibly stored and withdrawn at twice the energizing frequency. Part or all of it will be exchanged with reversibly stored electrostatic energy in the cable capacitance. Any remainder has to be transported to and from remotely located generators, reactors, and transformers. The maximum amount of electrostatically stored energy is fixed by the line voltage and independent of the

load current. However the inductive energy increases with current. For a certain load current, therefore, the energy stored in the inductance is equal to the energy stored in the capacitance, resulting in a resonance condition. Sending- and receiving-end voltages will then be the same, but for a displacement in phase, and no reactive power is exchanged via the line terminals. The amount of power transmitted with this current flowing is known as the surge impedance loading (SIL) of the line. If V is the line voltage and Z_s the surge impedance, the surge impedance loading is given by

$$SIL = \frac{V^2}{Z_s} \tag{1.160}$$

The next equation defines the surge impedance.

$$Z_s = \sqrt{\frac{L}{C}} \tag{1.161}$$

where L is the cable inductance and C the cable capacitance. Surge impedance loading becomes important for very long ac transmission lines. It can avoid the transportation of large amounts of idle reactive energy over several hundred miles and save the attendant line heating losses. Overhead lines are predominantly inductive and their surge impedance loading requires the reduction of current below thermally permissible limits. Cables, on the other hand, are predominantly capacitive and to achieve surge impedance loading the current would normally have to be increased to levels that lie above the thermal limit. One of the advantages claimed for superconducting cables is that their higher current carrying capability makes surge impedance loading possible [1.49]. The same objective can be achieved with low capacitance cables containing gaseous or vacuum insulation.

It has already been shown in Section 1.15 how to compute the self-inductance of a conductor when the current flowing in the subdivided filaments is known. The relevant inductance formula is (1.135). It contains the sum of the quadrature components of all the filament currents that make up the conductor. Furthermore, (1.135) also accounts for the stored energy associated with sheath and pipe currents.

The self-inductance of an isolated straight conductor carrying a uniformly distributed current is, according to Maxwell [1.15], equal to the mutual inductance between two parallel filaments separated by the geometric mean distance of the conductor cross section. Equation (1.46) explains that this particular mutual inductance is the average of all possible mutual inductances of the filament combinations that make up the conductor.

A well-known formula of the self-inductance per unit length of a parallel go-and-return wire line of length L is

$$\frac{L_i}{L} = \frac{\mu}{\pi} \ln\left(\frac{R}{a}\right) \quad H/m \tag{1.162}$$

where the permeability of vacuum is $\mu = 4\pi.10^{-7}$ (MKS units). R denotes the axial spacing of the wires and a the wire radius. This result has been derived from the flux linkage picture in which the self-inductance is equated to the flux linked by the circuit divided by the current in the circuit. A formal proof of (1.162) which makes use of the magnetic vector potential has been published by Silvester [1.50]. Without referring to the vector potential, it can be shown that the magnetic flux density outside a wire carrying a current i is given by

$$B = \frac{\mu i}{2\pi r} \tag{1.163}$$

Now consider the area $ABCD$ of Fig. 1.60. The magnetic flux of conductor one linking this area is

$$\Phi_1 = \int_0^X \int_a^R B\, dr\, dx = \frac{\mu i}{2\pi} \int_0^X \int_a^R \frac{1}{r}\, dr\, dx \tag{1.164}$$

or

$$\Phi_1 = \frac{\mu i X}{2\pi} \ln \frac{R}{a} \tag{1.165}$$

As the current in the second conductor flows in the opposite direction, it will add an equal amount of flux to the slightly shifted area $A'B'C'D'$. Although these areas do not exactly coincide, the self-inductance per unit length of the parallel wire line is usually taken to be

$$\frac{L_i}{L} = \frac{2\Phi_1}{iX} \tag{1.166}$$

The self-inductance formula (1.162) is then obtained by substituting (1.165) into (1.166). The resulting formula does not allow for the magnetic flux inside the wires (internal inductance) and is therefore an approximation to a more exact expression which will now be derived with the help of Neumann's formula and Fig. 1.61.

Conductors 1 and 2 of the go-and-return two-wire line have to be replaced by a pair of filaments m and n. They are separated by the GMD of the circular wire section which is $d = 0.7788a$. The loop is imagined to be completed at the remote ends through the generator and the load. In the

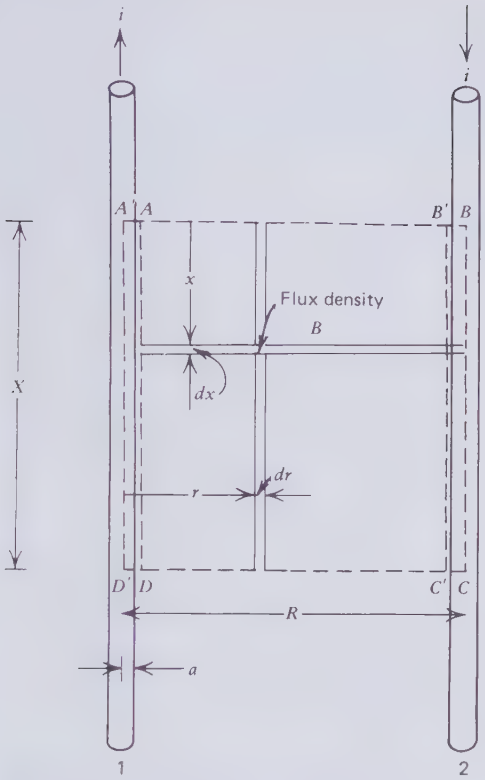

Figure 1.60 Flux linkage of parallel wire line.

vectorial form of Neumann's formula, the filament elements *dm* and *dn* are vectors in the direction of current flow.

$$M_{m,n} = \int_m \int_n (1/r)\,\mathbf{dm}\,\mathbf{dn} \tag{1.167}$$

where r is the distance between the element pair. The cosine of the angle of inclination between the filament elements is either $+1$ or -1 because the filaments are parallel lines and the angle is either 0 or 180°. Therefore (1.167) may be split into four terms as follows

$$M_{m,n} = (M_{m,n})_1 + (M_{m,n})_2 - (M_{m,n})_{1,2} - (M_{n,m})_{1,2} \tag{1.168}$$

The first term is the mutual inductance between m and n in conductor 1. The second term is the mutual inductance between m and n in conductor 2. These two terms are equal and assist each other. The third term of (1.168) is

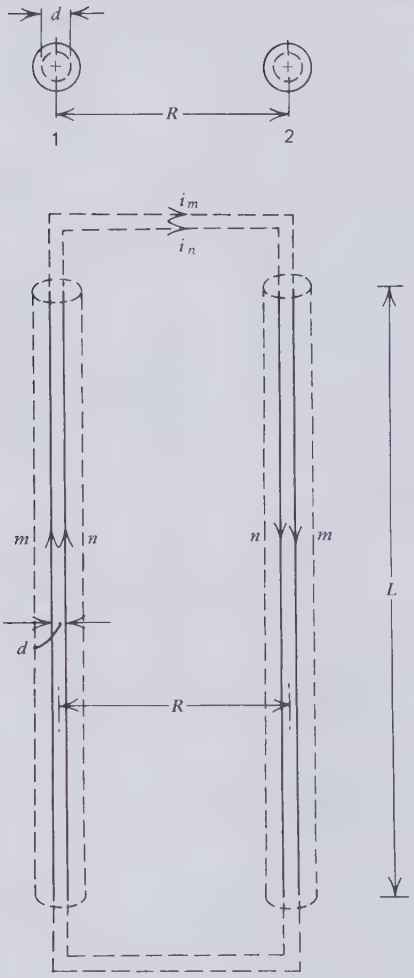

Figure 1.61 Self-inductance of two-wire line by Neumann's formula.

the mutual inductance between m in conductor 1 and n in conductor 2. This term is negative because the angle of inclination for all element combinations is 180°. Similarly, the fourth term is the mutual inductance of n in conductor 1 and m in conductor 2. The distance of filament separation to be used in the evaluation of the first two terms is clearly $d = 0.7788a$. But what is the distance of separation for the third and fourth term? At the top of Fig. 1.61, it is shown that the two representative filaments may be imagined to lie diametrically opposite anywhere on a circle that is coaxial with the wire and has the GMD of the wire section as diameter. Now it seems logical that the

filament separation for the last two terms of (1.168) should be the GMD of two circles which, from Maxwell's work [1.15], is known to be equal to the distance between the centers of the two circles. This is the distance R indicated on Fig. 1.61. Therefore the last two terms of (1.168) are equal. If we use approximation (1.36) for the mutual inductance between straight and parallel lines, (1.168) may be written

$$M_{m,n} = 2\times 2L(-1+\ln 2L-\ln d)-2\times 2L(-1+\ln 2L-\ln R) \quad (1.169)$$

This reduces to

$$\frac{M_{m,n}}{L} = \frac{L_i}{L} = 4\ln\frac{R}{d} \quad (1.170)$$

If this equation is expressed in MKS units it becomes

$$\frac{L_i}{L} = \frac{\mu}{\pi}\ln\frac{R}{d} \quad \text{H/m} \quad (1.171)$$

A comparison of (1.171) with (1.162) now shows that to obtain the exact expression of the self-inductance of the two-wire line, the GMD of the wire cross section has to be substituted for the wire radius in the formula that has been derived from flux linkage considerations. As would be expected, the exact formula gives a somewhat larger self-inductance, the difference being due to the flux linkage inside the wires.

The cable literature often describes the geometric mean distance (GMD) of a circular area as its geometric mean radius (GMR). The GMD can be associated with many different geometries apart from the circle. It is a distance between two points that bears no particular relationship to circles. Since the introduction of the finite-element analysis in the 1960s, the GMD has become quite important to the understanding of the conductor electrodynamics. To avoid any possible confusion the use of the term geometric mean radius will be avoided.

The GMD of a stranded conductor is greater than the GMD of the solid round conductor of the same cross-sectional area. The spaces between wires are responsible for increasing the average distance between filaments. This reduces the mutual inductances and with them the conductor self-inductance. The simple seven-strand conductor of Fig. 1.62 can be readily analyzed, provided it is assumed that the wires are not twisted about the axis and the current is distributed uniformly over all seven wires. We are then justified in treating each wire as a filament (finite element) and could write down the 7×7 mutual inductance matrix. The elements along the principal diagonal would be the wire self-inductances having a GMD of $0.7788r$,

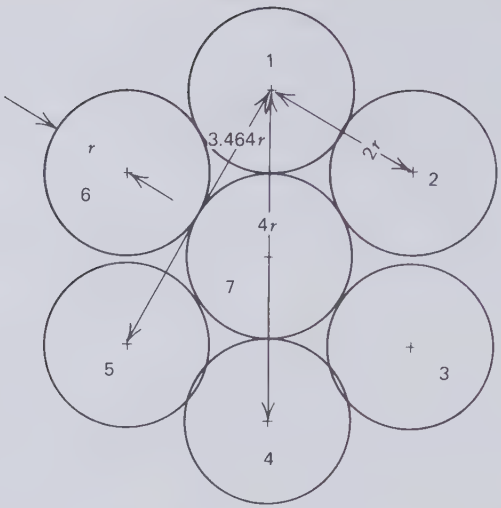

Figure 1.62 7-Strand conductor. GMD of single wire = 0.7788 r.

where r denotes the wire radius. However, according to (1.36), each mutual inductance may be written

$$M_{m,n} = C - \ln xr = C - \ln x_{m,n} - \ln r \tag{1.172}$$

where C and r are the same for each wire. Therefore to find the average of $M_{m,n}$ we need only find the average of $\ln x_{m,n}$. Figure 1.62 indicates that $x_{m,n}$ has the four distinct values of 0.7788, 2, 3.464, and 4. The logarithm of the average value of $x_{m,n}$ for all possible filament combinations is the GMD_7 of the seven-strand conductor.

$$\ln(\text{GMD})_7 = (1/49) \sum_{m=1}^{7} \sum_{n=1}^{7} \ln x_{m,n} + \ln r \tag{1.173}$$

The $\ln x_{m,n}$ matrix is written out in full in Fig. 1.63. Much of the information listed in this matrix is redundant because of the symmetries of the seven-strand configuration. It will be readily understood that the column sums of wires 1 to 6 must be the same. From this matrix it will be found that

$$(1/49) \sum_{m=1}^{7} \sum_{n=1}^{7} \ln x_{m,n} = 0.7778 = \ln 2.1766$$

Therefore the GMD of the seven-strand conductor is $2.18r$. The GMD of a solid rod of the same cross-sectional area as the seven-strand conductor

m	$n=1$	$n=2$	$n=3$	$n=4$	$n=5$	$n=6$	$n=7$
1	−0.250	0.6931	1.2424	1.3863	1.2424	0.6931	0.6931
2	0.6931	−0.250	0.6931	1.2424	1.3863	1.2424	0.6931
3	1.2424	0.6931	−0.250	0.6931	1.2424	1.3863	0.6931
4	1.3863	1.2424	0.6931	−0.250	0.6931	1.2424	0.6931
5	1.2424	1.3863	1.2424	0.6931	−0.250	0.6931	0.6931
6	0.6931	1.2424	1.3863	1.2424	0.6931	−0.250	0.6931
7	0.6931	0.6931	0.6931	0.6931	0.6931	0.6931	−0.250
$\sum_{m=1}^{m=7} \ln x_{m,n} =$	5.7004	5.7004	5.7004	5.7004	5.7004	5.7004	3.9086

$$\sum_{m=1}^{7} \sum_{n=1}^{7} \ln x_{m,n} = 38.111$$

Figure 1.63 $\ln x_{m,n}$ matrix of 7-strand conductor.

would be $2.06r$. For a conductor of 1000 m length made up of 7×61.2 mil (AWG 6) strands, this works out to a reduction of self-inductance of approximately 0.5 percent. It is a relatively small effect, which becomes larger as the number of wires in the conductor increases.

From (1.173) it can be seen that the GMD of a stranded conductor is proportional to the wire radius r. The $(\text{GMD})_g$ of a g-strand conductor may therefore be expressed as

$$(\text{GMD})_g = C_g \sqrt{A} \tag{1.174}$$

where C_g is a stranding coefficient for which the figures of Table 1.7 have been calculated according to [1.46]. To obtain the GMD in mils, the total conductor cross-sectional area A in (1.174) has to be expressed in circular-mils. When the conductor section is given in square millimeters, the stranding coefficient has to be multiplied by $\sqrt{4/\pi}$ to obtain the GMD in millimeters, or

$$(\text{GMD})_g = \sqrt{\frac{4}{\pi}}\, C_g \sqrt{A} \tag{1.175}$$

The decrease in inductance in large stranded conductors may now be estimated with the aid of Table 1.7 and (1.174) and (1.175). For example, in the case of a 2000 kcmil conductor made up of 127×125.5 mil wires, stranding reduces the inductance by 1.3 percent, which is still a small change.

Table 1.7 Stranding Coefficients for Self-Inductance Calculations

No. of wires	C_n
1	0.389
3	0.422
7	0.411
12	0.456
19	0.434
27	0.458
37	0.442
61	0.445
91	0.446
127	0.447
169	0.448
217	0.448
271	0.449

The GMD, and therefore the self-inductance, of round tubular conductors may be computed from Fig. 1.33. Round tubes have a smaller self-inductance than solid round rods of the same cross-sectional area because of the spreading apart of filaments. The tube formula in Fig. 1.33 may be used to make an order of magnitude estimate of the reduction of self-inductance due to skin current concentration. For example, if we take the 2000 kcmil stranded conductor, which has an overall diameter of 1.632 in., and assume that the current is uniformly distributed over an anular region of the same outside diameter and half that diameter on the inside, we would find a 2 percent reduction in self-inductance due to the "skin effect." This very rough estimate indicates that the stranded construction together with current skin formation may bring about an inductance reduction in the range of 1 to 10 percent.

For a go-and-return circuit of straight parallel conductors, the self-inductance per unit length is given by the two-wire line formula (1.171) provided the GMD of the stranded conductor is substituted for d.

Of greatest interest is the three-phase circuit because of its wide application in the field of power transmission. As has been explained before, a rigorous derivation of the self-inductance requires the finite-element analysis. Adequate approximations, however, are found quite easily for balanced circuits not involving sheath currents nor magnetic materials. These approximations are useful for crossbonded circuits using self-contained cables. If we label the three conductors 1, 2, and 3, which have driving voltages e_1, e_2, and e_3 applied along their lengths L and carry the balanced currents i_1, i_2, and i_3, we may equate the resistive voltage drop in each conductor to the

difference between the driving voltage and the back emf created by self- and mutual induction. If R and L_t are the resistance and self-inductance of an isolated conductor, and $M_{m,n}$ the mutual inductance between two of the conductors, we may write

$$i_1R = e_1 - (j\omega L_t i_1 + j\omega M_{1,2} i_2 + j\omega M_{1,3} i_3) \tag{1.176}$$

$$i_2R = e_2 - (j\omega L_t i_2 + jM_{2,3} i_3 + j\omega M_{2,1} i_1) \tag{1.177}$$

$$i_3R = e_3 - (j\omega L_t i_3 + j\omega M_{3,1} i_1 + j\omega M_{3,2} i_2) \tag{1.178}$$

The set of balanced three-phase currents requires that

$$i_1 + i_2 + i_3 = 0 \tag{1.179}$$

$$\begin{aligned} i_1 &= I\sin\omega t \\ i_2 &= I\sin(\omega t - 120°) = -0.5i_1 - 0.866ji_1 \\ i_3 &= I\sin(\omega t - 240°) = -0.5i_1 + 0.866ji_1 \end{aligned} \tag{1.180}$$

After substituting (1.180) into (1.176) and rearranging the terms, the impedance of conductor 1 is found to be

$$Z_1 = \frac{e_1}{i_1} = R + 0.866\omega(M_{1,2} - M_{1,3}) + j\omega[L_t - 0.5(M_{1,2} + M_{1,3})] \tag{1.181}$$

To find Z_2 we have to shift the phase of the currents of (1.180) through 120° so that

$$\begin{aligned} i_2 &= I\sin\omega t \\ i_3 &= I\sin(\omega t - 120°) = -0.5i_2 - 0.866ji_2 \\ i_1 &= I\sin(\omega t - 240°) = -0.5i_2 + 0.866ji_2 \end{aligned} \tag{1.182}$$

Substitution of (1.182) into (1.177) and rearrangement of the terms results in

$$Z_2 = \frac{e_2}{i_2} = R + 0.866\omega(M_{2,3} - M_{2,1}) + j\omega[L_t - 0.5(M_{2,3} + M_{2,1})] \tag{1.183}$$

It will be readily appreciated that repeating this process for the third

conductor yields

$$Z_3 = \frac{e_3}{i_3} = R + 0.866\omega(M_{3,1} - M_{3,2}) + j\omega[L_i - 0.5(M_{3,1} + M_{3,2})] \tag{1.184}$$

The following three conductor arrangements have to be considered:

1. Equilateral triangular conductor spacing

$$M_{1,2} = M_{2,3} = M_{3,1}$$

2. Regularly spaced conductors in flat formation

$$M_{1,2} = M_{2,3} \neq M_{3,1}$$

3. Irregular conductor spacing

$$M_{1,2} \neq M_{2,3} \neq M_{3,1}$$

The resistive terms of the three impedances depend on the difference between two mutual inductances. When the conductors are positioned at the corners of an equilateral triangle, this difference is zero. In the other two conductor arrangements the resistive term is modified by two mutual inductances because of the transfer of loss power between the conductors.

Equations (1.181), (1.183), and (1.184) show that the effective phase inductances are

$$L'_{i,1} = L_i - 0.5(M_{1,2} + M_{1,3}) \tag{1.185}$$

$$L'_{i,2} = L_i - 0.5(M_{2,3} + M_{2,1}) \tag{1.186}$$

$$L'_{i,3} = L_i - 0.5(M_{3,1} + M_{3,2}) \tag{1.187}$$

This proves that the self-inductance of an individual conductor is reduced by the presence of the two other conductors. It acknowledges the magnetic field cancellation that occurs when the conductors of a three-phase circuit are being brought together. Finally it should be noted that the effective phase inductances, rather like the self-inductance of a go-and-return circuit, are inductance differences that eliminate the nonlinear length dependence of solutions (1.35) and (1.36) of Neumann's mutual inductance formula.

To illustrate the use of the effective inductance formulas, let us consider a three-phase circuit of length L installed in a regularly spaced flat formation consisting of three 2000-kcmil stranded conductors. Denote the GMD of the conductors by d and the axial spacing between adjacent conductors by s, and

let 1 and 3 be the outside conductors. Then from (1.36) and (1.185) to (1.187)

$$\frac{L'_{i,1}}{L} = -\ln d^2 + \ln 2s^2 = \ln \frac{2s^2}{d^2}$$

$$\frac{L'_{i,2}}{L} = -\ln d^2 + \ln s^2 = \ln \left(\frac{s}{d}\right)^2$$

$$\frac{L'_{i,3}}{L} = L'_{i,1}/L$$

The GMD is $d = 0.632$ in. from (1.174) and Table 1.7. If $s = 12$ in. we find that

$$\frac{L'_{i,1}}{L} = 6.58 \text{ emu} = 6.58 \times 10^{-7} \text{ H/m}$$

$$\frac{L'_{i,2}}{L} = 5.88 \text{ emu} = 5.88 \times 10^{-7} \text{ H/m}$$

It is instructive to compare these results with the self-inductance per unit length of an isolated conductor. If $L = 1000$ m, this comes to

$$\frac{L_i}{L} = 21.5 \text{ emu} = 21.5 \times 10^{-7} \text{ H/m}$$

Enclosing the three conductors inside a nonmagnetic pipe would further reduce the effective cable inductance because the pipe currents would flow in opposite directions to the adjacent conductor currents and thereby produce additional magnetic field cancellation. The finite-element analysis explained in Section 1.15 would have to be employed to determine the magnitude of this effect. Up to the present time this analytical technique has not been adapted for dealing with ferromagnetic pipes. Hence to calculate the effective inductance of oil-paper insulated pipe-type cables, we have to rely on an empirical method, which, nevertheless, has proved adequate for most practical purposes.

Such a method for computing the reactance of pipe-type cables is outlined in [1.46, pp. 10–40]. The estimation charts plotted on Figs. 1.64 and 1.65 for concentrically and segmentally stranded conductors have been derived from empirically calculated data that has been published in [1.33, p. 74]. These graphs indicate that the effective inductance of pipe-type cables is quite small in spite of the presence of the magnetic pipe material. It will further be seen that the segmental conductor construction slightly increases the effective inductance because of the more uniform current distribution over the conductor cross section.

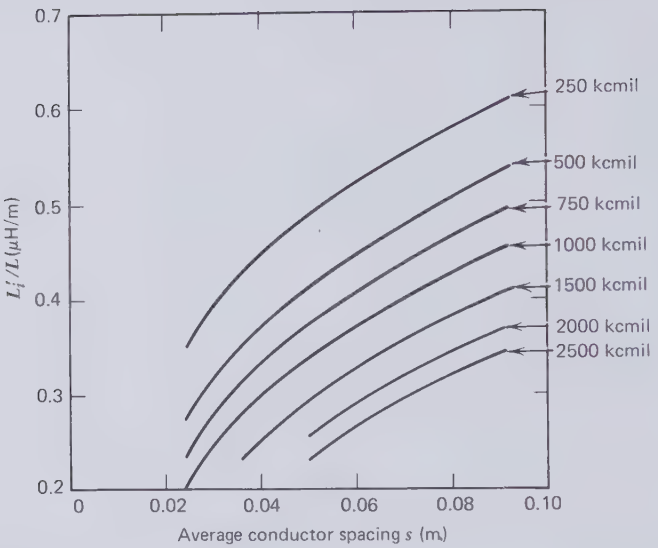

Figure 1.64 Self-inductance per unit length of oil-paper insulated pipe-type cables with concentrically stranded conductors.

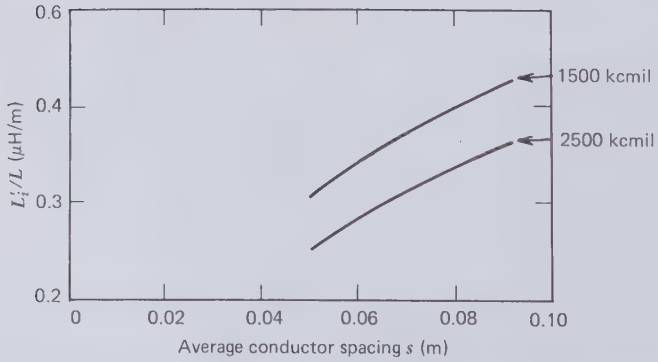

Figure 1.65 Self-inductance per unit length of oil-paper insulated pipe-type cables with segmentally stranded conductors.

1.20 COPPER

The metal that took man out of the stone age also introduced him, 10,000 years later, to the electrical era. Copper is second only to silver in electrical conductivity at ambient temperatures. Before the reduction of aluminum ore was invented in 1886, copper was the obvious choice for conveying electrical power over short and long distances. Even today it is preferred to aluminum whenever the conductor cross section has to be kept small. Oil-paper insulated high-voltage cables show how savings in sheath metal and paper insulation can be adequate compensation for the higher cost of copper.

Copper heralded the bronze age because sufficient quantities were found in nature in the metallic state. That the metal survived in this state on the geological time scale testifies to its corrosion resistance, which is a factor in the choice of conductor metals. If metallic aluminum was deposited in the early history of the earth's crust, it would long have withered to dust and caked to clay. Mechanically strong metals are usually poor electrical conductors. Copper represents a good compromise between strength and high conductivity.

The combination of malleability, strength and corrosion resistance have made copper alloys indispensable for the manufacture of ammunition. The two World Wars were a serious drain on copper resources. This strategic importance of copper has led to violent fluctuations of copper prices, which have been and continue to have an unsettling effect on the cable industry.

Apart from the rich copper deposits found and worked by Native Americans in the Lake Superior region, copper ore was discovered in Massachusetts as early as 1632. Since then Arizona, Montana, and Michigan have become the major copper producing states. Large copper suppliers on the international scene are Chile, central and southern Africa, Canada and Australia. Sulfide ores are the principal source of copper. Before smelting, the ore has to be crushed, milled, and concentrated by floatation methods. The first smelting process is carried out in a reverberatory furnace and produces copper matte, which is still rich in sulfides. Additional concentration of the metal is achieved with converter furnaces that produce blister copper of 99 percent purity. Sulfide dioxide blisters of the still porous and brittle copper gave rise to this name. Blister copper has to be refined to a purity in excess of 99.9 percent in order to arrive at tough-pitch copper suitable for electrical conductors. Electrolytic and fire refining methods are being used in the production of tough-pitch copper that may still contain up to 0.05 percent of oxygen. Several techniques are being employed for removing the oxygen to create oxygen-free high-conductivity (OFHC) copper, which has certain advantages particularly with regard to welding. Refined electrical grade copper is normally cast into "wire bars." They are

approximately 54 in. long and 4×4 in. in cross section, weighing 250 to 275 lb. The wire bars are converted to rod by hot rolling. After removal of the oxide surface, the rod can be drawn down to wire. The finished copper conductor should be as fully annealed as possible. Plastic strain due to cold working can decrease the conductivity at ambient temperature by as much as 2 percent.

In 1913 an International Annealed Copper Standard (IACS) was laid down by the International Electrotechnical Commission. According to this standard, 100 percent IACS conductivity copper will make the resistance of a wire, 1 m long and weighing 1 g, equal to 0.15328 Ω at 20°C, provided the density of the metal is 8.89 g/cm^3. On this scale, commercial high-conductivity copper usually exceeds 100 percent IACS. Certified OFHC copper has a conductivity of at least 102 percent IACS. Accurate measurements of the electrical conductivity of copper samples are quite difficult. The time-honored method first developed by Kelvin is designed for the specific purpose of giving the resistance per unit length of wires, stranded conductors, busbars, and other linear conductors. It requires an axial dc current to be passed along the conductor and the measurement of the potential drop over a shorter section, removed from the current contacts, by two contact probes. The potential drop over the accurately measured test section divided by the dc current is equal to the resistance between the potential probes. The conductivity can be calculated from this resistance, but the accuracy is usually low (1 to 2 percent) because of uncertainties in the average cross-sectional area of relatively long conductors.

A more accurate noncontact method, relying on induced eddy currents, has been described by Graneau [1.51]. This can be applied to accurately machined and compact metallic specimen. An appropriate measurement circuit is given in Fig. 1.66. It involves two sets of similar mutual inductance coils. They may consist of a single layer bifilar winding on a dielectric core tube. In this method a test specimen X of unknown conductivity σ_x is compared with a standard specimen S of known conductivity σ_s. The standard and test specimen may simply be short round rods of equal diameter and length that fit snuggly inside the core tubes of the S and X coils. The simple shape and compact size of the test objects, as well as the ease with which they may be maintained at uniform temperature, are significant advantages of this technique.

As shown in Fig. 1.66, the series-connected primary coils are energized by a variable-frequency oscillator. The energizing current is also passed through an accurate current meter and a noninductive resistance. The required frequency spectrum depends on the conductivity and size of the specimen. A band extending from 20 to 20,000 Hz is adequate for normal conductor metals at ambient temperature in the form of rods from 0.25 to

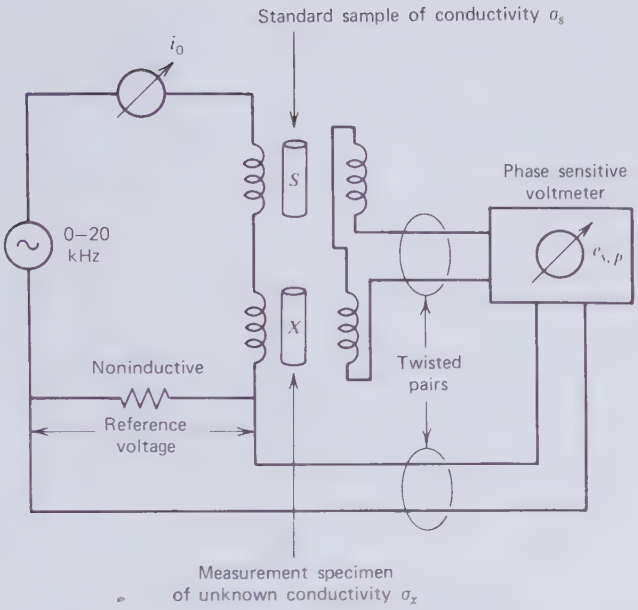

Figure 1.66 Eddy current method of measuring electrical conductivity [1.51].

1.00 in. diam and a few inches long. The energizing current may be derived from the voltage drop across the noninductive resistance or be directly measured by a thermojunction galvanometer. The secondary windings of the two mutual inductances are connected in opposition and the component $e_{s,p}$ of the difference-voltage induced in the secondaries that acts in phase opposition to the primary current i_0 is measured with a phase-sensitive voltmeter. The desired conductivity ratio σ_x/σ_s may then be derived from the measurements by the following reasoning.

Consider just one set of the mutual inductance coils. The voltages acting around the primary loop are the externally applied voltage e_0, the back emf e_b and the resistive voltage drop of the primary coil i_0R, where R is the coil resistance. These quantities are depicted as phasors in Fig. 1.67. In this diagram the back emf is further resolved into an in-phase and a quadrature component with respect to the energizing current i_0. The in-phase component must be equal to

$$e_{b,p} = i_0 R_e \tag{1.188}$$

where R_e stands for the "eddy current resistance" of the conducting core.

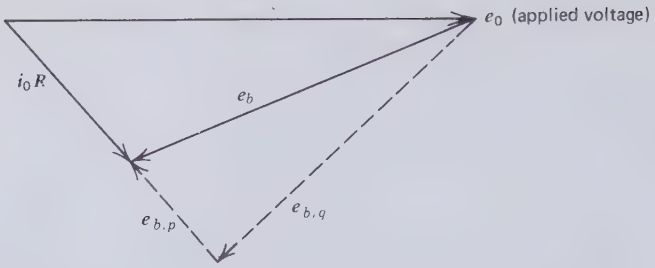

Figure 1.67 Phasor diagram for one primary coil of Fig. 1.66.

The total energy loss in one set of coils with the metallic core is

$$W = i_0^2(R + R_e) \tag{1.189}$$

The core loss alone is

$$W_e = i_0^2 R_e \tag{1.190}$$

Now if the mutual inductance coils are a bifilar winding, the induced secondary voltage e_s will be virtually equal to the back emf e_b of the primary. When the secondary winding consists of a different number of turns wound separately on top or below the primary winding, the voltages e_b and e_s will still be in phase with each other, but their amplitudes will differ by a constant k. In general, therefore

$$e_b = ke_s \tag{1.191}$$

The phase-sensitive voltmeter measures only that component of e_s which is in phase opposition with i_0. Let this be denoted by $e_{s,p}$. It is related to the eddy current resistance of the core by

$$R_e = k\frac{e_{s,p}}{i_0} \tag{1.192}$$

It will not be proved here that the eddy current resistance is a single valued function

$$R_e = k\omega F(\omega\sigma) \tag{1.193}$$

of the energizing frequency and the core conductivity. The function F can be mathematically defined with finite-element analysis and the power series expansion of the inverse mutual inductance matrix, or the power series may

be directly derived from an interaction diagram [1.51]. For the purpose of relative conductivity measurements, the function F is ascertained experimentally by measuring the eddy current resistance of the standard core over a range of frequencies. During these measurements the test core X is removed from the measurement circuit of Fig. 1.66. For this condition we may write from (1.192) and (1.193)

$$R_{e,s} = k\frac{e_{s,p}}{i_0} = k\omega F(\omega, \sigma_s) \tag{1.194}$$

If $R_{e,s}$ is plotted against the variable frequency ω we obtain a graph as OS in Fig. 1.68. The second curve OX on the same graph is obtained by inserting core X in the appropriate coil set and measuring the difference voltage induced in the secondaries, which is proportional to the eddy current resistance difference $R_{e,s} - R_{e,x}$. This latter difference is added to the standard curve OS. The result is curve OX of Fig. 1.68, which represents the eddy current resistance of the specimen core X. If a straight line OXS is drawn through the origin of the graph so that it intersects both curves and if this line is inclined at an angle θ to the abscissa we have

$$\begin{aligned} &\text{for point } S && R_{e,s} = k\omega_s F(\omega_s, \sigma_s) \\ &\text{for point } X && R_{e,x} = k\omega_x F(\omega_x, \sigma_x) \end{aligned} \tag{1.195}$$

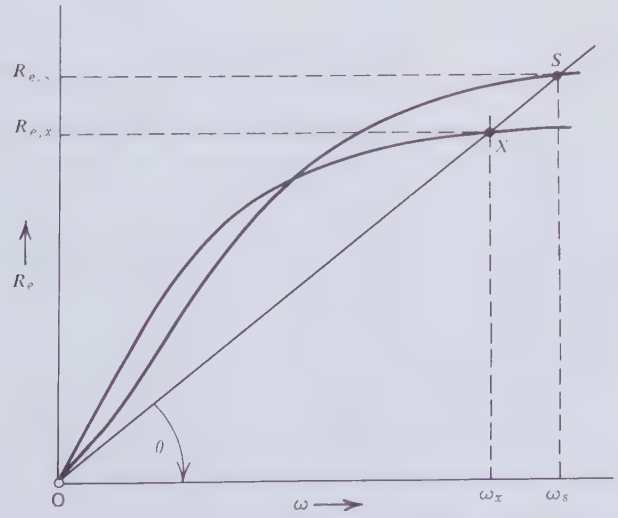

Figure 1.68 Measured eddy current resistance as a function of energizing frequency.

Furthermore

$$\tan\theta = \frac{R_{e,s}}{\omega_s} = \frac{R_{e,x}}{\omega_x} \tag{1.196}$$

From equations (1.195) and (1.196) we deduce that

$$kF(\omega_s, \sigma_s) = kF(\omega_x, \sigma_x)$$

and therefore

$$\frac{\sigma_x}{\sigma_s} = \frac{\omega_s}{\omega_x} \tag{1.197}$$

which gives the desired conductivity ratio as the ratio of two frequencies.

No solution will be obtained if θ is too large and the straight line intersects only one of the curves or passes through the point where the curves themselves intersect. It would be sufficient to measure the coordinates of only point S on the curve OS, draw the straight line OS and measure a small range of $R_{e,x}$ values, such that the short portion of curve OX intersects the straight line OS. However, the accuracy of the method can be improved by measurement and plotting of portions of both curves so that several straight lines of different inclinations can be drawn. But for experimental errors, each straight line should give the same conductivity ratio. The average ratio obtained in this way will be a more accurate result than a single ratio obtained from a single straight line.

1.21 ALUMINUM

Following the leap forward civilization took during the industrial revolution, our present century will probably be best remembered by the mobility it gave to man through flying machines and the conquest of space. Aluminum is one of the cornerstones on which these achievements rest. Eight percent of the accessible part of our planet is aluminum. By comparison 5 percent is iron and 0.0001 percent is copper. Aluminum is therefore one of the most plentiful metals in the earth's crust. Free metallic aluminum deposits are not found in nature because of the strong affinity this metal has to oxygen. The existence of aluminum was predicted by Sir Humphrey Davis, but he was unable to separate it from the oxide. The honor of having produced the first few grains of aluminum metal belongs to the Danish scientist Oersted [1.58] who is best known as the discoverer of electromagnetism. In 1825 he converted alumina to aluminum chloride, which he then reduced with potassium amalgam. After evaporating the mercury he was left with metallic

aluminum. For the first commercial process, which came into being in 1854, sodium was substituted for the costly potassium. This process was invented by Deville in France and became known as Deville's sodium process. In the years between 1855 and 1888 Deville separated about 100,000 lb of aluminum.

Relatively late in the industrial revolution, the young American chemist Hall and the Frenchman Heroult simultaneously discovered in 1886 a solvent of Al_2O_3 known as cryolite. The alumina-cryolite solution permitted the electrolytic separation of the light metal from oxygen on the scale that is now being supplied to the manufacturing industries. The electrolytic process requires quite pure oxide and has favored the working of only the beauxite ore containing approximately 60 percent or more Al_2O_3.

Large deposits of beauxite have been found in France, Canada, the Caribbean, and the United States. Most of the energy needed for separating aluminum from the extremely stable alumina (Al_2O_3) has to be provided as electricity. In 1976 the U.S. aluminum industry consumed 73.2 billion kWh of electricity, which was 10 percent of the total industrial consumption and 4 percent of all the electricity sold by U.S. utility companies. The cost of aluminum therefore is tied closely to the price of a kilowatt-hour of electricity. Large aluminum smelters are located in areas where electricity is abundant and cheap, as for example in the Northwest of the United States. Because of the widespread use of aluminum in the aircraft, ground transportation, building, and electrical industries, the demand for this metal and hence its price have been relatively stable. In this respect aluminum has had a decisive advantage over copper. In 1952 the tonnage of aluminum produced began to exceed the tonnage production of copper. By 1975 world production of aluminum had reached 10 billion tons/year. From the present rate of growth of aluminum utilization it has been estimated that the rich beauxite deposits will be exhausted in the next century. This realization has focused attention on scrap recovery and recycling, which not only conserves an important natural resource but also valuable electrical energy.

After cleaning, grinding, and concentration of the crude beauxite ore, almost pure alumina is deposited in the 900°C electrolytic baths of smelters that are equipped with carbon anodes and cathodes. This process yields electrical grade (EC) aluminum of 99.6 percent purity. Higher purities approaching 99.9 percent are achieveable by using both very pure oxide and carbon. Supplementary refining methods have been developed, and, in contrast to copper, it is quite easy to obtain 99.99 percent pure aluminum. Depending on their degree of annealing, samples of this grade of aluminum would be expected to have a resistance ratio (resistivity at 20°C to resistivity at 4°K) ranging from 800 to 1500. When the samples are fully annealed, this ratio is the best indication of the impurity content. The ideal resistivity

of aluminum at liquid-helium temperatures is virtually zero and the resistance ratio therefore depends essentially on the electron-phonon scattering at impurity atoms and lattice defects.

Aluminum lends itself to a higher degree of purification than any other metal. A grade known as "Super-Raffinal" is being produced in commercial quantities to a purity of 99.999 percent. Depending on the degree of crystalline perfection, this material may exhibit resistance ratios from 1500 to 2500. The National Bureau of Standards in conjunction with the aluminum industry has produced the highest purity of aluminum on record [1.52]. Its foreign matter content was as low as 0.2 parts per million, which gave rise to the astonishingly high-resistance ratio of 45,000. At the time the NBS experiment was performed it appeared possible that ultrapure aluminum might find application in cryogenically cooled magnets, but in recent years superconductors have been preferred for this purpose.

Elastic and plastic strain increases the resistivity of all metals. A certain amount of strain can be tolerated as long as it does not create plastic deformation. Therefore an important mechanical parameter of electrical conductors is the yield stress. It plays a part in the suspension of overhead line conductors and the tensile forces that may be applied to paper-insulated cables when they are pulled into pipes or ducts. Furthermore, tubular conductors are limited by yield stress as to the amount of internal pressure they can contain and also the maximum lateral thrust they can support due to short-circuit forces. Comparative yield stresses for copper and aluminum are displayed on Fig. 1.69. This data has been computed by Carlson [1.53]. The yield stresses for hard drawn materials are relevant only for cable sheaths and pipes. The relatively pure conductor metal will be self-annealing at the temperatures associated with full load current. In the case of annealed conductors of equal cross-sectional area, as can be seen from Fig. 1.69, copper will support almost three times as much tension as aluminum. But since the specific gravity of copper is nearly three times that of aluminum, the strength advantage of copper is lost when conductors of equal weight are considered. At the metal prices that have prevailed during the past 10 years, 1 lb of aluminum could be purchased for 50 to 90 percent of the cost of 1 lb of copper. In general, therefore, aluminum is the cheaper conductor when tensile yield stress is the primary criterion of choice. On an equal resistance basis, copper conductors turn out to be nearly twice as strong as aluminum. The most important conclusion that can be drawn from Fig. 1.69 is that for the same yield stress the two conductors will be approximately the same weight, but aluminum will have the lower resistance and the lower cost.

Therefore, it is not surprising that aluminum has superseded copper for overhead line conductors and made remarkable inroads in low-voltage distribution cables for underground installations. Aluminum overhead con-

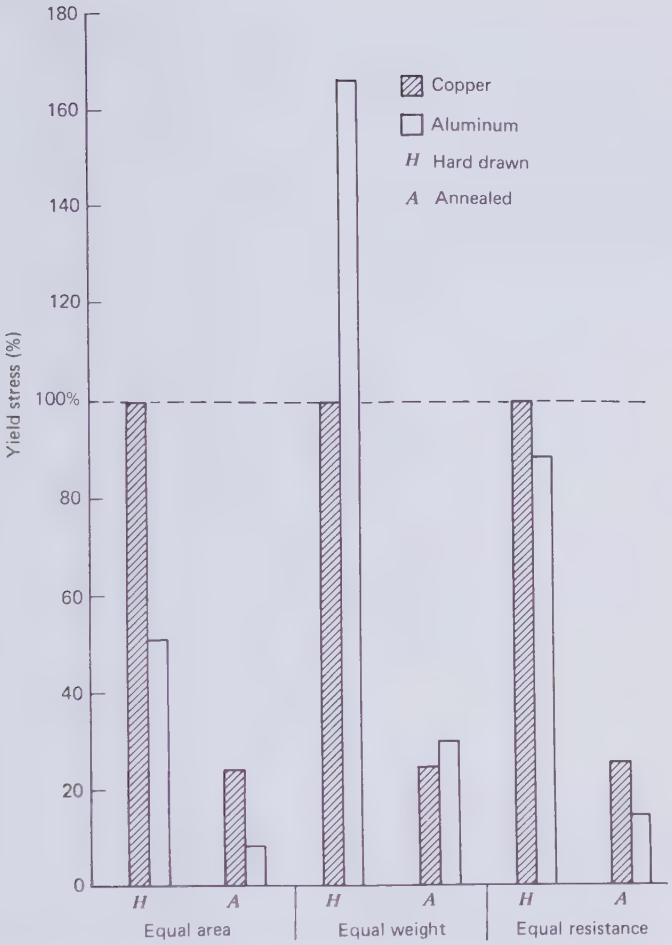

Figure 1.69 Yield stress of EC aluminum and electrolytic tough-pitch copper.

ductors were first installed in 1895 in California and in France. Steel-cored aluminum conductors came into use in 1908 and aluminum alloy conductors have been employed for many years throughout the world. Just before World War I, aluminum enjoyed considerable popularity because of the high price of copper. The first record of an aluminum conductor cable dates back to 1910 [1.59]. By the year 1913 over 800 miles of aluminum conductor cable had been installed in France, Germany and Switzerland. Copper has retained its position when strength is not a major factor and the smaller diameter of equal resistance conductors permits significant savings in insulation volume and sheath material. An example of this are high-voltage oil-paper insulated cables.

Aluminum is more susceptible to corrosion than copper. However pure aluminum forms a very tenacious and largely flawless oxide layer of high dielectric strength. This layer protects the metal against corrosion in the air and no further protective measures need be taken for overhead lines. Aluminum cable sheaths and pipes buried underground are subject to more severe electrolytic corrosion processes that penetrate the oxide layer. For this reason aluminum sheathed cables have to be covered by polyethylene or similar anticorrosion jackets. These jackets must be free of holes, which would concentrate the electrolytic action and penetrate through the aluminum pipe in a relatively short time. The conductors inside the cable are of course well-protected against corrosion by the electrical insulation.

The resistivity of aluminum as well as copper increases with temperature. From the approximate Bloch-Grueneisen formula (1.16), we expect the resistance increment to be proportional to absolute temperature. Hence when the conductor temperature increases from an ambient value of, say, 20°C (293°K) to 80°C this should result in approximately a 20 percent increase in resistance. So large an increase is a significant factor with regard to Joule losses and cable capability. Equation (1.16) is an approximation that applies to all metals. In practice, there exist deviations from this law and they are of different magnitude for different metals.

According to (1.16) we may state

$$\frac{R_x}{R_r} = \frac{T_x}{T_r} = \frac{273°\text{K} + T_x°\text{C}}{273°\text{K} + T_r°\text{C}} \tag{1.198}$$

where R_x is the unknown and R_r the reference resistance with T_x being the prevailing temperature and T_r the reference temperature. For $T_x = 80°\text{C}$ and $T_r = 20°\text{C}$ this gives $R_x / R_r = 1.2$, or a 20 percent resistance increase. However direct measurement would show that the actual resistance increment is approximately 24 percent for both aluminum and copper. To account for this discrepancy the following empirical formulas have been established that also allow for second-order differences between aluminum and copper.

For aluminum

$$\frac{R_x}{R_r} = \frac{234.5°\text{K} + T_x°\text{C}}{(234.5°\text{K} + T_r°\text{C})} \tag{1.199}$$

For copper

$$\frac{R_x}{R_r} = \frac{228°\text{K} + T_x°\text{C}}{228°\text{K} + T_r°\text{C}} \tag{1.200}$$

Using the previous example of $T_x = 80°\text{C}$ and $T_r = 20°\text{C}$, the resistance ratio for aluminum is now found to be 1.236 and that for copper is slightly larger at 1.242.

As nominally pure aluminum is cooled below ambient temperature, its resistance decreases more than that of nominally pure copper. At 70°K the two metals have approximately the same resistivity of 0.16 $\mu\Omega$·cm, which is less than 10 percent of the room temperature resistivity of copper. But since aluminum can be more easily refined to high purity than copper, it is fair to claim that aluminum is a somewhat better low-temperature conductor than copper. Figure 1.70 compares the measured low-temperature resistivities of copper by White and Woods [1.54], aluminum by Pawlek and Rogalla [1.55], beryllium by Reich, et al. [1.56], and finally sodium [1.57] in the

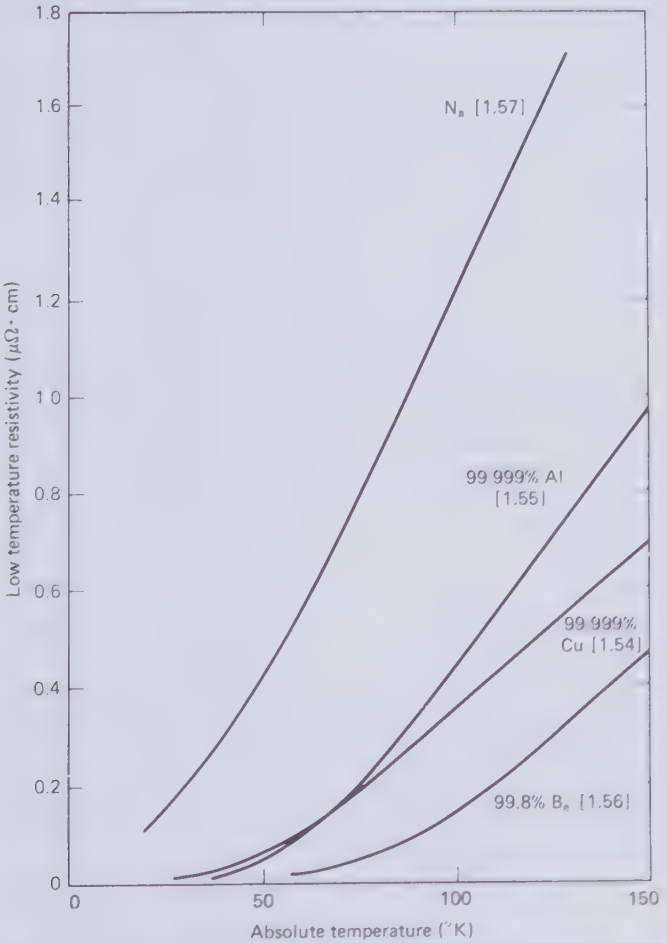

Figure 1.70 Measured low temperature resistivity of copper, aluminum, sodium, and beryllium.

temperature range from 20 to 150°K. This shows that beryllium of modest purity is a better electrical conductor at liquid-nitrogen temperatures than either aluminum or copper. However, in applications requiring high current density, part if not all of this advantage of beryllium may be eliminated by magnetoresistance as indicated by the Kohler plot of Fig. 1.4.

1.22 SODIUM

Although unable to separate aluminum from its oxide, Sir Humphrey Davis was successful in 1807 in his efforts to isolate sodium metal. Since then, some major processes in the chemical industry have come to rely on the availability of this very light alkali metal to make tetraethyl lead—the anti-knocking agent in leaded gasoline—sodium cyanide, sodium peroxide, fatty alcohols, and in the reduction of some unusual metals as for example titanium [1.63]. In a nonchemical application liquid sodium is used as a heat-exchange medium inside the valves of internal combustion engines. Prospects for the large-scale utilization of sodium exist in nuclear breeder reactors, sodium-sulfur batteries, and of course sodium cables.

In 1901 the Swiss inventor Sinclair patented the use of sodium for conductors of electricity [1.61]. Among the common metals, which exclude gold and silver, sodium ranks third on the scale of ambient temperature electrical conductivity after copper and aluminum. Sinclair recognized that this highly reactive metal has to be enclosed in an inert metallic or dielectric tube before it can be used as a conductor of electricity. He thought copper and aluminum made the best envelopes. But since these metals were better conductors and more expensive than sodium, there appeared to be little incentive for implementing Sinclair's ideas. In his time polyethylene was unknown.

Further patents for sodium conductors were issued in the United States and in France before World War I. All claimed major economic advantages over copper and aluminum. The first sizeable sodium conductor was put into service in 1927 in one of the plants of the Dow Chemical Company in Michigan. The conductor was 4 in. diam and 850 ft long. It was enclosed in a steel pipe. For 10 years it carried low-voltage dc current up to 4000 A and apparently gave completely satisfactory service. During 1941 Cantacuzene in France proposed lead-covered sodium conductors, which could be insulated with paper and oil in the same way stranded copper and aluminum conductors were insulated. Cantacuzene was also the first to suggest plastics and polymers for covering sodium conductors. This latter idea was finally reduced to practice by Humphrey and his colleagues of the Union Carbide Corporation [1.60] in the early 1960s. From 1965 to 1970 approximately

150,000 conductor-feet of polyethylene-insulated sodium cable was produced by the Union Carbide Corporation and the Simplex Wire and Cable Company. Most of this cable is in service in the United States, but token installations were also made in a number of the industrialized countries around the world. The major achievement of the Union Carbide Corporation was to show how sodium cables could be produced by extruding a polyethylene pipe and filling it simultaneously with liquid sodium. The extruded polyethylene tubes proved to be chemically compatible with sodium and suitable as moisture barriers, mechanical reinforcement, and excellent electrical insulation. The combination of polyethylene with sodium was a significant breakthrough in power cable development.

Sodium is one of the most abundant elements on earth with ample supplies in the United States and many other countries. The very light, soft malleable solid is easily cut with a knife and has a silvery luster with a hue of pink in it. It is so reactive in moist air and water that the free metal does not occur in nature. Sodium is a powerful reducing agent and its chemical reaction with water is violent to form sodium hydroxide (caustic soda) and hydrogen gas. If the hydrogen is released to air, the heat generated by the reaction usually ignites the gas. This results in explosions that are equivalent in force to those produced by firecrackers. Everyone who has taken high school chemistry remembers with delight the experiment of dropping a pellet of sodium in a bucket of water and the flame and noise this would produce. Memories of this experiment have contributed greatly to the fear of sodium cables, which so far has outweighed its economic advantages.

The principal users of sodium cables are the Portland General Electric Company, the Pennsylvania Power and Light Company, and the Jersey Central Power and Light Company. After 10 years of operation no failures of sodium underground cables have been reported. Difficulties have arisen, however, with the first generation of sodium-to-copper connectors. These difficulties do not appear to be insuperable. Users of sodium cables are satisfied that these cables can be safely installed and present no danger in underground service. Their light weight and flexibility are deemed to be additional advantages over and above the low cost of sodium metal. Gloves and safety glasses have to be worn by the crew that installs sodium cables because of the caustic nature of the hydroxide that forms within seconds of cutting a sodium cable. Touching this compound with bare hands would cause burns. When handling sodium it must also be remembered that the metal is self-igniting in air or oxygen at approximately 120°C and burns with the characteristic yellow flame giving off dense white smoke of predominantly sodium monoxide (Na_2O).

Fine dry crystalline common salt (NaCl) is the raw material from which sodium metal is produced. Of several cells invented for the electrolysis of

fused sodium chloride, the Downs cell is the most widely used today [1.63]. The duPont Company installed the first Downs cell in Niagara Falls, New York. Its modern version contains a set of four cylindrical graphite anodes inside steel tube cathodes. To lower the melting point of the salt bath, approximately 58 percent calcium chloride ($CaCl_2$) are added to the sodium chloride, which permits the cell to be operated at the relatively low temperature of 580°C. The cell separates calcium as well as sodium, but almost all the calcium with its high melting point of 842°C is precipitated in a cooler and returned to the bath while the still liquid sodium is allowed to float up in a riser pipe and out of the cell. Chlorine is the by-product of the electrolysis of sodium, and it is collected in gaseous form and piped away from the cell. A small amount of calcium remains in the sodium, which is removed later by filtering liquid sodium at approximately 110°C. The filtered product is 99.9 percent pure sodium ready for electrical conductor usage. In 1970 the United States produced 400 million lb of sodium of which more than 80 percent went into the production of gasoline additives [1.63]. The price of sodium fell dramatically in the first 50 years of production. From then onward it climbed due to inflation and lately because of the high cost of electricity. The history of sodium prices is reflected in Table 1.8.

Because of the reactivity of sodium with moisture in the atmosphere, the material is usually shipped in steel tanks that are topped with dry nitrogen gas. Sodium is equally inert to argon and helium gas. Kerosene, naptha, and other hydrocarbon liquids may also be used to cover sodium during storage. The easiest way of transferring the metal from one container to another or into the cable-making process is by heating it a few degrees above its melting point of 97.8°C and pumping the liquid or allowing it to flow under gravity. The viscosity of liquid sodium at 100°C is 0.682 centipoise compared to 32 centipoise of water at 20°C. Therefore, liquid sodium flows more freely than water. On the other hand, impurities in pipes quickly form slag, which tends to block small-diameter pipelines.

Table 1.8 Price of Sodium in Tank Car Loads

Year	¢/lb
1890	200
1906	25
1946	15
1953	16
1966	17
1976	29
1977	34

With regard to the application to cables, an important physical characteristic of sodium is its thermal coefficient of expansion, which is substantially higher than that of copper and aluminum. Table 1.9 lists the linear thermal expansion coefficients per degree centigrade of the conductor metals and extruded polyethylene insulation, which assumes ever greater importance in power cable technology. It will be recognized that as the cable temperature rises due to Joule heating, the conductor metals expand less than polyethylene. In the case of copper and aluminum conductors, this is likely to cause plastic deformation of the electrical insulation. The thermal mismatch is smallest between sodium and polyethylene. Besides the soft sodium will tend to follow the thermal motion of the polyethylene and is less likely to overstress or damage the sensitive high-voltage insulation. This explains the greater reliability of high-voltage solid dielectric sodium cables compared to similar cables with aluminum and copper conductors [1.64]. To fully appreciate this aspect of sodium, it should be recalled that the metal and the insulation are extruded together and freeze in roughly the same temperature range (100 to 120°C). However, after solidification, polyethylene will tend to contract more than the sodium and retains some elastic strain in the finished cable. This can be proved by cutting the cable with a sharp blade and observing the subsequent extrusion of a small amount of sodium until the elastic hoop stress in the polyethylene has been relieved. As the cable temperature rises under the influence of a load current, the initial thermal expansion relieves the strain in the insulation without forcing dimensional changes. In this way the already smaller differential thermal expansion between sodium and polyethylene is further reduced.

According to the *Sodium-NaK Engineering Handbook* [1.57], the most accurate measurements of the electrical resistivity (ρ_{Na}) of 99.9 percent pure sodium have been made by Dugdale and Gugan [1.62] from -223 to 22°C on self-supporting bare wires. Their experimental results may be expressed by the empirical formula

$$\rho_{Na} = 4.290 + 1.933 \times 10^{-2} T + 9.848 \times 10^{-6} T^2 \ \mu\Omega \cdot \text{cm} \qquad (1.201)$$

Table 1.9 Coefficient of Linear Thermal Expansion of Conductor Metals and Polyethylene at 20°C

Copper	16.5×10^{-6}/°C
Aluminum	23.6×10^{-6}/°C
Sodium	70.0×10^{-6}/°C
Thermoplastic Polyethylene	200.0×10^{-6}/°C
Crosslinked Polyethylene	250.0×10^{-6}/°C

where T is the metal temperature in degrees centigrade. Foust [1.57] recommends that the same formula should be used right up to the melting point of sodium, which is 97.8°C. The resistivity values listed in Table 1.10 have been computed in accordance with this recommendation for the important cable operating temperature range from 0°C to the melting point. During the melting process the resistivity of the material jumps from 6.3 to 10.1 $\mu\Omega \cdot$cm. The low-temperature resistivity of sodium in the liquid nitrogen temperature range has been plotted in Fig. 1.70. A comparison of sodium with standard copper and aluminum grades in the cable operating temperature range from 0 to 100°C is shown in Fig. 1.71. The sodium graph is for commercially pure (99.9 percent) material that would have 36.9 percent conductivity on the IACS scale. The two copper graphs refer to 100 percent IACS and oxygen-free high-conductivity copper of 102 percent IACS. The aluminum graphs represent EC grade metal for hard drawn 61 percent IACS overhead line conductors, and 61.8 percent IACS annealed aluminum used in cables.

Sodium is lighter than water, having a specific gravity of 0.97 at 20°C. The insulation encapsulating sodium is normally high-molecular-weight (low-density) polyethylene of 0.92 specific gravity. Unless heavy drain wires or armor surround sodium cables, they will float in water or be nearly of neutral buoyancy. This has a bearing on underwater cable installation when cables may be floated in position and lowered by weight. Buoyant power cables are of special interest as riser sections for floating power plants driven by nuclear, wind, or ocean-thermal energy. The lightness of the cable also reduces shipping expenses.

Table 1.10 Resistivity of Commercially Pure Sodium (99.9%) According to (1.201)

°C	$\mu\Omega \cdot$cm	°C	$\mu\Omega \cdot$cm	°C	$\mu\Omega \cdot$cm	°C	$\mu\Omega \cdot$cm
0	4.290	26	4.799	52	5.322	78	5.858
2	4.329	28	4.839	54	5.362	80	5.899
4	4.367	30	4.879	56	5.403	82	5.941
6	4.406	32	4.919	58	5.444	84	5.983
8	4.445	34	4.959	60	5.485	86	6.025
10	4.484	36	5.000	62	5.526	88	6.067
12	4.523	38	5.039	64	5.567	90	6.109
14	4.563	40	5.079	66	5.609	92	6.152
16	4.602	42	5.119	68	5.650	94	6.194
18	4.641	44	5.160	70	5.691	96	6.236
20	4.681	46	5.200	72	5.733	97.8	6.275
22	4.720	48	5.241	74	5.774		
24	4.760	50	5.281	76	5.816		

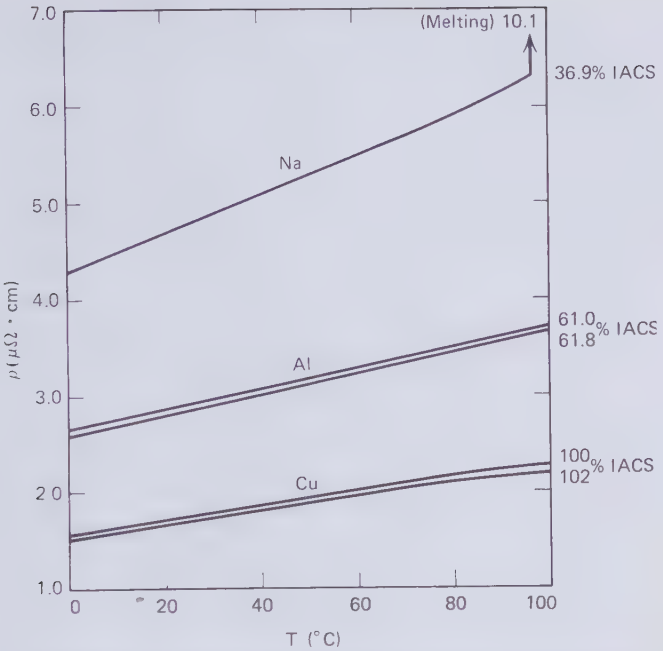

Figure 1.71 Resistivities of standard grades of copper, aluminum, and sodium in the cable operating temperature range.

1.23 BERYLLIUM

An awareness has arisen in the last 25 years that, in spite of their reliable performance, oil-paper insulated cables have thermal and economic limitations that will cause them ultimately to be superseded by some other kind of cable that will be a competitor to overhead lines. In the long run it seems inevitable that an alternative to overhead transmission has to be found or the landscape surrounding the populated centers of the world will gradually be converted to what sometimes has been called a "wirescape."

To cope with the thermal limitations of paper-insulated cables, the immediate remedy, which has been adopted both in New York and London, was artificial cooling. This made the cables less dependent on a good cooling environment and increased their transmission capability. Since the 1950s forced cooling of cables has become fairly common practice in congested areas where available underground space is scarce. The traditional approach to increasing the capability of individual cable circuits has been to raise the operating voltage. Going beyond the highest cable voltages now in use, however, gives rise to punitive dielectric losses in the paper insulation and

for long circuits also requires reactive compensation for the charging current.

These trends explain the growing interest in forcibly cooled and particularly cryogenically cooled cables that has come to the fore in the past few decades. Only a limited number of coolants are available for cryocables and research has been centered on liquid nitrogen, liquid hydrogen, and liquid or supercritical helium. Grave fire and explosion risks are associated with hydrogen and most experimental studies have relied on nitrogen and helium. The preferred conductor metal for liquid-nitrogen-cooled systems is aluminum because its conductivity in the low-temperature range is as good as that of copper. However, there is one metal that has several times the conductivity of copper and aluminum at the boiling point of liquid nitrogen. This metal is beryllium. Quite intensive research on beryllium conductors was carried out in France in the 1960s.

According to the low-temperature approximation of the Bloch-Grüneisen equation (1.17), the conductivity of a metal should be proportional to the sixth power of the Debye temperature Θ_D. Beryllium has by far the highest Debye temperature of the conductor metals, as can be seen from Table 1.2. Therefore it always has been expected to be the best of the low-temperature normal conductors. This consequence of the Bloch-Grüneisen formula with regard to the ideal resistivity of metals is given graphical expression in Fig. 1.3. Yet the anticipated high conductivity of beryllium at liquid nitrogen temperatures eluded experimenters for many years. Then Reich [1.65] zone refined a commercially pure (99.5 percent) specimen and achieved the breakthrough plotted in Fig. 1.72.

Notwithstanding this remarkable achievement by Reich, the interest in beryllium has faded again once the implications of the high magnetoresistance of this metal were fully appreciated. This effect virtually rules out applications of beryllium conductors in magnetic fields of the strengths encountered in power transformers and generators. The magnetic fields of cables are very much weaker and beryllium remains a possible conductor material for power transmission provided substantial economies in refining and fabrication techniques can be achieved with mass production.

The transverse magnetoresistance is caused by the lateral deflection of electrons that would otherwise travel in the direction of the electric field, and the extra collisions with phonons and lattice defects on the elongated electron path. The magnitude of the effect is a function of the electron mean free path, and it will therefore vary with conductor temperature. The magnetoresistance of beryllium was measured in the Center for Cryogenic Studies of l'Air Liquide in France [1.66] on the high-purity wire of 0.5 mm diam wound up as a solenoid of 56.5 cm length and 2 cm diam. The transverse magnetic field with its direction parallel to the solenoid axis was produced by a concentric superconducting coil. The measurements were

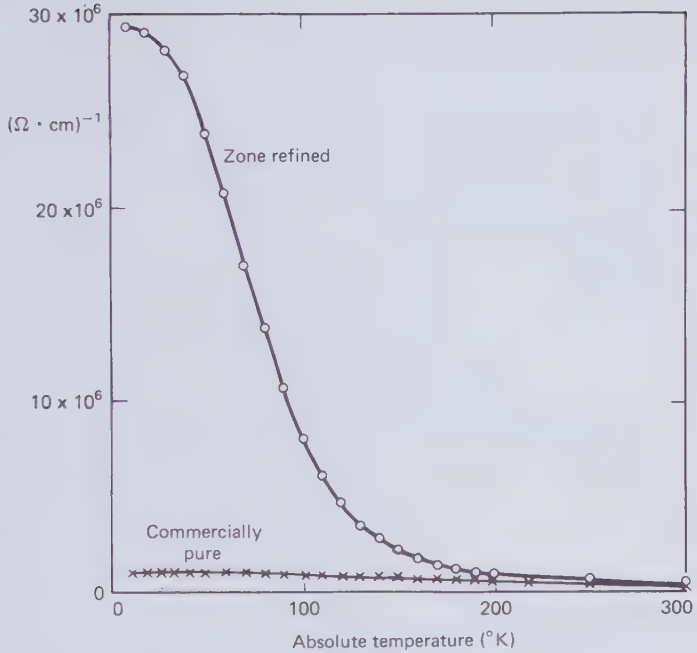

Figure 1.72 Electrical conductivity of commercially pure and zone refined beryllium measured by Reich [1.65].

repeated with the beryllium coil at the three temperatures of boiling liquid nitrogen (77°K), liquid hydrogen (20°K), and liquid helium (4.2°K) and the results are plotted in Fig. 1.73. The ratio ρ_H/ρ_0 on this graph is the resistivity of the beryllium wire at the magnetic field strength H divided by its resistivity in zero magnetic field. The magnetoresistance did not change significantly by cooling the solenoid from 20 to 4.2°K. This is an indication that the electron mean free path is constant over this temperature interval and it proves that the beryllium sample had reached its residual resistivity at the liquid-hydrogen temperature but not at the liquid-nitrogen temperature. The Bloch-Grüneisen theory in fact predicts that the temperature-dependent ideal resistivity should become vanishingly small between 40 and 50°K. Other metals do not reach their residual resistivity until the temperature is lowered to the boiling point of liquid helium.

The measurements indicate that a transverse magnetic field of just over 31 kG will multiply the electrical resistivity of high-purity beryllium at 77°K by a factor of 10, which more than eliminates the advantage that beryllium has over copper and aluminum in weak magnetic fields. However, in cable conductors the magnetic field will at most be of the order of one kilogauss

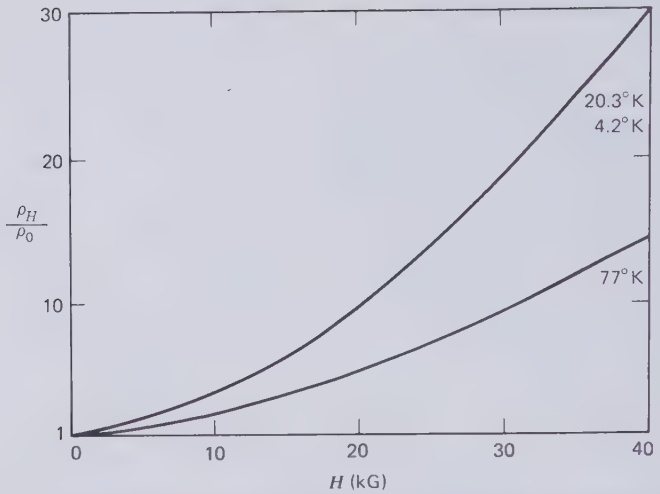

Figure 1.73 Magnetoresistance ratio of high-purity beryllium solenoid measured by Broniewski et al. [1.66].

and the magnetoresistance then increases the Joule losses by only a few percent. Therefore in cables the effective conductivity of beryllium in the liquid-nitrogen temperature range will be three to four times as large as that of copper and aluminum.

The yield strength of beryllium is higher than that of stainless steel and its specific gravity is only 1.85. The resultant high strength-to-weight ratio of beryllium has been of interest in the aerospace industry. Table 1.11 compares the ambient temperature elastic modulus, yield strength and linear thermal expansion of beryllium with other conductor metals and steel. The

Table 1.11 Ambient Temperature Mechanical Properties of Beryllium Compared to Other Conductor Metals and Steel

	Elastic Modulus (psi)	Yield Strength (psi)	Linear Expansion ($°C^{-1}$)
Beryllium	43×10^6	50,000	11.5×10^{-6}
EC aluminum	10×10^6	4,000	23.6×10^{-6}
OFHC copper	17×10^6	10,000	16.5×10^{-6}
Niobium	15×10^6	35,000	6.9×10^{-6}
304 stainless steel	28×10^6	42,000	11.9×10^{-6}
Ultrahigh strength steel	30×10^6	240,000	13.3×10^{-6}

high elastic modulus and yield strength are definite advantages of beryllium over aluminum for tubular cryoconductors that have to contain coolant under as high a pressure as possible. The amount of pressure that a conductor tube can withstand determines the spacing between refrigerators and the current that can be carried over a given distance between refrigerators. The lower coefficient of thermal expansion also favors beryllium over aluminum because telescopic joints have to accomodate less contraction during the cool-down process. When cooling an aluminum conductor from ambient temperature to 77°K, it will contract approximately 0.4 percent, whereas a beryllium conductor would contract only 0.3 percent. A disadvantage of beryllium is its susceptibility to brittle fracture. This would effect tubular conductors more than beryllium wires or tapes.

Although beryllium was first isolated in 1798, it was not obtained in a really pure state until 1855 [1.67]. The source of beryllium is the mineral beryl ($3BeO \cdot Al_2O_3 \cdot 6SiO_2$), a beryllium aluminum silicate, from which it derived its name. After subjecting the ore to various chemical treatments, fairly pure metal is obtained by electrolysis from anhydrous chloride or fluoride mixtures. The metal is lighter than aluminum and has the appearance of steel. Like aluminum, it is always covered with a strong thin film of oxide that resists corrosion. Most of the beryllium produced today is used as an alloying element for hardening and improving the fatigue strength of copper.

Inhaled beryllium powder is toxic. This imposes a number of restritions on the fabrication technology. Wire drawing, strip rolling, and tube extrusion are all possible with developed techniques that are generally more costly than the corresponding copper and aluminum manufacturing processes.

1.24 NIOBIUM AND ITS SUPERCONDUCTING ALLOYS

The fundamental difference between superconducting and all other transmission lines is that in the case of superconductors the magnetic field must in most designs be confined to a coaxial gap between go-and-return conductors. If the magnetic field is allowed to stray beyond this gap, it will cause circulating current Joule losses in normal metals that carry the full helium refrigeration penalty and cancel any benefit that can be derived from the use of superconductors. The circulating loss currents would be induced either by the sinusoidal variation of flux due to ac excitation or the inevitable load fluctuations in a dc cable. Therefore, to demonstrate the feasibility of superconducting power transmission, current has to be forced to flow to and fro in a coaxial line and the transmission voltage has to be maintained simultaneously across the coaxial gap. By the end of 1979 this had not yet

been achieved. Most countries have now suspended research on superconducting transmission lines. However work in this field continues in the United States and the Soviet Union.

The first major experiment was carried out by BICC in England between 1963 and 1967 [1.68], in which 2080 A (rms) of 50 Hz current at negligibly low transmission voltage were passed along a 10-ft-long coaxial superconducting niobium line. The Union Carbide Corporation later passed 60 Hz currents up to 2650 A (rms) around a 6-m-long coaxial superconducting line and superimposed pulsed currents up to 10,000 A (rms), which drove the niobium into the normal state [1.69]. The Union Carbide tests were also carried out at negligibly low voltage and therefore did not involve the transmission of significant amounts of power. In a series of separate investigations it has been shown that vacuum, helium, and laminated solid insulation impregnated with helium could operate at the low temperatures required by superconductors and withstand ac and dc voltages up to several hundred kilovolts.

Type I superconductors such as mercury, lead, and tin, which were the first to be discovered, held out little hope for power transmission because of the limited critical current density they could sustain. It was the discovery of the hard type II superconductors that seemed to open the door to almost lossless energy transmission. One of the first new superconductors was a niobium-zirconium alloy (Nb-25%Zr) with the relatively high transition temperature of 10.8°K and a critical magnetic field strength of the order of 70 kG. But very soon it was discovered that type II superconductors did dissipate energy when carrying power frequency currents. This so-called ac loss of niobium-zirconium guided researchers back to pure niobium, which behaved as a type I superconductor up to a certain current density and at higher currents transformed itself to a type II material with the associated deeper current penetration and the hysterisis loss. In general the ac performance of commercially pure niobium was superior to the niobium-zirconium alloy. Since then three more niobium alloy superconductors have been developed: niobium-titanium (Nb-48%Ti), niobium-tin (Nb_3Sn), and niobium-germanium (Nb_3Ge). The transition temperatures and critical magnetic fields were tabulated by Rechowicz [1.71] and his figures are reproduced in Table 1.12.

In recent years niobium-titanium and niobium-tin have become the preferred materials for both ac and dc superconducting transmission lines. Suitably prepared, these materials can sustain higher current densities than pure niobium, for the same ac loss, and therefore permit more compact cable designs. Niobium-germanium has the highest transition temperature of all superconducting materials so far discovered. This temperature lies clearly in the liquid-hydrogen cooling regime.

Table 1.12 Transition Temperatures and Critical Magnetic Fields of Niobium and Its Superconducting Alloys [1.71]

		Transition Temperature (°K)	Critical Field (kG)
Niobium	Nb	9.3	1.5 at 4.2°K
Niobium-Zirconium	Nb-25%Zr	10.8	70 at 4.2°K
Niobium-Titanium	Nb-48%Ti	9.5	120 at 4.2°K
Niobium-Tin	Nb_3Sn	18.4	220 at 4.2°K
Niobium-Germanium	Nb_3Ge	23.2	3 at 20°K

Niobium is a refractory metal that melts at 2470°C. Its name is connected with Niobe, the daughter of Tantalus of Greek mythology, probably because tantalum and niobium ores are usually found together. The discovery of niobium in America explains the alternative name of columbium derived from Columbus. The largest producer of columbite, the niobium ore, is Nigeria, and other substantial deposits exist in Africa. Niobium has a specific gravity of 8.57. Its elastic modulus, yield strength, and linear thermal expansion coefficient are given in Table 1.11. Niobium is significantly stronger than copper and aluminum and contracts less than these two conductor metals. It is a ductile material that has the appearance of steel.

Superconductors are notoriously poor thermal conductors. During the phase transition electrons are "condensed" into the superconducting state and are then no longer available for heat transport. This effect is exploited in superconducting thermal valves [1.73] in which the heat flow through a piece of superconductor is turned on and off by applying and removing a magnetic quench field. At the superconducting phase transition the thermal conductivity can change by as much as one to two orders of magnitude.

The low thermal conductivity of niobium and its superconducting alloys, combined with the low specific heat of all metals at liquid-helium temperatures, can easily give rise to thermal instability and quenching of the superconducting state. Small thermal disturbances caused, for example, by flux jumps, mechanical vibrations, or an electrical discharge, could escalate into a burn-out of the superconductor. This danger was brought to light when the first superconducting magnet coils were built. A remedy has since been found. It consists of using the thinnest possible superconductors and bonding them metallurgically to good thermal conductor materials as copper and aluminum. Thermally stabilized superconductors have thus become composite structures containing superconducting filaments, strips, or layers and substantially more normal metal.

One of the best methods of thermal stabilization is to disperse a large number of fine superconducting filaments in a copper matrix, the latter accounting for up to 90 percent of the metal cross-section. The backing or matrix material permits more efficient heat transfer to the helium coolant and therefore keeps the temperature of lossy superconductors down. This actually reduces the loss and permits additional current flow. Provided the backing material is of a high enough electrical conductivity, it may also be allowed to carry fault current pulses that are so large that they quench the superconductor for the duration of the pulse. Superconducting filaments embedded in a normal metal matrix are not deemed suitable for ac cables because of heavy eddy current losses that would arise in the normal metal situated in the magnetic field of the supercurrent. This loss is claimed to be acceptable up to a frequency of 1 Hz [1.71] and therefore filament superconductors are being considered for dc cables.

The ideal conductor arrangement for ac cables are coaxial tubes of normal metal clad with superconducting material on the surfaces that bound the coaxial gap, as proposed by Meyerhoff [1.69]. Such an arrangement results in a rigid transmission line. Very considerable difficulties have to be overcome if flexible conductors are desired. Helically wound wire or tape structures have to be designed that are thermally stable and do not permit significant amounts of magnetic flux to reach the backing material.

The metallurgy of niobium-based superconductors also has to concern itself with the surface finish of these conductors. It has been known for some time that surface currents flow even in type II superconductors and that the surface currents cause electron scattering and therefore Joule heating. The surface current loss, which is not hysteretic in nature, can be kept to a minimum by the elimination of surface roughness.

1.25 CONDUCTOR ECONOMICS AND KELVIN'S LAW

Conductor metals can be ranked on an economic merit scale. In calculating the figures of merit, the following conductor parameters will be required

A = cross-sectional area	m = cost per unit weight
L = length	M = conductor cost
δ = specific gravity or density	R = resistance
σ = electrical conductivity	C = conductance = $1/R$

The conductance and conductor cost are given by

$$C = \frac{\sigma A}{L} \tag{1.202}$$

$$M = mAL\delta \tag{1.203}$$

The ratio of these two parameters is

$$\frac{C}{M} = \frac{\sigma}{L^2 m \delta} \tag{1.204}$$

For a fixed length L, therefore, the most conductance that can be purchased per dollar depends on the electrical conductivity divided by the product of density and cost per unit weight of the conductor material. Let this ratio be the economic figure of merit of a conductor metal, i.e.,

$$X = \frac{\sigma(T)}{\delta \cdot m(t)} \tag{1.205}$$

Only δ is a constant of the material. As (1.205) indicates, σ is a function of the temperature T and m varies with time t. To normalize the figure of merit we express it relative to one of the conductor metals, say copper. For ranking aluminum and sodium with respect to copper, we calculate the ratios X_{Al}/X_{Cu} and X_{Na}/X_{Cu}. These ratios are plotted in Fig. 1.74 for the important temperature range from 20 to 80°C and the metal prices at 1965 and 1976.

The curves indicate, first of all, that the temperature of the conductors has hardly any effect on their economic merit and in further computations we use the intermediate temperature of 50°C. Also given in Fig. 1.74 are the metal prices for the two years of 1965 and 1976. They are in fact the prices per pound of electrolytically refined tough-pitch copper wire bars, EC aluminum ingots, and commercially pure sodium in tank cars. It will be seen that the variation of metal prices over the 11-year period has only had a secondary effect on the figures of merit and did not change the order of ranking of the three metals. By and large, aluminum is nearly three times better than copper, and sodium is about seven times better than copper. Metal prices will continue to fluctuate and not necessarily in proportion to the purchasing power of the dollar. However, the differences in merit rating are large enough to make a change in the ranking order unlikely.

As a next step in the economic analysis of conductors, the cost of conductor fabrication should be taken into account. Copper wire bars have to be rolled into rod and drawn down to wires, which are then laid up to form stranded conductors. Aluminum conductors are produced by a similar chain of operation, but the rod might be produced by extrusion. To convert sodium in tank cars to conductors, it is only necessary to melt the metal and pump it into an extrusion line. Average conductor fabrication costs are given in Table 1.13; with these costs it is possible to calculate relative figures of merit for finished conductors. The results of such calculations are displayed on Fig. 1.75 together with the figures of merit for the three metals alone. It will be seen that the fabrication costs slightly depress the relative value of

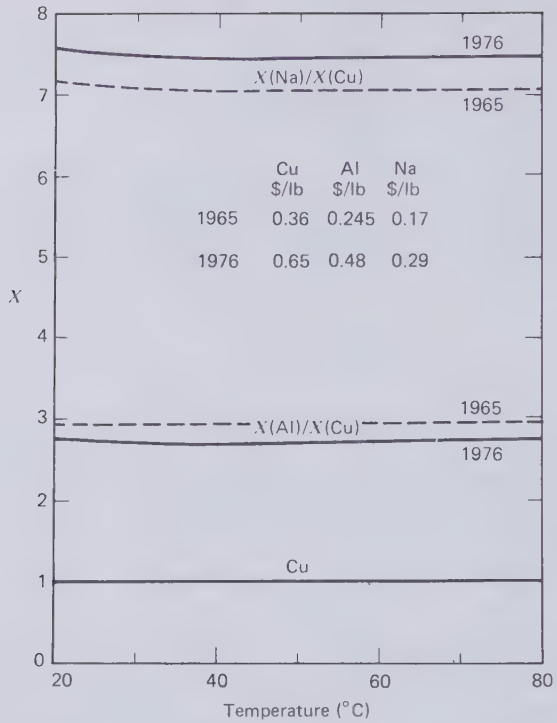

Figure 1.74 Economic figure of merit of copper, aluminum, and sodium as a function of conductor temperature.

aluminum conductors but increase the relative value of sodium conductors. Again the difference between the three metals is so large that fabrication costs do not upset the order of ranking.

The foregoing analysis explains why aluminum has all but eliminated copper from newly installed transmission and distribution lines. Sodium is unsuitable for bare overhead line conductors where steel-cored aluminum has no rivals.

In 1976 the gap between electricity generated and sold in the United States was 192.5 billion kWh [1.74]. There are no statistics available giving the fraction of this loss that can be ascribed to transmission and distribution

Table 1.13 Average Conductor Fabrication Cost

	Cu (¢/lb)	Al (¢/lb)	Na (¢/lb)
1965	8.0	8.0	1.0
1976	12.0	12.0	3.0

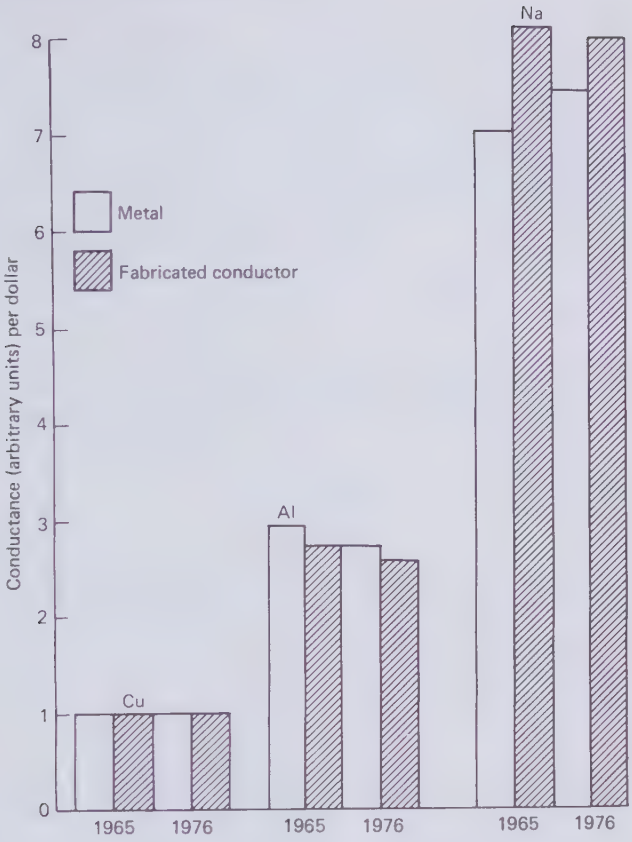

Figure 1.75 Conductance per dollar of fabricated conductors.

lines. It seems safe to assume, however, that approximately 60 billion kWh were converted to Joule heat. For some years to come, this is more energy than will be generated from solar sources. The potential for energy conservation by using more line conductance is therefore great. In monetary terms, the 60 billion kWh of Joule loss cost U.S. utilities an estimated $1.35 billion. At the then prevailing 8 percent bond rate, this was equivalent to raising nearly $17 billion of capital. The actual capital expenditure by U.S. power companies on transmission and distribution equipment in 1976 was about $7 billion [1.74]. The point of this comparison is that in the post-oil-embargo energy economy, and quite apart from any national energy conservation policy, the cost of conductor losses are now more important than the capital investment in lines.

Another energy consideration, although it carries far less weight, is the amount of energy consumed in producing copper, aluminum, and sodium conductors. Table 1.14 lists the electrical energy required for ore separation and refining. Additional energy has to be provided for melting and heating, chemical reduction, and metal fabrication processes. It will be seen that aluminum requires more electricity per unit conductance (Table 1.14) than the other two metals.

The overall economics of electrical conductors are usually discussed in terms of Kelvin's law, which was established at the dawn of the electrical age. It may be expressed in two equivalent ways [1.75].

1. The most economical conductor is that which makes the annual value of the interest and depreciation on the conductor equal to the annual value of the electrical energy loss due to the resistance of the conductor.
2. The most economical conductor is the one for which the acquisition cost is equal to the capitalized energy loss charge.

By capitalized loss charge is meant the amount of money that has to be invested so that the interest will just pay for the wasted energy.

To prove Kelvin's law, let K be the total capital cost, including capitalized losses, associated with the conductor, I the load current, and E the capitalized energy charge per watt of dissipation. The total capital cost, or present value, is then given by

$$K = AL\delta m + \frac{EI^2L}{\sigma A} \tag{1.206}$$

and the cost per unit length by

$$\frac{K}{L} = A\delta m + \frac{EI^2}{\sigma A} \tag{1.207}$$

With the definition of the figure of merit X of (1.205), this may be

Table 1.14 Energy Consumed in Metal Electrolysis

	Cu	Al	Na
δ/σ ($g \cdot cm^{-2} \cdot \mu\Omega$)	15.30	7.63	4.52
lb/arb. unit of cond.	3.38	1.69	1.00
electrolysis kWh/lb*	1.0	10.0	7.1
kWh/arb. unit of cond.	3.38	16.9	7.1

*Chemical Engineer's Handbook (1951).

transformed to

$$\frac{K}{L} = \frac{\sigma A}{X} + \frac{EI^2}{\sigma A} \tag{1.208}$$

When the conductor cross section A is the independent variable of (1.208), the first term increases linearly and the second term decreases hyperbolically with A. Differentiation of (1.208) results in

$$\frac{d(K/L)}{dA} = \frac{\sigma}{X} - EI^2(\sigma A^2) \tag{1.209}$$

This differential coefficient has to be zero for K/L to be equal to the Kelvin minimum cost. The minimum exist at

$$A = \frac{I}{\sigma}\sqrt{EX} \tag{1.210}$$

At this value of A the two terms of (1.208) are equal to each other, which is the proof of Kelvin's law. The actual value of the Kelvin minimum is

$$\left(\frac{K}{L}\right)_{\min} = 2I\sqrt{\frac{E}{X}} \tag{1.211}$$

Equation (1.211) indicates that for the economically optimized conductor, the transmission cost per unit length is proportional to the square root of the energy cost per watt of dissipation and inversely proportional to the square root of the conductor figure of merit. Figure 1.76 is a graphic representation of these results. In practical transmission line conductors, the current I is not constant and allowance for this should be made in (1.206) to (1.211). This can be done with a loss factor α, which is determined by the daily load cycle. First it is necessary to define the cable load factor CLF

$$\text{CLF} = \frac{\text{daily average load}}{\text{continuous cable rating}}$$

Cable load factors are lower than system load factors because the cable capacity is fixed, whereas the load peak may vary from day to day. Very approximately, a system load factor of 75 percent may be assumed to correspond to a cable load factor of 50 percent. No observed cable load factor statistics have been published that would permit more accurate estimates to be made. Two formulas have been used in the past to allow for

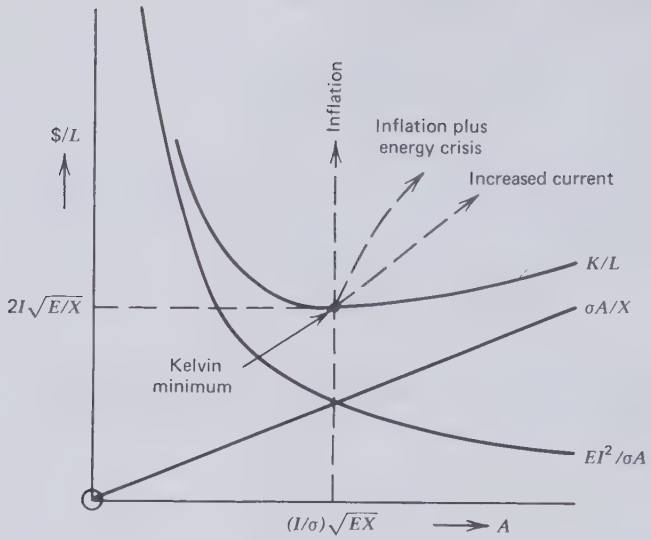

Figure 1.76 Graph of Kelvin's law.

the typical shape of a daily load cycle curve. They do not differ substantially. The one quoted by Neher and McGrath [1.19] is

$$\text{Loss factor} = \alpha = 0.3\ (\text{CLF}) + 0.7\ (\text{CLF})^2 \tag{1.212}$$

Therefore, in optimizing conductor sizes for cyclic loading by Kelvin's law, I/α has to be substituted for I in (1.206) to (1.211).

Figure 1.77 compares the 1976 transmission cost attributable to copper, aluminum, and sodium conductors for 200 A of constant current or 667 A at 50 percent cable load factor ($\alpha = 0.3$). The ranking of the three metals is again according to the figure of merit X, but the minimum transmission cost is governed by the square root of this figure. It is clear from Fig. 1.77 that in 1976 the economics favored large aluminum conductors and even larger sodium conductors. Sodium has so shallow a minimum that conductor cross sections below the optimum value of A incur only small penalties. Referring back to Fig. 1.76, it will be seen that both the ordinate and the abscissa of the Kelvin minimum are proportional to the current or I/α. When the current is larger than that used for plotting Fig. 1.77, therefore, the Kelvin minimum will move up along a straight line that passes through the origin and the cost minimum for the respective metal shown on Fig. 1.77.

An inflation factor β would raise m and E by the same fraction. Now we note that the ordinate of the Kelvin minimum is proportional to $\sqrt{E/X}$. With inflation this becomes proportional to $\sqrt{\beta E \beta m} \propto \beta$. The abscissa, on the other hand, is proportional to $\sqrt{E/X} \propto \sqrt{\beta E/(\beta m)}$ and is therefore

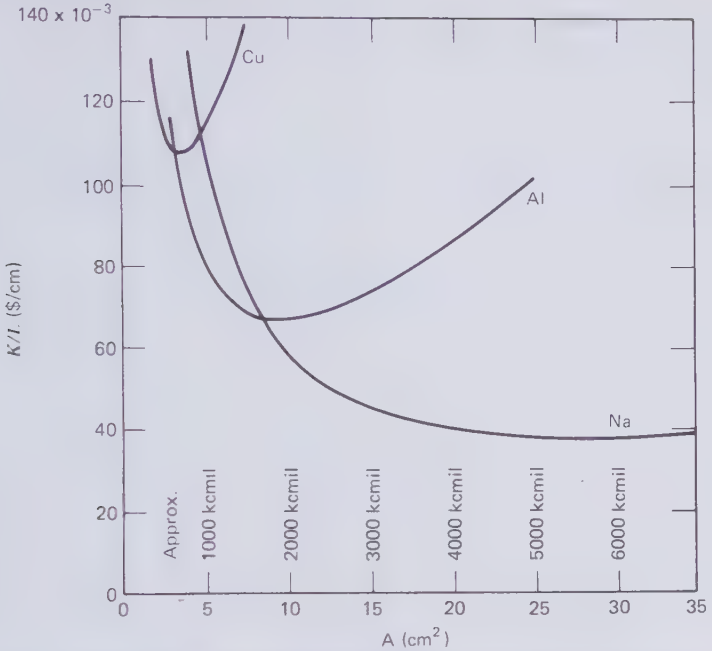

Figure 1.77 1976 Transmission cost attributable to the conductor for 200 A constant current or 667 A at 50% cable load factor.

independent of inflation. From this it follows that for pure inflation the Kelvin minimums would move upward in proportion to the inflation factor, which is equivalent to changing the vertical scale.

Owing to the energy crisis in the 1970s, the price of electricity has risen faster than the cost of conductor metals. If this trend is continuous in addition to inflation, the Kelvin minimum will be raised by a greater factor than β and it will also be deflected toward larger conductor cross sections A, as indicated in Fig. 1.76. The steep increase in the cost of energy that followed the 1973 oil embargo has left most installed conductors operating far to the left of the Kelvin minimum.

The cost ratios of optimized aluminum and sodium conductors with respect to optimized copper conductors were in 1976

$$\frac{K_{\min,\mathrm{Al}}}{K_{\min,\mathrm{Cu}}} = \sqrt{\frac{X_{\mathrm{Cu}}}{X_{\mathrm{Al}}}} = 0.62$$

$$\frac{K_{\min,\mathrm{Na}}}{K_{\min,\mathrm{Cu}}} = \sqrt{\frac{X_{\mathrm{Cu}}}{X_{\mathrm{Na}}}} = 0.35$$

The Joule loss J per unit length of the conductor is given by

$$\frac{J}{L} = \frac{I^2}{\sigma A} \tag{1.213}$$

If we compare the losses in two metals 1 and 2 per unit length of the conductor and for the same current I at the Kelvin minimum, we find that

$$\frac{J_1}{J_2} = \frac{\sigma_2 A_2}{\sigma_1 A_1} \tag{1.214}$$

where A_1 and A_2 are the conductor cross sections at the Kelvin minimums. But since $A = (I/\sigma)\sqrt{EX}$

$$\frac{A_2}{A_1} = \frac{\sigma_1}{\sigma_2}\sqrt{\frac{X_2}{X_1}} \tag{1.215}$$

and therefore

$$\frac{J_1}{J_2} = \sqrt{\frac{X_2}{X_1}} \tag{1.216}$$

In other words, the energy saving brought about by operating aluminum and sodium at the Kelvin minimum is in proportion to the transmission cost saving, or

$$\frac{J_{Al}}{J_{Cu}} = \sqrt{\frac{X_{Cu}}{X_{Al}}} = 0.62$$

$$\frac{J_{Na}}{J_{Cu}} = \sqrt{\frac{X_{Cu}}{X_{Na}}} = 0.35$$

Finally it has to be remembered that the cost of transmitting electrical power depends not only on the conductor but also on the insulation and the installation of the transmission line. Nevertheless, because of the dominant role the conductor plays with regard to energy losses, the overall transmission economics are strongly influenced by the conductor economics. This fact has been responsible for the swing from copper to aluminum conductors and probably will hasten the increased use of sodium conductors.

Part Two
HIGH-VOLTAGE INSULATION

2.1 RELIABILITY OF TRANSMISSION LINES

Public debates of the environmental merits of underground versus overhead transmission lines usually balance landscape aesthetics against the higher cost of undergrounding borne by the utilities and the consumers. At the time of writing, the most telling economic factor is the line conductor and, most of all, the energy that is being converted to heat inside the conductor. It is a historical fact, however, that the evolution of high-voltage cables, both for underground and underwater transmission, has been guided more by reliability consideration than economic pressure. The primary aspect of high-voltage cable reliability is the electrical insulation.

When studying the reliability of bulk power supply systems one has to distinguish between service reliability and equipment reliability, as has been pointed out by the Federal Power Commission [2.1]. Equipment may fail but power continuous to be supplied by standby or other underutilized equipment. The safest measure of ensuring the transport of electricity when one or more power lines have been damaged is to build a large amount of redundancy into the transmission network. This requires individual circuits to be capable of carrying substantially more power than they are normally called upon to convey. Redundancy may also be provided by duplicating circuits and particularly underground lines are often installed in pairs to form double circuits. Another method of ensuring supply continuity is to provide as many interconnections between generating plants as possible so that any given service area receives power from several directions.

Redundancy in the transmission network is inevitably coupled with low load factors and therefore reduced Joule heating losses. This is a positive way in which reliability and economy interact. More often, however, greater reliability has to be purchased at additional cost. It is well worth buying if it

can avert such catastrophies as the northeast blackout on November 9, 1965. This encompassed an area of 80,000 square miles and affected an estimated 30 million people in the United States and Canada, leaving 800 hospitals without commercial power [2.2]. The monetary loss was $ 100 million and would have been much higher had the outage not occurred on a mild moonlit evening. The cause of this blackout was the operation of a small relay in a power plant at Niagara Falls, but the extent of the disaster was attributed to general lack of reserve transmission capability.

The provision of adequate transmission capability lies in the hands of system planners. Just how much redundancy has to be built into a system depends to a considerable degree on the trust that can be placed in individual lines and therefore ultimately comes down to the question of equipment reliability. This parameter has two facets: (1) the frequency of line failures and (2) the outage time per failure, which is determined by the speed with which a circuit can be restored to service. The second point appears to be of greater importance than the first because damage-prone overhead lines are universally preferred by power companies to the more protected underground circuits. As the 1977 New York blackout demonstrated once again, overhead lines cannot be made to withstand all weather conditions. Yet in spite of several serious line failures, full service to the city was restored within a few days. An equally massive failure of underground lines could not have been repaired in so short a time. It is more difficult to locate underground faults, but the major problems are access in traffic bearing streets and the long time it takes to splice oil-paper insulated cables. The fear that utility executives have of underground cable failures was well expressed by Hauspurg [2.3] of the Consolidated Edison Company of New York when he reported on two 345-kV pipe-type cable failures in his city:

> Fortunately, both these failures occurred during off peak seasons because the time to locate, freeze, and replace faulty sections took from three to seven weeks because of the complexity required to handle 345 kV (paper) cable systems. We clearly need simpler methods for joining these cables. A seven week outage during the peak season would have been a very severe operating problem.

The difficulties of splicing and terminating high-voltage cables depend on the type of insulation. Joining overhead line conductors is a simple welding operation, requiring little time. The insulation around an overhead joint is the atmosphere, which continuously renews itself. Because of the great distances between conductors and grounded structures, the air may be saturated with moisture and particulate pollution. In contrast to this, many manhours of diligent and highly skilled work go into rebuilding the insulation surrounding a conductor joint in an oil-paper insulated cable. This insulation is not self-renewing. A conducting particle, moisture, or a crease or tear in one of the paper tapes can subsequently cause a little ionization,

which breaks further molecular bonds of the weak organic material setting free conducting carbon atoms, which on accumulation will give rise to voltage breakdown.

Compressed gas insulated cables are much easier to splice than oil-paper insulated cables because the jointing operation of conductors and the outer pipe consists of welding and no manual reconstitution of the insulation is required. Further simplifications of the jointing procedure seem feasible with vacuum insulation because it is easier to check for vacuum leaks than for pressure leaks and the vacuum insulation is more tolerant to loose particles and stress raising surface roughness and distortion. Besides this, it is more difficult to set up and maintain a destructive arc in vacuum than in a gaseous medium.

Most forced cable outages are the result of 'dig-ins'. This term stands for externally inflicted mechanical damage by excavation machinery used in the installation and repair of other underground services such as water, gas, and telephone lines. The solution to this problem resides in strong enclosure pipes or ducts or the burial of cables under protective concrete slabs.

Innate distrust of new high-voltage insulation systems has delayed innovation in the underground and underwater power transmission field. The general acceptance of new and more economical systems usually has to wait until quite a few installations have been in successful operation for 10 or 20 years. Even when a proven technology is stepped up in voltage, the power companies insist on extensive demonstration testing. An example of this was the 500-kV pipe-type cable program at Waltz Mill [2.4] which was jointly funded by the cable and utility industries. It lasted for 5 years and took an estimated expenditure in excess of $10 million to prove that it was safe to produce 500 kV oil-paper insulated cables in the same way, but with additional insulation thickness, as 345 kV cables had been produced for a number of years.

Excluding external mechanical damage, the scientific basis of insulation reliability is an understanding of dielectric breakdown. The present state of knowledge regarding this subject is far from adequate, particularly in the case of solid insulation. Ongoing research is however beginning to illuminate some of the darkest areas. As a result of this, high-voltage cable technology is now slowly but surely inching away from paper insulation, which was the first insulation tried on the first underground transmission line connecting a generating station outside London with the city center almost 100 years ago [1.59]. Because of the overriding importance of cable reliability, the first part of the discussion of high-voltage insulation will concern itself with the breakdown process.

The two other topics to be examined are cable capacitance and dielectric loss. The capacitance absorbs reactive power, which may have to be transported over long distances and thereby dissipates energy in the conductors.

The capacitive charging current also limits the power transmission capability of a cable. Dielectric losses together with the Joule loss raise the conductor and insulation temperatures and waste valuable energy. Dielectric breakdown, charging current limitations and dielectric loss all are problems that increase in severity with operating voltage. The march up the voltage ladder has been continuous since the beginning of large-scale electricity generation and the last rung is still out of sight.

2.2 THE TREND TO EVER INCREASING TRANSMISSION VOLTAGES

The first electric power systems were based on dc generators and dc distribution networks. In 1882 Gaulard and Gibbs in France invented the ac voltage transformer [1.59]. This immediately stimulated speculation about the best way of connecting large generators at or beyond the periphery of cities with the consumers in the center of urban areas. It developed into a struggle, filling the decade of the 1880s, between the conservatives, who preferred to stay with dc and had Thomas Edison as their chief spokesman, and the ac innovators headed by George Westinghouse and his colleague William Stanley. That the arguments were at times bitter may be judged from Edison's statement [1.59]: "My personal desire would be to prohibit entirely the use of alternating currents. They are as unnecessary as they are dangerous." Westinghouse responded with action on which Stanley reported as follows [1.33]: "We installed in the town plant of Great Barrington (Massachusetts) two 50-light and four 25-light transformers, the remainder being used in the laboratory for experimental work. The transformers in the village lit 13 stores, 2 hotels, 2 doctor's offices, one barber shop, and the telephone and post offices. The length of the line from the laboratory to the center of the town was about 4000 feet."

In the same year a 17-mile ac line was built in Cerchi, Italy, to transmit 112 kW of hydroelectric power at 2000 V. The first sizeable transmission line was installed by the London Electricity Supply Corporation in 1891 [1.59]. It was a 27-mile ac underground line operating at 10 kV. The paper-insulated cables of this line, known as Ferranti tubes, contained 7000 splices. Part of the installation was in use for over 40 years. The British government expressed misgivings regarding so high a transmission voltage running underground and for some distance along a railroad just above the ground surface. The question most frequently asked was what would happen if the cable be touched accidentally by human hands. To quench the remonstrations, Ferranti who had designed the line staged another historical ac demonstration, which Hunter and Hazell [1.59] describe as follows:

"One of his (Ferranti's) assistants, Harold Kolle, standing on an earthed (grounded) copper plate, held a cold chisel to the live main (cable) with his bare

hands: and a colleague armed with a sledge hammer then drove it through both conductors—with no more fatal results than the blowing of the main fuse link. The story goes that Kolle, asked later if he had not been frightened, replied: Frightened? I was scared out of my life! Young Henty had never used a sledge-hammer before."

In the United States the first important transmission line was built to carry hydroelectric power from Willamette Falls to Portland, Oregon, at a single-phase voltage of 3300 V. From then onward overhead transmission has been leading the way. The highest voltage now in use is 765 kV by the American Electric Power Company. Progressive transmission voltage increases as they occurred since 1890 are plotted on Fig. 2.1. At an average rate of approximately 10 kV/year, the small steps made early in our century have more recently been surplanted by giant steps of 300 to 500 kV a time with correspondingly long dwell periods. Underground transmission voltages have lagged behind a little, but from 1930 onward they have climbed up the voltage ladder almost as fast as overhead voltages.

Already in the 1960s, the Pirelli company in Italy satisfied itself by laboratory tests that it could supply 750 kV oil-paper insulated cables of the same reliability as lower voltage cables. Since 1974 the same company has offered to supply this type of cable up to 1100 kV [2.6]. However, no underground or underwater lines operating above 550 kV have been installed by 1979. In fact the evolution of high-voltage cables has reached a

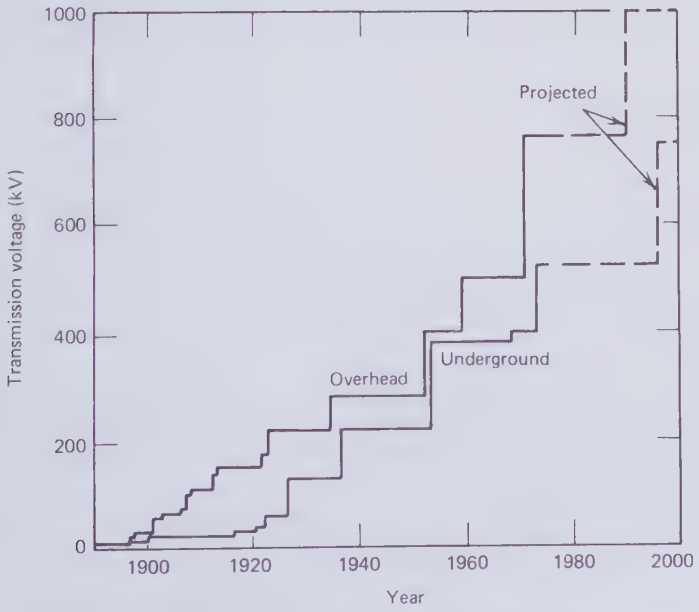

Figure 2.1 Worldwide increase of ac transmission voltages since 1890.

crisis point and significant expansions of underground systems have come to a halt in the 300–400 kV range. United States underground transmission additions reached a high in 1973 of 167 circuit-miles and since then have in fact declined to less than half this amount in 1977 [2.10]. Before examining this turn of events further it is helpful to study in a little more detail what the attractions of the highest transmission voltages should be.

The argument favoring ac over dc transmission was based on the simplicity of transformers with which it was easy to generate high ac voltage and back it with adequate power handling capability. The higher the voltage, the less current conductors have to carry. As the conductor loss is proportional to the square of current, doubling the line voltage brings with it a 75 percent saving in conductor loss. This trend is shown in more detail on Fig. 2.2 for the four power levels of 500, 1000, 2000, and 4000 MVA. The graphs actually depict the Joule heating loss as a percentage of transmitted power per ohm of conductor resistance. Consider a three-phase circuit of a line-to-line voltage V carrying a phase current I which has to overcome the phase resistance R. Then the total conductor loss W_J is

$$W_J = 3I^2R \tag{2.1}$$

But the power P transferred over the three-phase circuit is given by

$$P = \sqrt{3}\ VI \tag{2.2}$$

Combining these two equations gives the Joule power loss per unit resistance as

$$\frac{W_J}{R} = \frac{P^2}{V^2} \tag{2.3}$$

As a percentage loss per unit resistance it can be written

$$\frac{100\,W_J}{RP} = \frac{P}{V^2} \times 100\ (\%/\Omega) \tag{2.4}$$

This is the quantity that has been plotted on Fig. 2.2 against transmission voltage. Up to 1973 a reasonable rule of thumb would have been to operate lines close to 1 percent conductor loss/ohm of line resistance. This rule would have ensured low transmission cost somewhere in the vicinity of the Kelvin minimum of Fig. 1.76. To ensure the same result in post-oil-embargo years, lines have to be operated below the 1 percent/ohm conductor loss limit.

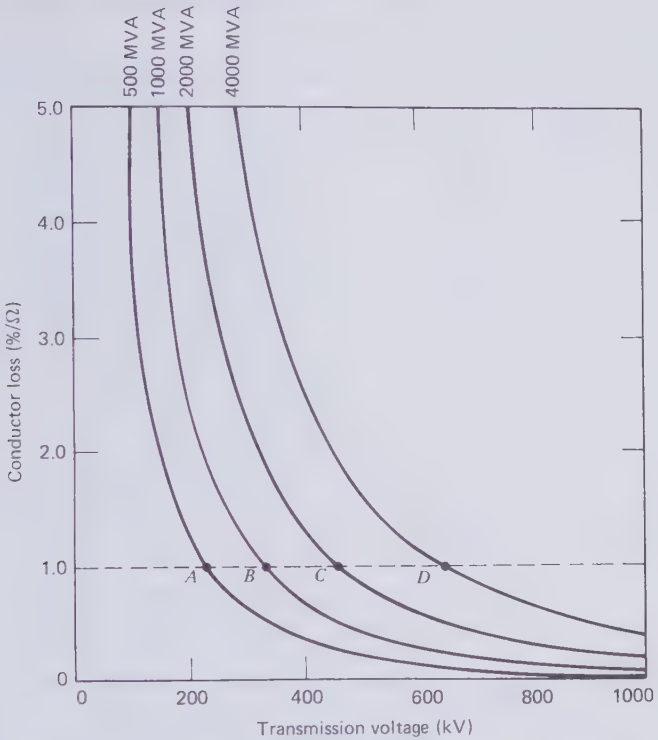

Figure 2.2 Conductor loss as a function of transmission voltage.

Data of typical U. S. overhead transmission lines is listed on Table 2.1. Column 6 of this table shows the ampacity, or normal full load current, of these lines and column 7 gives the current that would produce 1 percent of conductor loss/ohm. It will be seen that at the 1 percent limit the current is approximately the same as the line ampacity. Therefore past U. S. overhead line practice could be roughly represented by points *A*, *B*, *C*, and *D* of Fig. 2.2. These points indicate that a 500 MVA circuit should operate at 230 kV, the 1000 MVA circuit at 330 kV, the 2000 MVA circuit at 450 kV, and the 4000 MVA circuit at 630 kV.

Judging from the results of cost calculations given on Table 2.1, the sharp increase in the price of energy since 1973 has driven the operating point of typical U.S. overhead lines well to the left of the Kelvin minimum. That the cost of energy losses is now greater than the installed line cost is further illustrated in Fig. 2.3, which has been drawn up from the data on Table 2.1. It has to be stressed, however, that these particular results apply only when the load factor is 50 percent of the thermal line capability. For greater load

Table 2.1 Data of Typical U.S. Overhead Transmission Lines [2.7, 2.8]

1 Transmission Voltage (kV)	2 Number of Circuits/Tower	3 Number of Conductors/Phase	4 Conductor Size (ACSR) (kcmil)	5 Phase Resistance (Ω/mi)	6 Ampacity (kA)	7 Current at 1%/Ω Limit* (kA)	8 Thermal Line Capability MVA
138	1	1	795	0.140	0.88	0.80	210
138	2	1	795	0.140	0.88	0.80	420
230	1	1	1431	0.076	1.22	1.33	490
230	2	1	1431	0.076	1.22	1.33	980
345	1	2	795	0.070	1.75	1.99	1050
345	2	2	1590	0.035	2.64	1.99	3160
500	1	2	1780	0.031	2.85	2.89	2470
765	1	4	954	0.028	3.89	4.42	5150

*See Fig. 2.2.
†From [2.8].
‡Estimated by the author.

9	10	11	12	13	14	15	16
Installed Cost ($/mi)			Maximum Conductor Loss	Cost of Loss Generator	Energy Loss/Year at 50%	Capitalized Loss at 9% Interest Rate	1977
1971†		1977‡	(kW/mi)	@ $460/kW	Line Load Factor	and 1.76¢/kWh	Transmission Cost
Minimum	Maximum	Mean	(at load of col. 8)	($/mi)	(kWh/yr)	($/mi)	($/MVA·mi)
73,000	136,000	157,000	325	149,500	0.854×10^6	167,000	2255
97,000	184,000	211,000	650	299,000	1.708	334,008	2010
94,000	173,000	200,000	339	155,940	0.891	174,240	1082
128,000	237,000	274,000	678	311,880	1.782	348,480	953
101,700	171,000	205,000	643	295,780	1.690	330,489	792
183,500	393,000	432,000	1464	673,440	3.847	752,302	588
155,100	306,000	346,000	755	347,300	1.984	387,982	438
199,400	387,000	440,000	1271	584,660	3.340	653,155	326

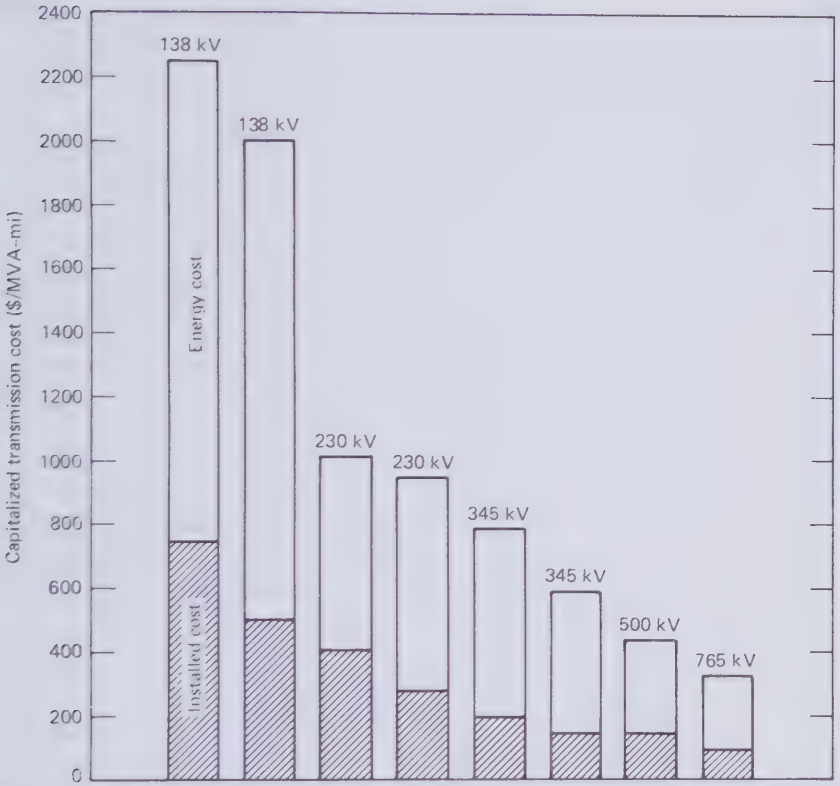

Figure 2.3 1977 Capitalized transmission cost of the typical U.S. overhead lines described in table 2.1.

factors the balance would be tilted even more heavily toward line losses. On the other hand, when lines are very long, reactive power flow problems usually require them to carry substantially less current than would be possible from thermal considerations alone. As the permissible load current is reduced, the capital cost component of Fig. 2.3 will increase while the loss energy cost component decreases. Therefore long lines are likely to operate nearer to the Kelvin minimum transmission cost than would be expected from Fig. 2.3.

Regardless of design optimization, Fig. 2.3 demonstrates that there exist compelling economic reasons to transmit power at the highest possible voltage. The greatest unit cost reduction occurs between 138 and 230 kV. There are no signs that the voltage race is likely to abate in the present century; but it seems inevitable that diminishing economic returns at the highest voltages will retard progress on the voltage ladder during the next

century. Other reasons that will reinforce this trend are the enormous size of transmission towers and the audible noise and radio and television interference of corona discharges in wet weather. Corona losses also have a small impact on the transmission economics.

Underground and underwater cables will undoubtedly progress beyond the present 500 kV level, but some hesitation in the employment of oil-paper insulated cables for this purpose has become obvious. Apart from the fact that oil-paper cables are very much more expensive to produce and install than overhead lines, they are further penalized by their dielectric losses and high dielectric constant. Based on information contained in [2.7] and [2.8], the 1977 value of the dielectric loss is plotted on Fig. 2.4 as a function of transmission voltage. This graph indicates that, for voltages beyond 600–700 kV, the financial outlay on the dielectric losses of oil-paper insulation becomes greater than the total cost of installed overhead lines and their losses. The cross over of the two curves of Fig. 2.4 has no particular significance except that it proves that overhead lines continue to benefit from increased operating voltages, whereas conventional underground transmission lines are running into serious economic hurdles as their voltages are pushed beyond the present level. When short sections of a transmission line

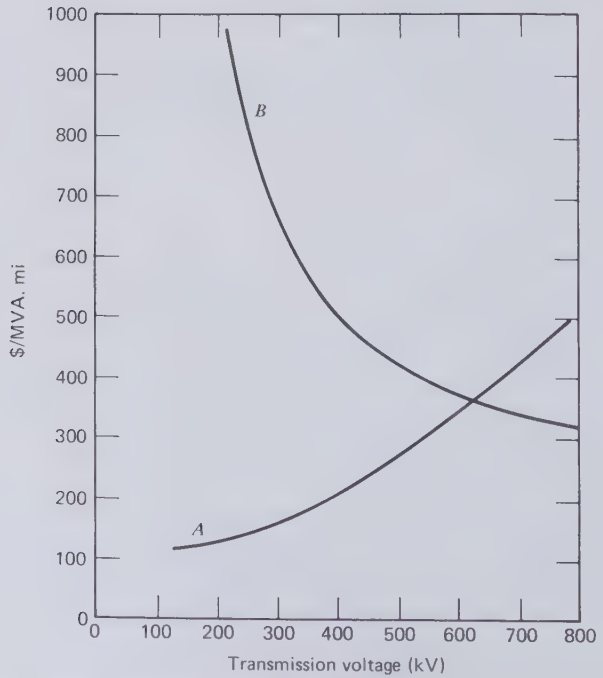

Figure 2.4 1977 Value of dielectric losses of oil-paper insulated pipe-type cables [2.7, 2.8] (curve *A*) compared with capitalized overhead transmission cost (curve *B*).

have to be underground for scenic reasons or because of natural obstacles, such as bodies of water, the cost of dielectric losses will be of minor importance and oil-paper insulated cables will undoubtedly be used for this purpose up to perhaps the 1100 kV cables that may already be purchased in Europe [2.6]. However, underground transmission lines of substantial length connecting major generating centers with urban areas will probably have to operate below 500 kV or depend on new kinds of high-voltage insulation with lower dielectric losses and smaller charging currents.

In spite of the resounding success of ac transmission, high-voltage dc transmission lines have also had their champions. Many years ago, series-connected dc generators were found capable of producing substantial voltages. The most notable example of early high-voltage dc transmission was the 138-mile Montiers-Lyons line in France installed in 1906. This was capable of transmitting 20 MVA at 125 kV and it contained a 23-mile underground section [2.9]. The cable was insulated with high-viscosity resin-oil impregnated paper, a design that is often described as "solid-type cable." After an eclipse lasting nearly 40 years, renewed interest in dc transmission was stirred by the development of mercury-arc power rectifiers. The next step-up in dc transmission voltage was a 72-mile cable installed in the Soviet Union in 1949 between Kashira and Moscow. This cable used substantially the same insulation as the early French dc cable. It was rated to carry 80 MVA at 200 kV. Since then ± 375 and ± 400 kV dc overhead lines have been installed in the United States and the Soviet Union. The largest dc cable is in use between Kingsnorth and London in England transmitting up to 640 MVA at ± 266 kV over a distance of 53 miles. This is a self-contained oil-paper insulated cable of about the same capacity as the 600 MVA ± 250 kV dc submarine transmission link between generating facilities on South Island and load centers on North Island of New Zealand. This latter cable, which crosses the hazardous Cook Strait, is 25 miles long. There exist several more high-voltage dc submarine cable links. The use of direct current not only eliminates dielectric losses, but makes reactive current compensation unnecessary, which is particularly important for long underwater circuits. Oil-paper insulated dc cables have no difficulty keeping in step with the race to higher transmission voltages, which is so obvious in the overhead line field. Whether they will ultimately find widespread use depends not so much on the cables themselves but on the economics of rectification and inversion plant.

2.3 DIELECTRIC BREAKDOWN OF GASES

Cables have been in use since the 1930s in which dry or preimpregnated paper insulation is filled with compressed nitrogen gas. Forty years later, in the early 1970s, rigid compressed gas insulated cables were introduced. They

contain sulfur-hexafluoride (SF_6). Gas is far from being the most important insulation of underground systems, but the gas breakdown mechanism will be discussed first because it is better understood than the breakdown of liquids and solids. This mechanism contains elements that serve as a model for the breakdown of the more dense media. Besides, high-voltage cable insulation has to compete with the air insulation of overhead lines.

Townsend Avalanches

Townsend, in his studies of gaseous discharge currents in uniform electric fields, arrived at the conclusion that under certain conditions, subject mainly to the state of the gas and the field strength, multiplication of charge carriers took place in the gas [2.11]. He assumed a free electron traveling in the gas could, over the length of one free path, acquire sufficient kinetic energy to produce a new pair of ions by collision with a neutral molecule. If the negative ion resulting from the collision is also an electron, then there are two electrons available to carry on the ionization process, which progresses as an avalanche across the gap until it strikes the electron-absorbing anode. This Townsend electron avalanche has become an important concept in all breakdown theories, because the chain of events in liquid and solid breakdown may encompass a vapor phase capable of supporting electron avalanches. The light emitted by the positive ions in the avalanche has been photographed. It showed that the avalanche is narrow and conical in shape, with a spherical head. Electron avalanches frequently, but not always, originate at or close to the cathode.

To estimate the number of electrons in an avalanche and to treat this ionization process quantitatively, Townsend introduced his first ionization coefficient α, which he defined as the number of electrons produced by one incident electron traveling 1 cm in the direction of the field. This α-coefficient is a function of the field strength E accelerating the electron between collisions and the length of the mean free path λ, which itself is inversely proportional to the gas pressure p. The kinetic energy gathered by the electron of charge e and mass m over one mean free path is

$$E\lambda e = (1/2)mv^2 \tag{2.5}$$

where v is the velocity with which it impinges on the neutral molecule. As $E\lambda$ is a potential difference given in volts, the energy of the electron may be expressed in electron-volts (eV). There exists a minimum energy with which the electron has to collide with the neutral molecule in order to split off another electron. This is known as the ionization energy, and it is listed in

Table 2.2 Ionization Energies of the Constituents of Air and Insulation Gases

		Ionization Energy (eV)
Helium	He	24.5
Argon	A	15.7
Hydrogen	H_2	15.4
Nitrogen	N_2	15.5
Oxygen	O_2	12.2
Carbon dioxide	CO_2	13.7
Sulfur hexafluoride	SF_6	15.7
Water vapor	H_2O	12.6

Table 2.2 for the major constituents of air and gases used for high voltage insulation. If the energy of free electrons in the gas is less than the ionization energy, α will be zero. However, if $E\lambda e$ is sufficiently large to cause ionizing collisions, then from a thin layer of thickness dx and perpendicular to the direction of the field, on which n electrons impinge, $(n+dn)$ electrons will emerge moving toward the anode. From the definition of α we have

$$dn = n\alpha dx$$

and over the full length d of the interelectrode gap containing the uniform field E

$$\int_{n_0}^{n_a} \frac{dn}{n} = \int_0^d \alpha dx \tag{2.6}$$

where n_0 electrons leave the cathode and n_a arrive at the anode. Since E and p are constant across the gap, α will also be constant. Therefore integrating (2.6) results in

$$n_a = n_0 e^{\alpha d} \tag{2.7}$$

This shows that the number of electrons in the avalanche increases exponentially with gap length, provided the initiating electron was located at or near the cathode surface and not in the middle of the gap. Since $\lambda \propto 1/p$, α is determined solely by the electric field per unit pressure E/p. In other words, if E and p are increased by the same fraction, α remains constant. The quantity α/p has been measured for many gases [2.13]. To show its general behavior as a function of (E/p), the results of Sanders [2.12] for mercury contaminated air have been plotted on Fig. 2.5. Curves for other gases are of a similar shape. The curves of the best insulating gases lie to the right of the air curve.

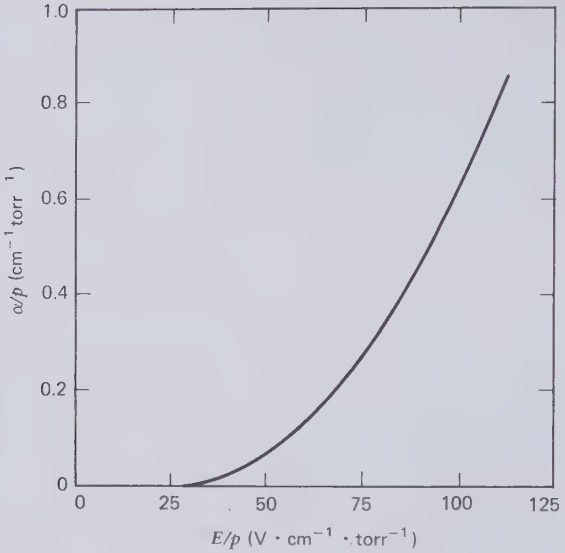

Figure 2.5 Townsend's first ionization coefficient for air [2.12].

Townsend originally suggested that positive ions would also produce ion multiplication by collisions with neutral gas molecules and for this purpose he introduced his second coefficient β. This hypothesis has long been contradicted by ionic mobility measurements. However, Townsend's third or γ-coefficient has survived, but its physical interpretation has undergone changes with time. In the beginning it was meant to account only for secondary electron emission at the cathode due to impinging positive ions. The modern trend is to employ it as a collective coefficient to account for all processes yielding free electrons on or near the cathode, other than the α mechanism. The most likely additional process could be ionization by photons. A strict definition of the γ coefficient is the number of secondary electrons generated at or near the cathode per ionizing collision in the avalanche [2.13]. If n_2 is the number of secondary electrons produced, (2.7) should be modified to

$$n_a = (n_0 + n_2)e^{\alpha d} \tag{2.8}$$

Now the number of ionizing collisions in the avalanche is $n_a - (n_0 + n_2)$, so that

$$\gamma = \frac{n_2}{n_a - n_0 - n_2} \tag{2.9}$$

By eliminating n_2 from (2.8) and (2.9) it is found that

$$n_a = \frac{n_0 e^{\alpha d}}{1-\gamma(e^{\alpha d}-1)} \tag{2.10}$$

The process described by (2.10) will become unstable and n_a will tend to infinity when

$$\gamma(e^{\alpha d}-1)=1 \tag{2.11}$$

But usually $e^{\alpha d}$ is very much greater than one and (2.11) reduces to the approximation

$$\gamma e^{\alpha d} \simeq 1 \tag{2.12}$$

which is known as Townsend's sparking criterion for uniform fields.

A single electron avalanche does not represent breakdown. When the sparking criterion is fulfilled, a string of avalanches cascades across the high-voltage gap and the discharge becomes self-sustaining. Each avalanche leaves behind it a cloud of positive ions because electrons are very much more mobile than the heavy ions. When the positive space charge is strong enough, it will retain electrons to form a conducting plasma. This plasma behaves almost like a metallic conductor, and as soon as it has been established the discharge current is limited only by the strength of the power source and the external circuit impedance. The only way of permanently extinguishing such an arc in a cable is by disconnecting it from the power source through a circuit interrupter. Temporary extinction of the arc takes place every time the ac power follow-current passes through a zero. At 50 or 60 Hz oscillations, the dwell time at the current zeros is too short to permit gap deionization and the arc will immediately reignite as the gap voltage reverses. This is not necessarily true for long gaps in which the electric field is very nonuniform. Flashover between two overhead line conductors is often self-extinguishing. If the fault current flows only for part of one ac cycle it should be called a spark. Whichever terminology is applied, the Townsend sparking criterion (2.12) defines dielectric gas breakdown in uniform electric fields.

From approximately 10 atm pressure down to the near vacuum region, Townsend's sparking criterion is in good agreement with breakdown measurements. Deviations have been observed at higher pressures and for gaps that are longer than 3 in. When the Townsend criterion holds, Pashen's law also applies. Pashen found by experiment that the breakdown voltage V_b across a uniform field gap depends on the product of gas pressure p and the

gap length d, or

$$V_b = f(pd) \tag{2.13}$$

Townsend's theory actually confirms this law. For example, if the pressure is doubled and the gap length is halved without changing the voltage, each electron is subject to acceleration by twice the field strength but will have its free path reduced to half and therefore aquires the same kinetic energy. Furthermore, since d/λ remains constant, the same number of ionizing collisions take place and n_a and n_2 remain unchanged. This implies that both α and γ remain constant. Because of Paschen's law it is convenient to present the breakdown strength of a gas as a function of the product pd rather than each quantity separately. As the determination of the ionization coefficients involves as much effort as actual breakdown measurements, it is common practice in cable research to determine only the latter as new gases are being studied. This does not detract from the value of the Townsend theory, which outlines the factors that contribute to breakdown and describes a mechanism that can be readily visualized.

Breakdown strength measurements are accompanied by statistical scatter due to causes that are not taken into account by the Townsend mechanism. The approximate uniform field breakdown voltages of air, nitrogen, and SF_6 at ambient temperature are plotted on Fig. 2.6 against the Paschen product pd. These curves apply to p and d values for which breakdown is determined by the Townsend sparking criterion. In this regime, it will be noted, the breakdown stress (V_b/d) is proportional to the gas pressure p. Nitrogen gas is only a slightly better insulation than air, but sulfur hexafluoride is substantially better than air. This is attributed to the fact that SF_6 is an electronegative gas. Because of its high dielectric strength, sulfur hexafluoride is used in compressed gas insulated cables.

The feature of electronegative gases, to which SF_6 belongs, is that some of the free electrons attach themselves to neutral molecules. This phenomenon removes electrons from the avalanche and consequently increases the sparking voltage. If this should seem strange, it has to be realized that even inside the avalanche the density of neutral molecules is much greater than the density of positive ions. Therefore the chance that an electron collides with a neutral molecule is much greater than its chance of meeting a positive ion. Geballe and Harrison [2.15] defined an attachment coefficient η given by the number of electrons combining with neutrals per centimeter of pathlength to form negative ions. Referring back to the equation preceding (2.6), this means that the number of electrons made available per centimeter of pathlength for avalanche multiplication now is only

$$dn = n(\alpha - \eta)dx \tag{2.14}$$

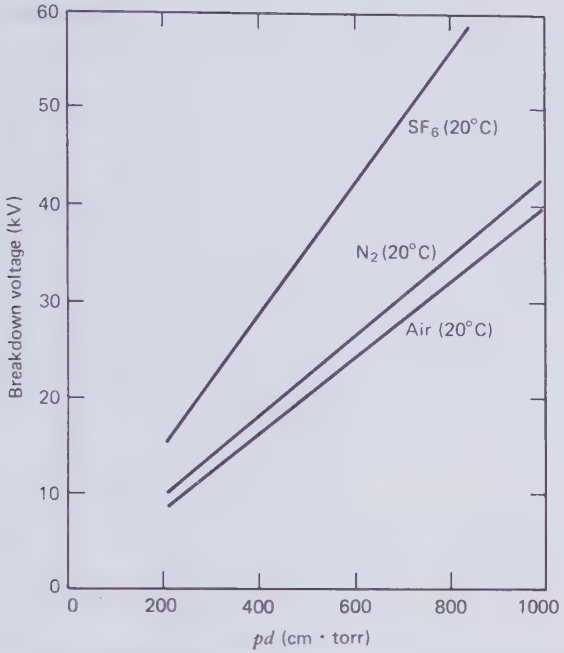

Figure 2.6 Uniform field breakdown strength of air, nitrogen and sulfur hexafluoride in the Townsend regime.

And the number of electrons reaching the anode becomes

$$n_a = (n_0 + n_2)e^{(\alpha-\eta)d} \tag{2.15}$$

The production of secondary electrons is governed by the number of positive ions reaching the cathode. This latter number is no longer equal to the number of electrons reaching the anode because a fraction of the electrons are lost through attachement but they leave behind a corresponding number of positive ions. Therefore γ has to be increased in the ratio of $\alpha/(\alpha-\eta)$. If γ_- is the secondary electron emission coefficient modified through electron attachment, it may be expressed in terms of the original coefficient by

$$\gamma_- = \left(\frac{\alpha}{\alpha-\eta}\right)\gamma \tag{2.16}$$

For electronegative gases, therefore, (2.15) and (2.16) modify Townsend's sparking criterion (2.11) to

$$\gamma\left(\frac{\alpha}{\alpha-\eta}\right)\left[e^{(\alpha-\eta)d}-1\right]=1 \tag{2.17}$$

When $\alpha = \eta$, all the electrons produced by collision ionization are absorbed by electron attachment, and the build-up of an avalanche, and therefore sparking, becomes impossible. It will be noted that the criterion (2.17) provides no finite solution for this case. Any solutions given when $\eta > \alpha$ must be meaningless because no avalanches can occur. Therefore the validity of the sparking criterion for electronegative gases has to be restricted to $\alpha > \eta$. This criterion very clearly indicates that the dielectric strength of electronegative gases is greater than that of normal gases. Only SF_6 has achieved prominence in practical applications, but other electronegative gases are known to have even higher dielectric strengths than sulfur hexafluoride. Mulcahy et al. [2.16] reported on a series of such gases. All of them have heavy complex molecules and are close to being liquids at cable operating temperatures. The breakdown strengths measured by these authors relative to air are recorded in Table 2.3.

Table 2.3 Breakdown Strength of Electronegative Gases Relative to Air in Small Sphere Gaps [2.16]

		Boiling Point (°C)	Breakdown Strength Relative to Air
Sulfur hexafluoride	SF_6	−64	2.5
Hexafluorocyclobutene	C_4F_6	− 5	3.9
Octafluorocyclopentene	C_5F_8	+25	5.5
Decafluorocyclopentane	C_5F_{10}	+22	4.3
Trifluoroacetonitrile	CF_3CN	−63	3.6
Pentafluoropropionitrile	C_2F_5CN	−30	4.7
Heptafluorobutyronitrile	C_3F_7CN	+ 1	5.8

Source: By permission of Lake Publishing Corporation.

Streamers in Nonuniform Fields

Breakdown of gases in uniform fields is of academic interest only. It serves to illucidate the breakdown mechanism. The field associated with power transmission lines is invariable divergent. Electron avalanches are normally confined to the high stress region close to conductors. If they cannot traverse the full length of the gap, they give rise to partial discharges or corona. When an increasing ac voltage is applied across a coaxial gap, the first ionic events observed are a series of small but well-defined pulse discharges from the center conductor when this is the negative electrode. These initial Trichel pulses, named after their discoverer, are all of equal magnitude, very fast and regularly spaced on the time scale. It is generally believed that

Trichel pulses are individual electron avalanches originating at the cathode surface and dissipating themselves some distance away in the weaker field region where α tends to zero. Trichel pulses are absent during the half-cycle of the voltage wave when the center conductor is anode. But one or more intense pulse discharges do occur during this half-cycle at a voltage slightly above the onset of trichel pulses. These isolated discharges usually produce audible noise and luminous filaments starting in midgap and terminating on the conductor. They have been called streamers and as a rule have the jagged and branched appearance of a minute lightning stroke. At a little higher voltage the same phenomenon can be observed during the negative half-cycle.

The filamentary nature of gas discharges in nonuniform fields and just preceeding breakdown is supported by a host of experimental evidence. Raether [2.17] captured cloud track photographs of streamers. Streamer theories have been developed by Raether and by Loeb and Meek [2.18].

The Townsend mechanism results in a more or less steady discharge current crossing the high-voltage gap. This is a continuous function of the applied voltage until breakdown takes place. It cannot account for the discontinuous nature of streamers and their well-defined spark channels. New concepts had to be evolved to explain the appearance of the pulse discharges that differs so dramatically from the glow that would be expected from the typical Townsend avalanche process. Although Raether and Loeb have made major contributions to the understanding of streamers, only the treatment of this topic by Meek will be explained in detail.

He argues that streamer formation is the consequence of transient space charge fields created by the positive ions left behind electron avalanches. When the transient space charge field reaches some critical value E_s one or more new avalanches will be drawn into it, thereby giving rise to the build-up of a conducting channel of intense ionization, which is the streamer. In the coaxial gap configuration of cables it is necessary to distinguish between positive and negative streamers, depending on whether the center conductor is anode or cathode. The positive streamer will start close to the anode, as indicated in Fig. 2.7, and grow backward by avalanches rushing into the tail of the space charge channel. The negative streamer starts out in the gap and grows backward to the cathode with new avalanches rushing into the partly established channel of positive ions. In both instances the streamer progresses against the flow of electrons. Only three avalanches are indicated in Fig. 2.7 for both positive and negative streamers. It has to be understood, however, that streamers usually consist of many more avalanches. The individual streamer can be a single filament or it may have branches and subbranches. The negative streamer progresses into a convergent field, whereas the positive streamer advances into a

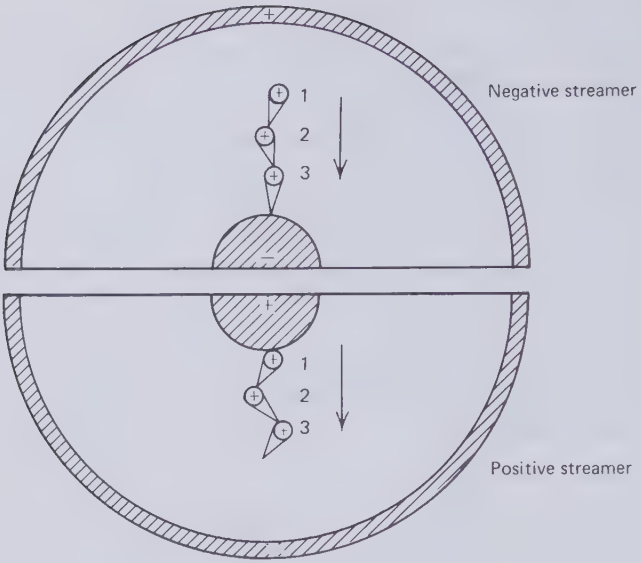

Figure 2.7 Growth of positive and negative streamers.

divergent field region. Therefore, the external field may be expected to have more of a guiding influence on negative streamers than on positive streamers. Positive streamers usually have more branches than negative streamers. This is particularly obvious from Lichtenberg figures that will be discussed later. Streamers that do not bridge the gap are partial discharges or corona events. However, when streamers cross the gap, they give rise to breakdown. It is imperative to operate cables below the streamer onset voltage. Overhead lines in wet weather operate in the streamer regime.

For a quantitative treatment of the streamer phenomenon two new parameters have to be introduced. They are the ionic mobility k and the diffusion coefficient D. An ion moving under the influence of an electric field E will acquire an average drift velocity v. The mobility of the ion is then defined as the drift velocity per unit field strength, or

$$k = \frac{v}{E} \tag{2.18}$$

If at any time like ions are generated cumulatively in a confined region of space, they will tend to diffuse in all directions and in the process collide with neutral molecules. Superposition of an electric field has the effect of orienting the diffusion in the direction of the field. Gas kinetic theory gives

the particle diffusion in the direction x as

$$\frac{dn}{dt} = -DS \cdot \frac{dn}{dx} \tag{2.19}$$

In (2.19) n is the number of ions and S the flow cross-sectional area. For a molecular concentration N at pressure p with the ionic charge being e, the diffusion coefficient and the ionic mobility are connected by

$$k = \frac{NeD}{p} \tag{2.20}$$

The average displacement of an ion, $\bar{a}$, after time t is

$$\bar{a} = \sqrt{2Dt} \tag{2.21}$$

It has been assumed by Meek that the electron avalanche takes the shape of a hemispherically ended cone, as depicted in Fig. 2.8. The apex of the cone is the origin O of the avalanche. As the electron mobility is several orders of magnitude greater than the ion mobility, the contour of the avalanche is assumed to be filled with virtually stationary positive ions. In a

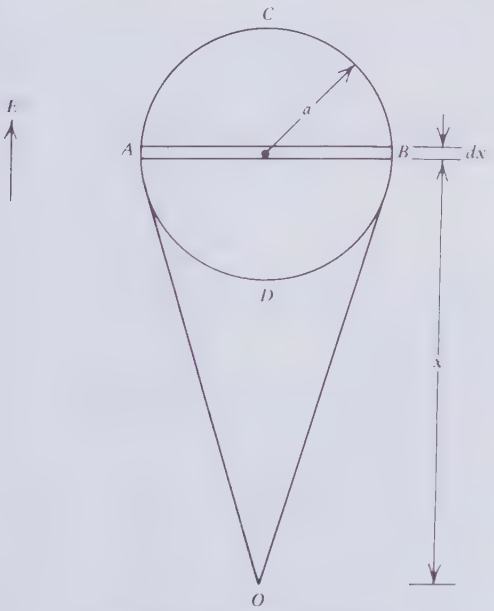

Figure 2.8 Electron avalanche.

small region of the field, over which E may be assumed to be constant, the number of electrons or positive ions generated by the avalanche progressing a distance x is $e^{\alpha x}$. If the avalanche continues to travel another short distance dx, it will generate $\alpha e^{\alpha x} dx$ additional electrons which leave behind an equal number of positive ions. The ion concentration in the layer AB of Fig. 2.8 then is

$$n = \frac{\alpha e^{\alpha x} dx}{\pi a^2 dx} = \frac{\alpha e^{\alpha x}}{\pi a^2} \tag{2.22}$$

Meek proceeds to assume that at any instant during the advancement of the avalanche, the positive ion concentration in the spherical volume $ADBC$ of radius a will be given by (2.22). The radius a is determined by diffusion and is therefore identical to $\bar{a}$ of (2.21). The radial field of a sphere of radius a and surface charge density s is

$$E_r = 4\pi s \tag{2.23}$$

But for a charge density n inside the sphere

$$s = \frac{(4/3)\pi a^3 ne}{4\pi a^2} = (1/3)ane \tag{2.24}$$

Substituting (2.24) into (2.23) gives

$$E_r = (4/3)\pi ane \tag{2.25}$$

With n from (2.22) and $a = \bar{a}$ from (2.21) this becomes

$$E_r = \frac{4e\alpha e^{\alpha x}}{3\sqrt{2Dt}} \tag{2.26}$$

If v is the drift velocity of electrons in the field E and therefore also the velocity with which the avalanche progresses, it follows that $t = x/v$ and from (2.18) $t = x/(kE)$. So that

$$E_r = (4/3)e\alpha e^{\alpha x}\sqrt{\frac{kE}{(2Dx)}} \tag{2.27}$$

With the electronic charge and data from the kinetic theory of gases, (2.27) in c.g.s. units can be shown to be equal to

$$E_r = 0.527 \times 10^{-6} \frac{\alpha e^{\alpha x}}{\sqrt{x/p}} \tag{2.28}$$

Meek's streamer onset criterion is

$$E_s = E_r = KE \tag{2.29}$$

Originally it was suggested that $K = 1$. In other words, subsidiary electron avalances will be drawn into the space charge of the first avalanche provided the radial field of the space charge is equal to the applied electric field E responsible for causing the first avalanche. Later experimental results indicated that K should be smaller than one and probably as low as 0.1. For any given gas K has to be determined experimentally.

To apply Meek's streamer onset criterion to the nonuniform field in a coaxial gap, we first of all recognize that up to a certain voltage E/p will everywhere be so small that $\alpha = 0$ and no Townsend avalanches can be set in motion. Just beyond the Townsend threshold α will be finite within a thin layer close to the inner conductor. The maximum avalanche length x_a is equal to the thickness of this layer. Raising the voltage further increases the maximum avalanche length, and therefore E_r until Meek's criterion is fulfilled and further avalanches are drawn into a developing streamer. Equation (2.28) may be adapted for streamers in a coaxial gap by writing

$$\frac{E_r}{p} = 0.527 \times 10^{-6} \alpha \exp \int_{r+x_a}^{r} \frac{\alpha dx}{\sqrt{px_a}} \tag{2.30}$$

In the c.g.s. units of (2.30) r is the radius of the inner conductor and x_a the maximum avalanche length. Now let the field strength at the surface of the inner conductor be E_c and take Meek's criterion as

$$E_s = E_r = KE_c \tag{2.31}$$

Combining (2.30) and (2.31) results in

$$\frac{E_c}{p} = \frac{0.527 \times 10^{-6}}{\left(K\sqrt{px_a}\right)} \exp \int_{r+x_a}^{r} \alpha dx \tag{2.32}$$

When a voltage V is applied to a coaxial line of inner radius r and outer radius R, the field strength E at a radial distance x from the axis is given by

$$E = \frac{V}{x \ln(R/r)} \tag{2.33}$$

Let $E = E_0$ when $x = r + x_a$. E_0 is then the stress below which no electron collision ionization can take place ($\alpha = 0$). From (2.33) it follows that the

maximum avalanche length is

$$x_a = r\{(E_c/E_0) - 1\} \tag{2.34}$$

Sanders' results for air, Fig. 2.5, suggest a value of E_0/p of 29 V/(cm·torr). The only way of solving (2.32) and (2.34) for E_c, the streamer onset conductor stress, in terms of the conductor radius r is still the trial-and-error method suggested by Meek. This is best carried out with a computer. For every value of r, a first value of E_c has to be guessed. Depending on the resulting inequalities, this value then has to be adjusted upward or downward until a solution of the required accuracy is obtained.

The calculations may be simplified by assuming that streamer onset occurs when the initiating avalanche reaches a critical size, as in the Townsend criterion (2.12). The size of an avalanche is measured by the number of positive ions contained in its contour and not by its physical extent. The magnitude of the critical number of ions, say N_c, has to be determined for every gas by experiment. Little is lost by this because Meek's more rigorous method, which involves the radial field strength of the positive space charge, also requires an experimental evaluation of the constant K of (2.31).

The number of ions in the initiating avalanche traveling through the nonuniform field of a coaxial line is

$$n = \exp \int_{r+x_a}^{r} \alpha dx \tag{2.35}$$

and for streamer onset we require that $n = N_c$. Next it is assumed that the α/p versus E/p graph is a straight line, using the best fit to the experimental curve over the range of field strength of interest. This results in an approximation, which, with the constant C, may be expressed by

$$\alpha = C(E - E_0) \tag{2.36}$$

The integral in (2.35) then becomes

$$\int_{r+x_a}^{r} \alpha dx = C \int_{r+x_a}^{r} (E - E_0) dx = CA \tag{2.37}$$

where A is the shaded area of Fig. 2.9. This area has the dimension of a voltage, and it can be readily shown to be equal to

$$A = rE_c \ln\left(\frac{E_c}{E_0}\right) - r(E_c - E_0) \tag{2.38}$$

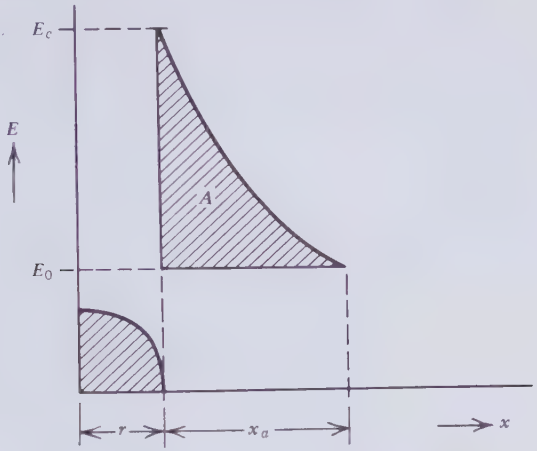

Figure 2.9 Field distribution in coaxial gap.

Now when $n = N_c$, $A = A_c$, which is the critical value for streamer onset. Separating the variables for the limiting case results in

$$f(r) = E_0 - \frac{A_c}{r} = E_c \left\{ 1 - \ln\left(\frac{E_c}{E_0} \right) \right\} = F(E_c) \tag{2.39}$$

Plotting graphs of $f(r)$ against r and $F(E_c)$ against E_c, as in Fig. 2.10, solutions (r', E_c') of (2.39) can be traced along the dotted lines. Reasonable values for the constants in (2.39) for atmospheric air are $A_c = 760$ V and $E_0 = 22$ kV/cm. Figure 2.11 compares solutions of (2.39) with these constants and experimental results obtained with thin copper wires in a brass tube [2.20]. No such experimental results have been published for the large

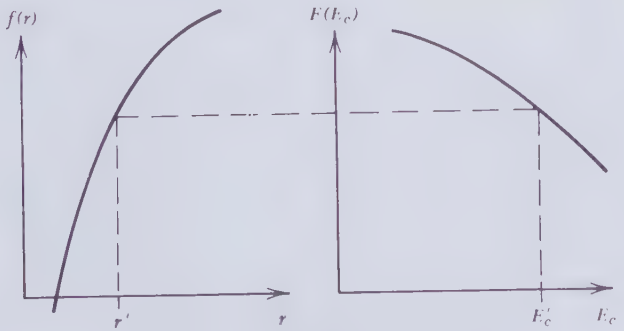

Figure 2.10 Graphical solution of (2.38).

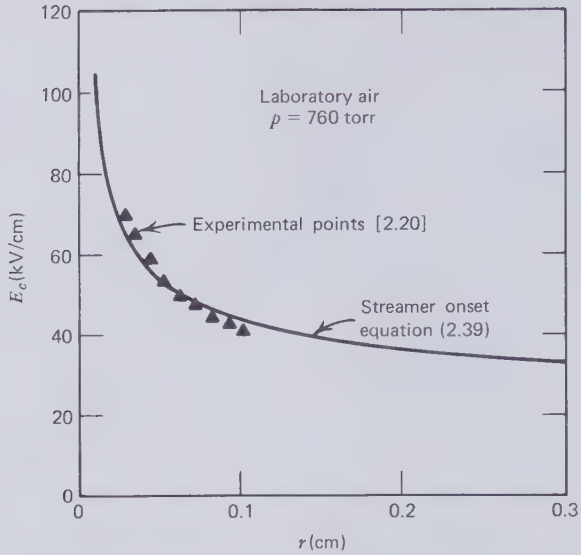

Figure 2.11 Streamer onset in atmospheric air between wire and cylinder electrodes.

conductors that find use in gas insulated cables. Figure 2.12 gives the conductor surface stress at streamer onset for large conductors according to (2.39) and the constants for atmospheric air. Considerably higher streamer onset stresses may be expected for sulfur hexafluoride because electron attachment will make it more difficult for the initiating electron avalanche to reach the critical size. It means that A_c will be larger for SF_6 than for air. E_0 is not expected to be very different for SF_6 because the ionization energy of this gas is about the same as that of nitrogen (see Table 2.2).

The critical avalanche size is

$$n = N_c = e^{CA_c} \tag{2.40}$$

From Sanders' data of Fig. 2.5, C comes to approximately $1/100$. Therefore N_c is of the order of 2000 positive ions. This appears to be a remarkably small number. Finally it should be realized that breakdown stresses will be significantly greater than those given by the sensitive streamer onset criterion. However, streamers represent a breakdown hazard and they would also result in unacceptably high energy losses. Therefore cables have to be operated below the streamer onset voltage, which is governed by the stress on the conductor surface and to a lesser degree by the spacing between the conductors.

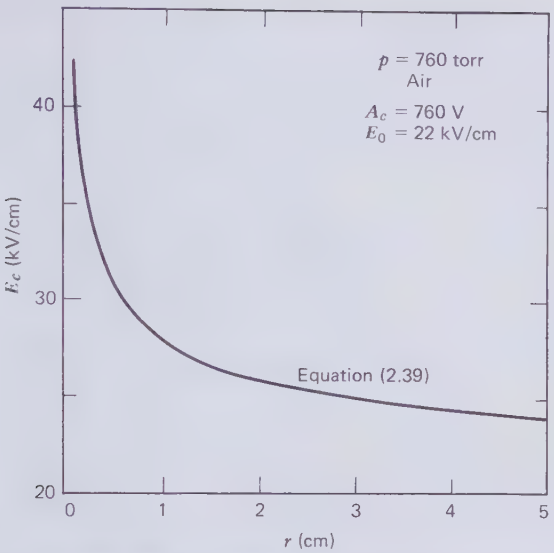

Figure 2.12 Streamer onset in atmospheric air between large coaxial conductors.

Lichtenberg Discharges and Insulator Flashover

As early as 1777 Lichtenberg [2.21] in Germany discovered that sparking resin blocks left characteristic surface charge patterns in the dust that had settled on the insulator. Since then "Lichtenberg figures" have been used to study gas discharges sliding over solid dielectric surfaces. The phenomenon also forms the basis of the Klydonograph which was developed to record voltage surges on power lines due to lightning strokes. This type of gas breakdown on the surface of insulators has to be taken into account in the development of gas insulated cables that must contain solid dielectric supports for holding conductors in the gas environment. It also plays a part in the design of open air terminations of high-voltage cables, which essentially consist of a dielectric tube, usually made of porcelain, separating the high-voltage connector from the grounded cable enclosure with air on the outside and the cable insulation on the inside. This tube has to be long to prevent flashover in air over the porcelain surface.

The setup normally employed for producing Lichtenberg figures is shown in Fig. 2.13. The voltage surge is applied to a rod-to-plane gap. A layer of insulation, frequently a glass plate, is placed between the electrodes. The upper surface of the dielectric layer is covered by a photographic plate that records the luminous traces of the discharges gliding over the insulator surface. The rod-to-plane geometry generates figures that radiate in all

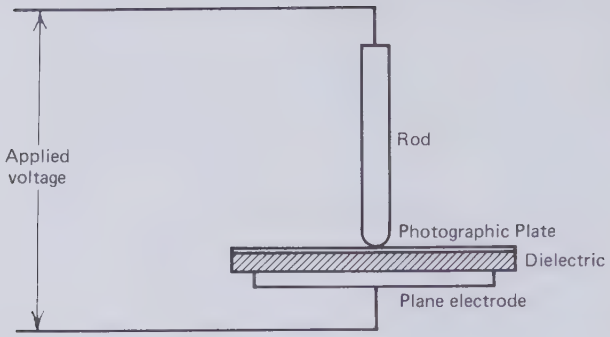

Figure 2.13 Conventional method of producing Lichtenberg figures (Klydonograph).

directions from a central point to an approximately circular boundary. Two Lichtenberg figures are sketched in Fig. 2.14. According to Merrill and von Hippel [2.22] these patterns are typical for air at atmospheric pressure. One is described as a positive figure because it forms when the rod is the positive electrode. The other is a negative figure. As Merrill and von Hippel have pointed out, differences in appearance of the Lichtenberg figures are helpful in the interpretation of the gas breakdown mechanism. The structure of the figures depends not only on electrode polarity but also on the nature and pressure of the gas.

The most surprising aspect of Lichtenberg discharges is that they are caused by quite low stresses and voltages. For example, if the insulation shield is stripped back from the end of a solid dielectric cable for approximately 6 in, a voltage pulse of 50 kV or less is sufficient to cause a spark to

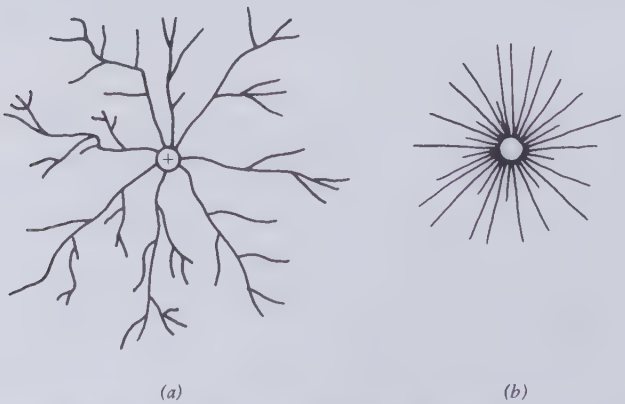

Figure 2.14 (a) Positive and (b) negative Lichtenberg figures in atmospheric air according to Merrill and von Hippel [2.22].

glide over the exposed insulation surface. Compared to this, it takes roughly three times this voltage to break down 6 in. of atmospheric air between spheres. This is all the more surprising when it is realized that the stress in the direction of the Lichtenberg discharge is even less than voltage and electrode separation suggest. The low breakdown strength of gasses at the interface with a solid dielectric medium is the result of the adhesion of positive gas ions to the solid surface. This adhesion is easily explained with regard to positive discharges in the Klydonograph configuration, where the negative plate electrode pulls positive ions against the insulator surface. It is less obvious why the same kind of immobility of positive ions should occur during negative discharges. The most likely explanation for this is dipole interaction. That the ionic motion during a negative discharge is largely due to electrons has been proved [2.22] by applying a magnetic field perpendicular to the glass plate and showing that it deflects the branches of the Lichtenberg figure in the direction in which electrons move under the influence of a magnetic field. A consequence of the adhesion of positive ions to the surface of insulators is that the head of a streamer will not diffuse as quickly as in the bulk of the gas. Therefore, the radial field of the space charge, given by (2.26), is correspondingly larger and causes more electron avalanches to cascade into the streamer. Otherwise the discharge is probably very similar to breakdown of the bulk of the gas, except that the Lichtenberg mechanism is constrained to two dimensions.

The light emitted by the Lichtenberg discharge and the energy required for evaporating loosely bound matter in the tracks of the figure are the result of intense ionization proceeding tangentially along the surface of the dielectric material. Electron avalanches certainly play an important part in the formative stages, but most of the liberated energy is likely to come from sparklike events following the path traced out by the electron avalanches. The size of any given figure is related to magnitude and rate of change of the applied voltage. Toepler [2.23] claimed that the radius of the figures is proportional to the rate of change of the applied potential difference and that very weak or no luminosity is observed when this falls below 10^6 kV/sec. Only a very high rate of change of the applied voltage is capable of creating the strong tangential electrical stress needed for streamer formation. At low rates of change, the surface charge concentration has time to diffuse without much ionization and temperature rise. This proves that the positive ions are not firmly trapped on the dielectric surface but only impeded in their motion. With time they disperse, but not as quickly as positive space charge in the midst of a gas.

Insulators bridging a high-voltage gas gap flash over most readily when their sides are parallel to the applied electric field. To increase the flashover strength, their shape must force sliding Lichtenberg discharges to move

perpendicular to the electric field. This is the explanation why projections and corrugations on insulator surfaces raise the flashover voltage.

Inscribed Lichtenberg figures have also been observed on dielectric surfaces that were exposed to electrical stress in vacuum [2.24]. In spite of the vacuum environment, surface discharges may proceed in the thin but dense gas layer adsorbed on dielectric surfaces. In some cases the dielectric material is the oxide coating on conductors. In badly outgassed systems the adsorbed gas layer may be up to 10 molecules thick. Further molecules may be contributed to the discharge through evaporation by ion impact on some of the dielectric surface. If an electric field of sufficient intensity exists parallel to the adsorbed gas layer, Townsend avalanches and streamers may be expected to form in this layer in the same way as in a more extensive volume of gas of the same species and density.

Field Emission

Townsend electron avalanches and streamers are precursors of complete gas breakdown. In the discussion of these phenomena it has been assumed that there is always a free electron available to kick off the initiating avalanche. Time delays between the application of voltage and the detection of a current pulse have established that triggering electrons may be relatively scarce. Statistical time lags of this kind can usually be reduced by exposing the breakdown gap to ultraviolet, gamma, or X radiation. Metal sheathed cables are well protected from radiation and statistical breakdown time lags should be long.

Quite apart from the way in which the initiating electron is produced, the Townsend γ mechanism described by (2.10) depends on the generation of secondary electrons at the cathode. If some of the γ electrons are being produced by a process other than positive ion bombardment they will also contribute to the self-maintenance of the discharge and breakdown of uniform field gaps. The most likely additional mechanism that will extract electrons from the cathode is field emission. In this process electrons are pulled out of the metal at ambient or lower temperatures by an electric field acting perpendicular to the metal surface. It is an important phenomenon contributing not only to the breakdown of gases, but also vacuum, liquid, and possibly solid insulation. A potential barrier exists at the surface of metals that prevents the escape of conduction electrons under normal conditions. The energy the electron must possess to overcome this barrier is its charge multiplied by what is known as the work function ϕ. As Gomer has explained [2.25], the work function consists of two parts. The larger part is the inner or chemical potential and the other is due to electrostatic effects at the surface discontinuity. The latter contribution is sometimes called the

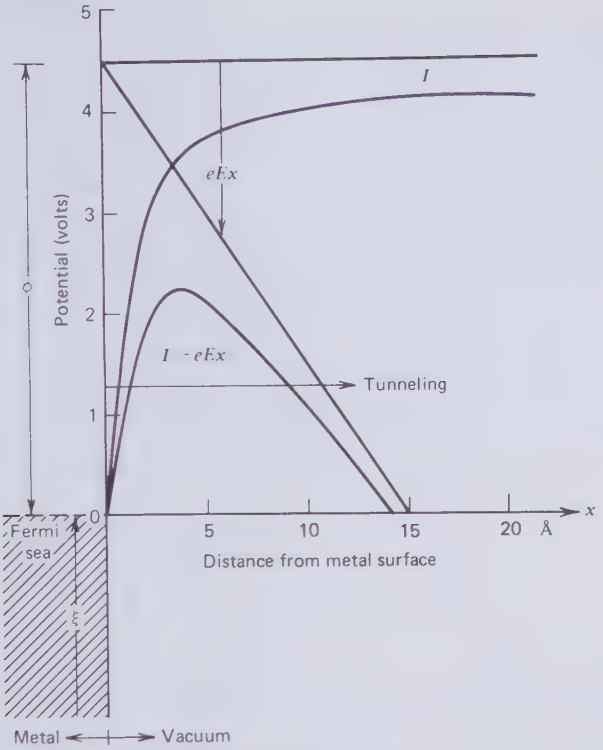

Figure 2.15 Electron potential at the surface of tungsten in the presence of a perpendicular surface field of $E = 0.3$ V/Å according to Gomer [2.25].

"image potential." Figure 2.15 is a potential energy diagram for an electron that tends to leap from the conduction band, or uppermost filled Fermi energy level in the metal, to an outside vacuum space. In the absence of an external electric field and the distortion of the surface barrier by the image potential, this electron in, for example, the tungsten lattice would have to aquire 4.5 eV of energy before it could permanently leave the metal. Thermionic emission is the process in which this energy is provided by heating. In tungsten this becomes possible when the temperature is raised to approximately 1500°K. Virtually no electrons can escape from the metal at normal ambient temperatures. Taking account of the barrier distortion by the electrostatic surface effect, the image potential I of Fig. 2.15 is obtained. This still is an effective obstacle preventing thermionic emmission at ordinary temperatures. The application of an electric field E perpendicular to the surface and in a direction that it will accelerate electrons away from the metal depresses the barrier further to $I - eEx$, where x is the distance

from the metal surface. The diagram of Fig. 2.15 is for $E = 3 \times 10^7$ v/cm = 0.3 v/Å, and over a distance of 15 Å in tungsten the electron can gain an energy equal to $e\phi$ for this metal. The effective surface potential that an electron in the metal has to overcome is therefore the hump shown in Fig. 2.15. The thickness of this barrier is $(I - eEx)/(eE)$. Provided the barrier is thin enough and low enough, electrons may tunnel through it. Tunneling is a quantum mechanical effect explained by the increased probability of finding one of the conduction electrons outside the barrier when the barrier thickness and height are being reduced. As is obvious from Fig. 2.15, extremely strong fields are required to bring about a significant weakening of the potential surface barrier.

Work function measurements are difficult and the values listed on Table 2.4 are averages from several experimental investigations. Of the conductor metals, copper has the highest and sodium the lowest work function. The field emission current density i_0 may be calculated from quantum mechanical principles. It results in the Fowler-Nordheim equation

$$i_0 = \frac{4\sqrt{\xi\phi}}{\xi + \phi} \cdot \frac{e^3 E^2}{8\pi h\phi} \exp\left(\frac{-8\pi\sqrt{2m\phi^3}}{2heE} \right) \tag{2.41}$$

where h is Planck's constant and ξ the Fermi energy. With constants A and D the Fowler-Nordheim equation takes the more simple form

$$i_0 = AE^2 e^{(-D/E)} \tag{2.42}$$

Equation (2.42) has been tested by many experimenters, and there is ample evidence that the cold emission current follows a Fowler-Nordheim type of relationship to the applied electric field. However, the coefficients A and D vary greatly with experimental conditions. In general, it has been observed that field emission occurs at considerably lower field strength than anticipated from the Fowler-Nordheim equation, and the emission current is often much greater than predicted.

Table 2.4 Work Function of Conductor Metals (Experimental Average)

		ϕ (eV)
Aluminum	Al	3.7
Beryllium	Be	3.7
Copper	Cu	4.3
Niobium	Nb	4.0
Silver	Ag	3.7
Sodium	Na	2.3

Two practical circumstances are believed to contribute to the prominence of field emission currents. The first is the magnification of field strength at the tip of surface protrusions. Field enhancement factors up to 500 have been suggested for surface projections and whiskers. Second, there are always foreign molecules adsorbed on the metal surface and, depending on the species and density of the adsorbed gases and vapors, they can depress the barrier potential by varying degrees. The situation is further complicated by the almost inevitable presence of oxide layers. The oxide may be a good dielectric as on aluminum or it can be a semiconductor as on copper. Dielectric surface layers tend to reduce field emission. But there exists the danger that positive ions are trapped on this layer, as in the Klydonograph configuration of Fig. 2.13, and eventually puncture the layer, eliminating whatever benefit it may have conferred on the breakdown strength of the gas insulation system. This appears to be the main reason why no reliance has been placed on anodized aluminum conductors for compressed gas insulated cables.

Field emission currents are more easily detected in vacuum insulation than in gas insulation. Electrons emitted into vacuum will be accelerated right across the high-voltage gap and have sufficient energy on impact with the anode to generate X radiation. With the aid of Geiger counters, it is possible to detect the resulting X rays remote from the high-voltage apparatus and through metallic enclosures. X ray measurements not only indicate the presence and magnitude of field emission currents [2.26], but they also show indirectly the location of emission sites by pinpointing the areas of the anode from which the X rays are emitted. This type of experiment usually reveals that the larger part of the field emission current is concentrated in a few electron beams and not uniformly distributed over the cathode surface. X ray pinhole cameras and fluorescent screen electrodes have been used to photograph electron beam field emission [2.27, 2.29]. Lichtenberg figures inscribed in oxide layers provide further evidence for the existence of electron beams in vacuum insulation [2.28]. Although no such easy methods of detecting point field emission into gas insulation are available, it seems safe to assume that the same type of concentrated emission will be experienced by gas insulation. Field emission currents are likely to initiate electron avalanches and lower the breakdown strength of the gas insulation in a uniform field gap. Furthermore, repetitive avalanching from the same field emission site into a divergent electric field should build up positive space charge in front of the electron source and eventually lead to streamer formation. Under all circumstances, it may be concluded, intense field emission from cathode points is a very likely cause of gas breakdown at reduced electrical surface stresses [2.33, 2.34].

Free Conducting Particles

Since the introduction of SF_6 insulated transmission lines and substation plant it has become obvious that free conducting particles in the high-voltage gap can greatly reduce the breakdown strength of gas insulation [2.30–2.36]. Loose dielectric particles, on the other hand, have proved to be harmless. The behavior of loose particles in vacuum insulation has also been studied [2.38]. At one time it was thought that loose dielectric particles accelerated across the vacuum gap would evaporate on impact with the other electrode and be a major cause of breakdown. The present state of knowledge suggests that only small conducting particles influence vacuum insulation in so far that they may create surface protrusions on electrode impact. Large conducting particles, which are responsible for the degradation of gas insulation, cannot acquire sufficient kinetic energy to cause electrode surface damage. The broad conclusion that may be drawn from these few facts is that it is the emission of conduction electrons from metal particles and avalanche-type ionization of the adjacent gas that affects the breakdown strength of gases.

A loose metal particle lying at the bottom of a gas insulated transmission line will acquire charge of the same polarity as the surface on which it rests in conducting contact. If this charge is denoted by q and the electric field at the particle by E, the particle experiences an electrostatic force of attraction $F = qE$. As the voltage across the gap is gradually increased a point will be reached when the electrostatic force begins to lift the particle. Should it be of elongated shape, it will first stand up. While in contact with the cathode, a standing particle will almost certainly make a field emission site. On increasing the field strength E even further, the particle will actually separate from the conductor. A small metal sphere would tend to retain most of its charge and move rapidly across the gap into a field of increasing strength as the center conductor is being approached. On impact with the latter the particle charge is removed and replaced by a charge of opposite sign. Gravitation, electrostatic force, and elastic rebound now assist each other in returning the particle to the outer conductor. There it will bounce again and reverse the polarity of its charge only to initiate a further cycle of motion between the conductors. Cooke et. al. described an experiment in which a bounce frequency of 30 Hz was observed [2.36]. This to-and-fro motion of a conducting particle does not necessarily cause breakdown.

The way in which a conducting particle can decrease the dielectric strength of a gas is by emitting electrons under concentrated electrical stress due to the particle geometry. The field emitted electrons then initiate avalanches and streamers in the normal manner. As already pointed out, an elongated conducting particle standing upright on the cathode surface makes an efficient field emitter. Field emission can and probably will continue as the particle is lifted off the cathode, but the loss of negative

charge after separation from the cathode reduces the electrostatic lift force and tends to arrest the particle motion toward the anode. Gravity may return it to the cathode, or the positive space charge surrounding it may attract sufficient electrons to renew its negative charge and reverse the particle motion once more. Ionization in the vicinity of the particle is a source of visible light and the particle can be seen and photographed as a moving and blinking point. Free conducting particles behaving like this have aptly been described as 'fireflies.' Yet gas breakdown and partial discharges, although caused by conducting particles, are not inevitably preceded by firefly action.

Diessner and Trump [2.31] have measured the dc sparking and discharge onset voltages in a coaxial line of 10 in. o. d. and 3 in. i. d. with nitrogen and sulfur hexafluoride gas contaminated by free conducting particles at pressures up to 300 psig. Their results are reproduced in Fig. 2.16. Compared to

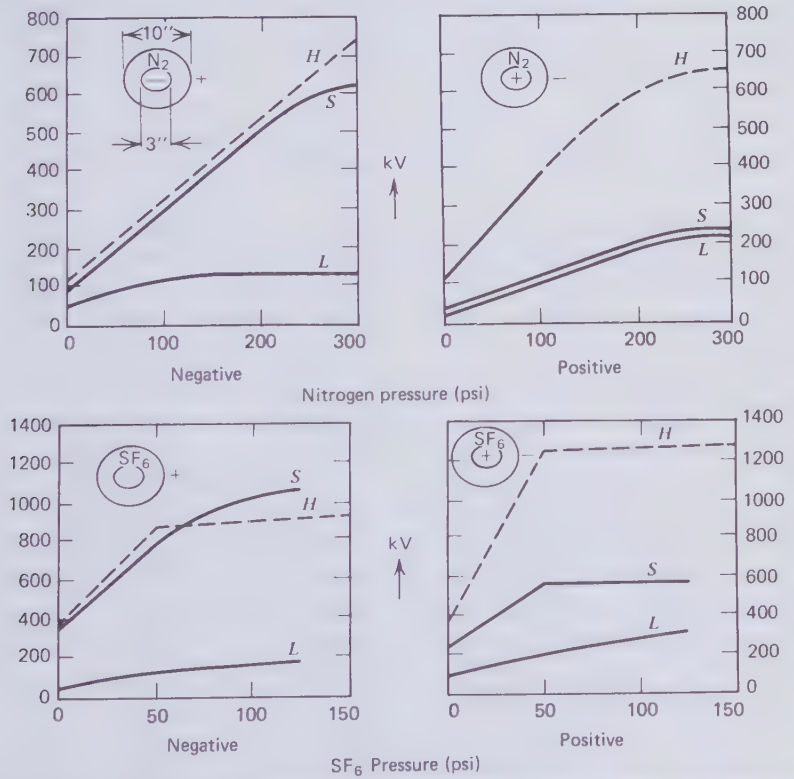

Figure 2.16 DC breakdown and discharge onset voltages in coaxial lines with nitrogen and sulphur hexafluoride insulation contaminated with conducting particles according to Diessner and Trump [2.31]. *H*—Breakdown voltage of clean system. *S*—Breakdown voltage with conducting particles. *L*—Discharge onset with conducting particles. (By permission of the Institute of Electrical and Electronics Engineers).

a clean system, the sparking voltage of the contaminated system is greatly reduced when the center conductor is positive but suffers little at the opposite polarity. Conductor polarity has apparently less effect on the discharge onset voltage. As loose conducting particles would probably be set in motion by the voltage at which discharges are first observed, it has to be assumed that the initial discharge activity actually takes place in the high field region close to the inner conductor. The triggering of an avalanche appears to be almost equally likely for both directions of travel of a field-emitted electron. The large depression of the positive sparking potential by conducting particles must be explained in terms of streamer formation. With the initiating avalanche triggered in the high field zone, the streamer has to grow backward to the outer conductor. Subsequent avalanches following the trigger event apparently are more easily set in motion when the field converges in the direction in which the electrons travel. A possible explanation of this fact is that the convergent field hinders diffusion of the positive space charge set up in the path of the electron avalanche. This idea complies with Meek's streamer onset criterion, which is governed by the radial field strength of this space charge.

2.4 DIELECTRIC BREAKDOWN OF LIQUIDS

The liquefied gases of nitrogen, hydrogen, and helium have been proposed for use as high-voltage dielectrics in cryocables. There they would assume the multiple function of electrical insulation, cooling fluid and heat-transport medium. The interest in these liquid insulated systems with point support insulators has waned again in favor of vacuum or a composite insulation consisting of flexible tapes impregnated with the cryogenic liquids.

Mineral, synthetic, and even vegetable oils find use in high voltage power systems. In the standard oil-paper insulation of cables, the liquid is essentially a filler of butt gaps between paper tapes and spaces between the fibers of cellulose. The breakdown strength of composite oil-paper insulation is largely determined by the paper. It increases with the fraction of paper contained in the insulation. The same can be said of tape insulation impregnated with cryogenic liquids. Therefore, the breakdown process in liquids is of minor importance in cable technology. A brief treatment of this difficult topic might, however, be helpful in trying to gain an overview of all electrical breakdown mechanisms.

It is tempting to assume that a liquid behaves like a gas in which the distance between molecules has been greatly reduced, but important experimental facts stand in the way of this simplification. With regard to gases it makes sense to speak of an intrinsic breakdown strength of the insulation medium. When this intrinsic strength or stress is reached in a uniform field,

runaway ion multiplication leads to breakdown. The intrinsic breakdown strength should be the same for dc, ac (peak), and pulses of greater length than the sum of the statistical and formative discharge time lags. Yet in liquids and even more strongly in solids, the breakdown stress in a uniform field decreases with insulation thickness. Therefore the "intrinsic" breakdown strength of a thin layer of liquid or solid insulation is no reliable guide to the technical performance of the insulation in a cable system. Furthermore, with liquid and solid dielectrics, the dc breakdown strength is markedly higher than the peak ac strength. The response of these two insulations to impulse voltages is similar to their reaction to dc provided the pulse is not of so short a duration that it would curtail the development of the discharge. Any useful breakdown theory must account for the thickness dependence of the breakdown stress and the dramatic lowering of dielectric strength that occurs with the application of power frequency voltages.

Some idea of the uniform field dc breakdown strength of gases, liquids and solids may be gained from the comparisons made in Fig. 2.17. There is little

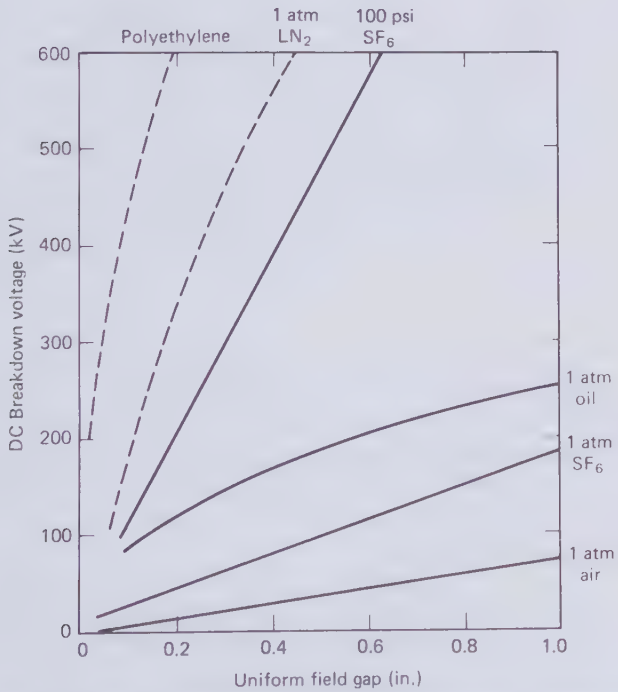

Figure 2.17 Uniform field dc breakdown of various materials as a function of insulation thickness. Solid curves from [2.39]; broken curves estimated by the author. (By permission of MIT Press).

doubt that the breakdown strength increases as the intermolecular distance is shortened. Consequently, in general, solids are better insulators than liquids, and liquids are better than gases. Nevertheless a good gas insulation, as for example SF_6 at 100 psi, can be better than the extensively used transformer oil liquid. Equally, there exist many solid dielectrics that are not as good as the best liquid dielectrics. The large difference in breakdown strength between liquid nitrogen (LN_2) and insulating oils is undoubtedly due to the electrical stability of the inert nitrogen molecule compared to the weaker interatomic bonds of hydrocarbons and similarly complex molecules.

Field Emission

The wide agreement on gas breakdown processes does not extend to breakdown in liquids and solids. Different and often conflicting breakdown mechanisms have been proposed for these two phases of matter, each being consistent with a limited range of experimental facts. However, on one point all scholars of the breakdown of liquids appear to be agreed. This concerns the importance of field emission as a source of electrons for initiating breakdown. The electron potential barrier at a metal surface in the presence of a perpendicular electric field E is depicted in Fig. 2.15. This particular diagram refers to electron emission into vacuum. When the vacuum space is filled with an insulating liquid, the potential barrier hindering the escape of electrons from the metal is lowered. This is the result of dielectric polarization given mathematical expression in the dielectric constant ε. Taking this effect into account, the image potential I, which differs from the work function energy $e\phi$ because of the slight overspill of conduction electrons, may be expressed by

$$I = e\phi - \frac{e^2}{(4\varepsilon x)} \tag{2.43}$$

The concentration of matter in liquids is such that $\varepsilon > 1$. All other aspects of field emission into a vacuum also hold good for electron emission into a liquid.

Electronic Breakdown

Once an electron has been injected into the liquid it will be accelerated by the field E. The amount of kinetic energy it can acquire is $eE\lambda$, where λ is the mean free path between collisions with liquid molecules. Because of the close packing of molecules in a liquid, where unit volume might contain several hundred times as many molecules as a gas, the electron should not be

able to reach a high enough velocity that would enable it to ionize neutral molecules. But Lewis [2.40] and Adamczewski [2.41] have explained how electrons in the liquid may interact with hydrocarbon molecules exchanging only part of their kinetic energy to mostly heat. This kind of exchange retards the electron, but allows it to carry on its way with reduced velocity. In this manner the electron can gather increasing momentum over a number of mean free paths until it is capable of producing an ionizing collision. The electrons generated by this multiplication process are then subject to the same stepwise acceleration that causes further ionizing collisions. Therefore, electron avalanches may also progress through the liquid dielectric, but a stronger electric field is required than that which can initiate the Townsend α mechanism in a gas. Having shown that ionization by collisions of electrons with neutral molecules is possible, Lewis proceeds to a breakdown criterion of the form

$$eE_b\lambda = Ch\nu \tag{2.44}$$

In (2.44) E_b is the breakdown field strength, $h\nu$ a quantum of vibration energy supplied to the liquid molecule and C a constant to be established by experiment. The mean free path λ is that between retarding collisions and not ionizing collisions. The criterion (2.44) would not be very instructive unless the mean free path can be related to molecular structure so that various liquids may be ranked according to breakdown strength. Lewis has assumed that each CH_x group in the hydrocarbon molecule acts as a separate center of electron retardation, which results in a mean free path of

$$\frac{1}{\lambda} = N\sum_x n_x Q_x \tag{2.45}$$

where N is the number of molecules per cubic-centimeter and n_x the number of CH_x groups per molecule which have corresponding collision cross sections Q_x.

Adamczewski, on the other hand, assumes the electron retardation is due to vibrations set up in the C–C bond of the oil molecules. He believes the electron passes along the molecular chain of radius r and there meets $n-1$ carbon bonds, each $h_0 = 1.23$ Å long in the axial direction. The effective cross section of the molecule he takes to be

$$Q = 2rh_0(n-1) \tag{2.46}$$

making the active collision area per cubic centimeter

$$S = NQ = 2rh_0N(n-1) \tag{2.47}$$

The mean free path then becomes

$$\frac{1}{\lambda} = 2rh_0N(n-1) \tag{2.48}$$

To establish his own breakdown criterion Adamczewski reasons that for avalanche formation the kinetic energy of the triggering electron must be at least equal to the known excitation $h\nu$ of the C–C bond. In other words, he sets the constant in Lewis' criterion (2.44) to C = 1 and then substitutes the C–C activation energy. It results in the following equation for the breakdown voltage of hydrocarbon liquids

$$E_b = \frac{h\nu}{e} 2rh_0N(n-1) \tag{2.49}$$

From this simple relationship Adamczewski has calculated the breakdown voltage of a number of hydrocarbon liquids and compared his theoretical results with the experimental findings of other investigators. As Table 2.5 shows, excellent agreement was obtained with (2.49).

Table 2.5 Breakdown Stress of Hydrocarbon Liquids [2.41]

Liquid		E_b (MV/cm)	
		Experimental	Theoretical
Pentane	C_5H_{12}	1.44	1.44
Hexane	C_6H_{14}	1.56	1.57
Heptane	C_7H_{16}	1.66	1.68
Octane	C_8H_{18}	1.79	1.77
Nonane	C_9H_{20}	1.84	1.85
Decane	$C_{10}H_{22}$	1.92	1.91
Tetradecane	$C_{14}H_{30}$	2.00	2.08
2-Methylpentane		1.49	1.44
2.2-Dimethylbutane		1.33	1.21
2.3-Dimethylbutane		1.38	1.21
isoHeptane	C_7H_{16}	1.44	1.44
isoOctane	C_8H_{18}	1.40	1.44
Benzene	C_6H_6	1.63	1.56
Toluene	C_7H_8	1.99	1.98
Ethylbenzene	C_8H_{10}	2.26	2.28
n-Propylbenzene	C_9H_{12}	2.50	2.53
i-Propylbenzene	C_9H_{12}	2.38	2.18
n-Butylbenzene	$C_{10}H_{14}$	2.75	2.73
i-Butylbenzene	$C_{10}H_{14}$	2.22	2.44

By permission of Taylor & Francis, Ltd.

Figure 2.18 Breakdown channels in very viscous hexachlordiphenyl according to Krasucki et al. [2.42]. (Photograph by the Electrical Research Association.)

Of course cryogenic liquids do neither contain C–C bonds or hydrocarbon groups and Lewis' and Adamczewski's breakdown theories cannot be directly applied to them. At the same time there is good reason to believe that electron retardation should also be possible with the more simple molecules of liquified nitrogen, hydrogen, and helium. Quantitative proof of this speculation is still outstanding.

A fact in support of the electronic breakdown theory is the appearance of discharge and breakdown channels photographed in transparent liquids. They exhibit the characteristics of gas discharges in so far as the luminous traces are narrow, jagged, and carry the imprint of treelike branching as can be seen in Fig. 2.18.

Vapor Bubble Breakdown

An old explanation of liquid breakdown is founded on gas discharges in vapor bubbles. These bubbles may be formed by evaporation or dissociation of the liquid molecules or they may be filled with gas originally dissolved in the liquid or trapped at the electrode surfaces. At least qualitatively, the bubble mechanism easily explains the dependence of breakdown voltage on temperature and hydrostatic pressure. It presents an immediate answer to the question of why breakdown occurs at much lower ac than dc stresses. It

is the only theory that, through bubble motion, has the beginnings of explaining the gap length dependence of breakdown strength in uniform fields.

Adamczewski [2.41] believes the pressure and temperature dependence is also explicable by an electronic process but Sharbough and Watson [2.43] expressed doubt on this point. These investigators recognized that a considerable amount of heat might be supplied to a small volume of liquid close to an intense field emission site at the cathode. This could be sufficient to evaporate a quantity m of the liquid. If c_p is the specific heat at constant pressure, T_b the boiling temperature and H_l the latent heat of evaporation, the consequence of supplying an amount of heat ΔH can be expressed by

$$\Delta H = m\left[c_p(T_b - T_o) + H_l\right] \tag{2.50}$$

where T_o is the bulk temperature of the liquid. It has further been proposed that the heat input is given by

$$\Delta H = AE^n\tau \tag{2.51}$$

In (2.51) τ is a residency time of the liquid, it being assumed that the rise in temperature will set the hot liquid in motion and if it has not evaporated in the residency time it will have moved away from the field emission site to a colder region. Sharbough and Watson argue that the residency time should be equated to the measured formative time lags. AE^n of (2.51) is proportional to the space charge limited emission current. The constant A depends on local conditions and n usually lies in the range 1.5 to 2.0. With this information and (2.50) and (2.51) Sharbaugh and Watson have been able to account for the breakdown strength of hexane, heptane, decane, and benzene at varying hydrostatic pressure and temperature.

The vapor bubble breakdown model received a strong impetous from the work of Krasucki and his colleagues [2.42–2.46], mainly through photography and filming, at 16 frames/s, of the prebreakdown and discharge processes in the very viscous hexachlorodiphenyl. The first event detected was the appearance of a vapor bubble in the region of highest field strength, usually near the cathode. This bubble then moved toward the anode. Krasucki's work also confirmed the dependence of breakdown voltage on hydrostatic pressure and liquid temperature. Bubbles were observed to elongate in the direction of the electric field. This can be understood from energy considerations. Less electrostatic energy is stored by the bubble if it is elongated rather than of spherical shape. The motion of the bubble against gravity could possibly be explained by electrostatic forces acting on charge accumulations and polarizations on the vapor cavity surface.

It is well known that corona onset voltages in a gas cavity are much lower for ac than for dc. Without continuous polarity reversal, the ionic charges trapped on the cavity wall suppress the field responsible for sustained avalanche discharging after an initial burst. But if the field reverses direction, the charges that before suppressed avalanching now aid this process. Therefore bubble breakdown provides a good reason for the low ac breakdown strength of liquids. Should bubble motion and the distance traversed by them be an essential step in the progress of partial discharges to complete breakdown, then this mechanism would also provide an explanation of the gap length effect on uniform field breakdown stresses in liquids.

Liquid Purity and Foreign Particles

Small amounts of impurities and additives often profoundly change the dielectric strength of liquids. This finding is quite compatible with the electronic and vapor bubble breakdown models. The ionization process can obviously be influenced by the presence of molecules that are more easily ionized than the bulk of the liquid, or other molecules that capture electrons and build up negative space charge. Additives and impurities are capable of changing the boiling temperature and also the latent heat of evaporation. This modifies the energy required for creating vapor bubbles.

A particularly harmful impurity is water. In dispersion it provides a copious supply of ions in relatively weak electric fields. Therefore every effort has to be made to prevent the contamination of cable oil with moisture. The most likely source of water are the paper tapes. High-voltage cable manufacturers take great pains to dry the paper and store it in a dry environment. Paper taping of the cable conductors is normally being carried out in an air-conditioned enclosure.

By the same token, the breakdown strength of a liquid can be improved by additives. Adamczewski [2.41] quotes an example where the addition of seven percent nitrobenzene to pure hexane lifts the breakdown strength by 20 percent.

It has been established beyond doubt that foreign particles drastically impair the insulation strength of liquids. Metal particles respond to the electric field in the same way as in gas, except that their motion is greatly hindered by the viscosity of the liquid. They give rise to additional centers of electron field emission.

In gases dielectric particles are relatively harmless but they become a major hazard in liquids. Polarization makes dielectric particles subject to electrostatic forces. These forces are directed toward the more intense region of the field, provided the dielectric constant of the solid matter exceeds that of the liquid which is almost always the case. As each dielectric particle of

this kind is the cause of field intensification at its surface, numbers of them attach themselves to each other, end-to-end, to form strings which might completely bridge the high voltage gap. The growth of fiberlike particle strings can readily be observed in transparent liquids. They start at the high-stress electrode and grow toward the opposite electrode. When they approach the latter the field between the end of the bridge and the electrode intensifies which can lead to visible discharges and breakdown. In a uniform field the first particle on an electrode creates a stress point to which other particles thrive and therefore the bridging process is not limited to nonuniform fields. It is the viscous and hydraulic suspension of the dielectric particles in the insulating liquid which makes the bridge building possible.

Of course many dielectric fiber bridges do exist in the laminated oil-paper insulation of high-voltage cables without causing any deleterious effects. The situation in the free liquid differs from this mainly in the field intensification caused by isolated material fibers.

In concluding the topic of dielectric breakdown of liquids it should be mentioned that the three breakdown mechanisms (electronic, bubble, and particle) are not so much in conflict with each other, but probably combine under many sets of circumstances to bring about insulation failure. Particles will generally introduce additional stress and may also supply free electrons. The motion of electrons generates ions and heat both furthering evaporation. Bubbles permit normal gas discharges to take place, which may become initiators of more electronic heating and ionization, and so on. The mass of accumulated experimental evidence rules out that any one of the three mechanisms alone could explain the breakdown of liquid dielectrics.

2.5 DIELECTRIC BREAKDOWN OF SOLIDS

Solid insulation has been and continues to be far more important to high-voltage cables than all the other dielectric substances. The demand for flexible cables has narrowed the choice of solid dielectrics to organic materials such as paper, rubber, and polymers. Glasses and ceramics are of secondary interest only for cable terminations and conductor spacers in gas and vacuum insulated systems. Just one new insulation material has so far been able to compete with the long-established oil-impregnated paper. This is extruded polyethylene. Although attractive for certain very flexible low voltage cables, natural and synthetic rubbers have not been found suitable for the more arduous duties of high-voltage transmission cables.

An understanding of the causes of breakdown of thick-wall-extruded polyethelyne is invaluable to the advancement of underground and under-

water power transmission because of significant cost savings resulting from the use of this insulation.

A number of unexplained insulation failures of solid dielectric cables in the United States, where these cables were pioneered, and elsewhere have hampered progress in this field over the past 20 years. A hopeful sign is that 225-kV polyethylene insulated cables have now been in service in France for some years with a reliability record similar to that of oil-paper insulated cables. The variance in cable reliability can be traced back to differences in the polyethylene material, cable design, and operating conditions. Widely different views are held on these matters; this is the result of our inadequate understanding of the breakdown mechanism operative in solids. Both on the scientific and technological planes, this subject stands on less firm foundations than breakdown in vacuum, gases, and liquids. The complexity of phenomena in amorphous and crystalline solids arises from the interactions and bonds between closely spaced atoms and molecules, which involves much more than the mobilities and kinetic energies of electrons and ions in a gaslike substance.

Clarifying the breakdown mechanism is of course a scientific objective in itself, but it also helps to develop confidence in the long-term reliability of specific dielectrics. Thermal breakdown theories were the first to be developed as a natural continuation of electron and hole conduction through solid insulators. Although positive ions are prevented from moving through solid matter, an electron vacancy at an atom or at a molecule may be passed on to neighboring atoms by electrons jumping into the hole and leaving another hole behind. In this way it may be said that a "positive hole" has a finite mobility, although this is usually much smaller than the electron mobility. Collision ionization models probably received the most attention. From them arose the concept of intrinsic electric strength, and they dealt with electron avalanches and space charges. O'Dwyer [2.47] refers to them collectively as "purely electrical breakdown." A later proposed mechanism is "mechanical breakdown," first suggested by Stark and Garton [2.48], which assumes that the dielectric material collapses under electrostatic compression. Budenstein [2.49] developed an interesting new breakdown theory. In some respects this is compatible with thermal, electrical, and mechanical models, but it is more specific about the later stages of the breakdown process, which involves a breakdown channel filled with high temperature gas or a plasma. Cable oriented breakdown studies have concentrated on the incipient breakdown that manifests itself by a system of branched channels, known as "trees," and dielectric degradation by corona discharges at free surfaces and in cavities. This wide range of breakdown mechanisms will be briefly reviewed. To be useful for the further evolution of high-voltage cable insulation systems,

breakdown theories should explain why solids lose a substantial part of their dielectric strength when:

1. they are subject to power frequency ac voltage;
2. the insulation thickness is increased;
3. the temperature rises to the 50–150°C range;
4. tensile strain is applied perpendicular to the direction of the electric field.

Each breakdown theory will be tested by these four questions.

Thermal Breakdown

The thermal breakdown theory has evolved over a span of 50 years. Prominent contributors to it were Fock [2.50], Moon [2.51], Whitehead [2.52], O'Dwyer [2.47], Sze [2.53], Klein [2.54], Hanscombe [2.55], and others. We will essentially follow the review of this subject by O'Dwyer in [2.47].

If an electric field E is applied across a dielectric slab of material, a small current will flow through the insulation that may be quantified with the aid of an average electrical conductivity σ. The steady direct current will cause Joule heating. In an infinitesimally small volume of the dielectric the Joule power is σE^2. The heat flowing away from the volume element is given by $\nabla \cdot (\kappa \nabla T)$, where ∇T is the temperature gradient and κ is the thermal conductivity of the medium. The remainder of the Joule energy is stored in the volume element. With c_v being the specific heat of the dielectric material at constant volume and t the time, the rate of stroing energy is $c_v(dT/dt)$. The fundamental law of thermal breakdown is the heat flow equation

$$\sigma E^2 = c_v \frac{dT}{dt} - \nabla \cdot (\kappa \nabla T) \tag{2.52}$$

The theory then postulates that the insulation will fail when the temperature reaches a critical value. Solving (2.52) in space and time is a formidable task because both σ and κ are temperature-sensitive parameters. The way around this difficulty has been the further assumption that breakdown takes place when the temperature of the hottest point in the material reaches the critical level. The position of this point can usually be specified from the appearance of thermal and electrical field plots. The theory does not give the critical temperature, nor does it consider the chain of electrical events that create the low-resistance breakdown channel. The most helpful result flowing from (2.52) is that, for one particular constant field E, the temperature of the hottest part of the dielectric will approach the highest possible asymptotic

limit T_a. This is true regardless of the material and specimen geometry. T_a normally lies well below the melting point of the material. The field strength associated with it will be denoted by E_a. When E is greater than E_a, T_a will be reached in finite time and for sufficiently large values of E this can be a very short time. At a stress E that is smaller than E_a the temperature of the hot spot will stabilize below T_a. Therefore E_a defines a boundary between thermal stability and instability. This is further illustrated in Fig. 2.19.

The crucial point of the thermal breakdown model is that only a temperature instability can set up the runaway conditions of insulation failure. This condition will always be reached when $E > E_a$ and therefore the breakdown field is said to be equal to the asymptotic field, or $E_b = E_a$.

For the steady state ($dT/dt = 0$) and one-dimensional heat flow ($\partial T/\partial x = \partial T/\partial y = 0$), (2.52) reduces to

$$\frac{\partial}{\partial z}\left(\kappa \frac{\partial T}{\partial z}\right) + \sigma\left(\frac{\partial V}{\partial z}\right)^2 = 0 \tag{2.53}$$

In (2.53) V is the potential difference, or voltage, in the direction of heat flow z. Since thermal breakdown is due to current heating without charge accumulation, we may express the current density i by

$$i = \sigma(\partial V/\partial z) \tag{2.54}$$

To solve (2.53) and (2.54) for a flat layer of thickness d and infinite lateral extent with a voltage V applied between electrodes on either side of the layer we measure z from the center plane at which the temperature will be a maximum and, at breakdown or just before, equal to T_a. This situation is

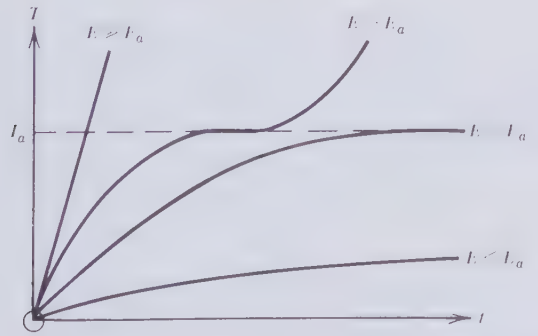

Figure 2.19 Temperature-time relationship for various electric field strengths according to O'Dwyer [2.47]. (By permission of Oxford University Press.)

sketched in Fig. 2.20. Combining equations (2.53) and (2.54) gives

$$\frac{\partial}{\partial z}\left(\kappa\frac{\partial T}{\partial z}\right)-i\frac{\partial V}{\partial z}=0 \tag{2.55}$$

Integration results in

$$iV=\int_0^z\frac{\partial}{\partial z}\left(\kappa\frac{\partial T}{\partial z}\right)dz=\kappa\frac{\partial T}{\partial z} \tag{2.56}$$

and substituting for i from (2.54) gives V as

$$V=-\frac{\kappa}{\sigma}\frac{\partial T/\partial z}{\partial V/\partial z} \tag{2.57}$$

It has been noticed by most investigators that the dielectric strength of widely different materials, as for example mica, quartz, polyethylene, and paraffin, is not so very different. This might suggest that the conductivity ratio (κ/σ) in (2.57) is of a similar order of constancy. It is a reminder of the Wiedemann-Franz law (1.10) which must not be taken for more than a vague signpost in the maze of materials science.

How to proceed from (2.57) depends on just how strong a function σ and κ are of E. The thermal conductivity is usually not affected by the field, and it is only a slowly varying function of temperature. Let it have the average value κ_0 over a reasonable temperature range containing T_a. For most materials σ may also, to a first approximation, be taken as field independent and its variation with temperature is customarily expressed by

$$\sigma=\sigma_0\exp\left(-\frac{C}{KT}\right) \tag{2.58}$$

The constants σ_0 and C have to be determined for the material concerned by conductivity measurements over an appropriate range of temperatures. K is Boltzmann's constant. With the help of these empirical facts it is permissible to separate the variables in (2.57)

$$V\,dV=-\left(\frac{\kappa}{\sigma}\right)dT \tag{2.59}$$

and integrate with inverted limits and over the full gap voltage which is also the breakdown voltage V_b

$$V_b^2=8\int_{T_c}^{T_a}\left(\frac{\kappa}{\sigma}\right)dT \tag{2.60}$$

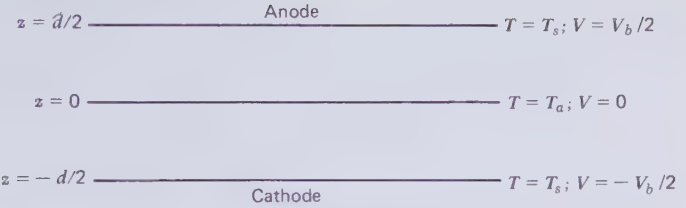

Figure 2.20 One-dimensional heat flow in infinite dielectric slab for the thermal breakdown voltage V_b.

T_s is the surface temperature of the dielectric slab, which in a well-cooled system will be equal to the environmental temperature or nearly so. T_a and V_b are critical values in the dielectric delineating thermal instability and electrical breakdown. With κ_0 and (2.58), the equation for the breakdown voltage becomes

$$V_b^2 = 8\int_{T_s}^{T_a}\left(\frac{\kappa_0}{\sigma_0}\right)\exp\left\{\frac{C}{(KT)}\right\}dT$$

$$V_b^2 = \frac{8\kappa_0}{\sigma_0}\left[\frac{KT^2}{C}\exp\left\{\frac{C}{(KT)}\right\}\right]_{T_a}^{T_s} \tag{2.61}$$

To eliminate T_a from (2.61) it is argued that V_b is a relatively insensitive function of T_a because the conductivity in (2.60) increases with T_a. This is true only for the one-dimensional flow of heat. Furthermore, when C is very much greater than KT and of course T_a is greater than T_s, the quantity $T_a^2\exp\{C/(KT_a)\}$ becomes negligible compared to $T_s^2\exp\{C/(KT_s)\}$. Therefore (2.61) approximates to

$$V_b = E_b d \simeq \left(\frac{8\kappa_0 KT_s^2}{\sigma_0 C}\right)^{1/2}\exp\left\{\frac{C}{(2KT_s)}\right\} \tag{2.62}$$

where E_b is the breakdown stress. This stress, in accordance with (2.62), is inversely proportional to the insulation thickness.

O'Dwyer [2.47] has calculated E_b for sodium chloride (NaCl) using the following data available from the literature

$\kappa_0 = 0.05$ (J cm^{-1} °K^{-1} s^{-1}) $\quad C = 12000$K (°K)

$\sigma_0 = 71.8$ (Ω^{-1} cm^{-1}) $\quad T_s = 523$ (°K)

His results are given by the straight line on the log-log plot of Fig. 2.21. Few

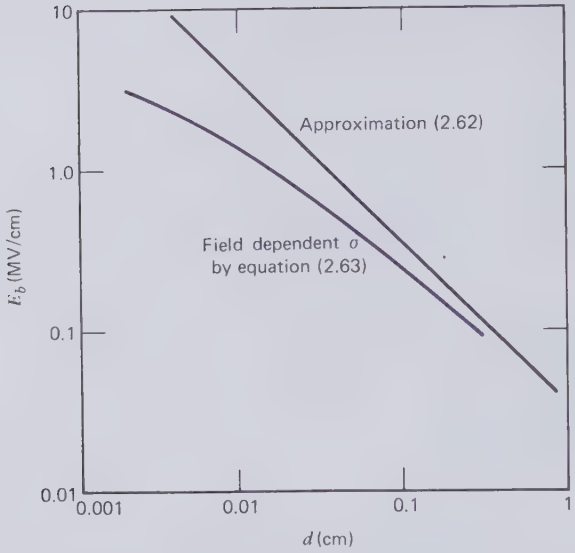

Figure 2.21 Thermal breakdown strength of NaCl slab at 250°C surface temperature according to approximation (2.62) and with allowance for variations in σ due to E by equation (2.63) [2.47]. (By permission of Oxford University Press).

attempts appear to have been made to confirm (2.62) by experiment. Sometime ago Inge et. al. [2.57] found that the breakdown voltage of NaCl slabs at 700°C was approximately constant and independent of d for $d > 0.15$ cm, which tends to support the thermal breakdown mechanism. But the magnitude of V_b was only about half the value predicted by (2.62).

Chou and Brooks [2.56] modified the equations of the thermal breakdown model by allowing for the field dependence of the electrical conductivity by

$$\sigma = \sigma_0 \exp\left\{ \frac{-(C - \beta E)}{(KT)} \right\} \tag{2.63}$$

This prevents the separation of variables in (2.57) and forced these investigators to use numerical methods for the subsequent integration. Their results are also plotted on Fig. 2.21. It will be seen that the variation of conductivity with the electric field strength can become a significant factor in thin layers below 1 mm. It should not influence the much thicker insulation layers in cables to any great extent.

When the voltage applied across the dielectric slab is undergoing sinusoidal polarity reversals, polarization losses due to dipole friction come into play. They furnish additional heat, which should contribute to the

thermal breakdown process. In the case of ac excitation the charging current I_c associated with the dielectric material leads the applied voltage by a phase angle ϕ, which is just a little smaller than 90°, as shown in Fig. 2.22. The quadrature component I_X is a truly lossless polarization or displacement current. The remaining component I_R behaves like a resistive Joule loss current, although part of it must be due to dipole rotation losses rather than charge transport. If i_C is the charging current density and $V/d = E$ the uniform field strength, then the power dissipation density in the dielectric may be written

$$p = i_C E \cos\phi \tag{2.64}$$

Let C_e be the geometric capacitance of the electrodes in vacuum and ε the dielectric constant of the slab of area A, then the polarization current density is given by

$$i_X = \omega\varepsilon\left(\frac{C_e}{A}\right)E \simeq i_C \tag{2.65}$$

and this is very nearly equal to the charging current density. Substituting the approximate value of i_C into (2.65) and noting that $C_e = A/(4\pi d)$ results in

$$p \simeq \omega\left(\frac{C_e}{A}\right)E^2\varepsilon\cos\phi \simeq \omega\left(\frac{C_e}{A}\right)E^2\varepsilon\tan\delta \tag{2.66}$$

Both forms of (2.66) can be found in the cable literature; $\cos\phi$ is usually called the power factor of the dielectric and $\tan\delta$ is referred to as the loss factor.

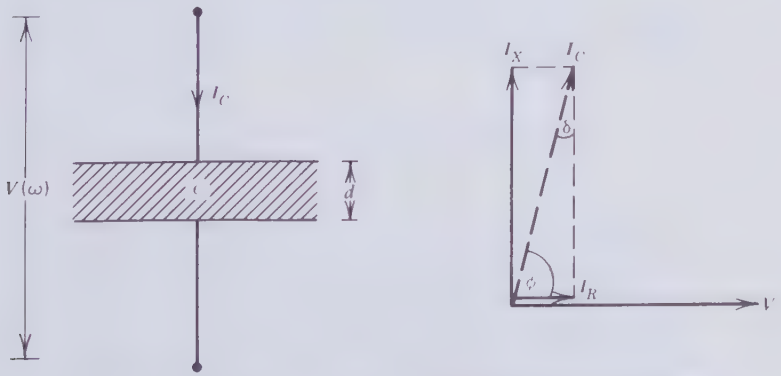

Figure 2.22 Charging current phasor diagram for a dielectric slab.

Comparing (2.66) with the left-hand side of (2.52), it will be appreciated that with ac excitation we are dealing with an effective electrical conductivity

$$\sigma_{ac} = \omega\left(\frac{C_e}{A}\right)\varepsilon\cos\phi \tag{2.67}$$

To evaluate this quantity at power frequency ($f=60$ Hz, $\omega=2\pi f$) for polyethylene cable insulation a dielectric constant of 2.3 may be assumed. The geometric capacitance of a paralle plate capacitor is

$$\frac{C_e}{A} = \frac{10^{-11}}{(36\pi d)}\text{F/cm} \tag{2.68}$$

The power factor of polyethylene is unlikely to be less than 10^{-4}, which works out to a minimum ac conductivity of this material of $\sigma_{ac}=9\times 10^{-15}/d$. Unlike the dc conductivity, σ_{ac} is thickness dependent. Even in insulation for the highest voltage systems, d is unlikely to be greater than 9 cm, so that $10^{-15}\ \Omega^{-1}$ is a lower bound of the ac electrical conductivity of polyethylene. It is by no means easy to measure the dc conductivity for as good a dielectric as polyethylene. Widely different values have been reported by a number of experimenters. Somewhere in the middle of the spread of data lie the results of Stannet and Schroff [2.58], who found dc conductivities of 1×10^{-18} and $125\times10^{-18}\ \Omega^{-1}\ \text{cm}^{-1}$ at 40 and 84°C, respectively. These figures cover about the normal operating temperature range of polyethylene insulation and indicate strongly that the ac conductivity is always larger than the dc conductivity, possibly by as much as several orders of magnitude. Therefore, at least qualitatively, the thermal breakdown model explains why the dielectric strength of polyethylene is lower for ac than for dc voltages. Substituting the ac conductivity of (2.67) and (2.68) into the breakdown formula (2.62), it will be found that the thickness dependence is made less strong

$$E_b = \left(\frac{1}{\sqrt{d}}\right)\left(\frac{288\pi\times10^{11}\kappa_0 KT_s^2}{\omega\varepsilon\cos\phi\cdot C}\right)^{1/2}\exp\left\{\frac{C}{(2KT_s)}\right\} \tag{2.69}$$

Thermal instability is the normal mode of failure of paper insulation when subjected to increasing dc and ac voltages. This was first shown by Brazier [2.59]. Robinson [2.60] recognized this kind of breakdown by the geometry of the breakdown path, and was able to distinguish it from tracking, treeing, and corona activity, which produced failure by slow erosion. He demonstrated that thermal breakdowns produce radial punc-

tures of the insulation wall, whereas corona discharges track along the surfaces of individual paper tapes. Another proof of thermal breakdown was found to be scorching and brittleness of the paper for 2 or 3 ft on either side of the breakdown channel. Robinson claimed that if the voltage was removed at the threshold of thermal instability, but just before runaway took place, the insulation was left completely unharmed. In contrast to this, damage due to tracking and treeing left its marks long before the insulation strength collapsed. Since these discoveries were made, thermal instability has become the overriding design criterion of oil-paper insulated high-voltage cables. As the conductor heat also flows through the dielectric wall, the thermal criterion affects not only the voltage rating of the cable but also its power transfer capability.

Steady state heat flow in a coaxial cable differs in two ways from that in the dielectric slab model used hitherto. First, the dielectric losses are not the only source of heat to be considered and, second, heat flow is unidirectional from the center outward. There is no doubt about the temperature dependence of the dielectric loss, or power factor, of oil-paper insulation beyond a certain critical temperature. Figure 2.23 shows this for one of the early impregnated paper insulations investigated by Robinson [2.60] and a modern insulation, which has been developed to keep the dielectric loss in oil-paper insulation to a minimum. Although the modern insulation has an essentially flat characteristic up to 80°C, it will be appreciated that eventually it must rise just as steeply as that of the old insulation. The best that can be achieved is to move the transition beyond the 100–120°C band.

An analytical solution of steady state heat flow in a coaxial dielectric, as shown in Fig. 2.24, is possible provided the maximum temperature at the

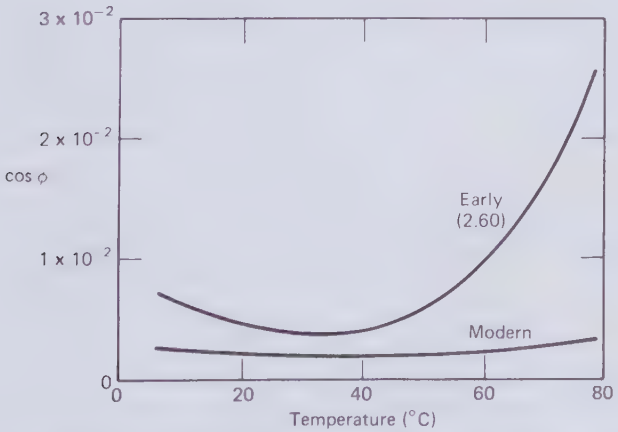

Figure 2.23 Power-factor/temperature characteristic of oil impregnated paper insulation.

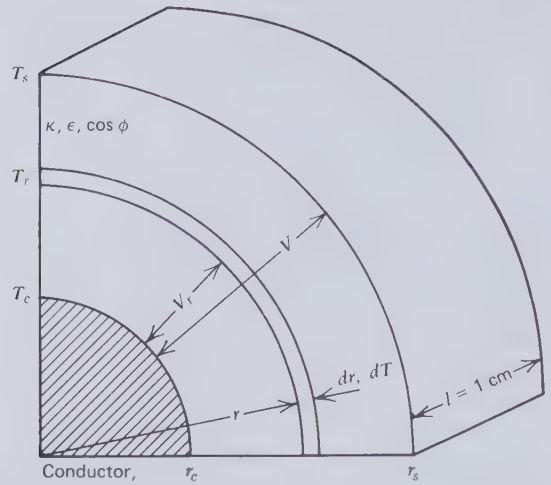

Figure 2.24 Dielectric heating of coaxial cable dielectric.

conductor surface, T_c, is limited to the extent that the power factor may be taken as constant for all parts of the dielectric wall. This is very nearly true for the normal operating temperature range of oil paper insulated cables. We start by considering a portion of the dielectric wall from the conductor outward to the radius r, as illustrated in Fig. 2.24. The voltage across this portion will be denoted by V_r and is given by

$$V_r = V\frac{\ln(r/r_c)}{\ln(r_s/r_c)} \tag{2.70}$$

where V is the total voltage applied between conductor and sheath and r_s and r_c are the sheath and conductor radii, respectively. The capacitance in esu of the same portion of the insulation wall and one centimeter long is

$$C_r = \frac{\varepsilon}{\{2\ln(r/r_c)\}} \tag{2.71}$$

This enables us to calculate the polarization current I_r by

$$I_r = \frac{V_r}{(1/\omega C_r)} = \omega C_r V_r \tag{2.72}$$

and substituting from (2.70) and (2.71)

$$I_r = \frac{\omega\varepsilon V}{2\ln(r_s/r_c)} \tag{2.73}$$

It will be noted that this current is the same for all values of r and, just like an ionic current, the polarization current causes no charge accumulations and obeys the law of continuity. The dielectric loss occurring in this portion of the insulation is

$$P_{d-r} = V_r I_r \cos\phi \tag{2.74}$$

With (2.70) and (2.73) this loss becomes

$$P_{d-r} = \frac{\omega\varepsilon V^2 \cos\phi}{2\left[\ln(r_s/r_c)\right]^2} \ln(r/r_c) \tag{2.75}$$

Next we consider the temperature differential dT across the thin layer dr. This is equal to the product of P_{d-r} and the thermal resistance dR_i of the layer. But with a thermal conductivity κ of the dielectric we have

$$dR_i = \frac{dr}{2\pi r\kappa} \tag{2.76}$$

so that

$$dT = \frac{\omega\varepsilon V^2 \cos\phi}{4\pi\kappa\left[\ln(r_s/r_c)\right]^2} \ln(r/r_c)\frac{1}{r} \tag{2.77}$$

Without axial heat flow and no cooling provided in the conductor, the steady state heat flow has to be radially outward. The cable sheath will attain a temperature T_s, which lies above the ambient temperature T_0 and ensures heat transfer to the environment. The temperature differential between conductor and sheath may be calculated from

$$T_c - T_s = \int dT = \frac{\omega\varepsilon V^2 \cos\phi}{4\pi\kappa\left[\ln(r_s/r_c)\right]^2} \int_{r_c}^{r_s} \ln(r/r_c)\frac{dr}{r} \tag{2.78}$$

The solution of the integral in (2.78) can be found in tables in [2.61] and the temperature drop across the insulation is

$$T_c - T_s = \frac{\omega\varepsilon V^2 \cos\phi}{8\pi\kappa} \frac{1}{9\times 10^{11}} (^\circ\mathrm{C}) \tag{2.79}$$

The Joule heat of the conductor P_c also has to flow radially outwards and overcome a total thermal resistance of the insulation R_i which can be

calculated by integrating (2.76)

$$R_i = \int_{r_c}^{r_s} \frac{dr}{2\pi r\kappa} = \frac{\ln(r_s/r_c)}{2\pi\kappa} \text{ (Therm. } \Omega \text{ of 1 cm length)} \qquad (2.80)$$

At this stage it might be pointed out that the total dielectric loss in the insulation wall

$$P_d = \frac{\omega\varepsilon V^2 \cos\phi}{2\ln(r_s/r_c)} \times \frac{1}{9\times 10^{11}} \quad \text{(W/cm)} \qquad (2.81)$$

flowing through half the thermal resistance of the insulation wall ($R_i/2$) gives the same temperature drop as (2.79). In cable design this has been found to be more convenient than the use of (2.79).

For simultaneous heat transfer of conductor and dielectric losses we obtain, by superposition, the combined temperature drop

$$T_c - T_s = \frac{P_c \ln(r_s/r_c)}{2\pi\kappa} + \frac{\omega\varepsilon V^2 \cos\phi}{18\times 10^{11}\pi\kappa} \quad (^\circ\text{C}) \qquad (2.82)$$

In (2.82) the factor $1/(9\times 10^{11})$ converts the electrostatic units of capacitance to farads.

Oil-impregnated paper insulation can be broken down even though the conductor carries no current and the sheath is well cooled to almost ambient temperature. If any thermal mechanism is going to explain this, it must be shown that dielectric heating alone can raise the conductor temperature to approximately 100°C above the sheath temperature. The results plotted on Fig. 2.25 are a test of this hypothesis. They refer to typical parameters of oil-paper cable insulation of $1/\kappa = 500$ therm·Ω·cm; $\varepsilon = 3.5$; $f = 60$Hz and power factors ranging from 1×10^{-3} to 5×10^{-3} and were calculated with (2.82) for $P_c = 0$.

Note might be taken of the remarkable fact that the dielectric heat, and thermal breakdown from this cause alone, is independent of the conductor and sheath radii and indeed the electrical stress. It is, however, a strong function of voltage and insulation power factor as well as the dielectric constant. No precise figures have been quoted for the temperature at which thermal instability will arise. Experience indicates that oil-impregnated paper insulation is in danger above 100°C, which implies that $T_c - T_s$ should not be more than 80°C. Therefore the maximum voltage this type of insulation could safely withstand at a 5×10^{-3} power factor is no more than 350 kV(rms). But significantly higher voltages can be supported at the lowest power factors of the best oil-paper insulation.

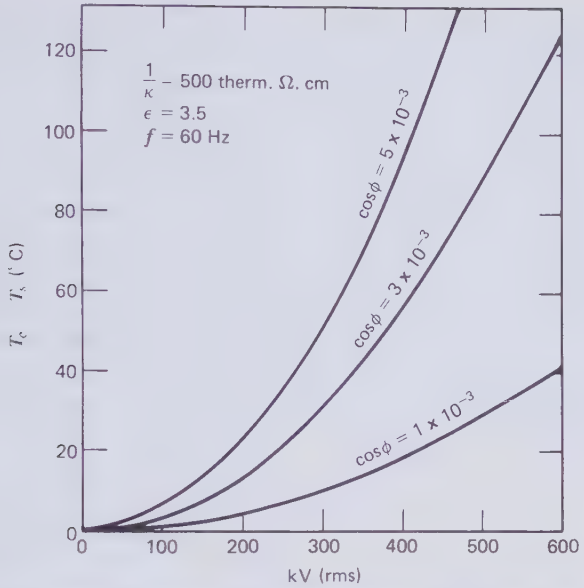

Figure 2.25 60 Hz dielectric heating of oil-paper insulation. T_c = conductor temperature; T_s = sheath temperature.

Figure 2.25 demonstrates quite clearly that ac dielectric heating alone can drive the insulation temperature at the conductor into a range where the power factor is expected to rise steeply with temperature. This would inevitably lead to the thermal instability and breakdown described by Brazier and Robinson.

The operating conditions that a high-voltage cable has to meet are, of course, much more severe than indicated by Fig. 2.25, because the insulation temperature will be further increased by the Joule heat from the conductor and the imperfect cooling of the cable sheath. When these two effects are taken into account, the temperature drop between the conductor and the ambient temperature T_0 becomes

$$T_c - T_0 = P_c\left(\frac{\ln(r_s/r_c)}{2\pi\kappa} + R_e\right) + \frac{\omega\epsilon V^2\cos\phi}{18\times10^{11}}\left(\frac{1}{\pi\kappa} + \frac{R_e}{\ln(r_x/r_c)}\right) \quad (2.83)$$

where R_e is the external thermal resistance between the cable sheath and the ambient heat sink. Equation (2.83), unlike (2.79), shows the conductor temperature to be dependent on r_s/r_c and therefore related to the maximum electrical stress at the conductor. For example if we take a fixed conductor radius of 2.5 cm and increase the insulation thickness from 0.75 to 4.5 cm,

whereas the voltage is kept constant at 200 kV (rms), $T_c - T_0$ will pass through a minimum at about $r_s/r_c = 2$, as shown in Fig. 2.26. Although the electrical stress continues to fall beyond the minimum temperature drop, the conductor temperature starts to rise because of the increasing thermal resistance of the insulation. Therefore nothing is gained in breakdown reliability if the electrical stress is reduced too far.

Brazier [2.59] outlined a numerical step-by-step method of determining the threshold of thermal instability in a coaxial cable when the local power factor varies significantly with temperature. For this purpose he subdivided the dielectric wall into a number of n thin cylindrical layers. The larger n, the greater is the accuracy of the method. To start with the conductor temperature is fixed at some particular value T_1. Then the dielectric loss P_1 in the insulation layer nearest to the conductor is computed with the assumption that this layer is at temperature T_1. When R_1, the thermal

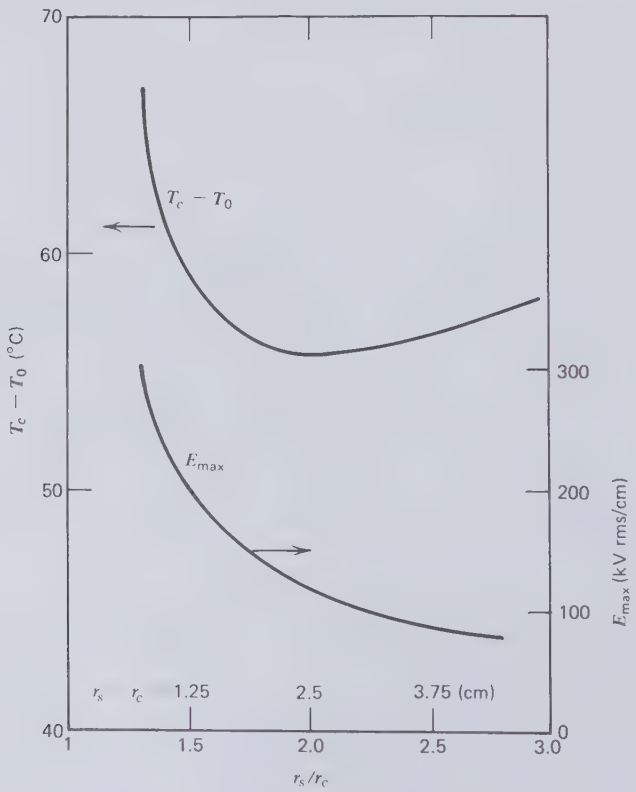

Figure 2.26 Oil-paper insulation temperature as a function of r_s/r_c for $r_c = 2.5$ cm; $V = 200$ kV(rms); $f = 60$ Hz; $\cos\phi = 5 \times 10^{-3}$; $\varepsilon = 3.5$; $1/\kappa = 500$ thermal-$\Omega \cdot$cm.

resistance of this layer, has been calculated it is possible to determine the temperature drop across the layer by

$$T_1 - T_2 = P_c R_1 + \tfrac{1}{2} P_1 R_1 \tag{2.84}$$

where P_c is the Joule heat emanating from the conductor. Equation (2.84) makes use of the previously established rule that the temperature drop across the dielectric due to dielectric heating is given by the total dielectric loss flowing through half the thermal resistance of the insulation. The process of calculations can now be repeated for the second dielectric shell, and so on. Figure 2.27 shows a thermal circuit that should be helpful in the computational work and it also includes the effect of the external thermal resistance R_e. The whole chain of operations has to be repeated for as many conductor

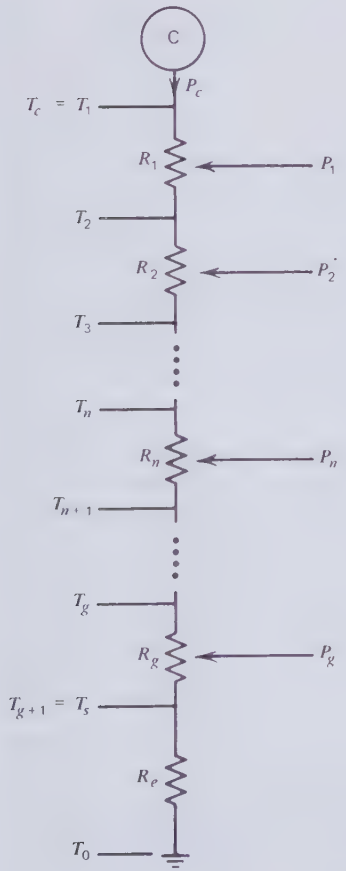

Figure 2.27 Thermal circuit for Brazier's step-by-step method of calculating the thermal instability criterion.

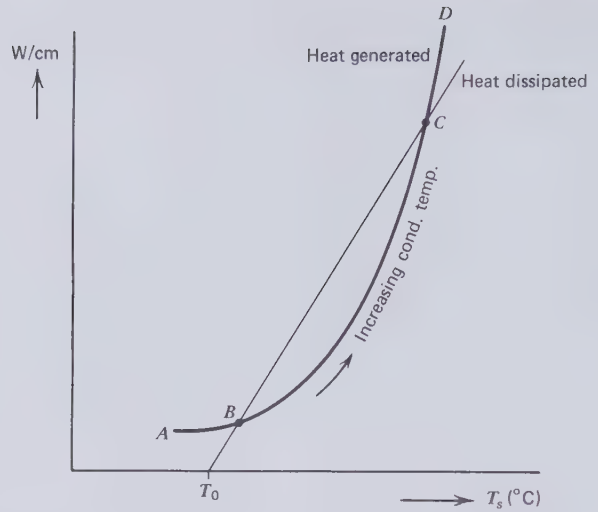

Figure 2.28 Thermal stability diagram according to Brazier [2.59].

temperatures as are of interest. Any one conductor temperature gives one point on the thermal stability diagram of Fig. 2.28. The straight line on this diagram stands for the power that is being dissipated from the cable sheath to the environment at some lower temperature T_0. The curve *ABCD* represents the conductor and dielectric loss power genereated in the cable per unit length for a range of conductor temperatures. *B* is obviously a stable point of operation with the heat generation being balanced by the dissipation. *C* is a metastable point. When the heat produced in the cable rises above this point, thermal runaway and breakdown of the insulation must follow.

The steady state thermal breakdown model has been much less successful in explaining the breakdown of polyethylene insulation than it was in first elucidating the failure mechanism in oil impregnated paper. Thermoplastic polyethylene softens in about the same temperature range in which paper insulation meets with thermal instability problems. For this reason cables insulated with these two very different materials are designed to operate at about the same temperature. The power factor of polyethylene is approximately an order of magnitude smaller than that of oil-impregnated paper. Therefore significantly less dielectric heating occurs in the polyethylene insulation, and it is customary to neglect this when determining the current rating of polyethylene insulated cables. To justify this practice, the temperature drop across coaxial solid polyethylene insulation has been calculated from (2.79). The results are plotted on Fig. 2.29 for three different power factors. The largest power factor of 1×10^{-3} is very high for polyethylene

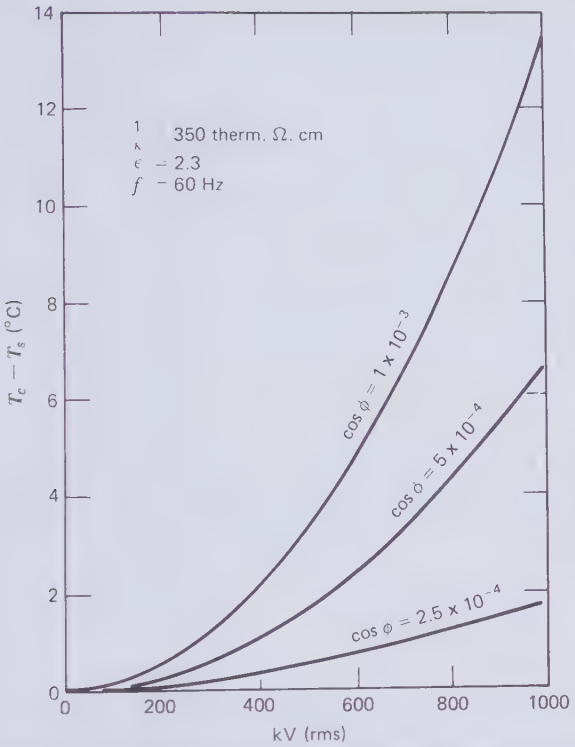

Figure 2.29 60 Hz dielectric heating of extruded polyethylene. T_c = conductor temperature; T_s = sheath temperature.

and the lowest power factor used is more typical of polyethylene cable insulation. According to these graphs, solid polyethylene insulation should be suitable for higher voltages than oil-impregnated paper. This is not borne out by experience and it must be concluded that the average breakdown of extruded polyethylene is not due to thermal instability of the dielectric.

The thermal breakdown criteria (2.62) and (2.69) are of the form

$$E_b = AT_s \exp(B/T_s) \tag{2.85}$$

This indicates a steeply falling breakdown characteristic in the cryogenic temperature region up to ambient temperature. Using the previously quoted data for sodium chloride in (2.62) for a 1-cm-thick NaCl slab, the curve on Fig. 2.30 is obtained. It has about the expected shape from 400°K upward, but the extremely high breakdown levels suggested by (2.62) and (2.69) for the cryogenic temperature range are certainly false. All experimentally

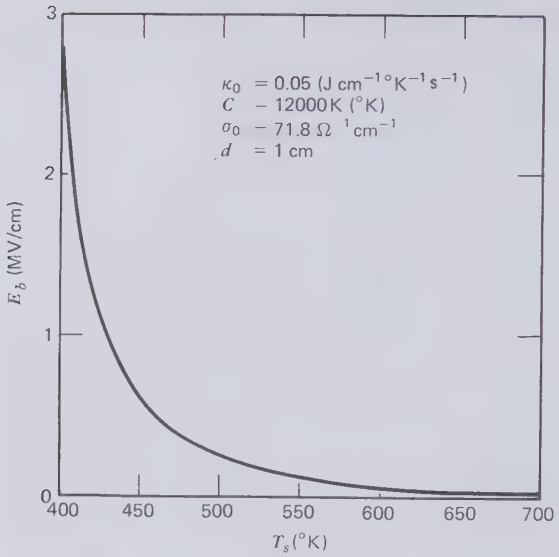

Figure 2.30 Thermal breakdown of a 1-cm-thick sodium chloride (NaCl) slab from approximation (2.62).

determined breakdown versus temperature characteristics of polyethylene and other polymers are essentially flat up to ambient temperature and then fall toward the melting point of the materials. It seems very likely that breakdown mechanisms other than the thermal one are operative below ambient temperature.

The thermal model does not deal with the later stages of the breakdown process and it therefore cannot elucidate the connection between electrical strength and mechanical stresses and strains in the material. For an explanation of the electrical weakening of polyethylene by stretch and its reinforcement by hydrostatic pressure we have to look to other breakdown theories, which concentrate on the bonds between atoms and molecules.

Before considering breakdown mechanisms that appear to be more appropriate for extruded polymeric insulation, another success of the thermal mechanism will be mentioned. In Fig. 2.26 it has been shown that the maximum steady state temperature attained in oil-paper insulation, and therefore also the ac breakdown voltage, is relatively insensitive to the electrical stress in the dielectric. This curious situation arises from the fact that, for a given voltage across the concentric insulation wall, any increase in stress is accompanied by more effective heat transfer through the insulation. In practice this means that the ac breakdown voltage of a paper insulated cable is not sharply defined by a limiting electrical stress. Nonetheless, the

electrical stress governs the cable size, and it is therefore of great concern to cable designers. In this confusion they have at times disagreed whether the maximum stress near the conductor or the average stress throughout the wall is more important, with the former being preferred by European designers and the latter by Americans. That an argument of this kind could have persisted for many years without experimental resolution is by itself a confirmation of the thermal breakdown mechanism in oil-impregnated paper insulation. In contrast to the uncertainty about the ac breakdown stress, there has been general agreement and supporting experimental evidence that the impulse breakdown performance of oil-paper insulation depends on the maximum electrical stress at the conductor shield. The question now arises: can this also be explained by the thermal breakdown mechanism?

For the steady state solution of (2.52), the first term of it was ignored because dT/dt was zero. A pulse voltage lasting for only microseconds must lead to quite different phenomena as there is hardly any time for the heat to flow away from the source. It is then appropriate to ignore the heat-conduction term of (2.52) and start by expressing the local events at a point in the dielectric by

$$\sigma E^2 = c_v \, dT/dt \tag{2.86}$$

As before, the electrical conductivity of the dielectric material will be assumed to increase with temperature according to (2.58), which involves the factor $\exp[-C/(KT)]$. This must be viewed as an equivalent conductivity, which in addition to ion transport also embraces the polarization process and the losses associated with it. For the sake of simplicity E will be taken as a ramp function of time t.

$$E = (E_b/t_b)t \tag{2.87}$$

where E_b is the field strength at breakdown and t_b the time it takes to reach E_b. Even with the simple form of (2.87) we can only derive an approximate solution of (2.86). Any more involved time functions of E, as the standard impulse wave would be, create greater mathematical difficulties. With the substitution of (2.58) and (2.87) into (2.86) it can be shown that

$$\int_{T_0}^{T} \exp\left[\frac{C}{(KT)}\right] dT = \frac{\sigma_0 E_b^2}{c_v t_b^2} \int_0^{t_b} t^2 \, dt \tag{2.88}$$

The integration of the left side of (2.88) is fraught with the same difficulty that had to be overcome in going from (2.60) to approximation (2.62). To

obtain the approximate solution it has to be shown that

$$\left(\frac{KT^2}{C}\right)\exp\frac{C}{(KT)} \simeq \int \exp\left[\frac{C}{(KT)}\right] dT \tag{2.89}$$

Differentiating (2.89) gives

$$\left(\frac{d}{dT}\right)\left(\frac{KT^2}{C}\right)\exp\left[\frac{C}{(KT)}\right] = -\exp\left[\frac{C}{(KT)}\right] + \left(2\frac{KT}{C}\right)\exp\left[\frac{C}{(KT)}\right]$$
$$\simeq -\exp\left[\frac{C}{(KT)}\right] \tag{2.90}$$

The last step in (2.90) is justified by the fact that for most dielectric materials C is very much greater than KT. Therefore the solution (2.89) is permissible provided the limits of integration are reversed. Equation (2.88) then becomes

$$\left[\frac{KT^2}{C}\exp\left[\frac{C}{(KT)}\right]\right]_T^{T_0} \simeq \frac{\sigma_0 E_b^2 t_b^3}{3c_v t_b^2} \tag{2.91}$$

For any practical situation when C/K is very much greater than T, the term of the T-limit becomes negligible compared to the T_0-term. For thermal instability, which is being reached when $t = t_b$, the breakdown field strength may be expressed as

$$E_b \simeq \sqrt{\frac{3c_v KT_0^2}{\sigma_0 C t_b}}\ \exp\left[\frac{C}{(2KT_0)}\right] \tag{2.92}$$

O'Dwyer [2.47] quotes several experimental investigations on sodium and potassium chloride that are in excellent agreement with the thermal impulse breakdown formula (2.92). Thinking of power transmission, this criterion affirms, at least qualitatively, some of the facts that have been of major importance in the development of oil-paper insulated high-voltage cables. They are as follows:

1. Impulse voltage breakdown is governed by the maximum electrical stress near the conductor shield.
2. The impulse strength increases with the specific heat of the dielectric material. This calls for dense and strongly calendered thin paper tapes wound as tightly over the conductor shield as cable bending will permit.

3. As the T_0 in the exponential factor of (2.92) overrides the effect of T_0^2 under the square-root sign, the impulse strength of the insulation decreases as the initial temperature of the most highly stressed region T_0 increases. Therefore a voltage pulse applied to the insulation at elevated temperature is more dangerous than when the same pulse is applied at ambient temperature. This has led to the coining of the phrase "hot impulse strength."
4. The impulse breakdown voltage, or the breakdown stress E_b, increases as the pulse length t_b decreases. Oil-paper insulation is therefore more vulnerable to the slower switching surges than the fast lightning impulses.
5. For maximum impulse strength, the insulation resistance should be as high as possible. This is equivalent to saying that σ_0 should be as low as possible.

Electromechanical Breakdown

In 1955 Stark and Garton [2.62] measured the electric strength of the first cross-linked polyethylene samples from 0 to 220°C. They found that cross-linking improved the dielectric strength at temperatures above 100°C and their results are shown in Fig. 2.31. The material was cross-linked by electron irradiation and the larger of two radiation doses produced the greater amount of cross-linking and therefore the stiffer material. Quite unexpectedly, the investigators noticed that the change in electric strength, which presumably was caused by the cross-linking of molecular chains,

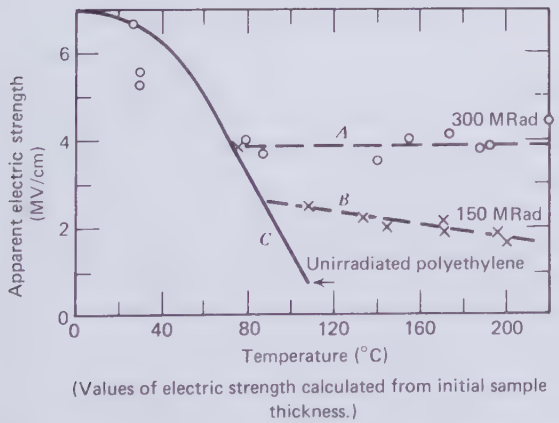

Figure 2.31 Electric strength of polyethylene irradiated with 4-MeV electrons [2.62]. (By permission of Macmillan).

resembled the modification of the modulus of elasticity. This caused them to suspect that the breakdown mechanism in polyethylene was of electromechanical nature. Electrostatic forces compress the dielectric in the direction of the electric field. In thin layers, which have the highest dielectric strength, the electrostatic pressure can amount to 10 to 100 atm. In more conservatively stressed cable dielectrics, this pressure can still be as high as 10 psi. When the field is alternating, the pressure pulsates at twice the power frequency.

Block and LeGrand [2.63] actually measured the electromechanical deformation of a copolymer specimen with a birefringence technique. Their most important finding was that local field inhomogeneities, caused by imperfections, converted the compressive stress to shear stress over a region no larger than a few microns. This is also the cross-sectional dimension of treeing channels. Breakdown was observed when the electric field in one of the deformed regions reached some critical value, which could be called the intrinsic dielectric strength of the material.

Parkman et al. [2.64] increased the breakdown stress of polyethylene specimen 50 to 80 percent by subjecting them to hydrostatic pressure through a viscous membrane. The membrane apparently prevented the hydraulic fluid from penetrating the dielectric material and thereby ensured that all the pressure was exerted on the outside surfaces of the test specimen. At first sight the increase in dielectric strength with hydrostatic pressure appears to contradict the electromechanical breakdown hypothesis of electrostatic compression, but it is compatible with Block and LeGrand's discovery that electrical failure is caused by shear stress.

It is well known, but apparently not documented, that breakdown experiments on bent solid dielectric cable samples invariably produce punctures on the outside of the bend where the insulation is in tension, rather than on the inside where it is in compression. This is further evidence favoring the shear mechanism. Figure 2.32 reproduces a set of measurements published by Yahagi and Mita [2.65]. These authors stretched 50-μm-thick low-density polyethylene films transverse to the electric field at ambient temperature. The ac, dc, and impulse voltages were applied 3 mins after elongation. In all cases they noticed a sharp drop in the breakdown stress (voltage divided by reduced film thickness) for the first 30 percent of elongation and then a recovery followed by a further downward trend. The first decline in electric strength is detrimental to cable reliability. Transverse tensile strain not only depresses the dc strength of the dielectric but has an even greater effect on the impulse and ac strength. In percentages, the ac strength suffers the most. These facts make it tempting to think of electromechanical breakdown in terms of a purely mechanical model. With regard to Yahagi and Mita's experiments, this would mean disconnecting the spherical top electrode from

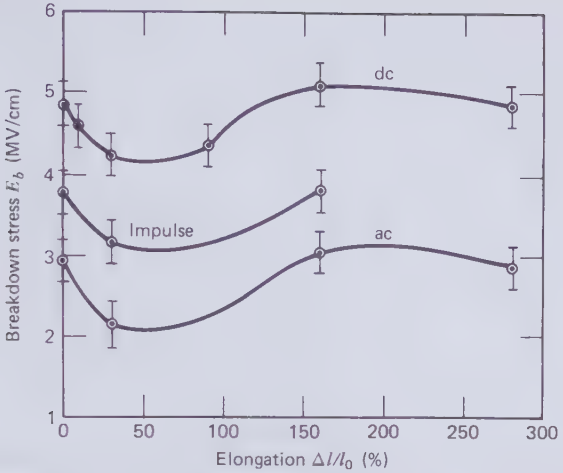

Figure 2.32 Breakdown strength of 50-μm-thick low-density polyethylene films at room temperature three minutes after elongation according to Yahagi and Mita [2.65]. (By permission of the Institution of Electrical Engineers.)

the voltage supply and load it mechanically with a weight to simulate the compression that dc would achieve. In this model impulse voltage would have to be replaced by a hammer blow and a 120-Hz vibrator could simulate the ac voltage. If electrical breakdown can be equated to the rupture of interatomic bonds then it must in some way be related to the mechanical properties of the material. The results of Fig. 2.32 lend a good deal of support to this view because the dc breakdown relates to tensile failure, impulse breakdown to impact failure and ac breakdown to fatigue failure in this order of ranking. This is, of course, a very tenuous analogy because the electrostatic forces are distributed through the volume of the dielectric and not confined by mechanical contact points. Furthermore, such mechanical quantities as the elastic modulus, tensile strength, impact and fatigue strength, which have precise meanings in metals, are ill defined in plastic materials.

Further support for the existence of some mechanical breakdown process in thick-wall polyethylene cable insulation comes from an experiment carried out over a number of years at the Waltz Mill, Pennsylvania, cable test site of the Electric Power Research Institute [2.66]. Five 138-kV cables with cross-linked polyethylene insulation were subjected to an extensive test program after carefully screening them with discharge detectors. The culmination of the tests was a series of load cycles in which conductor temperatures up to 140°C were reached. All cables broke down at one stage or another during the load cycle program, usually during the cool-down

period. Relatively large differences in the coefficients of thermal expansion between the polyethylene insulation and the aluminum or copper conductors forced the insulation to undergo plastic deformation within every load cycle. This deformation had to be brought about by mechanical stresses in the insulation [2.67]. The axial forces in the insulation, depending on its thickness, can be of the order of 5000 lb. Since the conductor is in effect bonded to the insulation, it has to take strong axial reaction forces that have, at times, broken individual wires or whole soldered conductor joints. The sequence of events in one load cycle leads to the simultaneous application of axial tension and hoop stress to the electrical insulation during the cool-down phase. Figure 2.33 is a diagram that explains this step by step.

A new cable (a) in the mechanically relaxed state progresses to (b) where full load current is passed through the conductor. This causes the conductor and the insulation to heat up. The polyethylene expands 1 to 2 percent more than the conductor both in the axial and in the radial direction. This has three consequences: (1) the insulation is forced into axial compression, (2) a cavity will form between the conductor and the semiconducting polyethylene conductor shield which is bonded to the insulation, and (3) the outer part of the insulation is under hoop stress because it is cooler and expands less than the inner part. Given sufficient conductor temperature rise, the

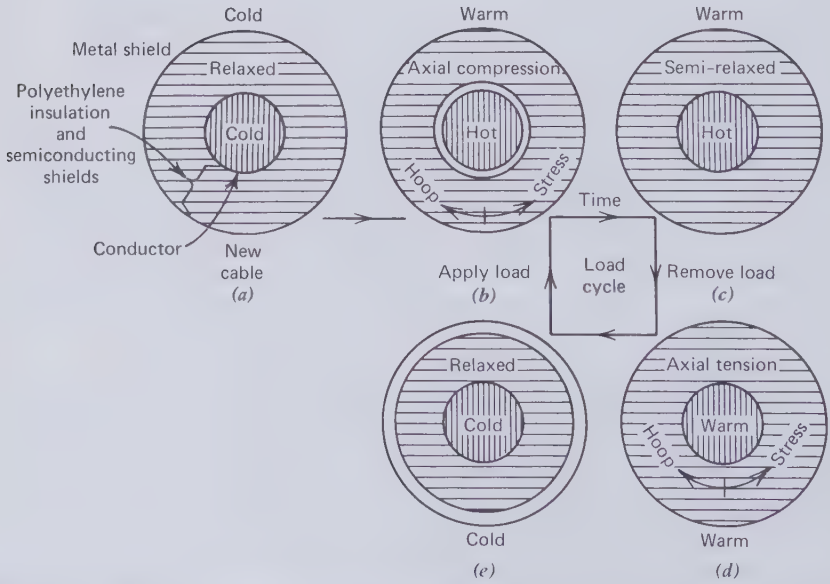

Figure 2.33 Load cycle induced mechanical stresses in solid dielectric cable [2.67]. (By permission of the Institute of Electrical and Electronics Engineers).

mechanical stresses inside the insulation easily exceed the yield strength of polyethylene and the material begins to flow. The only room it has for plastic expansion is the cavity on the conductor surface. This will fill up and after a few hours the semirelaxed state (c) is reached. Now the load current is reduced or removed and the insulation begins to contract more than the conductor. It creates axial tension in the dielectric and, because of shrink-down, hoop stress in the electrically most sensitive insulation layer near the conductor. This is the potentially dangerous phase (d) of the load cycle when breakdowns are prone to occur. Finally, when the cable reaches the cold state (e) it will be tight on the conductor, conceivably leaving a cavity between the bonded semiconducting insulation shield and any metal shield. In some of the Waltz Mill cable samples radial cracks were found in the insulation, indicating just how severe the thermally induced mechanical stresses can be and electrical failure usually occurred in phase (d).

Stark and Garton [2.62] equated the electrostatic pressure to the elastic restoring force in the dielectric. An easy way of calculating the electrostatic force F_e is to take the gradient of the stored electrostatic energy, or

$$F_e = -\left(\frac{d}{dx}\right)\left(\frac{1}{2}CV^2\right) \tag{2.93}$$

where C is the capacitance of the dielectric sample and V the voltage applied across it. The negative sign in (2.93) indicates compression or a shortening of the distance of separation x between the electrodes. For a flat plate arrangement of area A the capacitance is given by

$$C = \frac{\varepsilon A}{4\pi x}\frac{1}{9\times 10^{11}} \quad \text{F} \tag{2.94}$$

To obtain the force this has to be differentiated with respect to x

$$\frac{dC}{dx} = -\frac{\varepsilon A}{4\pi x^2}\frac{1}{9\times 10^{11}} \tag{2.95}$$

Noting that the electric field strength is $E = V/x$, the electrostatic pressure per unit area of the dielectric becomes

$$\frac{F_e}{A} = \frac{\varepsilon E^2}{8\pi}\frac{1}{9\times 10^{11}}\frac{10^5}{9.807} \quad \text{g/cm}^2 \tag{2.96}$$

The factor $10^5/9.807$ converts the pressure unit from J/cm/cm^2 to g/cm^2. A significant feature of this theory is that the electrostatic pressure depends

only on the electric stress and not the thickness of the slab. In addition the pressure is proportional to the dielectric constant.

To find the electrostatic force on the walls of coaxial cable insulation, the appropriate formula for the capacitance per unit length is

$$C = \frac{\varepsilon}{2\ln(r_s/r_c)} \frac{1}{9\times10^{11}} \quad \text{F} \tag{2.97}$$

where r_s is the sheath radius and r_c is the conductor radius. There exist different capacitance gradients at the two electrodes.

$$\frac{dC}{dr_s} = -\frac{\varepsilon}{2r_s[\ln(r_s/r_c)]^2} \frac{1}{9\times10^{11}} \quad \text{F/cm} \tag{2.98}$$

$$\frac{dC}{dr_c} = \frac{\varepsilon}{2r_c[\ln(r_s/r_c)]^2} \frac{1}{9\times10^{11}} \quad \text{F/cm} \tag{2.99}$$

Using (2.98) and (2.99) in (2.93) and dividing by the circumference, the external and internal pressures at constant voltage are seen to be

$$\frac{F_s}{A} = \frac{\varepsilon E_s^2}{8\pi} \frac{1}{9\times10^{11}} \frac{10^5}{9.807} \quad \text{g/cm}^2 \tag{2.100}$$

$$\frac{F_c}{A} = \frac{\varepsilon E_c^2}{8\pi} \frac{1}{9\times10^{11}} \frac{10^5}{9.807} \quad \text{g/cm}^2 \tag{2.101}$$

Stark and Garton experimented with 50-μm-thick polyethylene films and observed breakdown stresses of the order of 5 MV/cm. Taking the dielectric constant of polyethylene as 2.3, (2.96) indicates an electrostatic pressure of 25.9 kg/cm^2. It is not surprising that so large a pressure should cause breakdown in a relatively weak polymeric film. But the electrostatic pressure exerted on the insulation of a solid dielectric high-voltage cable at the observed breakdown stresses is much smaller. Consider the following example: $\varepsilon = 2.3$; $r_s = 4$ cm; $r_c = 2$ cm; $V = 10^6$ V (dc at breakdown). From (2.100) and (2.101) the pressures at the conductor and insulation shields are found to be 748 and 374 g/cm^2, respectively. This alone proves that electromechanical breakdown of a given material is not merely a matter of establishing a critical electrostatic pressure on the dielectric surfaces.

One major difficulty of any electromechanical breakdown model is to find an adequate mathematical description of the mechanical properties of polymers and plastic materials in general. Figure 2.34 is a stress-strain diagram of a low-density non-cross-linked polyethylene at 25°C. The data for this graph has been taken from [2.68]. Even at strains below 2 percent,

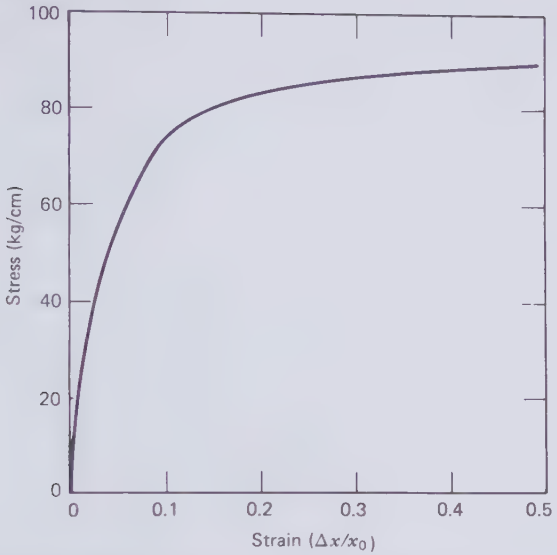

Figure 2.34 Stress-strain curve of low-density polyethylene at 25°C [2.68].

the stress-strain graph is not a straight line. Young's modulus of elasticity, which is the slope of this graph, is a well-defined constant parameter for each metal, but an uncertain quantity in plastics. Stark and Garton [2.48] suggested the stress-strain relationship of polyethylene might be adequately approximated to

$$\text{stress} = Y \ln \frac{x_0}{x} \tag{2.102}$$

where Y is taken as a constant modulus of elasticity, x_0 is the original length of the specimen, and x its compressed length. Equating this to (2.96) and substituting $E = V/x$ and $n = x/x_0$, it is found that

$$\frac{k\varepsilon V^2}{Yx_0^2} \frac{1}{n^2} = \ln \frac{1}{n} = \frac{X}{n^2} \tag{2.103}$$

This last equation may be solved graphically as illustrated in Fig. 2.35. As the voltage is increased, until $X = 0.1$, n will decrease from unity and stabilize at $n = 0.9$ where $X/n^2 = \ln(1/n)$. At this point of stability the dielectric will be compressed to 90 percent of its original thickness. The voltage, which achieved this 90 percent compression, is given by

$$V = \sqrt{\frac{0.1\, Yx_0^2}{k\varepsilon}} \tag{2.104}$$

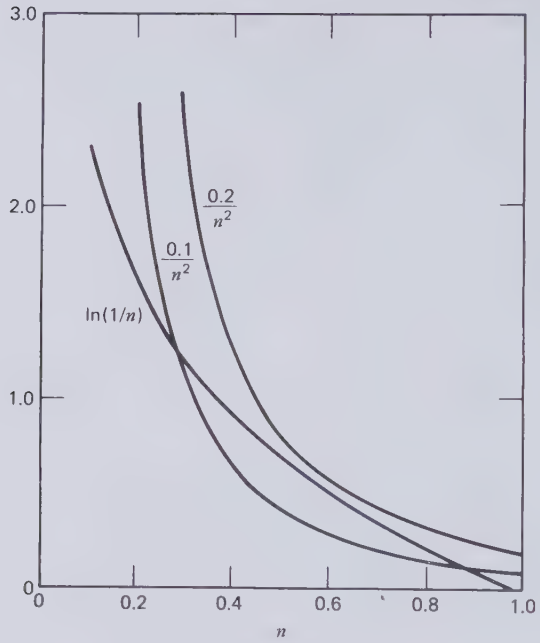

Figure 2.35 Graphical solution of (2.103).

If Y is given in grams per centimeter squared and x_0 in centimeters, the numerical constant k from (2.96) is $10^5/(8\pi \cdot 9\times 10^{11}\cdot 9.807)=4.508\times 10^{-10}$. Solutions for the voltage, like (2.104), may be found for all values of $X<0.1$. When $X=0.2$ the dielectric will collapse because even if n could decrease to zero, $0.2/n^2$ is everywhere greater than $\ln(1/n)$. At some intermediate value of $0.1<X<0.2$ the curve of X/n^2 will just touch the curve of $\ln(1/n)$, which gives the breakdown voltage V_b. The largest stable value of $X_{\max}$ is obtained through differentiation

$$\frac{dX}{dn}=-n+2n\ln\frac{1}{n}=0 \tag{2.105}$$

Therefore

$$n=\frac{1}{e^{0.5}} \tag{2.106}$$

and

$$X_{\max}=\frac{1}{2e}=0.1839 \tag{2.107}$$

Substituting this value into (2.103) gives the breakdown voltage and the electrical breakdown stress due to compressive collapse as

$$\frac{V_b}{x_0} = E_b = \sqrt{\frac{Y}{2ek\varepsilon}} \tag{2.108}$$

To derive an equivalent electromechanical breakdown criterion for a coaxial cable dielectric it will be assumed that the insulation is rigidly supported on the outside and any thinning due to electrostatic compression is being brought about by an increase of the inner radius. This is feasible in practice because of the bonding of a semiconducting conductor shield to the inside wall of the insulation. Let the original insulation thickness be $s_0 = r_s - r_c$, as shown in Fig. 2.36. This thickness will be compressed to $ns_0 = r_s - r$. The force balance equation, corresponding to (2.103), may then be derived from (2.101) and (2.102) and written

$$k\varepsilon E_r^2 = Y \ln \frac{s_0}{ns_0}$$

$$\frac{k\varepsilon V^2}{r^2\left[\ln(r_s/r)\right]^2} = Y \ln \frac{1}{n} \tag{2.109}$$

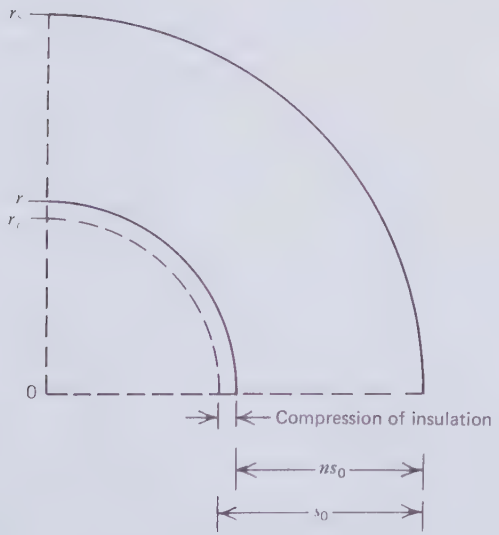

Figure 2.36 Radical compression of coaxial insulation due to electrostatic pressure.

but

$$r^2\left[\ln\left(\frac{r_s}{r}\right)\right]^2 = r_s^2\left[1-n\left(\frac{s_0}{r_s}\right)\right]^2 \ln\frac{1}{1-n(s_0/r_s)} \tag{2.110}$$

Combining (2.109) and (2.110) results in

$$\frac{k\varepsilon V^2}{r_s^2 Y}\frac{1}{\left[1-n(s_0/r_s)\right]^2} = \ln\frac{1}{n}\ln\frac{1}{1-n(s_0/r_s)}$$

or

$$\frac{X}{\left[1-n(s_0/r_s)\right]^2} = \ln\frac{1}{n}\ln\frac{1}{1-n(s_0/r_s)} \tag{2.111}$$

The graphic solution of (2.111) for the specific case of $s_0 = r_c = 0.5r_s$ is shown in Fig. 2.37. As for the flat plate dielectric, X_{max} is found by setting the differential coefficient of X with respect to n equal to zero. The result is $X_{max} = 0.1421$, which gives

$$X_{max} = 0.1421 = \frac{k\varepsilon V^2}{(4r_c^2 Y)} \tag{2.112}$$

because $r_s = 2r_c$. When (2.112) holds V will be the breakdown voltage V_b, which is associated with the breakdown stress E_b at the conductor surface. Therefore

$$\frac{V_b}{r_c} = E_b \ln\left(\frac{r_s}{r_c}\right) = \sqrt{\frac{0.1421\times 4Y}{k\varepsilon}} \tag{2.113}$$

If (2.113) is compared with (2.108), we find that

$$\frac{E_b(\text{coax cable})}{E_b(\text{flat plate})} = \frac{1}{\ln 2}\sqrt{0.1421\times 4\times 2e} = 2.54 \text{ for } s_0 = r_c \tag{2.114}$$

The compressive electromechanical breakdown theory therefore predicts that the breakdown strength of coaxial insulation should be significantly greater than that of flat plate insulation. In fact the flat plate will collapse when, from (2.106), the compression reaches 40 percent, whereas the coaxial insulation will not collapse until it reaches 74 percent.

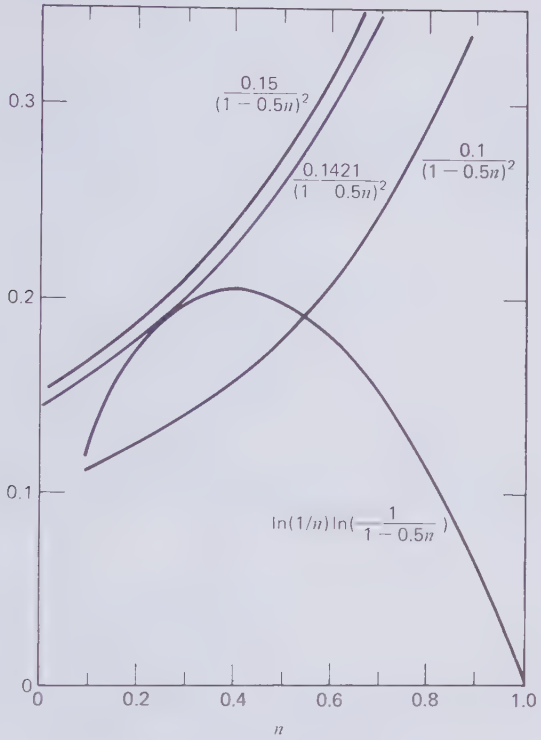

Figure 2.37 Graphical solution of (2.111).

Stark and Garton [2.48] found reasonable agreement between the electromechanical breakdown criterion (2.108) and measurements on two cross-linked 50-μm-thick polyethylene films at the elevated temperature of 150°C. Another success of this theory was the correlation of a decrease in breakdown strength of polyisobutylene at approximately -40°C with a sharp decrease in elastic modulus in the same temperature range.

It is by no means easy to fit the logarithmic law (2.102) to an actual stress-strain plot. If an experimentally determined plot is available, the breakdown voltage for a given initial film thickness can be found by iterations. The first step is to guess an electrical breakdown voltage, say V_1, and calculate the corresponding electrostatic pressure. This indicates a certain strain on the graph, and an adjusted electrical stress may be calculated for V_1. The new mechanical stress gives a second strain figure from the graph, and so on. If the strain increases with successive iteration, the system is unstable and V_1 is greater than V_b. On the other hand, decreasing strain indicates stability and V_1 is smaller than V_b. From this

knowledge an improved value V_2 can be guessed. By successive approximations carried out in this way a value V_n will be found that is close to V_b. Iterations of this kind have been performed on the stress-strain plot of Fig. 2.34. They predicted a breakdown stress of approximately 8 MV/cm at 25°C. Measurements on low-density polyethylene films at this temperature indicated breakdown stresses from 5.5 to 9.0 MV/cm [2.69].

DC breakdown stresses at the conductor interface of high-voltage solid dielectric cables are on the average only one-tenth to one-fifth of the stress predicted by the electromechanical criterion. The discrepancy is so large that simple uniform compression failure cannot be the cause of breakdown. Uniform compression of the insulation requires the accompaniment of a substantial elongation of the cable, which the conductor would not permit. All the indications are that the breakdown area in a polyethylene insulated cable is quite small. As already discovered by Block and LeGrand [2.63], local shear action is likely to play a part in the breakdown process and this could conceivably account for part of the discrepancy with the electromechanical breakdown criterion.

Furthermore, the electrostatic force would be aided by material contraction due to any superimposed transverse extension, as in the cool-down phase of a cable load cycle. This interaction is illustrated in Fig. 2.38(a). The magnitude of the contraction is governed by Poisson's ratio and it could amount to 0.25 to 0.5 of the transverse strain. The opposite of this is transverse compression or restraint, as in Fig. 2.38(b). Experiments have shown that restraint increases the dielectric strength of thin films by as much as 40 percent [2.64].

In addition to shear action and transverse tension, it is possible to think of a third factor that could help to depress the breakdown strength of a practical cable below the level of the electromechanical criterion. This is field enhancement resulting from local caving-in of the insulation under the electrostatic pressure. This effect might become particularly severe if a conducting surface protrusion on the electrode was responsible for starting the caving-in process. It remains to be seen whether these more complicated actions will eventually yield to quantitative analysis. Any credible mathematical theory would have to explain, among other things, the formation of tree-channels that are the precursors of breakdown in polymeric insulation.

Besides, a really useful breakdown theory must throw some light on the further decrease in dielectric strength when the insulation is stressed with 50 or 60 Hz alternating voltage. In thick-wall cables this brings the observed breakdown stress of polyethylene down to less than 0.5 MV/cm. The thermal breakdown model could explain this for oil-paper insulation by dielectric heating, but had no answer to the question of why the same phenomenon is present in low-loss polyethylene. An electromechanical

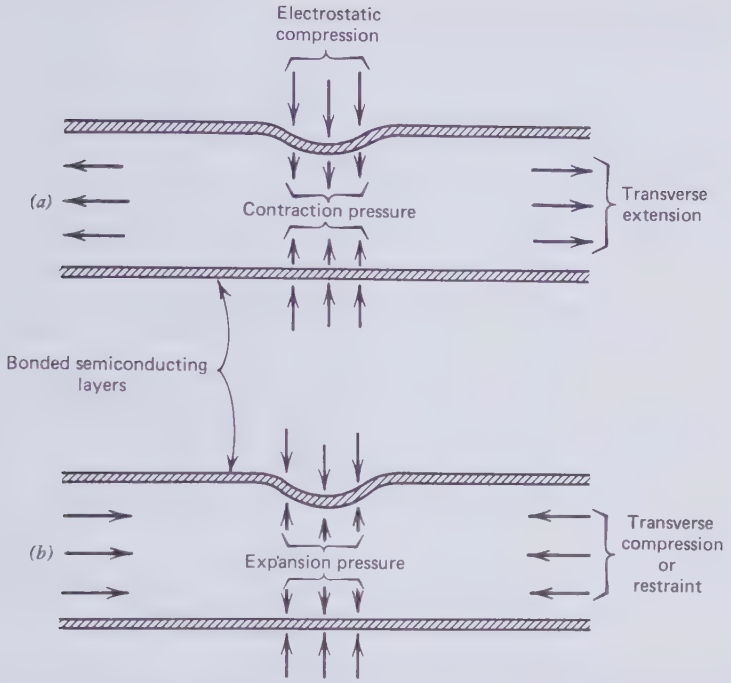

Figure 2.38 The effect of transverse strain on local electrostatic compression in a dielectric slab.

mechanism can probably account for this in terms of vibration fatigue. With respect to metals, it is not unknown that the fatigue strength is only 0.25 to 0.5 of the tensile, shear, or compressive strength of the material. Vibrating electrostatic forces provide at least a qualitative explanation of the difference between ac and dc dielectric strength of polymers. The quantitative treatment would again have to address itself to the excavation of ac tree channels prior to breakdown of polyethylene.

Thermal and electromechanical breakdown models are not mutually exclusive. The prebreakdown generation of heat, which lies at the root of the thermal theory, weakens interatomic bonds and with them the elastic moduli. Hence electromechanical actions almost certainly come into play in the later stages of thermal breakdown. Yet under other circumstances the electromechanical process can proceed without being aided by heat.

According to (2.108) the breakdown stress of a flat plate dielectric does not decrease as the slab is made thicker. This contradicts experimental findings and is probably the weakest link in the electromechanical breakdown explanation.

Gas Channel Breakdown

Thermal and electromechanical breakdown are characterized by stability limits beyond which events cannot be easily arrested in a divergent electric field. But partial breakdowns are a common occurrance. They are particularly obvious in transparent insulation, such as polyethylene, because of the telltale tree patterns. For the development of high-voltage solid dielectric cables, there is great interest in breakdown theories that can teach something about the formation and growth of the branched channel system described as an electrical tree to distinguish it from water and chemical trees. Appropriate theories should preferably incorporate the proven facts of the thermal and electromechanical models. It seems certain that the uncovering of the mechanism of debrisless drilling of very fine round tree channels must concern itself on a sophisticated level with the atomic structure of the dielectric material. Budenstein's gas channel breakdown model [2.49] appears to be the first attempt that comes to grips with this problem.

His new concept is reminiscent of vapor bubble breakdown in liquids, which is also a gas channel breakdown process. But there the similarity ends. A convenient starting point of the gas channel model of breakdown in solids is the recognition that each and every breakdown involves the vaporization of solid matter in one or more small holes penetrating the insulation. Ordinarily it would be assumed that this vaporization is the consequence of electrical breakdown. However, Budenstein maintains it is the cause of breakdown conduction. In other words, the insulation is punctured and the channel filled with a hot gas before the breakdown current begins to flow. Supporting evidence for this view comes from the discovery by Cooper and Elliott [2.70] of light being emitted from a channel in potassium bromide approximately 20 nsec prior to voltage collapse. The implication is that had the voltage been removed in the 20-nsec interval it would have been found that the channel had been formed without a spark having passed through it.

This reversal of cause and effect appears to resolve one of the most puzzling experimental facts first noticed when dielectric materials began to be irradiated with electron beams in the 1950s. A transparent plastic disc may be charged negatively by the incident electrons and hold this charge for a long time. Tapping it later with a grounded piece of metal removes the excess electrons and, in the process, creates a fully developed branched system of discharge channels, or a tree. Even though this treeing is clearly associated with electron transport through the dielectric material, as was the initial planting of the charges, it is not caused by the collapse of voltage and sparking between a pair of electrodes.

The model proposed by Budenstein divides the breakdown mechanism into five stages:

1. Creation of a critical electron charge density in a region of the dielectric material.
2. Chemical bond disruption in the dielectric molecules caused by the critical electron charge density.
3. Chemical chain reaction between the unbonded atoms, which liberates considerable quantities of energy.
4. Completion of the gaseous channel bridging the electrodes by pressure cracking of the dielectric material.
5. Hot plasma conduction and voltage collapse.

The electron charge density for step 1 may be set up directly by electron beam irradiation or laser light excitation. In cable dielectrics, however, one or more of the following three sources of excess electrons are assumed to be present: field emission from the cathode, charge injection from an ionized gas cavity, or charge multiplication by electron avalanches. Although Budenstein did not comment on this point, it probably has to be assumed that alternating voltage will not remove the charge but may add to it in every cycle.

The next two steps in the chain of events leading to breakdown hypothesize some of the fastest known and essentially explosive chemical reactions. The drastically new idea in this theory is that energy stored in the material is actually used to destroy it and, in a way of speaking, the electric field is merely the catalyst that triggers the reaction. In the previous two models the energy that destroyed the dielectric was actually taken from the source that sustained the electric field.

As a feasible example of chemical bond disruption, Budenstein points out that the neutral hydrogen molecule H_2 will quite easily become a negative ion by electron attachment. The addition of yet another electron to the negative ion results in the unstable H_2^{2-} ion. This may disintegrate in one of the following ways:

$$\begin{aligned} H_2^{2-} &\rightarrow H + H + 2e \\ &\rightarrow H + H^- + e \\ &\rightarrow H^- + H^- \\ &\rightarrow H^+ + H^+ + 4e \end{aligned} \qquad \begin{aligned} H_2^{2-} &\rightarrow H_2 + 2e \\ &\rightarrow H_2^- + e \\ &\rightarrow H_2^+ + 3e \end{aligned}$$

The energetically most favorable reactions should dominate and it will be realized that this type of chemical bond disruption can actually increase the electron charge density that started the disruption.

After the breaking of chemical bonds by an excess of electrons, the liberated atoms are free to react with each other, releasing considerable amounts of heat to the dense gas in which the reactions take place. As an example of a chain reaction that would accomplish the necessary and rapid heat generation for excavating the gas channel, Budenstein cites the explosive combination of hydrogen and chlorine

$$\begin{aligned} H_2 + \text{light} &\rightarrow H + H \\ H + Cl_2 &\rightarrow HCl + Cl \\ Cl + H_2 &\rightarrow HCl + H \\ H + Cl &\rightarrow HCl + \text{light} \end{aligned}$$

In each step the reaction products must have the potential of causing further reactions to keep the fire burning. The chain reaction preceding breakdown must create a cavity filled with the gaseous reaction products, which, in spite of severe lateral heat loss, stay at a temperature of several thousand degrees so as to be a conducting plasma when the breakdown channel is completed.

As the size of the gas cavity increases, feeding on the chain reaction, high mechanical stresses will be induced in the vicinity of it due to the extremely high pressure in the reaction zone. Cracks should form exposing fresh surface area to which the chain reaction can spread. In this way the breakdown channel grows longer while being driven by the chain reaction rather than the electric field.

When the gas channel finally bridges both electrodes, breakdown conduction begins immediately because the trapped gas in the channel is already thermally ionized. Should cooling overwhelm the chain reaction or the crack propagation be stopped by some obstacle, the channel "drilling" operation is halted and the material suffered a partial breakdown leaving tree channels behind as evidence.

The gas channel breakdown model has no doubt arisen from an effort to bring the breakdown process more in line with the visual traces of the phenomenon. Much of the science has to be taken for granted. Budenstein himself has pointed out some of the unresolved questions. For example, how can excess charge in the form of low-energy electrons impart 4 to 6 eV of energy to the host molecules to break their chemical bonds? If it should turn out to be some resonance absorption of electrons into the structure of the molecules, as Budenstein speculates, why does the process not proceed continuously but depend on a critical charge density to trigger explosive dissociation? Should the rate of crack propagation not be controlled by the velocity of sound and is this not too slow to explain the very brief interval between prebreakdown light emission and voltage collapse? Can cracking plus chain reaction fabricate channels of circular cross section?

As the gas channel mechanism is based on the rupture of chemical bonds, it is consistent with the fact that the breakdown strength of a material should decrease as the bulk temperature approaches the melting point. Transverse tension in the material should help crack propagation and in this way lower the breakdown strength. Compression would have the opposite effect, which is in agreement with experiment. The gas channel model appears to have no good answers to the important technological queries of why the breakdown stress is reduced by ac voltage and insulation thickness.

Intrinsic Breakdown

The literature on dielectrics contains many references to the "intrinsic electric strength" of insulating materials. It is not possible to give a precise definition of this parameter. What is meant by it in practice is the maximum breakdown strength measured on thin films. The word "intrinsic" suggests that electric strength is a material property like density or specific heat. If it does exist at all, it should not be affected by the dimension of the dielectric object, the nature of the electrodes, nor the rate of change of the electric field. But it is precisely these extrinsic circumstances that appear to determine the breakdown strength of high-voltage cable insulation. The thin-film electric strength is unattainable in high-voltage cables and therefore only of academic interest.

An intrinsic breakdown theory would have to concern itself with the interaction of the electric field with a very small region of the dielectric material away from the electrodes. It would have to show how this interaction gives rise to instabilities that can destroy the chemical bonds and the crystal lattice. For the process to be intrinsic, it should be capable of sustaining itself without assistance from neighboring material regions. Therefore, in a uniform field, the destruction would have to take place simultaneously in all regions, leaving little scope for a sequence of events that would explain the formation of breakdown channels and puncturing. Intrinsic mechanisms also rule out avalanche ionization, which depends on the size of the dielectric sample. In a recent review of breakdown theories, O'Dwyer [2.47] felt compelled to abandon the term intrinsic breakdown in favor of "purely electrical breakdown."

A purely electrical mechanism concerns itself with electrons and holes operating above the valency band and in the presence of virtually empty conductions bands of dielectric crystals under the quantum mechanical constraints of crystalline solids. There is much similarity with semiconductor theory. Electronic events in crystals produced by external electric fields are of fundamental importance. Studies of this subject have not yet influenced the development of insulation materials. For a comprehensive treatment of this topic the reader is referred to O'Dwyers book [2.47].

Treeing in Polymers

Kitchen and Pratt [2.71] described the prebreakdown process in polyethylene by "treeing" because of the branched structure and the single stem of communicating fine channels that were left behind as evidence of a partial discharge of the dielectric. Discharge trees have been observed in virtually all solid insulating materials, including glass and porcelain, but they are difficult to find unless the insulation is transparent. They have the appearance of three-dimensional Lichtenberg figures, and it is therefore tempting to think of them as having been created by electron avalanches and streamers.

The tree channels are approximately circular and typically 5 to 20 μm in diam. Eichhorn [2.73] has photographed tree channel cross sections with a scanning electron microscope and found them to have rough walls to which molecular debris adheres as shown in Fig. 2.39. Several investigators have observed the growth of trees under an optical microscope. They found it to proceed in distinct steps, one or more branches being added at a time. The growth process could be speeded up or slowed down by raising or lowering the applied voltage. At sufficiently high voltage a tree can be grown in a microsecond, whereas it may take years to develop under low dc stress. The Kitchen and Pratt hypothesis [2.71] that every breakdown in polymers is preceeded by tree formation is now widely accepted. No absolute proof of

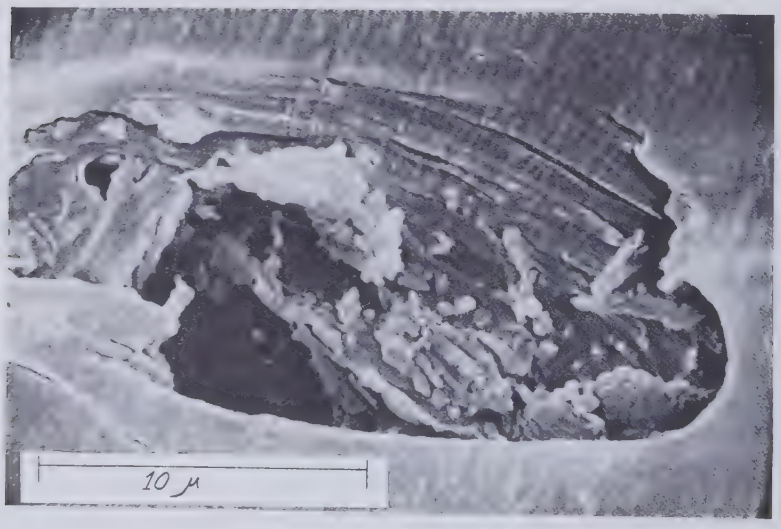

Figure 2.39 Section through tree channel photographed by Eichhorn [2.73] with scanning electron microscope. (By permission of the National Academy of Sciences, Washington, D.C.).

this fact appears to have been provided but much convincing evidence is available in the form of tree branches emanating from the much larger breakdown channels.

A tree developing at constant voltage in uniform or divergent fields does not inevitably lead to breakdown during the lifespan of a cable. This is true even if the tree grows from the low field region at the insulation shield into the stronger field near the conductor. Breakdown is likely to occur when a tree completely bridges the interelectrode gap but it need not take place the instant the tunnel has been finished. At times the leading branches of two trees growing from opposite electrodes have been observed to pass each other quite closely before breakdown took place.

Dielectric material excavated during the tunnelling operation is somehow converted to gas, which diffuses to the root of the tree or from the branches directly into the insulation. The gassification and the breaking of molecular bonds that this implies could possibly be explained by Budenstein's gas channel breakdown mechanism [2.49]. Although free carbon has been detected on the walls of tree channels, they are usually not blackened like the much wider breakdown channels. Most trees are grey in appearance; few have color with blue, green, brown, and yellow tints prevailing. Sletbak and Botne [2.74] analyzed colored deposits on tree channel walls with an electron microprobe and found them to contain sulfur, iron, and copper. Colorless trees also contained foreign elements, among them sodium, potassium, calcium, and chlorine. From these experimental findings it may be deduced that conducting and semiconducting matter is drawn into the tree from the root. If water is present at the root this will also be pumped into the tree by electrostatic forces and it is likely to bring with it dissolved salts. Trees of this kind have become known as "water trees" [2.75]. Wet and dry trees containing elements that do not belong to the dielectric material are also described as "chemical trees" [2.76]. Sulfur trees have received particular attention. They were found in cables containing copper conductors and were installed in locations where hydrogen sulfide gas was present and diffused through the polymer to the copper conductors. Corrosion products may then initiate treeing over an extended area and copper sulfide migrates into the tree channels.

Conflicting reports exist on the effect that water immersion has on tree growth in polyethylene-insulated cables. Experience gathered in Japan suggests that the wet environment reduces cable life, whereas polyethylene insulated underwater cables in the U.S. have been at least as reliable as underground cables [2.77, 2.78]. In experiments with needle electrodes embedded in the insulation, Eichhorn [2.73] actually found that immersion of thermoplastic polyethylene (PE) and cross-linked polyethylene (XLPE) samples in water made it more difficult to produce trees and delayed

breakdown. The American underwater cables were insulated with "voltage-stabilized" thermoplastic polyethylene and this material is believed to be more resistant to water treeing than other grades of polyethylene.

It is a remarkable fact that all trees have their origin or root at a free surface of the insulation or at an interface between the insulation and electrodes or foreign particles. This proves that tree initiation is not only determined by electrical stress but has something to do with the property of surfaces. The convenient practice of studying tree growth from the point of a needle molded into the polymer specimen has highlighted the importance of local field enhancement at conductor surface projections. It is undoubtedly a factor contributing to the site selection for the tree root. Less voltage is required to grow a tree from a needle point when the tip is positive rather than negative.

Just as the dielectric strength of a material is greatest when exposed to dc and lowest when placed in an ac field, so the tree starting voltage is much higher for dc than for ac. Impulse voltage tree initiation lies between dc and ac values.

Applied electric stress cannot be the only factor governing tree growth because the tree channels do not follow the field lines of flux. The way branches grow simultaneously at different distances from the opposite electrode and in directions that can be almost perpendicular to the applied field is perhaps the most puzzling aspect of treeing in polymers. Figure 2.40 is an attempt to classify the appearance of trees. The most photographed trees are those grown deliberately from the tip of needles. They resemble the shape of natural trees. Other trees have the appearance of a bush with many branches going directly back to the root. Bush trees are often observed when water is present at the root. Bow-tie trees grow in the middle of the dielectric wall from cavities and foreign particles. Bahder and Katz [2.79] have

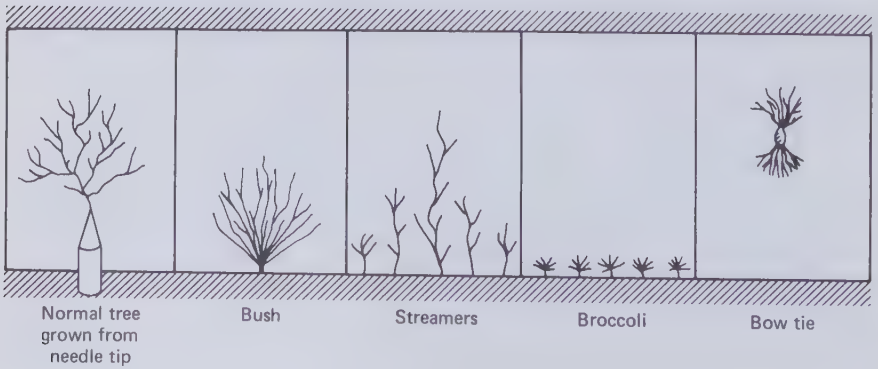

Figure 2.40 Classification of trees in polymers.

described streamer and broccoli trees which were found in cables removed from service. The significant feature of the last two groups is the large number of roots per unit electrode area, which suggests that they are caused by area contamination rather than stress raising asperities. The similarity of the geometry of gas discharges (Lichtenberg figures) and polymer trees is striking. A noteworthy aspect of all these discharges is that, in spite of the irregular paths of discharge channels, the branches never cross each other and are all connected to a common root.

The early development of polyethylene insulated cables revealed that the tree inception voltage could be increased by mixing staining rather than nonstaining antioxidant into the insulation compound [2.80]. The results plotted in Fig. 2.41 show this effect for varying amounts of DPPD (*NN*-diphenyl-*P*-phenolyne-diamine) antioxidant. The half-life refers to the time after which half the number of samples tested under identical conditions showed tree growth. This finding set in motion extensive research on polyethylene additives. The additives have become known as voltage stabilizers or tree inhibitors and the intension is to disperse them uniformly through the insulation. Although voltage stabilizers are not able to eliminate tree initiation, they retard tree growth sufficiently to have a significant influence on insulation life in the presence of some inevitable defects. The performance of a large number of voltage stabilizing additives has been discussed by Ashcraft et al. [2.81]. Their work also revealed that polysulfone has the highest tree initiation resistance; chemically cross-linked polyethylene is almost as good as commercially available voltage stabilized thermoplastic polyethylene, and polypropylene rubber has very low treeing resistance. The decomposition products of dicumyl peroxide, which is being

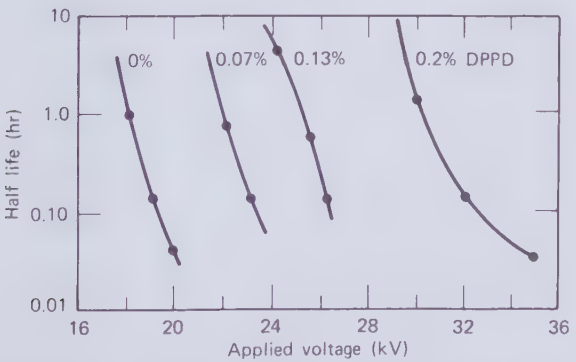

Figure 2.41 Voltage life curves of needle test polyethylene samples containing varying amounts of DPPD staining anti-oxidant according to Kitchin and Pratt [2.80]. (By permission of the Institute of Electrical and Electronics Engineers).

employed for chemical cross-linking, have been found to be excellent voltage stabilizers but they slowly diffuse out of the insulation and thereby lower the treeing resistance. Fillers also increase the treeing resistance of polyethylene [2.82] and so does dispersed water vapor [2.81].

Since trees in polymers are precursors of complete insulation failure we must expect all previously discussed breakdown mechanisms to play a role in their formation. By the same token it would be unrealistic to expect us to understand treeing any better than the breakdown of solid dielectrics. When they were first discovered it was thought that trees were the result of erosion by discharges in cavities and the tree channels themselves. Sputtering of dielectric material under the impact of impinging positive ions should make the channels straight and parallel to the applied electric field. As this is not so, the sputtering explanation has to be abandoned. Cooper and Auckland [2.83] have gone one step further and actually showed by experiment that the first luminous event of the discharge takes place in the solid material rather than in the gas channel.

Today the most widely accepted starting assumption is that treeing is caused by space charge trapped in the insulation. Direct evidence of treeing by negative space charge comes from polymer specimen that were irradiated with electron beams. Materials of high insulation resistance will retain the trapped electrons for days. Within this period a tree may be grown by deliberately discharging the excess electrons to ground through a metal contact and with the help of a small mechanical shock, like the tap of a hammer. No tree will form if the negative charge is allowed to leak away slowly. The same type of experiment may be performed with a needle embedded in a polymer sample. If the needle is negative with respect to a contact plate electrode which faces the needle point, electrons will be field-emitted from the needle and trapped in the dielectric. After the supply of a sufficient charge to the dielectric a tree may be produced by simply short circuiting the electrodes [2.84]. "Short circuit trees" can be created with even lower charging voltage when the needle is positive with respect to the plate. This latter result suggests that both positive and negative space charges are involved in the initiation and growth of trees. Positive space charge would be the result of extracting electrons from the insulation and leaving behind a collection of trapped positive holes.

The needle point emits the space charge and also becomes the site where the charge is again removed from the insulation after the damage is done. Whether this is true for all trees formed in cable insulation is still a subject for speculation. It is likely to depend on how far the space charge can migrate through the dielectric and the relative mobility of electrons and holes.

In the normal growth of polymer trees, new branches are added only around the periphery of a tree. This suggests that every new branch

generates its own space charge and that much of it is drained from the insulation when the next branch is formed. Electron transport along the tree channels during the build-up of space charge must be made possible by gas discharges or water or conducting impurities in the channels. The development of bushy trees with many branches radiating from a common root indicates a dearth of conduction mechanisms to the tips of the branches. Almost all bow-tie trees from voids and foreign particles in the body of the insulation are of this nature.

There is little doubt that the trapped space charge strains molecular bonds and cross-links within its sphere of influence over and above the strain they have to withstand on account of the externally applied field. Young's modulus is a measure of bond strength and stiffness. Rupture will be made easier by any weaknesses in molecular bonding. The excavation of tree channels that necessarily depends on bond rupture may therefore be expected to be influenced by all the factors that were discussed in connection with electromechanical breakdown of solid dielectrics.

The modulus of elasticity declines with increasing temperature and therefore tree initiation and growth should be aided by heating the insulation. This was already confirmed by the experiments of Kitchen and Pratt [2.80]. Increasing temperature not only lowers the tree inception voltage, but it also speeds up tree growth and therefore has an impact on all stages of tree development.

A free surface brings disorder and imbalance to the molecular array. Free surfaces may be torn apart by electromechanical shear forces. This view is strongly supported by the favorable experience with semiconducting shields that are firmly bonded to the insulation. In the early polyethylene insulated cables these shields consisted of unbonded tapes. As Vahlstrom's [2.72] investigation proved, cables with tape shields have been very prone to treeing. The problem was overcome by coextruding semiconducting polyethylene layers with the insulation, which strengthened the insulation surface. At one time it was thought that air trapped between shields and insulation was the major factor in initiating tree growth from tape shields.

A further reason that favors trees to take root at interfaces with conductors is the need to transport charge to the tip of tree branches. Once a channel is of a certain length this can probably be accomplished by the gas discharge mechanism, but in the nascent stage the tree may have to draw electrons or ions directly from a conductor.

That the prevailing strength of molecular bonds influences tree growth is also proved by the preferred paths tree branches take in a single crystal. Polyethylene insulation is partially crystallized, and it has for some time been suspected that the morphology of the material might influence treeing. Direct proof of this fact was provided by Wagner [2.85]. Figure 2.42 shows one of his photographs of a cross section through a discharge channel

wedged between spherulites in high-density polyethylene. As Fig. 2.42 indicates, spherulites are regularly grouped polymer crystals around a center. They grow out of the amorphous phase of the material and usually trap some amorphous material between their boundaries. The amorphous phase in its disordered state is mechanically weaker than the crystalline phase and apparently discharges seek out the mechanical weaknesses of the material. Another photograph in [2.85] shows a whole tree to have been grown in an amorphous region of polypropylene. In this photograph tree growth was arrested at the boundary with crystalline material. Extruded polyethylene exhibits molecular orientation in the direction of polymer flow. This produces mechanical weakness in the cross-bonding between oriented molecular chains. Preferred tree growth in the extrusion direction [2.71] provided an early clue to the electromechanical breakdown model.

On the basis of erosion by gas discharges it was expected that tree growth could be accelerated by oscillating the applied voltage and stepping up the energizing frequency. The rapid development of trees at power frequencies compared to slow growth with dc exitation well-confirmed this line of thought. A recent series of measurements by Noto and Yoshimara [2.86] revealed that the time lag between voltage application and tree initiation could in a certain experiment be reduced from 100 sec at 50 Hz to 0.2 sec at

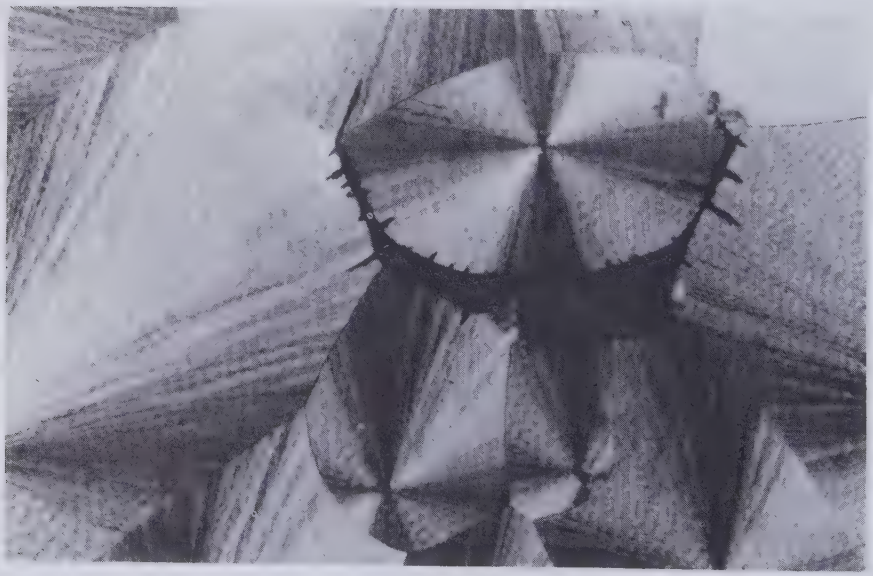

Figure 2.42 Microtome cut through tree channel between spherulites in high-density polyethylene [2.85]. (By permission of the National Academy of Sciences, Washington, D.C.; photograph: AEG-Telefunken).

10,000 Hz. This result was obtained with needles firmly pushed into polyethylene. If the needle was partially withdrawn so as to grow the tree deliberately from an air-filled cavity the corresponding time lags for tree initiation were 60 sec at 50 Hz and 0.3 sec at 10.000 Hz. The gas discharge clearly helped tree initiation, but it was not found to be essential for tree formation. A more plausible explanation for the time lag reduction at high frequency appears to be fatigue cracking of molecular bonds at the interface with the needle point. Fatigue failure would also explain the large difference in the treeing resistance of polymers to ac and dc.

In fact a single mechanical stress reversal, as in the production of short circuit trees, can set off the bond-breaking chain reaction. Of course a single jerk is not as effective as the continuous oscillation in an ac field. Therefore impulse voltages lower the tree inception stress less than ac voltages.

Extensive research on polymer treeing in the decade of the 1970s has given no indication of a connection between treeing and thermal instability of the dielectric. The conclusion drawn from Fig. 2.29 that dielectric heating in polyethylene is insufficient to cause thermal runaway holds as well for treeing as it does for breakdown. The major remaining uncertainty in polymer breakdown are the events that lead from the existence of the space charge to the excavation of tree channels. As in the progress of gas discharge streamers, it is obviously a discharge from the healthy insulation to the damaged parts. Budenstein's gas channel mechanism is the first ray of light in this obscure area.

An understanding of how voltage stabilizing additives to polymers inhibit and retard tree growth is of considerable practical importance to the further development of polyethylene insulated high-voltage cables. With our present knowledge we have to assume that tree growth and breakdown are the result of space charge in the insulation and the mechanical rupture of molecular bonds. The benefits from voltage stabilizing additives could flow from a tendency to limit the space charge or the strengthening of molecular bonds or both. Most researchers tend to believe that stabilizers reduce or disperse the space charge or render it harmless in some other way. The possibility of bond strengthening cannot be entirely overlooked because of the great change in the mechanical properties of metals, which can be brought about by the fine dispersion of small amounts of other materials through the host lattice.

2.6 BREAKDOWN OF VACUUM INSULATION

The first application of vacuum in the power transmission field was to circuit interrupters. Since then vacuum insulated fuses have become available and vacuum lightning arresters are a good prospect for the future. In all

these examples the vacuum insulation properties are incidental to the unique advantage of vacuum with regard to spontaneous arc extinction. High-voltage vacuum insulations in its own right could become an important facet of cryocables. It is the only electrical insulation that at the same time is also good thermal insulation and this simplifies the design of cryogenically cooled transmission lines.

Vacuum breakdown is actually low-pressure gas breakdown. The gas involved is mainly metal vapor from the conductors. Vacuum insulated transmission lines would operate at a pressure of 10^{-6} torr or lower. The mean free path between residual gas molecules at these low pressures is at least 50 m, whereas the distance between the conductors of the cryocable of Fig. 1.42 is only 8 cm. Ionizing collisions between electrons and residual gas molecules are therefore not a significant factor.

Cranberg's Clump Hypothesis

Research on vacuum breakdown has delved primarily into the prebreakdown processes, which have to create sufficient local gas or vapor pressure for collision ionization to take over and develop into plasma conduction. One of the simplest mechanisms proposed for vapor generation is Cranberg's clump hypothesis [2.87]. This assumes that a charged particle, originally in contact with one of the electrodes, becomes detached by electrostatic forces and in transit across the gap gathers sufficient kinetic energy to evaporate some metal of the electrode on which it impinges. Cranberg's hypothesis gained credibility from the following quantitative consideration. Let the energy per unit area delivered to the target electrode be C. This will be equal to the potential difference V through which the particle has fallen multiplied by the charge density on the projectile. If the particle lost or gained no charge during the flight, its charge density must be proportional to the electric field E at the originating electrode, so that

$$C = kVE \tag{2.115}$$

where k is a constant. For a uniform field gap of length d between plane parallel electrodes

$$E = \frac{V}{d} \tag{2.116}$$

If C' is the critical impact energy density at which sufficient vapor is produced for breakdown, the corresponding value of the voltage becomes the

breakdown voltage V_b, or

$$V_b = \left[\frac{C'd}{k} \right]^{1/2} \tag{2.117}$$

Hence the breakdown voltage in a uniform field gap should be proportional to the square root of gap length. Cranberg found this prediction to be in reasonable agreement with the experimental results available in 1950.

The clump mechanism is reminiscent of gas breakdown by free conducting particles. There are however these differences to be considered. In the vacuum gap the particle moves unimpeded by gas drag, and it will not be surrounded by ionized gas. Menon and Srivastava [2.88] pointed out that particles would have to be at least 10 μm in size before they could cause breakdown, rather than merely initiate a self-extinguishing discharge. They built an apparatus to search for particles of this size and larger, just prior to vacuum breakdown, and found none.

By now the clump hypothesis has been largely discarded because it cannot explain the precision of vacuum breakdown in a well-conditioned system in which the scatter of breakdown voltages in many repeated shots from low-energy sources is usually less than a few percent. It does not seem possible that a loose particle of the correct size would be available time and again in say 100 successive breakdowns. Nevertheless there is every reason to believe that microparticles cause ionizing events in vacuum [2.89, 2.90] that are disturbances of the underlying vapor generation process.

High-Voltage Conditioning

Just as tree growth in polymers is leading to a fuller understanding of the breakdown of solids, so partial discharges in vacuum must hold the key to vacuum breakdown. When the voltage across a vacuum gap is gradually increased, the first prebreakdown phenomenon observed is the onset of field emission. Initially the emission current is very erratic and changes discontinuously up and down. Finally the current may die out or settle down to a steady small value. The steady field emission current can be reduced by lowering the voltage and it normally obeys the trend of the Fowler-Nordheim equation (2.42). Electrons impinging on the anode will generate a small X-ray flux. The detection of X rays therefore proves that the current is being carried by electrons rather than positive ions.

When the emission current has settled down to a small value, an increase of a few percent in voltage will drive it back up to a high level and the erratic behavior. After some time the current will again die down and the process may be repeated once more. Stepping up the voltage between the

electrodes in this manner is known as high-voltage conditioning of vacuum insulation. It has to be terminated when the current crossing the gap remains permanently at some elevated level.

The discontinuous current changes are usually accompanied by luminous and sometimes faintly audible discharges at points on the electrode surfaces. These events have also been described by the term "microdischarges." The conditioning process is usually terminated when the frequency of microdischarges remains uncomfortably high, say one per minute, and shows no sign of abating.

It is natural to speculate that the variability of the field emission current during conditioning is due to the removal of old and the creation of new field emission sites in the form of sharp surface protrusions. Heating by Joule loss and the Nottingham effect can account for the melting and evaporation of small asperities and the extrusion of new ones with the aid of electrostatic forces. The first major study of this subject was carried out by Alpert and his colleagues [2.91]. They convinced themselves that many field emission sites were involved and quoted 1 to $10/cm^2$ of clean tungsten surfaces. In their opinion the individual emission site had quite a short life and the whole system of field emitters therefore gives the impression of being in continuous motion. Alpert et al. were able to condition small tungsten electrodes that had been baked to 420°C in approximately 30 sec. This compares with 30 hours conditioning of the short cryocable loop described in [2.92], which was mildly baked at temperatures ranging from 100–200°C and had an active internal surface area of approximately 4 m^2.

An important aspect of conditioning is the liberation of adsorbed gases from the conductor surfaces. Much of the liberated gas is produced in bursts accompanying microdischarges. Figure 2.43 is a typical pressure record for a conditioning step of the cryocable loop. In this case conditioning was carried out with 60 Hz ac. It will be seen that at 112.5 kV (rms) the pressure was steady at less than 2×10^{-9} torr. When the voltage was raised by only 2.5 kV, the pressure shot up into the 10^{-6} torr range and returned to the 10^{-9} torr range within 1 min because the cable was connected to an ion pump. A number of smaller pressure bursts occurred in the next 30 mins. Within the hour, the pressure settled down again in the low 10^{-9} torr range but slightly above the level it had reached at 112.5 kV.

DC conditioning proceeds along similar lines. But when the polarity of the electrodes is reversed for the first time, the conditioning process has to be repeated from the beginning. These facts are consistent with the hypothesis that high-voltage conditioning of vacuum insulation is removal of gas from the conductor surfaces. Further confirmation of this hypothesis can easily be obtained by admitting air to a conditioned conductor pair and then pump it out again. It will be found that the exposure to air deconditions the

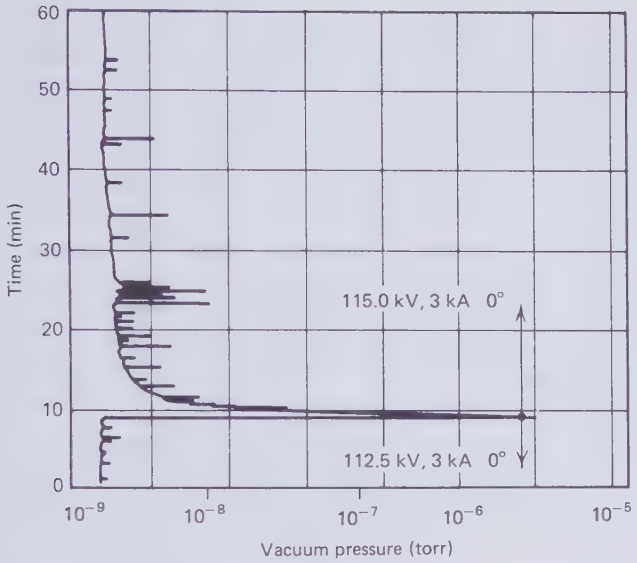

Figure 2.43 Pressure response to conditioning step [2.92]. (By permission of the Institute of Electrical and Electronics Engineers).

conductors. When a previously conditioned hollow conductor is suddenly filled with liquid nitrogen the pressure in the vacuum gap will drop due to condensation of some of the residual gas on the cold surface, and this also causes deconditioning.

Experiments in the author's laboratory have established that it is the anode that is being cleaned during dc conditioning. It may be explained by the desorption of gases by electron bombardment from the cathode [2.93]. For this mechanism to be effective field emission has to be spread fairly uniformly over the cathode area in accordance with the findings of Alpert et al. [2.91]. Differences between ac and dc conditioning teach us another fact. With ac the emission current dies out at the same relative rate as the gas evolution. However, with dc the current decreases much more slowly than the pressure. Yet when the dc polarity is reversed, so that a conditioned anode becomes the new cathode, a large drop in emission current can be observed. From these findings it may be deduced that adsorbed gas on the cathode contributes to field emission. That sorption processes on the cathode influence field emission has also been established by Juettner et al. [2.94].

The detrimental effect of hydrocarbon deposits on conductors has been known for many years and it led investigators to abandon oil diffusion pumps in high-voltage vacuum experiments. In the development of cryocables [2.95] it was discovered that water vapor backstreaming through a

turbomolecular pump froze on the cold conductor and thereby degraded the insulation. Cross and Chatterton [2.96] independently found that a layer of condensed water molecules on the electrode surfaces dramatically lowers the breakdown voltage. To avoid the contamination of electrodes by vapors that are backstreaming from vacuum pumps it is now almost universal practice to employ ion pumps, without which vacuum insulated cables could not be contemplated.

High-voltage conditioning is also observed when the conductors are coated with a dielectric material. Anodized aluminum conductors have received special attention [2.24]. The aluminum oxide layer does not prevent field emission but the conditioning process is very much slower than with nominally bare aluminum conductors.

The vacuum breakdown process that emerges from research on cryocables may be described as follows. Gas or vapor adhering to insulator and conductor surfaces is the primary cause of the initiation of sudden partial discharges. The individual discharge creates its own atmosphere in the vacuum gap permitting ion multiplication by collisions between electrons and vapor molecules. The further escalation of the discharge depends on the balance between vapor molecules lifted into the gap and those lost to the vacuum background. The easy diffusion of space charge is a unique property of vacuum insulation. If the surfaces in the vicinity of the discharge do not supply sufficient vapor molecules to make up the loss, the discharge becomes self-extinguishing. On the other hand, if ample gas is available on the surfaces the discharge continues to escalate until it produces enough heat to evaporate conductor metal and thereby initiate a self-sustaining metal vapor arc. This constitutes breakdown. In any given setup the conditioning process can only be driven to the point where electrical stresses at some location are high enough to immediately generate and maintain a metal vapor atmosphere.

Ion Exchange Mechanism

According to the gas laws the average thermal velocity of a molecule is given by

$$v_a = 14{,}551\sqrt{\frac{T}{M}} \quad \text{cm/sec} \tag{2.118}$$

where T is the absolute temperature in degrees Kelvin and M is the molecular weight. Therefore a nitrogen molecule (N_2) of $M = 28.02$ at the temperature of liquid nitrogen (77°K) travels at an average velocity of 24,121 cm/sec. At 25°C the average velocity would be 47,453 cm/sec.

Hence gas evolved from the conductor surfaces escapes quickly, not permitting the slow build-up of an atmosphere. Only some explosive event, as for example the collision of a clump of matter with a conductor or the sudden disintegration of a field emitter protrusion, is capable of creating the atmosphere. Although both types of explosion may occur from time to time, the experimental facts of high-voltage conditioning point to the involvement of adsorbed gas.

A third mechanism of rapidly generating a discharge atmosphere from the conductor surfaces was first proposed by van de Graaf [2.97, 2.98]. It assumes that one electron striking the anode will on the average produce A positive ions and C photons (X or γ radiation). The positive ions are accelerated to the cathode and one of them is assumed to produce B secondary electrons. Furthermore each photon released at the anode is taken to produce D new electrons at the cathode. Therefore the total yield of one starting electron, which will be absorbed by the anode, is the release of $AB+CD$ new electrons at the cathode. This ion exchange becomes a runaway chain reaction when

$$AB+CD>1 \tag{2.119}$$

This inequality is van de Graaf's vacuum breakdown criterion. He and Trump measured the various exchange coefficients for one particular electrode setup [2.98] and thereby showed that this simple theory can predict a breakdown instability. However it has not enjoyed much quantitative success in the intervening period. As far as vacuum insulation in high-voltage cables is concerned any ion exchange mechanism must be supplemented by the release of neutral gas molecules at the anode and possibly also at the cathode.

An order of magnitude estimate of the quantity of liberated gas may be made for the 2×10^{-6} torr pressure pulse of Fig. 2.43. This was measured by the ion pump located a number of feet away from the discharge. The volume V_1 of the vacuum vessel was 220 liter. Many of the liberated gas molecules will have been quickly condensed again on the liquid-nitrogen-cooled conductor without contributing to the measured pressure pulse. Let us assume, therefore, that without readsorption the pressure would have risen to 10^{-5} torr $=p_1$. The quantity of gas defined by the product V_1p_1 must have originally been concentrated in the discharge volume V_2 at a pressure p_2. To obtain some idea of the discharge volume let it be assumed that the discharge lasted for 50 μsec, which represents a short microdischarge. If the neutral molecules moved with an average thermal velocity of 30,000 cm/sec, at a temperature intermediate between that of the cold conductor and the warm enclosure, the lateral radius of diffusion would

have been approximately 1.5 cm. The gap length was 5.5 cm. A cylindrical column of that length and 1.5 cm radius has a volume of 39 cm^3. If we take this to be equal to the discharge volume, the discharge pressure may be calculated from

$$p_2 = \left(\frac{V_1}{V_2}\right) p_1 \tag{2.120}$$

In this order of magnitude estimate it is found to be 0.056 torr giving a Paschen product pd of 0.31. The Paschen breakdown minimum for air is 0.4 kV at $pd = 0.5$. Therefore, normal gas breakdown due to surface gas evolution appears to be a distinct possibility.

Singh and Chatterton [2.99] were the first to address themselves to the evaluation of gas evolution concurrent with ion exchange. The problem is very complex because of the gradual exhaustion of the gas deposit and the random direction in which sputtered and thermally emitted neutrals move into the gap. In this first attempt the effect of electrons and photons was ignored and it was assumed that A negative ions are released at the cathode per incident positive ion, and B positive ions are released at the anode per incident negative ion. With no analytical method being available to handle this problem, a numerical computer technique was used to simulate a large number of ion transits and the circular electrode area was resolved into finite ring elements.

Disregarding the thermal velocity, the transit time t of a singly charged ion is

$$t = x\left(\frac{2m}{eV}\right)^{1/2}$$

where x is the gap length, m the mass of the ion, V the voltage between the electrodes, and e the charge of an electron. The nitrogen molecule has a mass of 4.6×10^{-23} g. In a 100 kV gap of 5 cm length it can cross over from one electrode to the other in 1.2×10^{-12} sec. A large number of transits can therefore be accomplished during a discharge lasting for a number of microseconds. The results obtained by Singh and Chatterton for a confined electrode area initially holding a certain surface gas concentration at ambient temperature and with some assumptions as to the exchange coefficient product AB give microdischarge pulses between 1 and 10 ampere lasting from 1 to 50 μsec and being accompanied by pressure bursts up into the 10^{-3} to 10^{-1} torr range. These figures appear reasonable and are certainly in coarse agreement with the cryocable conditioning experience.

An ion-exchange mechanism that embraces gas desorption seems to hold out the greatest promise of explaining how the breakdown atmosphere between cable conductors is established. It will have to deal with electron desorption of the anode and possibly also photon effects.

Insulator Flashover

Breakdown experiments on plain vacuum gaps are only made possible by placing the support insulator of the high-potential electrode into a region of low electric field behind the breakdown gap. This is impractical in a cable because it would require an enlarged vacuum enclosure pipe at the insulator positions. Economic considerations make it mandatory to place support insulators of vacuum-insulated conductors into strong electric fields. Unless special precautions are taken, the flashover strength of an insulator in vacuum will be much smaller than the breakdown strength of the gap that the insulator bridges.

It is generally believed that only one layer of chemically bound gas molecules can reside on a thoroughly cleaned metal surface [2.100]. This is known as the monolayer. Dielectric materials, however, have the potential of tightly binding a greater quantity of surface gas, probably due to polar interactions. Dushman and Lafferty [2.101] in their review of this subject mention layers of water vapor on glass that were three to four monolayers thick with a monolayer density of 2×10^{-5} cm^3 (STP)/cm^2. The gas held by one square centimeter of dielectric surface could therefore raise the pressure in one cubic centimeter of the vacuum space from 0 to 6×10^{-3} torr.

If an electric field of sufficient intensity exists parallel to the gas layer, then discharges will occur in this layer much in the same way as in a more extensive volume of gas of the same species and density. Electron avalanche and streamer breakdown of high-pressure gas is characterized by filamentary discharge channels. Low-pressure gas breakdown, by comparison, has a diffuse appearance resembling a glow discharge. The gas density in the adsorbed layer is almost that of a liquid. Therefore breakdown channels within this layer and running parallel to the solid dielectric surface must necessarily be narrow filaments. Furthermore, for the insulator flashover to be entirely due to a gas discharge, the filamentary channels must follow the insulator profile even if this be convoluted.

Figure 2.44(a) shows a conductor support insulator, or spacer, which was used in an experimental length of coaxial cryocable. The adjacent photograph, Fig. 2.44(b), depicts a series of successive discharges across the spacer as they appeared to the camera during high-voltage conditioning [2.102]. The filamentary nature of the discharges can be clearly discerned and they are seen to be clinging to the concave contour of the glass insulators. Hundreds of photographs of this kind left no doubt that insulator flashover in the vacuum insulated cable was triggered by gas discharges in the adsorbed layer on dielectric surfaces. Every one of these discharges was accompanied by gas evolution and an observable pressure pulse. Insulator surfaces in cable terminations of the vacuum insulated system were found to behave in the same way [2.103].

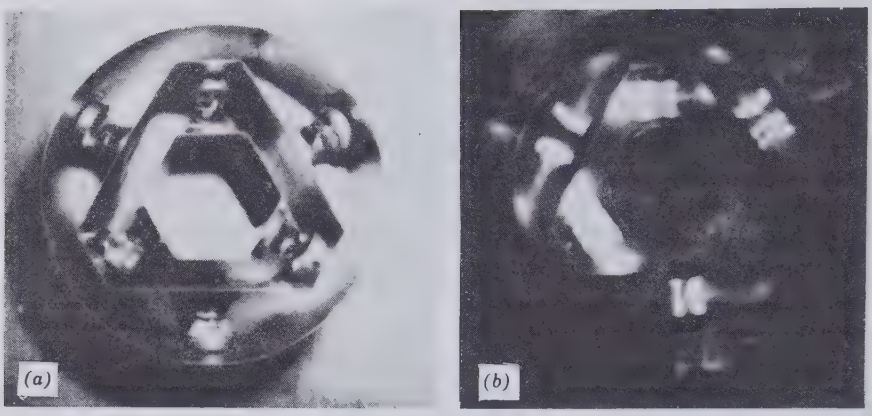

Figure 2.44 (a) Triangular spacer of glass insulators between metal shields. (b) Open shutter photograph of successive discharges across this cryocable spacer [2.102] (By permission of the American Institute of Physics).

Figure 2.44(b) also provides evidence that gas is streaming away from the discharge channels on the insulators. This gas has the potential of causing breakdown in the open vacuum gap. The purpose of the metallic ion shield is to place two vacuum gaps in series with each other in the immediate vicinity of the support insulators. This increases the ac flashover strength of insulators in vacuum [2.104] and makes them more resistant to conditioning discharges [2.105]. For complete breakdown two separate gas discharges have to occur, one on either side of the ion shield. Statistical time lags in the development of the discharges may combine to delay breakdown until the crest of a 60-Hz voltage wave has passed. As the breakdown level is normally established by slowly increasing the applied voltage, a situation is reached when during some cycles the time lag is short enough for breakdown, whereas during others it is too long. This was actually the case when the oscillogram of Fig. 2.45 was taken.

Insulator flashover occurred approximately 1 msec beyond one of the voltage peaks. At that instant the voltage fell sharply to the IR-drop across an external current limiting resistor. By the time the flashover took place the ac voltage had fallen 7 percent below the crest value. With double the time lag it would have decreased by 27 percent, making breakdown unlikely. At present it is not understood how statistical time lags of the order of milliseconds can arise. The formative time lag in normal gas discharges is measured in microseconds.

One mechanism that could possibly contribute to the time lag is the process of charging insulator surfaces in vacuum. The work of DeTourreil

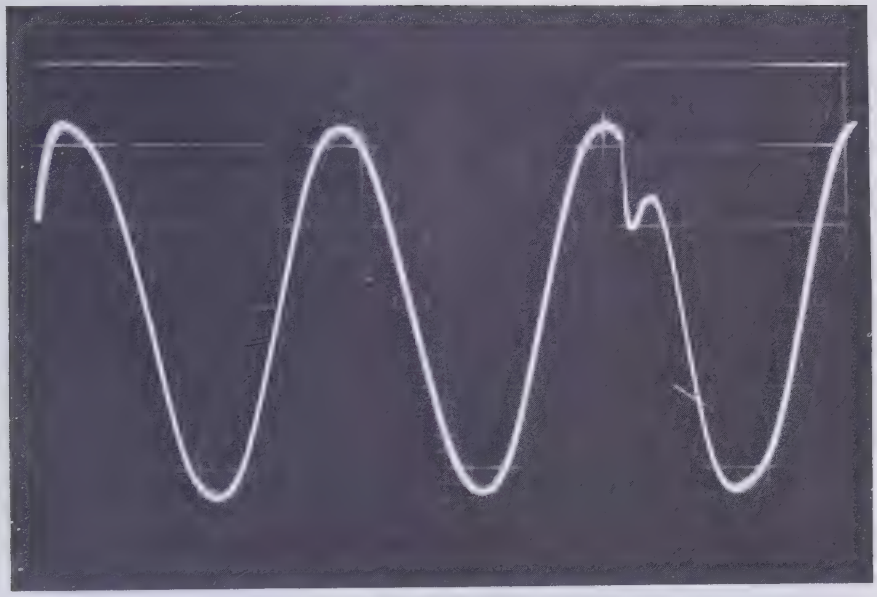

Figure 2.45 Oscillogram of ac insulator flashover. (By permission of the American Institute of Physics).

and Srivastava [2.106, 2.107] shows that dielectric surfaces acquire positive charge. This enhances the electric field strength at the cathode-insulator junction. The resulting stress concentration is likely to produce the necessary free electrons for starting a gas discharge. Surface charging time lags seem to be of the order of 1 μsec but the charge resides on the insulator surface for a long time and successive voltage cycles may add to it.

Shannon et al. [2.108] were the first to report the effect the insulator profile has on the flashover strength in vacuum. Since then the unsymmetric behavior of conical insulators has been discovered [2.107]. With the base of the cone in contact with the cathode the flashover voltage is significantly higher than the other way around. This effect has been observed when the insulator is subjected to short voltage pulses and almost disappears when dc is applied. The cone behavior can be explained if it is assumed that the surface charge is produced by electron bombardment from the cathode and secondary electron emission from the dielectric material. With the base of the conical insulator on the anode, electrons emitted from the cathode have better access to the insulator surface and this accounts for the difference in pulse voltage flashover strength. DC breakdown occurs at a substantially lower voltage and complete surface charging can take place with either polarity.

The insulator profile has also a decisive influence on the tangential electric field component, which drives electron avalanches along the gas layer on the insulator surface. Predominantly concave profiles have a higher ac flashover voltage than predominantly convex profiles. This again points to the importance of the insulator-charging mechanism by electron bombardment. Steps in the insulator profile appear to be more effective than smooth convolutions, presumably because the portions of the surface that run parallel to the electrodes hinder the progress of electron avalanches. All investigators found that right cylinders bridging the high-voltage gap between parallel electrodes have the lowest flashover strength. They also have to support the largest tangential stress parallel to the gas layer.

Of a number of various concave and convex insulator profiles tried in cryocable experiments, profile (a) of Fig. 2.46 has given the best result. It shields most of the insulator surface from direct electron impact. At the same time it has surface segments of low tangential stress. Insulator (b) has not yet been tested but might have an even higher ac flashover strength than (a) because of the additional low-tangential-stress surfaces. This advantage could conceivably be canceled by surface charging of the edge of the center disc.

The most important function of the ion shield is to prevent surface erosion of the insulator surfaces by heavy arc currents. It is energetically more favorable for a metal vapor arc to burn beyond the edge of the ion shield, and this protects the insulators against overheating. Conditioning steps may be made so small that only self-limiting microdischarges will occur and they do no harm to insulator surfaces. However the accidental development of a metal vapor arc when conditioning a long cable with a large stored energy cannot be ruled out. This problem has been investigated by discharging high-voltage capacitors across ion shielded insulators [2.109]. The experiments established that inorganic insulators (glass and ceramics) can survive the discharge of all the electrostatically stored energy in a 50-mile-long cable. In some experiments peak discharge currents of 50 kA were reached. How effective one ion shield is in protecting insulators from arc damage may be judges from the following observations:

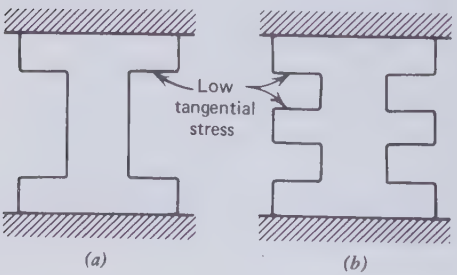

Figure 2.46 Insulator profiles for supporting ac conductors in vacuum.

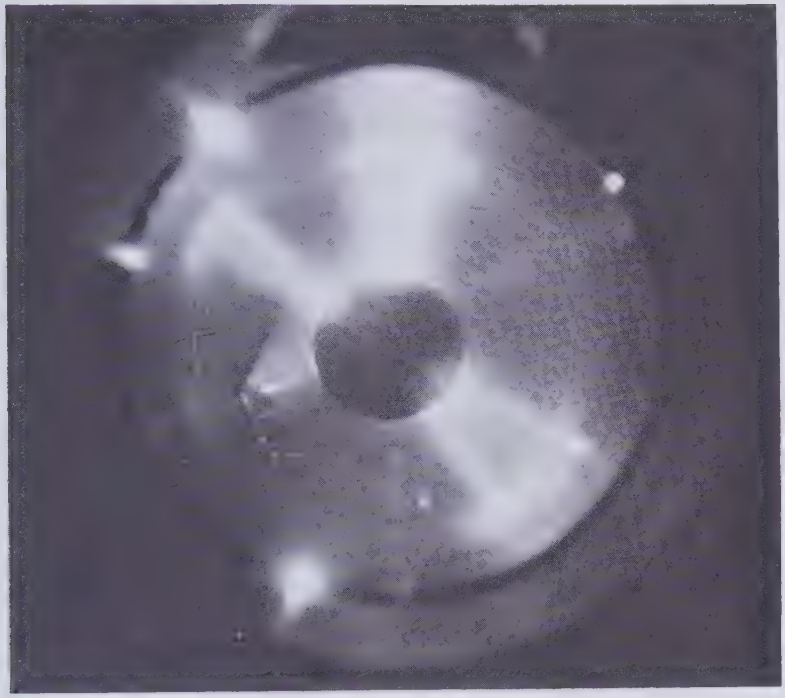

Figure 2.47 Open shutter photograph of capacitor discharge beams beyond reach of ion shield [2.102]. (By permission of the American Institute of Physics).

arc damage may be judges from the following observations:

1. Virtually all cathode spots photographed in over 300 capacitor discharges formed outside the 3-in. wide shadow band of the ion shield.
2. Permanent arc marking of the conductors was heaviest just outside the ion shield shadow and almost nonexistent on the inside of it and on the shield itself.
3. The heaviest current discharges gave rise to slightly conical beams of intense ionization just beyond the reach of the ion shield, as shown on the photograph of Fig. 2.47.

Metal Vapor Arc Between Conductor Surfaces

In every other insulation an electric arc is destructive and requires repair of the transmission line, but vacuum can tolerate a certain amount of arcing. The feasibility of vacuum insulated cables depends on this fact unless means

of high-voltage conditioning are found that positively prevent the development of metal vapor arcs. How much the conductor surfaces suffer from arcing depends on the arc current magnitude and duration as well as the conductor material.

It has been proposed that long vacuum circuits should be conditioned with low-energy dc sources and periodic reversals of polarity. Under these circumstances a conditioning arc might involve thousands of ampere but it could not be sustained for very long. The discharge of the cable capacitance results in an oscillating exchange of stored energy between cable capacitance and inductance with damping being provided by the conductor resistance. Lumped capacitance and inductance have been used to simulate the discharge of a long cable. A typical arc current oscillogram resulting from these experiments is reproduced in Fig. 2.48 [2.109].

Nearly all arc current oscillograms taken during high-voltage conditioning showed brief breaks in the waveform close to but not directly at the current zeros. Figure 2.48 is a clear example of this. In the first seven cycles brief current interruptions took place a short time *after* the current had passed through zero. In the eighth cycle a longer interruption of approximately 80 μsec is indicated. From this it may be estimated that the earlier interruptions lasted for less than 10 μsec. Furthermore, at the beginning of the discharge, temporary extinction of the arc occurred after current reversal and renewed rise to 700 A in the opposite direction. This unexpected delay in the interruption can be explained by the sweep-up of space charge immediately after current reversal followed by an interruption and then the restriking of the arc with cathode spots on the opposite electrode. Reignition must be caused by the sharp induced voltage transient that accompanies the almost

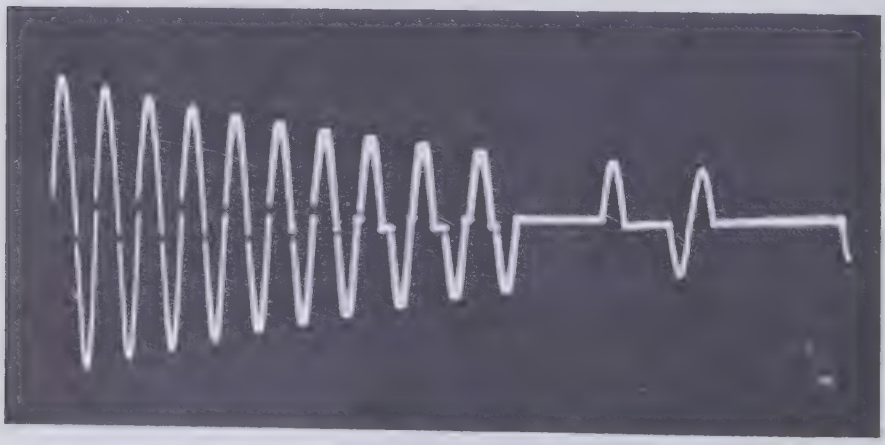

Figure 2.48 Vacuum arc current of 4870 A ringing down at 3950 Hz [2.109].

instantaneous interruption of several hundred amperes. Later in the discharge of Fig. 2.48 the extinction current dropped to 200 A and the reignition voltage transient became proportionately smaller until finally the arc remained permanently extinguished.

The interruption of 60 Hz vacuum arcs is of course well understood from the development of vacuum circuit breakers that are capable of quenching arcs up to 40 kA at the first current zero of the 60 Hz wave. The reignition voltage transient for 60 Hz currents is not as large as in the high-frequency arc to which Fig. 2.48 refers. There is more time available for deionizing the vacuum gap and this keeps the transient voltage low.

The dangers flowing from a fully developed metal vapor arc are (a) gross melting of the conductors, (b) condensation of metal vapor on insulator surfaces, and (c) the liberation of gas which may condense on previously conditioned surfaces. It has been shown in the author's laboratory at MIT that conditioning arcs are not capable of producing significant melting on aluminum, nickel and titanium surfaces [2.109]. There is no doubt however that a 60 Hz arc of 20 kA or more and burning two or three cycles would cause gross melting of all three metals.

Conditioning arcs in the kiloampere range inscribe many Lichtenberg figures into the oxide layers of aluminum and titanium. They left no trace on a nickel-plated aluminum conductor until differential thermal expansion was beginning to crack the nickel layer. The Lichtenberg figures prove the existence of adsorbed gas layers but they do not appear to affect the breakdown strength of the vacuum gap.

Some metal vapor will inevitably be condensed on the insulator surfaces. Unless the arcing continues for hours, it does not accumulate in quantities that reduce the flashover voltage. Glass insulators stay clean longer than ceramic insulators. The diffusing arc plasma liberates considerable quantities of gas from surfaces that face the vacuum space. This can be troublesome in the early stages of conditioning when the discharge frequency can become so high that the conductors overheat. A useful rule is to condition at the highest possible temperature to minimize recondensation of the vapor products that have been lifted off conductor and insulator surfaces.

2.7 POLARIZATION, CABLE CAPACITANCE, AND DIELECTRIC LOSS

A fundamental difference between conductors and insulators, or metals and dielectrics, is the tenacity with which electrical charge is bound to atoms and molecules. Dielectric molecules holding on to their charges nevertheless respond to electric fields. The reaction to the external field is internal charge displacement and strain. In this electrically strained state, the material is said to be polarized. Polarization is a cooperative phenomenon in the sense

that the polarization of one molecule increases the field strength in its immediate vicinity, which causes additional polarization in the neighboring molecules with a further strengthening of the field, and so on.

Concepts

Four basic mechanisms of polarization are known and von Hippel [2.110] has given them graphic expression by the diagrams of Fig. 2.49. Induced electronic polarization is due to the displacement of the electronic charge with respect to the positive nucleus of the atom. Absorption of energy through electronic polarization is a quantum mechanical effect that can lead to the emission of photons in the visible and ultraviolet spectrum. The contribution of this polarization mechanism to the behavior of cable insulation is negligible.

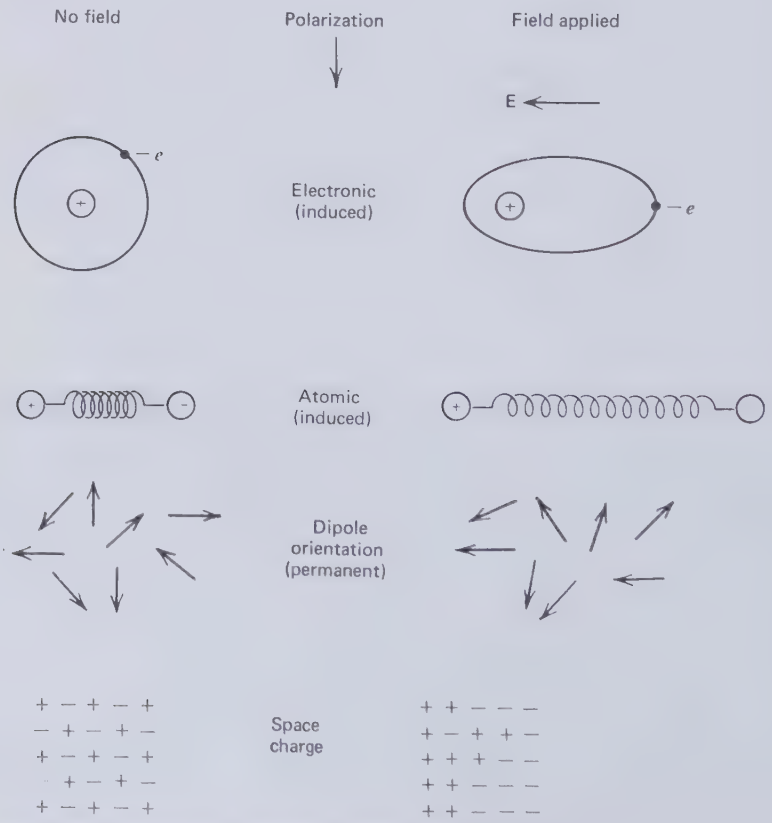

Figure 2.49 Polarization mechanisms [2.110]. (By permission of the MIT Press).

In the binding of two atoms some electronic charge may be transferred from one partner to the other. The two atoms then become ions that respond to the application of an electric field by atomic polarization and energy can be withdrawn from the field and converted to heat in the material by infrared photons. Both the induced electronic and atomic polarizations give rise to electrostriction, which implies a dimensional change in the unstrained dielectric specimen due to the application of an electric field. The effect is not reversible because mechanical deformations only strain the bonds between molecules and leave the charge distribution untouched. Both induced polarization mechanisms are observable in gases and liquids where the resulting dipoles are free to rotate. The polarization of gases is a very feeble effect because of the large distance between gas molecules which results in a small number of polarizable charges per unit volume. Induced polarization is largely temperature-insensitive, which serves to distinguish it from polarizing responses of sets of permanent dipoles.

The charge unsymmetry in complex molecules usually causes permanent dipole moments. This and space charge polarization account for virtually all of the dielectric constant and loss of cable insulation. The alignment of permanent molecular dipoles can only be achieved through rotation or movement of individual or groups of molecules. The higher the temperature or thermal agitation of the material, the easier it is for permanent dipoles to move. Their collective motion is accompanied by changes in specimen dimensions. Unlike electrostriction, this phenomenon is reversible because a displacement of molecules changes the polarization and can generate a voltage between two points in the material. It is known as the piezoelectric effect. In some predominantly crystalline materials permanent dipoles may be relatively free to rotate. This creates a tendency for large groups of dipoles to spontaneously align themselves with each other and the phenomenon is described as *ferroelectricity* because of the similarity with the spontaneous alignment of paramagnetic moments in ferromagnetic materials.

Space charge polarization arises from the fact that both electrons and ions (holes) have limited mobility in dielectric materials. The charges are ultimately trapped at imperfections, the boundaries between crystalline and amorphous phases and at the surfaces of the specimen itself. An applied electric field will displace a fraction of the space charge and this produces macroscopic dipoles that can move with difficulty and lose some energy in the process.

The dielectric polarization vector P acts parallel to the electric field vector E and it may be written

$$P = N\alpha E' \tag{2.121}$$

where N is the number of elementary particles per unit volume contributing

to polarization and α their polarizability. E' is the local electric field which is the sum of the applied field and a component produced by dipole alignment. P has the same dimension as E and α is therefore a volume. A more useful form of (2.121) is

$$P = \chi \varepsilon_0 E \tag{2.122}$$

because the experimenter knows the strength of the applied field E and the permittivity of free space

$$\varepsilon_0 = 8.854 \times 10^{-12} \quad \text{F/m} \tag{2.123}$$

The dielectric susceptibility χ is related to the relative dielectric constant ε of the material by

$$\varepsilon - 1 = \chi \tag{2.124}$$

To arrive at a relationship between the molecular parameter $N\alpha$ and the dielectric constant of the material it is necessary to determine E' in terms of the applied field E.

It brings us up against the classical difficulty of field theory, which apparently predicts an infinite field strength at the location of a point charge. This problem was overcome a long time ago by Masotti [2.114]. His model is depicted in Fig. 2.50. It presumes that a small sphere of radius r has been excavated from the material around the point A at which the field is to be determined. The excavation must leave the polarization of the remaining

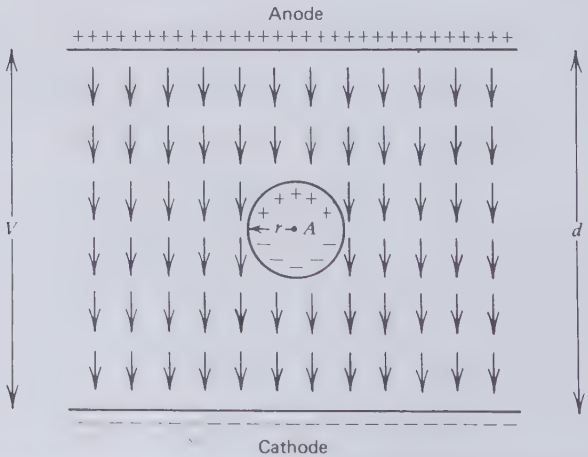

Figure 2.50 Masotti model for calculating the internal field in a dielectric medium.

material undisturbed. The local field E' at A may then be taken as the sum of three components.

$$E' = E_1 + E_2 + E_3 \tag{2.125}$$

E_1 is equal to the excitation field E, which in the case of a parallel plate capacitor is simply the voltage V between the anode and cathode divided by the plate separation d, or

$$E_1 = E = V/d \tag{2.126}$$

The charge density on the cavity wall is the component of the polarization P, which acts normal to the dielectric surface and binds free charge to it. If dA is an element of the spherical surface and θ the angle of inclination between P and dA, then the surface charge density q_s is given by

$$q_s = P\cos\theta\, dA \tag{2.127}$$

Now by placing unit charge at the point A we find from Coulomb's law that

$$dE_2 = \frac{P\cos\theta}{4\pi r^2\varepsilon_0}\, dA \tag{2.128}$$

where dE_2 is the radial field contribution at A due to the surface charge q_s at the element dA. For each surface element, there exists a counterpart that produces the same field component in the anode-cathode direction but an equal and opposite component in the transverse direction. Hence to calculate the value of E_2 in the direction of the applied field E_1, only the resolved components in the E_1 direction need be summed, or

$$E_2 = \int \frac{P\cos^2\theta}{4\pi r^2\varepsilon_0}\, dA \tag{2.129}$$

To carry out the integration in (2.129) it is convenient to divide the spherical surface in ring elements

$$dA = 2\pi r\, d\theta \sin\theta \tag{2.130}$$

and it will be found that

$$E_2 = \frac{P}{2\varepsilon_0} \tag{2.131}$$

This field is not only parallel to E_1 but also acts in the same direction.

With the aid of (2.122) and (2.124) E_2 may be expressed in terms of E by

$$E_2=\left(\frac{\chi}{3}\right)E=\frac{(\varepsilon-1)E}{3} \tag{2.132}$$

The E_3 component of the Masotti model should account for the dipole-dipole interactions within the spherical volume around A. If it is assumed that only the interaction of two dipoles has physical meaning—in other words there exists no self-interaction—r may be reduced to the molecular radius of the dipole at A and then

$$E_3=0 \tag{2.133}$$

Substituting the three field components into (2.125) we obtain

$$E'=\frac{E(\varepsilon+2)}{3} \tag{2.134}$$

The E' given by (2.134) is known as the Masotti field.

By equating (2.121) to (2.122) and substituting for E' from (2.134) it can be shown that

$$N=\frac{3\varepsilon_0(\varepsilon-1)}{(\varepsilon+2)} \tag{2.135}$$

which is the desired relationship between polarization and dielectric constant. N is known for most gases, liquids, and solids and ε may be determined experimentally by capacitance measurements. Therefore (2.135) can be used to calculate the polarizability α of dielectric materials.

Polarization is detrimental to cable insulation because it increases the charging current and leads to dielectric heating. These disadvantages make themselves felt when transmitting ac power. For sinusoidal excitation the permittivity or dielectric constant may be considered to be a complex quantity

$$\varepsilon=\varepsilon'-j\varepsilon'' \tag{2.136}$$

The phasor diagram Fig. 2.22 of the charging current through a dielectric slab defines the power factor angle ϕ of the insulation and also the loss angle δ. The reactive impedance of the capacitor is

$$X_C=\frac{1}{\omega\varepsilon\varepsilon_0 C} \tag{2.137}$$

In this expression $\varepsilon_0 C$ is the geometric capacitance that becomes equal to the actual capacitance when the space between the plates is vacuum. With (2.136) and (2.137) the total charging current I_c may be expressed as

$$I_c = \omega\varepsilon'' \varepsilon_0 CV + j\omega\varepsilon' \varepsilon_0 CV \tag{2.138}$$

This defines the real and imaginary parts of the relative dielectric constant in terms of the reactive and resistive current components of Fig. 2.22, or

$$\varepsilon' = \frac{I_X}{\omega\varepsilon_0 CV} \tag{2.139}$$

$$\varepsilon'' = \frac{I_R}{\omega\varepsilon_0 CV} \tag{2.140}$$

and the dielectric loss factor is seen to be

$$\tan\delta = \frac{\varepsilon''}{\varepsilon'}. \tag{2.141}$$

Permittivity

Gases have the lowest permittivity (*dielectric constant*) of all cable insulation materials. This is primarily due to the low matter density. Besides this, the insulating gases of nitrogen and sulfur hexafluoride are nonpolar; that is to say their molecules do not exhibit a permanent dipole moment. In a nonpolar gas in the absence of ionization the polarization is produced by induced electronic and atomic charge distortions. The electronic contribution is normally the dominant factor, but SF_6 is an exception to this rule [2.115]. As the density of a gas increases with pressure, the dielectric constant must also go up. This effect is negligible over the pressure range employed in cables. For example the dielectric constant of argon at 25°C and 64.4 psi is 1.00223. It rises to 1.015 at 427 psi. Air at 20°C and atmospheric pressure has a dielectric constant of 1.0006.

The permittivity of insulating liquids is higher than that of gases firstly because of the density and secondly because some of the oils are polar dielectrics. Mathes [2.116] assembled the dielectric constants of the cryogenic liquids and compared them with transformer oil and water. Of them helium has the lowest permittivity, which is not much higher than that of gases. Mathes' figures are reproduced in Table 2.6. Complex hydrocarbon molecules are polar in nature and that accounts for the higher dielectric

Table 2.6 Low-frequency Dielectric Constants of Insulating Liquids [2.116]

	Temperature (°K)	Density (g/cm^3)	Dielectric constant (ε')
Helium	1.83	0.1465	1.0562
	2.24	0.1471	1.0563
	4.21	0.1251	1.0469
Hydrogen	14.4	0.0772	1.259
	20.4	0.0712	1.231
Nitrogen	63.1	0.870	1.467
	77.3	0.881	1.431
Transformer Oil	273	0.900	2.22
	373	0.835	2.12
Water	273	0.9998	88
	293	0.998	80

constant of insulating oil. The H_2O molecule is inflicted with an exceptionally large dipole moment and this is reflected by the dielectric constant of water which can be as high as 80.

Of greatest interest is the permittivity of solids because of its influence on the charging current of the commonly used high-voltage cables. All other factors being equal, nonpolar insulation materials are to be preferred, and polyethylene stands out among them. It was because of its dielectric properties that this material was first developed for high-frequency communication cables. In the meantime it has become apparent, however, that polyethylene is not entirely free of permanent dipoles.

Forster [2.111] measured the dielectric constant and the loss tangent of four extruded samples of commercially available polyethylene brands. His results are listed in Table 2.7. Two of the samples were high-density thermoplastic polyethylene (HDPE), one of them was low-density thermoplastic material (LDPE), and the remaining one was chemically cross-linked low-density polyethylene (XLPE). Forster's measurements confirmed that the permittivity increases with density provided the molecular weight distribution is constant. In cable design it is common practice to take the dielectric constant of both thermoplastic and thermosetting (cross-linked) polyethylene as 2.3. Some manufacturers blend polyethylene insulation with filler powders following the tradition of mineral powder filled rubber dielectrics. The powder is often clay and its purpose is to increase the mechanical toughness of the insulation. Mineral fillers raise the dielectric constant of polyethylene to a nominal value of 2.7. The only rubber material employed as high-voltage cable insulation is mineral filled ethylene propylene rubber (EPR) and its nominal dielectric constant is 3.3, which is almost as high as that of oil-paper insulation.

Table 2.7 Dielectric Properties of Extruded Polyethylene Samples According to Forster [2.111]

	Sample			
	1	2	3	4
Type	HDPE	HDPE	LDPE	XLPE
Density (g/cm^3)	0.960	0.952	0.918	—
Dielectric constant	2.3406	2.3316	2.2692	2.2758
Dielectric power factor at 100 Hz ($\cos\phi = \tan\delta$)	2.2×10^{-4}	1×10^{-4}	3.1×10^{-4}	5.5×10^{-4}

In a nonpolar material temperature has a small effect on permittivity in so far as it increases the thermal agitation which disturbs the alignment of induced dipoles. This small temperature effect is evident in the polyethylene graph of Fig. 2.51. Dry paper, by comparison, is a polar dielectric and the motion of permanent dipoles becomes easier as the temperature is raised. In other words, the cooling of paper insulation seems to freeze out some of the dipole activity. The curves of Fig. 2.51 are based on measurements by Allan and Kuffel [2.117].

This last graph also shows that the dielectric constant of dry paper at ambient temperature is nearly the same as that of polyethylene. However when taped paper insulation is impregnated with insulating oil the permittivity of the oil-paper combination leaps to 3.5. At first this may appear surprising because the oil alone has a dielectric constant that is not very different from that of dry paper. Ionic conduction in the oil and the resulting space charge polarization (see Fig. 2.49) explain this effect [2.119], which continues to be a serious disadvantage of oil-paper insulated cables. Ions in the oil have sufficient mobility to be swept to the many paper interfaces where they are trapped until the polarity reverses and ionic

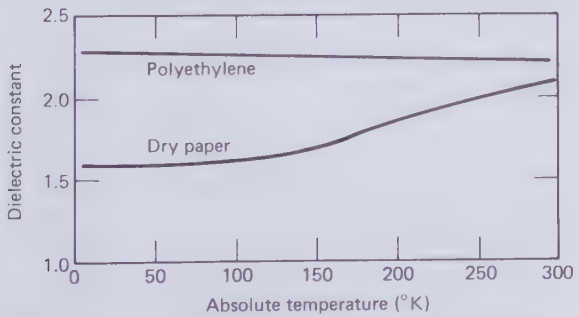

Figure 2.51 Permittivity of polyethylene and dry paper at low temperatures [2.117]. (By permission of the Institution of Electrical Engineers).

transport in the opposite direction takes place. The charge separation between paper barriers is large compared with intermolecular distances, and the resulting dipoles are therefore also large. Hence a relatively small number of space charge dipoles can account for a significant amount of polarization.

Impregnants with few free ions for creating space charges at liquid-solid boundaries should keep the permittivity of the composite insulation close to that of the constituent dielectric materials. The cryogenic liquids of helium, hydrogen, and nitrogen might achieve this. Hardly any measurements of the permittivity of taped insulation impregnated with cryogenic liquids have been published. Jefferies et al. [2.118] found that a 40-ft-long cable sample insulated with spun-bonded polyethylene fiber paper and impregnated with liquid nitrogen had a capacitance of 1500 pF. The conductor and insulation diameters were 2.75 and 4.45 in., respectively. Using equation (3.55), the dielectric constant of the cryocable insulation comes out to be

$$\varepsilon = \frac{1500 \cdot 10^{-12} \cdot 9 \cdot 10^{11} \cdot 2 \ln(4.45/2.75)}{40.12 \times 2.54} = 1.07$$

This is an extremely small permittivity considering that polyethylene alone should have a dielectric constant of the order of two. More research is required before anything definite can be said about the polarization mechanism in tape insulated cryocables. Forsyth et al. [2.120] expect synthetic insulation tapes impregnated with supercritical helium to have a permittivity of 2.2.

Another composite insulation that has received much attention in recent years is polypropylene laminated paper impregnated with oil. Matsuura et al. [2.121] described the development and testing of cable samples made with this kind of dielectric. In their various insulating tapes a layer of polypropylene binder was sandwiched between two other layers which might consist of cellulose paper or synthetic paper of polypropylene fibers or of a synthetic polypropylene film. Using the following notation

C = cellulose paper	S = synthetic paper
P = polypropylene binder	F = polypropylene film

five different composite tapes were tested with the three-layer combinations CPC, CPF, SPS, SPF, SPC. The dielectric constants of the best of these tape materials impregnated with DDB cable oil are listed in Table 2.8.

Polypropylene alone has a permittivity of approximately 2.2 and this low value has been attained in the oil impregnated SPS system. From this fact it may be concluded that space charge polarization is a peculiarity of the

Table 2.8 Dielectric Constant and Other Electrical Properties of Polypropylene Laminate Oil Impregnated Insulation According to Matsuura et al. [2.121]

	Sample		
	CPC	CPF	SPS
Density (g/cm^3)	0.88	0.87	0.76
Dielectric Constant	2.8	2.5	2.2
Power Factor at 80°C and 200 kV/cm	8×10^{-4}	5×10^{-4}	1×10^{-4}
Impulse strength (kV/cm)	2500	2700	1400
AC strength (kV(rms)/cm)	1350	1500	900

cellulose-oil combination. Table 2.8 indicates that an increasing amount of cellulose in the tape make-up raises the permittivity. The CPC construction has a dielectric constant of 2.8 which lies significantly below the 3.5 value of oil-paper insulation and with the reduction in permittivity comes a 50 percent saving in dielectric loss.

Polyethylene film tapes swell and degrade excessively when immersed in insulating oil. Iwata and his colleagues [2.122] have claimed that this problem can be overcome with a polyethylene paper made of highly oriented crystalline fibers. Their measurements showed that this material provides oil impregnated cable insulation of a dielectric constant of 2.2 and an 80°C power factor of 2.4×10^{-4}.

Dielectric Loss

The two mechanisms that dissipate energy in electrical insulation are ionic collisions of transport currents and atomic and molecular distortions caused by polarization. Good insulators have few free ions that can carry transport currents and in the majority of cases the dielectric losses are produced by polarization. A further justifiable generalization is that materials of low permittivity also dissipate little energy. The most direct way of producing an almost loss-free insulation is to use a minimum of polarizable matter as in vacuum and gas insulation.

Polyethylene has the lowest loss of all solid dielectric cable insulation materials. In the normal cable operating temperature range the power factor of various grades of high molecular weight, low density, thermoplastic polyethylene falls in the $1-5\times10^{-4}$ bracket. Cross-linking of the polyethylene chain molecules increases the dielectric loss, but it is rarely more than twice as large as that of the corresponding thermoplastic material. The best of the extruded polyethylene insulations have a power factor of one tenth of

that of the best oil-paper insulation. Forster [2.111] concluded from his measurements (Table 2.7) that the dielectric loss in polyethylene depends on the degree of crystallinity with most of the dissipation occurring in the amorphous material. This conclusion has been derived from the lower loss of the more crystalline high-density material of Table 2.7. Forster suspects that the higher loss in cross-linked material is due to additional molecular chain motion.

Polyethylene is also one of the lowest-loss materials at cryogenic temperatures as is evident from the results compiled by Fallou and Bobo [2.123], which have been reproduced in Fig. 2.52. Compared to its ambient temperature value, the power factor of low-density polyethylene is down by one order of magnitude at liquid-nitrogen temperatures and two orders of magnitude at liquid-helium temperatures. The loss reduction at low temper-

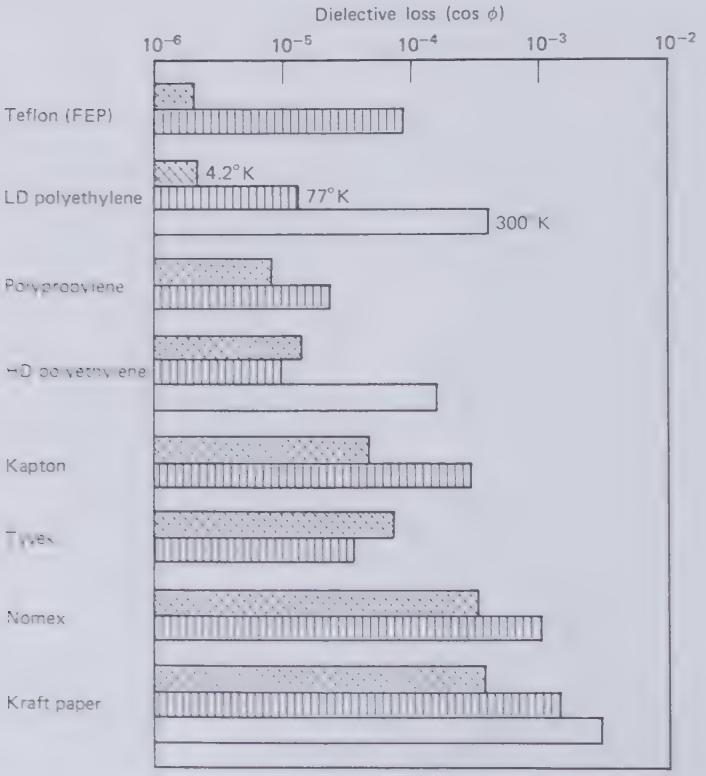

Figure 2.52 Low temperature dielectric loss of various materials according to Fallou and Bobo [2.123] at 1 kHz (< 100 V). (By permission of the National Academy of Sciences, Washington, D.C.).

atures is not well understood except when the polarization is due to the orientation of permanent dipoles, which lose some of their ability to move as the temperature falls. Cellulose paper shows the smallest and polyethylene the largest loss dependence on temperature. Kraft paper insulation is unsuitable for ac superconducting cables because its loss is not sufficiently reduced to compensate for the energy penalty of refrigeration. To make the refrigeration load bearable the dielectric power factor at liquid-helium temperatures should not be greater than 10^{-5} and at liquid-nitrogen temperatures it should not be greater than 10^{-4}.

The temperature dependence of the dielectric loss of oil-impregnated taped insulations is plotted on Fig. 2.53. Apart from having the highest loss, oil-paper insulation exhibits a characteristic dip, between 20 and 120°C, in the power factor versus temperature curve. The drooping portion of this curve is indicative of the involvement of permanent dipoles and the rising portion is the beginning of thermal instability. It will be seen that the impregnated polypropylene laminated insulations have more of a flat power factor versus temperature characteristic. Whether their ultimate dielectric strength is determined by thermal instability or another breakdown mechanism is not yet known.

The dielectric power factor of high-voltage cable insulation may vary not only with frequency and temperature but also with electrical stress. Between certain limits, the loss factor of oil-paper insulation will actually decrease with increasing electrical stress. This has become known as the Garton effect.

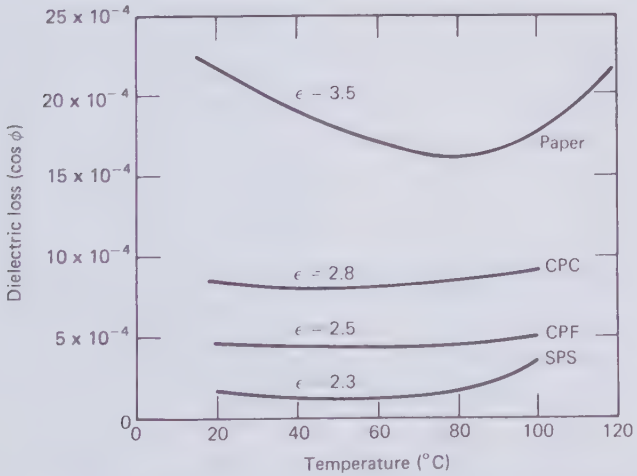

Figure 2.53 Dielectric loss of oil impregnated taped insulation systems above ambient temperature [2.121, 3.5]. CPC, CPF and SPS are the polypropylene-paper laminates of Table 2.8. (By permission of the Institute of Electrical and Electronics Engineers (New York) and the Institution of Electrical Engineers (London)).

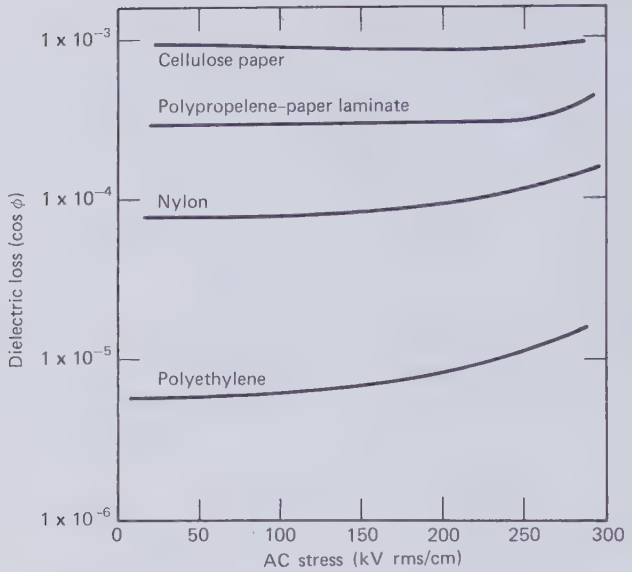

Figure 2.54 Dielectric loss of various tape materials impregnated with liquid nitrogen according to Rigby and Weedy [2.126]. (By permission of the Institute of Electrical and Electronics Engineers).

It is explained by the shorter time for which ions move in liquid layers as the field strength is increased [2.124]. In other composites increasing electrical stress is known to drive the losses upward. For example, Bogner [2.125] reported a sharp increase in the dielectric loss factor of polyethylene tapes immersed in boiling liquid helium from 10^{-6} at 30 kV/cm to 3×10^{-5} at 80 kV/cm. However, this poor performance of liquid-helium-impregnated insulation can no doubt be improved by applying pressure to the impregnant and thereby reduce ionization in the gaseous phase.

Loss-versus-stress characteristics show greater stability when the insulating tapes are impregnated with liquid nitrogen. This can be seen from Fig. 2.54, which depicts the results of Rigby and Weedy [2.126] for an unspecified liquid pressure. All the materials investigated by these authors show some increase in the loss factor as the stress approaches 300 kV(rms)/cm, which is probably caused by the onset of ionization in the butt gaps between tapes.

Cable Capacitance

By definition the capacitance C of a pair of electrodes is the electrical charge Q that will be set free at the electrode surfaces when a potential difference V

is applied between them, or

$$C = \frac{Q}{V} \tag{2.142}$$

When Q is expressed in coulombs and V in volts, (2.142) gives the capacitance in farads. The capacitance of a pair of electrodes is known to depend only on the geometry of the electrodes and the permittivity of the insulation that separates them. If the gap between the conductors of a coaxial cable contains a dielectric of permittivity ε, the electric field strength E at a radial distance x from the cable axis is

$$E = \frac{4\pi q}{2\pi x\varepsilon} = \frac{2q}{x\varepsilon} \tag{2.143}$$

where $q = Q/L$ is the charge per centimeter length on either conductor. Therefore, the voltage between the coaxial conductors of inner and outer radii r and R may be expressed in terms of the charge by

$$V = \int_r^R E\,dx = (2q/\varepsilon)\int_r^R \frac{dx}{x} = \left(\frac{2Q}{L\varepsilon}\right)\ln\left(\frac{R}{r}\right) \tag{2.144}$$

The fundamental capacitance formula of a coaxial line may now be obtained by substituting (2.144) into (2.142).

$$C = \frac{\varepsilon L}{2\ln(R/r)} \quad \text{esu} \tag{2.145}$$

For C to be given in electrostatic units L has to be expressed in centimeters and capacitance is seen to have the dimension of length. The practical unit of capacitance is given by

$$\begin{aligned} 1 \text{ Farad} &= 9\times 10^{11} \text{ cm} \\ 1 \text{ pF} &= 0.9 \text{ cm} \end{aligned} \tag{2.146}$$

To obtain the capacitance of a coaxial line of length L (cm) in practical units the formula must be written

$$C = \frac{\varepsilon L \text{ (cm)}}{2\ln(R/r)}\,\frac{1}{9\times 10^{11}} \quad \text{F} \tag{2.147}$$

which for 1 cm length is equivalent to (2.71) and (3.55). In this form of the capacitance equation, ε is the permittivity of the insulation. For vacuum this is unity. It should be noted that (2.147) does not involve the permittivity of free space.

Gas and vacuum insulated underground power transmission lines have been proposed in which three conductors are enclosed in the same grounded metal pipe, which is also the neutral conductor of the three-phase system. Figure 2.55 shows the three interconductor capacitances C_c and the three conductor-to-neutral capacitances C_n in the star-delta network. The delta connected reactances $1/\omega C_c$ involving the interconductor capacitances may be transformed to star connected reactances by the delta-star transformation

$$\frac{1}{\omega C_c'} = \frac{\left(\frac{1}{\omega C_c}\right)^2}{3\left(\frac{1}{\omega C_c}\right)} = \frac{1}{3\omega C_c} \tag{2.148}$$

Therefore each C_n capacitance is in effect shunted by

$$C_c' = 3C_c \tag{2.149}$$

Hence the total capacitance C_n' between each conductor and neutral is

$$C_n' = C_n + 3C_c \tag{2.150}$$

and this is the capacitance that determines the charging current and the critical length of the circuit.

When the conductors and the enclosure pipe are circular cylinders both C_n and C_c may be calculated from Smythe's formula [2.127]

$$C = \frac{\varepsilon L\ (\text{cm})}{2\cosh^{-1}\left[\pm(D^2 - R^2 - r^2)/2Rr\right]} \frac{1}{9\times 10^{11}} \quad \text{F} \tag{2.151}$$

D is the distance between the axes of the two cylinders of radii R and r between which the capacitance is being computed. The negative sign in the denominator of (2.151) applies when the smaller cylinder of radius r lies within the larger cylinder. It has to be used when computing C_n. The positive sign gives the capacitance of the two-wire line, which has to be used for computing C_c when $R = r$. Knowing that

$$\cosh^{-1} x = \ln\left(x + \sqrt{x^2 - 1}\ \right) \tag{2.152}$$

(2.151) reduces to the formula (2.147) for the coaxial line by setting $D = 0$.

If the conductors are not circular cylinders, as in the example of Fig. 1.42, it is probably easier to measure the capacitances on a scaled cable model than to compute them. The cross-sectional dimensions of the cable appear as

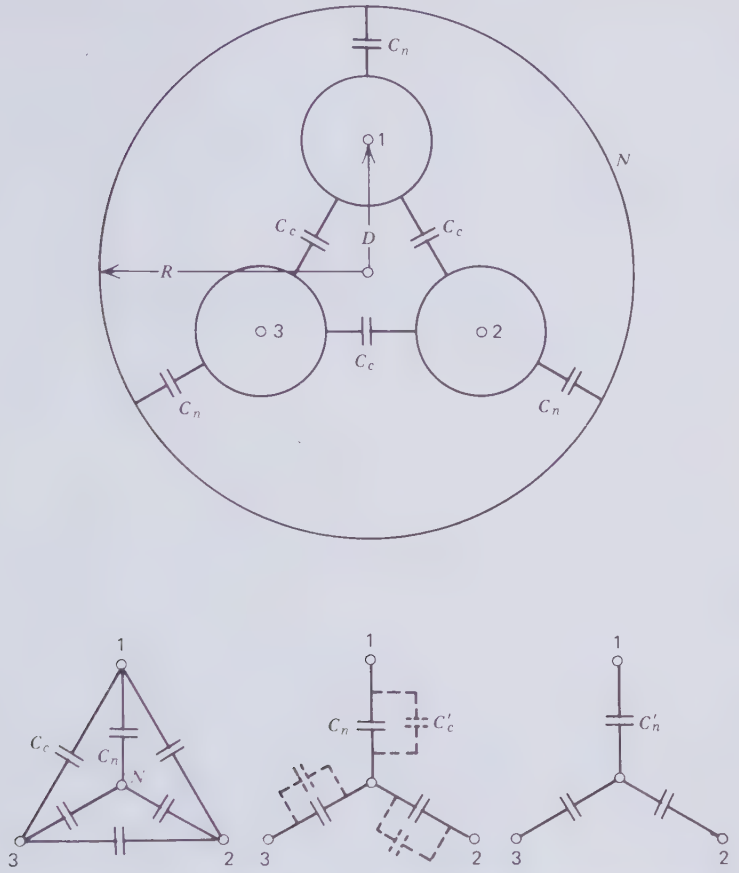

Figure 2.55 Capacitances in a collectively shielded three-conductor cable.

ratios in the capacitance formulae, which proves that geometrically similar models of different scale factors have the same capacitance.

It is possible to compute the capacitance between noncircular conductors by first establishing the electric field distribution with a numerical relaxation technique [2.128]. This will also yield the potential differences per unit charge from which the capacitance may be derived.

Part Three

CABLE TECHNOLOGY AND ECONOMICS

3.1 HISTORICAL EVOLUTION OF HIGH VOLTAGE CABLES

Paper Insulated Cables

The early pioneer of underground power transmission was Sebastian de Ferranti. Hardly 20 years old, he proposed that a power plant should be built 7 miles away from the center of the city of London and the output of the generators should be brought to the metropolis by a high-voltage cable. Within a few years, by 1891, he saw his plan implemented and succeed. When the cable manufacturers of the time told him, 2 years before the completion of the generating station, that they could not supply a 10-kV ac cable operating at three times the voltage they had handled previously, the energetic Ferranti took it upon himself to design, produce, and install the first underground power transmission line.

Figure 3.1 shows the make-up of the "Ferranti Tubular Main" as his paper insulated cable was called. The old jute or rubber insulations proved to be unsuitable for 10-kV, 50-Hz transmission. Paper had been used as insulation in telephone cables and Ferranti found that by impregnating it with ozokerite, a by-product of the manufacture of candle wax, it could withstand very high voltage. As Hunter and Hazell report [1.59], dc tests with a Wimhurst machine convinced the young inventor that a half-inch layer of paper would give him a 16 : 1 safety factor. Only after the cable had been placed in service was it discovered that the ac strength of the paper insulation was very much lower, reducing the safety factor to 2 : 1.

An 1888 patent by Ferranti mentions the rigid tubular design of Fig. 3.1 and also a flexible cable with tape-wound paper insulation. There is little

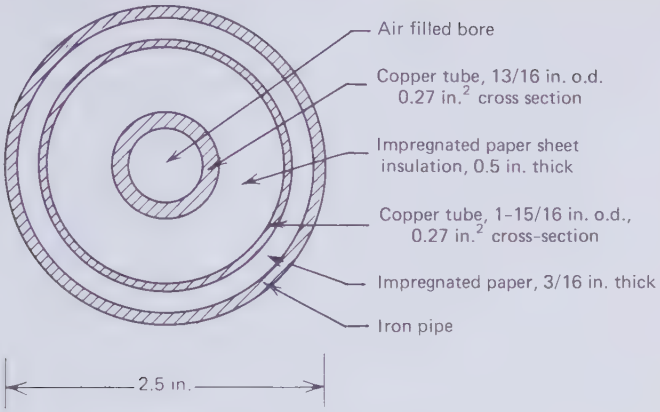

Figure 3.1 Ferranti 10-kV ac tubular main.

doubt that Ferranti would have preferred long flexible cables on reels, but his 2-year construction deadline did not permit the development of paper taping machinery. It forced him to wrap 20-ft-wide paper sheets spirally around copper tubes and insert the insulated conductor into another copper tube that served as return conductor of a single-phase circuit. These operations could be carried out quite quickly in a metal fabrication shop. But the penalty he had to accept for low-cost manufacture was 7000 plug-in joints on the 4×7 mile single-phase circuits. The ingenious Ferranti cable joint was a forerunner of modern slip-on splices and elbow connectors. Like all splices in cables containing solid insulation, the Ferranti joints had their problems with thermal expansion. He therefore lost no time, after 1891, to develop the flexible cable. With it came the large and complex paper taping machinery, the lead presses, cabling, and the armoring plant, which have been the tools of the power cable industry for nearly a century. Ironically, the very latest high-voltage cables that employ SF_6 gas insulation may again be produced in metal fabrication shops. So the wheel has turned full circle.

Ever since the days of the Ferranti Tubular Main, paper insulated cables have stayed in the forefront of underground power transmission. With the introduction of three-phase systems at the turn of the century, there came three-core cables. For several decades they were the main concern of cable engineers. As demonstrated by the pipe-type cable, their importance has not diminished, but European practice returned to single-core high-voltage cables to gain the benefit of more effective ground cooling.

In the 1920s, before the modern pipe-type and self-contained cables came into being, the development of underground transmission had reached a crisis. Overhead lines were by then transmitting power at 200 kV, whereas

cables struggled to break through the 100-kV barrier. The number of cable insulation failures in all countries had reached alarming proportions when Emanueli in Italy found the solution by impregnating the paper insulation with low viscosity oil and allowing the oil to permeate into and out of the cable during thermal cycling. To achieve this end Emanueli provided the conductor with a central oil duct, which at intervals along the route was connected to riser tanks. Gravity was sufficient to make the cable absorb oil from the tanks during the warm-up and expansion phase of the cycle. The excess oil would be squeezed out again during the cool-down period. Current practice is to connect the oil duct to sealed underground tanks with pressurized expansion bellows. This landmark invention ensured that no gas- or air-filled cavities could form and permit the slow deterioration of the paper insulation by gas discharges. A full scientific explanation of the breakdown of viscous compound impregnated cables was furnished by Robinson [2.60] in 1936. The Emanueli patent for a central oil duct dates back to 1917, illustrating how technology often drives ahead of scientific analysis.

In the United States the gas cavity problem was solved in a different way. Bennet in 1931 pulled three paper insulated cable cores in an oversize steel pipe, filled the pipe with low viscosity oil and maintained it under high pressure. He required no central oil duct and could operate his cable at significantly higher oil pressure than Emanueli's reinforced lead sheaths would safely withstand. This was the beginning of pipe-type cables, which are preferred to low-pressure oil-filled cables when mechanical protection against dig-ins and installation in congested urban areas are of overriding concern.

Barnes [1.34] published Fig. 3.2 which shows how the corona inception stress in a gas-filled impregnated paper insulated cable can be raised fourfold by stepping the nitrogen gas pressure up to 200 p.s.i. This is made possible by the reduction of the mean free path of electrons, over which they have to acquire 15.5 eV of kinetic energy to cause collision ionization. It provided the incentive for developing gas-pressure-assisted cables in competition with low-pressure self-contained and high-pressure pipe-type cables. The challenge was taken up in Europe and particularly in Britain. Although an entirely dry paper and gas cable was developed by Arman [1.59], it did not go into production because the voltage impulse strength was only about 40 percent of the compound impregnated version. This can be explained in terms of the thermal impulse breakdown mechanism, which associates high impulse strength with high density of the dielectric.

Over a period of about 30 years, starting in 1931, gas pressure cables enjoyed a fair degree of success. Mainly three different types were produced. The first to be placed in service operated at 66 kV. Hochstadter and Vogel

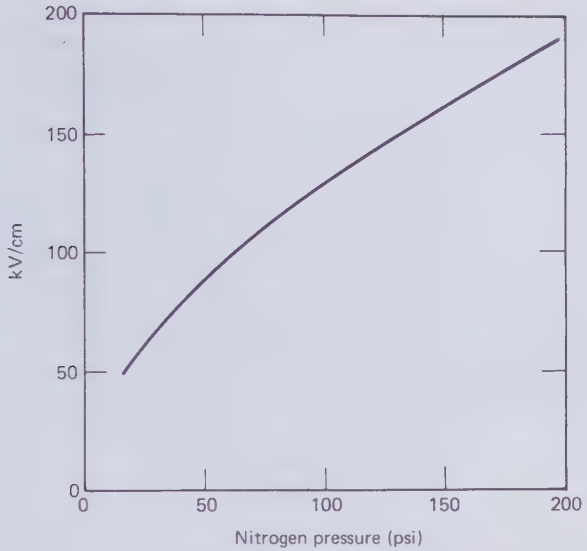

Figure 3.2 Corona inception voltage of nitrogen gas filled impregnated paper insulation as a function of gas pressure according to Barnes [1.34]. (By permission of C. C. Barnes and Chapman & Hall).

in Germany and Bowden in England cooperated in its development and their design is shown in the photograph of Fig. 3.3. It is seen to be a three-phase cable in which the mass-impregnated paper insulated cores were collectively covered with a somewhat triangular lead sheath. The nitrogen gas at 180 p.s.i. was contained in a welded steel pipe and transmitted via the pliable lead sheath to the high-voltage insulation.

Fear of detrimental chemical reactions between the gas and impregnated paper led to the indirect application of gas pressure through the lead membrane. As far as dry nitrogen gas was concerned, the fear of chemical reactions seemed to be unfounded as proved by Beaver and Davey [1.59] in a successful field trial of a 132 kV single-core cable in 1937. Significant features of this cable were that the paper tapes were impregnated with a greaselike compound prior to being lapped on the cable conductors and nitrogen gas was later brought in direct contact with the preimpregnated dielectric. The alternative method of mass-impregnation required the insulated conductors to be loaded into tanks where they were flooded with the impregnation compound. The size of the tanks determined the distance between insulation splices on the finished transmission line. But with preimpregnation almost any cable length could be produced without insulation splices. This proved attractive for long underwater installation. The Beaver-Davey gas-pressure-assisted cable was therefore used for the important

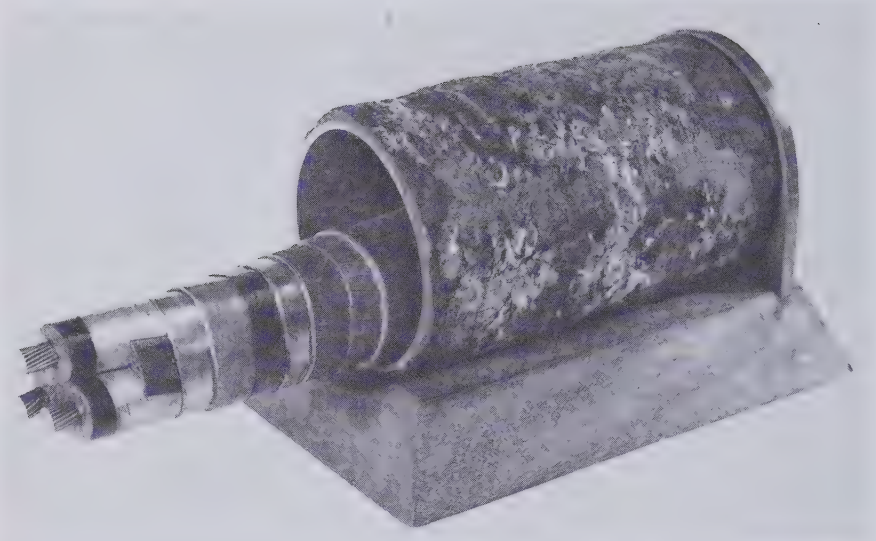

Figure 3.3 Hochstadter-Vogel-Bowden compression-type cable [1.59]. (By permission of George Newnes; Photograph: BICC).

Figure 3.4 Hunter-Brazier 3-core 132-kV gas pressure assisted mass-impregnated paper insulated cable. (By permission of George Newnes; Photograph: BICC).

submarine interconnections between British Columbia and Vancouver Island, part of the England-France link, and the Cook Strait cable between the North and South Islands of New Zealand.

A mass-impregnated gas pressure assisted cable was developed by Hunter and Brazier [1.59]. In 1943 it resulted in the installation of the first compact three-core cable at the high voltage of 132 kV. In this cable an operating stress of 100 kV/cm was reached through the use of 220 psi internal nitrogen pressure. The design of the Hunter-Brazier cable is shown in Fig. 3.4. This shows the longitudinal and circumferential steel tapes needed to contain the high gas pressure.

For several reasons the era of gas-pressure-assisted paper insulated cables appears to be coming to an end. Foremost among them is the fact that low-pressure oil-filled cables have now been shown to withstand higher operating stresses and do not use the expensive pressure containment components. Because of magnetic hysteresis losses, steel enclosures can only be employed on three-core cables. The large conductors that are now commonplace demand a steel pipe for containing pressure of the order of 200 psi and the pipe may as well be filled with oil, which, although more costly than nitrogen gas, permits higher dielectric operating stresses than the cheaper gas filling.

Over the last 20 years, more and more of the oil-paper insulated cable installations have been provided with forced cooling. This increases the transmission capability of a given circuit and safeguards against hot-spot instabilities, which may be caused by some local disturbance of the soil cooling process. Pipe-type cables may be readily cooled by circulating the oil and extracting heat from it in external cooling stations. Self-contained cables were first cooled by running water through pipes laid alongside the cable, which reduces the ambient soil temperature and thereby cools the cable. A more efficient way of cooling the outside of the cable is to pull it into an oversize waterpipe and circulate the water through heat exchangers. Oil-filled cables are also being cooled by oil circulation through an enlarged oil duct. The most powerful forced cooled cable circuits now in use have been installed under the river Severn in England. They are self-contained 400-kV oil-paper insulated cables with conductor cooling by oil circulation and surface cooling with water. One of these circuits has a transmission capability of 2640 MVA which is more than the output of a modern generating station. The successful testing of an internally water-cooled 110 kV oil-paper insulated cable has been reported [3.2]. In this case the water flowed through a stainless steel central duct in the conductor.

It is very much easier to transmit dc than ac power. A steady current does not give rise to electromagnetic induction and the accompanying ac conductor and pipe losses, and a steady voltage eliminates dielectric losses and is

less likely to cause ionization in gas-filled cavities of the insulation. However, ac voltage transformation is so much more economical than ac-dc conversion that, in the past, virtually all efforts have been devoted to the development of ac transmission lines. In the few instances where dc underground or underwater transmission has been justified for special reasons, as for example the control of load flow, the limitation of fault currents or the difficulty of providing underwater reactive compensation, ac cables have been readily adapted for dc use. The most substantial underground dc line now in use stretches for 53 miles from Kingsnorth to London. It relies on low-pressure oil-filled cables to transmit 640 MVA at ± 266 kV. Almost as powerful, but only 25 miles long, is the ± 250 kV, 600 MVA submarine crossing of the Cook Strait between generating facilities on South Island and load centers on North Island of New Zealand. This is a splice-free gas-pressure-assisted cable insulated with preimpregnated paper.

Solid Dielectric Cables

The very high cost of producing, splicing, and terminating all paper insulated high-voltage cables has placed them in a difficult and seemingly hopeless competitive position in relation to overhead lines. Only where land acquisition is prohibitively expensive or other circumstances of the installation favor underground or underwater lines do cable systems find their use. The development of polyethylene in the Second World War as a low loss dielectric for communication cables raised hopes of reducing the cost of underground power transmission with solid dielectric cables. In this case and from then onwards the United States has taken the lead in the development of new power cables. The first 15-kV cable with extruded polyethylene insulation went into service in 1955 and by 1963 Crowdes [3.1] announced that his company had set its sight on a 138-kV solid dielectric cable. The first short length of this cable was supplied in 1965 to Puerto Rico where it has been operating ever since. In the low voltage distribution field, polyethylene insulated cables have been a resounding success, but progress in the high-voltage area has been slow. Power companies have hesitated to adopt high-voltage solid dielectric cables because of a series of splice failures caused by thermal expansion and more splice and cable failures on the Waltz Mill test site [2.66] on load cycling to the exceptionally high conductor temperature of 130°C and more. A significant amount of 225-kV solid dielectric cable is in service in France. In contrast to the American experience, the French cables have a perfect record of performance over the first 5 years of their life [3.3]. The French practice is to run conductors in solid dielectric

cables at significantly lower temperatures than proposed for American cables.

In the early 1960s, Humphrey and his colleagues in the United States developed polyethylene insulated cables with sodium conductors [1.60]. The first in service was a 15-kV URD cable installed in 1965. In the following 5 years approximately 50 sodium cables were installed mainly in the United States but also in other countries. A short length of a 138-kV sodium transmission cable was placed in service by the American Electric Power Corporation at Lima, Ohio, in 1971. After an initial termination failure this cable has continued to operate without incident. Another short length of the same cable was, in 1976, subjected to 100 daily load cycles in the author's laboratory at the Massachusetts Institute of Technology. The conductor temperature reached 85°C and during the final five cycles the ac test voltage was 133 kV, which is equal to the phase-to-ground voltage of a 230-kV system. At the highest voltage the maximum stress at the conductor was 111 kV (rms)/cm which is beginning to be comparable with the performance of oil-paper insulation.

Gas Spacer Cables

In the slow evolution of underground power transmission lines two spurts occurred. Right in the beginning Ferranti created a rigid tubular line in a mere 2 years. Two American groups of engineers took not much longer, at around 1970, to bring out SF_6 gas spacer cables, which are already operational up to 550 kV. Easy construction, good heat transfer through the dielectric, low losses, and inexpensive terminations are obvious advantages of the compressed gas insulated cable. In the isolated phase design, these advantages have to be offset against the large quantity of aluminum contained in the cables and the wide trenches in which they have to be installed. For short lengths as station getaways, river crossings, and highway crossings, the simple terminations make gas spacer cables an attractive proposition. There remain some questions to be resolved regarding the effect of street traffic on large diameter aluminum pipes directly buried at normal depth. This problem would not arise in cross-country installations along overhead line right-of-ways for which the gas spacer cable appears very suitable. The Electric Power Research Institute is currently devoting much effort to the development of flexible isolated phase and rigid three-conductor gas spacer cables. The former would avoid the field welding of many pipe joints and the latter should achieve economies in metal consumption and trench width.

3.2 SELF-CONTAINED OIL-PAPER INSULATED AC AND DC CABLES

Description

The principal elements of a naturally cooled, selfcontained oil-paper insulated cable are shown on Fig. 3.5. It may be produced with flexible copper or aluminum conductors of diverse construction. The concentric strand configuration is deemed adequate up to 1000 to 1500 kcmil. Conductors as large as 5000 kcmil are now in use and the Conci or the Milliken construction are preferred for the largest sizes. Cable samples with these two types of conductor are shown in Fig. 3.6. The Conci conductor is built up of keystone-shaped strip with alternate layers wound in opposite directions. It is a very compact conductor having approximately 98 percent the density of a tube with the same inside and outside diameters. For the purpose of computing skin and proximity effects, the Conci conductor may be treated as a solid tube. Its construction creates a self-supporting oil duct. The Milliken segmental construction makes for greater flexibility, which is important on the largest sizes. As explained in Section 1.17, the ac-dc resistance ratio of Milliken conductors can be quite small provided the wires are insulated from each other. Without definite provision for this insulation the ac loss is a variable and unpredictable quantity. Concentrically stranded and Milliken conductors are laid around a wire helix, which keeps the oil duct open. Metal tapes are wrapped around the outside of Milliken conductors to hold the bundle of segments together before it is passed through the paper taping machine.

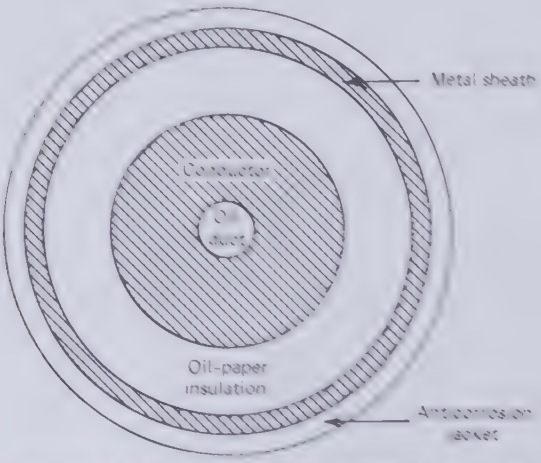

Figure 3.5 Elements of a naturally cooled self-contained oil-paper insulated cable.

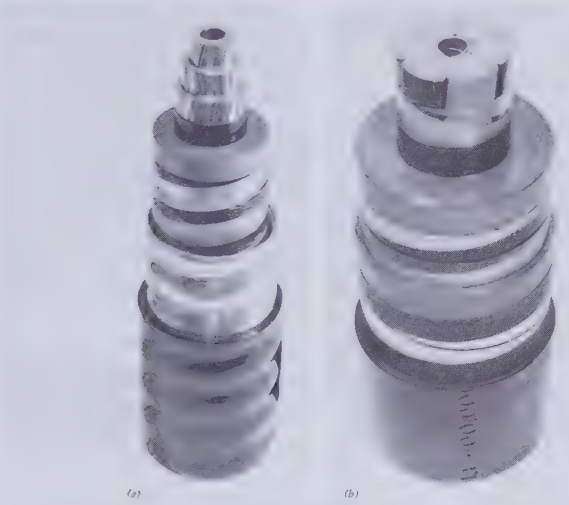

Figure 3.6 Two popular constructions of self-contained oil-paper insulated cables [3.4]. (a) 1580 kcmil Conci conductor, corrugated aluminum sheath. (b) 2570 kcmil Milliken conductor, reinforced lead sheath. (By permission of the Institution of Electrical Engineers). Photograph: Pirelli General.

The thickness of the insulation wall depends on the cable operating voltage, the conductor diameter, and the design stress. Miranda and Gazzana Priaroggia [3.4] have measured breakdown stresses of modern oil-paper insulation and their results are plotted in Fig. 3.7. As has been discussed in Section 2.5, the breakdown of oil-paper insulation is not determined solely by the maximum electrical stress. Cable designers allow for this by generous safety factors. Figure 3.7 gives the 50 Hz rms breakdown stress. The 60 Hz value is not expected to be significantly different. It will be seen that the ratio of impulse to rms ac breakdown stress varies from 2.5 at 10 psi to 1.9 at 200 psi. Underground cable insulation has to be coordinated with the electrical insulation of the rest of the power network. All components of the system should have the same chance of surviving voltage surges due to switching operations and lightning strokes. The surge withstand voltage that has to be met by the components is called the basic insulation level, abbreviated by BIL. Standardized BIL values for various U.S. system voltages are listed on Table 3.1. If a certain component is protected against surges by a lightning arrester, the BIL of this component may be reduced. Reduced basic insulation levels (RBIL) in use in the United States are also given on Table 3.1. It will be seen that the ratio of BIL stress at the conductor to ac operating stress is approximately eight. For reduced basic

insulation levels, this ratio falls into the range 6 to 7. Comparing these ratios with Fig. 3.7 it is clear that the BIL voltage will, in general, determine the insulation thickness to be applied to the cable for any given conductor radius r_c.

To obtain an idea of the minimum insulation thickness needed for the RBIL of Table 3.1 and a design impulse stress of, say, 1325 kV/cm, let us consider a range of conductor radii 2 cm $\leqslant r_c \leqslant$ 4 cm. This particular design stress provides only a 10 percent safety margin at 25 psi oil pressure with respect to the impulse strength curve of Fig. 3.7. For any BIL voltage V_i the

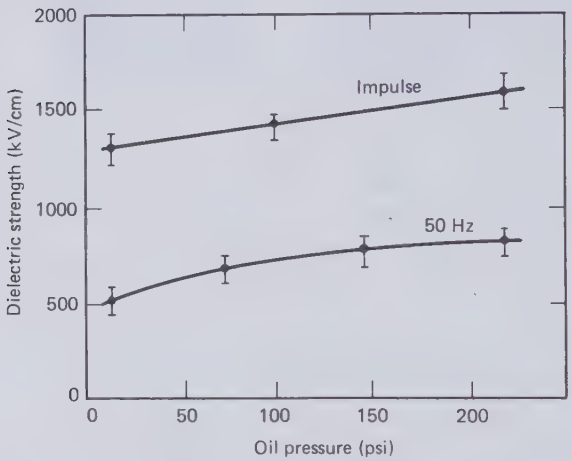

Figure 3.7 Breakdown strength of oil-paper insulation according to Miranda and Gazzana Priaroggia [3.4]. (By permission of the Institution of Electrical Engineers).

Table 3.1 Basic Insulation Levels (BIL) in the U.S. Voltage Classes

System Voltage	BIL	RBIL	BIL Stress	RBIL Stress
(kV)	(kV)	(kV)	AC Stress	AC Stress
115	550	450	8.3	6.8
138	650	550	8.2	6.9
230	1050	900	7.9	6.8
345	1550	1300	7.8	6.5
525	–	1800	–	5.9

electrical stress at the conductor shield is given by

$$S_c = \frac{V_i}{r_c \ln[(r_c + t)/r_c]} \tag{3.1}$$

And therefore the insulation thickness t is

$$t = r_c(e^{V_i/(r_c S_c)} - 1) \tag{3.2}$$

Having calculated the minimum insulation thickness to satisfy the BIL requirement, we may check back on the rms ac stress, S_{ac}, at the conductor shield. This is

$$S_{ac} = \frac{1}{\sqrt{3}} \frac{V_{ac}}{r_c \ln[(r_c + t)/r_c]} \tag{3.3}$$

where V_{ac} is the ac three-phase system voltage. On Fig. 3.8, t has been plotted for three conductor radii and the 1325 kV/cm RBIL stress. It is clear from this graph that the conductor radius has little impact on the insulation thickness until the system voltage becomes greater than 250 kV. At the very least the insulation wall will be 0.5 cm thick and at the highest voltages it is likely to exceed 2 cm. This wall may be built up from several hundred paper tapes varying in thickness from 1 to 10 mil.

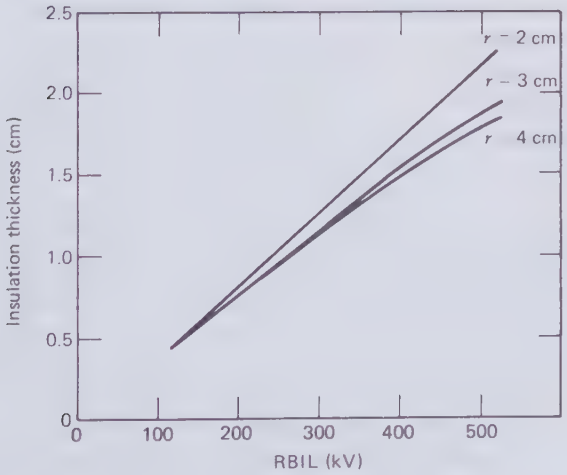

Figure 3.8 Minimum insulation thickness for reduced BIL.

For the insulation thicknesses shown on Fig. 3.8, the ac stress falls within a bracket of 170 to 200 kV/cm. From the experimental results of Fig. 3.7, this would appear to be safe. In practice, however, ac design stresses rarely go beyond 150 kV/cm. This is the result of using larger safety margins for the impulse design stress. The paper for high-voltage cables is carefully chosen with regard to impermeability, density, and impurity content, which have a bearing on dielectric losses, breakdown strength, cable capacitance, thermal resistivity, taping and bending operations, and the chemical degradation that takes place with age. The wrapping tensions are also important as they must ensure that the dielectric wall is firm, yet the tapes should be able to slide a little during cable bending.

Dielectric and conductor shields provided on the outside and the inside of the insulation wall, respectively, consist of conducting or semiconducting tapes that are applied by the paper taping machine. Shield designs have undergone changes with time and they are subject to manufacturers' preferences. A recently developed shield construction is described in reference [3.5]. The nature of the shields has a noticeable effect on dielectric losses, breakdown voltage and the aging of the insulation.

After the paper insulation has been wrapped around the conductor, it is dried with heat under vacuum and subsequently flooded with cable oil. From the oil tank, the impregnated core passes directly into the lead or aluminum sheathing extruder to minimize the risk of water pick-up. A method for maintaining vacuum in the paper insulation while the metal sheath is being extruded around it has also been developed. In that case the cable is filled with oil at a later stage. Different impregnation oils have been employed over the years. Most existing installations are filled with mineral oil. In the 1960s dodecylbenzene (ddb) became popular. More recently alkylates as, for example, linear decylbenzene (db) and branched nonylbenzene (nb) have come to the fore because of their even lower viscosity and their ability to absorb water vapor that is being liberated during the aging of cellulose. Their behavior has been studied by power factor measurements under accelerated aging conditions at 120°C [3.5]. Nonflammable Askarel cable oils are also available. They are more costly and have disadvantages with regard to dielectric losses and cable capacitance.

As paper insulation is extremely sensitive to small traces of moisture, the provision of a watertight metallic enclosure is mandatory. Water slowly diffuses through the wall of plastic pipes and they are therefore not acceptable for protecting oil-paper insulation. The first cable sheathing metal was lead and this is still being used extensively for underwater installations. The majority of new underground installations rely on extruded and corrugated aluminum sheaths. Corrugations are necessary to ensure sufficient cable flexibility. Relatively thin aluminum alloy pipes are capable of containing a

certain amount of internal oil pressure without the reinforcing tapes that have to be wrapped around lead pipes. Five millimeter thick corrugated aluminum sheaths on quite large cables can tolerate oil pressures of the order of 300 psi. Heavily reinforced lead pipes are still preferred for deep water installations because unreinforced aluminum could not readily support the laying tension. Aluminum and lead alloy sheathing materials have been developed that combine optimum mechanical properties with reasonable corrosion resistance.

On underground cables the anticorrosion jacket is normally a layer of polyethylene or PVC. It has to be adequate electrical insulation against the standing voltage on cross-bonded metal sheaths. Pinholes in the jacket have a tendency to concentrate electrolytic corrosion currents that have proved to be particularly harmful to aluminum sheath cable. A semiconducting layer of graphite-containing paint is usually applied over the anticorrosion jacket so that the latter may be tested for pinholes with voltage applied across it.

Installation

To fully exploit the thermal advantage of self-contained cables, they have to be directly in contact with the soil. But these cables are also installed in ducts or tunnels. The typical trench arrangement of a three-phase circuit in flat formation is depicted in Fig. 3.9. D is the burial depth which varies from about 30 to 50 in., depending on local circumstances, other utilities under the same street, and the load road surfaces have to carry. The greater D, the safer the cables are from dig-ins and surface deformation. On the other hand D should be kept small to save trenching cost and keep the thermal soil resistance between cables and atmosphere to a minimum. The bottom part B of the trench contains the cables and is filled with sand selected for low thermal resistivity and good moisture retention. Sand also makes good contact with the cable surface for heat transfer. It has become customary to lay concrete slabs or other protective tiles on top of the thermal sand to prevent excavation tools from directly striking the cables. In many instances it is possible to backfill some of the excavated material on top of the protective slabs. The backfill has to be well compacted to distribute the load carried by the road surface. In selecting the lateral cable spacing S, a compromise has to be made between the affordable degree of thermal isolation and keeping the trench width W within economic limits. Typical lateral spacings S are 10 to 20 in. When an underground line consists of two circuits, they are often installed with one on either side of the same street.

All forms of transmission cable may also be installed along overhead line right-of-ways, across agricultural land, through forests, and wastelands as long as there is access for installation and repair. An important precaution

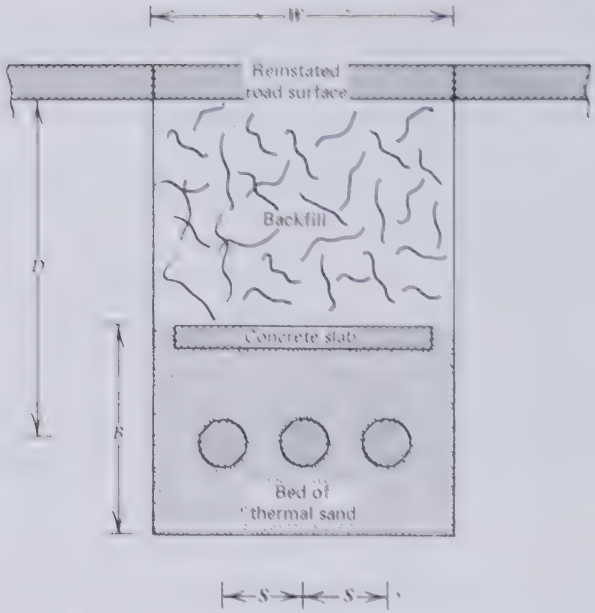

Figure 3.9 Direct burial of self-contained cables.

that has to be taken everywhere is the elimination of tree roots close to the cables. The roots interfere with heat transport and reduce the moisture content of the soil.

In open areas it is usually possible for a reel trailer to lay the cable directly into the trench. But in towns and cities the cables may have to be pulled under water pipes, telephone cables and other utilities that cross their path. This method of installation requires the trench to be kept open for a whole reel length, which may amount to 1000 to 2000 ft. Many municipalities stipulate the maximum length of trench that may be kept open at any one time in order to prevent serious traffic obstructions. This installation difficulty gives pipe-type cables an advantage over self-contained cables.

Cables are no better than their splices and terminations. Accessories for oil-filled cables have been improved over many years and they are now as reliable as the cable itself. The basic elements of a straight-through splice are indicated in Fig. 3.10. Connections between conductors may be made in a number of different ways from compression jointing to explosive welding. The oil duct may be blocked by the connector because a flow space is provided between the splice case and the permeable electostatic shield. For the sake of clarity, the transverse scale of Figs. 3.10 to 3.12 has been exaggerated to show the build-up of insulation. The extra insulation thick-

ness reduces the electrical stresses in splices and terminations to about half of what it is in the cable. Preimpregnated paper rolls and tapes are wound around the connector and the stepped back cable insulation. When the installation calls for sheath cross-bonding, the grounded layers are interrupted in the electrostatic shield by an oil gap, and in the metal splice case by a pressure tight epoxy gap. Both gaps are shown in Fig. 3.10. More pressure tight joints have to be made, usually by plumbing, between the cable sheath and the splice housing. The electrostatic shield is made up of metal or carbon tapes, or both. Wires bind the tapes down to the insulation.

Splicing operations have to be carried out in a dry and relatively clean environment. This can be provided in permanent manholes or temporary

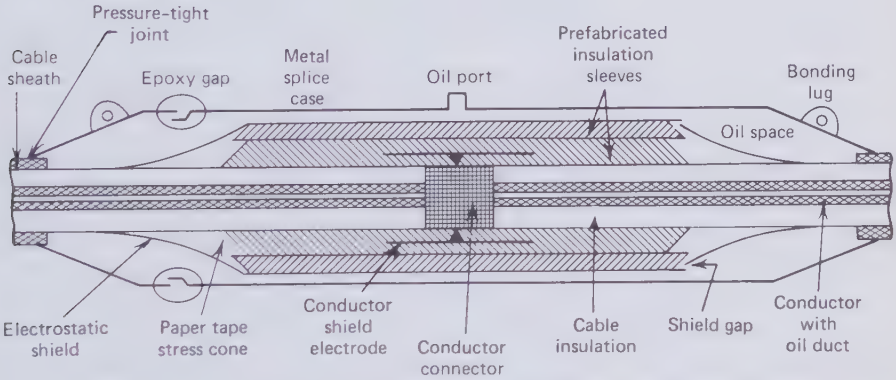

Figure 3.10 Major elements of a straight-through splice of an oil-filled cable.

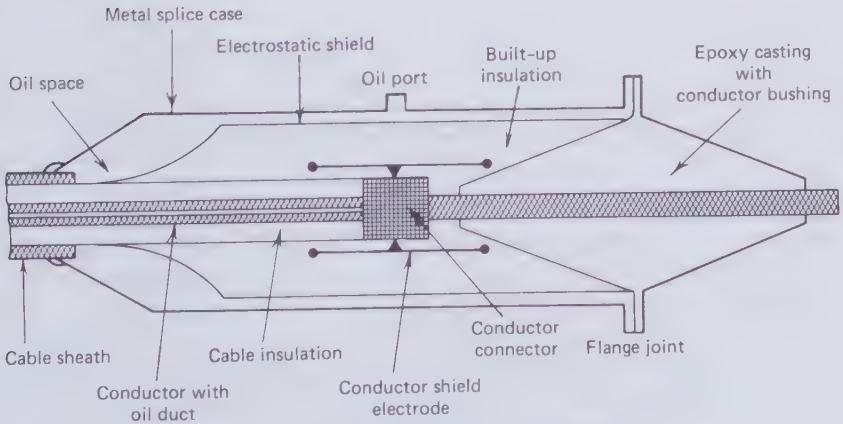

Figure 3.11 Half of a stop-joint of an oil-filled cable.

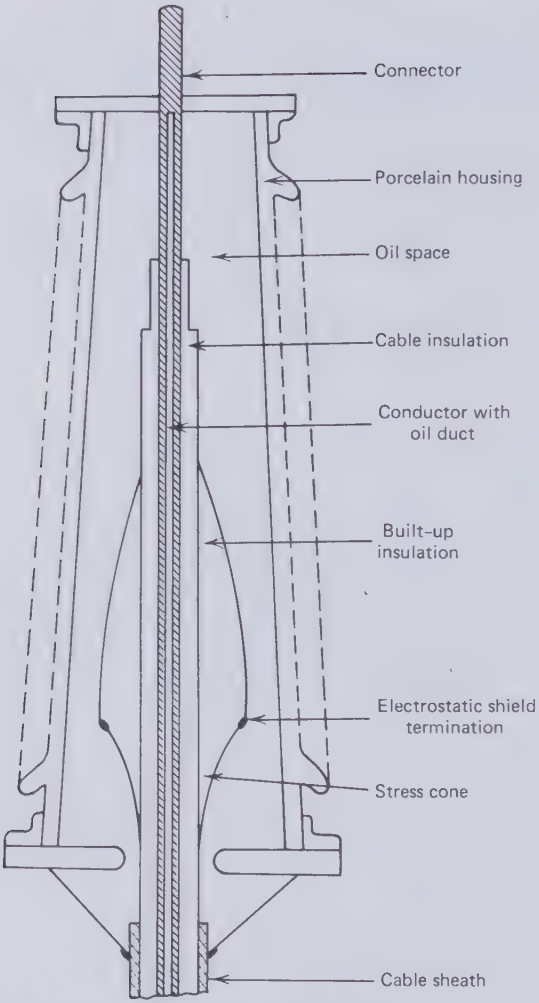

Figure 3.12 Diagramatic representation of oil-filled cable termination.

shelters depending on whether the splices have to be kept accessible or are directly buried. As the cable is shipped fully filled with oil, fluid will leak out during the splicing process, and the fluid has to be replenished at another point along the cable route to ensure that no air is drawn into the insulation. Alternatively the cables may be frozen on either side of the splice with liquid nitrogen. The finished splice must then be evacuated through the oil port before it is filled with oil. Insulated link boxes have to be provided at splice positions for sheath crossbonding.

Some of the splices have to be stop-joints for interrupting the oil flow. Stop-joints have two purposes. First they limit excessive hydrostatic heads when the cable is installed in hilly areas. Their second function is to sectionalize the oil system so that only part of the circuit drains when the cable is accidentally ruptured. The basic elements of half a stop-joint are sketched on Fig. 3.11. The heart of the stop-joint is an epoxy resin casting around a conductor stub. The cable ends are connected to either end of the stub which, together with the epoxy casting, blocks the longitudinal oil flow. The remainder of the stop-joint is built up rather like an ordinary joint with a flange connection in the middle of the housing.

Oil tanks may be installed underground near the splices through which they are connected to the cable oil duct. They should preferably be hermetically sealed and housed in a concrete enclosure. To maintain relatively constant pressure in the cable, the oil is allowed to expand a bellows against spring force or gas pressure cushions.

The principle of an oil-filled cable termination is illustrated in Fig. 3.12. The ordinary cable termination also known as a pothead or a sealing end, must separate the oil-paper insulation from air insulation. This is achieved with a long porcelain tube with rain petticoats. A special problem is the termination of the electrostatic shield. To prevent breakdown at this point additional paper insulation is wrapped over the cable insulation so that the thickest part of the wall coincides with the stress-relieved end of the shield. Above this point the insulation thickness is gradually reduced to form a stress cone, which keeps the tangential stress to a minimum. This will prevent sliding discharges along the critical interface between solid and oil insulation.

Ampacity

The highest safe operating temperature of the oil-paper insulation sets a limit to the current that the conductor may be allowed to carry. In a self-cooled cable the hottest part of the insulation is the layer right next to the conductor. For all practical purposes this is considered to be at the conductor temperature T_c, which thereby becomes the limiting parameter of cable ampacity.

Temperature endangers oil-paper insulation for two reasons. At some level, normally above 120°C, it gives rise to thermal instability breakdown which has been discussed in Section 2.5. But even below this level, temperature does do some harm through accelerated aging of the insulation. The slow decomposition of cellulose proceeds at a strongly temperature-dependent rate. As Endacott [3.6] has pointed out, chemical reactions of this sort double their rate with about every 9°C rise in temperature. He quotes the

example of a cable that has a 300 year life at 40°C and would last only 10 years at 85°C, which is the temperature to which many power companies allow their cable conductors to rise. Of course the cable temperature is never constant and therefore the specified 85°C limit gives a much longer cable lifespan than 10 years.

To find the maximum permissible ac cable current, and therefore the transmission capability of the circuit, it is necessary to calculate all the heat generated at the various sources and a number of thermal resistances per unit length of cable. The cable considered in this section contains essentially three sources of heat. They are the conductor loss P_c, the dielectric loss P_d, and the sheath loss P_s. All three losses per unit length of cable may be computed with formulas developed in Sections 1.8 to 1.17 and 2.5. The thermal resistivity of the metallic components is negligible compared to that of the insulation and the soil. It may therefore be assumed that all the conductor heat arises at the conductor surface and the sheath heat at the sheath surface. By the same token, the flow of the conductor and dielectric heats through the cable sheath causes no measurable temperature drop across the sheath.

Referring to Fig. 3.13, we may express the temperature drop between the conductor and the soil surface temperature T_s in Endacott's form [3.6]

$$T_c - T_s = P_c(R_i + R_j + kR_e) + P_d(0.5R_i + R_j + kR_e) + P_s(R_j + kR_e) \quad (3.4)$$

R_i is the thermal resistance of unit length of the insulation wall given by (2.80). As proved with (2.79) and (2.81), the temperature drop across the insulation due to the dielectric losses is equal to the product of the loss and half the thermal insulation resistance R_i. R_j, the jacket resistance, may also be calculated with (2.80). The numerical factor k, known also as the thermal proximity factor, is greater than unity and accounts for the heating of the central cable by the two outside cables. The middle cable of Fig. 3.9 will run hotter than the two adjacent cables and therefore its current carrying capability will fix the ampacity of the three-phase circuit.

To calculate the soil thermal resistance R_e, the ground is assumed to be of uniform thermal resistivity ρ_e and advantage is taken of the fact that the ground surface is an isothermal of the heat sink temperature T_s. Because of the good thermal conductivity of the metallic cable sheath, the cable surface temperature T_0 may also be taken as an isothermal. Figure 3.14(a) shows the heat flux field from the cable to the soil surface. This flux is equivalent to the field between the cable C and its thermal image I as indicated on Fig. 3.14(b), both being immersed in a medium of resistivity ρ_e. Given the heat generated per unit length of cable as P/L, the flux density along a line of

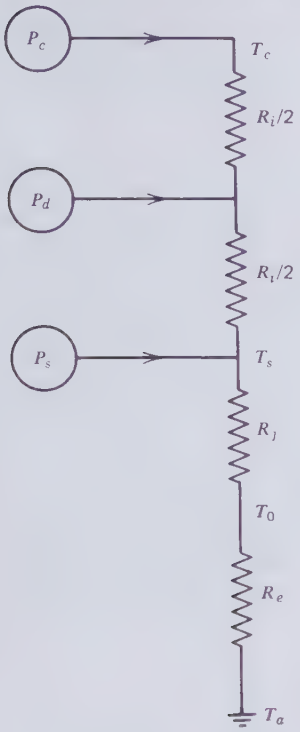

Figure 3.13 Thermal circuit of naturally cooled self-contained cable.

flux is $P/(2\pi L)$. It will be recognized that the thermal image field corresponds to the electrostatic field of a two-wire line. The temperature T_X (potential) at some point X (see Fig. 3.14) is given by

$$T_X = -\frac{P\rho_e}{2\pi L}\frac{1}{x_c} + \frac{P\rho_e}{2\pi L}\frac{1}{x_i} \tag{3.5}$$

The temperature differential $(T_X - T_a)$ between X and the image heat sink may be obtained by integrating the potential.

$$T_X - T_a = -\frac{P\rho_e}{2\pi L}\int_r^{x_c}\frac{dx}{x} + \frac{P\rho_e}{2\pi L}\int_r^{x_i}\frac{dx}{x} \tag{3.6}$$

where r is the radius of the cable and its image. The integration of (3.6) results in

$$T_X - T_a = \frac{P\rho_e}{2\pi L}\ln\frac{x_i}{x_c} \tag{3.7}$$

To obtain the temperature difference between the cable surface and the heat sink ($T_0 - T_a$), the point X must be moved to X' on Fig. 3.14(b), which lies on the periphery of the cable. Writing (3.7) for X' gives the soil thermal resistance

$$R_e = \frac{T_0 - T_a}{P} = \frac{\rho_e}{2\pi L} \ln \frac{2D - r}{r} \tag{3.8}$$

The cable length L has been retained to show that (3.8) is dimensionally correct with R_e being expressed, for example, in thermal-Ω, ρ_e in thermal-Ω·cm and L in cm. In most practical cases $D \gg r$ and (3.8) approximates to

$$R_e \simeq \frac{\rho_e}{2\pi L} \ln \frac{2D}{r} \tag{3.9}$$

To derive the thermal proximity factor k use is again made of the method of thermal images as indicated in Fig. 3.15. According to (3.7), the temperature rise of cable 2 above T_a due to the heat it receives from cable 1 may be

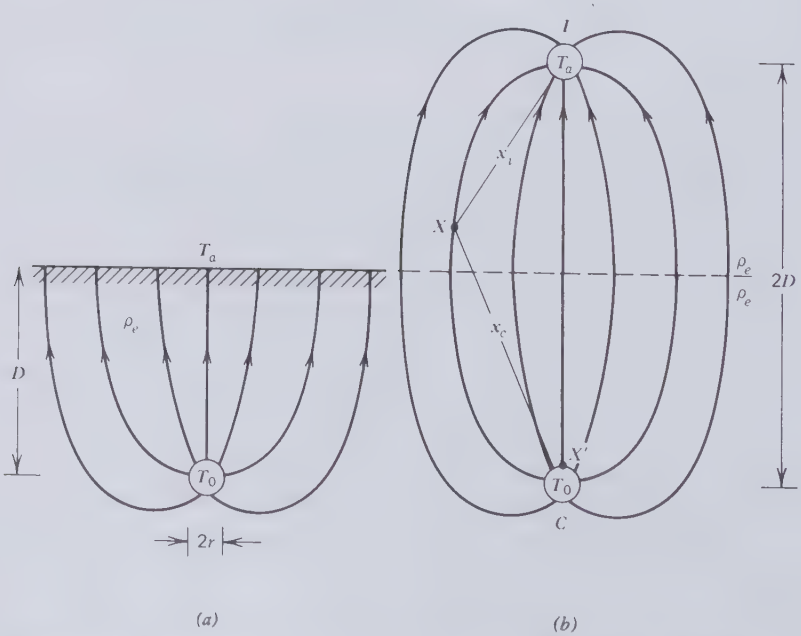

Figure 3.14 Thermal image method of calculating the soil thermal resistance R_e.

expressed by

$$T_{2,1} - T_a = \frac{P\rho_e}{2\pi L} \ln \frac{x_{1',2}}{x_{1,2}} \tag{3.10}$$

Similarly, the temperature rise of cable 2 due to the heat it receives from cable 3 may be written

$$T_{2,3} - T_a = \frac{P\rho_e}{2\pi L} \ln \frac{x_{3',2}}{x_{3,2}} \tag{3.11}$$

And from (3.9), the temperature rise of cable 2 due to its own heat dissipation is

$$T_{2,2} - T_a = \frac{P\rho_e}{2\pi L} \ln \frac{2D}{r} \tag{3.12}$$

The total temperature rise at the surface of cable 2 above ambient is given by the sum of equations (3.10), (3.11), and (3.12), or

$$T_0 - T_a = \frac{P\rho_e}{2\pi L} \left(\ln \frac{2D}{r} + \ln \frac{x_{1',2} x_{3',2}}{x_{1,2} x_{3,2}} \right) \tag{3.13}$$

If R_e is the soil thermal resistance of an isolated cable as given by (3.9), the thermal proximity factor k is defined by

$$kR_e = \frac{\rho_e}{2\pi L} \left(\ln \frac{2D}{r} + \ln \frac{x_{1',2} x_{3',2}}{x_{1,2} x_{3,2}} \right) \tag{3.14}$$

Dividing both side of (3.14) by R_e finally gives

$$k = 1 + \frac{\ln \dfrac{x_{1',2} x_{3',2}}{x_{1,2} x_{3,2}}}{\ln \left(\dfrac{2D}{r} \right)} \tag{3.15}$$

How important the thermal proximity factor is will be seen from the following typical example.

$$D = 36 \text{ in.} \qquad S = 12 \text{ in.} \qquad r = 2 \text{ in.}$$

Then

$$x_{1',2} = x_{3',2} = \sqrt{72^2 + 12^2} = 73$$

$$k = 1 + \frac{\ln \dfrac{73^2}{12^2}}{\ln \dfrac{72}{2}} = 2$$

Therefore mutual cable heating can have the effect of doubling the soil thermal resistance.

The thermal resistivity of the soil will almost certainly vary along the cable route. In addition, at any given spot, it will also vary with time depending largely on the moisture content. For these reasons a conservative figure has to be chosen in the calculation of cable ampacity and it must also make an allowance for interface resistances, which have been ignored in the analysis. Frequently the choice of a soil resistivity value is based on the results of field surveys. Typical figures used in cable design fall into

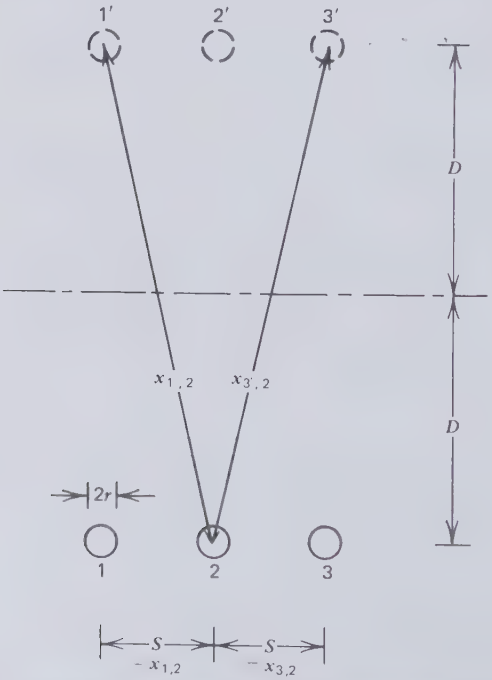

Figure 3.15 Thermal images of three naturally cooled cables in flat formation.

the range 80 to 120 thermal-Ω·cm. Taking $\rho_e = 90$ thermal-Ω·cm, the soil thermal resistance in the example just quoted comes to

$$R_e = \frac{90}{2\pi} \ln \frac{72}{2} = 51.33 \text{ thermal-}\Omega \text{ (per cm)}$$

$$= 1.68 \text{ thermal-}\Omega \text{ (per ft)}$$

If the cable has the following dimensions

conductor diam = 2 in.	sheath thickness = 0.12 in.
insulation thickness = 0.7 in.	jacket thickness = 0.18 in.

and the thermal resistivities of the oil-paper insulation and the jacket material are 500 and 350 thermal-Ω·cm respectively, the remaining two thermal resistances come to

$$R_i = \frac{500}{2\pi} \ln 1.7 = 42.23 \text{ thermal-}\Omega \text{ (per cm)}$$

$$= 1.39 \text{ thermal-}\Omega \text{ (per ft)}$$

$$R_j = \frac{350}{2\pi} \ln \frac{2}{1.82} = 5.25 \text{ thermal-}\Omega \text{ (per cm)}$$

$$= 0.17 \text{ thermal-}\Omega \text{ (per ft)}$$

Before computing the maximum permissible current from (3.4), it must be recognized that both the conductor and the sheath loss will be proportional to the square of the current.

$$P_c = I^2 R_{ac} \tag{3.16}$$

$$P_s = I^2 R_s' \tag{3.17}$$

where R_s' is the equivalent sheath resistance defined in Section 1.13. Substituting (3.16) and (3.17) into (3.4) and solving for the current, it is found that

$$I = \sqrt{\frac{T_c - T_a - P_d(0.5R_i + R_j + kR_e)}{R_{ac}(R_i + R_j + kR_e) + R_s'(R_j + kR_e)}} \tag{3.18}$$

The dielectric loss P_d may be calculated from (2.81). For a system voltage of 300 kV, an insulation power factor of $\cos\phi = 3 \times 10^{-3}$ and the dielectric

constant $\varepsilon = 3.5$, we find for the foregoing example

$$P_d = \frac{2\pi \times 60 \times 3.5 \left(\frac{300 \times 10^3}{\sqrt{3}} \right)^2 \times 3 \times 10^{-3}}{2 \ln 1.7 \times 9 \times 10^{11}}$$
$$= 0.124 \text{ W/cm} = 3.79 \text{ W/ft}$$

For the sake of completing the example and without considering the details of the conductor design, assume it to be made of copper and that at the maximum conductor temperature of $T_c = 85°C$ it has an ac resistance of 4.6×10^{-6} Ω/ft, whereas the sheath adds 5 percent to the effective conductor resistance, or $R_s' = 0.2 \times 10^{-6}$ Ω/ft. Taking the ambient temperature to be $T_a = 20°C$, we have all the data needed to compute the maximum permissible steady current from (3.18).

$$I = \sqrt{\frac{85 - 20 - 3.79(0.5 \times 1.39 + 0.17 + 2 \times 1.68)}{4.6 \times 10^{-6}(1.39 + 0.17 + 2 \times 1.68) + 0.2 \times 10^{-6}(0.17 + 2 \times 1.68)}}$$
$$= 1449 \text{ A}$$

Ampacity computations are seen to be tedious asnd when a range of design parameters have to be evaluated it is advantageous to employ a computer.

A more descriptive term than ampacity is continuous current rating. In the unlikely event of a transmission circuit being installed in ducts, it would have to be adjusted downward. The additional thermal resistances of the duct wall and the air space then have to be inserted between the jacket and soil thermal resistances. Equation (2.80) may be used for the duct wall but the radiation and convection heat transfer in the air space poses a more difficult problem. Buller and Neher [3.7] derived the following formula for the resistance R_g of the air space between cable and duct wall

$$R_g = \frac{1}{2r\left[A\left(\frac{\Delta T p^2}{2r} \right)^{1/4} + B + CT_m \right]} \quad \text{thermal-}\Omega \text{ (per ft)} \qquad (3.19)$$

where

r = cable radius in inches

p = gas pressure in atmospheres

ΔT = temperature drop across gas space in °C

T_m = mean gas temperature in °C

Table 3.2 Constants of (3.19) according to Neher and McGrath [1.19]

	A	B	C	Average ΔT (°C)
Cable in metallic conduit	0.07	0.121	0.0017	20
Cable in fiber duct in air	0.07	0.036	0.0009	20
Cable in fiber duct in concrete	0.07	0.043	0.0014	20
Cable in transit duct in air	0.07	0.086	0.0008	20
Cable in transit duct in concrete	0.07	0.079	0.0016	20
Gas-filled pipe-type cable at 200 p.s.i.	0.07	0.121	0.0017	10

A, B, and C are constants, which, together with ΔT, are listed in Table 3.2. This table has been compiled by Neher and McGrath [1.19].

From time to time and for a variety of reasons, short sections of an underground line may have to be installed above ground in free air. An example is a river crossing underneath a bridge. It is fair to assume, in general, that air cooling is more effective than ground cooling, provided the cable is not exposed to direct sunlight. Figure 3.16 brings out the difference between soil and air cooling. For the same current and voltage, the surface temperature of the cable in air will be lower than that of the buried cable. Besides, the temperature of the underground cable rises very slowly because of the thermal mass of the soil.

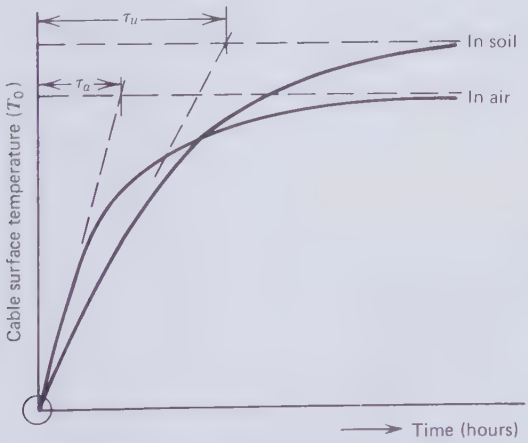

Figure 3.16 Rise of cable surface temperature after switching on full load current.

The radiation loss from the cable in air is given by the Stefan-Boltzmann law

$$W_r = 2\pi r k_r \xi \left[(T_0 + 273)^4 - (T_a + 273)^4 \right] \quad \text{W/cm} \tag{3.20}$$

where k_r is the radiation constant equal to 5.67×10^{-12} W·cm^{-2}·°K^{-4}, ξ is a factor depending on the emissivities of the emitting and receiving surfaces, r is the cable radius in centimeters, and the temperatures have to be expressed in degrees Kelvin. Little is usually known about the emissivities, but for a black plastic jacket a figure of 0.8 to 0.9 for ξ should be reasonable. A further difficulty with (3.20) is that T_0 cannot be established until the total heat dissipation from the surface is known.

For the convective loss W_c in still air at the ambient temperature T_a Neher and McGrath quote the following formula

$$W_c = 2\pi r k_c \Delta T \left(\frac{\Delta T}{2r} \right)^{1/4} \quad \text{W/cm} \tag{3.21}$$

where r is the cable radius in centimeters, $\Delta T = T_0 - T_a$, and $k_c = 3.32 \times 10^{-4}$ is a convection constant chosen for best agreement with experiment. On Fig. 3.17 the radiative and convective heat transfer from a cable of 5 cm radius, an emission factor of 0.8 placed in still ambient air of 25°C has been plotted against surface temperature T_0 in accordance with (3.20) and (3.21). This shows the relative importance of radiation cooling. In a gentle wind, however, the convection term would have to be increased considerably. The heat generated in the previously considered cable is indicated on Fig. 3.17 by the broken line. This amount of heat can be dissipated from the cable when the surface temperature is 41.3°C. The conductor temperature corresponding to this surface temperature may be derived from the thermal circuit of Fig. 3.13 by

$$T_c - T_0 = \frac{P_c R_i}{2} + \frac{(P_c + P_d) R_i}{2} + (P_c + P_d + P_s) R_j \tag{3.22}$$

Earlier the various parameters were calculated to be

$$P_c = 0.317 \text{ W/cm} \qquad R_i = 42.23 \text{ thermal-}\Omega \text{ (per cm)}$$

$$P_d = 0.124 \text{ W/cm} \qquad R_j = 5.25 \text{ thermal-}\Omega \text{ (per cm)}$$

$$P_s = 0.014 \text{ W/cm}$$

From this data and (3.22), it may be confirmed that the conductor temperature lies less than 20°C above T_0 and therefore well below the safe limit of

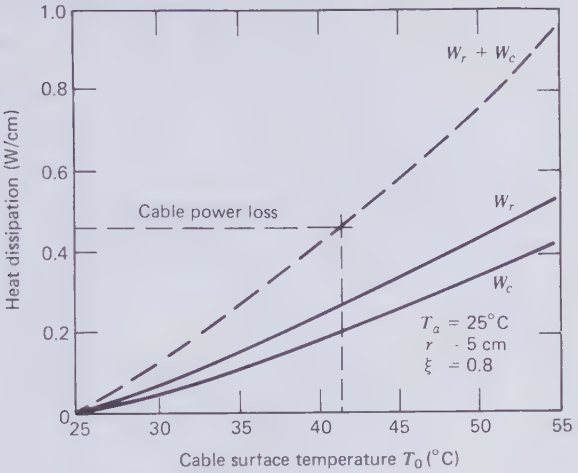

Figure 3.17 Heat dissipation of cable in air.

85°C for which the underground section was designed. This example illustrates how effective air cooling is if the cable is not exposed to direct sunlight.

Daily Cycle Rating

Power transmission lines are rarely called upon to carry their nominal ampacicity for long periods of time. Under normal circumstances most lines are subject to recurring daily load cycles. Shape and peak value of the cycle may change over the years. Because of the large time constant τ_u of the underground circuit indicated on Fig. 3.16, the conductor temperature will not reach the steady state value corresponding to the peak load. Therefore the cable may safely be allowed to carry more current than the ampacity rating. The additional load transfer capability can be calculated from the time constant and the daily load cycle curve.

Figure 3.18 shows a possible shape of the recurring load cycle. Consider the extreme case when the peak load (100%) is equal to the cable ampacity. The particular load cycle of Fig. 3.18 is associated with an average load of 70 percent, which is also called the load factor. Except when the load is 100 percent, the cable loss percentage will be less than the load percentage because the current dependent loss is proportional to the square of load. The loss cycle curve also shown in Fig. 3.18 has been calculated for a fixed dielectric loss of 20 percent of the total peak loss. The average loss for this load cycle was then found to be 63 percent.

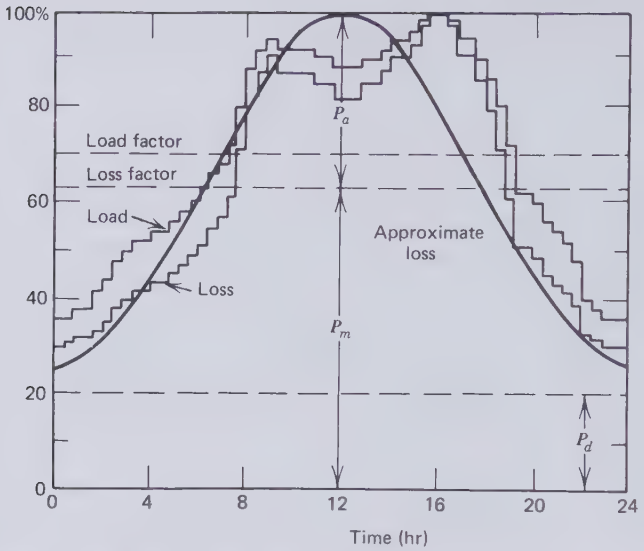

Figure 3.18 Daily loss and load cycles and sinusoidal approximation to loss cycle.

For analytical purposes it is convenient to divide the loss in a constant part, or the mean loss P_m, and a sinusoidally varying loss with an amplitude P_a. As already mentioned, the underground time constant is largely due to the thermal capacity of the soil. To examine its transient behavior as a heat transfer medium, the soil will be represented by the thermal circuit of Fig. 3.19 in which the thermal resistance R_e is shunted by the soil thermal capacity C_e. This can only be an approximation as both the resistance and the capacitance will to some extent be temperature sensitive. P is the heat flow from unit length of cable leaving the surface at temperature T_0 and arriving at the atmospheric heat sink at temperature T_a. From the electrostatic equivalent of this circuit it is known that the heat fluxes through the capacitive and resistive branches are

$$P_x = Pe^{-t/\tau_u} \tag{3.23}$$

$$P_r = P(1 - e^{-t/\tau_u}) \tag{3.24}$$

The heat flowing through the thermal resistance must be driven by the temperature difference

$$T_0 - T_a = P(1 - e^{-t/\tau_u})R_e \tag{3.25}$$

The heat flow in the capacitive branch fills the thermal capacity, or

$$T_0 - T_a = \frac{1}{C_e}\int_0^t P e^{-t/\tau_u}\,dt$$

$$= \frac{P\tau_u}{C_e}(1 - e^{-t/\tau_u}) \tag{3.26}$$

From (3.25) and (3.26) the thermal time constant is found to be

$$\tau_u = R_e C_e \tag{3.27}$$

The average heat flow P_m is accompanied by the temperature differential $P_m R_e$ and this will be modulated by the cyclic heat flow through the complex circuit of Fig. 3.19. Sinusoidal heat flow through the parallel $R-C$ combination will encounter the thermal impedance

$$Z_e = \frac{R_e}{\sqrt{1+\omega R_e C_e}} = \frac{R_e}{\sqrt{1+\omega\tau_u}} \tag{3.28}$$

Therefore the cyclic part of the heat flow meets a smaller impedance than R_e and this accounts for the increase in cyclic cable rating over the continuous ampacity.

The temperature difference between cable surface and the atmospheric heat sink may now be written

$$T_0 - T_a = P_m R_e + P_a Z_e \tag{3.29}$$

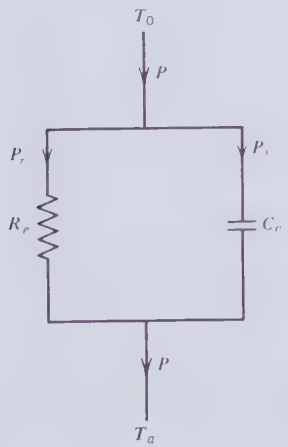

Figure 3.19 Thermal circuit of soil.

Substituting (3.28) into (3.29) and dividing throughout by P_{max}, the heat flow at 100 percent load, it is found that

$$R_e' = \frac{T_0 - T_a}{P_{max}} = \left(\frac{P_m}{P_{max}}\right) R_e \left(1 + \frac{P_a/P_m}{\sqrt{1+\omega\tau_u}}\right) \tag{3.30}$$

where R_e' is the cyclic thermal resistance of the soil modified for the particular load and loss cycles of Fig. 3.18. If $P_m/P_{max} = \alpha$, the loss factor, (3.30) may also be written

$$R_e' = \left(\alpha + \frac{1-\alpha}{\sqrt{1+\omega\tau_u}}\right) R_e = \beta R_e \tag{3.31}$$

Hence to obtain the cyclic thermal resistance of the soil, the previously derived soil resistance R_e has to be multiplied by a factor β, which is a function of the loss factor and the thermal time constant of the soil.

It is easy to compute the loss factor from the load cycle curve and the formulas for conductor, dielectric, and sheath losses. However, the only reliable way of obtaining the thermal time constant is by direct experiment with a piece of cable in the appropriate soil environment. In Fig. 3.20 the cyclic soil resistance factor β has been charted over representative ranges of τ_u and the loss factor α. The time constant increases with cable laying depth D and cable radius r. Transmission circuits laid 36 in. deep would be

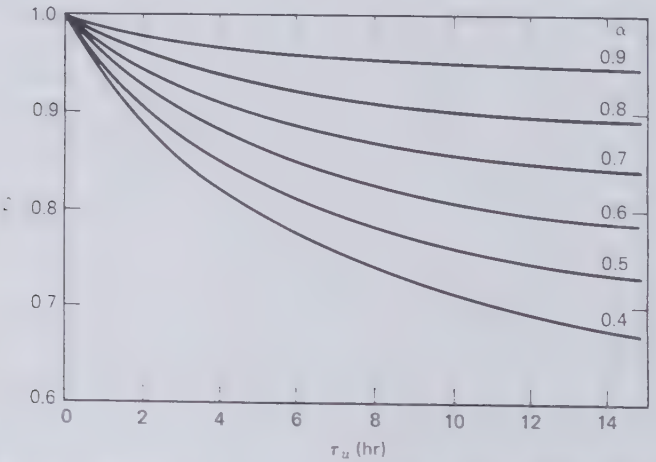

Figure 3.20 Cyclic soil resistance factor β as a function of the soil thermal time constant and the loss factor α.

expected to have thermal time constants between 5 and 10 hr depending on soil density and water content. The radian frequency in (3.21) is given by

$$\omega = 2\pi f = \pi/12 \quad \text{rad/hr} \tag{3.32}$$

To compute the daily cycle rating of a naturally cooled self-contained cable system, R_e' has to be substituted for R_e in (3.18). Assuming $\beta = 0.85$, the peak current of the numerical example on page 300 works out to be 1570 A instead of the continuous ampacity of 1449 A. This represents an 8 percent increase or, as it is sometimes called, a cyclic rating factor of 1.08. Barnes [1.34] quotes a blanket cyclic rating factor of 1.13 for all naturally cooled self-contained transmission cables. With respect to the numerical example of page 300, this would imply $\beta = 0.75$, which is attainable with a loss factor of $\alpha = 0.5$ and a thermal time constant $\tau_u = 11$ hr. These figures are typical for large underground cable circuits.

Forced Cooling

Forced cooling of underground circuits was introduced in the 1950s to guard against hot spots at unforeseen and also some predictable locations along cables. Axial flow cooling makes cables largely, if not completely, independent of their thermal surroundings and therefore permits greater freedom in the selection of cable routes. Installation at greater depth, to pass under obstructions, and through less conducting underground environments becomes possible. Forced cooling has become a means of increasing trench power density and in some instances it has been traded for conductor metal. Ultimately forced cooling must be justified by savings in transmission cost. Without going to cryogenic temperatures it does not reduce the energy wastage, but rather increases it through pumping losses and the power required for driving heat-exchange equipment, and savings have to come from reduced capital investment per unit installed transmission capability. The drastic increase in the price of energy since the 1973 oil embargo has changed the economics of power transmission in a direction that makes forced cooling less attractive than it has been before. After all, for the extra cooling to be effective, a considerable amount of electricity has to be first converted to waste heat. If the high cost of energy persists, it inevitably places renewed emphasis on the reduction of losses with larger conductors and the increase of transmission capability without additional cooling.

Some important self-contained oil-paper insulated cables are being cooled with flowing water or oil in a variety of ways. No two installations appear to be exactly alike and the whole field of forced cooling is in a state of evolution. The first water-cooled cables were installed by Ontario Hydro, and they have been described by Ralston and West [3.8]. Their method

relies on indirect cooling via the soil close to the cables and in contact with parallel water pipes, as can be seen on Fig. 3.21(a). Extensive use of this form of indirect cooling has been made on the 275 kV underground system of London [3.9].

While the Canadian installation utilized plastic water pipes, the early forced cooled cables in London relied on corrugated aluminum tubes of 2.6

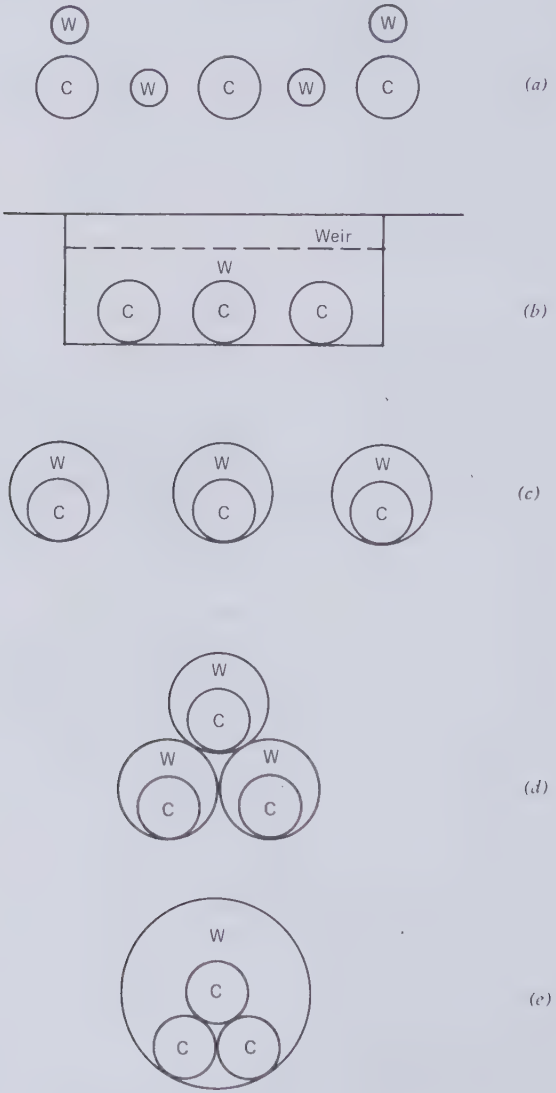

Figure 3.21 External water cooling arrangements.

in. bore operating at 125 psi and being covered with a polyethylene anticorrosion jacket. Induced currents in the aluminum pipes added 20 percent to the heat load and the corrugations were found to cause extra pressure drop. Since then polyethylene pipes reinforced to withstand 50 psi at 50°C have been employed. The parallel water pipes are small enough in diameter to be reeled and laid in long length.

Artificial cooling highlighted a splice problem, which until then had been glossed over. The greater thickness of paper insulation over the conductor splice raises the splice temperature over the average conductor temperature. As can be seen in Fig. 3.22, on a naturally cooled cable, this temperature elevation is of the order of 5 to 10°C. But with external forced cooling, a large part of the heat no longer has to flow through the soil and the thermal resistance of the insulation becomes the dominant factor governing the conductor temperature. This can result in the splice temperature rising as much as 30°C above the average conductor temperature, according to an analysis by Hitchcock and Thewell [3.14] of 275 kV, 2500 kcmil cable. This

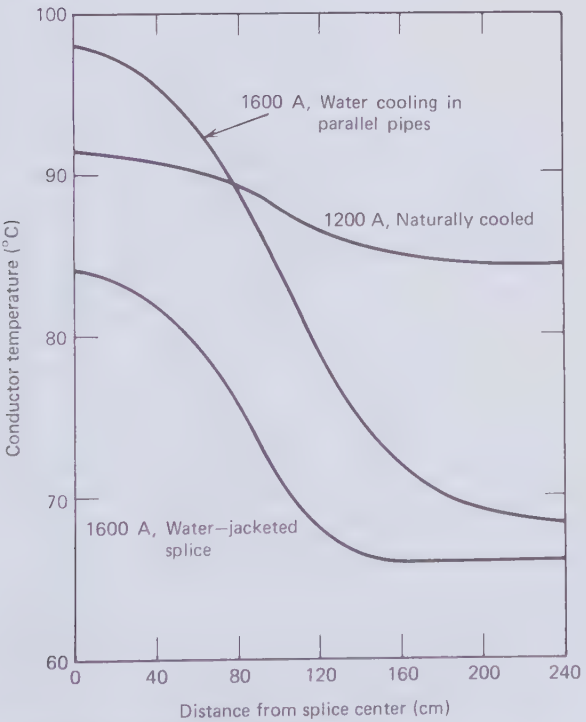

Figure 3.22 Conductor temperature distribution along 275 kV, 2500 kcmil oil-paper cable splice [3.14]. (By permission of the Institute of Electrical and Electronics Engineers).

calculated temperature distribution is also plotted on Fig. 3.22. A water jacket around the splice housing, as Hitchcock and Thewell have shown, can reduce the temperature differential to 18°C. Another method of dealing with the overheating of splices is to reduce the thermal resistance above the conductor joint by substituting epoxy resin for oil-paper insulation.

Figure 3.23 by Cox [3.9] outlines the basic elements of a water-cooling station with air blast heat exchangers. Where conditions allow it, cooling towers and water chillers may be used that have the advantage of being more effective and less noisy. In Cox's design water is being pumped for 1 mile in both directions away from the cooling station and then turned around by manifolds to flow back to the heat exchangers. This results in a cooling module of 2 mile length. The purpose of the header tank is to permit free expansion and contraction of the water volume in the pipes with variations in ambient temperature and during load cycles. In addition the tanks provide make-up water and generally control the static pressure in the system.

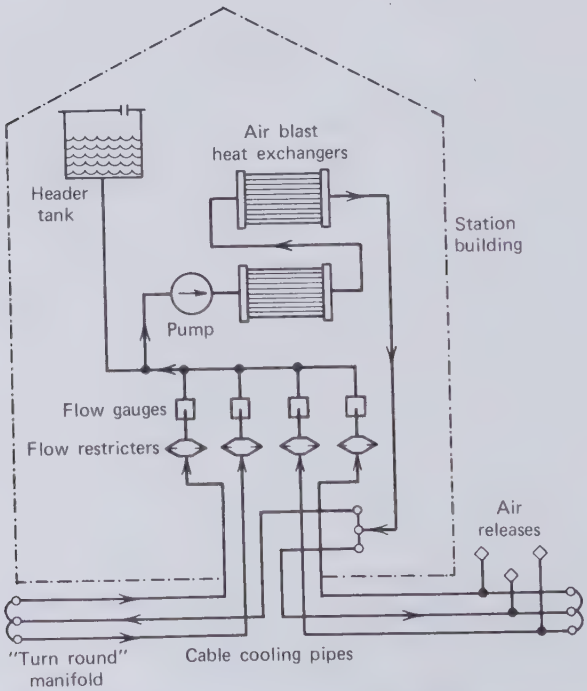

Figure 3.23 Water cooling station with air blast heat exchangers according to Cox [3.9]. (By permission of Electrical Review).

Forced cooling with parallel water pipes has not proved to be as cost effective as water immersion of the cables in troughs or the large surrounding pipes shown in Fig. 3.21(b–e). Troughs are feasible only when the cable route is nearly horizontal and some have been installed along railroads and canals. Just as in canals, the water flow in cooling troughs is controlled by gravity and a series of weirs. Troughs constructed of concrete channels with a protective lid may contain considerable quantities of water. Flow restrictions due to sediments and the use of impure water are not as detrimental as they would be in enclosure pipes.

The integral sheath cooling of Fig. 3.21(c–e) appears to be the preferred method of forcibly cooling self-contained cables with oil-paper or extruded polyethylene insulation. Quite large water pipes are required even if they enclose just one of the three cores. Rigid PVC pipes with and without glass fiber tape reinforcement may be jointed by welding. Fiberglass reinforced epoxy resin pipes would be stronger but more costly. Metal pipes may be considered for the three-core design of Fig. 3.21(e) which is similar to pipe-type cables. Water corrosion would appear to rule out carbon steel pipes, but there are no technical reasons that would eliminate stainless steel, cement-lined cast iron or aluminum pipes. The magnetic losses in cast iron should be less than in the steel of pipe-type cables.

Enclosing water pipes have to have clear internal diameters ranging from 6 to 12 in. They cannot be stored and shipped on reels and short pieces from 20 to 60 ft length have to be joined in the field. The water pipes must not only be able to withstand considerable hoop stress but also external pressure applied during installation, the abrasion of cable pulling-in, and the impact forces caused by short-circuit currents that repel the cables cores from each other. Clean and preferably demineralized water should be used to prevent the build-up of deposits and the constriction of flow area. It is uneconomical to install water pipes that are large enough to accept cable splices. Therefore special provision has to be made for splice cooling. The cooling pipe should extend right up to the cable terminations or larger conductor cable sections have to be inserted between potheads and the main cable run.

Loss reductions brought about by sheath cross-bonding are so valuable that they cannot be given up in water-cooled systems. The cleanest water that can be afforded is still too much of a conductor of electricity that it would in fact bridge the sheath gap. Therefore the cable sheath has to be insulated from the cooling water by a polyethylene or similar watertight jacket. At splice positions, insulated sheath connections have to be made and brought out through the waterjacket to cross-bonding links.

More so than in connection with naturally cooled cables, the design of forced cooled circuits has to take note of the large thermomechanical forces of expansion and contraction set up mainly by the conductor. These forces

are proportional to the cross-sectional area of the conductor. Copper, aluminum, and lead have linear thermal expansion coefficients of 16.5, 23.6, and 29.2×10^{-6}, in this order. The axial expansion of a copper conductor during warm-up from 25 to 85°C amounts to 0.1 percent. If the cable is constrained from movement by the soil and fixed terminations, the end thrust of the conductor will correspond to 0.1 percent of strain. As the longitudinal compression modulus of a stranded conductor is not a well-defined quantity, this thrust must be measured [3.15]. A typical figure for a 4000 kcmil constrained conductor is 10 tons. Lateral freedom of motion of the cable relieves much of the compressive stress. As the cable is being pulled into the water pipe, it is likely to retain some reel set rather than lie straight in the duct. While trying to expand, the cable is most likely to assume some helical shape and act like a compression spring. After accommodation in the water pipe, some of the compressive stress may be relieved, giving rise to tension during the cool-down phase of the load cycle. Since the large cable splices cannot move inside the water pipe, it becomes necessary to anchor each splice to the ground in such a way that it will withstand the slowly oscillating forces without harm to the high-voltage insulation.

A further complicating factor is the differential thermal expansion between conductor and sheath. Although both aluminum and lead have larger coefficients of expansion than copper, the sheath temperature rise with integral cooling is only approximately one third that of the conductor. The length mismatch is then of the order of 0.05 percent. Conductors as large as those used in forced cooled cables are stronger than lead or corrugated aluminum sheath, with the result that the conductor will deform the sheath in lateral cable motion. There is reason to fear that this cyclic deformation could produce fatigue failures in lead pipes but not in aluminum. It will certainly strain the joints between cable sheaths and splice casings and is known to have caused oil leaks at these positions. Relative axial motion in the oil-paper insulation can be accommodated by the layered tape structure, which is a unique advantage that this type of insulation has over solid polyethylene. It will further be appreciated that during the warm-up phase the insulation wall is subject to additional radial compression because of the expanding diameter of the stranded and slightly birdcaging conductor.

Figure 3.24 is a diagram to aid coolant temperature calculations. A single-core cable enclosed in a water pipe is being considered. The various physical quantities entering the calculations are also defined by the diagram. It will be appreciated that water flow in parallel pipes or the enclosure of more than one cable core in the same pipe can be treated in a similar manner.

Consider the length element dx in Fig. 3.24. The coolant contained in this element will receive heat from the cable at the rate of $(P/L)dx$. Part of this

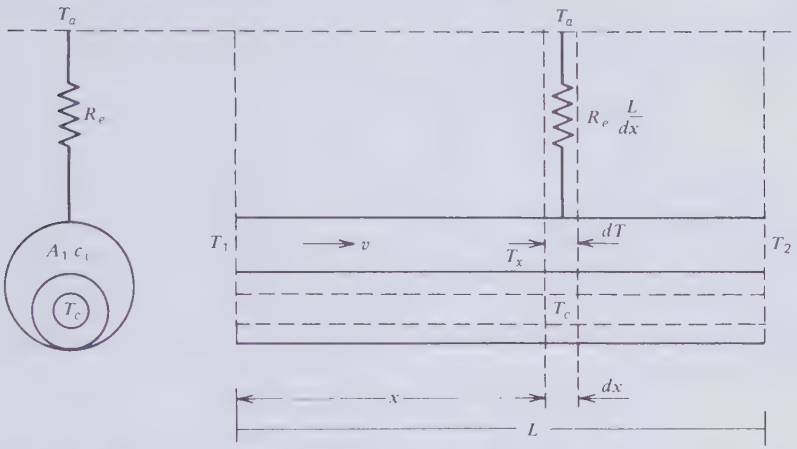

Figure 3.24 Rise in coolant temperature. A—Coolant flow area (cm^2). c_v—Specific heat at constant volume of coolant (J/cm^3). T_x—Coolant temperature at distance x from inlet (°C). T_1—Coolant inlet temperature (°C). T_2—Coolant outlet temperature (°C). L—Cable length (cm). P—Total heat flow from cable to coolant (W). R_e—Thermal resistance between ambient and coolant water over total length of cable (thermal-Ω). v—Coolant flow velocity (cm/sec).

will be stored in the coolant as sensible heat and the rest is transmitted through the coolant to the soil. The transmitted part is $[(T_x - T_a)/(LR_e)]dx$. In the case of water the thermal resistance of the coolant itself may be ignored and the pipe wall resistance is also very small compared to R_e. Therefore the heat balance equation for the coolant element is

$$\frac{P}{L}dx = c_v Av \cdot dT + \frac{T_x - T_a}{LR_e}dx \tag{3.33}$$

Separating the variables x and T_x of this equation and integrating from the water inlet to x results in

$$\int_0^x \frac{dx}{Lc_v AvR_e} = \int_{T_1}^{T_x} \frac{dT}{PR_e - (T_x - T_a)} \tag{3.34}$$

The solution of (3.24) is

$$\frac{x}{Lc_v AvR_e} = \ln\left[\frac{PR_e - (T_1 - T_a)}{PR_e - (T_x - T_a)}\right] \tag{3.35}$$

and therefore

$$T_x - T_a = PR_e - [PR_e - (T_1 - T_a)]e^{-x/(Lc_v AvR_e)} \tag{3.36}$$

When $x = L$, (3.36) gives the coolant temperature rise $T_2 - T_1$ which determines the cable ampacity, or

$$T_2 - T_a = PR_e - [PR_e - (T_1 - T_a)]e^{-1/(c_v A v R_e)} \tag{3.37}$$

The implications of (3.37) can best be seen from a practical example. Water has a specific heat of $c_v = 4.18$ J/cm°C. A pipe of 20 cm i. d. will be assumed to enclose a cable of 10 cm diam. This leaves a flow area of $A = 236$ cm^2. Let the ac transmission circuit be installed in flat formation at a depth of $D = 100$ cm and with a cable spacing of $S = 22$ cm. Taking the distance between coolant inlet and outlet to be $L = 2000$ m and the soil thermal resistivity $\rho_e = 120$ thermal-Ω·cm, (3.8) gives

$$R_e = \frac{120}{2\pi \times 2 \times 10^5} \ln \frac{200 - 5}{5} = 3.5 \times 10^{-4} \quad \text{thermal-}\Omega$$

This is the thermal resistance of the soil for the whole 2000 m length of cable. For unit length of 1 cm it is of course 2×10^5 times as large. The thermal proximity factor due to the mutual heating of the cables is given by (3.15).

$$k = 1 + \frac{\ln[(200^2 + 22^2)/22^2]}{\ln(200/5)} = 2.2$$

When using (3.37) for the three-phase circuit, R_e has to be multiplied by k. Let the power dissipation from each core be 1 W/cm, or $P = 2 \times 10^5$ W for the total length. The water inlet temperature and the ambient temperature will be taken as $T_1 = 30$°C, $T_a = 25$°C. Substituting figures into (3.37) then results in

$$T_2 = 25 + 154 - [154 - 5]e^{-1.317/v} = 179 - 149e^{-1.317/v}$$

The variation of T_2 with v is plotted in Fig. 3.25. Whether or not a certain flow velocity can be supported depends on the strength of the pipe, the static pressure due to route gradient and the pressure drop associated with pipe friction. Pressure drops for water pipes may be readily derived from flow charts as the one published in [3.17]. In the example under consideration the pressure drop over the 2000 m cooling length at a flow velocity of 100 cm/sec would be approximately 45 psi. Glass-fiber-reinforced rigid PVC pipes are available that can withstand 100 psi. In most cases it should be easy to achieve flow velocities of at least 50 cm/sec, which in the example

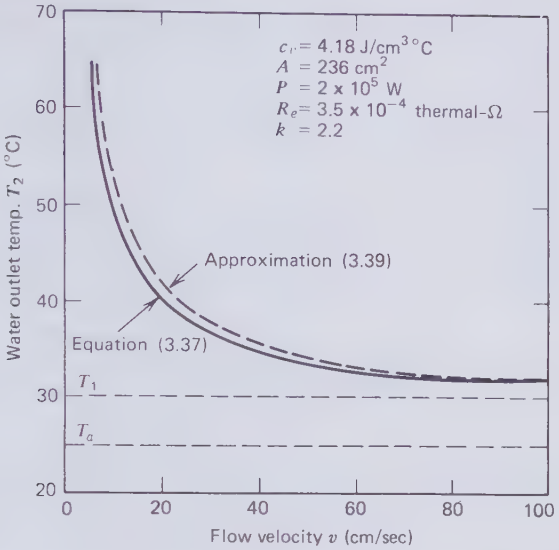

Figure 3.25 Water outlet temperature as a function of flow velocity of a 2000-m-long cooling section.

would bring the water outlet temperature within 4°C of the inlet temperature. Hence the cable surface temperature is virtually independent of the soil thermal resistance and the heating by adjacent cables.

Having recognized this fact, further calculations may be simplified by making the conservative assumption that all the cable heat is transported along with the coolant. In this simplified model the heat balance may be expressed by

$$P = c_v A v (T_2 - T_1) \tag{3.38}$$

The approximate coolant outlet temperature is

$$T_2 \simeq T_1 + \frac{P}{c_v A v} \tag{3.39}$$

This approximation is also plotted on Fig. 3.25. The ampacity of the cable is that steady current which brings the conductor temperature at the coolant outlet up to the thermal limit set by the insulation. Figure 3.26(a) shows the thermal circuit for this last piece of cable. There the temperature drop between conductor and coolant is

$$T_c - T_2 = I^2 R_{ac}(R_i + R_j) + P_d(0.5R_i + R_j) + I^2 R_s' R_j \tag{3.40}$$

Either (3.37) or (3.39) has to be substituted into (3.40). Using approximation (3.39) it is found that

$$T_c - T_1 = I^2 R_{ac}(R_i + R_j + R_w) + P_d(0.5R_i + R_j + R_w) + I^2 R_s'(R_j + R_w) \tag{3.41}$$

where $R_w = 1/(c_v A v)$, which is a thermal resistance associated with coolant flow as indicated in the thermal circuit of Fig. 3.26(b). A close approximation to the ampacity of the forced cooled circuit therefore is

$$I = \sqrt{\frac{T_c - T_1 - P_d(0.5R_i + R_j + R_w)}{R_{ac}(R_i + R_j + R_w) + R_s'(R_j + R_w)}} \tag{3.42}$$

R_w for the 20-cm-diam water pipe and a flow of 50 cm/sec would be $1/(4.18 \times 236 \times 50) = 2 \times 10^{-5}$ thermal-Ω of 1 cm length of cable. This is negligible compared with the thermal resistance of the insulation and the

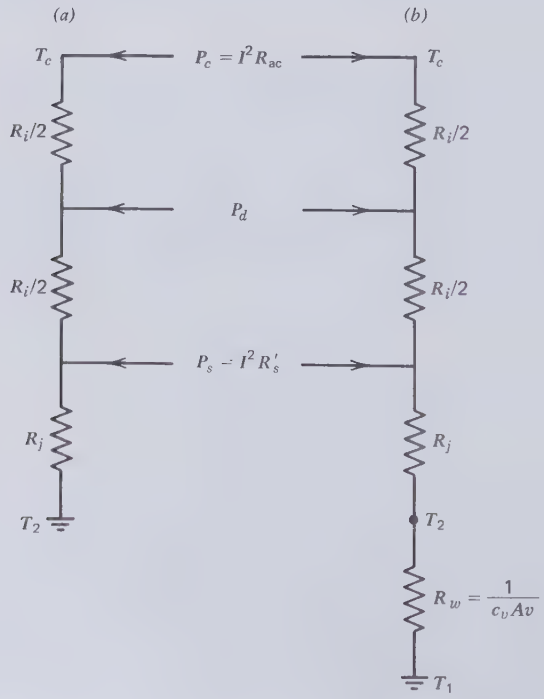

Figure 3.26 Thermal circuit for unit length of cable at the coolant outlet.

Table 3.3 Comparison of the 2000-m-long Naturally Cooled Circuit of Page 300 with the Forced Cooled Circuit of Page 314

	Naturally Cooled	Forced Cooled
Ampacity	1449 A	2678 A
Conductor loss	190.2 kW	649.8 kW
Sheath loss	8.3 kW	28.2 kW
Dielectric loss	74.4 kW	74.4 kW
Pumping loss	–	10.0 kW

jacket. As expected, therefore, the result of intensive cable surface cooling is the elimination of the soil thermal resistance as a factor limiting the cable ampacity given by (3.18) at the expense of raising the heat sink temperature from T_a to T_1. With $T_1 = 30°C$ instead of $T_a = 20°C$ in the example of page 314, integral water cooling of the self-contained cable circuit increases the ampacity from 1449 A to 2678 A. Table 3.3 compares the three-phase losses associated with these two ampacities, assuming that the 50 cm/sec flow rate can be achieved with a pumping loss of 10 kW over the three 2000-m-long pipes. The comparison indicates an 85 percent increase in ampacity due to forced cooling obtained at a loss penalty of 180 percent. These figures are typical of externally forced cooled underground lines.

As the soil is no longer participating in the cable cooling process, its heat storage capacity becomes unavailable for daily cycle rating purposes. The coolant outlet temperature follows load variations with a time lag that depends on the flow velocity and the length of the cooling module. Coolant transit times are of the order of 1 to 2 hr, which is relatively short compared to the thermal time constant of the soil. The daily cycle rating of an externally forced cooled cable is therefore the same or only a little higher than the continuous ampacity.

Self-contained oil-paper insulated cables may also be cooled by oil circulation through enlarged oil ducts. This makes possible heat extraction at the highest cable temperature and reduces the size of heat exchangers in the cooling stations. Enlarged oil ducts render the cable less flexible and increase the amount of insulation and sheathing material required. Consequently the duct diameter has to be kept reasonably small. Five centimeter ducts are readily achiveable. Figure 3.27 shows the cross section through a 345 kV, 5000 kcmil internally forced cooled cable, which has an overall diameter of approximately 6 in.

Oil flow in pipes will be treated in greater detail in a later section dealing with forced cooled pipe-type cables. For the time being, it may be assumed that a 1-mile coolant module relying for pressure containment on a strong

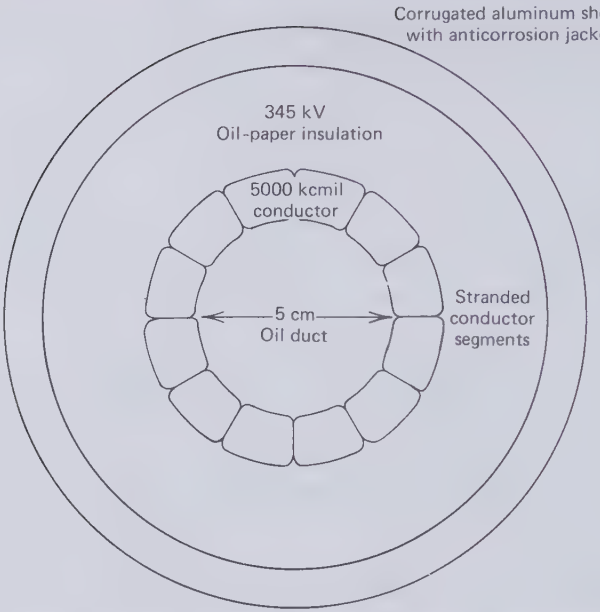

Figure 3.27 345 kV, 5000 kcmil internally forced cooled cable. Overall diameter = 6 in.

corrugated aluminum sheath can support flow velocities up to 150 cm/sec. Representative figures for oil density and specific heat at constant volume are $\delta = 0.86$ g/cm^3 and $c_v = 2.1$ J/g·°C. To ensure cooling of the last piece of the cable, the oil outlet temperature T_2 has to lie a few degrees below the maximum permissible conductor temperature. For oil inlet and outlet temperatures of $T_1 = 25°C$, $T_2 = 80°C$, the maximum flow rate of 150 cm/sec would extract 292.6 kW of heat from one conductor. The ac resistance of a 5000 kcmil copper conductor at the average temperature of 52.5°C would be approximately 0.015 Ω/mile. Hence the oil stream could remove all the conductor heat of one mile of cable when the current is 4 kA corresponding to a power flow of nearly 2400 MVA.

If the coolant flow area is A, the oil velocity v, and the module length L, the average rate of extracting heat per unit length of cable core may be written

$$\frac{P_0}{L} = \frac{1}{L} Av\delta c_v (T_2 - T_1) \quad \text{W/cm} \tag{3.43}$$

It would be uneconomical to make this larger than the average conductor loss per unit length P_c/L. With the proviso $P_c > P_0$, the temperature drop

across the series connected radial thermal resistances (see Fig. 3.13) is

$$T_c - T_a = (I^2 R_{ac} - P_0)(R_i + R_j + kR_e) + P_d(0.5R_i + R_j + kR_e) + I^2 R_s'(R_j + kR_e) \tag{3.44}$$

Therefore the ampacity of the internally cooled cable becomes

$$I = \sqrt{\frac{T_c - T_a + P_0(R_i + R_j + kR_e) - P_d(0.5R_i + R_j + kR_e)}{R_{ac}(R_i + R_j + kR_e) + R_s'(R_j + kR_e)}} \tag{3.45}$$

In naturally cooled oil-filled cables, the oil duct is not continued through splices because the impregnant adequately permeates through the insulation to an outer oil space in the splice housing which bridges the plug in the central oil duct. This would obviously not be acceptable for the high flow rates of internally cooled cables that depend on unobstructed flow through tubular connectors. Internal cooling overcomes the previously encountered difficulty with excessive splice temperatures. Even though the extra electrical insulation will impede the radial heat dissipation from the splice, the conductor and insulation temperatures are held down by the stream of cool oil. A special problem exists at the oil inlet and outlet ports where stop-joints have to be provided with a clear oil passage from the conductor to the joint casing. In principle, the stop joints with oil feed ports must consist of two back-to-back connected cable terminations or potheads. Designs of this critical element of internally cooled cables aim at as compact an arrangement as the difficult engineering requirements permit; all of it is housed in a common metallic enclosure.

An important aspect of internal oil cooling is continuous filtration of the coolant to prevent the contamination of the high-voltage insulation. The method just described utilizes the same oil as coolant and impregnant. The separation of these two functions has been considered. If an impermeable barrier is being provided between duct and insulation it seems quite feasible to cool the conductor with water, which has a higher specific heat and lower viscosity than oil. Successful experiments with an internally water cooled high-voltage cable have been reported by Brakelmann and Rasquin [3.2].

Fault Current Rating

Accidental short-circuit faults on transmission systems are unavoidable. Automatic circuit interrupters will isolate the fault from the system in the shortest possible time. But for a brief moment, until the breakers open, lines

feeding power to the fault must be capable of handling very large overload currents. It is difficult to predict the magnitude of fault currents because of their dependence on the location of the fault in relation to the line considered. Furthermore, fault current levels are growing with time as generators and transmission facilities are added to the power system. Fault current levels are specified for every new line. A rule-of-thumb is 10 times the ampacity, and in some instances it may be as much as 20 times. The faster overcurrent relays and circuit interrupters respond, the better is the protection of the system against fault current damage. Modern interrupters can clear a fault within two cycles of the 60-Hz voltage wave. In case of overhead line faults, it is customary to allow one automatic reclosing operation, because the initial flashover may not have caused permanent damage. Every breakdown of paper insulation will be destructive and reclosing should not be allowed. But cables may have to carry the through-fault current to an adjacent overhead line and they must for this reason be capable of surviving a second rush of fault current during the reclosing operation. The very minimum the cable has to withstand are four cycles of fault current. However power system designers specify much longer fault periods, often up to 1 to 2 sec.

The damage that fault current may inflict upon healthy circuits arises from two causes. First, mechanical damage may be produced by the electromechanical forces of repulsion between conductors or conductors and sheaths. Second, the sharp increase in Joule heating may drive the conductor and sheath temperatures so far up that thermal instability breakdown of the paper insulation is being initiated.

The electromechanical forces have been discussed in Section 1.16. Only the conductor currents need be considered in installations with sheath cross-bonding. When the current distribution over the conductor area is known, (1.145) gives accurate values of the steady and oscillating force components. An approximate estimate of the forces may be made by treating the currents as if they were concentrated in the conductor center lines. With the aid of Fig. 3.28, equation (1.145) may then be simplified to

$$\frac{F_{1,2}}{L} = -\frac{2I^2}{S}(-0.25 - 0.25\cos 2\omega t - 0.433\sin 2\omega t) \tag{3.46}$$

$$\frac{F_{2,3}}{L} = -\frac{2I^2}{S}(-0.25 - 0.5\cos 2\omega t) \tag{3.47}$$

$$\frac{F_{3,1}}{L} = -\frac{2I^2}{S}(-0.125 - 0.125\cos 2\omega t + 0.217\sin 2\omega t) \tag{3.48}$$

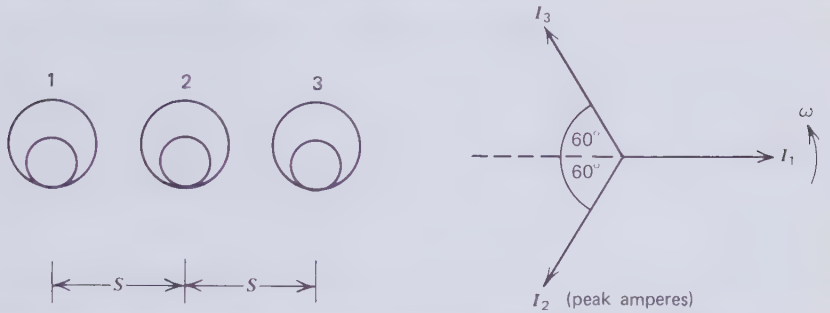

Figure 3.28 Diagram for estimating approximate fault current forces on conductors of a forced cooled circuit with sheath cross-bonding.

The force per unit length on conductor 1 is

$$\frac{F_{1,2}}{L} + \frac{F_{3,1}}{L} = -\frac{2I^2}{S}(-0.375 - 0.125\cos 2\omega t) \tag{3.49}$$

and on conductor 2

$$\frac{F_{1,2}}{L} + \frac{F_{2,3}}{L} = -\frac{2I^2}{S}(0.5 - 0.75\cos 2\omega t - 0.433\sin 2\omega t) \tag{3.50}$$

Because of symmetry, the force per unit length on conductor 3 is the same as that on 1, but it acts in the opposite direction. These forces on individual conductors will be maximum when the oscillating parts add to the steady parts. Therefore the maximum forces on conductors 1 and 2 are

$$F_{1,\max} = -\frac{2I^2}{S} \times (-0.808) = 1.6\frac{I^2}{S} \tag{3.51}$$

$$F_{2,\max} = -\frac{2I^2}{S} \times (-1.366) = 2.7\frac{I^2}{S} \tag{3.52}$$

With the currents expressed in absolute amperes and S in centimeters, (3.51) and (3.52) give the forces in dynes per centimeter. The center conductor is seen to be subject to the largest lateral force, which has to be computed with the current amplitude and not the rms value. Assuming a fault current of, for example, 30,000 A and $S = 22$ cm, the peak force on conductor 2 is 1.105×10^6 dyne/cm or 1126 g/cm, which is considerable. The mechanical impulse loading depends, however, only on the steady force component of 417 g/cm multiplied by the duration of the fault.

The Joule heat generated in the conductor by the fault current has no time to flow into the insulation or even an internal coolant. It has to be absorbed in its entirety as sensible heat in the conductor metal. The normal operating temperature limit of the conductor is fixed to keep the cellulose aging process under control. Brief spells of overheating have little effect on aging. During fault periods the conductor temperature may therefore be allowed to rise to the point where thermal breakdown of the insulation has to be considered. Most users of oil-paper insulation accept an emergency operating temperature of 120°C. Since short-circuit faults may occur at any time during the life of a cable it is not safe to rely on a greater temperature differential than that between the maximum operating temperature and 120°C or $\Delta T_F = 120 - 85$°C. Denoting the symmetrical rms fault current by I_F and the fault period by t_F, the amount of heat that has to be stored in the conductor is $I_F^2 R_{ac} t_F$. The ac resistance must allow for the high conductor temperature and should not include components that stand for induced losses in the sheath. The heat balance per unit length of conductor is

$$I_F^2 R_{ac} t_F = A_c \delta c_v \Delta T_F \tag{3.53}$$

where A_c is the conductor cross-sectional area, and δ and c_v are the density and specific heat of the conductor metal. The following numerical values may be used.

	δ	c_v
Copper	8.94 g/cm^3	0.384 J/g·°C
Aluminum	2.70 g/cm^3	0.899 J/g·°C

From (3.53) the short-circuit current rating is

$$I_F = A \sqrt{\frac{\delta c_v \Delta T}{t_F \rho_{ac}}} \tag{3.54}$$

The dc resistivity ρ_{dc} may be averaged over the temperature interval and must then be multiplied by an ac/dc ratio to convert it to the ac resistivity. For the 85 to 120°C range, the average dc resistivities of copper and aluminum are 2.28 and 3.77 $\mu\Omega$·cm. Let us take the example of a 3000 kcmil aluminum conductor and compare it with a copper conductor of the same cross section for a fault period of 12 cycles of 60 Hz or 0.2 sec. Assuming a conductor ac/dc ratio of 1.1 and $\Delta T_F = 35$°C, the fault current rating of the aluminum conductor is 153.8 kA and of the copper conductor it is 235.3 kA.

Critical Length and Reactive Compensation

The critical length L_c of a cable circuit is that length at which the charging current I_c becomes equal to the thermally limited ampacity I. If r_s and r_c are the radii of the insulation and conductor shields, ε the dielectric constant, then the capacitance C of one cable core per centimeter length is

$$C = \frac{\varepsilon}{2\ln\left(\frac{r_s}{r_c}\right)\cdot 9\times 10^{11}} \quad \text{F/cm} \tag{3.55}$$

It is directly proportional to the dielectric constant, which, among all cable insulations, is highest for oil-paper. This has been a factor hindering the expansion of underground transmission networks particularly with pipe-type cables. The trend to larger conductors also increases the cable capacitance and so do thinner insulation walls, which are desired to save materials; but both these disadvantages are outweighed by the greater ampacity that large conductors and insulation walls of lower thermal resistance make possible.

The charging current is given by

$$I_c = \omega CLV \tag{3.56}$$

where L is the circuit length and V the voltage across the insulation. L is equal to L_c when I_c is equal to I. Hence the critical circuit length may be expressed by

$$L_c = \frac{I}{\omega CV} \tag{3.57}$$

Flexibility in power-system planning demands that L_c should be as long as possible. Harmful as the cable capacitance is, we see from (3.57) that high voltage has the same effect. In spite of the excellent reliability of oil-paper insulated cables, the high charging currents have not allowed them to reap the full economic benefit of transmission at the highest voltages. Forced cooling raises the cable ampacity and thereby increases the critical length. This is likely to be as costly a solution as reactive compensation. Endacott [3.6] has provided guidelines to the ampacity of 5000 kcmil copper conductor cables. Table 3.4 lists these ampacities for the voltage classes from 138 to 500 kV, together with typical insulation thicknesses. From this data the cable capacitance and the critical length have been calculated. The results have been included on Table 3.4. Whereas at 138 kV the critical length is 111 km, at 500 kV it has come down to 53 km. For cables with aluminum conductors or smaller copper conductors L_c will be less.

Table 3.4 Critical Lengths of Naturally Cooled Self-contained Oil-paper Insulated Cables with 5000 kcmil Copper Conductors; Ampacities According to Endacott [3.6]

	138 kV	230 kV	345 kV	500 kV
Insulation thickness (cm)	1.28	2.12	2.60	3.18
Ampacity (A)	2000	1900	1850	1690
Trans. capability (MVA)	478	757	1105	1464
Capacitance (pF/cm)	6.07	4.01	3.42	2.95
Critical length (km)	110	95	72	53

The phasor diagram of Fig. 3.29 indicates how the useful load current I_L combines with the charging current I_c for a resistive load of unity power factor. This idealized load keeps I_L in phase with the voltage across the insulation. The product $\sqrt{3}\ VI_L$ is the power transmitted over the three-phase circuit. The charging current amplitude is proportional to circuit length or L/L_c. When L/L_c tends to zero, I_L is nearly equal to the ampacity I and the circuit is capable of carrying almost 100 percent of its continuous rating. But for greater lengths I_L has to be reduced to keep I on the circle of Fig. 3.29 and prevent overheating of the cable. At the other extreme, when L tends to L_c, the permissible load current becomes very small and the circuit has lost its capability of transmitting useful power. Reactive compensation is a method of restoring the transmission capability of long oil-paper insulated cable circuits. It becomes worth considering when the ratio L/L_c is greater

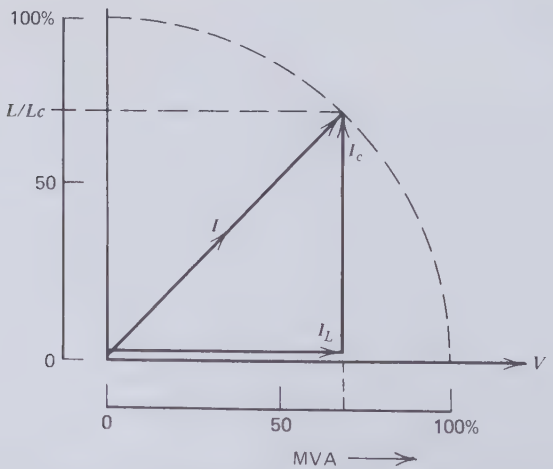

Figure 3.29 Circle diagram of transmission capability as a function o. circuit length for unity power factor.

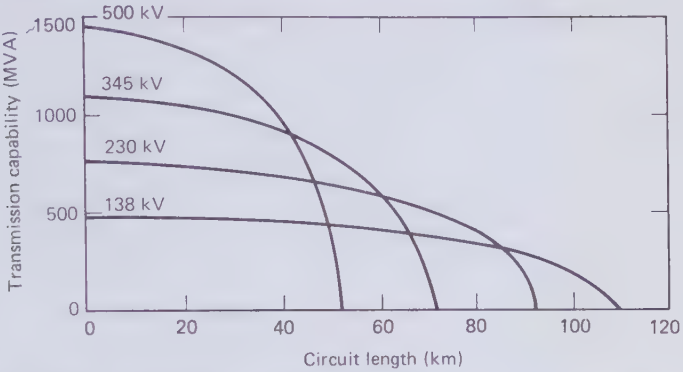

Figure 3.30 Length dependence of transmission capability of 5000 kcmil copper conductor self-contained oil-paper insulated cables.

than 0.6 and the transmission capability has been lowered by more than 20 percent. How the transmission capability of 5000 kcmil copper conductor cables with oil-paper insulation and natural cooling varies with circuit length and system voltage is shown in Fig. 3.30.

Cables exchange reactive power with inductive loads, and this raises their transmission capability. On short cables the useful load current that may then be transported can actually be greater than the rated ampacity. When long cables supply an inductive load, charging currents that are greater than the ampacity could be allowed without overheating the circuit. Both the short and long length operation at a lagging power factor angle of $-\phi$ degrees is illustrated in Fig. 3.31(a). An inductive load compensates for some of the charging current whereas a capacitive load adds to it. The effect which a load with a leading power factor angle has on the useful current I_L that may be carried by the cable can be seen in the phasor diagram Fig. 3.31(b).

To calculate the load current I_L for any phase angle ϕ between I_L and V consider the phasor triangle made up of I_c, I_L, and I. The law of cosines states

$$I^2 = I_c^2 + I_L^2 - 2I_c I_L \cos(90° + \phi) \tag{3.58}$$

Solving (3.58) for I_L and noting that

$$I_c = \frac{L}{L_c} I \tag{3.59}$$

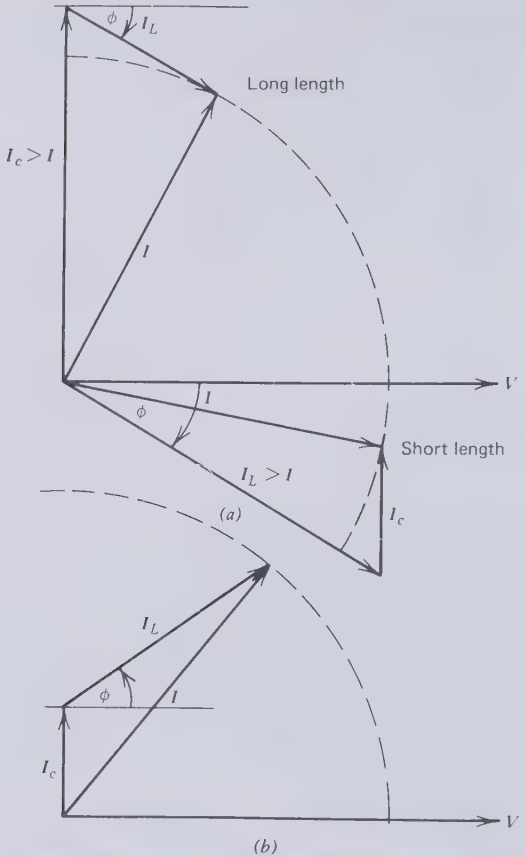

Figure 3.31 Circle diagrams of transmission capability for inductive and capacitive loads. (a) Inductive load. (b) Capacitive load.

the ratio I_L/I is found to be

$$I_L/I = (L/L_c)\cos(90^\circ + \phi) + \tfrac{1}{2}\sqrt{4(L/L_c)^2\cos^2(90^\circ + \phi) + 4\left[1 - (L/L_c)^2\right]} \tag{3.60}$$

For a resistive load (i.e., $\phi = 0$) equation (3.60) reduces to

$$I_L/I = \sqrt{1 - (L/L_c)^2} \tag{3.61}$$

Figure 3.32 is a plot of I_L/I against L/L_c for power factor angles of -15, 0, and $+15$ degrees. It clearly shows the benefits that can be derived from an

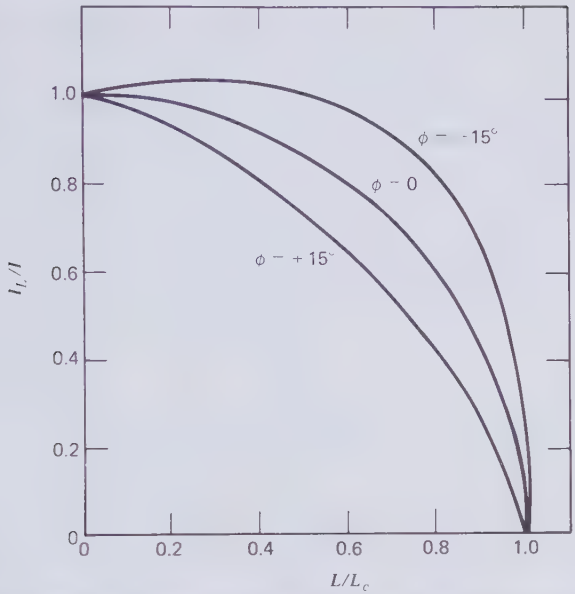

Figure 3.32 Useful load current as a function of length and load power factor angle.

inductive load. Reactive compensation with shunt reactors achieves this to a greater degree and without reliance on any specific load.

The basic idea of reactive compensation is to resonate the cable charging current through one or more parallel inductances. Perfect tuning is not possible as the cable capacitance is distributed and the reactors must necessarily be lumped inductances. Moreover, since the line has series inductance, which also stores energy, but in proportion to the square of current rather than voltage, any tuning would be continuously upset by load fluctuations. A further complication is the voltage drop along the line. In the general case, where the line is a link of a network, power flow and voltage drop not only vary but they may actually reverse direction.

Sizes and positions of shunt reactors have to be tailored to the needs of any particular line. Figure 3.33 shows two arrangements that increase the critical length of the transmission circuit by factors of two and four. The diagrams have been drawn for just one phase of a three-phase circuit. In the highly idealized circuits of Fig. 3.33, line resistances and inductances are ignored and the distributed cable capacitance has been replaced by lumped capacitances. With reactive compensation, cable circuits can be extended indefinitely. Practical shunt reactors are approximately of the same physical size as transformers. If at all possible they will be located at substations where the cable is in any case being terminated. In principle it should be

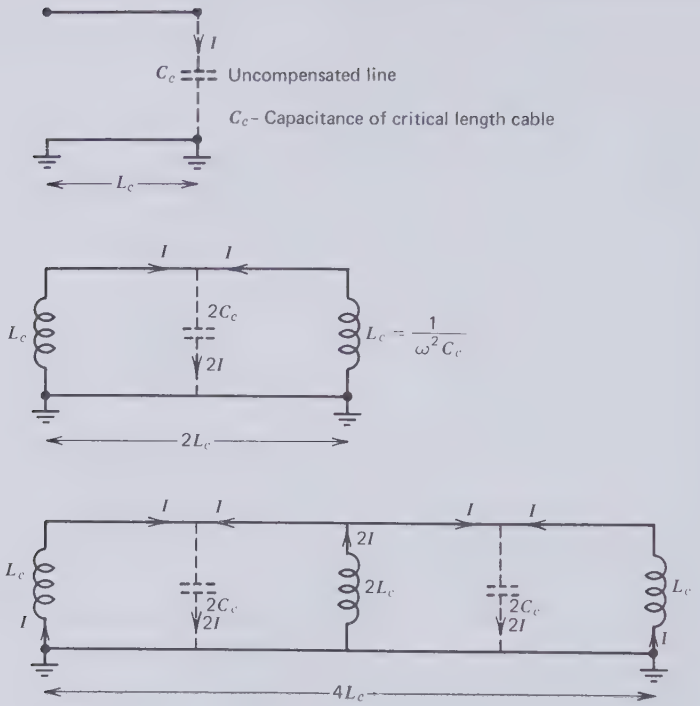

Figure 3.33 Shunt reactor compensation of cable charging current.

possible to seal shunt reactors permanently and install them underwater. However, this has not yet been attempted. With shunt reactors at the terminals, underwater circuits have to be limited to approximately 1.2 to 1.5 times the critical length of the uncompensated circuit. Reactive compensation brings with it a severe financial penalty, not least because of the standing loss in the reactors.

DC Cables

The number of high-voltage dc power transmission lines is steadily increasing. Overhead lines have been chosen for long distances and the most important one for the time being is the U.S. Pacific Intertie of 850 mile length and a capability of 1440 MW at ±375 kV. Currently the largest dc cable links Kingsnorth with London over a distance of 53 miles and has a capability of 640 MW at ±266 kV. A 60-mile-long dc submarine cable connects Sweden with the Baltic Island of Gothland and a 75-mile-long dc underwater cable ships power from Italy to Sardinia in the Mediterranean.

High-voltage dc is particularly attractive for long underwater lines as it avoids the installation of underwater shunt reactors for charging current compensation.

The early French [2.9] and Russian [2.8] experience with viscous compound impregnation of the cable insulation, rather than filling it with oil, proves that paper is more tolerant to dc than to ac voltages. The actual ac and dc stresses reached in practical cables are strongly influenced by impulse withstand specifications that may differ for ac and dc systems. Nonetheless the major paper cable producers believe that dc design stresses up to 400 kV/cm are feasible while ac stresses appear to be leveling out at 150 kV/cm [3.5, 3.6]. The behavior of oil-paper insulation under dc stress has been discussed in Part Two.

Any given self-contained oil-paper insulated cable designed for a certain three-phase rms line-to-line voltage can carry dc power at the same voltage between line and ground. In Fig. 3.34 a 2000 kcmil aluminum conductor cable with 0.8-in. insulation wall is analyzed when employed (a) in a 230 kV three-phase circuit with sheath cross-bonding, and (b) in a ± 230 kV dc circuit. Specified and derived parameters of the two circuits are listed on the diagram. The ampacity of the three-phase circuit is 831 A resulting in a transmission capability of $\sqrt{3}\ VI = 331$ MVA accompanied by a full load loss of 5.1 percent/100 miles. The dc circuit requires two instead of three cables, and it may be installed in a narrower trench. In addition to these savings it can transmit 28 percent more power than the ac circuit and does so at lower loss.

This example quite clearly illustrates the advantages of dc underground transmission accruing from the absence of dielectric and sheath losses as well as the lower thermal proximity factor. Unfortunately these advantages have to be traded against the cost of rectifier and inverter stations. In a cost study carried out in 1971 [2.8], it was found that for 50-mile-long underground circuits the transmission cost for dc systems, including terminal equipment, was lower than for ac systems. Breakeven distances as short as 20 miles have been mentioned for dc lines when both the ac and dc cables rely on oil-paper insulation.

Underwater Cables

The traditional high-voltage ac cable for deep water power transmission contains a copper conductor insulated with impregnated paper, which is pressurized with either low-viscosity oil or nitrogen gas and hermetically sealed into a lead sheath. DC cables may be of the same makeup or they can be impregnated with a viscous compound that is kept in compression by the hydrostatic head above the cable. As a result of its mechanical weakness,

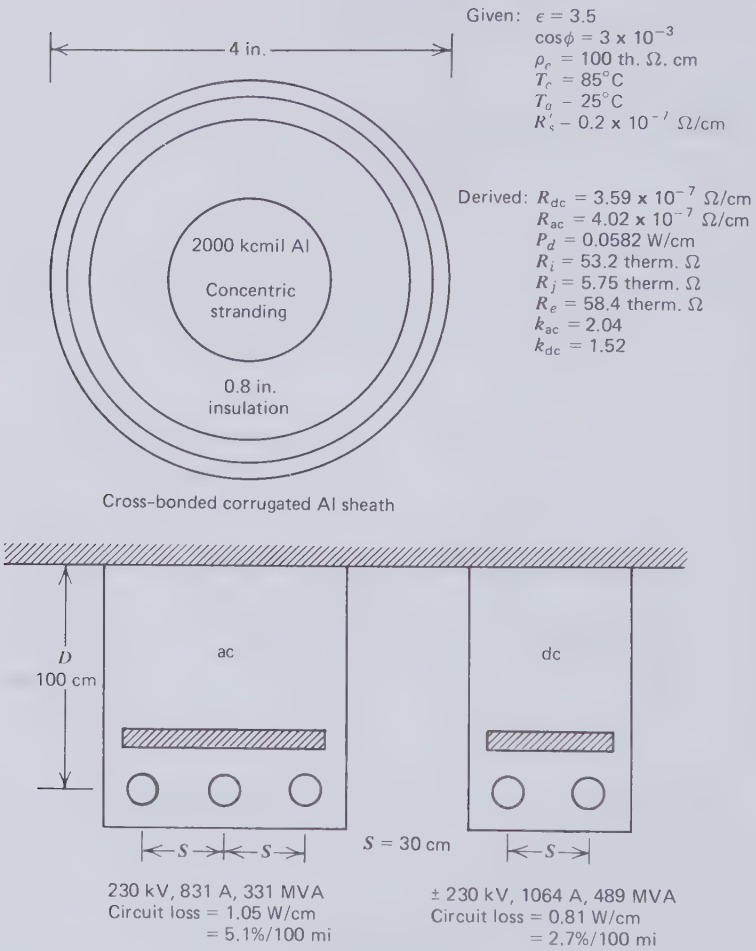

Figure 3.34 Comparison of ac with dc circuit.

lead must be reinforced on the water side by other metals to withstand the internal pressure of the impregnant and some longitudinal forces applied to it during cable handling. Owing to the hazard of galvanic corrosion between dissimilar metals it becomes essential to prevent water from having access to both metals. At least one of them or both metallic layers are normally enclosed in a waterproof polyethylene jacket. In addition to the longitudinal reinforcement of the lead sheath, the submarine cable requires armoring against abrasion in handling and installation. Bare and covered armor wires of galvanized steel, aluminum and its more corrosion-resistant alloys, pure copper, and copper alloys have all been used in the past for this purpose. In

the majority of cases a single layer of substantial and closely packed armor wires has been wound on with a short pitch of several cable diameters. Reverse lay double wire armor has been applied in a few instances.

Copper, lead, reinforcing tapes and armor wires make for very heavy cables. They have to be strong enough to support their own weight in water while hanging from the cable ship to the sea bottom. In deep water this imposes severe strain on the cable endangering the insulation. There exists of course a limit to the depth of water in which lead covered cables may be installed. Gazzana-Priaroggia and Maschio [3.19] believe this limit to be approximately 1000 m. Transatlantic telephone cables have been installed in substantially deeper water. The tendency with telephone cables has been to make them lighter by eliminating the external armor and building tensile strength into the conductor. However the lead sheath has prevented this practice from being adopted for paper insulated power cables. Some weight reduction is achieved by using aluminum conductors instead of copper. Replacing the lead sheath by an aluminum sheath has not been attempted mainly because of the limited tensile rigidity of corrugated tubing that would transfer all the laying tension to the conductor.

Whereas cables may be designed to take large tensile forces, it has generally been felt that they are more reliable if they do not contain splices, at least not in the lead sheath, the reinforcement, and the armor. Splices have been laid satisfactorily in water of moderate depth, as for example in the English Channel. Nevertheless, the major underwater cables have been produced splice-free in long lengths stretching from shore to shore.

Many-mile long cables require special manufacturing plants located on deep water piers where the splice-free product can be loaded directly on cable ships. Overland transportation of these long cables is virtually impossible. Only a few plants in the world exist that have the long-length dockside capability, and this necessarily adds to the cost of underwater circuits.

The long cables have to be coiled on the deck or in holds of the cable ship. This applies torsion and twist to the cables, which, together with locked-in torsion in the armor, creates a tendency of the cable to fall in loops to the seabed. Cable loops are highly undesirable because the moving ship may pull a loop into a kink and damage the high-voltage insulation. Throwing loops has been a major hazard in the installation of deep-sea cables. Some installers have tried to guard against it quite successfully by laying the cable with residual tension. Others have relied on the opposite method of laying slack cable.

Once the ship is in position in favorable weather, high-voltage underwater cables can be laid as fast as 1 or 2 miles/hr. Special arrangements have to be made for floating the shore ends on land and burying the cable in shallow water to protect it against trawling gear and anchors. Cable laying at

reasonably high speed is important to avoid the risk of running into foul weather in which the cable can easily be severed from the ship. In spite of the high laying speed, compared with undergrounding, the installation of underwater cables is not necessarily cheaper than undergrounding because of ship charter fees, which have to cover a period of time that is much longer than the actual cable laying operation.

An important consideration is the spacing between underwater cables. It has to be a compromise of conflicting objectives. Two cables should never cross over each other as this would create dangerous hot spots in both cores. To keep up the laying speed, which is dictated by weather, it is frequently deemed undesirable to lay more than one cable at a time. Granted the remarkable precision of navigational methods, it would be too much to expect successively laid cores to come to rest side by side within a few feet. Close spacing reduces the sheath and armor losses of an ac circuit and the compass error produced by the steady magnetic field of a dc circuit. When one or the other of these two concerns overrides the cost of installation, a complete circuit with spare cores can be laid simultaneously with spacer pieces being attached to the cables as they move over the deck of the ship to the laying sheave. This technique was adopted for the England-France dc cable. AC circuits involve usually at least four cores (three phases plus a spare core). Additional sheath and armor losses and some derating of the cable may then be considered the lesser evil compared to the complications and risks of laying four cables at one and the same time. The cable spacing adopted for the successive laying of seven cores of the Long Island Sound crossing was a nominal distance of 275 m [3.20].

Saltwater has adequate electrical conductivity to act as return conductor. The early dc underwater cable connecting Sweden with Gothland made use of this fact [3.24]. Sea water remains an emergency conductor for two-pole dc installations in which one cable has failed. The neutral current of an ac circuit can be readily absorbed by the lead sheath and armor.

Figure 3.35 illustrates the construction of two important submarine cables in use in North American waters. One is the 138 kV ac intertie between Long Island and Connecticut and the other is the 300 kV dc cable supplying Vancouver Island with power from British Columbia. In an oil-filled ac cable the pressure of the impregnant can rise to 250 psi, depending on depth of water and load fluctuations. Viscous compound impregnation was chosen for the dc cable because it saves cable materials and oil pressurization equipment. An interesting feature of the Vancouver dc cable is the oval cross section. It becomes more circular as the cable expands under full load. The thermal cycling of a circular lead sheath can produce grooves in and cracking of the lead.

Both cables of Fig. 3.35 depend on a lead alloy water barrier but the reinforcement is arranged in different ways. In the ac cable nonmagnetic

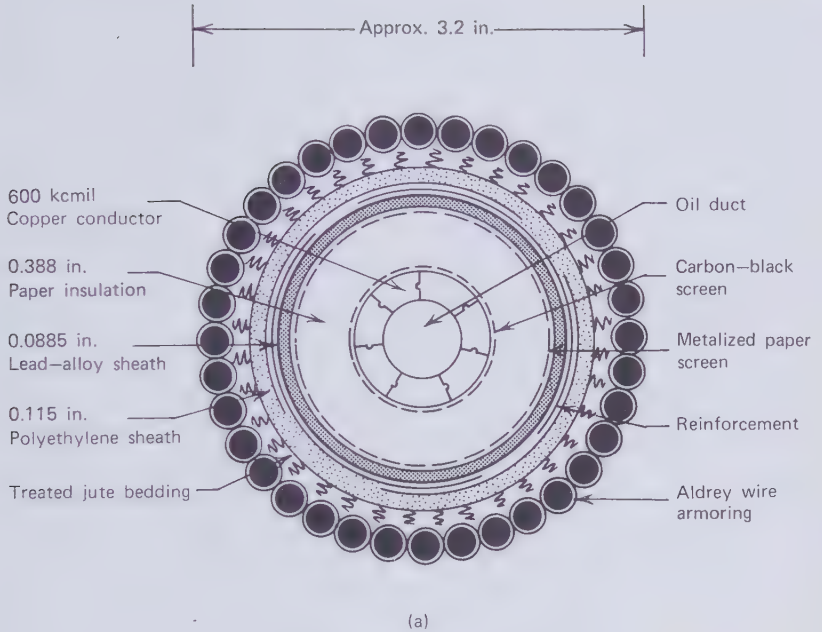

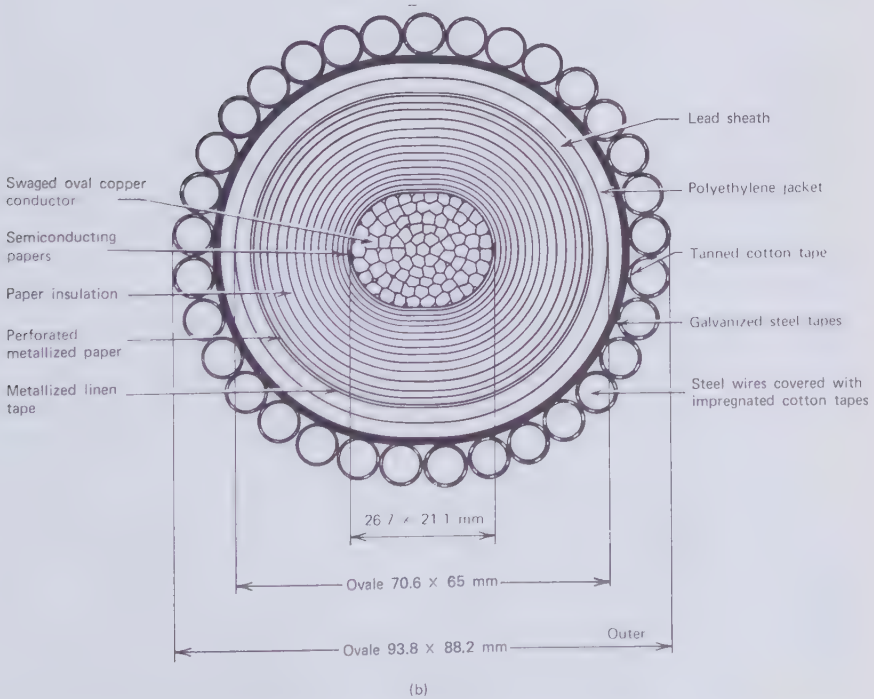

Figure 3.35 Two major submarine cables in use in North America. (a) 138 kV Long Island Sound ac cable [3.20]. (b) 300 kV Vancouver Island dc cable [3.21]. (By permission of the Institute of Electrical and Electronics Engineers).

metal tapes are wound directly on the lead pipe, and they in turn are covered by a waterproof polyethylene jacket, which separates the two inner metal layers from the aluminum wires on the outside. Steel reinforcing tapes and steel armor wires have been chosen for the dc cable. They are avoided on ac cables because of the magnetic hysteresis losses. The combined steel layer is placed on the outside of the polyethylene jacket, which separates it from the lead sheath.

Sheath cross-bonding is impossible on cables that do not contain splices and would be very difficult in the underwater environment even if splices were provided. The circulating current flowing in the combination of sheath, reinforcing tapes, and armor wires can be nearly as large as the current carried by the enclosed conductor, as explained in Section 1.12. This results in large energy losses, which can easily be greater than the conductor loss unless substantial metallic layers are used to keep the resistance of the outer current path low. Furthermore, since two layers of metal are separated by a polyethylene jacket, the longitudinal emf's induced in them will differ by an amount given by (1.112). This difference will drive eddy currents around the sheath-armor loop through bonds at both ends of the cable, and so generate additional Joule heat. The potential difference given by (1.112) also subjects the polyethylene jacket to some electrical stress. Under normal operating conditions the voltage across the jacket may amount to only a few hundred volts determined by circuit length. But when the conductor current is suddenly interrupted ωi_c in (1.112) has to be replaced by the rate of change of current and then causes high-voltage transients, which may puncture the jacket and admit water to the lead sheath. The Long Island Sound cable is protected against voltage surges, which could jeopardize the integrity of the anticorrosion jacket, by making conducting connections between the lead sheath and the aluminum armor every 2 miles. This reduces L in (1.112) and therefore the surge voltage by approximately a factor of five. Another solution of this problem would be the use of a semiconducting polyethylene jacket, but the manufacturers of the L.I. Sound cable were not confident that the conducting properties of carbon-filled polyethylene could be guaranteed to persist for many years.

It might be thought that installing cable under water is as good as forced cooling. There is little doubt about the cool environment that exists at depth below, say, 200 ft; yet its benefits cannot be fully realized because the cable also has to pass through shallow water near the shores where it is likely to be buried under sediments of poor thermal conductivity. The ampacities of submarine circuits are dictated by the shore ends. To overcome this bottleneck large conductor shore ends have sometimes been spliced to the deep-water section. Whether or not such splices are acceptable will depend on the line voltage. Silt sediments in deep water can spoil the effect of a lower ambient temperature. Silt in contact with the cable may dry out

during a spell of sustained heavy load. Dry silt can be inpenetrable to the water and actually form a kind of thermal insulation initiating thermal breakdown of the paper insulation. One of the more recent underwater failures of this nature occurred in 1969 on a 115 kV oil-filled cable installed across Lake Champlain, New York [3.22].

As the Lake Champlain cable demonstrates, not all submarine cables are installed in salt water. As a rule inland water installations are quite short. Some are river crossings. It seems surprising that few, if any, underwater circuits have been laid along river and canal beds. These waterways pass through the most densely builtup areas and would appear to make ideal power corridors. A study of the installation of 275-kV ac cables in the canals of London revealed that static water not free to convect, as water entrapped in silt would be, has a thermal resistivity of 165 thermal-$\Omega \cdot$cm [3.23]. Low thermal conductivity of the canal beds and difficulties concerning underwater sheath cross-bonding were the primary reasons for the rejection of canal cables. The increase in the cost of energy since the time the study was made in 1967 makes cross-bonding even more important but it deemphasizes the significance of the thermal environment of the canal bed. River and canal cables would have to be plowed into the bottom sediments for mechanical protection. A solution of the cross-bonding problem is certainly not impossible and the changing energy economics may one day reopen the subject of power lines in rivers and canals.

Repairing underwater cables can be an extremely costly task, not so much in shallow inland waters, but on the open sea. Splicing a repair length requires the repair vessel to remain almost stationary for one or even more days without its anchor chains becoming entangled with the rising portions of the cable. Not very long ago it was discovered that the spare core of the dc intertie laid across Cook Strait, New Zealand, failed [3.25]. Repair is now being contemplated at a cost greater than that of the installation of all three cores 15 years ago. The solution to the high repair cost of deep sea cables must eventually be the development of much lighter and therefore less expensive underwater cables that can easily be laid in parallel with damaged circuits.

Prospect of Synthetic Tape Insulation

The scientific aspects of synthetic tape insulation have been discussed in Part Two. Substituting polyethylene or other polymeric tapes for paper promises significant reductions in cable charging current and dielectric loss. There may also exist some potential for lowering the thermal resistance of the high-voltage insulation. Serious studies of this topic began in 1960. Beale et al. [3.26] reported the first tests of 275 kV cable samples with polyethylene tape insulation filled with SF_6 gas at 150 psi. As might be expected, these

pioneering experiments were not entirely successful, but they provided sufficient encouragement to continue the research. A serious differential thermal expansion problem had been revealed which, on thermal cycling, caused premature breakdown of the insulation. Besides, the thermal resistivity of the gas-polyethylene combination turned out to be greater than anticipated. These difficulties were overcome with further research, and Beale [3.27] claimed in 1973 that, compared with oil-paper cables, the new insulation system would reduce cable capacitance by 37 percent, dielectric losses by 95 percent and the thermal resistivity by 33 percent. Later Stannett and Gibbsons reported [3.28] that a commercial 400 kV self-contained cable with SF_6 gas pressure assisted polyethylene tape insulation is being developed in Great Britain.

The majority of cable manufacturers appear to favor oil impregnated synthetic tape insulation [3.29, 3.30]. Polymeric tapes unfortunately swell substantially if they are immersed in insulating oils. Laminating the synthetic tape between two layers of paper prevents elongation by swelling. Increases in tape thickness have to be accepted or controlled with constraining metal tapes wound on top of the insulation. Edwards and Melville [3.29] reported the successful manufacture and testing of experimental 132-kV cable samples insulated by oil impregnated polypropylene-paper composite tapes. These authors concluded that their new insulation may well be suitable for 750 kV self-contained ac cables.

What in the early 1960s appeared to be a simple substitution of new for old materials has turned out to be a difficult research and development challenge. However prospects are now good that synthetic tape insulated self-contained cables with superior performance to oil-paper insulated cables will become commercially available in the 1980s.

Economics

The economics of electric power transmission revolve around three topics: (1) the actual cost of transmitting unit energy over unit distance, (2) the relative transmission cost as it varies from one type of line to another and particularly of underground lines with respect to overhead lines, and (3) the energy loss per unit energy conveyed over unit distance. These three aspects will be discussed for all types of cable and the treatment of the oil-paper insulated self-contained cable serves as the model for this discussion.

To arrive at the actual cost of power transmission, it is necessary to have up to date information on three major cost components, which are (a) the installed cost of transmission lines per unit length, (b) the cost of the fixed energy losses (dielectric, pumping, etc.), which accrue all the time regardless of the amount of energy that the line is carrying, and (c) the cost of the Joule losses, which are proportional to the square of current or power flow. A

comprehensive survey of transmission cost data appertaining to the U.S. electric utility industry in 1971 was published by the Edison Electric Institute [2.8]. Extensive use will be made of this information, which is contained in a document also known as the ADL-Report. Since 1971 the installed cost of transmission lines has risen roughly in proportion to the rate of inflation. In deriving the 1976 installed cost figures, the 1971 data will be multiplied by the inflation factor of 1.4026, which represents a 7 percent compound inflation rate over the 5-year period.

The Arab oil embargo occurred half way between 1971 and 1976 and with it came an increase in the price of electricity, which was out of proportion to the then prevailing inflation rate. According to the ADL-Report, the 1971 price of electricity to the electric power companies was 0.8¢/kWh. This was of course less than the price charged to consumers.

Another important economic parameter is the "annual capital charge." This refers to depreciation, interest that would have been earned or saved had the capital plant not been built, and the annual maintenance cost, which for transmission lines is quite low. The annual capital charge as a fraction of the installed cost of transmission lines used throughout reference [2.8] is 15 percent. Depreciation rates do not vary with inflation and interest charges have remained relatively constant. Therefore the 15 percent annual charge may be applied to the 1976 capital cost figures.

The average price of electricity to the U.S. utility industry in 1976 was stipulated by the Philadelphia Electric Company in a later survey of transmission costs for U.S. utilities [3.31]. It was given as 1.76¢/kWh plus a "demand charge" of $460/kW. The demand charge is the installed cost of 1 kW generating capacity. This will also incur an annual capital charge of 15 percent, which comes to $69. It has to be distributed over the kilowatt-hours generated by the 1 kW generator in one year and therefore adds a further 0.79¢ to the 1.76¢/kWh. Hence the average price of electricity for utility consumption in 1976 was 2.55¢/kWh, or more than three times the 1971 price.

Relatively few self-contained oil-paper insulated cables have been installed in the United States. Their costs were not compiled in the ADL-Report. Yet these cables are widely used in Europe and particularly in Great Britain. A graph comparing the installed cost of self-contained with pipe-type oil-paper insulated cables was published in 1967 [3.32]. It is reproduced in Fig. 3.36. The British cost actually applies to 1965 and it is seen to be only about half that of U.S. pipe-type cable installations at corresponding voltage and power levels. In the discussion of [3.32] it was argued that part of the differential might be explained by the higher wages that prevailed in the United States. Most experts seem to agree that self-contained cables are more economical than pipe-type cables. But since no hard figures are available for U.S. installations it will be assumed that the installed cost of

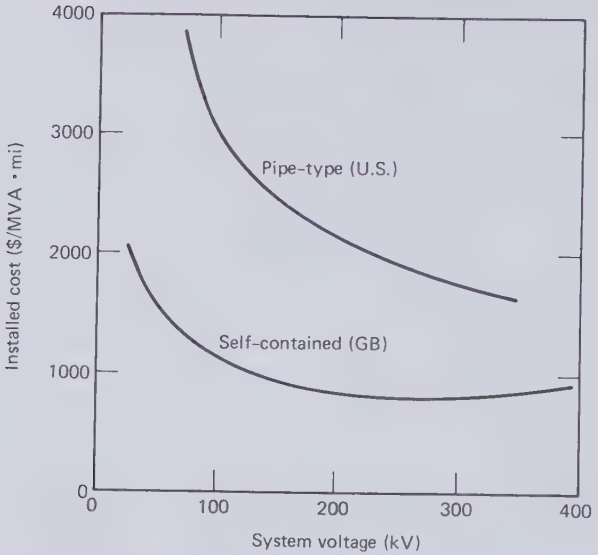

Figure 3.36 1965 Installed cost comparison of self-contained with pipe-type oil-paper insulated cables [3.32]. (By permission of the Institute of Electrical and Electronics Engineers).

the self-contained cable in the United States is the same as that of the pipe-type cable for equal voltages and conductors. However, the advantages of self-contained cables with regard to the lower current-dependent loss and the higher ampacity will be retained in the following economic analysis.

On this basis the 1971 and 1976 transmission costs for the four underground (UG) and four overhead (OH) lines listed on Table 3.5 have been computed. The eight lines fall into the four standard U.S. voltage classes of 138, 230, 345, and 500 kV. Conductors for the individual lines were chosen in accordance with the ADL-Report so that the installed costs listed in this report for 1971 could be used without modification. In the case of overhead lines the ADL-Report gives maximum and minimum costs and the figures shown on Table 3.5 are mean values between the two extremes. It is assumed that they apply to average suburban conditions 10 to 30 miles out from the center of metropolitan areas. The installed costs of underground lines (Table 3.5) also apply to the average suburban scenario rather than the downtown or open country scenarios that have been covered in the ADL-Report.

The lowest cost overhead system is one in which two three-phase circuits are suspended from the same steel tower. This has been chosen for the 138 to 345 kV systems, but at 500 kV it is common practice to mount only one circuit on one tower. A sufficient number of UG circuits were taken to match the thermal transmission capabilities of these overhead lines.

Table 3.5 Details of overhead (OH) and underground (UG) transmission lines used in the economic analysis of naturally cooled self-contained oil-paper insulated cables

	138 kV		230 kV		345 kV		500 kV	
	UG	OH	UG	OH	UG	OH	UG	OH
Conductor size (kcmil)	2000	795	2000	1431	2000	2×1590	2000	2×1780
Metal	Copper	ACSR	Copper	ACSR	Copper	ACSR	Copper	ACSR
Ampacity (A)	1300	880	1200	1220	1100	2640	1000	2850
Number of circuits	2	2	2	2	5	2	3	1
Dielectric loss (kW/mi)	23.22	—	44.04	—	214.65	—	189.63	—
J-loss resistance (Ω/mi)	0.036	0.140	0.036	0.076	0.036	0.035	0.036	0.031
Insulation thickness (in)	0.505	—	0.835	—	1.025	—	1.250	—
1971 Inst. cost ($/mi)	462,184	141,184	624,666	182,700	1,789,665	288,250	1,223,799	230,550
1976 Inst. cost ($/mi)	648,237	197,760	876,126	256,246	2,510,098	404,286	1,716,441	323,358
1971 Diel. loss ($/mi)	1627	—	3086	—	15,043	—	13,289	—
1976 Diel. loss ($/mi)	5186	—	9837	—	47,950	—	42,359	—

Both the insulation thickness and the dielectric loss per mile have also been taken from the ADL-Report, but the Joule loss resistance has been specially computed for self-contained cables at the average conductor temperature of 50°C and taking the effect of sheath cross-bonding into account. The ADL-Report assumes constant current at any load level, which is equivalent to setting the Joule loss factor α of (1.212) to unity. For the present analysis, however, daily load cycling at a 0.75 load factor has been assumed which, when substituted into (1.212), results in a Joule loss factor of $\alpha = 0.62$. Therefore the present loss estimates are lower than those of the ADL-Report.

The ampacities of the UG lines of Table 3.5 are based on the self-contained cables being installed in flat formation at a depth $D = 42$ in. with a spacing $S = 12$ in. in soil of a thermal resistivity of 90 thermal-$\Omega \cdot$cm. For naturally cooled lines the transmission cost TC, measured in \$/MVA-yr-mi, is given by

$$TC = \frac{0.15IC + YDL + YJL}{n\sqrt{3}\ V(uI)(CLF)} \tag{3.62A}$$

where

IC = installed cost of line containing n circuits (\$/mi)
0.15 = annual capital charge factor (yr^{-1})
YDL = yearly cost of dielectric losses (\$/yr·mi)
YJL = yearly cost of Joule losses (\$/yr·mi)
V = line voltage (kV)
I = line ampacity (kA)
u = line utilization factor or daily peak current as a percentage of ampacity
CLF = cable (line) load factor

If P_d is the dielectric loss in watts per centimeter of cable core, and E is the cost of unit electricity to the power company in \$/kWh,

$$YDL = 3nP_d \times 2.54 \times 12 \times 5280 \left(\frac{24 \times 365}{1000} \right) E \quad (\$/\text{yr} \cdot \text{mi}) \tag{3.62B}$$

Similarly if R' is the effective J-loss per centimeter of cable core (in self-contained cables with sheath crossbonding $R' = R_{ac}$), α the loss factor defined by (1.212), then

$$YJL = 3n\alpha(uI)^2 R' \times 2.54 \times 12 \times 5280 \left(\frac{24 \times 365}{1000} \right) E \quad (\$/\text{yr} \cdot \text{mi}) \tag{3.62C}$$

All this information results in the 1976 underground transmission cost graph of Fig. 3.37. The unit of energy is the MVA·year and the unit of distance the mile. The transmission cost in \$/MVA·yr·mi drops as the average load carried by a given line increases. Most transmission lines appear to operate in the 50 to 100 percent utilization range. "Full load" in all the economic discussions should be taken as the maximum thermal transmission capability and not any superimposed emergency rating. The horizontal load scale is also a measure of the total amount of energy conveyed by the line in 1 year. Figure 3.37 shows the economic advantage of transmitting electricity at the highest possible voltage. At the same time the 500 kV line has only a marginal advantage over the 345 kV line mainly because of the ampacity limitation due to the thick paper insulation.

The picture is not so different when considering Fig. 3.38 for the four overhead lines, except that on the average the transmission cost is reduced by a factor of two. There is, however, one other observation that should be made when studying Figs. 3.37 and 3.38. At full load the curves for the UG lines are still dipping, whereas the OH line cost graphs have leveled out and are in fact climbing. This means the overhead lines have passed through the

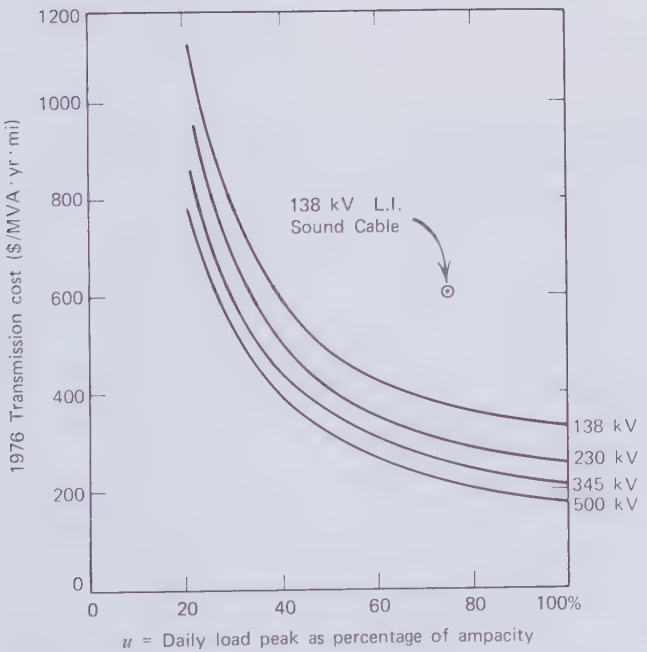

Figure 3.37 1976 transmission cost for naturally cooled self-contained oil-paper insulated cables (CLF = 0.75, $\alpha = 0.62$).

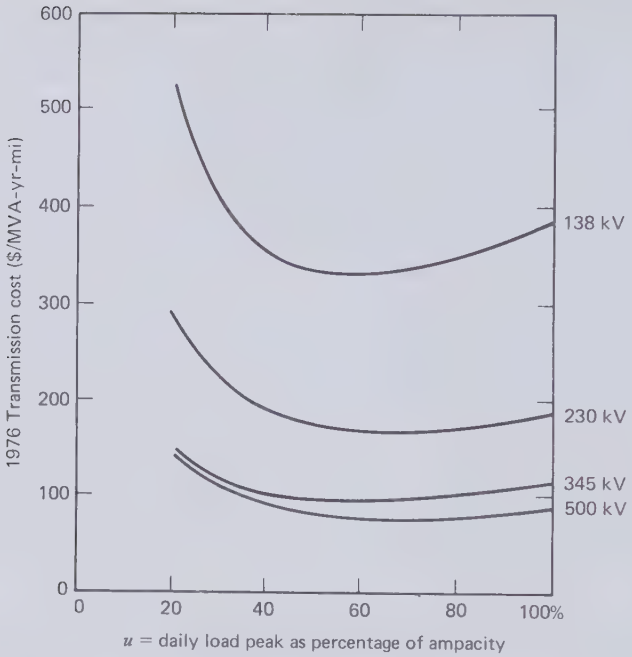

Figure 3.38 1976 Transmission cost for overhead lines (LF = 0.75, $\alpha = 0.62$).

Kelvin cost minimum, which was explained in Section 1.25, whereas the underground lines are prevented by thermal restrictions from reaching the minimum. Air cooling takes overhead lines through the minimum but underground lines require forced cooling to attain the same goal.

Another conclusion that may be drawn from Fig. 3.38 is that the economics of overhead transmission can only be slightly improved by selecting larger conductors. The additional metal would roll the cost minimum to the right. Only in the case of the 138 kV line could this bring about a significant cost saving within the load range of interest. The four overhead lines chosen for the ADL-Report are seen to be about the most cost-effective transmitters of electric power known to us which justifies using them as a standard of comparison. This state of affairs would change if the existing relationship between the cost of materials and energy were fundamentally altered.

Figure 3.39 presents the UG/OH transmission cost ratio for the four voltage classes at a 75 percent cable load factor and $u = 100\%$. As this is also the load factor on which the Joule-loss factor $\alpha = 0.62$ is based, it implies that once per day the cyclicly varying load will just reach the thermal capability of the line. Figure 3.39 gives the breakdown of the relative transmission cost in terms of the capital, dielectric loss, and Joule loss

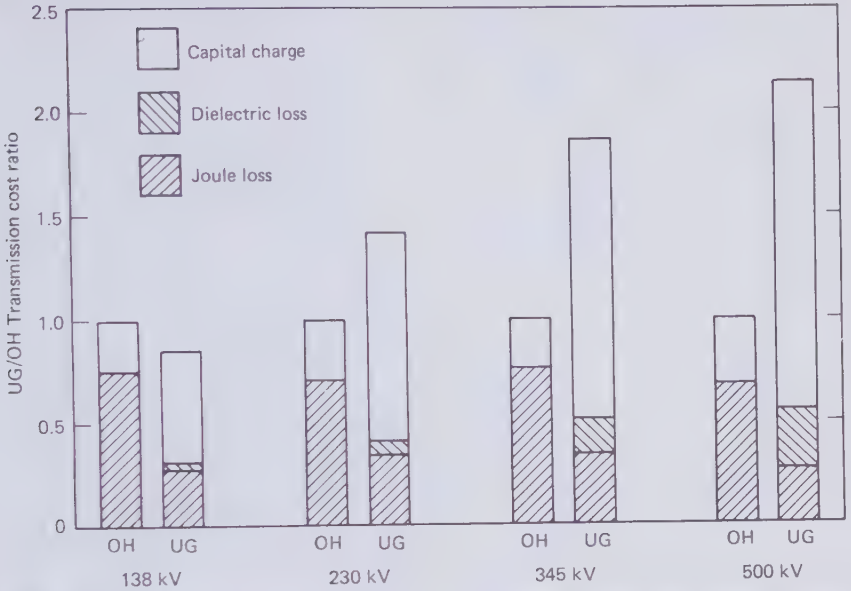

Figure 3.39 UG/OH transmission cost ratio for naturally cooled self-contained oil-paper insulated cables ($u = 100\%$, CLF $= 0.75$, $\alpha = 0.62$).

components. It will be seen that the oil-paper insulated cable lines are overburdened by capital charges, which is the primary reason for the high cost of underground power transmission at the higher voltages. If more power could be transmitted through the individual UG line, the capital component would shrink and the Joule component would increase. This would result in an overall economic gain until a balance is achieved between capital and loss charges, and it has motivated the introduction of forced cooling.

The loss component of the overhead lines is seen to be greater than their capital component. As undesirable as this may be from an energy conservation point of view, bringing the two components into perfect balance is not likely to reduce the transmission cost by much as the shallow minima of Fig. 3.38 indicate.

The ratio of energy to materials cost that existed in 1976 will not hold forever. When it changes it will influence the ratio of UG to OH transmission cost. For example, the tripling in the price of electricity between 1971 and 1976, when capital costs increased by 40 percent, reduced the UG/OH transmission cost ratio as shown in Fig. 3.40. It is obvious that the higher loss overhead lines suffered more by this nonuniform cost movement than the UG lines. A return to cheaper electricity in relation to manufactured goods

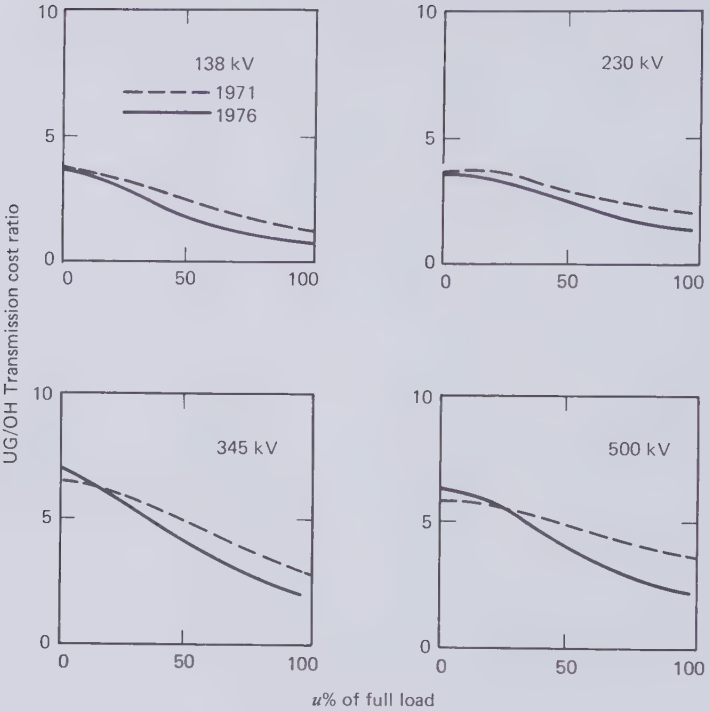

Figure 3.40 Comparison of 1971 and 1976 UG/OH transmission cost ratios.

seems unlikely and therefore the energy/material relationship established in the late 1970s might well hold for the remainder of the century.

Although Fig. 3.39 stresses the economic importance of energy losses, it is not a yardstick of transmission efficiency. When conservation of energy is a goal in itself, not necessarily coupled to the lowest transmission cost, then the fraction of energy that is being converted to heat in unit length of line has to be considered. A convenient unit of circuit length for this purpose is 100 miles, as this makes the loss fraction a few percent. It will be understood that in the assessment of transmission efficiency it is irrelevant that 100 miles is more than the average underground circuit length and in some instances even more than the critical length. The percentage transmission loss per 100 miles has been plotted on Fig. 3.41 against line utilization u at constant current ($CLF = 1.0$) of the four UG and the four OH lines examined previously. It now becomes very clear how inefficient a transmitter of electricity the 138 kV overhead line is and in future such lines will almost certainly have to be equipped with larger conductors to eliminate this deficiency. Another fact standing out is the poor efficiency of the UG lines at light loads caused by the standing dielectric loss of the oil-paper insulation.

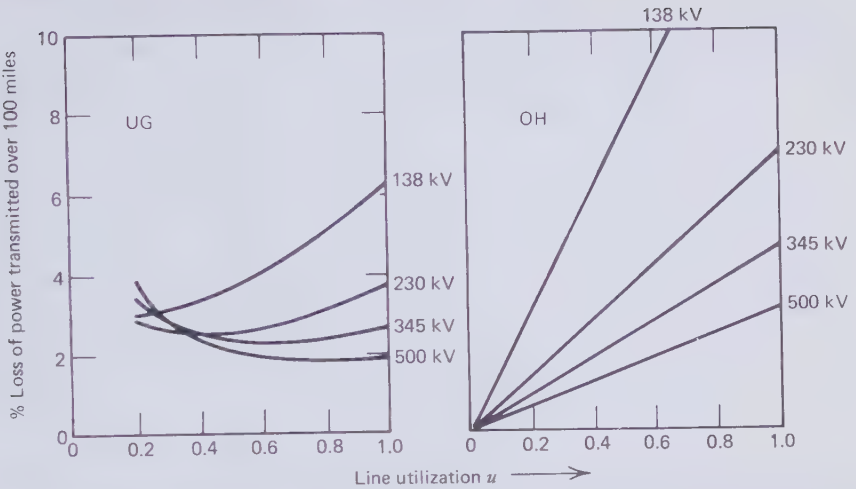

Figure 3.41 Transmission loss of naturally cooled self-contained oil-paper insulated cables (UG) and overhead lines (OH). CLF = 1.0.

To estimate the effect forced cooling has on transmission cost we express the underground to overhead transmission cost ratio at a given voltage and MVA-rating as

$$\frac{\text{UG}}{\text{OH}} = \frac{CC + DL + JL}{OH} \tag{3.63}$$

where

UG = underground transmission cost

OH = overhead transmission cost

CC = capital charge component of UG

DL = dielectric loss component of UG

JL = Joule loss component of UG

Let forced cooling increase the transmission capability of unit length of line by the factor of $(1+x)$ where x would typically assume values between zero and one. If forced cooling increases the capital cost of unit length of line by the factor $(1+y)$, CC in (3.63) has to be multiplied by $(1+y)/(1+x)$. The dielectric loss component of the forced cooled system will be diluted in a larger number of MVA's and DL therefore has to be multiplied by $1/(1+x)$. The Joule loss component increases as the square of transmission capability but it will also be diluted in the larger number of MVAs, so that JL has

to be multiplied by $(1+x)$. Hence for the forced cooled line (3.63) becomes

$$\frac{\text{UG}}{\text{OH}} = \frac{1}{\text{OH}} \frac{1+y}{1+x} \text{CC} + \frac{DL}{1+x} + (1+x)JL \tag{3.64}$$

Consider first of all the case $y=x$ and $JL>DL$. Then for any value $x>0$ the cost ratio will be greater for forced cooling then for natural cooling. Hence to benefit from forced cooling y must be smaller than x. Set $y=mx$ where $0<m<1$ and $m=y/x$. Table 3.6 lists UG/OH ratios for the 500 kV system at 75 percent load factor for values of m and x varying between zero and one. These results show, for example, that a 2.02 transmission cost ratio is obtainable at 500 kV provided $x=0.8$ and $m=0.4$. It requires a cooling system which adds no more than 32 percent to the installed cost in return for 80 percent additional transmission capability. The table also suggests that it would be difficult to reduce the UG/OH ratio much below two.

Forced cooling is likely to decrease the transmission efficiency because the increase in Joule loss will probably outweigh the dilution of the dielectric loss. However in the 500 kV example, in which the annual cost of the dielectric loss of the naturally cooled line is greater than the Joule-loss cost, there is little deterioration of the transmission efficiency provided the driving power in the cooling plant does not add appreciably to the total loss. For example the 2.02 UG/OH ratio for 500-kV self-contained cables requires $x=0.8$ and this increases the sum of dielectric and Joule loss/MVA·yr·mi transmission by merely 4 percent.

The cost of underwater transmission is not firmly established. It varies greatly from one installation to another. As an example we will consider the 138-kV Long Island Sound cable shown in Fig. 3.35(a). It was in service in 1971 and the installed cost has been given as exceeding $10 million for two circuits and one spare core of 11.8 mile length [3.20]. The annual capital charge per mile in 1971 was therefore $127,119. For $\varepsilon=3.5$, $\cos\phi=2.5\times10^{-3}$ the dielectric loss of this underwater line comes to 18.8 kW/mi. The

Table 3.6 Effect of forced cooling on the 1976 UG/OH transmission cost ratio at 500 kV

	UG/OH				
x	$m=1.0$	$m=0.8$	$m=0.6$	$m=0.4$	$m=0.2$
0.2	2.46	2.40	2.33	2.27	2.21
0.4	2.47	2.36	2.26	2.15	2.04
0.6	2.49	2.35	2.21	2.07	1.92
0.8	2.52	2.35	2.18	2.02	1.85
1.0	2.55	2.36	2.17	1.98	1.79

Joule loss factor was specified as 0.63, suggesting a daily load factor of 75 percent. Approximate values of the resistances of the conductor and the outer metallic layers are 0.102 Ω/mi and 0.05 Ω/mi. As the sheaths of the submarine cable cannot be cross-bonded, the aluminum armor wires and the lead sheath will carry a circulating current which is nearly equal to the conductor current. The combined capability of the two circuits has been given as 300 MVA, corresponding to a current of 628 A. Noting the Joule-loss factor, the result is a current dependent loss of 227 kW/mi.

Assuming the cable was utilized as originally specified, the 1976 transmission cost would have been

$$\frac{1}{300}(127{,}119 + 18.8 \times 24 \times 365 \times 0.0255 + 227 \times 24 \times 365 \times 0.0255)$$
$$= \$607/\text{MVA} \cdot \text{yr} \cdot \text{mi}$$

This result is represented by the single point in Fig. 3.37. Although the underwater transmission cost for the self-contained oil-paper insulated L.I. Sound cable is rather high compared with underground lines, it is nevertheless an economical solution to a particular transmission problem considering the length of the alternative overhead line along the L.I. and Connecticut shores.

3.3 OIL-PAPER INSULATED PIPE-TYPE CABLES

U.S. pipe-type cables have much in common with the European self-contained oil-paper insulated cables of Section 3.2. Both have profited from cross-fertilization in the development of conductors and high-voltage insulation. There remain, however, some important differences in installation procedures, ancillary equipment, ampacity and forced cooling which will all be considered in the present section.

Description

Pipe-type cables are commercially available up to 550 kV and 750 kV cables are clearly feasible [3.34]. Most of the installed circuit mileage falls into the voltage classes up to and including 138 kV. Significant quantities of 345 kV cable are in operation, particularly in New York City. The useful range of pipe-type cables is illustrated in Fig. 3.42. Inside diameters of the pipes vary between 8 and 12 in.

Conductors of pipe cables do not require an oil duct. Concentric stranding is commonplace with smaller conductors but the segmental construction is used universally for the popular 2000 kcmil size. Conductor flexibility is at a

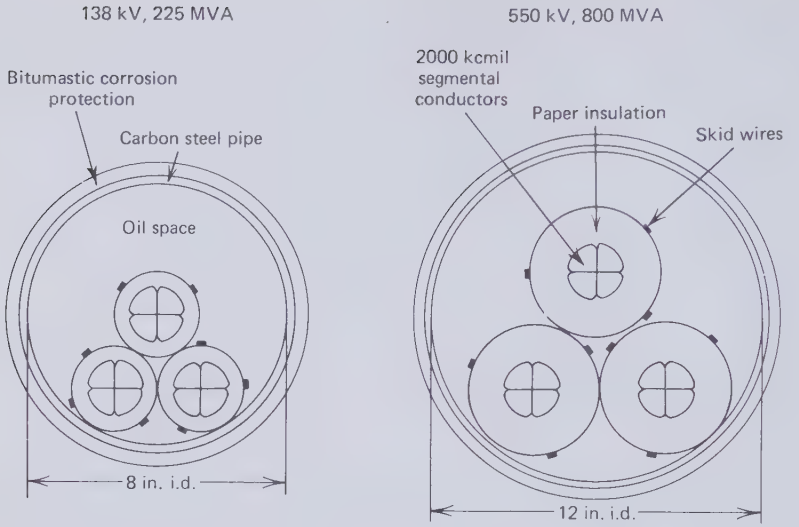

Figure 3.42 Useful size range of pipe-type cables.

premium in pipe-type cables because the insulated cores have to be pulled around bends in the pipeline. This mitigates against compact and rigid conductors as for example the Conci construction of Fig. 3.6(a) on page 285. It partly explains why conductor development for pipe cables has apparently come to a halt at 2500 kcmil while self-contained cables have raced on to 6000 kcmil. Large conductors in pipes do not offer as high a return in ampacity as might be expected. This was shown by Kilar and Engelhardt [3.33] who have published the graph of Fig. 3.43, which applies to 345 kV pipe-type cables. It will be seen that doubling the conductor area from 2000 to 4000 kcmil increases the ampacity by only 25 percent. The diminishing return in transmission capability is the result of mutual heating of the three cable cores and the sharing of the heat flow path through the soil.

Many small differences in paper density, preparation, air permeability, tape thickness, wrapping tension, shield design, oil composition, and so on, lead to slight variations in the insulation performance. Disregarding the preferences of individual cable manufacturers, it can be said that all oil-paper insulated cables have about the same permittivity (3.5), insulation power factor (0.1–0.3 percent), and thermal resistivity (500 thermal-$\Omega \cdot$cm). The higher pressure in the pipe will make it more difficult for vapor bubbles to form in the oil contained in the butt gaps between paper tapes and this should interfere with the progress of thermal instability failure. Oil pressure does not influence the insulation power factor in a significant way and therefore it should not change the temperature at which thermal instability

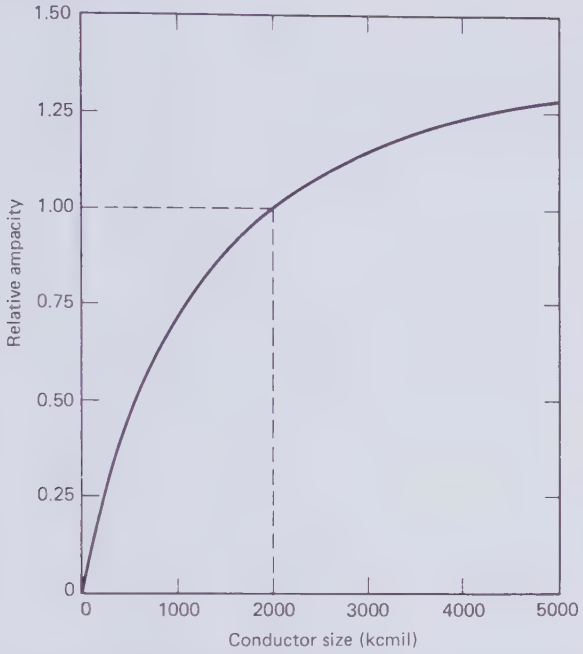

Figure 3.43 Naturally cooled 345-kV pipe-type cable ampacity as a function of conductor size according to Kilar and Engelhardt [3.33]. (By permission of the Institute of Electrical and Electronics Engineers).

will occur. Although different permissible conductor temperatures are sometimes specified for pipe and self-contained cables, there exists no scientific basis for this. The suppression of vapor bubbles, on the other hand, does permit higher design stresses in pipe-type cables. The measured impulse and ac breakdown strength as a function of oil pressure is plotted on Fig. 3.7. Particularly with regard to the overriding impulse strength, the pipe-type cable is seen to have at least a 10 percent advantage over self-contained cables. The latter may be assumed to operate at an average pressure of 50 psi compared to the 200 psi of pipe-type cables. The higher breakdown strength of pipe cables has been born out in some tests at Waltz Mill on 550 kV cables, where one of the successful samples was designed to a stress of 170 kV(rms)/cm at the conductor surface [3.39].

The cores of pipe cables are factory impregnated with quite a viscous oil and then protected against moisture pick-up during storage, transportation, and pulling into the pipe. Metal or metallized tapes are wrapped around the cores to make it difficult for atmospheric moisture to reach the paper. These tapes also help to retain the impregnant. As a further precaution against moisture contamination, the finished cores are stored on sealed metal reels

filled with dry gas. These measures and further protective steps taken during installation have proved entirely successful in maintaining the insulation quality over the relatively long period of time between factory impregnation and filling of the oil pipe.

To aid the sliding of cores in the pipe, *D*-shaped skid wires of stainless steel, bronze or a strong plastic material as for example high-density polyethylene are wound over the insulation shield with a short lay. The flat side of the *D* rests against the core and the round side comes in contact with the pipe and other cable cores.

So far all the oil pipes have been made of a high-grade carbon steel. Since the first installation of a pipe-type cable in the 1930s, steel has represented the best compromise between strength and economy in spite of substantial energy losses in the pipe wall and the corrosive nature of steel. Possible alternative materials are aluminum, stainless steel and glass fiber reinforced epoxy resin [3.35]. When designed for the same internal pressure and external street traffic load, steel pipes are considerably less costly than these three alternatives. However, no up to date analysis appears to have been performed which takes the cost of energy losses into account.

Steel pipes have to be internally cleaned before installation to remove rust and other contamination [3.37]. After cleaning they may be internally coated with a thin layer of material—often an epoxy compound [3.36]—which is chemically compatible with the cable oil and prevents internal corrosion until the pipe is filled with oil. The internal coating should also ensure smooth sliding of the cores through the pipe. Corrosion protection on the outside of the pipe follows standard pipeline practice [3.38]. The rule is to apply a layer of approximately 0.5 in thickness of an asphalt mastic containing sand, mineral fillers and fibers. Where appropriate, cathodic protection is provided in addition to the anticorrosion covering.

Installation

It is in the installation technology that pipe cables have a number of advantages over self-contained cables. To mention just two: concrete slabs are not required for mechanical protection and two three-phase circuits can more easily be housed in one trench. This is apparent from comparing Fig. 3.9 with Fig. 3.44. The latter refers to a 345 kV double circuit placed in a 5-ft-wide and 4.5-ft-deep trench. In New York the trenches are filled entirely with thermal sand up to the pavement level [3.36] and the sand is compacted to a minimum dry density of 115 lb/ft^3. The compacted dry sand was found to have a thermal resistivity of 80 to 90 thermal-$\Omega \cdot cm$ which fell to 30 to 35 thermal-$\Omega \cdot cm$ when 10 percent moisture was added. Other utilities backfill some of the excavated soil on top of thermal sand and then

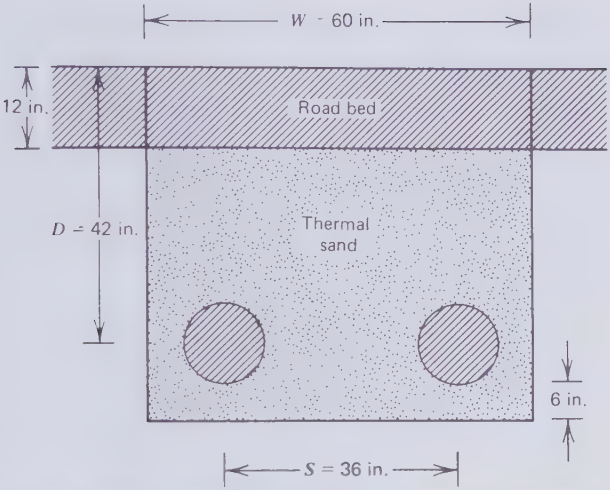

Figure 3.44 Typical trench cross section of 345 kV double-circuit installed in New York [3.36]. (By permission of the Institute of Electrical and Electronics Engineers).

make an adjustment in the average soil thermal resistivity when calculating the cable ampacity.

Wherever possible pipe welding and weld inspection should be carried out above ground level just before lowering the pipe into the trench. A final leak check of manhole-to-manhole lengths is made in the trench with a pressure drop test. Dry nitrogen gas up to a pressure of 500 p.s.i. is being used for this purpose. Three different pipe joints have been developed over the years. Least use is made of the sleeve joint, which requires two circumferential weld seams. It is rarely possible to match two pipe sections in diametrical dimensions and roundness so that they will not form an internal step under the sleeve, which could harm the cable cores during pull-in. Most cable pipelines are joined with the aid of smooth internal backing rings (chill rings) which are located under the slightly flared ends of abutting pipe sections. This method requires only one weld seam and the ring prevents welding icicles from projecting into the cable run. The same result can be achieved with a bell and spigot joint but this requires an additional weld seam for attaching the bell section. All weld seams should be inspected radiographically to ensure that the molten metal has properly penetrated and the inside profile of the joint is smooth. Leak testing has to be performed in addition to radiography. Internal pressurizing plugs or 'pigs' are available with which a short section of pipe can be set under gas pressure and an external water bath surrounding the pipe will indicate leaks by gas bubbles emerging from the surface. When weld inspection and leak testing routines

are carefully followed steel pipelines give long years of trouble free service. Part of the pipe jointing process is the restoration of the corrosion covering over the joint length. Pipe bends are produced in the field and welded in position. The radius of these bends should be kept as large as possible to facilitate core pulling.

The splices of self-contained cables may be directly buried but the splices of pipe cables are customarily housed in permanent manholes at the locations were the cable cores were first pulled into the pipe. Another important function of the manhole is to provide a weather shelter and air conditioned enclosure for the duration of the splicing operations, which last a number of days. Splices are the weakest points of all types of cable. Having them installed in accessible manholes makes for easy repair. The manholes are usually precast concrete enclosures with entrances for cables and personnel. To compliment the trench layout of Fig. 3.44, a typical manhole would by 18 ft long, 7 ft wide and of sufficient height for splicers to work in it comfortably. The distance between manholes is governed first by the maximum pulling tension that can safely be applied to the cable cores and deviations from a straight line pull, and second on the length of cable core that can be stored on a reel and transported to the manhole. For the larger circuits a typical spacing is 2000 ft. Substantially longer lengths have been pulled into pipes when the cores are of small diameter. Splices in pipe cable cores are spaced at least twice as far apart as they would be on a self-contained cable system. A further advantage of pipe-type cable is that splice pits are uncluttered by cross-bonding and oil tank equipment.

In the densely built-up areas in which most pipe cables have been installed, pipe laying and the burial of manholes may proceed by opening short sections of road at a time and close them again shortly afterwards, causing a minimum of traffic disruption. Trench sections of a cross-bonding length of self-contained cable are usually kept open much longer until the splices are made and tested in case one of the cores has to be replaced.

To ensure the removal of any moisture that may have accumulated inside the pipe during installation, sections between manholes are dried by evacuating them with a mechanical pump to a pressure of approximately 10^{-1} torr. To check that the drying process is complete, a valve between the pump and the line is closed and the subsequent pressure rise observed. When this is less than 10^{-2} torr/hr the pipe has reached adequate dryness and the vacuum may be broken to dry nitrogen gas to keep out moist air.

All three cable cores are pulled together into the pipe by a single grip at the end of the cores that are fed from weather protected reel trailers standing close to the manhole. The pulling tension is continuously monitored and safe guidelines are available in the Underground Reference Book [1.46] for not overstraining the conductors while they slide around horizontal and vertical

bends of different radii. The pipe has to be of a certain minimum diameter to allow adequate clearance for the core pulling operation. Depending largely on pipe size, the three cores may arrange themselves in triangular or cradled configuration as shown in Fig. 3.45. The clearance c between the uppermost cable core of diameter d of the triangular arrangement and the inside diameter of the pipe can be shown to be

$$c = D/2 - 1.366d + 0.5(D-d)\sqrt{1-\left[\frac{d}{(D-d)}\right]^2} \tag{3.65}$$

For any desired clearance and core diameter the pipe/core diameter ratio may be read from the graph of Fig. 3.45. When D/d is smaller than 2.5, the cables are more or less compelled to stay in the triangular array which results in more magnetic field cancellation and therefore lower pipe loss than that associated with the cradled core arrangement.

The principal aspects of splicing oil-paper insulated cables are the same for pipe-type and self-contained systems. Both have benefitted equally from the development of improved connectors and prefabricated parts that can be slipped over the insulation. It is also true to say that both still depend to a considerable extent on many hours of skilled manual work, which continues to have an adverse effect on cable installation costs and repair times. One

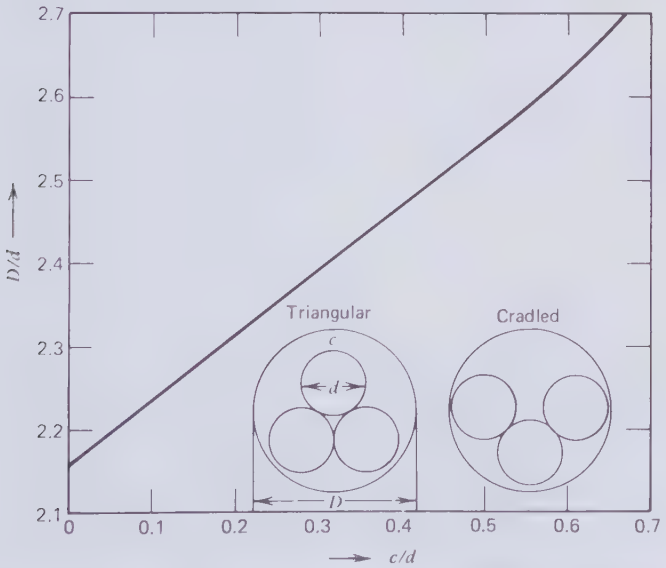

Figure 3.45 Pipe to core diameter ratio as a function of desired core clearance [1.46].

difference between the two splice versions is that all three core joints of the pipe cable can be housed inside the same enlarged steel sleeve which interconnects the two pipe sections.

As the steel pipe is capable of withstanding much more internal pressure than is normally required for the insulated cores it is unnecessary to provide pipe-type cables with complex stop joints of the kind that are required for self-contained cables in hilly country to protect the weak cable sheath against hydrostatic heads. This point in favor of pipe cables has to be weighed against the danger of spilling the larger oil volume in pipes into the ground and possibly pollute water supplies when the pipe is accidentally punctured. Semistop joints have been developed for pipe cables that limit the accidental oil spillage to a section between two such joints.

The principle of the semistop joint is outlined by the schematic sketch of Fig. 3.46. Oil flow barriers that grip the three cable cores individually are provided on either side of the otherwise normal core splices. An external oil-bypass is fitted which also connects to the space between the barriers to keep the splices under pressure. Various valves on the by-pass may be operated manually or automatically to isolate oil sections from each other. The adjective "semistop" is used because a little oil may penetrate the barrier through the taped insulation of the cores. In another design of a semistop joint, inflatable collars are placed between the cores and the barrier plates. During normal operation of the circuit these collars are left deflated so that oil can pass along the cable. In an emergency in which the pipe springs a major leak, the collars are automatically inflated so that only the oil in the section that is inflicted by the leak will spill into the surrounding soil.

The terminations of pipe cables differ in two respects from those of self-contained cables. In the first place, to establish adequate clearances between the potheads, the three cores have to be broken out from the

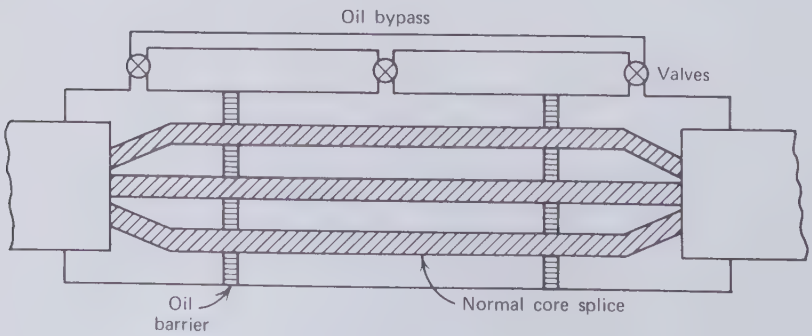

Figure 3.46 Principle of semi-stop joint of pipe-type cable.

collective pipe into three single pipes. This transition through a "spreader" is usually made 10 or 20 feet below the potheads of an open air installation. No restriction of the oil passage is built into the spreader and therefore the potheads are subject to the same pressure as the pipe. It is customary to make the short pieces of single pipe enclosures out of nonmagnetic stainless steel to avoid them becoming overheated by the magnetic loss due to the stronger field surrounding the isolated cores.

The second feature that distinguishes terminations of pipe cables from those on self-contained cables is the greater pressure the porcelain shell has to withstand. Some manufacturers use a small diameter high-pressure tube to contain the pipe pressure and then surround this tube with oil at lower pressure which is enclosed in a standard porcelain housing. Others prefer a single pressure arrangement and a suitably reinforced porcelain body.

In typical naturally cooled pipe cables the oil pressure is maintained with duplicate pumps located on one end of the transmission line, or on both when the circuit is long. Pumping and control plant are commonly housed in above-ground structures in the substation in which the cable is terminated. Pump duplication is deemed necessary because running machinery requires servicing and is not quite as reliable as static plant. Careful thought has to be given to the power supply of the pumps. Difficulties may arise in energizing a pipe cable system after a major power failure if the pumps have to be driven by electricity from the public distribution system. Pumping stations also have to be provided with oil tanks which allow for thermal expansion and contraction of the oil volume in the pipe. The pumping stations have to run unattended and have to be fully automated for this purpose. Alarms in load control centers give warning of the loss of pressure in pipe cable systems.

Before filling a newly installed, spliced, and terminated pipe cable with oil it is advisable to evacuate it once more to remove any moisture that may have accumulated on the insulation during the latter stages of the installation work.

Ampacity

To be able to calculate the maximum steady rms current which a self-cooled pipe cable may carry, it is necessary to have three kinds of information. They are (1) the strengths of the heat sources inside the cable, (2) the temperature limits set by the cable and its environment, and (3) the thermal resistances through which the cable heat must be conducted away. The strengths of current related heat sources in pipe cables have been discussed in Section 1.18. The major heat sources in the cable are the three conductors. When I amperes of 60-Hz current flow in each conductor the heat

dissipated in unit length is

$$P_c = I^2 R_{ac} \tag{3.66}$$

For segmental conductors in pipe-type cable the ac resistance per unit length may be determined from the dc resistance at the appropriate temperature and the ac-dc resistance ratio plotted on Fig. 1.56. For reasons given in Seection 1.18, it is suggested that the broken curve of Fig. 1.56 should be used for segmental copper conductors operating at 60 Hz. Figure 1.71 may be consulted for the resistivities of standard grades of copper and aluminum at the design temperatures. The segmental conductor construction is intended to suppress the proximity effect. If the conductors are concentrically stranded, an allowance for the proximity effect can be made with (1.154).

It will be appreciated that the energy losses in the insulation shield and skid wire assembly P_s, as well as those in the pipe P_p, will make themselves felt as ac resistance components in the conductor—see (1.159)—but they must not be included in the conductor heat source (3.66). With (1.159b) the shield loss may be expressed as

$$P_s = I^2 R_s' = \frac{I^2 R_s}{1 + \left(\dfrac{R_s}{\omega M_{c,s}} \right)^2} \tag{3.67}$$

where R_s is the dc resistance per unit length of the shield assembly and $M_{c,s}$ the mutual inductance between the conductor and the surrounding shield. As the shield is normally quite thin the mutual inductance is given by (1.94).

Finally the empirical formula (1.159c) should be used to calculate the pipe loss, or

$$P_p = I^2 R_p' = I^2 (0.34S + 0.175 D_p) \cdot 10^{-6} \quad \text{W/ft} \tag{3.68}$$

where S is the average axial spacing between the cores in inches and D_p is the inside diameter of the steel pipe in inches. Equation (3.68) applies to the more common case of the cores lying in cradled formation. If the pipe is so small that close triangular spacing may be assumed, the pipe loss will be less and the following empirical formula from [1.19] is available

$$P_p = I^2 R_p' = I^2 (0.89S - 0.115 D_p) \cdot 10^{-6} \quad \text{W/ft} \tag{3.69}$$

The only other heat source to be considered is the dielectric loss given by (2.81). As has been proved with (2.79), the correct temperature drop across the insulation due to dielectric heating alone is obtained by allowing the

total dielectric loss P_d per unit length to flow through half the thermal resistance R_i of the insulation.

In the discussion of the ampacity of self-contained cables it was explained that the choice of the maximum permitted conductor temperature has an effect on cable life because it is also the temperature of the insulation next to the conductor and therefore controls the slow decomposition or ageing of the cellulose. Every 9°C temperature rise is believed to double the decomposition rate. Not all users of oil-paper insulated cables agree on the value of T_c, and cable designs have been based on conductor temperatures ranging from 70 to 95°C. Some power companies chose a single temperature, and others distinguish between the "normal" and "emergency" temperature. Restrictions may be placed on the time the cable is allowed to operate at the emergency temperature. The ampacity of a cable is its current rating when the conductor has reached the "normal" temperature.

All the heat generated in naturally cooled cables is dumped into the atmosphere. Therefore the sink temperature is continuously fluctuating. A single temperature value has to be chosen for ampacity calculations. This is called the ambient temperature T_a and it would be the soil temperature at burial depth in the absence of the cable. The soil temperature is governed by the surface air temperature but varies quite slowly with a time constant of weeks. Some utilities rate their cables for two ambient temperatures, one giving the summer ampacity and the other the winter ampacity. More than two seasonally adjusted current ratings may of course be used in any cable loading program. The summer rating, which is frequently the only rating assigned to a cable, commonly is based on T_a values between 20 and 30°C.

A heat flow diagram with sources, sink, and thermal resistances of the naturally cooled pipe-type cable is shown in Fig 3.47. As before, this ignores the negligibly small thermal resistances of the metallic components. Both the thermal resistance of the oil-paper insulation R_i and that of the somastic corrosion jacket R_j may be calculated from (2.80). The thermal resistivities ($\rho = 1/\kappa$) of typical oil-paper insulation and somastic coatings are 500 and 100 thermal-$\Omega \cdot$cm, respectively.

To arrive at the heat flux through the soil, the pipe surface is considered to be an isothermal surface. With this assumption Fig. 3.14 can also be applied to pipe cables where the pipe takes the place of the metal sheath surrounding a self-contained cable core. It follows that the thermal resistance between an isolated pipe and atmosphere is given by (3.8) on page 296 and the approximation (3.9). If two or more pipes are installed in close proximity, that is in the same trench, then the method of thermal images explained by Fig. 3.15 (page 298) has to be employed to derive the thermal proximity factor k. For an isolated pipe $k = 1$. Should three pipes be installed in the same trench, k is given by (3.15). The most common arrangement is that of Fig. 3.44, where two circuits are installed in the same trench. In this

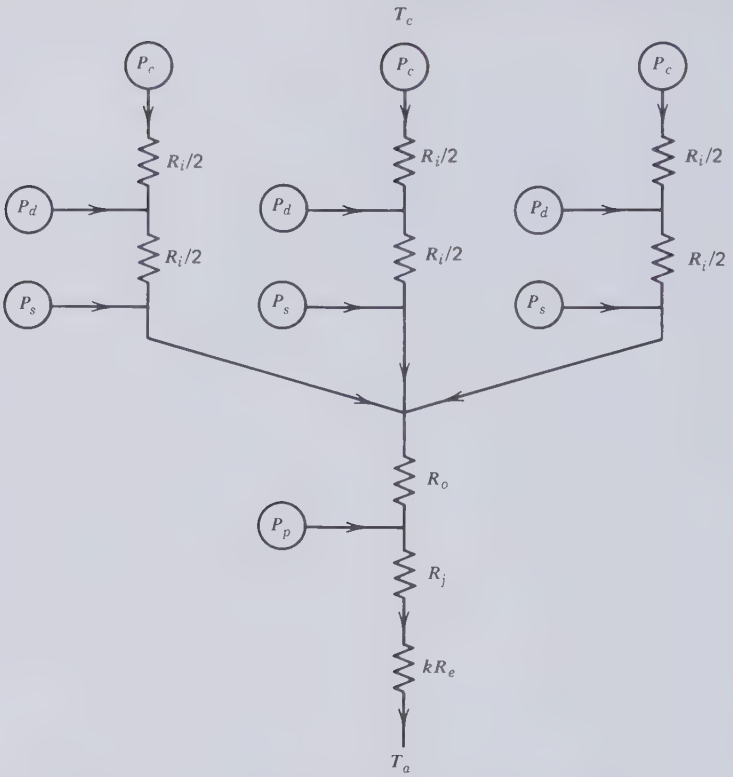

Figure 3.47 Thermal circuit of naturally cooled pipe-type cable.

case the temperature rise in pipe 2 due to the heat it receives from pipe 1 is given by (3.10), and (3.12) shows the temperature rise of pipe 2 due to its own heat dissipation. The sum of these two temperature increments divided by (3.12) defines the thermal proximity factor, which therefore is

$$k = 1 + \frac{\ln \dfrac{x_{1',2}}{x_{1,2}}}{\ln \dfrac{2D}{r}} \tag{3.70}$$

where r is the pipe radius, D the burial depth, and the x-distances are defined in the thermal image diagram of Fig. 3.15. Because of symmetry the same value of k applies to both pipes.

R_0 on Fig. 3.47 stands for the heat transfer impedance of the oil. An analytical assessment of this parameter has proved to be difficult [3.40]. The

heat is being carried by convection through the bulk of the oil with little hinderance and the resistance arises mainly in the surface films on the cable cores and the pipe. It is common practice to compute R_0 from one of two formulas recommended by Neher and McGrath [1.19]. The first of them is

$$R_0 = \frac{2.52}{1+0.0065D'T_0} \quad \text{thermal-}\Omega\text{ (per ft)} \tag{3.71}$$

In this formula D' is the diameter in inches of a circle circumscribing the three cores, and T_0 is the mean oil temperature in °C. The usefulness of (3.71) is limited by the fact that T_0 cannot be calculated explicitly without prior knowledge of T_0. To avoid time-consuming iterations Neher and McGrath suggested the second and approximate formula

$$R_0 = \frac{6.3}{2.45+D'} \quad \text{thermal-}\Omega\text{ (per ft)} \tag{3.72}$$

which has been derived making assumptions about the most likely range of oil temperatures. Equation (3.72) should be treated as an empirical relationship in adequate agreement with practical experience. D' will be a minimum when the three cores are touching each other in close trefoil formation. If d is the core diameter it can be shown that

$$D'_{\min} = 2.15d \tag{3.73}$$

and the maximum circumscribing circle is of course limited by

$$D'_{\max} = 3d \tag{3.74}$$

The selection of a value of D' between these two extremes is a matter of judgement rather than computation.

To derive the ampacity equation for pipe cable we sum the temperature drops along one of the resistance chains of Fig. 3.47 from the atmospheric sink to one of the conductors.

$$T_c - T_a = \left[3(P_c+P_d+P_s)+P_p\right](R_j+kR_e) + 3(P_c+P_d+P_s)R_0 + (P_c+P_d)\left(\frac{R_1}{2}\right) + P_c\left(\frac{R_1}{2}\right) \tag{3.75}$$

Next we substitute for P_c, P_s, and P_p from (3.66) to (3.68) using the ac conductor resistance R_{ac} and the equivalent shield and pipe resistances R'_s

and R_p'. The resulting equation may be solved for I^2 to give

$$I^2 = \frac{T_c - T_a - P_d\left[\left(\frac{R_i}{2}\right) + 3R_0 + 3R_j + 3kR_e\right]}{R_{ac}R_i + 3(R_{ac} + R_s')(R_0 + R_j + kR_e) + R_p'(R_j + kR_e)} \tag{3.76}$$

To further clarify the involved computation of the ampacity of pipe cables let us consider the following numerical example.

EXAMPLE:

1. 345-kV double-circuit installed according to Fig. 3.44. $D = 42$ in.; $S = 36$ in.
2. Pipe: 0.25-in.-thick grade A steel; inside diameter $D_p = 10.25$ in.; 0.5-in.-thick somastic coating of 100 thermal-$\Omega \cdot$cm.
3. Conductors: 2000 kcmil, 4 segments, 102% IACS copper, 1.632 in. diam.
4. Insulation: 1.025 in. thick, 3.682 in. overall diameter, 500 thermal-$\Omega \cdot$cm, $\varepsilon = 3.5$, $\cos\phi = 2.5 \times 10^{-3}$.
5. Electrostatic shield and skid wire assembly: metallized (aluminum) mylar tapes, 1 in. wide, 1/8 in. overlap, total metal thickness 1 mil. Two D-shaped stainless steel skid wires, 0.25 in. diam half-round, 3 in. lay, 77×10^{-6} $\Omega \cdot$cm at 60°C, diameter over skid wires 3.95 in.
6. To show the variation of ampacity with ambient conditions and conductor temperature, the calculations will be carried out for soil thermal resistivities from 70 to 120 thermal-$\Omega \cdot$cm, three ambient temperatures of 20, 25, and 30°C, and three conductor temperatures of 70, 80, and 90°C.

Conductor resistance R_{ac}. The cross-sectional area of the conductors is converted as follows: 1 circular mil $= (\pi/4) \times 10^{-6}$ in^2 $= (\pi/4) \times 10^{-6} \times 2.54^2$ $= 5.067 \times 10^{-6}$ cm^2. With a 2% stranding factor the conductor dc resistance is

$$R_{dc} = \frac{1.02\rho_c(T_c)}{(2 \times 10^6 \times 5.067 \times 10^{-6})} = 0.1\rho_c(T_c) \quad \Omega/\text{cm}$$

The conductor resistivity as a function of temperature may be read off Fig. 1.71. Furthermore the broken curve of Fig. 1.56 indicates $R_{ac}/R_{dc} = 1.085$. This information is sufficient to calculate the conductor loss resistance $R_{ac} = R_{dc}(R_{ac}/R_{dc})$.

T_c(°C)	70	80	90
$\rho_c(\Omega \cdot \text{cm})$	2.02×10^{-6}	2.10×10^{-6}	2.14×10^{-6}
$R_{dc}(\Omega/\text{cm})$	0.202×10^{-6}	0.210×10^{-6}	0.214×10^{-6}
$R_{ac}(\Omega/\text{cm})$	0.219×10^{-6}	0.228×10^{-6}	0.232×10^{-6}

EQUIVALENT RESISTANCE OF SHIELD AND SKID WIRE ASSEMBLY R_s'. For the purpose of this calculation we assume all the shield metal to be concentrated on one tape. The back of the tape is insulated and therefore the induced shield currents have to follow the lay of the tape. To advance 0.875 in. along the cable core the induced current has to cover a pathlength of $[0.875^2+(3.682\pi)^2]^{1/2}=11.6$ in. where 3.682 in. is the cable core diameter. The resistivity of aluminum at an assumed shield temperature of 60°C is, from Fig. 1.71, $3.3\times10^{-6}\ \Omega\cdot$cm. Therefore, the tape resistance per cm core length is

$$R_t=3.3\times10^{-6}\frac{\left(\frac{11.6}{0.875}\right)}{(1\times10^{-3}\times2.54^2)}=6.78\times10^{-3}\quad\Omega/\text{cm}$$

Similarly, each skid wire advances 3 in. during one turn around the core so that the induced current has to cover a pathlength of $[3^2+(3.682\pi)^2]^{1/2}=11.95$ in. in one 3 in. lay. The dc resistance of the two skid wires in parallel is

$$R_{sw}=0.5\times77\times10^{-6}\frac{11.95/3}{0.5(\pi\times0.125^2)\times2.54^2}=0.969\times10^{-3}\quad\Omega/\text{cm}$$

The dc resistance of the assembly for the parallel combination of R_t and R_{sw} is

$$R_s=\frac{R_t\cdot R_{sw}}{R_t+R_{sw}}=\frac{6.78\times10^{-3}\times0.969\times10^{-3}}{6.78\times10^{-3}+0.969\times10^{-3}}=8.48\times10^{-4}\quad\Omega/\text{cm}$$

The shields are in contact with each other in the pipe and the longitudinal circulating current loss is given by (3.67). Before this can be used, it is necessary to compute the mutual inductance between conductor and shield from (1.94). It has been proved in Section 1.11 that the mutual inductance *per unit length* of parallel conductors is itself length dependent. To calculate $M_{c,s}$ it will be assumed that the cable length is $L=10^5$ cm. Ten times this length would only make a small difference to the ampacity. Furthermore, we treat the shield as a thin layer so that

$$r_0=r_i=\frac{3.682}{2}\times2.54=4.676\text{ cm}$$

$$M_{c,s}=2\times10^5\left[-1+\ln(2\times10^5)-\ln 4.676\right]=1.93\times10^6\text{ cm}=1.93\times10^{-3}\text{ H}$$

$$M_{c,s}/L=1.93\times10^{-3}/10^5=1.93\times10^{-8}\quad\text{H/cm}$$

Hence from (3.67)

$$R_s' = \frac{8.48\times10^{-4}}{1+\left[\dfrac{8.48\times10^{-4}}{(2\pi\times60\times1.93\times10^{-8})}\right]^2} = 6.24\times10^{-8} \quad \Omega/\text{cm}$$

EQUIVALENT PIPE RESISTANCE R_p'. From (3.68)

$$R_p' = \frac{(0.34S+0.175D_p)\times10^{-6}}{12\times2.54} \quad \Omega/\text{cm}$$

$$D_p = 10.25; \qquad S_{\min} = d = 4.13; \qquad S_{\max} = 1.5d = 6.20$$

Let us take the mean value of $S_{\text{mean}} = 5.17$

$$R_p' = \frac{(0.34\times5.17+0.175\times10.25)\times10^{-6}}{12\times2.54} \doteq 0.117\times10^{-6} \quad \Omega/\text{cm}$$

DIELECTRIC LOSS P_d. The phase voltage of a 345 kV system is

$$V = 345{,}000/\sqrt{3} = 199{,}186 \quad \text{V}$$

From (2.81)

$$P_d = \frac{2\pi\times60\times3.5\times199186^2\times2.5\times10^{-3}}{2\ln\left(\dfrac{3.682}{1.632}\right)\times9\times10^{11}} = 0.0894 \quad \text{W/cm}$$

THERMAL RESISTANCE OF THE INSULATION R_i. From (2.80)

$$R_i = \frac{500}{2\pi}\ln\frac{3.682}{1.632} = 64.75 \quad \text{thermal-}\Omega\text{ (per cm)}$$

THERMAL RESISTANCE OF THE SOMASTIC JACKET R_j. From (2.80)

$$R_j = \frac{100}{2\pi}\ln\frac{11.75}{10.75} = 1.42 \quad \text{thermal-}\Omega\text{ (per cm)}$$

SOIL THERMAL RESISTANCE R_e. From (3.8)

$$R_e = \frac{\rho_e}{2\pi} \ln \frac{84 - (11.75/2)}{11.75/2} = 0.4118\rho_e \quad \text{thermal-}\Omega\text{ (per cm)}$$

ρ_e(thermal-Ω·cm)	70	80	90	100	110	120
R_e(thermal-Ω)	28.83	32.95	37.06	41.18	45.30	49.42

THERMAL PROXIMITY FACTOR k. From (3.70)

$$k = 1 + \frac{\ln \dfrac{(84^2 + 36^2)^{1/2}}{36}}{\ln \dfrac{84}{(11.75/2)}} = 1.35$$

THERMAL RESISTANCE OF OIL R_0. Assume the intermediate value of $D' = 2.5d = 2.5 \times 3.682 = 9.2$. Then from (3.72)

$$R_0 = \frac{6.3 \times 12 \times 2.54}{2.45 + 9.2} = 16.5 \quad \text{thermal-}\Omega\text{ (per cm)}$$

AMPACITY GRAPHS. To show the variation in current rating with ambient conditions and conductor temperature the computations have been extended to a range of soil thermal resistivities from 70 to 120 thermal-Ω·cm, three ambient temperatures of 20, 25, and 30°C, and three conductor temperatures of 70, 80, and 90°C. The graphs of Fig. 3.48 have been obtained by substituting all the information into (3.76). Over the full range of externally imposed conditions the ampacity of the 345-kV double circuit is seen to stretch from approximately 400 to 870 A. It corresponds to a continuous transmission capability in one trench of 480 to 1040 MVA.

CURRENT RATING IN AIR. Equation (3.20) and (3.21) on page 302 give radiation and convection heat transfer from the surface of the cable jacket in still air at ambient temperature T_a. The heat dissipated from the somastic coating of the pipe cable used in the present example has been calculated and plotted in Fig. 3.49 as a function of the jacket surface temperature T_0 and a single ambient temperature of 25°C. In soil of a thermal resistivity of 90 thermal-Ω·cm at $T_a = 25$°C and permitting the conductor temperature to rise to 80°C, the ampacity of the pipe cable is 650 A (see Fig. 3.48). The energy dissipated in the cable at this current comes to 0.7 W/cm. If suspended in still air, instead of being buried, the cable surface temperature would rise only to 35°C, as seen on Fig. 3.49. Knowing this temperature we

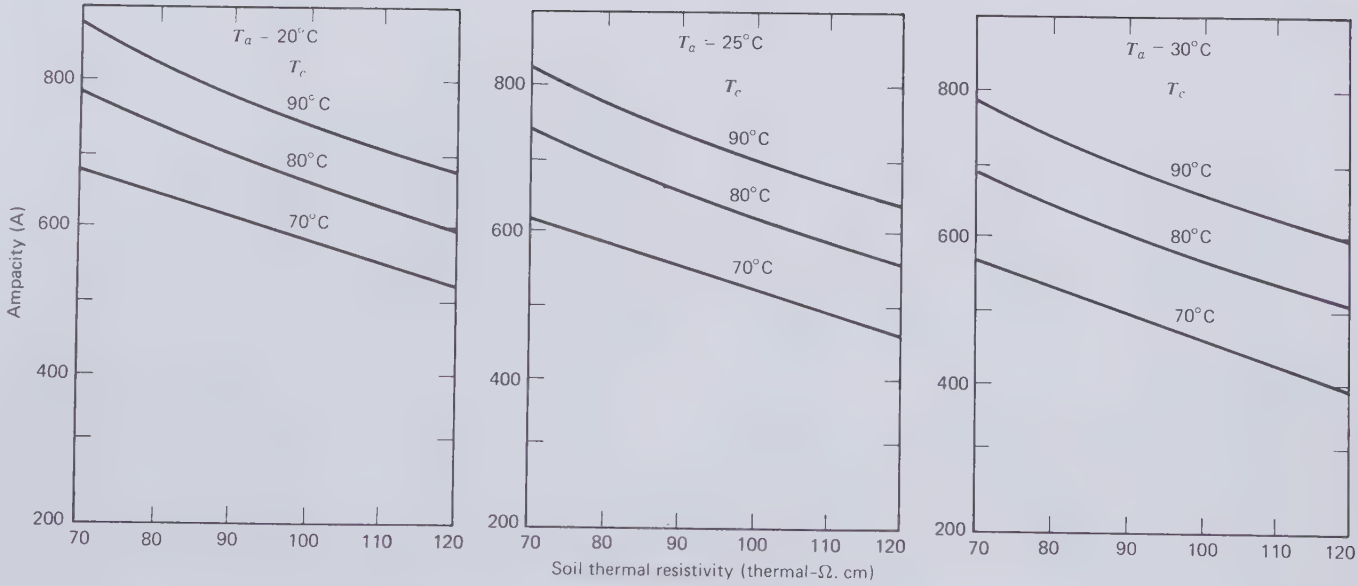

Figure 3.48 Ampacity graphs for naturally cooled pipe-type cable example.

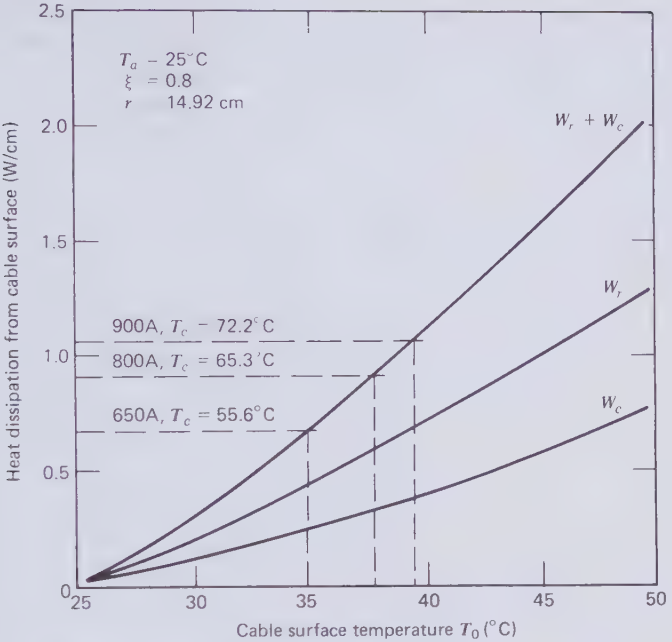

Figure 3.49 345 kV, 2000 kcmil pipe-type cable ampacity in air.

are in a position to calculate the conductor temperature T_c from the heat flow circuit of Fig. 3.47.

$$T_c - T_0 = \left[3(P_c + P_s + P_d) + P_p\right]R_j + 3(P_c + P_s + P_d)R_0 + (P_c + P_d)\frac{R_i}{2} + P_c\frac{R_i}{2} \tag{3.77}$$

With the appropriate data, which is all available from the worked example, this equation indicates a conductor temperature of 55.6°C. Therefore, as already found in connection with self-contained cables, air is a more effective natural cooling medium than soil. This is important for the cooling of splices in manholes, which would otherwise overheat because of the additional insulation thickness.

Disregarding the splices, the ampacity of a pipe cable suspended in free air may be determined by iteration on the $W_r + W_c$ graph of Fig. 3.49. For example, take a current of 800 A and calculate the heat generated in the cable. This comes to 0.9 W/cm and corresponds to a cable surface temperature of 38°C. Substituting this value into (3.77) indicates that the conductor

temperature is 65.3°C. Hence a larger current has to be tried to reach $T_c = 80°C$. With 900 A it would be found that $T_c = 72.2°C$, and so on. Not only does air cooling greatly increase the ampacity of a single cable, it virtually eliminates the mutual heating between adjacent cables.

Daily Cycle Rating

If the daily load cycle curve can be adequately approximated to a single period of a sine wave, then the cyclic rating method explained in conjunction with Fig. 3.18 may also be applied to pipe cables. It requires kR_e in the ampacity equation (3.76) to be multiplied by the cyclic soil-resistance factor β, which has been plotted on Fig. 3.20 (page 306) for experimentally determined time constants up to 14 hr and a range of loss factors α. For example a short time constant of 4 hr and a loss factor of 0.5 would result in $\beta = 0.85$.

Customarily, however, the daily load cycle rating of pipe-type cables is computed with a rule that was proposed by Neher and McGrath [1.19]. An advantage of this rule is that it does not require the experimental determination of the soil thermal time constant τ_u. To appreciate the form that the Neher-McGrath rule takes, we consider first the product of the thermal proximity factor k from (3.70) and the soil thermal resistance R_e of an isolated pipe from (3.9)

$$kR_e = \left\{ 1 - \frac{\ln(x_{1',2}/x_{1,2})}{\ln(2D/r)} \right\} \frac{\rho_e}{2\pi} \ln \frac{2D}{r} \tag{3.78}$$

This may also be written

$$kR_e = \frac{\rho_e}{2\pi} \left\{ \ln \frac{R_x}{r} + \ln \frac{2D}{r} \frac{x_{1',2}}{x_{1,2}} \right\} \tag{3.79}$$

R_x is a linear dimension that has to be given in the same units as r, the pipe radius, and D, the burial depth. Neher and McGrath suggested that R_x should be taken as 4.13 in. = 10.54 cm and the second logarithmic term in (3.79) should be multiplied by the loss factor α to obtain βkR_e, the effective soil thermal resistance for cyclic rating calculations. The Neher-McGrath rule (in centimeter units) is given mathematical expression by

$$\beta kR_e = \frac{\rho_e}{2\pi} \left\{ \ln \frac{10.54}{r} + \alpha \ln \frac{2D}{10.54} \frac{x_{1',2}}{x_{1,2}} \right\} \tag{3.80}$$

With only one cable in the trench $x_{1',2}/x_{1,2} = 1$.

The arbitrary nature of this rule has often been criticized, but no better analytical formula has been forthcoming that does not require the measurement of the soil thermal time constant. Neher and McGrath suggested that R_x stands for a radius about the pipe axis beyond which the thermal inertia of the soil becomes effective. It should be noted that this radius is so small that it will lie inside the pipe of the larger circuits.

The loss factor may be determined graphically, as on Fig. 3.18, or it may be calculated from (1.212). In the foregoing numerical example of an ampacity calculation, we had the following data:

$$D = 42 \text{ in.} = 106.68 \text{ cm} \qquad r = 5.875 \text{ in.} = 14.92 \text{ cm}$$

$$S = 36 \text{ in.} = 91.44 \text{ cm}$$

Therefore

$$\frac{x_{1',2}}{x_{1,2}} = \frac{(84^2 + 36^2)^{1/2}}{36} = 2.539$$

For a loss factor of $\alpha = 0.5$ and a soil thermal resistivity of $\rho_e = 90$ thermal-$\Omega \cdot$ cm we obtain from the Neher-McGrath rule (3.80)

$$\beta k R_e = \frac{90}{2\pi}\left\{\ln\frac{10.54}{14.92} + 0.5\ln\left(\frac{2\times 106.68}{10.54}\times 2.539\right)\right\}$$

$$= 23.24 \quad \text{thermal-}\Omega \text{ (per cm)}$$

But the thermal proximity factor was found to be $k = 1.35$ and $R_e = 37.06$ thermal-Ω. Therefore

$$\beta = \frac{23.24}{1.35 \times 37.06} = 0.47$$

This value of the cyclic soil resistance factor is significantly lower than any shown in Fig. 3.20. The Neher-McGrath rule may therefore be expected to give higher cyclic cable ratings than the other method.

Returning to the ampacity of the 345-kV double circuit, which has just been studied, this was found to be 650 A for an ambient temperature of 25°C, a conductor temperature of 80°C and a soil thermal resistivity of 90 thermal-$\Omega \cdot$cm. Applying the Neher-McGrath rule to this example the daily cycle rating with $\beta = 0.47$ is found to be 873 A which represents a 34 percent increase over the continuous rating.

Forced Cooling

Pipe-type cables lend themselves readily to forced cooling by simply pumping the oil along the cable and then bringing it out to heat exchangers or refrigerators. The basic approach to calculating the ampacity of a forced cooled cable has already been outlined in connection with self-contained cables (see Fig. 3.24). As a coolant, cable oil differs significantly from water. Its specific heat is usually less than half that of water and the relatively high viscosity of oil gives rise to stagnant boundary layers with appreciable thermal impedance. The higher viscosity of oil is also responsible for greater pumping losses.

Whatever little thermal impedance the water stream offered to radial heat flux could be ignored. However, the radial temperature drop across the oil stream is not negligible. It is caused by two film resistances, one on the surfaces of the cores and the other on the inside of the pipe. At the outlet, hot oil leaves the pipe between the two film resistances. Uncertainties in the geometrical arrangement of the three cable cores and others arising from the flow pattern and degree of turbulence make a meaningful division between the two resistances difficult. Erring on the safe side, it will be assumed that the oil outlet temperature T_2 is equal to the pipe temperature at the outlet and all of the oil thermal resistance R_0 lies between the pipe and the core surfaces, as indicated in Fig. 3.50. The heat flow diagram for the forced cooled system is identical to Fig. 3.47, except for the heat extraction P_0 by the oil.

Let the total power dissipated in the pipe cable of length L be

$$P = 3(P_c + P_s + P_d) + P_p \tag{3.81}$$

with the symbols having the same meaning as in the self-cooled case. If the total heat extracted by the oil at the end of L is P_0, the heat balance for the short section dx of the cable shown in Fig. 3.50 is

$$\frac{P}{L}\,dx = \frac{P_0}{L}\,dx + \frac{T_x - T_a}{R_j + R_e}\,\frac{dx}{L} \tag{3.82}$$

T_x is the pipe temperature at x and T_a is the heat sink temperature, as before. Over the short distance dx the pipe temperature increases by dT. The heat carried away by the oil of specific heat at constant volume c_v is

$$\frac{P_0}{L}\,dx = c_v A v\,dT \tag{3.83}$$

In (3.83) A is the cross-sectional area of the oil stream and v the flow velocity. Substitution of (3.83) into (3.82) leads to

$$\frac{P}{L}\,dx = c_v A v\,dT + \frac{T_x - T_a}{R_j + R_e}\,\frac{dx}{L} \tag{3.84}$$

Equation (3.84) may be solved by separating the variables and integrating x from 0 to L and T from the oil inlet temperature T_1 to the outlet temperature T_2, that is

$$\int_0^L \frac{dx}{L(R_j + R_e)c_v A v} = \int_{T_1}^{T_2} \frac{dT}{P(R_j + R_e) - (T_x - T_a)}$$

$$\frac{\lambda}{\left[(R_j + R_e)c_v A v\right]} = \ln\left[\frac{P(R_j + R_e) - (T_1 - T_a)}{P(R_j + R_e) - (T_2 - T_a)}\right] \tag{3.85}$$

$$T_2 - T_a = P(R_j + R_e) - \left[P(R_j + R_e) - (T_1 - T_a)\right]e^{-1/F} \tag{3.86}$$

where

$$F = \frac{(R_j + R_e)c_v A v}{\lambda} \tag{3.87}$$

It should be noted that since P is the total power dissipated in the cable over the whole length L, R_j and R_e are the radial resistances—not per foot or cm —for the whole length L. But in the terms of (3.86), which are products of power and thermal resistance, we may treat P as the power per unit length and then multiply it by the resistance of unit length. As the latter is the customary way of handling cable ampacity calculations, we must remember that if thermal resistances of unit length are used throughout (3.85), those on the left side have to be divided by the dimensionless number λ which is the number of unit lengths contained in L.

Next we consider the temperature drop between one of the conductors at the oil outlet and the oil or pipe temperature T_2. In Fig. 3.50 this can be seen to be equal to

$$T_c - T_2 = 3(P_c + P_s + P_d)R_0 + P_d(R_i/2) + P_c R_i \tag{3.88}$$

Adding (3.86) and (3.88) and grouping the terms in T_a terms, P_d-terms, and current-dependent terms, it can be shown that

$$T_c - T_a - (T_1 - T_a)e^{-1/F} - P_d\left[3(R_j + R_e)(1 - e^{-1/F}) + 3R_0 + \frac{R_i}{2}\right]$$

$$= P_c R_i + 3(P_c + P_s)\left[(R + R_e)(1 - e^{-1/F}) + R_0\right] + P_p(R_j + R_e)(1 - e^{-1/F}) \tag{3.89}$$

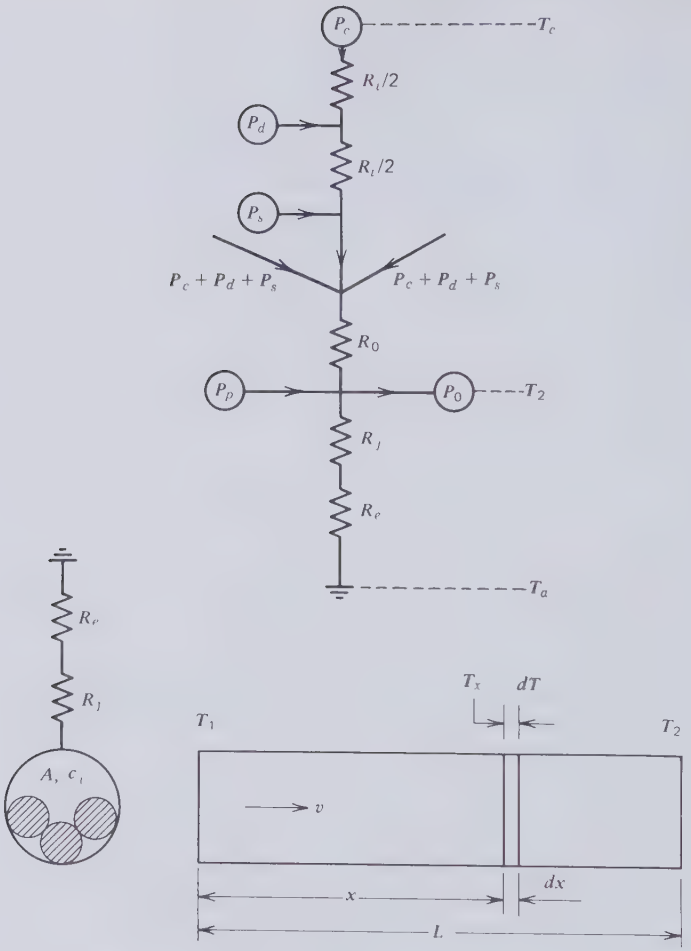

Figure 3.50 Forced cooling of pipe-type cables.

Remembering that $P_c = R_{ac}I^2$; $P_s = R_s'I^2$; $P_p = R_p'I^2$; the ampacity equation is found to be

$$I^2 = \frac{T_c - T_a - (T_1 - T_a)e^{-1/F} - P_d\left[3(R_j + R_e)(1 - e^{-1/F}) + 3R_0 + \frac{R_i}{2}\right]}{R_{ac}R_i + 3(R_{ac} + R_s')\left[(R_j + R_e)(1 - e^{-1/F}) + R_0\right] + R_p'(R_j + R_e)(1 - e^{-1/F})} \tag{3.90}$$

When $v = 0$, $F = 0$, and $e^{-1/F} = 0$. Hence when the oil flow is stopped (3.90) reduces to (3.76), which is the ampacity equation for self-cooled cables when

$k=1$. Should more than one cable be installed in the same trench, R_e of (3.90) has to be multiplied by the appropriate thermal proximity factor.

The function $e^{-1/F}$ is plotted on Fig. 3.51. It approaches unity asymptotically and at $F=100$ it is within 1 percent of that limit. As $e^{-1/F}$ tends to one, the ampacity of the forced cooled cable also tends to an upper limit given by

$$I_{\lim}^2 = \frac{T_c - T_1 - P_d[3R_0 + (R_i/2)]}{R_{ac}R_i + (R_{ac} + R_s')R_0} \tag{3.91}$$

The maximum possible current rating of a forced cooled pipe-type cable is therefore independent of the thermal environment and also the jacket resistance R_j. It is strongly dependent on the oil inlet temperature, which may lie above or below the ambient temperature T_a depending on whether the oil is cooled by simple heat exchange to air or water or with the aid of refrigerators. Implicit in (3.91) is the statement that the limiting ampacity could only be reached when $T_2 = T_1$. That this condition can be approached in practice will be seen from the following consideration.

Using dissipation factors per unit length and thermal resistances of unit length, the total heat generated by the cable is λP. This may be equated to the heat removed by the oil and the heat conducted away to the soil at the average pipe temperature $(T_2 - T_1)/2$.

$$\lambda P = c_v A v (T_2 - T_1) + \lambda \frac{(T_2 - T_1)/2}{R_j + R_e} \tag{3.92}$$

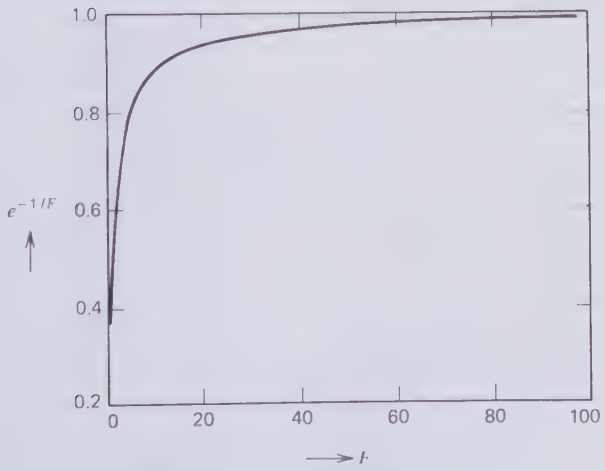

Figure 3.51 The exponential $e^{-1/F}$.

From this it is found that

$$T_2 - T_1 = \frac{2P(R_j + R_e)}{1 + 2F} \tag{3.93}$$

Now $P(R_j + R_e)$ is the temperature drop between the pipe surface and ambient of a self-cooled pipe cable. This is rarely more than 40°C. Hence for the limiting ampacity of the forced cooled cable, when $F > 100$, $T_2 - T_1$ is only a fraction of one degree.

Williams et al. [3.41] quote the specific heat at constant volume of several cable oils over the important temperature range from 10 to 45°C. It varies between 1.7 and 2.8 J/cm^3-°C. The oil flow areas of pipe cables commonly fall between 200 and 500 cm^2. Flow velocities can be as high as 50 cm/sec. The thermal resistance $(R_j + R_e)$ of 1 cm length of pipe is likely to be of the order of 50 thermal-Ω. From these figures one can obtain an idea of the magnitude of the forced cooling parameter F given by (3.87). In the specific case of a 1-km-long pipe ($\lambda = 10^5$), $R_j + R_e = 45$ thermal-Ω, $c_v = 2$ J/cm^3-°C, $A = 300$ cm^2, we find that

$$F = 45 \times 2 \times 300 \times 10^5 v = 0.27v$$

The unreasonably large flow rate of 370 cm/sec would be required in this example to bring F up to 100. It shows that in the large majority of forced cooling applications it will not be possible to closely approach the limiting ampacity of (3.91).

Equation (3.72) is an expression for the radial thermal resistance of the oil under stagnant conditions when the main heat-transfer mechanism is free convection. Notaro and Webster [3.40] have derived analytical expressions of the two boundary layer resistances on the assumption that even with forced cooling free convection dominates over forced convection. The two film resistances are not independent of heat flow and therefore require iterative solution with the ampacity equation (3.90). In one of the examples considered by Notaro and Webster the film resistance at the cable core surface for an oil temperature of 50°C varied between 7.6 and 16.7 thermal-Ω of 1 cm length of core. In the sample ampacity calculation for a self-cooled pipe cable the oil thermal resistance computed with (3.72) and $D' = 10.33$ in. came to 15.03 thermal-Ω for 1 cm of length. This should be compared with the insulation resistance in the same example of $R_i = 55$ thermal-Ω. It seems that, even though the method of computing the oil resistance will have some effect on the ampacity result, it is not of overriding concern.

Forced convection is the more likely mode of heat transfer when the flow in the forced cooled cable is turbulent, which will be the case unless extremely small flow velocities are employed. Williams et al. in the discus-

sion of [3.40] present data of the oil film resistance on the core surface based on forced convection. At the oil temperature of 50°C, this varied between 7.6 and 22 thermal-Ω, which is not very different from the free convection result. The same authors also published [3.41] information about the film resistance at the pipe wall as observed during field tests. The most likely value indicated in the tests was 7.6 thermal-Ω of 1 cm length.

As discussed by Slutz et al. [3.42], the pressure drop Δp over a distance L along the pipe of internal diameter D arising from the flow of an incompressible liquid of density ρ and traveling with a velocity v may be expressed with the help of a friction factor f by

$$\Delta p = 2f\left(\frac{L}{D_H}\right)\rho v^2 \tag{3.94}$$

D_H is the hydraulic diameter of the flow section, which for an empty round pipe is equal to D. The friction factor is solely a function of the dimensionless Reynolds number

$$Re = \frac{\rho v D_H}{\mu} \tag{3.95}$$

where μ is the viscosity of the incompressible fluid. The friction factor of pipe-type cable models was measured by Slutz et al. [3.42] for various core configurations and an empty pipe. Their results are plotted in Fig. 3.52. The

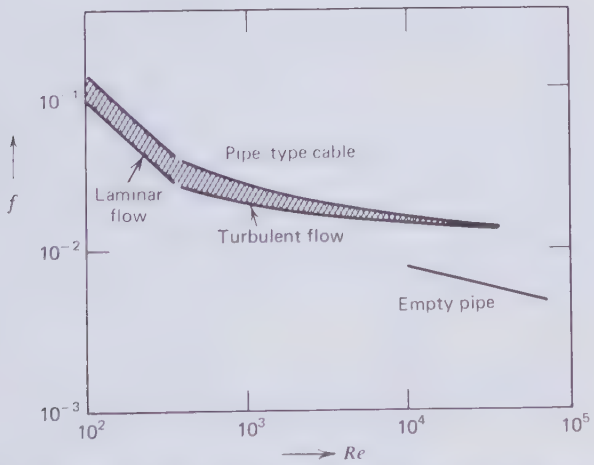

Figure 3.52 Oil friction factor as a function of the Reynolds number according to Slutz et al. [3.42]. (By permission of the Institute of Electrical and Electronics Engineers).

break in the pipe cable curve corresponds to the transition from laminar to turbulent flow. The Reynolds number at which the transition occurs can be influenced by the height of the skid wires that induce turbulence. In the turbulent regime the friction factor should, ideally, be constant and independent of viscosity. This is not entirely true for pipe cables presumably because of the division of the oil stream in separate channels by the cable cores. Figure 3.52 indicates that oil flow in the empty pipe remains laminar, at any rate up to $Re = 8 \times 10^4$.

D_H, the hydraulic diameter, is defined by

$$D_H = \frac{4 \times (\text{flow area})}{\text{wetted perimeters}} = \frac{D^2 - 3d^2}{D + 3d} \tag{3.96}$$

where d is the cable core diameter. To obtain an upper limit of the Reynolds number that might be encountered in pipe-type cables, consider the case where $D = 12$ in., $d = 4$ in. ($D_H = 10.16$ cm), $\rho = 0.85$ g/cm^3, $\mu = 100$ centipoise $= 1.02 \times 10^{-2}$ g·sec/cm^2, and $v = 100$ cm/sec.

$$Re = \frac{0.85 \times 100 \times 10.16}{1.02 \times 10^{-2}} = 8.47 \times 10^4$$

The turbulent flow region of Fig. 3.52 will therefore cover the operation of most pipe cables. The model results of this graph indicate that a friction factor of $f = 0.02$ sec should give conservative pressure drops provided the Reynolds number is greater than 1000.

Williams et al. actually measured the pressure drop in a 138 kV pipe-type cable of 1.5 mile length. The cable contained 2000 kcmil copper conductors in an 8 in. i.d. steel pipe. Estimates of the hydraulic diameter and oil flow area of this cable are $D_H = 8.6$ cm and $A = 202$ cm^2. The density of most cable oils is close to 0.85 g/cm^3. With this information the pressure drop over a 1000-ft section of the 138-kV cable has been computed. The result is plotted on Fig. 3.53 together with some measurements obtained by Williams et al. [3.41]. It will be seen that the measured pressure differential is considerably larger than that predicted from scale-model measurements of the friction factor. Williams and his colleagues suggested the following empirical formula, which gave the best agreement with their field measurements

$$\Delta p(\text{psi/ft}) = \frac{2.73 \times 10^{-3} \mu(\text{centipoise}) Q(\text{gpm})}{\left\{ [D(\text{in.})]^2 - 4.22[d(\text{in.})]^2 \right\}^2} \tag{3.97}$$

The measurements were carried out at an average oil temperature of 36°C, and the average viscosity was taken to be 187 centipoise. Line B on Fig. 3.53

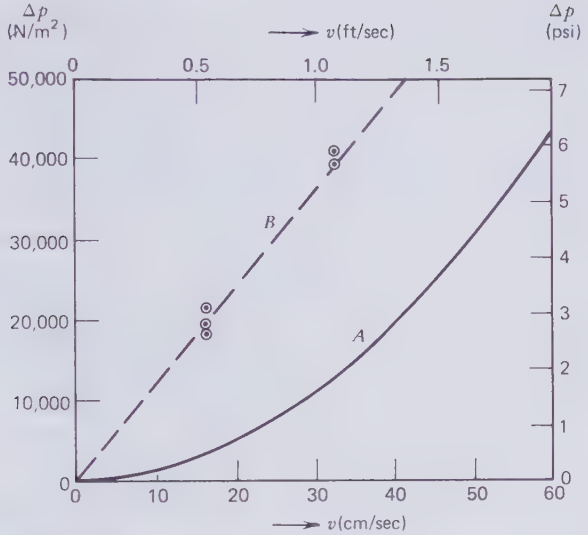

Figure 3.53 Pressure drop in a 1000 ft long 138 kV, 2000 kcmil pipe-type cable as a function of oil flow velocity. *A*—equation (3.94) with $f=0.02$ sec; *B*—empirical equation (3.97) and measurement points from [3.41]. (By permission of the Institute of Electrical and Electronics Engineers).

represents (3.97) applied to the field test installation and this viscosity. The proportionality of pressure drop to flow velocity revealed by the field measurements suggests that the oil flow was predominantly laminar, although the Reynolds number indicates that it should have been turbulent.

Theory and experiment agree that the pressure drop in an oil return pipe not containing cable cores is inversely proportional to the Reynolds number and therefore proportional to viscosity. As the oil entering the return pipe will normally be above ambient temperature, heat will flow from the pipe into the soil and the oil temperature will drop along the pipe. Hence the viscosity will increase as the oil progresses to the exit. Slutz et al. [3.42] have pointed out that the pressure drop of laminar flow and variable viscosity may be derived by differentiating (3.94) with respect to x, the distance along the pipe, and subsequently integrating the viscosity from one end of the pipe to the other.

$$\frac{dp}{dx} = \frac{2f\rho v^2}{D_H} = \frac{2\mu C v}{D_H^2} \tag{3.98}$$

where

$$C = fRe \tag{3.99}$$

The viscosity-temperature relationship may be approximated to

$$\mu = Ae^{-BT_x} \tag{3.100}$$

A and B are constants and T_x is the oil temperature at distance x along the pipe. Integrating (3.98) gives the pressure drop

$$\Delta p = \left(\frac{2Cv}{D_H^2}\right)\int_0^L \mu\, dx \tag{3.101}$$

The integral can be solved if T_x in (3.100) increases linearly with x, as it would if the heat loss to the ground were negligible, so that

$$\int_0^L \mu\, dx = \int_0^L Ae^{-B(T_1+cx)}dx = \frac{1}{cB}(Ae^{-BT_1} - Ae^{-BcL}) \tag{3.102}$$

As before, T_1 is the oil temperature at $x=0$, and T_2 at $x=L$. But $cL = T_2$ and therefore

$$\Delta p = \frac{2Cv}{D_H^2 cB}(\mu_1 - \mu_2) \tag{3.103}$$

where μ_1 and μ_2 are the viscosities at the oil inlet and outlet, respectively.

Mean values of the upper and lower viscosities of cable oils have been plotted in Fig. 3.54. The exponential law is seen to hold approximately for low-viscosity oils that are usually preferred for forced cooling. The value of B for these oils is approximately 1.6. When the heat flux to the soil is not negligible and high-viscosity oils are employed, Williams et al. recommend the following formula for the pressure drop in the return pipe

$$\Delta p\ (\text{psi/ft}) = \frac{2.73\times10^{-3}\mu(\text{centipoise})Q(\text{gpm})}{[D(\text{in.})]^4} \tag{3.104}$$

The potential energy lost by the coolant in overcoming the flow resistance has to be restored to the fluid by the circulating pump. As the oil velocity is normally kept constant regardless of the power carried by the cable, the energy supplied to the drive motor is a standing loss like the dielectric loss. Denoting the pump efficiency by η, the flow loss P_v per unit length of pipe is

$$P_v = \frac{\Delta pAv}{\eta} \tag{3.105}$$

where the pressure drop must be expressed per unit length. When a return pipe is involved P_v consists of two components, one for the cable itself and the other for the return pipe.

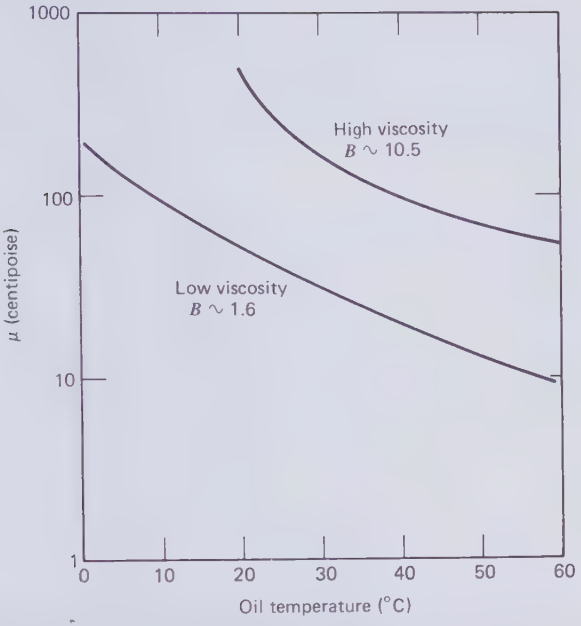

Figure 3.54 Viscosity of cable oils as a function of temperature [3.41]. (By permission of the Institute of Electrical and Electronics Engineers).

A double circuit could be cooled by oil circulation without a return pipe but with heat exchangers at both ends of one cooling module. However, if one of the cables fails, the oil circulation may have to be interrupted in both of them and the surviving circuit then has to revert to the ampacity of a naturally cooled cable. A thermally remote return pipe, that is a pipe installed several feet away from the cables, not only increases the firm rating (one circuit out of order) of the double circuit system, but it also reduces the load on the cooling stations by dissipating some of the heat collected in the oil to the surrounding soil.

The return pipe is usually the most costly item of the cooling equipment. It can be omitted if large oil reservoirs are provided at both ends of the transmission line and the oil flow is forced to reciprocate between the two tanks. Oscillatory cooling of this kind moves the hot spot (T_2) to and fro over one cooling module and makes better use of the thermal capacity of the soil in which the forced cooled circuits are embedded. With oil circulation, the hot spot remains stationary at the oil outlet. At the inlet virtually no heat flows to the ambient sink. The motion of the hot spot of an oscillatory system is indicated in Fig. 3.55. The instant $t=0$ corresponds to the temperature distribution along the module length L, which would prevail in a circulatory system, with T_1 and T_2 being the inlet and oulet oil temperatures. As the

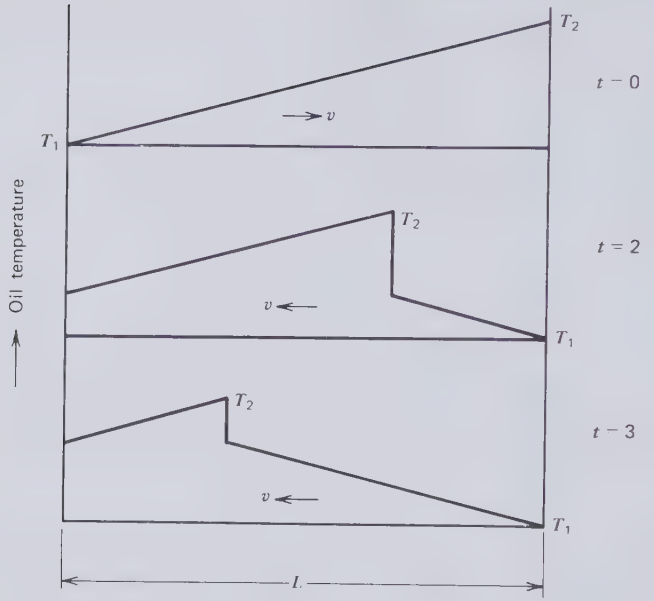

Figure 3.55 Movement of hot-spot in reciprocating oil flow cooling.

flow is reversed, cool oil enters the pipe at the far end and the last slug of hot oil moves back into regions where the cable cores are likely to be at a lower temperature than the oil.

A 230 kV, 2000 kcmil pipe-type cable contains approximately 7300 gal oil/mile. Therefore a 10,000-gal tank on either end of a 1-mile length would be adequate for oil oscillation. Any number of cooling modules with cooling stations at their ends may be linked together without increasing the tank size.

Most of the early forced cooled pip-type cables relied on air-blast heat exchangers. In recent years more use has been made of refrigeration plant to cool the oil close to or even below the ambient temperature. A significant drop below the ambient soil temperature would be counterproductive because heat from the soil would then flow into the cable. Bender and Purnhagen [3.44] have discussed the various options that exist with regard to cooling station plant and equipment. The many different approaches range from simple free convection oil to air heat exchangers to sophisticated refrigerators. In certain locations water will be chosen as an intermediate coolant, and it may be coupled to cooling towers, spray ponds, or wells. Reference [3.44] also considers the capital and maintenance cost of the cooling plant.

A numerical example will now be considered to conclude this section on the forced cooling of pipe-type cables. For this we choose the 345 kV double-circuit which has already been examined with respect to its operation in the naturally cooled mode.

EXAMPLE

1. 345 kV double-circuit installed according to Fig. 3.44; $D = 42$ in.; $S = 36$ in.
2. Cable pipe: 0.25 in. thick grade A steel; inside diameter $D_p = 10.25$ in.; somastic coating corrosion protection of 0.5 in. thickness and a thermal resistivity of 100 thermal-$\Omega \cdot$cm.
3. Conductors: 2000 kcmil, 4 segments, 102% IACS copper, 1.632 in. diam. Maximum conductor temperature $T_c = 80°C$.
4. Insulation: 1.025 in. thick; 3.682 in. overall diameter; $\varepsilon = 3.5$; $\cos\phi = 2.5 \times 10^{-3}$; $\rho_{th} = 500$ thermal-$\Omega \cdot$cm.
5. Electrostatic shield and skid wire assembly: metallized (aluminum) mylar tapes, 1 in. wide; 0.125 in. overlap; total metal thickness 0.001 in. Two D-shaped stainless steel skid wires 0.25 in. diam half-round; 3 in. lay; 77×10^{-6} $\Omega \cdot$cm at 60°C.
6. Soil thermal resistivity $\rho_e = 90$ thermal-ohm$\cdot$cm; ambient temperature $T_a = 25°C$.
7. Oil return pipe: in separate trench (thermally remote from cables); grade A steel, 0.25 in. thick, 10.25 in. i.d.; installed at the same depth as the cables and provided with the same corrosion protection.
8. Coolant oil: low-viscosity polybutene; c_v (at 35°C) = 2.5 J/cm.°C; μ (at 35°C) = 25.5 centipoise; density = 0.85 g/cm^3; minimum pressure required for dielectric strength 200 psi; maximum pressure permitted by potheads 400 psi; installed in level ground.
9. Cooling module: $L = 1$ mile as shown in Fig. 3.57 with the distance between cooling stations being 2 miles.
10. Cooling stations: deliver oil at $T_1 = 20°C$ from refrigerators with drive power requirements according to Fig. 3.56. The cooling stations also contain oil circulating pumps of 80% efficiency. It will be assumed that all the energy expended by the pumps appears as heat in the coolant and has to be removed from it by the refrigerators.

RESULTS PREVIOUSLY OBTAINED FOR THE NATURALLY COOLED SYSTEM. $R'_{ac}(80°C) = 0.228 \times 10^{-6}$ Ω/cm; $R'_s(60°C) = 6.24 \times 10^{-8}$ Ω/cm; $R'_p = 0.117 \times 10^{-6}$ Ω/cm; $P_d = 0.0894$ W/cm; $R_t = 64.75$ thermal-Ω; $R_0 = 16.5$ thermal-Ω; $R_j = 1.42$ thermal-Ω; $R_e = 37.06$ thermal-Ω; $k = 1.35$.

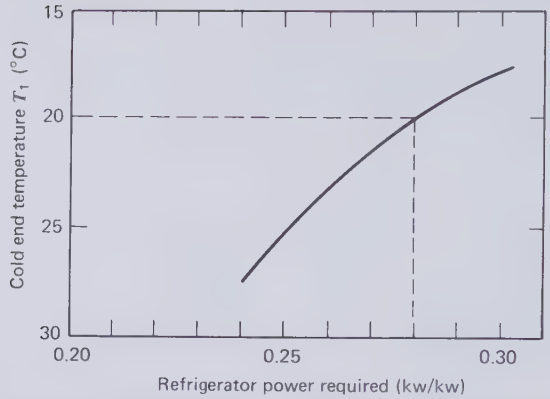

Figure 3.56 Refrigerator power requirement according to Bender and Purnhagen [3.44]. (By permission of the Institute of Electrical and Electronics Engineers).

FLOW AREAS. Let A_c be the flow area in one cable pipe and A_r the flow area of the return pipe.

$$A_c = \frac{\pi}{4}(10.25^2 - 3\times 3.93^2)\times 2.54^2 = 298 \text{ cm}^2$$

$$A_r = \left(\frac{\pi}{4}\right)\times 10.25^2 \times 2.54^2 = 532 \text{ cm}^2$$

FORCED COOLING PARAMETER F. Let F_c be the forced cooling parameter of the cable and F_r that of the return pipe. λ is the number of unit lengths (cm) in one cooling module (1 mile), i.e., $\lambda = 1.61\times 10^5$. Then from (3.87) and noting that R_e for the cable, but not for the return pipe, must include the thermal proximity factor k

$$F_c = \frac{(1.42 + 1.35\times 37.06)\times 2.5\times 298\times v_c}{1.61\times 10^5} = 0.238 v_c$$

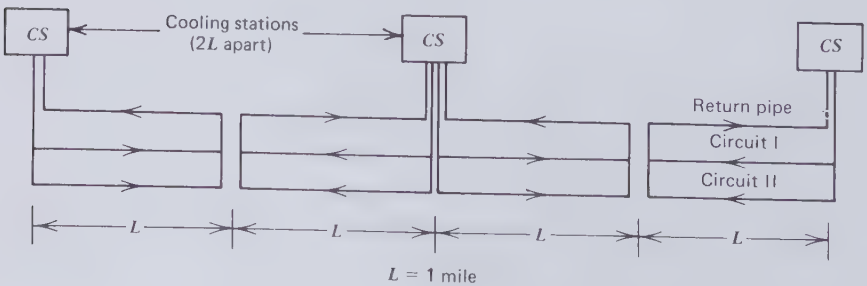

Figure 3.57 Cooling module layout.

where v_c is the oil velocity in the cable in centimeters per second.

$$F_r = \frac{(1.42+37.06)\times 2.5\times 532\times v_r}{1.61\times 10^5} = 0.318 v_r$$

where v_r is the oil velocity in the return pipe. But since the oil of two cables is returned in one pipe we have

$$v_r = (2A_c/A_r)v_c \text{ and } F_r = 0.356 v_c$$

AMPACITY. Substituting the data into the ampacity equation (3.90) gives

$$I = \left[\frac{33.9+18.8e^{-1/F_c}}{8.01\times 10^{-5} - 5.09\times 10^{-5} e^{-1/F_c}} \right]^{1/2} \quad \text{A}$$

I is listed in Table 3.7 and plotted on Fig. 3.58 as a function of the oil flow velocity v_c. It varies from 651 A ($v_c = 0$) to 1255 A ($v_c = 60$ cm/sec).

PRESSURE DROP. We distinguish between the pressure drop Δp_c in the cable and Δp_r in the return pipe. From (3.97) and 1 U.S. gal = 3785 cm^3, noting that the volume flow rate is

$$A_c v_c \text{ cm}^3/\text{sec} = 4.72[v_c(\text{cm/sec})] \quad \text{gpm}$$

$$\Delta p_c = \frac{2.73\times 10^{-3}\times 25.5\times 4.72[v_c(\text{cm/sec})]}{[10.25^2 - 4.22\times 3.93^2]^2}$$

$$= 2.07\times 10^{-4}[v_c(\text{cm/sec})] \quad \text{psi/ft}$$

and over the 1-mile module

$$\Delta p_c = 1.09[v_r(\text{cm/sec})] \quad \text{psi}$$

From (3.104) and noting that the volumeric flow rate in the return pipe is $Q_r = 2Q_c = 2\times 4.72 v_c$

$$\Delta p_r = \frac{2.73\times 10^{-3}\times 25.5\times 4.72[v_c(\text{cm/sec})]}{10.25^4}$$

$$= 5.95\times 10^{-5}[v_c(\text{cm/sec})] \quad \text{psi/ft}$$

and over the 1-mile module

$$\Delta p_r = 0.314[v_c(\text{cm/sec})] \quad \text{psi}$$

Table 3.7 Example of Forced Cooling of 345-kV Pipe-Type Cable

CLF (%)	α	v_c (cm/sec)	F_c	I (A)	F_r	P_v (kW)	λP (kW)	T_2 (average °C)	T_3 (average °C)	dH/dt (kW)	P_R (kW)	ΣP (kW)	Transm. loss fraction (%)
100	1.000	0	—	658	—	—	111	55.5	—	—	—	111	2.85
		10	2.38	996	3.56	0.4	201	31.2	29.7	72.7	20.4	222	3.73
		20	4.76	1124	7.12	1.4	244	27.4	27.1	107.2	30.0	275	4.09
		30	7.14	1184	10.68	3.2	266	25.6	25.5	126.1	35.3	305	4.31
		40	9.52	1218	14.24	5.8	279	24.5	24.5	139.9	39.2	324	4.45
		50	11.90	1240	17.80	9.0	288	23.7	23.8	150.6	42.2	339	4.58
		60	14.28	1255	21.36	13.0	294	23.2	23.3	160.5	44.9	352	4.69
75	0.619	0	—	651	—	—	85	47.2	—	—	—	85	
		10	2.38	996	3.56	0.4	141	27.8	27.1	53.3	14.9	156	
		20	4.76	1124	7.12	1.4	168	25.1	25.1	77.4	21.7	191	
		30	7.14	1184	10.68	3.2	181	23.8	23.9	90.4	25.3	210	
		40	9.52	1218	14.24	5.8	189	23.0	23.1	98.2	27.5	222	
		50	11.90	1240	17.80	9.0	195	22.5	22.6	105.9	29.7	234	
		60	14.28	1255	21.36	13.0	198	22.1	22.2	111.3	31.2	242	
50	0.325	0	—	651	—	—	65	40.8	—	—	—	65	
		10	2.38	996	3.56	0.4	94	25.2	25.2	39.1	10.9	105	
		20	4.76	1124	7.12	1.4	108	23.3	23.5	53.6	15.0	124	
		30	7.14	1184	10.68	3.2	116	22.4	22.6	61.3	17.2	136	
		40	9.52	1218	14.24	5.8	120	21.9	22.1	68.4	19.2	145	
		50	11.90	1240	17.80	9.0	123	21.6	21.8	76.1	21.3	153	
		60	14.28	1255	21.36	13.0	125	21.4	21.6	84.5	23.7	162	

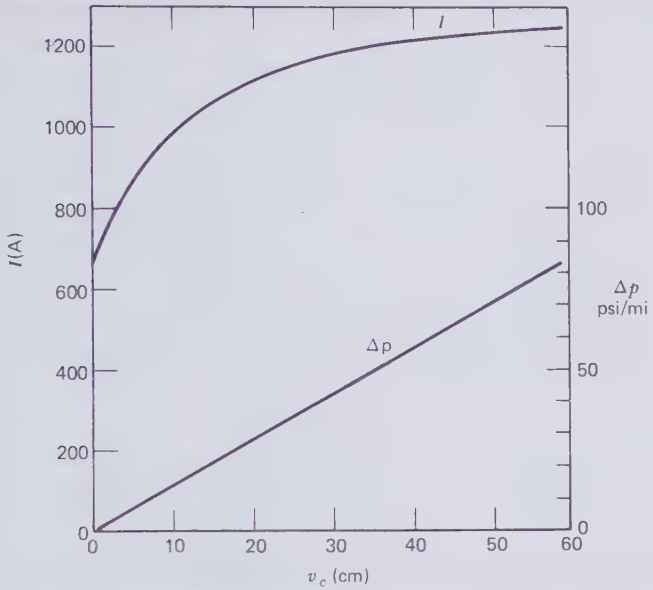

Figure 3.58 Ampacity and pressure drop (cable + return pipe) as a function of oil flow velocity in forced cooled pipe-type cable example.

Hence the total pressure drop in the 1-mile loop which has to be made good by the circulating pump is

$$\Delta p = \Delta p_c + \Delta p_r = 1.40[\, v_c(\text{cm/sec})\,] \quad \text{psi}$$

The pressure drop is plotted in Fig. 3.58. For the maximum velocity considered, i.e., $v_c = 60$ cm/sec, the total pressure drop is 84 psi. This has to be superimposed on the static pressure of 200 psi giving a maximum pressure of 284 psi, which is less than the 400 psi limit of the porcelain potheads.

PUMPING POWER. To obtain P_v in watts from (3.105) the pressure drop has to be converted to the appropriate metric units, that is,

$$\Delta p = 1.40[\, v_c(\text{cm/sec})\,] \times \frac{453.6}{2.54^2} \times 981 \times 10^{-7} \quad \text{W}\cdot\text{sec/cm}^3$$

$$P_v = 1.40[\, v_c(\text{cm/sec})\,] \left(\frac{453.6}{2.54^2}\right) \times \frac{981 \times 10^{-7} \times 298 v_c}{0.8} \quad \text{W}$$

$$= 3.60 v_c^2 \quad \text{W}$$

TOTAL CABLE HEAT LOAD λP. The per unit length power loss in the cable is

$$P = 3P_c + 3P_s + 3P_d + P_p$$
$$= \left[3(R_{ac} + R_s') + R_p'\right]\alpha I^2 + 3P_d$$

where α is the loss factor defined by (1.212) in terms of the cable load factor (CLF). For constant current equal to the cable ampacity I the loss factor is unity.

$$P = \left[3(0.228\times10^{-6} + 6.24\times10^{-8}) + 0.117\times10^{-6}\right]\alpha I^2 + 3\times0.0894 \quad \text{W/cm}$$
$$= 1.06\times10^{-6}\alpha I^2 + 0.268 \quad \text{W/cm}$$
$$\lambda P = 1.61\times10^{5}(1.06\times10^{-6}\alpha I^2 + 0.268) \quad \text{W}$$

λP is listed on Table 3.7 for the three cable load factors of 100, 75, and 50% corresponding to loss factors of 1.0, 0.619, and 0.325.

CABLE OUTLET OIL TEMPERATURE T_2. Note that (3.88) applies only to unity loss factor, but T_2 may be calculated for any loss factor from (3.93) provided the reduction in P due to the loss factor is taken into account. Therefore

$$T_2 = 20 + \frac{P(1.42 + 1.35\times37.06)}{1 + 2F_c}\,^\circ\text{C} = 20 + \frac{51.5P}{1 + 2F_c} \quad ^\circ\text{C}$$

T_2 has been listed on Table 3.7 for the 100, 75, and 50% cable load factors.

RETURN PIPE OUTLET OIL TEMPERATURE T_3. T_3 may be computed from (3.86), but for the return pipe $P = 0$ and T_2 has to be replaced by T_3 and T_1 by T_2.

$$T_3 = T_a + (T_2 - T_a)e^{-1/F_r}$$

F_r has already been computed under "forced cooling parameter" and therefore

$$T_3 = 25 + (T_2 - 25)e^{-1/0.356v_r} \quad ^\circ\text{C}$$

At smaller than unity loss factors both T_2 and T_3 are time averages. The average value of T_3 has been listed in Table 3.7.

REFRIGERATION LOAD. Let the heat that has to be removed per unit time from the coolant of two cable circuits be dH/dt.

$$\frac{dH}{dt} = c_v A_r v_r (T_3 - T_1) + 2P_v$$

Therefore for one cable circuit

$$\frac{dH}{dt} = 0.5 \times 2.5 \times 532 \times 1.12 v_c (T_3 - 20) + P_v = 745 v_c (T_3 - 20) + P_v \quad \text{W}$$

dH/dt for a single circuit is listed in Table 3.7 for 100, 75, and 50% cable load factors.

Refrigerator drive power requirement. Figure 3.56 shows the refrigerator drive power requirement for a range of cold-end temperatures. It will be seen that for $T_1 = 20°\text{C}$ the compressor calls for 0.28 kW per kW of the refrigeration load dH/dt. Therefore the mechanical power input into the heat pump P_R is given by

$$P_R = 0.28\, dH/dt$$

P_R for a single circuit is listed in Table 3.7 for 100, 75, and 50% cable load factors.

Total rate of energy loss ΣP. The sum of all the power loss components is $\Sigma P = \lambda P + P_v + P_R$. Both λP and P_R depend on the loss factor α. ΣP is listed in Table 3.7 and plotted on Fig. 3.59 for just one circuit.

Discussion of results. The relatively large diameter oil return pipe is responsible for the significant increase in the power transmission capability of the double-circuit obtained with a 2-mile distance between cooling stations. In this particular example the ampacity at an oil flow velocity of 60 cm/sec is nearly twice as large as that of the naturally cooled cable system. However, taking the 75 percent cable load factor, the 93 percent increase in transmission capability incurred a 185 percent penalty in power losses.

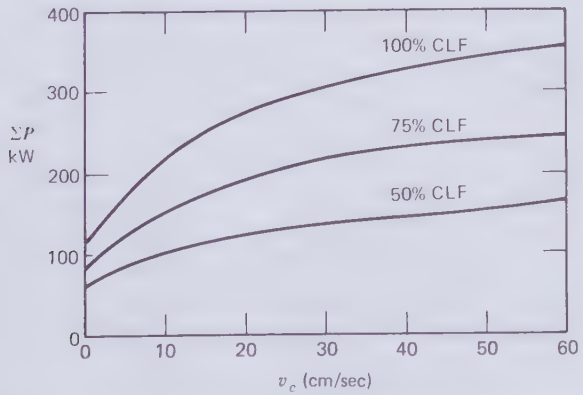

Figure 3.59 Power loss of one circuit of forced cooled pipe-type cable example (1 mile).

The low values of T_2 at the higher coolant velocities indicate that little heat flows through the soil to the atmospheric heat sink. It also means the soil thermal capacity cannot be exploited for increasing the cable ampacity when the daily load factor is less than unity. The consequences of this fact will be appreciated from the following consideration.

Let a third set of cable cores be pulled into the return pipe and examine the naturally cooled performance of the three-circuit system. The third circuit will have a higher ampacity than the other two because it is operating in thermal isolation, but if all three circuits are connected in parallel nothing will be gained from this because of equal current sharing. Let it be assumed, therefore, that the current in the third circuit is the same as in the other two. Ampacities, transmission capabilities and power losses for this case have been listed in Table 3.8 and compared with the forced cooled double-circuit system with the high flow velocity of $v_c = 60$ cm/sec. In many practical situations the daily load factor falls between 50 and 75 percent. In these instances the transmission capability of the naturally cooled 3-circuit system can be greater and the loss smaller than that of the forced cooled 2-circuit system.

It is important to recognize that in these numerical examples no effort has been made to optimize the lines for any particular transmission duty and therefore no generalizing conclusions should be drawn from them. There is no doubt, however, that the economics of forced cooling have to be carefully compared with what can be achieved by naturally cooled lines of equivalent capability.

Fault Currents

A more general discussion of fault currents in cables will be found in Section 3.2. The writings on pipe-type cables are vague or silent on this subject. A dearth of information on the current distribution in pipe-type cables has already been revealed in Sections 1.15 and 1.19. But it is the nature of the current distribution that governs both the excess Joule loss and interconductor forces during a short-circuit fault in the cable itself or a connected line (through-fault).

Equation (3.54) determines the fault current that each conductor can carry without overheating the insulation. Typical figures entering this equation in the case of copper conductors are: $\Delta T = 40°C$ (from 80 to 120°C); $t_F = 0.2$ sec; $\rho_{ac} = 1.2 \times 0.28 \times 10^{-6}\ \Omega \cdot$cm; $\delta = 8.94$ g/cm^3; $c_v = 0.384$ J/g-°C. For these values (3.54) permits fault currents from 80 kA for a 1000 kcmil conductor to 200 kA for a 2500 kcmil conductor, which is adequate in most circumstances.

The excess Joule heat generated in the electrostatic shield and skid wire assembly by a line-to-line fault is proportional to the effective resistance R_s'.

Table 3.8 Sample Comparison of 2-Circuit Forced Cooled with 3-Circuit Naturally Cooled Pipe-Type Cable System

	Ampacity			Transmission Capability			Transm. Loss per Mile		
	100% CLF (A)	75% CLF (A)	50% CLF (A)	100% CLF (MVA)	75% CLF (MVA)	50% CLF (MVA)	100% CLF (kW)	75% CLF (kW)	50% CLF (kW)
2 circuits forced cooled $v = 60$ cm/sec	1255	1255	1255	1500	1500	1500	704	484	324
3 circuits naturally cooled	651	819	1007	1167	1468	1805	332	328	287

This is very much smaller than the ohmic resistance R_s of the metallic path carrying the shield circulating currents because, as revealed by (3.67), the mutual inductance between the conductor and the shield is involved. For the previously analyzed 345 kV, 2000 kcmil cable we found that $R_s = 8.48 \times 10^{-4}\ \Omega/\text{cm}$, whereas the effective shield resistance was only $R_s' = 6.24 \times 10^{-8}\ \Omega/\text{cm}$. Since the induced Joule loss in the shield assembly is proportional to R_s' and not the ohmic resistance R_s, the shield metal has to absorb less heat per unit volume than the conductor metal. Besides ΔT will be greater for the shield than for the conductor. It is therefore safe to conclude that provided the conductor temperature will stay within permitted temperature limits during a short-circuit fault, so will the electrostatic shield assembly.

The steel pipe with its large metal cross section and low initial temperature should have no difficulty in storing the heat pulses from fault currents.

Little is known about the interconductor forces of pipe-type cables other than that they increase with the square of the current amplitude and will therefore be at least 100 times as large during fault conditions than in normal cable operation. An approximate value of the interconductor forces between the self-contained cables of a three-phase circuit was derived with an analysis in which the distributed conductor currents were replaced by concentrated line currents. This can be justified when the distance between conductors is large compared to their diameters, which is definitely the case for overhead line circuits and to a lesser degree also for self-contained cables with sheath cross-bonding. Not only lie the cores of a pipe-type cable too close together for this approximation to be valid, but the distributed circulating currents and the magnetization of the steel pipe have a strong influence on the interconductor forces. The pipe currents actually reduce the interconductor forces. This would be confirmed by a finite-element analysis. What has prevented this mathematical technique from being applied to pipe-type cables is the uncertain location of the cores and the complication introduced by the magnetic permeability of the pipe material.

Nevertheless an order of magnitude estimate of interconductor forces likely to be encountered when pipe cables carry fault currents can be gleaned from the results of a finite element analysis described in Section 1.16. The relevant results are presented in Fig. 1.51 and Table 1.4. $F_{c,s}$, the radially outward directed steady force acting on each conductor during a symmetrical three-phase fault, is the most important component. For the particular cable considered in Section 1.16, in which symmetrically spaced conductors were enclosed in an aluminum pipe of approximately 12 in. diam, $F_{c,s}$ was found to be 4.4 kg/m with a fault current of $I_F = 20$ kA. Twice this current would set up forces that are four times as large. The core of a 345 kV, 2000 kcmil copper cable weighs about 15 kg/m. A 50-kA fault current must be expected to lift one of the cable cores of a pipe-type cable and press the other two with twice their weight against the pipe wall. This

indicates that interconductor forces due to fault currents may become troublesome before overheating of the insulation adjacent to the conductors reaches dangerous levels.

The fact that no fault current damage of pipe-type cables has been reported in the 40 years since their introduction rather suggests that they can tolerate the fault current levels now prevailing on the transmission systems to which they are connected. Fault current levels are drifting upward as generation capacity is added to the transmission network and a time may come when the fault current performance of pipe-type cables has to be placed on a firm analytical or experimental basis.

Critical Length and Reactive Compensation

The reader is referred to Section 3.2 for a full discussion of this topic. Identical methods are used for deriving the critical length of pipe-type and self-contained cables and the way shunt reactors are used to overcome the charging current limitation is also the same. The lower ampacities of pipe-type cables lead of course to shorter critical lengths for various voltages and conductor sizes. The plot shown on Fig. 3.60 was published in [2.7] and it should be compared with Fig. 3.30 for 5000-kcmil self-contained cables.

DC Application

Two cable cores pulled into a steel pipe are eminently suitable for bipolar dc transmission. In this application the steel pipe performs the two functions of pressure container and mechanical shield without carrying the heavy

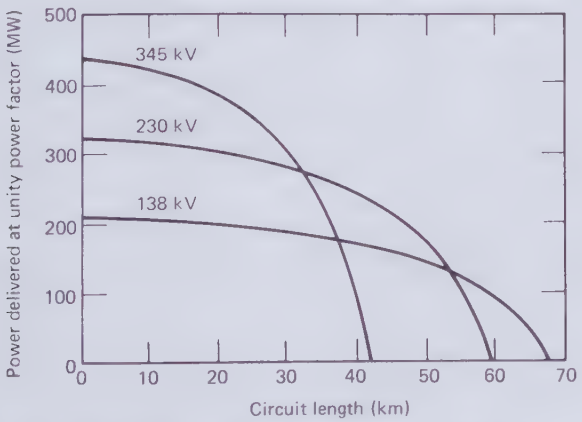

Figure 3.60 Length dependence of transmission capability of 2000 kcmil copper conductor pipe-type cables acccording to [2.7]. $\cos\phi = 2.5 \times 10^{-3}$; $T_c = 75°C$; CLF = 100%.

Table 3.9 Proposed Bipolar Double-circuit dc Transmission Lines [2.7]

Operating Voltage (kV)	Cu-conductor Size (kcmil)	Pipe Size D_p (in.)	Circuits per Trench	Capability per Trench (MVA)
±200	900	6.625	2	600
±400	1000	8.625	2	1200
±600	1500	10.750	2	2160

penalty of additional induced energy losses. The absence of the dielectric loss is a further advantage of dc transmission. Although the pipe-type high-voltage dc cable was recommended for use in the United States by two prominent investigations [2.7, 2.8] carried out in 1967 and 1971, none have been installed at the time of writing. Virtually all underground and underwater dc transmission lines in operation throughout the world depend on self-contained cables. An advantage of self-contained cables over two-core pipe cables is that three cores can make up a bipolar line with a spare core to be utilized when one of the other two cores fails. To establish the same backup capability with pipe-type cables requires at least four insulated conductors. Table 3.9 lists three dc systems based on double-circuit pipe-type cables. Their transmission capabilities under average conditions have been suggested by an Advisory Committee to the Federal Power Commission [2.7].

Underwater Installation

Some pipe-type cables have been installed underwater. No particular difficulties arise in river crossings and short off-shore applications in moderate water depth. Pipe-type cables were seriously considered for the Long Island Sound crossing [3.20] but rejected for the following reasons:

"1. With a single pipe, complete loss of capacity would result from a single contingency.
2. Repair time would be extensive.
3. Positive prevention of water ingress at fault location presented difficulties."

As self-contained submarine cables cannot be readily cross-bonded, their circulating sheath current loss is of the same order of magnitude as the Joule and magnetization losses caused by the pipe. There are limits to the core length that can be pulled into a pipe even when the pipe is almost straight.

In general, self-contained submarine cables are preferred over pipe-type cables because:

1. Mechanical damage by bottom fishing gear and anchors will in the majority of cases affect only one self-contained cable core which can subsequently be bridged by a spare core, leaving ample time for repairing the damaged cable while power continues to flow.
2. It is easier to plow flexible cables rather than rigid pipes into the bottom sediments near the shores.

Prospect of Synthetic Tape Insulation

The discussion of this topic in connection with oil-paper insulated self-contained cables in Section 3.2 also applies to pipe-type cables.

Economics

The method that has been developed for economically evaluating self-contained oil-paper insulated cables will now also be applied to pipe-type cables. It is based on the average installed cost in suburban environments of 2000 kcmil copper conductor cables in the 138, 230, 345, and 500 kV voltage classes as reported by the Edison Electric Institute in 1971 [2.8], a 7 percent compound inflation rate to bring these costs up to the 1976 level, and the 1976 cost of electricity to the utilities as published by the U.S. Department of Energy [3.31]. The same data sources have been used to compile the cost information for overhead lines. The comparison is expressed by the underground (UG) to overhead (OH) transmission cost ratio for the year 1976. It is argued that this ratio is likely to remain valid for the remainder of the present century unless oil-paper insulated cables change their character or the relationship between the cost of materials and energy is altered once more in a significant way.

A quantitative definition of the transmission cost of naturally cooled cables has been provided with (3.62A). With this equation the results presented here may be reviewed and updated at a later time. Table 3.10 lists the relevant details of approximately equal capability 138, 230, 345, and 500 kV pipe cable and lowest cost overhead transmission lines. The 1971 installed costs and the dielectric and Joule loss parameters have all been taken from [2.8]. New data not mentioned in this reference is the 7 percent compound inflation rate and the 1976 cost of electricity to power companies.

With this information, (3.62A) on page 340 yields the UG/OH transmission cost ratios of Fig. 3.61 which apply to 100 percent utilization ($u = 1$) and a daily load factor of 75 percent (CLF = 0.75). The diagram compares both

Table 3.10 Example of Transmission Cost Calculations of Naturally Cooled Pipe-type Cables and Overhead Lines

	138 kV		230 kV		345 kV		500 kV	
	UG	OH	UG	OH	UG	OH	UG	OH
Conductor: Size (kcmil)	2000	795	2000	1431	2000	2×1590	2000	2×1780
Metal	copper	ACSR	copper	ACSR	copper	ACSR	copper	ACSR
*Ampacity (A)	937	880	864	1220	758	2640	659	2850
Number of circuits	2	2	3	2	4	2	4	1
*Dielectric loss (kW/mi)	23.22	–	66.05	–	171.71	–	252.81	–
*J-loss resistance (Ω/mi)	0.046	0.140	0.048	0.076	0.050	0.035	0.053	0.031
*Insulation Thickness (in.)	0.505	–	0.835	–	1.025	–	1.250	–
*1971 Inst. Cost ($/mi)	462,184	141,184	936,999	182,700	1,431,732	288,250	1,631,732	230,550
1976 Inst. Cost ($/mi)	648,236	197,760	1,314,189	256,246	2,008,078	404,285	2,288,588	323,358
1976 Diel. Loss ($/mi)	5,186	–	14,754	–	38,360	–	56,479	–
1976 J-Loss ($/mi)								
$u=1.0$	33,506	89,946	44,591	93,998	47,745	202,704	38,253	104,619
0.8	21,444	57,565	28,584	60,159	30,557	129,731	24,482	66,956
0.6	12,062	32,380	16,079	33,839	17,188	72,974	13,771	37,663
0.4	5,361	14,391	7,146	15,040	7,639	32,433	6,120	16,739
0.2	1,340	3,598	1,787	3,760	1,910	8,108	1,530	4,185
1976 Transmission Cost ($/MVA·yr·mi)								
$u=1.0$	405	380	331	182	285	111	256	83
0.8	461	346	388	169	340	101	310	80
0.6	568	328	491	165	438	94	403	78
0.4	802	349	707	183	639	98	593	88
0.2	1544	527	138	289	1257	145	1172	142

$T_c=75°C$; $T_a=25°C$; $\rho_e=90$ thermal-Ω·cm; CLF=0.75; 1976 cost of electricity to power companies $E=\$0.0255/kWh$.

self-contained and pipe-type cables with overhead lines. As might have been expected, the results confirm that self-contained oil-paper insulated cables are more economical than pipe-type cables and, except at 138 kV, overhead lines are very much more economical than the two underground systems. Besides this, Fig. 3.61 reveals that in fully utilized lines the loss cost associated with overhead lines is greater than that of underground circuits, but the difference diminishes as the voltage increases and it nearly disappears at 500 kV because of the dielectric loss in the oil-paper insulation. There is little doubt that the balance between capital and loss charges, which was upset by the threefold increase in energy cost following the oil embargo, and which is required for the Kelvin minimum cost of Fig. 1.76, will in newly installed overhead lines be restored by providing them with larger conductors. This would lead to a small reduction in the cost of overhead transmission.

A striking advantage of overhead lines is that their transmission cost remains low almost regardless of utilization. This fact is demonstrated by Fig. 3.62 which shows, for example, that at 138 kV the transmission cost is nearly the same for overhead and both underground transmission lines at $u = 100\%$, but the UG/OH ratio increases to almost 4 : 1 at $u = 20\%$.

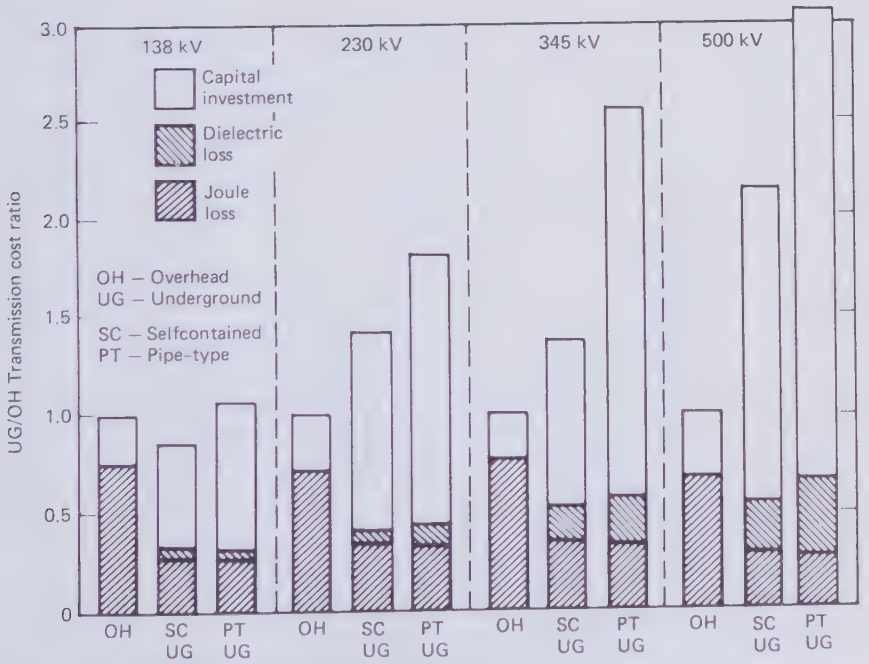

Figure 3.61 1976 UG/OH transmission cost ratios for naturally cooled self-contained and pipe-type cables. CLF = 0.75, $\alpha = 0.62$.

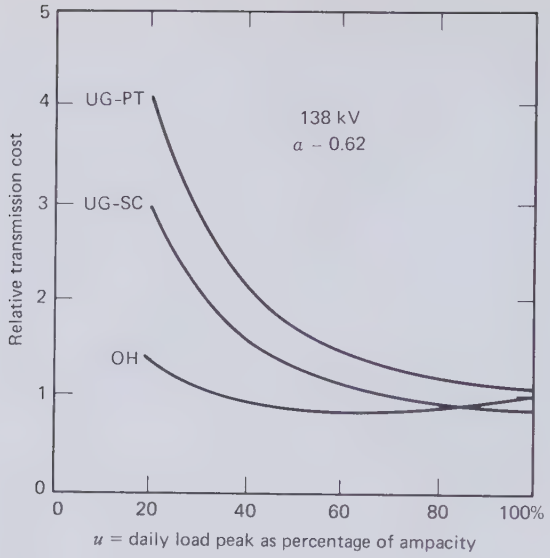

(a)

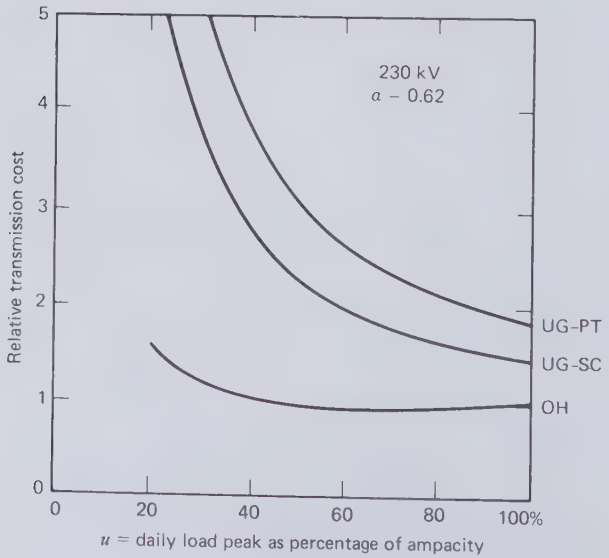

(b)

Figure 3.62 Transmission cost with oil-paper insulated naturally cooled cables relative to overhead lines as a function of utilization. (a) 138 kV; $\alpha = 0.62$. (b) 230 kV; $\alpha = 0.62$. (c) 345 kV; $\alpha = 0.62$. (d) 500 kV; $\alpha = 0.62$.

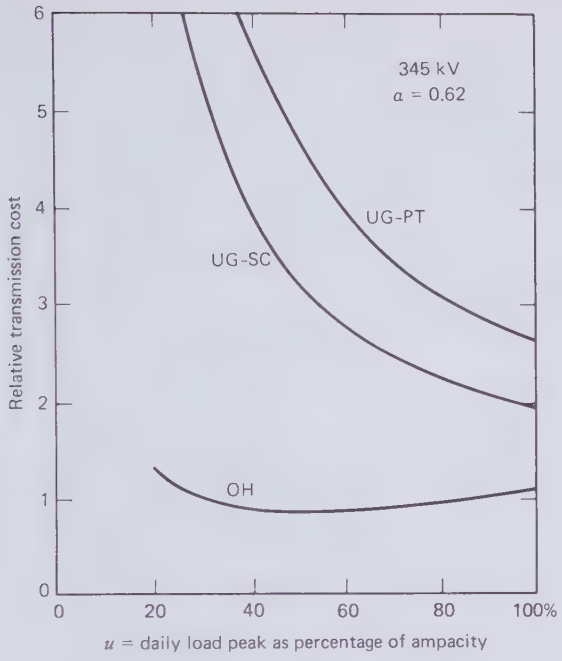

(c)

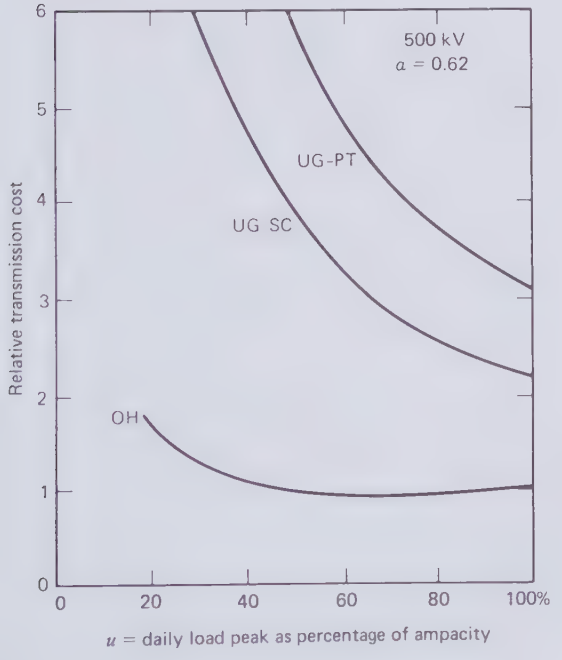

(d)

Figure 3.62 *Continued.*

In the United States the economic shortcomings of pipe-type cables have been accepted in the hope that these lines will be more reliable than self-contained cables because of the higher oil pressure and the mechanical protection provided by the steel pipe. Figure 3.61 shows little difference in the cost of losses in the two cable systems although the 2000 kcmil copper conductor used in either is associated with a total J-loss resistance R' of 0.036 Ω/mi in the self-contained cable and 0.046 to 0.053 Ω/mi in the pipe-type cable. The higher current density in the self-contained cable reduces the capital charge component per MVA at the expense of the loss components.

The economic assessment of forced cooling meets with special difficulties because of the variety of ways in which a cooling module may be set up. It can be short or long, use coolant return pipes that are small or large, and be located in the cable trench or remote from it. There exist options for heat exchange to air, water, or a refrigerant below ambient temperature. Compared with the external water-cooling method described in Section 3.2, the energy losses associated with oil circulation and refrigeration of pipe-type cables are not negligible and have to be factored into the economic analysis.

To achieve a certain amount of generality we ask the question: how much may the forced cooling equipment cost without increasing the transmission cost beyond that attainable with naturally cooled cables? We start with the transmission cost (3.62A). The denominator of this expression has the dimension of power (MVA) and it will be called the time average of the transmitted power *TP* so that

$$TP = n\sqrt{3}\ V(\text{kV})uI(\text{kA})(\text{CLF}) \tag{3.106}$$

where n is the number of circuits that constitute the line, u the utilization factor or the peak power transmitted in the daily load cycle as a fraction of ampacity, and CLF is the daily load factor. The transmission cost TC_1 with the naturally cooled line may be expressed as

$$TC_1 = \frac{0.15IC}{TP} + \frac{YDL}{TP} + \frac{YJL}{TP} \tag{3.107}$$

As before, *IC* is the installed cost per unit length of line, *YDL* the yearly cost of the dielectric loss per unit length, and *YJL* the yearly cost of the current dependent or Joule loss per unit length. Each term of (3.107) has the dimension if \$/MVA·mi·yr.

The result of forced cooling the pipe cable system will be: (1) an increase in ampacity by a factor of $(1+x)$; (2) an increase in the installed cost by a factor of $(1+y)$; (3) an additional term in (3.107) for the yearly

cost of energy losses associated with the cooling plant and given by $YCL/[(1+x)TP]$. Note that in this term TP is the transmitted power of the naturally cooled line. The cooling losses are due to pumping (P_v) and refrigeration (P_R). If E is the cost of electricity to the power company in \$/kWh the yearly cost of the cooling losses is given by

$$YCL = (P_v + P_R) \times 24 \times 365 E \tag{3.108}$$

Whether or not forced cooling is economical obviously depends on the relationship of x to y, and we will express this by

$$y = mx \tag{3.109}$$

Instead of comparing the forced cooled line with an overhead line, as was done in Section 3.2, in the case of pipe cables we will consider the ratio of transmission cost with forced cooling TC_2 to that with natural cooling TC_1. A cost ratio rather than an absolute cost is again the choice in order to isolate the result as far as possible from the effects of inflation.

$$\frac{TC_2}{TC_1} = \frac{1}{TC_1}\frac{1+mx}{1+x}\frac{0.15IC}{TP} + \frac{1}{1+x}\frac{YDL}{TP} + (1+x)\frac{YJL}{TP} + \frac{1}{1+x}\frac{YCL}{TP} \tag{3.110}$$

The first term of (3.110) indicates that the installed cost is proportional to $(1+y)$ and the transmitted power to $(1+x)$. Forced cooling will not change the yearly cost of the dielectric loss and therefore in the second term only the transmitted power has to be multiplied by $(1+x)$. Now the yearly cost of Joule losses is of course proportional to $(1+x)^2$ but TP has to be multiplied by $(1+x)$, which makes the net factor of the third term $(1+x)$.

When $m=1$, that is to say the installed cost and the transmission capability increase in the same proportion, and $YJL > YDL$, as would normally be the case, then $TC_2/TC_1 > 1$. Hence for forced cooling to be economical m should be smaller than one. Furthermore, using Table 3.7 as a guide, it seems that in most practical cases x will also be smaller than one. Knowing the economic parameters of the naturally cooled line, a table of TC_2/TC_1 ratios may be computed from (3.110) with x and m varying between zero and one. If the objective of forced cooling is to achieve a transmission cost saving of, say, ten percent or more, the table has to be searched for transmission cost ratios of 0.9 or smaller, noting the associated x and m coordinates. This has to be followed by trial design of cooling schemes for which x and m can be evaluated and compared with the target figures.

The prospect of reducing transmission costs by forced cooling of pipe cables will be better appreciated by considering the following numerical example.

EXAMPLE

1. 345 kV, 2000 kcmil (copper) double circuit in the same trench with remote oil return pipe of the same diameter as one cable pipe.
2. Cost components of the naturally cooled line as given in Table 3.10 for $u=1$ and CLF$=0.75$, that is
   $IC(1976) = \$2{,}008{,}078/\text{mi}$
   $YDL(1976) = \$38{,}360/\text{mi}$
   $YJL(1976) = \$47{,}745/\text{mi}$
   $n = 4$
   $TP = 1359$ MVA
   $TC_1 = \$285/\text{MVA}\cdot\text{mi}\cdot\text{yr}$.
3. 1976 cost of electricity to power companies $E = \$0.0255/\text{kWh}$.
4. Use Table 3.7 (CLF$=0.75$) for the pumping P_v and refrigeration loss P_R. Data from this table have been used to draw the graph of the yearly cost of cooling losses as a function of $(1+x)$ shown in Fig. 3.63.

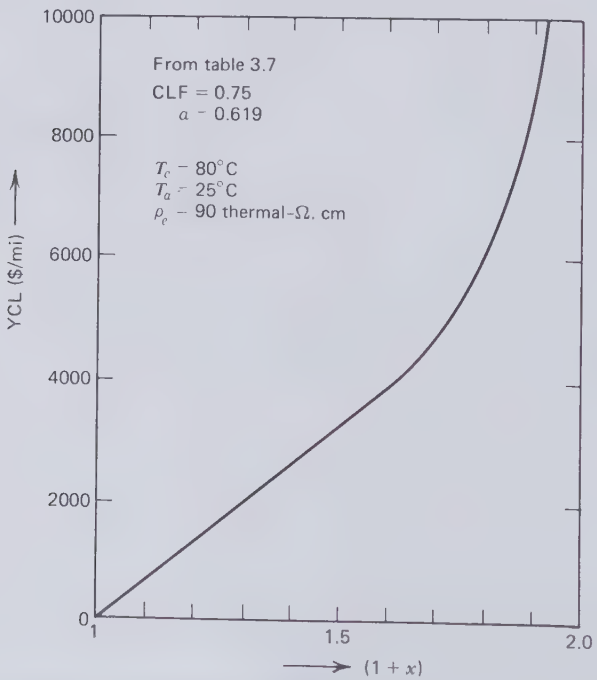

Figure 3.63 Yearly cost of cooling losses (3.108) in the 345 kV, 2000 kcmil pipe-type cable example.

RESULTS. To obtain the desired of TC_2/TC_1 ratios substitute the m and x coordinates into (3.110). The results for some of the coordinates are listed on Table 3.11.

DISCUSSION. In this particular example an 11 percent saving in transmission cost can be obtained when $m=0.4$ and $x=0.4$. Then $y=0.4\times0.4=0.16$. Hence the 11 percent saving presupposes that a 40 percent uprating in transmission capability can be achieved with a 16 percent increase in the installed cost of the transmission line. In 1972 Bender and Purnhagen [3.44] considered it possible to obtain a 25 percent uprating of a 345-kV double circuit with heat exchangers costing \$100,000/mi and an oil return pipe of an installed cost of \$280,000/mi. Bringing these capital cost items up to the 1976 value with the 7 percent compound inflation factor of 1.31 gives an installed cost increment of \$498,102. Therefore

$$y=498102/2008078=0.248; x=0.25; m=y/x=0.248/0.25=0.992.$$

For these coordinates Table 3.11 indicates $TC_2/TC_1=1.01$. Hence this system would with present energy costs not result in a transmission cost saving. On the other hand, as Bender and Purnhagen have pointed out, the addition of the forced cooling plant at some stage in the life of a pipe-type cable may delay the installation of a new transmission line. Then further economic incentives come into play due to the saving of capital charges on more extensive plant which can make forced cooling of pipe-type cables more attractive than it would otherwise appear. The Bender and Purnhagen example indicates that the oil return pipe is the major cost item of forced cooled pipe cables.

Energy conservation may be an end in itself apart from the effect it has on the transmission economics. As before in Section 3.2, we consider for this

Table 3.11 Effect of Forced Cooling on the Transmission Cost of a 345 kV, 2000 kcmil Pipe-type Cable TC_2 Relative to the Transmission Cost TC_1 of a Naturally Cooled Cable

	TC_2/TC_1				
x	$m=1$	$m=0.8$	$m=0.6$	$m=0.4$	$m=0.2$
0.2	1.01	0.99	0.96	0.93	0.91
0.4	1.03	0.98	0.94	0.89	0.85
0.6	1.04	0.98	0.93	0.87	0.81
0.8	1.06	0.99	0.92	0.86	0.79
1.0	1.09	1.01	0.93	0.86	0.78

purpose the transmission loss over a 100-mile-long line as a fraction of the transmitted power. The loss is of course proportional to line length and the 100-mile distance was chosen to make the loss fraction a few percent.

$$\%\text{loss of 100 mi} = 100u\frac{3\left[(uI)^2R_{100}+\lambda P_d\right]}{\sqrt{3}\ V(uI)} \tag{3.111}$$

where u is the utilization factor, I the ampacity, R_{100} the J-loss resistance of 100 miles of one conductor which includes components for shield and pipe losses, λP_d is the dielectric loss of one 100-mile-long cable core, and V is the line voltage. This 100-mile loss fraction has already been calculated for the overhead lines and self-contained cables listed on Table 3.5. The results are in Fig. 3.64 compared with those obtained for naturally cooled pipe-type cables. For the transmission loss fraction to have meaning the power flow must be constant and therefore all the graphs of Fig. 3.64 imply a load factor of CLF = 1.0. For example at $u = 0.6$ the constant line current is 60% of the ampacity. At 138 and 230 kV, the fractional loss in the two cable systems is almost identical; but at 345 and 500 kV the self-contained cable conserves distinctly more energy than the pipe-type cable. Heavily loaded cables in the 138 and 230 kV classes are significantly more efficient than overhead

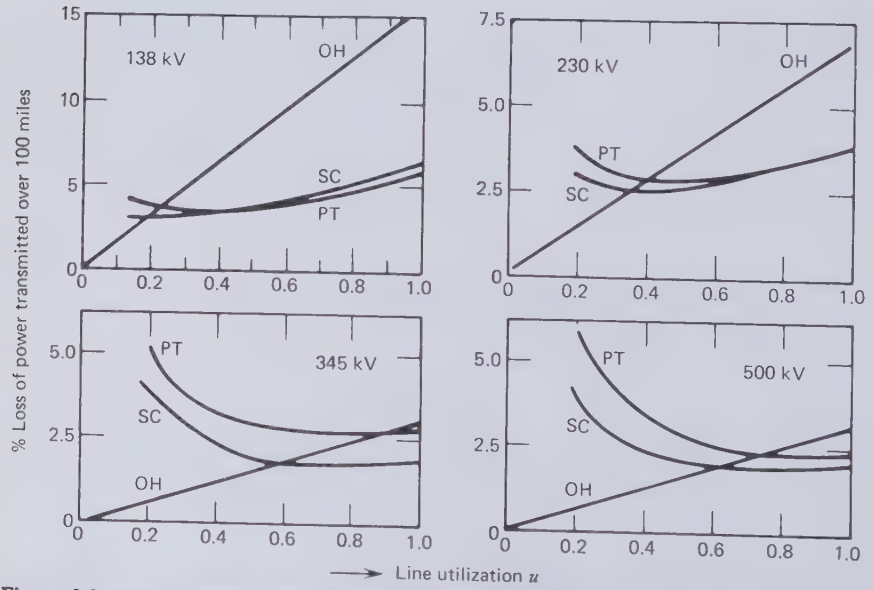

Figure 3.64 Transmission loss of naturally cooled oil-paper insulated pipe-type (PT) and self-contained (SC) cables compared with overhead lines (OH). CLF = 1.0.

lines, yet this advantage of the underground lines disappears in the 345 and 500 kV classes because of the severity of the dielectric loss.

Forced cooled lines must inevitably have higher loss fractions per unit length because the primary purpose of cooling is to increase the current density in the conductors and besides some energy is expended in the cooling equipment. To show the magnitude of the energy loss fraction of a 100-mile-long 345-kV pipe-type cable, the appropriate figures for constant full load and a range of oil flow velocities have been included in Table 3.7. At a typical flow velocity of $v = 30$ cm/sec the loss fraction is seen to be 4.31 percent compared to 2.85 percent of the naturally cooled system.

3.4 GAS PRESSURE ASSISTED PAPER INSULATED CABLES

A brief description of the various oil-paper insulated cables that are pressurized with nitrogen gas rather than insulating oil has been provided in Section 3.1. The original incentive for gas pressurization was a thinner insulation for the same operating voltage. Over the past 40 years this advantage has been slowly eroded by improvements in dielectric strength of both self-contained and pipe-type oil filled cables. As far as the dielectric constant, power factor, and thermal resistivity of the insulation are concerned, there is hardly any difference between gas pressure assisted and other paper insulated cables.

Only one gas-filled pipe-type cable installed in the United States in the 1970s received attention [3.45]. The methods of constructing and installing gas pressure assisted cables are closely parallel to those mentioned in Sections 3.2 and 3.3. Because of the similarity of properties to oil pressurized cables, the gas assisted ones have a comparable performance record with respect to ampacity, economics, efficiency and reliability.

3.5 SOLID DIELECTRIC CABLES

At the 1976 IEEE Underground Transmission and Distribution Conference Deschamps et al. [3.3] claimed that: "...at the present time in France, at the 225 kV level, the polyethylene insulated cable is superseding all its competitors." In the same year Mattison and Wretemark [3.46] reported to CIGRE that approximately 200 km of 123 to 145-kV cross-linked polyethylene cable had been manufactured in Sweden and installed in Scandinavia and other countries. Both the French and Swedish experience with solid dielectric high-voltage cables appears to be very satisfactory. Although the first successful installations of this new type of cable were made in the United States in the mid 1960s, here solid dielectric transmission cables

suffered a severe setback through a series of splice failures and adverse test results at Waltz Mill [2.66].

History has taught us that the success of a new type of high-voltage cable is not secure until at least 20 years of service experience are at hand. However, the growing understanding of breakdown in solid dielectrics, which is the subject of Section 2.5, gives us reasons to be optimistic. Many cable engineers now believe that at long last a more economical means than oil-paper insulated cables has been found for transmitting electrical energy underground. Let us begin by looking at the various cable designs currently in use throughout the world.

French 225-kV Cable

In 1969 the first and still the highest voltage cable with extruded polyethylene insulation became a part of the French 225-kV transmission network [3.47]. By 1976 some 14 circuit-kilometers were in service. Figure 3.65 is a photograph of this cable, which is being produced by the SILEC Company. Its excellent performance record appears to be due to the conservative design.

To obtain a three-phase circuit capability of 300 MVA, the 225 kV cable is furnished with either a 805 mm^2 (1589 kcmil) copper conductor or a 1200 mm^2 (2368 kcmil) aluminum conductor. Both are of the standard four-segment construction familiar from pipe-type cables. High-molecular-weight plain polyethylene is coextruded with semiconducting (carbon filled) polyethylene layers on either side. All manufacturers of solid dielectric cables agree that firm adhesion of the shielding layers to the insulation is imperative. SILEC claims that this requires simultaneous bonding at a temperature of 200°C. Furthermore, Charoy and Jocteur [3.47] point out that the resistivity of the semiconducting material is of minor importance and may vary up to $10^6\ \Omega \cdot cm$, but the mechanical and chemical properties of this material are critical. The bonding strength is required to withstand the shear forces tending to separate the layers during load cycling (see Fig. 2.33). SILEC produce the insulation sandwiched between the semiconducting shields with a 50-m-high vertical extrusion line. This helps to keep the heavy conductors concentric with the initially very soft insulation.

It may seem surprising that the highest voltage solid dielectric cable relies on non-cross-linked and unstabilized thermoplastic polyethylene. This material was used in the United States in distribution cables and has a poor performance record. It is particularly vulnerable to water and this fact may have decided the French manufacturers to enclose their cables in a conventional 3-mm-thick lead sheath. The insulation wall of 2.4 cm (0.944 in.)

Figure 3.65 French 225-kV solid dielectric cable.

thickness is more substantial than in a paper cable, but quite highly stressed as far as extruded polyethylene goes.

The most conservative aspect of the French cable is the conductor temperature rating. Originally 65°C was recommended by the manufacturers [3.47]. Electricite de France appears to have relaxed this to 70°C [3.3]. As cables are never subjected to constant full load over extended periods of time, the French 225-kV cables are unlikely to operate above 60°C. This will keep the differential thermal expansion between conductor and insulation wall within 1 percent [2.67], which prevents serious plastic deformation of the dielectric during load cycling. The lead sheath has to be protected against corrosion. SILEC chose for this purpose a 3.5-mm PVC jacket extruded directly on the lead.

Three advantages are claimed by the French utility for solid dielectric over self-contained oil-paper insulated cables. They are (1) lower manufacturing costs, (2) less maintenance of the dry cable system, and (3) easy adaptability to external water cooling.

Swedish 123 to 145-kV Cables

The major difference between the Swedish and French practice is the use of cross-linked polyethylene insulation without a metallic water barrier. The ground conductor of the Swedish cables consists of copper wires wound on the semiconducting insulation shield. Copper is preferred for this purpose to aluminum because of its higher corrosion resistance in spite of the protection of the wires with a PVC or polyethylene jacket. The ground conductor has to carry fault currents and it is sized so that the fault current density does not exceed 210 A/mm^2. In most cases the outer copper conductor has a cross section of 95 mm^2, which implies a fault current level of the order of 20 kA.

Mattison and Wretemark [3.46] do not mention a recommended conductor temperature. The Swedish engineers appear to keep an open mind on this important issue while service experience is being accumulated. However, they developed solid dielectric cables with both copper and aluminum conductors up to the exceptionally large size of 2000 mm^2 (3947 kcmil), which rather indicates that they intend to operate their cables at low temperature and conserve energy.

U.S. 138-kV Cables

In 1965 the first 138-kV solid dielectric cable was installed in Puerto Rico [2.78]. It contained a 750-kcmil copper conductor and was insulated with voltage stabilized high-molecular-weight polyethylene. Both the conductor and insulation shields were extruded semiconducting layers of polyethylene adhering firmly to the insulation. Two copper tapes wound on the insulation shield carried the charging currents. This first cable was only 123 m long and contained no splices.

This first generation of polyethylene cables was developed by the Simplex Wire and Cable Company, which had discovered that the breakdown strength of high-molecular-weight polyethylene was better than that of the more rigid high-density polyethylene and furthermore that the addition of up to 2 percent of staining antioxidant DPPD impaired tree growth and thereby lengthened the voltage life of the insulation, as shown in Fig. 2.41 on page 241. The resulting brown thermoplastic dielectric became known as voltage-stabilized polyethylene. It has performed more reliably than the nonstabilized material, which was later employed by other manufacturers.

More recently it was found that the decomposition products of the chemical cross-linking process in polyethylene linger on for several years and confer voltage stabilizing properties to the insulation. Ashcraft et al. [2.81] determined by experiment that voltage-stabilized thermoplastic and chemically cross-linked polyethylene show about the same resistance to tree initiation.

Short lengths of the Simplex cable have given satisfactory service, but the splice that this company developed was an utter failure. The Simplex splices usually broke down when the cables were heavily loaded, which suggests that the failure mechanism was due to thermomechanical causes.

Other U.S. cable manufacturers advanced cross-linked polyethylene insulation to the stage where it could be employed in high-voltage cables. The General Electric Company, which was primarily responsible for the introduction of cross-linked polyethylene insulation in addition filled the polyethylene with mineral or organic powder which acts as a voltage stabilizer [2.82]. For some years cross-linked polyethylene was promoted on the strength of its higher softening temperature and the higher conductor temperatures and current densities which this permitted. It was claimed that cables with this insulation could safely operate at 90°C and under emergency conditions at 130°C. At Waltz Mill 138 kV cables with cross-linked polyethylene insulation were put to the test, and most of them broke down at the elevated temperatures. This and the poor performance of the Simplex splices constituted a severe setback to the expansion of power transmission with solid dielectric cables in the United States.

Better splices have become available in the meantime and new voltage-stabilized cross-linked polyethylene compounds are likely to restore confidence in this product. Besides this, the incentive for high-temperature operation has largely disappeared because of the higher cost of energy losses since the oil embargo in 1973. Whether or not solid dielectric cables should be protected by a metallic moisture barrier remains an unresolved question and will be further discussed in connection with submarine cables.

EP-Rubber Insulated Cables

Vulcanized rubber was the first solid dielectric material that was applied to power cables. Rubber insulated cables were employed by the New York Subway Commission as long ago as 1888 [1.59]. Wherever flexibility is of overriding importance, rubber insulated cables are still in great demand. An example are trailing cables for mining machinery. Synthetic butyl rubber is being preferred to natural rubber. Not until the copolymerization of ethylene and propylene in an ordered structure became a practical reality did rubber insulation have a chance to compete with polyethylene in dielectric strength.

Ethylene propylene rubber (EPR) insulated cables were quickly developed in the 1960s up to 138 kV [3.48]. Unfortunately the first 138 kV EPR cable tested in Waltz Mill broke down at an early stage because of a manufacturing defect in the insulation wall. EPR cables have since then been confined to distribution voltages below 100 kV.

McAvoy and McIlveen [3.48] stressed the high corona resistance of EPR compared to polyethylene in the presence of surface eroding gas discharges. However, this type of discharge is unlikely to occur in the insulation of a high-voltage cable and no advantage can then be taken of the corona resistance. A more significant property of EPR is the high softening temperature of 135°C, which is equal to that of cross-linked polyethylene. EPR is toughened with a filling of mineral powder, but it retains sufficient elasticity so as not to have to undergo plastic deformation during load cycling. This appears to be an advantage, yet at the same time the small modulus of elasticity is potentially hazardous if the conditions for electromechanical breakdown are fulfilled. This topic has been discussed in Section 2.5.

On the basis of experiments with small cable models in 70°C water, Metra and Lombardi [3.49] claim that EPR cables should have a longer life under water than cross-linked and thermoplastic polyethylene without voltage-stabilizing additives. Their experiments lead to the conclusion that all long solid dielectric submarine cables should be enclosed in a hermetically sealed metal sheath.

Even if the mineral filled EPR rubber insulation should in the long run prove to be more reliable than the various forms of polyethylene, its high dielectric loss and thermal resistivity make it a doubtful competitor to oil-paper insulation. The critical insulation parameters are compared in Table 3.12, which also lists frequently used abbreviations of the insulation compounds.

Sodium Cables

A splice-free short length of high-voltage sodium cable has been in operation since June 1972 on the 138-kV system of Lima, Ohio. Up to the time of writing, this cable has given faultless service. Figure 3.66 shows the design of the Lima sodium cable. It is provided with a relatively small conductor surrounded with 0.8-in. voltage-stabilized thermoplastic polyethylene. Laboratory and field experience has proved that sodium cables do not require a semiconducting conductor shield and are probably all the more reliable for this omission. The process of filling the soft polyethylene tube with sodium, as it is being extruded, at least initially ensures excellent adhesion between the conductor and the insulation. Later a layer of hydroxide forms at the interface, but this does not lead to discharges, treeing and insulation failures.

The outside of the insulation, which is not in contact with sodium, must be protected with an adhering layer of semiconducting polyethylene. Beyond this layer the construction of the first high-voltage sodium cable follows conventional lines. Two copper tapes were employed to carry charging and fault currents. The tapes have been covered with a polyethylene anticorrosion jacket.

Table 3.12 Comparison of Critical Properties of Solid Dielectric Materials with Oil-paper Insulation

Material	Filler Powder	Abbreviation	Dielectric Constant (ε)	Power Factor ($\cos\phi$)	Loss Factor ($\varepsilon\cos\phi$)	Thermal Resistivity (Thermal-$\Omega\cdot$cm)	Deformation (Instability) Temperature (°C)
Oil-paper	–	–	3.5	2.5×10^{-3}	8.8×10^{-3}	500	120
Polyethylene	none	PE	2.3	3×10^{-4}	0.7×10^{-3}	350	90
Voltage stabilized polyethylene	none	VSPE	2.3	3×10^{-4}	0.7×10^{-3}	350	90
Cross-linked polyethylene	none	XLPE	2.3	3×10^{-4}	0.7×10^{-3}	350	135
Voltage stabilized cross-linked polyethylene	none	VSXLPE	2.3	3×10^{-4}	0.7×10^{-3}	350	135
Cross-linked polyethylene	filled	XLPE(f)	2.8*	3×10^{-3}*	8.4×10^{-3}*	350*	135
Ethylene propylene rubber	filled	EPR	2.8*	4×10^{-3}*	11.2×10^{-3}*	610*	135

*These values vary with the volume fraction of filler powder.

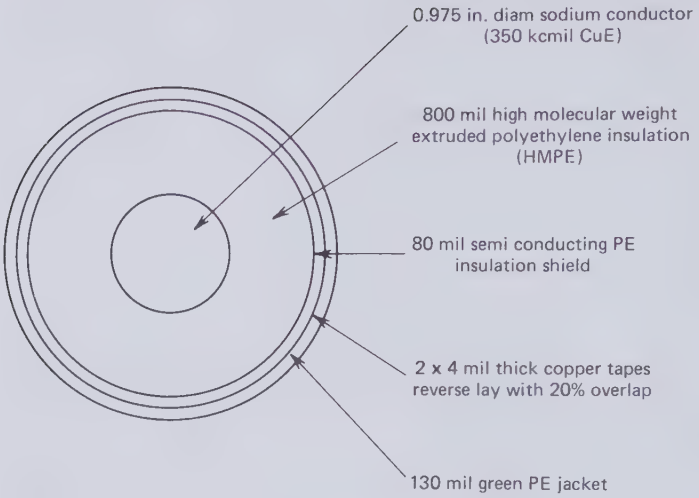

Figure 3.66 138-kV sodium cable in service at Lima, Ohio, since 1972.

An unusual feature of the first generation of sodium cables is that water vapor is allowed to diffuse through the insulation and slowly corrode the conductor. As water molecules arrive at the conductor they react with sodium according to the formula

$$\begin{aligned} &2\text{Na} + 2\text{H}_2\text{O} \rightarrow 2\text{NaOH} + \text{H}_2 \\ &46g + 36g = 80g + 2g \end{aligned} \tag{3.112}$$

The density of sodium is 0.97 g/cm^3. Therefore every cubic centimeter of water reacts with $(46/36) \times 0.97$ cm$^3 = 1.24$ cm^3 of sodium and converts it into sodium hydroxide (caustic soda) and hydrogen gas. NaOH is a white crystalline nonconducting compound. The reaction (3.112) creates a layer of this material, which separates the conductor metal from the insulation. The hydrogen generated by the reaction easily diffuses through the polyethylene to leave the cable. Water vapor penetrates the layer of sodium hydroxide and therefore perpetuates the growth of this layer indefinitely.

Eichhorn [3.50] has determined quantitatively how much water permeates through the polyethylene insulation by measuring the resistance increment of the enclosed sodium conductor. With reference to Fig. 3.67, the volume of water (liquid) V_w that reaches the sodium conductor of length L and initial radius r_i is proportional to the time and the area A through which diffusion takes place. Furthermore V_w is inversely proportional to the thickness s of the polyethylene through which the vapor has to diffuse. For A Eichhorn takes the cylindrical mean area between the conductor and insulation

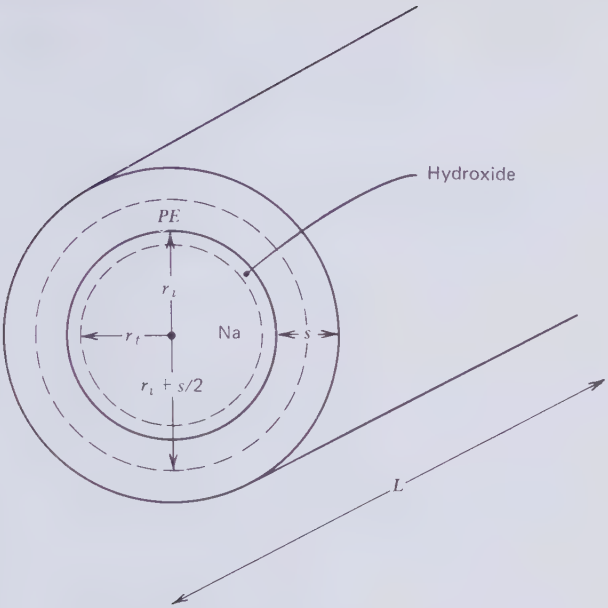

Figure 3.67 Hydroxide layer on sodium conductors.

surfaces, which is nearly equal to the logarithmic mean, or

$$A = \pi(2r_i + s)L \tag{3.113}$$

Hence the volume of water reaching the conductor is

$$V_w = \frac{k_w \pi(2r_i + s)Lt}{s} \tag{3.114}$$

where k_w is the volume diffusion constant of proportionality that has the dimension cm^2/sec. Let ΔV be the volume of sodium converted to hydroxide and hydrogen by V_w, then

$$\Delta V = \frac{k_w \pi(2r_i + s)Lt}{1.24s} \tag{3.115}$$

The initial volume of sodium present in length L of the cable is

$$V_i = \pi r_i^2 L \tag{3.116}$$

Therefore

$$\frac{\Delta V}{V_i} = \frac{k_w t(2r_i + s)}{1.24 s r_i^2} \tag{3.117}$$

After time t the axial resistance of the conductor will have increased from R_i to R_t with erosion producing the increment $\Delta R = R_t - R_i$. It can easily be shown that

$$\frac{\Delta R}{R_t} = \frac{\Delta V}{V_i} \tag{3.118}$$

Equation (3.118) indicates how resistance measurements may be used to determine the fraction of sodium that has been lost in the reaction with water. By this means Eichhorn measured the water diffusion constant k_w and his results are plotted on Fig. 3.68 against the reciprocal of absolute temperature. As would be expected, the vapor diffusion increases sharply with polyethylene temperature. Figure 3.68 actually indicates a 20-fold increase in the amount of water reaching the sodium conductor when the insulation temperature is raised from 40 to 80°C. Eichhorn also proved by experiment that the diffusion rate is proportional to the relative humidity of

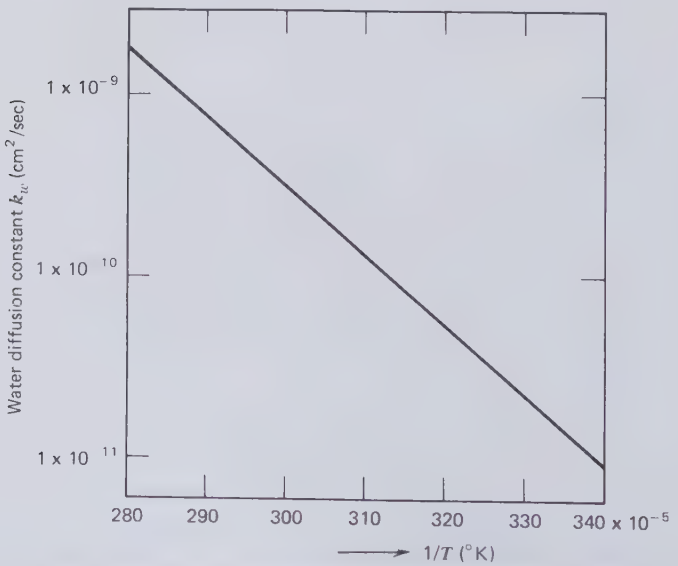

Figure 3.68 Water vapor diffusion through polyethylene [3.50]. (By permission of the Society of Plastics Engineers).

the air at the insulation surface. The plot of Fig. 3.68 applies to 100 percent relative humidity or immersion in liquid water.

To assess the seriousness of the water permeation problem let us calculate the time it would take to convert 10 percent of the sodium volume in the cable of Fig. 3.66 to hydroxide when the cable operates under water at an average insulation temperature of, say, 40°C = 313°K. On Fig. 3.68 for $1/313°K = 319 \times 10^{-5}$ we find $k_w = 6 \times 10^{-11}$ cm^2/sec. The total thickness of polyethylene including the insulation shield and jacket is $s = 1.01$ in. = 2.57 cm and the initial conductor radius is $r_i = 1.24$ cm. For $\Delta V / V_i = 0.9$ it follows from (3.117) that

$$t = \frac{0.9}{6 \times 10^{-11}} \frac{1.24 \times 2.57 \times 1.24^2}{2 \times 1.24 + 2.57} = 1.455 \times 10^{10} \text{ sec} > 400 \text{ years}$$

Therefore the life of this particular cable is not limited by water-vapor diffusion through the polyethylene. Another calculation of this kind would show that in 10 years the sodium conductor radius would be reduced by approximately 1 percent or 5 mils.

The cable of Fig. 3.66 was manufactured in 1969. Seven years later a 60-ft length of it was subjected to load cycles at the author's laboratory at MIT. While terminating the test length it was established that the conductor was covered with a layer of sodium hydroxide, which, as far as could be judged, was several mils thick. During a total of 50 load cycles the line-to-ground voltage was taken up to 133 kV, while the conductor temperature reached 85°C. The tests proceeded without incident indicating that a 0.8-in. wall of voltage-stabilized polyethylene is likely to be adequate for 230-kV sodium cables in spite of the layer of hydroxide.

Service and test experience gathered with this cable over a period of nearly 10 years suggests that solid dielectric sodium cables will be more reliable than the same type of cable furnished with aluminum or copper conductors. The primary reasons for this optimism are the good thermomechanical compatability of sodium and polyethylene [2.67] and the desication of the high-voltage insulation by the presence of the sodium. No water can possibly exist for any length of time near the sodium conductor. Not only is the linear thermal expansion of sodium (70×10^{-6}) a better match to thermoplastic polyethylene (200×10^{-6}) than copper (16.5×10^{-6}) and aluminum (23.6×10^{-6}), but the plasticity of the sodium makes the conductor follow the thermal deformation of the insulation without creating strain.

In the years from 1965 to 1970 U.S. utilities placed some 50 low-voltage sodium cable installations underground and have been able to operate them very much in the same way as other solid dielectric cables. Considering the inovative nature of sodium cables, there were remarkably few incidents of

malfunction in 10 years of operation. The fear of sodium fires has not materialized, nor has the more real danger of thermal instability at the melting point of sodium (97.8°C) become a significant problem. On the basis of the service record and the economic merit of sodium metal shown in Fig. 1.74, sooner or later these cables are likely to become a major factor in the underground transmission of electrical energy.

The first high-voltage sodium cable has much too small a conductor to exploit the economic advantages of sodium. Developments in the remainder of this century are expected to tend to the design illustrated in Fig. 3.69. This should be suitable for 230 kV and possibly even 345 kV. Apart from the large conductor, a new feature of this cable is the sodium sheath that replaces the copper tapes or wires or the lead sheath normally used for carrying the charging and fault currents. The sodium sheath is a positive barrier to the the penetration of water vapor and keeps the insulation completely dry. Any moisture trapped in the polyethylene during the manufacturing process will in time be permanently removed by reaction with the sodium boundaries. However water vapor will diffuse through the polyethylene jacket and gradually erode the sodium sheath from the outside in. For the cable size shown in Fig. 3.69, this erosion rate comes to approximately 1 mil/year and has to be taken into account in designing the thickness of the sheath.

Splices

Welds make the best conductor joints with the lowest contact resistance. However the high temperature required for welding, together with the thermal conductance of the metal, endanger the adjacent electrical insulation. To avoid the heating problem, soldered and compression joints have been developed for copper conductors in paper insulated cables. They are equally suitable for solid dielectric cables. Compression jointing has not been entirely satisfactory on aluminum conductors because the tenacious aluminum oxide severely limits the number of contact points and if some of them break during thermal cycling the joint will overheat and may damage the insulation. Therefore methods of soldering and welding aluminum conductors had to be developed that do not burn the insulation. Explosive welding with a powder charge is one way of achieving this end. This eliminates the sustained heat flow down the conductors during slow arc or torch welding. Another solution is the use of a welding jig with coolers that extract heat from the conductor on both sides of the weld.

The jointing of large sodium conductors in high-voltage cables presents special problems, which still await solution.

By far the most serious aspect of splicing is the bridging of the electrical insulation between the pencil-shaped ends of two solid dielectric cables.

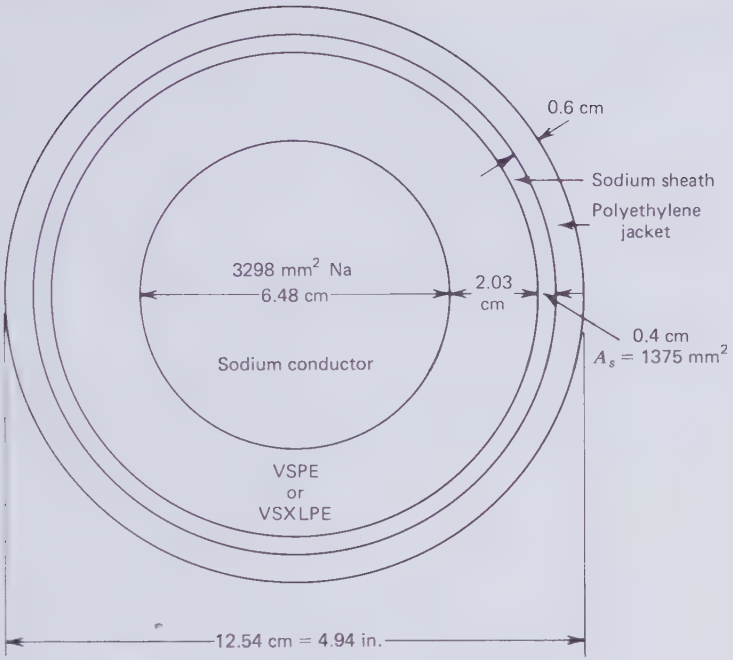

Figure 3.69 230/345 kV sodium cable of the future.

What makes a good splice in extruded polyethylene is still not fully understood. The taped structure of the oil-paper dielectric permits a little axial motion of the insulation relative to the conductor. Solid insulation that is bonded to the conductor prevents this relative motion and any axial displacement has to be taken up in elastic or plastic deformation of the splice material. Some elasticity would be expected to help and indeed splices made with EP-rubber tapes have outperformed others that were built up from polyethylene tapes [3.51–3.56]. This may seem surprising because the extra dielectric loss and the low modulus of rubber tapes should make them more vulnerable to thermal and electromechanical breakdown. The experimental facts indicate that the thermomechanical advantage of elasticity outweighs the dielectric shortcomings of EPR. Ethylene propylene rubber has a lower impulse strength than polyethylene and therefore splices made with EPR tapes have to be built up beyond the diameter of the cable. Since EPR also has a higher thermal resistivity than polyethylene this means the splices will run hotter than the cable. If they are directly buried with the cable they become the limiting factor of transmission capability. However, this is no longer a major concern because the loss economics favor generally lower conductor temperatures.

Taped insulation splices almost inevitably contain some air-filled cavities and the tapes may separate from the pencilled down solid insulation on either side. Therefore newly made taped splices usually show a considerable degree of discharge (corona) activity, but this dies out with time as the splice settles down under thermal cycling. The danger of discharge damage has led some manufacturers to develop molded splices in which the cavity-free splice insulation is firmly bonded to the cable insulation.

The first attempt in this direction was the ill-fated Simplex splice which was constructed of polyethylene tapes that were subsequently fused together and to the insulation by heat and external pressure. On sectioning, these splices have the appearance of extruded insulation. Their impulse strength is also comparable with that of the cable and they were therefore made of the same diameter as the cable. Despite this apparent integrity of the Simplex splice it could not deal with thermal cycling and many of these splices failed when the cables were fully loaded. Under light load they have been surviving for a long time.

The highest voltage solid dielectric cable splices are in use on the French 225-kV transmission grid. Their construction is an extrapolation of the extensively used field molded splice of coaxial submarine telephone cables [3.57]. Figure 3.70 is a cross section through the 225-kV splice.

The conductor joint is soldered or welded and then covered by a layer of molded semiconducting polyethylene, which is fused to the conductor shield of both cable ends projecting out from under the pencilled down insulation. The partially completed joint is then placed in a larger mold casing. Polyethylene is heated under nitrogen in an adjacent extrusion chamber. When liquid, the polyethylene is injected into the mold surrounding the conductor splice and kept there under pressure and heat for several hours to ensure complete filling and bonding to the cable insulation. After a period of controlled cool-down the mold is removed and the insulation splice painted with semiconducting paint and wrapped over with semiconducting nylon tapes. The winding of metal tapes on the insulation shield and bonding a metal sleeve on both ends to the lead sheath of the cable complete the

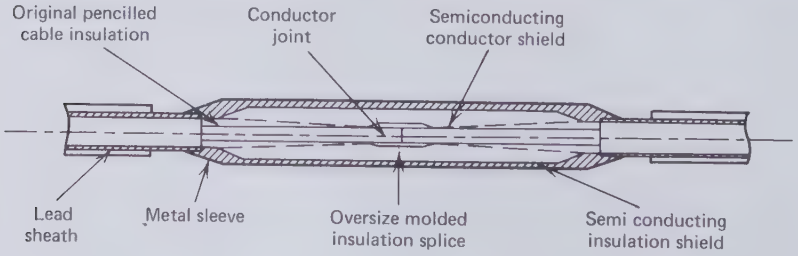

Figure 3.70 Injection molded splice of French 225 kV solid dielectric cable.

splicing operation. For sheath cross-bonding the metallic path through the metal sleeve has to be interrupted by an epoxy gap and also a shield gap has to be provided in the same way this is accomplished in the splices of self-contained oil-paper insulated cables shown in Fig. 3.10 on page 291.

The jointing of low-voltage solid dielectric cables has been greatly simplified by the prefabrication of slip-on insulation splices. Efforts are underway to apply this same labor saving technology to high-voltage solid dielectric cables. The principle of the slip-on splice is illustrated in Fig. 3.71. Premolded elastomeric insulation (D) with its integral semiconducting jacket (E) is forced to slide over the conductor splice. The bore in the splice sleeve is a little smaller than the diameter of the cable insulation (C) causing the premolded elastic insulation to be compressed and bear down tightly on the interface. While the conductor joint is being made, the splice sleeve assembly has to be pushed over the shielded cable (F). The discontinuity caused by the conductor joint is covered by a conducting shield (B). This shield is in contact with the conductor and has to be smooth so that the splice will easily slip over it.

Premolded splices are inevitably large in diameter but this need not be a disadvantage if the cable conductor away from the splice is operated in the 60 to 70 °C temperature range which leaves a fair margin up to 20°C of excess splice temperature. It seems possible that the axial and radial elasticity of slip-on insulation may prove to have certain thermomechanical advantages over molded polyethylene splices.

Installation

Apart from splicing and terminating, the installation of solid dielectric cables is identical to that of self-contained oil-paper insulated cables described in Section 3.2.

Referring to Fig. 3.12 (page 292), it will be appreciated that the pothead of an oil-paper insulated cable is automatically kept filled with oil from the reservoirs that maintain a positive pressure inside the cable. The termina-

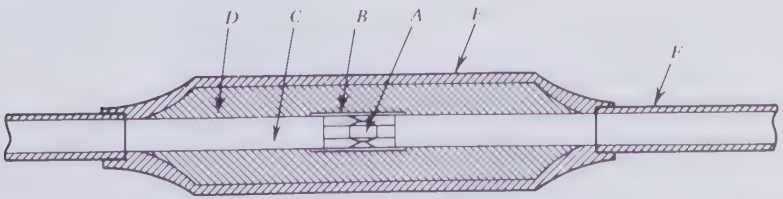

Figure 3.71 Principal elements of a slip-on insulation splice. *A*—Conductor splice. *B*—Conducting shield. *C*—Cable insulation. *D*—Slip-on insulation. *E*—Semiconducting splice jacket. *F*—semiconducting insulation shield.

tions of solid dielectric cables, by contrast, have to contain their own oil and some arrangement that will keep the oil under pressure to prevent air from being drawn into the pothead. Both these special requirements are fulfilled in the slip-on pothead of Fig. 3.72. This is supplied with a metal tube, instead of the cable, and elastomeric diaphragm oil seals through which tube and cable may slide without spilling oil. To install the pothead on the

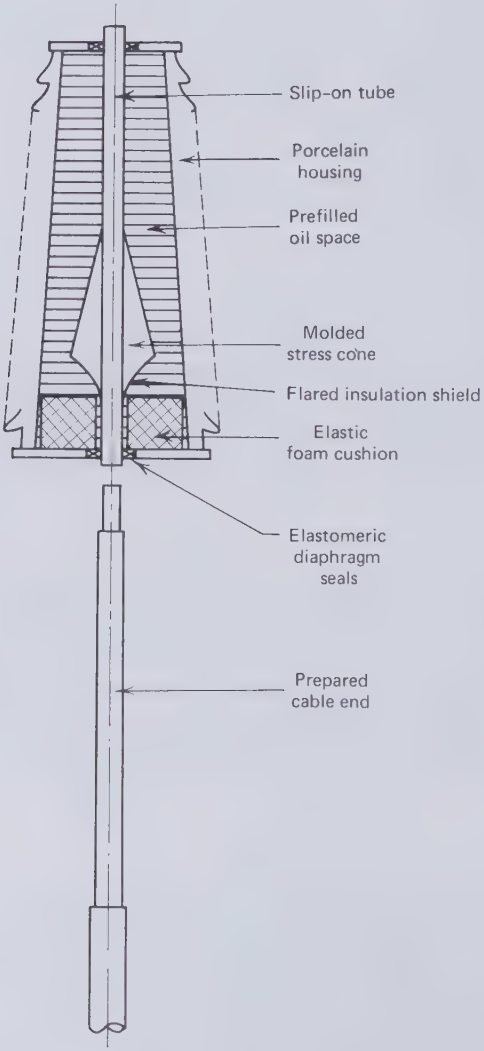

Figure 3.72 Slip-on oil-filled termination for solid dielectric cables.

prepared cable end and high-voltage connector, the latter is inserted into the metal tube and the pothead lowered onto the cable. This slides the tube out of the top of the pothead while the cable enters at the bottom. Slip-on potheads have to be manufactured to fit the dimensions of the cable.

Prefabricated terminations contain a molded stress cone and insulation build-up which, as in the slip-on splice, grips the cable insulation firmly. Also housed in these oil-filled terminations is an elastic foam cushion containing sealed gas-filled cells. As the cable is loaded and the insulation expands, displacing some of the incompressible liquid, the cushion is compressed and this process is reversed during cool-down of the cable.

Attempts have been made to design a dry pothead for solid dielectric cables analogous to dry slip-on splices, but they have not been entirely successful. Although a future completely dry cable transmission system appears to be a distinct possibility.

Ampacity

The thermal circuit of a naturally cooled solid dielectric cable is identical to that of Fig. 3.13 on page 295 and the equation governing radial temperature drops is (3.4), which leads to the ampacity equation (3.18).

For equal voltage, conductor and insulation dimensions the dielectric loss from (2.81) is proportional to the product $\varepsilon \cos\phi$. This is listed in Table 3.12 on page 407 for oil-paper and solid dielectrics. The unfilled polyethylene materials have a loss factor which is generally less than one-tenth of that of oil-paper insulation. For this reason it has been common practice to ignore the dielectric loss of polyethylene cables so far as ampacity calculations are concerned. In a typical cable containing a 2000 kcmil conductor and 0.8 in. extruded polyethylene with a 50 mil conductor shield and an 80 mil insulation shield operating at 138 kV with $\varepsilon = 2.3$ and $\cos\phi = 3 \times 10^{-4}$, (2.81) on page 212 gives

$$P_d = \frac{2\pi \times 60 \times 2.3 \times \left(\frac{138000}{\sqrt{3}}\right)^2 \times 4 \times 10^{-4}}{2\ln\left(\frac{8.463}{4.399}\right) \times 9 \times 10^{11}} = 1.87 \times 10^{-3} \quad \text{W/cm}$$

and if the same cable is used at 230 kV

$$P_d = \left(\frac{230}{138}\right)^2 \times 1.87 \times 10^{-3} = 5.19 \times 10^{-3} \quad \text{W/cm}$$

Noting that the thermal resistivity ($1/\kappa = \rho$) of polyethylene is 350 thermal-$\Omega \cdot$cm, we may calculate the thermal resistance of the insulation wall from (2.80)

$$R_i = \frac{350}{2\pi} \ln\left(\frac{8.463}{4.399}\right) = 36.45 \quad \text{thermal-}\Omega\cdot\text{(per cm)}$$

Therefore the temperature drop across the insulation due to the dielectric loss is

$$\Delta T_d = \left(\frac{1}{2}\right) R_i P_d \text{ (and at 138 kV)} = \left(\frac{36.45}{2}\right) \times 1.87 \times 10^{-3} = 0.034 \text{ °C}$$

$$\text{(and at 230 kV)} = \left(\frac{36.45}{2}\right) \times 5.19 \times 10^{-3} = 0.095 \text{ °C}$$

If the conductor is made of copper its ac resistance will be at least 1.77×10^{-7} Ω/cm. A typical current in a 2000 kcmil conductor is 800 A which would result in a Joule loss of 0.113 W/cm and a temperature drop across the insulation of

$$\Delta T_J = 0.113 \times 36.45 = 4.13 \text{ °C}$$

Therefore at 138 kV the temperature drop across the insulation due to dielectric losses is less than 1 percent of that caused by the conductor Joule loss. It lies within the uncertainty of Joule loss computations and may safely be neglected.

At 230 kV the temperature drop due to dielectric losses is of the order of 2 percent of that created by the conductor losses and may still be ignored in ampacity computations. However, at 230 kV the dielectric loss itself amounts to 5 percent of the conductor loss, and since the dielectric loss is not subject to load factor reductions it should be considered in economic studies. At 345 kV both the temperature drop and the economic penalty of dielectric losses in polyethylene have to be taken into account.

For a sample ampacity calculation we compare the performance of XLPE with EPR insulation and show that ground conductor crossbonding is imperative.

EXAMPLE

1. 138 kV three-phase circuit buried at a depth of $D = 36$ in. in flat formation with a center spacing of $S = 12$ in.; thermal resistivity of sand $\rho_e = 90$ thermal-$\Omega \cdot$cm; ambient temperature $T_a = 25$°C. Cable design as in Fig. 3.73.

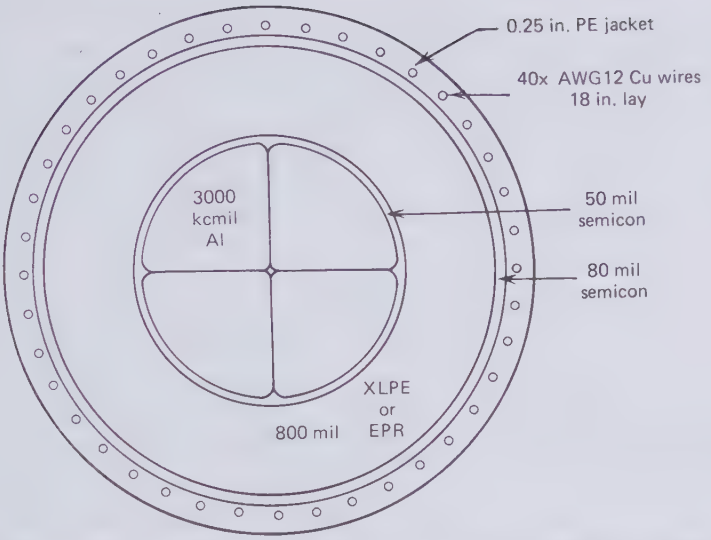

Figure 3.73 138 kV Solid dielectric cable for ampacity calculation example.

2. Conductor: 3000 kcmil, 4 segments, aluminum of 61.8% IACS, 2.18 in. diam.
3. Conductor shield: 50 mil semiconducting polyethylene.
4. Insulation: (a) 800 mil XLPE, $T_c = 90°C$; $\varepsilon = 2.3$; $\cos\phi = 3 \times 10^{-4}$; $\rho_t = 350$ thermal-$\Omega \cdot$cm. (b) 800 mil EPR; $T_c = 90°C$; $\varepsilon = 2.8$; $\cos\phi = 4 \times 10^{-3}$; $\rho_t = 610$ thermal-$\Omega \cdot$cm.
5. Insulation shield: 80 mil semiconducting polyethylene.
6. Ground conductor: 40 × AWG12 100% IACS copper drain wires wound on the semiconducting insulation shield with a lay of 12 in.
7. Jacket: 250 mil of polyethylene.

CONDUCTOR RESISTANCE R_{ac}. Conductor area = 3000 kcmil = $3 \times 10^6(\pi/4) \times 10^{-6} \times 2.54^2 = 15.2$ cm^2. With a 2% stranding allowance the conductor dc resistance per cm is $R_{dc} = 1.02\rho_c(T_c)/15.2\ \Omega$/cm. From Fig. 1.71 $\rho_c(90°C) = 3.55\,\mu\Omega \cdot$cm. Therefore $R_{dc} = 0.238 \times 10^{-6}\ \Omega$/cm. The oxide layer on aluminum wires prevents interwire conduction and thereby suppresses the proximity effect. For the skin effect of a 4-segment conductor, Fig. 1.56 (lowest curve) indicates $R_{ac}/R_{dc} = 1.11$. Hence $R_{ac} = 1.11 \times 0.238 \times 10^{-6} = 0.264 \times 10^{-6}\ \Omega$/cm.

EFFECTIVE CIRCULATING CURRENT RESISTANCE OF DRAIN WIRES R_s'. The drain wires are wound over the insulation shield diameter $d_s = 4.04 \times 2.54 = 10.26$

cm. The length of one turn is $[(\pi d_s)^2+(12\times 2.54)^2]^{1/2}=44.36$ cm. Therefore the wire length per centimeter of cable length is $44.36/12\times 2.54=1.46$. Assume the drain wires operate at 60°C. The 100% IACS copper resistivity at this temperature from Fig. 1.71 is 2 $\mu\Omega\cdot$cm. Furthermore each AWG 12 wire has a diameter of 0.0808 in. The cross-sectional area of the ground conductor therefore is $A_g=40\times(\pi/4)(0.0808\times 2.54)^2=1.323$ cm^2. The dc resistance per unit length of the ground conductor is given by

$$R_s=\frac{2\times 10^{-6}\times 1.46}{1.323}=2.21 \quad \Omega/\text{cm}.$$

To calculate the mutual inductance between the conductor and the drain wires it will be assumed that the cable length is 10^5 cm. Ten times this length makes only a small difference to the ampacity. Furthermore we treat the ground wires as a thin tube coinciding with the cylindrical surface in which the wire axes lie. Then $r_0=r_i=(4.04+0.0808)(2.54/2)=5.23$ cm. From (1.94):

$$M_{c,g}/L=2(-1+\ln 2\times 10^5-\ln 5.23)\times 10^{-9} \quad \text{H/cm}=1.91\times 10^{-8} \quad \text{H/cm}$$

From (3.67):

$$R_s'=\frac{2.21\times 10^{-6}}{1+\left[2.21\times 10^{-6}/2\pi\times 60\times 1.91\times 10^{-8}\right]^2}=2.02\times 10^{-6} \quad \Omega/\text{cm}.$$

Effective eddy current resistance of drain wires R_e'. From the discussion in Section 1.14 and Fig. 1.41 it will be seen that two kinds of eddy currents may flow in the tubular sheath of a single core cable. However, if the ground conductor is made up of wire helices the longitudinal voltages induced in each wire due to the current in an adjacent conductor will all be equal because of the wire transposition and eddy currents of the second kind cannot flow. To make an order of magnitude estimate of the eddy currents of the first kind we equate the layer of drain wires to a tube of a thickness equal to the drain wires, but of axial resistance $R_s=2.21\times 10^{-6}$ Ω/cm, as determined above. Using again a length of $L=10^5$ cm, we find from (1.112) with $r_0=5.33$ cm, $r_i=5.13$ cm, $r_m=5.23$ cm:

$$\Delta e=2\pi\times 60\times 2\times 10^5\times 10^{-9}I\ln(5.33/5.13)=2.88\times 10^{-3}I \quad \text{V}$$

and from equation (1.114):

$$L_e = 2\times10^5\{-2+2\ln 8\times10^5-\ln[(5.33+5.23)(5.23+5.13)]\}\times10^{-9} \quad \text{H}$$

$$= 4.10\times10^{-3} \quad \text{H} \quad \text{and} \quad \omega L = 1.54 \quad \Omega$$

Therefore

$$|Z_e| = \left[(10^5\times2.21\times10^{-6})^2+1.54^2\right]^{1/2} = 1.56 \quad \Omega$$

$$i_e = \Delta e/|Z_e| = \frac{2.88\times10^{-3}I}{1.56} = 1.85\times10^{-3}I \quad \text{A}$$

$$W_e/L = \frac{I^2R_s}{L} = \frac{(1.85\times10^{-3})^2I^2\times0.221}{10^5} = 7.57\times10^{-12} \quad \text{W/cm};$$

$$R_e' = 7.57\times10^{-12} \quad \Omega/\text{cm}$$

which is completely negligible compared to R_{ac}. Therefore in a crossbonded installation of the cable of Fig. 3.73 only the conductor and dielectric loss need be considered in ampacity calculations.

Dielectric loss P_d. From (2.81)

$$\text{XLPE} \quad P_d = \frac{2\pi\times60\times2.3\left(\dfrac{138000}{\sqrt{3}}\right)^2\times3\times10^{-4}}{2\ln\left(\dfrac{3.88}{2.28}\right)\times9\times10^{11}} = 1.73\times10^{-3} \quad \text{W/cm}$$

$$\text{EPR} \quad P_d = \frac{2\pi\times60\times2.8\left(\dfrac{138000}{\sqrt{3}}\right)^2\times4\times10^{-3}}{2\ln\left(\dfrac{3.88}{2.88}\right)\times9\times10^{11}} = 0.028 \quad \text{W/cm}$$

Thermal resistance of polyethylene wall R_t. From (2.80)

$$\text{XLPE} \quad R_t = \left(\frac{350}{2\pi}\right)\ln\left(\frac{4.04}{2.18}\right) = 34.37 \quad \text{thermal-}\Omega$$

$$\text{EPR} \quad R_t = \left(\frac{610}{2\pi}\right)\ln\left(\frac{4.04}{2.18}\right) = 59.89 \quad \text{thermal-}\Omega$$

THERMAL RESISTANCE OF JACKET R_j. From (2.80)

$$R_j = \left(\frac{350}{2\pi}\right)\ln\left(\frac{4.54}{4.04}\right) = 6.50 \quad \text{thermal-}\Omega$$

SOIL THERMAL RESISTANCE R_e. From (3.8)

$$R_e = \left(\frac{90}{2\pi}\right)\ln\frac{2\times 36 - 2.27}{2.27} = 49.06 \quad \text{thermal-}\Omega$$

THERMAL PROXIMITY FACTOR k. From equation (3.15)

$$k = 1 + \frac{\ln\left[(72^2 + 12^2)/12^2\right]}{\ln\left(\frac{72}{2.27}\right)} = 2.04$$

AMPACITY OF XLPE CABLE. From (3.18) (1) Without cross-bonding, that is

$$R_s' = 2.02\times 10^{-6} \quad \Omega/\text{cm}$$

$$I^2 = \frac{90 - 25 - 1.73\times 10^{-3}(0.5\times 34.37 + 6.5 + 2.04\times 49.06)}{0.264\times 10^{-6}(34.37 + 6.5 + 2.04\times 49.06) + 2.09\times 10^{-6}(6.5 + 2.04\times 49.06)}$$

$$I = 499 \quad \text{A}$$

(2) With cross-bonding, that is, $R_s' = 0$

$$I^2 = \frac{90 - 25 - 1.73\times 10^{-3}(0.5\times 34.37 + 6.5 + 2.04\times 49.06)}{0.264\times 10^{-6}(34.37 + 6.5 + 2.04\times 49.06)}$$

$$I = 1319 \quad \text{A}$$

AMPACITY OF EPR CABLE. (1) Without cross-bonding

$$I^2 = \frac{90 - 25 - 0.028(0.5\times 59.89 + 6.5 + 2.04\times 49.06)}{0.264\times 10^{-6}(59.89 + 6.5 + 2.04\times 49.06) + 2.09\times 10^{-6}(6.5 + 2.04\times 49.06)}$$

$$I = 479 \quad \text{A}$$

(2) With cross-bonding

$$I^2 = \frac{90 - 25 - 0.028(0.5\times 59.89 + 6.5 + 2.04\times 49.06)}{0.264\times 10^{-6}(59.89 + 6.5 + 2.04\times 49.06)}$$

$$I = 1180 \quad \text{A}$$

Discussion of results. This example illustrates that cross-bonding of the ground conductors is essential to prevent serious derating of solid dielectric transmission cables. With cross-bonding the XLPE cable has a 12 percent higher ampacity than the EPR cable.

Daily Cycle Rating

The peak cyclic current that may be carried by a solid dielectric cable without overheating the insulation is determined by its environment and not the cable itself. Therefore the daily cycle rating of solid dielectric cables is established by the same procedure that was adopted for oil-paper insulated cables on pages 303 to 307.

Forced Cooling

As the solid dielectric cable does not contain a dielectric liquid, the obvious choice of a cooling fluid is water. Internal conductor cooling with water has been applied experimentally to lower voltage cables and proposed for high-voltage cables [3.58]. But the most convenient way of forced cooling solid dielectric cables is to immerse them in flowing water. Trials of externally water cooled 225-kV solid dielectric cables have been in progress in France for some years [3.59]. Water is the cheapest cooling fluid and it can be pumped over long distances with relatively small pressure drops. The heat exchange equipment for water is well established and also of relatively low cost. The major economic factors entering external forced cooling are the cost of the water pipes, sheath losses if cross-bonding proves impossible, and the higher level of Joule loss.

All the arrangements of external water cooling of self-contained oil-filled cables depicted on Fig. 3.21(a–c) may also be applied to solid dielectric cables. Research in France has concentrated on arrangements (d) and (e) which require the least trench space. If each cable core is enclosed in its own water pipe, as in arrangement (d), the pipes can be kept of small enough diameter for reeling and transportation in long length. This saves much of the pipe jointing work. The smaller diameter water pipes can also withstand higher internal pressure, but the pressure drop in arrangement (d) will be larger than in (e). High-density polyethylene and PVC seem to be the preferred pipe materials.

The French 225-kV cables are provided with a lead sheath and in the forced cooling experiments this was left bare and in contact with the water. It makes the suppression of sheath circulating currents by cross-bonding impossible when all three cables are enclosed in the same water pipe. Because of the great cooling capacity of the water, the heat from the sheath

losses can easily be carried away in the coolant stream without seriously reducing the cable ampacity, but the economic penalty of the energy loss is appreciable.

External water cooling is compatible with sheath cross-bonding when the ground conductors are covered with a plastic jacket or the cable cores are housed in separate nonmetallic water pipes.

The economic future of externally water cooled and underwater solid dielectric cables in general strongly depends on whether or not a metallic membrane is required to positively keep water away from polyethylene insulation. At the time of writing this crucial question has not been resolved. There is supporting evidence on both sides of the argument. Not the least of it is the success of the French 225-kV cable with its protective lead sheath.

In 1968 the first major 138-kV solid dielectric submarine cable circuit was energized. It is three and a half miles long and crosses Cook Inlet at Anchorage, Alaska. This cable is insulated with voltage stabilized thermoplastic polyethylene. Water vapor is allowed to diffuse through its insulation. The installation contains approximately 20 factory made splices of the same diameter as the cable and made of heat fused polyethylene tapes. For a few years the submarine circuit operated fault-free, but then splices began to fail. As already pointed out, the heat fused polyethylene tape splice apparently cannot cope with the axial thermomechanical forces. The underwater performance of this splice in the Alaskan waters appears to have been a little better than in underground installations elsewhere. This can be readily explained by the lower temperature at which the Alaskan splices must be operating.

Because of the confusion created by the splice failures, the experience with the Cook Inlet cable does not conclusively prove the need for a metallic sheath when the polyethylene insulation is voltage stabilized. A further point to be borne in mind is that thousands of miles of transatlantic telephone cable has given excellent service without a metallic sheath. Liquid water penetration would certainly have caused insulation failures in the presence of the 5 to 10 kV dc which these cables carry to supply power to the repeaters. The diffusion of water vapor through polyethylene has even been reported to be beneficial to the dielectric strength [3.60]. There is no doubt, however, that when water molecules can conglomerate to droplets they will become the cause of water trees and present a potential hazard to the insulation. Liquid water conglomeration is only possible if the insulation contains cavities in its body or at the interfaces with the semiconducting shields.

Assuming for the time being that it will ultimately be possible to operate voltage stabilized polyethylene reliably in direct contact with water, this would open the prospect of a solid dielectric pipe-type cable. Water would

replace the oil in a metallic pipe and the three cable cores could operate without a metallic shield. The choice of the pipe metal would be largely dictated by cost and corrosion considerations. One possibility would be cement-lined cast iron pipes which have been widely used as water pipes.

Ampacity calculations should be based on the discussion of forced cooling in Sections 3.2 and 3.3. For metal shielded cores in nonconducting pipes (3.42) on page 316 is the ampacity equation. Up to and including 230 kV cables, P_d may be set to zero. The effective "radial" thermal water resistance is

$$R_w = \frac{1}{(c_v A v)} \quad \text{thermal-}\Omega \tag{3.119}$$

with the specific heat at constant volume of water being $c_v = 4.18\ \text{J/cm}^3 \cdot °\text{C}$. A is the flow cross-sectional area and v the flow velocity. Equation (3.42) is a conservative approximation in so far as it assumes that all heat generated in the cable is absorbed in the water stream, which Fig. 3.25 shows to be very nearly true. The thermal circuit associated with this ampacity equation is Fig. 3.26 on page 316. It implies that each cable core is enclosed in its own water pipe.

When the three cores share the same water stream in one large pipe the thermal circuit of Fig. 3.74 applies, which ignores the dielectric loss P_d and assumes that all three cores are covered by a plastic jacket to prevent corrosion and permit metal shield cross-bonding. The temperature drop equation for this arrangement is

$$T_c - T_1 = P_c R_i + (P_c + P_s) R_j + 3(P_c + P_s) R_w \tag{3.120}$$

and the corresponding ampacity equation becomes

$$I^2 = \frac{T_c - T_1}{R_{ac} R_i + (R_{ac} + R_s') R_j + 3(R_{ac} + R_s') R_w} \tag{3.121}$$

Should water cooled solid dielectric cables in a metal water pipe become a reality, then the ampacity equation will be (3.90). Again P_d may be neglected for 138- and 230-kV cables. Instead of involving an effective water resistance R_w, (3.90) depends on the forced cooling parameter F defined by (3.87). No radial thermal resistance need be substituted for R_0 in (3.90) because of the excellent heat transfer to water. Unless the equivalent pipe resistance R_p' has been determined by finite element analysis, there seems to be no alternative to (3.68) which will give an order of magnitude estimate.

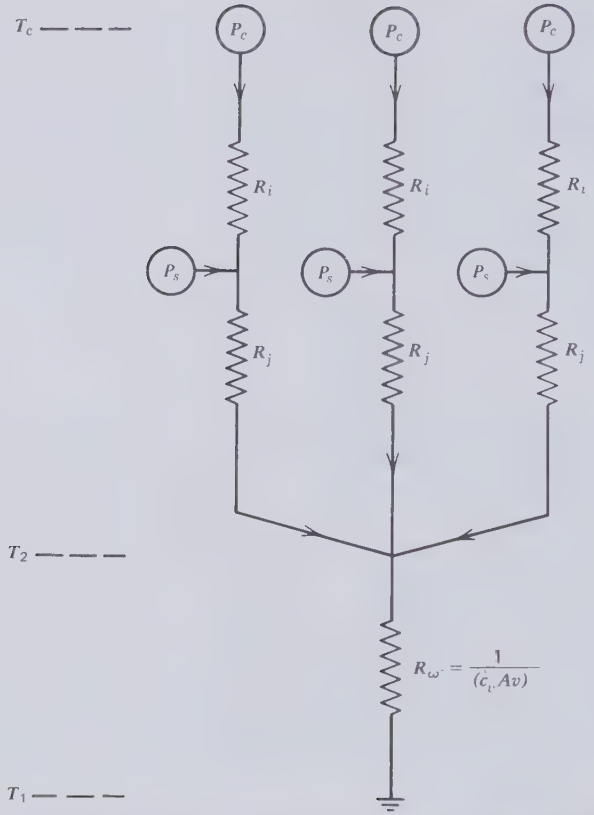

Figure 3.74 Thermal circuit for three solid dielectric cables sharing the same water coolant stream.

Fault Current Rating

As far as fault currents in solid dielectric cables are concerned the discussion of this subject in connection with self-contained oil-paper insulated cables in Section 3.2 should be consulted. For a brief moment the conductor temperature in all solid dielectric cables may be allowed to reach 120°C and when the insulation is cross-linked polyethylene or EPR this may be extended to 150°C. If these temperatures were maintained over longer periods of time they would of course lead to insulation softening and melting.

Critical Length and Reactive Compensation

One of the factors determining the critical length of an ac underground circuit is the cable capacitance per unit length and therefore the dielectric

constant. In this respect extruded polyethylene has an advantage over oil-paper insulation. But the critical length is also strongly dependent on the ampacity and this is a function of such varied factors as conductor metal and size, insulation thermal resistance, and the method of cable cooling.

To present some guidelines to the critical length of solid dielectric cables of the future, certain cable designs have to be preferred over others, and there is no certainty that these designs will prevail. One of the principal questions is: should the solid dielectric cable be surrounded by a lead sheath or other metallic moisture barrier? In most situations a metal sheath would almost certainly be cross-bonded and then have little effect on ampacity and critical length. For this reason R_s' will be set to zero in the ampacity formula used for critical length computations.

Polyethylene of $\varepsilon = 2.3$, $\rho_t = 350$ thermal-$\Omega \cdot$cm and $\cos\phi = 3 \times 10^{-4}$ is the most likely insulation material of future generations of high-voltage solid dielectric cables. An important design choice is the maximum permissible sustained conductor temperature. For the critical length computations we choose $T_c = 70°C$ because higher temperatures cause severe thermal expansion difficulties that have been at the root of a number of cable failures.

Another design variable is the insulation thickness. At 138 kV a 0.8 in. polyethylene insulation wall seems to be fairly well established for all conductor sizes. The French 225-kV cable relies on 0.944 in. of insulation. Since extra insulation thickness does not necessarily confer additional reliability on the cable, because of thermomechanical complications, it seems quite certain that with time thinner insulation walls will come into use. The following critical length computations are based on 0.8-, 0.9-, and 1.0-in. insulation walls for 138-, 230-, and 345-kV cables, respectively. No 345-kV solid dielectric cables are presently in service and their prospects are a matter of speculation.

There is no reason to believe that conductor sizes in solid dielectric cables will be limited to any greater extent than they are in selfcontained oil-paper cables. Because of the trends to more economical aluminum conductors, critical length calculations will be made for aluminum conductors up to 5000 kcmil.

Only naturally cooled cables will be considered that are directly buried at a depth of $D = 36$ in. with a lateral spacing of $S = 12$ in. in thermal sand of $\rho_e = 90$ thermal-$\Omega \cdot$cm in an ambient temperature of $T_a = 25°C$. The burial depth and spacing fix the thermal proximity factor at $k = 2.04$.

Figure 3.75 explains the notation used for the various cable diameters from d_1 to d_5. Conductor shields from 50 mil thickness for 1000 kcmil conductors to 80 mil for 5000 kcmil are suggested. An 80 mil semiconducting insulation shield has been chosen for all cables. The cross-bonded metallic ground conductors are assumed to be embedded in the 0.25-in. thick polyethylene jacket.

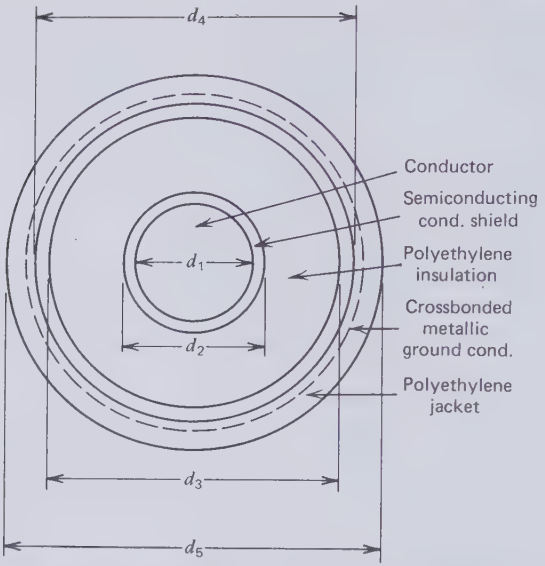

Figure 3.75 Dimensions of solid dielectric cables used in critical length computations.

The ampacity, capacitance, and critical length results for 15 different cables in the 138-, 230-, and 345-kV voltage classes are listed on Table 3.13. They show that continuous current ratings up to 1400 A can be achieved in spite of the conductor temperature restriction. Dielectric losses have been ignored at 138 and 230 kV. The critical length is not proportional to ampacity because the greater dielectric volume surrounding the larger conductors increases the cable capacitance per unit length.

The transmission capabilities of the 15 cables are displayed on Fig. 3.76 as a function of circuit length. The graphs should be compared with Fig. 3.30 for self-contained and Fig. 3.60 for pipe-type oil-paper insulated cables. At equal conductor size, the oil-paper insulated cable carries more power because it employs copper rather than aluminum. In all cases, however, the aluminum-polyethylene cable has the greater critical length, although the difference becomes small at the highest voltage. Pipe-type cable circuits with their conductor size limitation carry much less power and consequently have more severe critical length restrictions than oil-paper or polyethylene insulated self-contained cables. EPR insulation reduces the ampacity and also the critical length of solid dielectric cables.

Reactive compensation should be considered when the circuit length is 60 percent or more of the critical length. Shunt reactors may be employed for this purpose as illustrated in Fig. 3.33 on page 328 and explained in the accompanying text.

Table 3.13 Ampacity I, Capacitance C, and Critical length L_c of 138 to 345-kV Polyethylene Insulated Cables with Cross-bonded Ground Conductors and Aluminum Conductors from 1000 to 5000 kcmil

kV	kcmil	d_1 cm	d_2 cm	d_3 cm	d_4 cm	d_5 cm	R_{dc} $\mu\Omega$/cm	R_{ac} $\mu\Omega$/cm	R_i th. Ω	R_j th. Ω	R_e th. Ω	I A	C pF/cm	L_c km
138	1000	2.93	3.18	7.24	7.65	8.92	0.674	0.682	53.46	8.56	52.85	623	1.55	134
	2000	4.15	4.40	8.46	8.87	10.14	0.337	0.354	42.31	7.45	50.97	909	1.95	155
	3000	5.15	5.46	9.52	9.93	11.45	0.225	0.259	36.57	7.93	49.17	1095	2.30	159
	4000	5.96	6.32	10.38	10.79	12.57	0.169	0.199	33.06	8.51	47.79	1275	2.58	165
	5000	6.60	7.01	11.07	11.48	13.51	0.135	0.163	30.83	9.07	46.72	1429	2.80	170
230	1000	2.93	3.18	7.75	8.16	9.43	0.674	0.682	57.05	8.06	52.03	621	1.43	87
	2000	4.15	4.40	8.97	9.38	10.65	0.337	0.354	45.43	7.07	50.24	906	1.79	101
	3000	5.15	5.46	10.03	10.44	11.96	0.225	0.259	39.36	7.57	48.53	1091	2.10	104
	4000	5.96	6.32	10.89	11.30	13.08	0.169	0.199	35.64	8.15	47.20	1271	2.35	108
	5000	6.60	7.01	11.58	11.99	14.02	0.135	0.163	33.26	8.71	46.17	1424	2.55	112
345*	1000	2.93	3.18	8.26	8.67	9.94	0.674	0.682	60.43	7.61	51.26	612	1.34	61
	2000	4.15	4.40	9.48	9.89	11.16	0.337	0.354	48.37	6.73	49.55	892	1.66	72
	3000	5.15	5.46	10.54	10.95	12.47	0.225	0.259	42.02	7.24	47.91	1074	1.94	74
	4000	5.96	6.32	11.40	11.81	13.59	0.169	0.199	38.09	7.82	46.63	1249	2.17	77
	5000	6.60	7.01	12.09	12.50	14.53	0.135	0.163	35.58	8.38	45.63	1399	2.34	80

*Dielectric losses have been neglected for 138 and 230 kV but not for 345-kV cables.

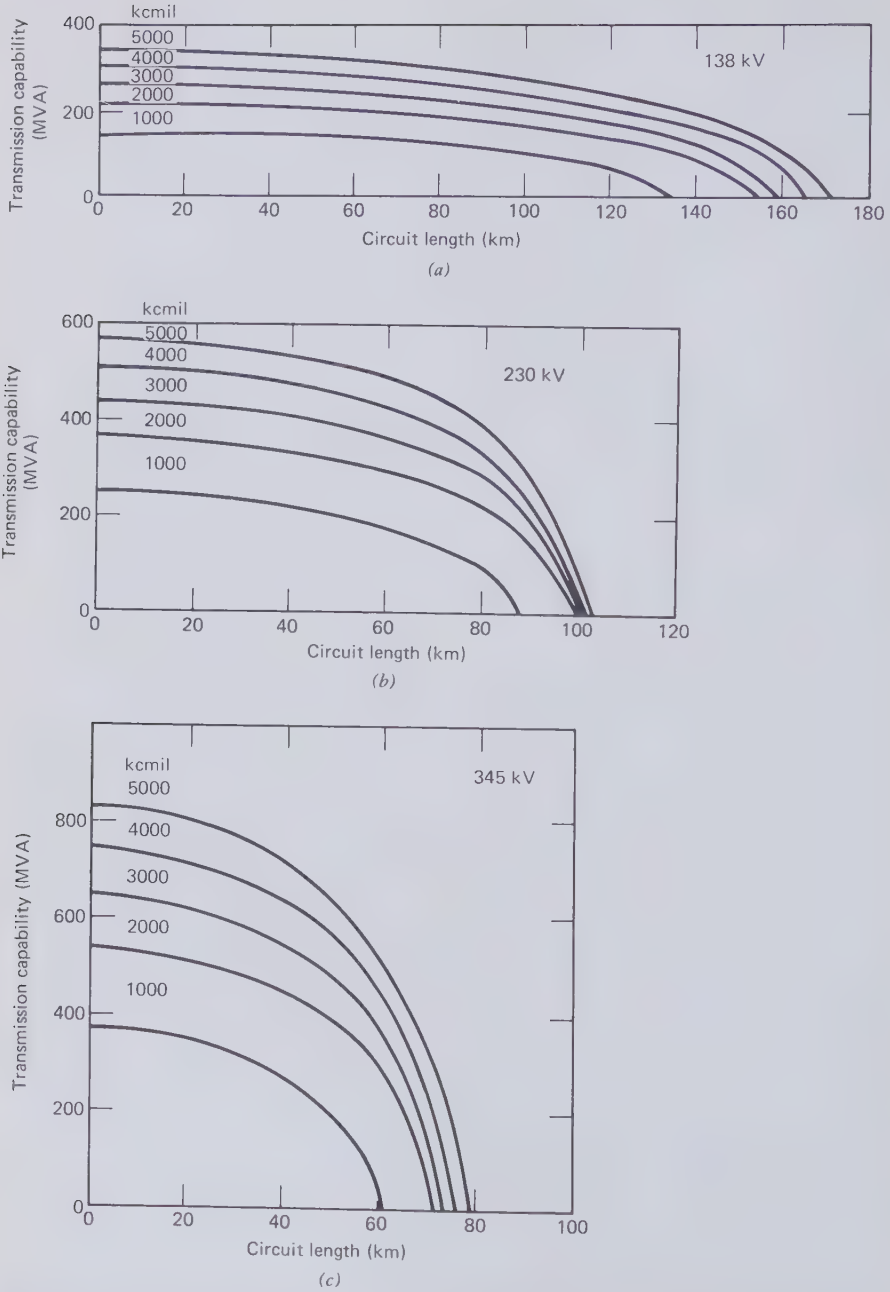

Figure 3.76 Critical length of directly buried polyethylene insulated cables with ground conductor crossbonding and aluminum conductors from 1000 to 5000 kcmil.

DC Application

At the present time no high-voltage solid dielectric dc cables have been installed. There is no reason to believe that extruded polyethylene will not be successful in this application. Some of the advantages flowing from the lower dielectric constant and power factor are lost when the insulation is subject to dc stress. For dc transmission, therefore, solid dielectric cables are not expected to compete quite as strongly with paper insulated cables as they do in ac applications.

Underwater Installation

The test case of high-voltage solid dielectric underwater cables turns out to be a 138-kV line running across Cook Inlet outside Anchorage, Alaska. Forty foot tides running at 9 knots made this installation particularly difficult. Ease of installation is an important criterion in the choice of submarine cables and the solid dielectric cable is lighter and less vulnerable in the cable laying process than lead-sheathed oil-paper insulated cable. Figure 3.77 is a cross section of the Cook Inlet cable [3.61]. The underwater

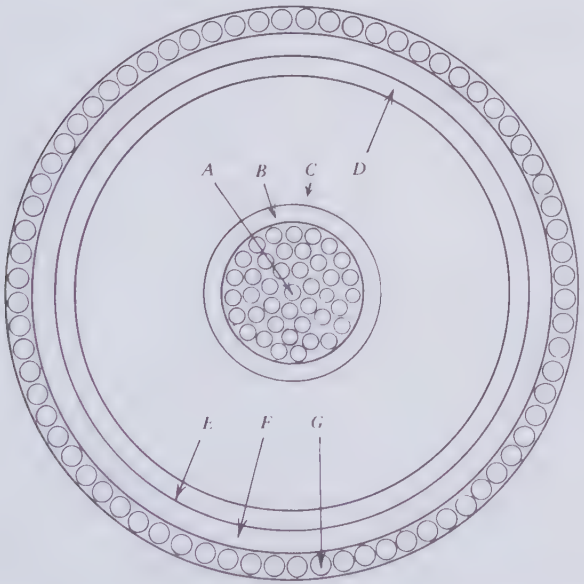

Figure 3.77 138 kV, 3.8 in o.d. Cook Inlet solid dielectric submarine cable. *A*—500 kcmil copper conductor. *B*—Semiconducting conductor shield. *C*—900 mil Polyethylene insulation wall. *D*—Semiconducting insulation shield. *E*—Two copper shielding tapes. *F*—Polyethylene anticorrosion jacket. *G*—Copper armor wires.

transmission line originally contained some 20 factory-made splices under copper armor. The latter was applied in unbroken length to the four 22,000-ft-long cable cores. One of the cores was ruptured during or soon after cable laying. Water entered the conductors at the severed ends but was contained by the air between the conductor strands, which was compressed by the water head. It proved possible to repair the cable by splicing in a short length of new cable.

Voltage stabilized thermoplastic polyethylene is the insulation of the Cook Inlet cable and water vapor is allowed to diffuse through it. The circuit was first energized in March 1968 and operated satisfactorily for a few years. Splices began to fail in 1972. They had been made with heat fused polyethylene tapes having insufficient elasticity to withstand repeated axial thermal expansion and contraction forces exerted by the conductor. The cable was still in service, but at reduced load, in 1978. Repair splices have been made with self-amalgamating EPR tapes. Notwithstanding the splice troubles, there appears to be some hope that voltage-stabilized polyethylene insulation can operate reliably over a long period of time in direct contact with water and without a metallic moisture barrier.

To gain mechanical protection, this cable was embedded 10 foot deep into the sediments of Cook Inlet. Embedment was carried out with a water jet plow subsequent to laying the cable on the seabed. For fear it might move laterally in the strong tides in the time between laying and embedment, it was felt the cable had to be heavy and this is one of the reasons why copper wire armor was chosen. The other reasons were (1) the greater corrosion resistance of copper to salt water as compared with aluminum and its alloys, (2) copper tapes were used for shielding and with the same armor metal no bimetallic corrosion could occur, and (3) as explained in connection with Fig. 1.38 on page 72, the higher conductivity of the copper reduces the inevitable circulating current loss. The large amount of copper in the Cook Inlet cable adds significantly to the cable cost and it is doubtful that copper armoring will become standard practice.

In any case the need for externally armoring solid dielectric submarine cables is not fully established. Deep-water submarine telephone cables are installed without it but they contain a tensile strength core in the center conductor that is usually steel but could also be made of a strong fibrous material. This strength member is required for supporting the weight of the cable while it hangs from the cable laying vessel. Overhead line conductors are provided with steel cores and so could power cable conductors. Some additional loss occurs in the steel but not as much as in the external armor. As the telephone cable experience proves, the armor is not required for abrasion resistance, at least not in deep water.

Should it become practical to operate underwater solid dielectric cables without external armor, then the metallic shield would probably also be

eliminated to completely stop the flow of circulating currents. This would save a large amount of energy. Charging and fault currents would then have to be carried in the water. Removing all metal from the outside of the cable would also obviate corrosion problems that have been very troublesome to submarine cables. However, without a metallic covering, the cable becomes vulnerable to toredos and other marine boring animals.

Economics

To calculate the cost of transmitting electric power through solid dielectric cables, it is necessary to know the capital investment involved and the price of the energy that is being lost in transmission. Of the installed cost, that portion which may be attributed to the trenching operation is not significantly different from the expense of installing self-contained oil-paper insulated cables. The major uncertainty of the economics of solid dielectric cables resides in the price of the cables themselves. They have not been mass produced and the most useful sizes have not even been produced on a pilot scale.

There exists a mass market for solid dielectric distribution cables and the best that can be done is to extrapolate the prices of polyethylene insulated low-voltage cables into the high-voltage region. One way of approaching this problem is to apply an appropriate multiplication factor to the accurately known materials cost. The materials involved are polyethylene chips as they are fed into extruders, copper in wire bars, aluminum in extrusion ingots, and sodium in tank cars. A good guide to the selling price of distribution cables in the 15 to 35-kV classes has been 1.5 times the materials cost. The multiplication factor for 138- to 345-kV oil-paper insulated cables varies between two and three. Even in mass production some increase in the multiplication factor with voltage is inevitable because of the greater research and development, testing and selling expenses associated with the more sophisticated transmission cables. At present it seems reasonable to assume that ultimately, when the mass market has been established, solid dielectric high-voltage cables will sell for not more than three times the materials cost. This may be easier to achieve with copper conductors rather than the less costly aluminum and sodium conductors. For an exercise in the economics of solid dielectric transmission cables, therefore, the ratio of selling price to materials cost will be fixed at $\chi = 3$.

If the materials cost is denoted by MC and the cost of the civil engineering operations and the installation of the cable in the trench by CE, the transmission cost equation (3.62A) on page 340 may be written

$$TC = \frac{0.15(\chi \cdot MC + CE) + YDL + YJL}{n\sqrt{3}\ V(uI)(\mathrm{CLF})} \tag{3.122}$$

As a rule each directly buried three-phase circuit will be installed in its own trench, and the installed cost of two circuits is then simply twice the cost of one circuit. Hence for the typical installation it is sufficient to compute the transmission cost *TC* for a single circuit or $n = 1$. It has already been shown that for 138- and 230-kV polyethylene insulated cables the yearly cost of the dielectric loss *YDL* may be neglected.

As an illustration of the method of economically assessing solid dielectric cables and also to obtain some guidance to the future prospects of these cables let us consider a group of 27 different designs, nine each in the voltage classes of 138, 230, and 345 kV. It has to be stressed that 345-kV polyethylene insulated cables are still in the research and development stage and may not become a practical reality. In each voltage class we will examine the economic effect of copper, aluminum, and sodium conductors. The size of the conductors is an important design variable and we will analyze the economics of 2000, 3000, and 5000 kcmil conductors.

The configuration of the PE-Cu and PE-Al cables is shown in Fig. 3.75. Diametrical dimensions for the three voltages and conductor sizes are given in Table 3.13. Sodium cables of the same overall diameter and insulation thickness have been chosen, but both semiconducting polyethylene layers have been replaced by sodium. Therefore the kcmil dimension of the sodium conductors is only a nominal figure, the actual cross-sectional area being larger than the nominal figure. The grounded layer of sodium under the cable jacket is assumed to be cross-bonded along the circuit length. For the remaining 18 copper and aluminum cables a 200 kcmil copper ground conductor has been selected which is covered by the 0.25-in. thick polyethylene jacket and also cross-bonded along the circuit. The two types of ground conductor are adequate for fault currents up to 20 kA. Eddy current losses in the ground conductors will be ignored.

The 27 cables together with three overhead lines, three pipe-type and three self-contained oil-paper insulated cables are coded on Table 3.14. Intermediate and final results of the transmission cost computations are listed on Table 3.15. In all cases the 1976 transmission cost refers to a fully utilized line ($u = 1$) and a cable load factor of CLF = 0.75. It will be realized that most transmission lines are only partially utilized and *TC* can be substantially greater than indicated in these particular calculations.

The ampacities of the solid dielectric cables have been calculated for the thermal resistances of Table 3.13. This presupposes the cables are directly buried at a depth of 36 in. and spaced 12 in. apart. For the sodium cables the thermal resistances had to be recalculated to allow for the absence of the semiconducting polyethylene layers and Table 3.15 lists the modified values of R_i. Also given on this table are the quantities of copper, aluminum, sodium, and polyethylene contained in one conductor-foot in each of the 27

Table 3.14 Coding of 36 Transmission Lines Used in Transmission Cost Studies and on Fig. 3.78.

Line	
0	138 kV, 795 kcmil ACSR, two overhead circuits on one tower
1	138 kV, 2000 kcmil Cu, pipe-type cable
2	138 kV, 2000 kcmil Cu, self-contained paper cable
3	138 kV, 2000 kcmil Cu, solid dielectric cable
4	138 kV, 3000 kcmil Cu, solid dielectric cable
5	138 kV, 5000 kcmil Cu, solid dielectric cable
6	138 kV, 2000 kcmil Al, solid dielectric cable
7	138 kV, 3000 kcmil Al, solid dielectric cable
8	138 kV, 5000 kcmil Al, solid dielectric cable
9	138 kV, 2000 kcmil Na, solid dielectric cable
10	138 kV, 3000 kcmil Na, solid dielectric cable
11	138 kV, 5000 kcmil Na, solid dielectric cable
△	230 kV, 1431 kcmil ACSR, two overhead circuits on one tower
12	230 kV, 2000 kcmil Cu, pipe-type cable
13	230 kV, 2000 kcmil Cu, self-contained paper cable
14	230 kV, 2000 kcmil Cu, solid dielectric cable
15	230 kV, 3000 kcmil Cu, solid dielectric cable
16	230 kV, 5000 kcmil Cu, solid dielectric cable
17	230 kV, 2000 kcmil Al, solid dielectric cable
18	230 kV, 3000 kcmil Al, solid dielectric cable
19	230 kV, 5000 kcmil Al, solid dielectric cable
20	230 kV, 2000 kcmil Na, solid dielectric cable
21	230 kV, 3000 kcmil Na, solid dielectric cable
22	230 kV, 5000 kcmil Na, solid dielectric cable
□	345 kV, 2 / 1590 kcmil ACSR, two overhead circuits on one tower
23	345 kV, 2000 kcmil Cu, pipe-type cable
24	345 kV, 2000 kcmil Cu, self-contained paper cable
25	345 kV, 2000 kcmil Cu, solid dielectric cable
26	345 kV, 3000 kcmil Cu, solid dielectric cable
27	345 kV, 5000 kcmil Cu, solid dielectric cable
28	345 kV, 2000 kcmil Al, solid dielectric cable
29	345 kV, 3000 kcmil Al, solid dielectric cable
30	345 kV, 5000 kcmil Al, solid dielectric cable
31	345 kV, 2000 kcmil Na, solid dielectric cable
32	345 kV, 3000 kcmil Na, solid dielectric cable
33	345 kV, 5000 kcmil Na, solid dielectric cable

Table 3.15 Intermediate and Final Results of Transmission Cost Computations

Line Voltage	kV	138	138	138	138	138	138	138	138	138
Conductor Material		Cu	Cu	Cu	Al	Al	Al	Na	Na	Na
Line #		3	4	5	6	7	8	9	10	11
*Conductor Size kcmil		2000	3000	5000	2000	3000	5000	2000	3000	5000
Ampacity	A	1071	1293	1679	909	1095	1429	854	1047	1285
Capability CLF = 1	MVA	256	309	401	217	262	342	204	250	307
R_{ac}	$\mu\Omega$/cm	0.255	0.186	0.118	0.354	0.259	0.163	0.417	0.295	0.210
†R_i	thermal-Ω	—	—	—	—	—	—	36.42	30.97	25.45
Copper	lb/ft	6.80	9.88	16.06	0.62	0.62	0.62	—	—	—
Aluminum	lb/ft	—	—	—	1.88	2.82	4.69	—	—	—
Sodium	lb-ft	—	—	—	—	—	—	1.35	1.94	2.99
Polyethylene	lb/ft	4.16	5.08	6.75	4.16	5.08	6.75	3.82	4.69	6.30
Materials	$/ft	5.83	8.15	12.73	2.72	3.48	4.95	1.69	2.16	3.01
1976 Cable Cost	$/mi	277042	387288	604930	129254	165370	235224	80309	102643	143035
1976 Installation	$/mi	168000	168000	168000	168000	168000	168000	168000	168000	168000
1976 Inst. Cost	$/mi	445042	555288	772930	297254	333370	403224	248309	270643	311035
‡YJL	$/mi	19558	20793	22243	19559	20765	22257	20336	21623	23186
1976 TC	$/MVA·mi·yr	450	449	459	394	360	323	376	332	303

Line Voltage	kV	230	230	230	230	230	230	230	230	230
Conductor Material		Cu	Cu	Cu	Al	Al	Al	Na	Na	Na
Line #		14	15	16	17	18	19	20	21	22
*Conductor Size	kcmil	2000	3000	5000	2000	3000	5000	2000	3000	5000
Ampacity	A	1067	1288	1674	906	1091	1424	850	1042	1280
Capability CLF = 1	MVA	425	513	667	361	435	567	339	415	510
R_{ac}	$\mu\Omega$/cm	0.255	0.186	0.118	0.354	0.259	0.163	0.417	0.295	0.210
†R_i	thermal-Ω	—	—	—	—	—	—	39.68	33.88	27.96
Copper	lb/ft	6.80	9.88	16.06	0.62	0.62	0.62	—	—	—
Aluminum	lb/ft	—	—	—	1.88	2.82	4.69	—	—	—

Sodium	lb/ft	—	—	—	—	—	—	1.27	1.96	3.01
Polyethylene	lb/ft	4.67	5.66	7.43	4.67	5.66	7.43	4.30	5.25	6.96
Materials	$/ft	6.01	8.35	12.97	2.89	3.68	5.18	1.86	2.35	3.24
1976 Cable Cost	$/mi	285595	396792	616334	137333	174874	246154	88387	111672	153965
1976 Installation	$/mi	182000	182000	182000	182000	182000	182000	182000	182000	182000
1976 Inst. Cost	$/mi	467595	578792	798334	319333	356874	428154	270387	293672	335966
‡YJL	$/mi	19412	20632	22111	19430	20614	22101	20146	21417	23006
1976 TC	$/MVA·mi·yr	281	279	284	249	227	203	239	210	192
Line Voltage	kV	345	345	345	345	345	345	345	345	345
Conductor Material		Cu	Cu	Cu	Al	Al	Al	Na	Na	Na
Line #		25	26	27	28	29	30	31	32	33
*Conductor Size	kcmil	2000	3000	5000	2000	3000	5000	2000	3000	5000
Ampacity	A	1051	1267	1645	892	1074	1399	837	1025	1257
Capability CLF = 1	MVA	628	757	983	533	642	836	500	612	751
R_{ac}	μΩ/cm	0.255	0.186	0.118	0.354	0.259	0.163	0.417	0.295	0.210
†R_i	thermal-Ω	—	—	—	—	—	—	42.76	36.64	30.36
Copper	lb/ft	6.80	9.88	16.06	0.62	0.62	0.62	—	—	—
Aluminum	lb/ft	—	—	—	1.88	2.82	4.69	—	—	—
Sodium	lb/ft	—	—	—	—	—	—	1.40	1.98	3.04
Polyethylene	lb/ft	5.21	6.26	8.14	5.21	6.26	8.14	4.82	5.81	7.62
Materials	$/ft	6.19	8.55	13.21	3.08	3.89	5.42	2.04	2.55	3.47
1976 Cable Cost	$/mi	294149	406296	627739	146362	184853	257558	96941	121176	164894
1976 Installation	$/mi	196000	196000	196000	196000	196000	196000	196000	196000	196000
1976 Inst. Cost	$/mi	490149	602296	823739	342362	380853	453558	292941	317176	360894
‡YJL	$/mi	18834	19965	21351	18834	19976	21332	19534	20724	22187
YDL	$/mi	806	939	1135	806	939	1135	806	939	1135
1976 TC	$/MVA·mi·yr	198	196	198	178	162	144	171	151	138

*Sodium conductor diameter equal to copper and aluminum conductor diameters including shield.
†For Cu and Al cables as in Table 3.13.
‡$u = 1$, CLF = 0.75, $\alpha = 0.62$.

different cable designs. The 1976 materials prices have been taken as

Copper	65¢/lb
Aluminum	48¢/lb
Sodium	29¢/lb
Polyethylene	34¢/lb

The polyethylene figure is an average price for thermoplastic, cross-linkable, and semiconducting materials.

The rows of figures in table 3.15 showing the material cost leave no doubt about the price advantage of aluminum and sodium cables for the same overall diameter. But the transmission economics depend not only on this and are greatly influenced by cable ampacity and energy losses. It will be noticed that in accordance with the assumption that the finished cable price is a multiple of the materials cost, the 1976 cable cost is simply three times the materials value.

The civil engineering charges for excavating the trench, filling it, and reinstating road surfaces is the same for all cable sizes and insulation. Edison Electric Institute [2.8] published 1971 figures for the trench installation of pipe-type cables in average suburban areas. Escalated by a compound annual inflation rate of 7 percent, these figures have again been used for the 1976 cost comparison. Apart from the civil engineering tasks, the published average installation costs include cable pulling, splicing, and terminating. As solid dielectric cables do not contain oil, some of these operations are simplified, but no cost reduction has been made to allow for this. A comparison of the data on Tables 3.10 and 3.15 will reveal that with the above assumptions the installed cost of solid dielectric cables with 2000 kcmil copper conductors is greater than that of 2000 kcmil pipe-type cables at 138 and 230 kV and less at 345 kV. The differences are not very large and advantageous transmission costs can only arise from cable ampacity and loss.

It should be observed that the yearly cost of the Joule loss YJL of all 27 solid dielectric cables lies in a relatively narrow band spreading from \$19,000 to \$23,000 per circuit-mile. This has to be so because the major restriction in heat flow between the conductor and the atmospheric heat sink is the soil thermal resistance kR_e. Some variation in heat flux arises from differences in the internal thermal resistance of the cables. A consequence of the nearly constant Joule loss is that the cable ampacities must be approximately proportional to the square-root of the conductor cross-section area A. This can be verified on the ampacities listed in Table 3.15.

Assuming constant YJL, only the materials cost MC and the ampacity I of the transmission cost equation (3.122) depend on the conductor section A. There will be an optimum conductor size for every metal at which the

transmission cost TC is a minimum. This is reminiscent of the Kelvin minimum discussed in Section 1.25. To find the optimum conductor sizes, (3.122) has to be differentiated with respect to A.

$$\frac{d}{dA}(TC)=\frac{0.15\chi}{n\sqrt{3}\,uV(\mathrm{CLF})}\frac{d}{dA}\left(\frac{MC}{I}\right)+\frac{0.15CE+YDL+YJL}{n\sqrt{3}\,uV(\mathrm{CLF})}\frac{d}{dA}\left(\frac{1}{I}\right) \tag{3.123}$$

For the particular case of solid dielectric cables which are naturally cooled let

$$M=f(A) \tag{3.124}$$

$$I=C\sqrt{A} \tag{3.125}$$

where C is a constant of proportionality. Substituting (3.124) and (3.125) into (3.123) and equating the differential coefficient to zero, we find that for the optimum conductor sizes we must have

$$A\frac{d}{dA}f(A)-\frac{1}{2}f(A)=\frac{0.15CE+YDL+YJL}{0.3\chi} \tag{3.126}$$

With this equation and the data on Table 3.15 it can be shown that the transmission cost minima lie near 2000 kcmil for copper, 5000 kcmil for aluminum, and 7500 kcmil for sodium. Hence the underground transmission costs could be reduced below the levels shown in Table 3.15 by using larger sodium conductors but not by using larger copper or aluminum conductors.

On Fig. 3.78 the transmission costs obtained for the 27 solid dielectric cables are compared with those previously calculated for overhead lines, and pipe-type and self-contained oil-paper insulated cables. The transmission costs for overhead lines and pipe-type cables have been taken from Table 3.10 and are shown on Fig. 3.78 as UG/OH ratios for each of the three voltage classes. The UG/OH transmission cost ratios for self-contained cables have been taken directly from Fig. 3.39. It has to be recalled that the results shown on Fig. 3.78 are for fully utilized transmission lines ($u=1$). Fractional utilization will result in higher UG/OH transmission cost ratios because overhead line transmission is largely independent of u, as can be seen on Fig. 3.38 on page 342.

The broad conclusions that may be drawn from the economic analysis of naturally cooled solid dielectric cables are as follows:

1. The transmission cost is about the same for overhead and any underground line when transmitting power at 138 kV.

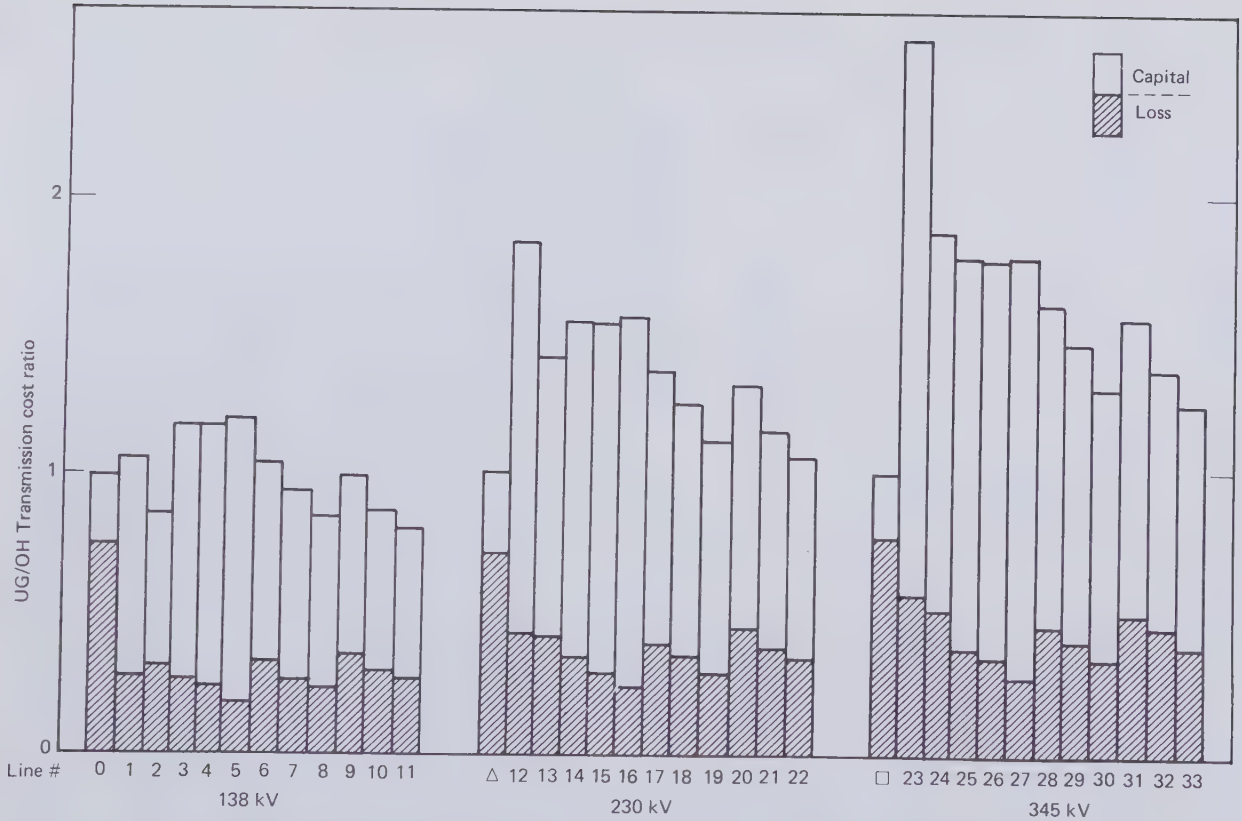

Figure 3.78 Transmission cost comparison for $u = 1$, CLF = 0.75. See Table 3.14 for transmission line code.

2. In general solid dielectric cables are more economical than pipe-type oil-paper insulated cables.
3. The economic advantage of solid dielectric cables increases with voltage because the low dielectric loss not only saves energy but also permits more power to be transmitted through a given size of cable.

The economic merits of forcibly cooling solid dielectric cables may be assessed with the technique outlined in connection with self-contained and pipe-type oil-paper insulated cables.

3.6 GAS INSULATED CABLES

The practice of enclosing generator leads and station busbars in metallic pipes has lead to the evolution of gas insulated transmission lines. Bus ducts usually contain air, but for the more rigorous duties of high-voltage cables sulfur hexafluoride gas (SF_6) is now being universally employed. Figure 2.6 on page 173 compares the uniform field breakdown strength of air and nitrogen with the electronegative SF_6 in the Townsend regime.

The first 345 kV-gas insulated transmission line was energized in 1971 and only four years later the technology had been advanced to 800 kV [3.62]. This rapid development was possible because gas insulated cables can be fabricated from readily available extruded aluminum tubing in modestly sized metal shops. Gas insulation by-passes specialized and capital intensive traditional cable manufacturing processes as for example wire drawing, stranding, paper taping, polyethylene extrusion, lead sheathing, and so on.

By 1976 a total of 22 gas insulated transmission lines had been energized in North America at voltages from 138 to 800 kV, carrying currents between 1.00 and 3.85 kA, and being 100 to 3300 ft long [3.62]. The terminations of gas insulated cables are decidedly cheaper than those for oil-paper insulated cables. This and the absence of oil pressurization plant explains why gas cables are popular for short station getaways and underpasses. The average length of the first 22 installations is 1000 ft.

Isolated Phase Rigid Cables

Almost all the gas cables presently in service consist of three separate coaxial lines assembled from rigid aluminum pipes. The overall diameter of the smallest single-phase enclosure is 9 in. and the largest 29 in. Enclosures of 0.25-in. thickness have proved generally adequate, but the largest pipes are 0.375 or even 0.500 inch thick. To gain mechanical strength and reasonable extrusion tolerances, the enclosure pipes are made of an appropriate aluminum alloy. Higher conductivity EC aluminum may be used for the

smaller conductor pipes. The conductors consist of hollow tubes rather than solid rods for (a) greater rigidity, (b) lower electrical surface stress, and (c) lower ac-dc resistance ratios.

As proved by overhead lines, aluminum alloys have adequate corrosion resistance in open air, but the metal requires added protection when in direct contact with soil. Directly buried gas cables are therefore covered with a corrosion protection jacket similar to that employed on pipe-type cables. Connecting the pipe to a source of 1 to 2 V negative potential with respect to ground (cathodic protection) represents an additional safeguard against corrosion attack.

A typical shipping length of isolated phase gas insulated cable is shown in Fig. 3.79. The length of individual sections is governed by the method of transportation. Up to 60-ft-long pipes have been shipped on trucks. Construction details vary from manufacturer to manufacturer. In the example of Fig. 3.79 each of three conductor spacers in a length of 60 ft is combined with a welded joint in the enclosure pipe. In this design one end of the pipe is enlarged to slip over the other end and keep the outer edge of the spacer disc in position. A pipe overlap of approximately 5 in. ensures that the epoxy spacer is not overheated during welding. The field weld between shipping lengths is of similar design but it does not coincide with a spacer position.

Although in the earliest gas insulated cables conductor tubes were also welded end to end, it has now become common practice to joint conductors with a plug-in connector. A major advantage of the plug-in arrangement is that it permits telescopic motion in thermal expansion and contraction without imposing mechanical stress on the conductor. Aluminum is a poor contact material because of its tough oxide layer. Aluminum surfaces of busbar connections have been traditionally silver plated for this reason. Silver plating is now also in use on plug-in connectors of gas insulated cables. Fingerlike contact springs on both male and female parts of the

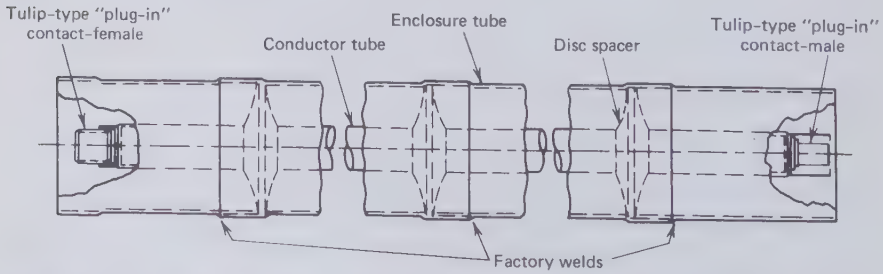

Figure 3.79 Typical shipping length of isolated phase gas-insulated cable [3.62]. (By permission of the Institute of Electrical and Electronics Engineers).

connector will ensure sufficient and sustained contact pressure. In spite of these precautions, the plug-in connector may run 5 to 10° hotter than the conductor itself.

In directly buried situations the outer pipe cannot expand axially and the cable heat will therefore subject it to axial compressive stress. The pipe wall has to withstand this without buckling and care has to be taken to design the circumferential welds so that they will not be sheared by the thermo-mechanical forces. In above ground installations the outer shell may be provided with expansion bellows. Alternatively short lines may be anchored on one end and allowed to move at the other end.

One of the most challenging aspects of the design of gas insulated cables is the spacer that holds the conductor in position. It has to meet stringent mechanical, thermal, and electrical demands. Three spacer geometries presently in use in rigid gas insulated cables are illustrated in Fig. 3.80. The most rugged of them is undoubtedly the disc spacer but its flashover performance is not always as good as that of the conical spacer. Both these latter forms of spacer impede easy axial gas flow and thereby prevent the migration of contaminant particles and arc motion beyond the spacer. The least solid dielectric material is contained in the post spacer which has certain advantages with respect to dielectric losses and material defects.

Filled epoxy compounds are the preferred materials from which spacers are produced by vacuum casting. As far as possible the thermal expansion of the spacer material should be matched to that of aluminum. This can be controlled to some extent by the nature and volume fraction of the filler material [3.64]. Puncture strength, surface tracking resistance, and low dielectric constant and power factor are important electrical properties of the spacer material. They should permit low energy nondestructive surface discharges during testing and high-voltage conditioning, which transplant the most dangerous conducting particles to regions of low electric stress. The dielectric constant strongly influences the tangential surface stress, and this should obviously be kept as low as possible. Thermal deformation of the spacer would be harmful. The softening point of the material of which it is made should lie well above 95°C, which presently is considered to be the limiting conductor temperature.

Insulator flashover in gases and its relation to sliding Lichtenberg discharges has been discussed in Section 2.3. The adhesion of positive ions, and also electrons, to the solid dielectric surface in the wake of electron avalanches make flashover and conduction possible at extremely low tangential fields. Particle contamination of the spacer surface would be expected to assist streamer formation by providing triggering electrons for multiple avalanching. The Lichtenberg discharge mechanism suggests that the spacer geometry should make the tangential surface stress a minimum. This can be

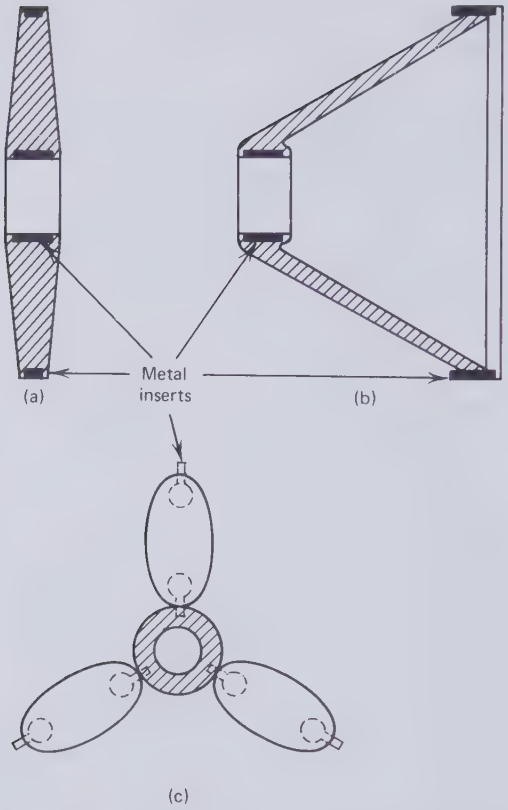

Figure 3.80 Spacer designs presently in use in rigid isolated phase gas insulated cables. (a) Disc. (b) Cone. (c) Post.

achieved with conical and other designs that avoid radial surfaces coinciding with the principal electrical stress.

To prevent the formation of Townsend electron avalanches in the highly stressed gap between the solid dielectric material and the electrodes, the spacer should be bonded to both aluminum pipes. This is not feasible because, among other things, different thermal expansion rates between the inner and outer aluminum pipes. An alternative to bonding is the attachment of metal rings to the spacer body, which then make contact with the aluminum pipes and so eliminate the high electrical stress regions.

The detrimental effect of free conducting particles has been discussed in Section 2.3. To mitigate against breakdown of cables due to these particles, low electric field regions are now provided near the outer rim of spacers. Particles landing in these regions will become immobilized or "trapped." Low or zero electric field regions are described as particle traps. Figure 3.81

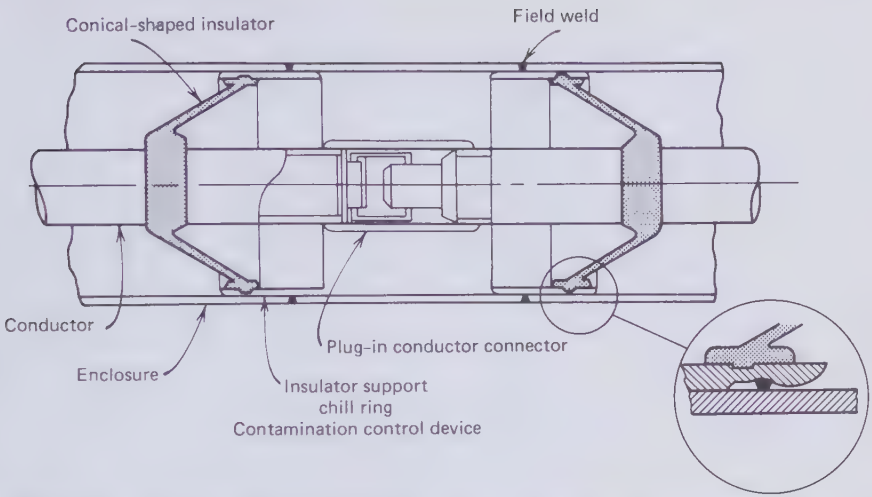

Figure 3.81 Conductor plug-in joint and field weld in pipe combined with conical spacer and particle trap [3.65]. (By permission of McGraw-Hill).

gives an example in which a particle trap is combined with the spacer mounting on the enclosure wall.

The latter diagram also shows details of a plug-in connector and a second method of combining circumferential welds with locating spacers. In this particular example *O*-rings prevent weld products from reaching the insulation space.

Up to the present time, it appears, all isolated phase gas insulated transmission lines have been solidly bonded at both ends, permitting the flow of sheath circulating currents which are approximately equal to the conductor currents. It would not seem impossible to cross-bond the outer enclosures, although it would mean giving up an all-welded gas-containing vessel and take some risks with gas leaks. The circulating current loss is a function of the dimensions and the conductivity of the enclosure pipe and subject to the trends indicated on Figs. 1.38–1.40 on pages 72–74. In general an increase in pipe wall thickness will reduce the loss and this is an additional reason for making the enclosure pipe of relatively strong material and construction.

Prefabricated modular accessories as for example terminations, elbows, and T-joints are commercially available. The interior of the termination communicates directly with the gas space in the cable and it does not require a stress cone. Figure 3.82 is an outline sketch of accessories for isolated phase gas insulated transmission lines. The corners of the enclosure pipe in mitered elbows and T-joints are not sources of damaging gas ionization.

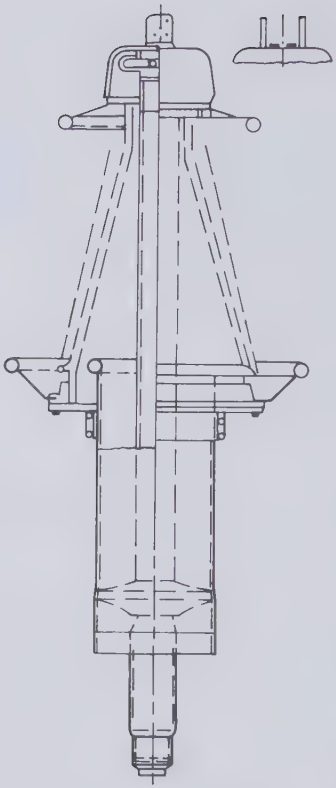

(a)

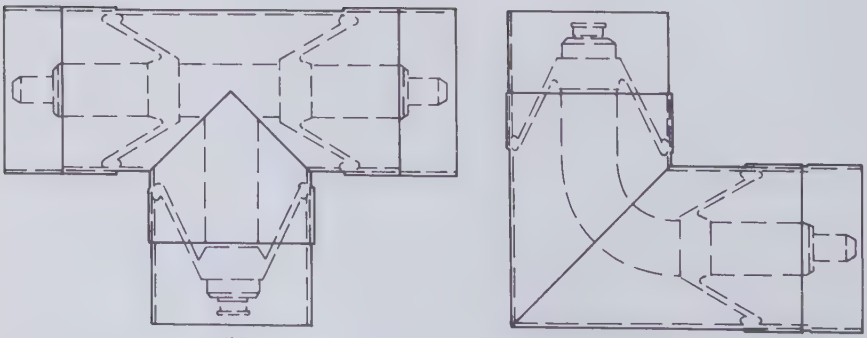

(b) (c)

Figure 3.82 Accessories of isolated phase gas insulated transmission lines [3.62]. (a) Termination. (b) T-Joint. (c) Elbow. (By permission of the Institute of Electrical and Electronics Engineers).

Isolated Phase Flexible Cables

Serious research on flexible gas insulated cables was set in motion in the early 1960s [3.66] and it still continues although rigid lines have met with success in the meantime. The Electric Power Research Institute recently reported [3.69] that a production line for flexible gas cables will be shipped to the United States from Germany in 1979 and the manufacture of this cable should start in 1980. EPRI estimates that flexible gas cables will be 25 percent less expensive on an installed cost basis than the rigid version. The savings are expected to result from the greater ease of handling and shipping, less field assembly work, and the convenience of routing the cable around obstacles.

Two different types of flexible gas insulated cable are being developed in the United States [3.67] and in England [3.68]. Both teams agree on the use of stranded aluminum conductors covered with another material to prevent aluminum dust from contaminating the gas insulation. The American proposal is to seal the stranded conductor in a thin longitudinally welded and corrugated copper sheath, whereas in England an extruded layer of electrical insulation is preferred for this purpose.

Two current designs of spacers for flexible gas cables are shown in Fig. 3.83. Tests on the U.S. cable have started at Waltz Mill; it relies on an *I*-section disc-type spacer that is relatively flexible and not provided with metal inserts. The proposal is to mass-produce it by injection molding in two halves which are later assembled around the conductor. Some spacer flexibility is needed for a close fit to the corrugated conductor and to survive the process of corrugating the enclosure, which has to be carried out with the spacer in position. A very different approach to the spacer problem is being pursued in England. There the conductor is subdivided into three separate strands, each is covered by a layer of insulation, and the subconductors are twisted together with a cabling machine while the spacers are inserted between them. The three subconductors are connected to each other at every cable joint. The distance between spacers in flexible cables has to be quite short, typically of the order of two feet. Therefore a large number of spacers is required that represent a significant cost factor and probably also a noticeable source of dielectric loss.

The object in Britain is to develop a compact flexible cable of approximately the same diameter of a self-contained oil-paper insulated cable of similar transmission capability. This requires relatively high gas pressure of the order of 200 psi. Rigid cables are operated at around 50 psi. At this lower pressure, the gas will remain in the gaseous phase down to $-40°C$. A higher operating pressure would lift the condensation temperature, and this has been deemed unacceptable in the U.S. climate. The first flexible U.S. cable is being designed for 50 psi and it has a correspondingly large overall

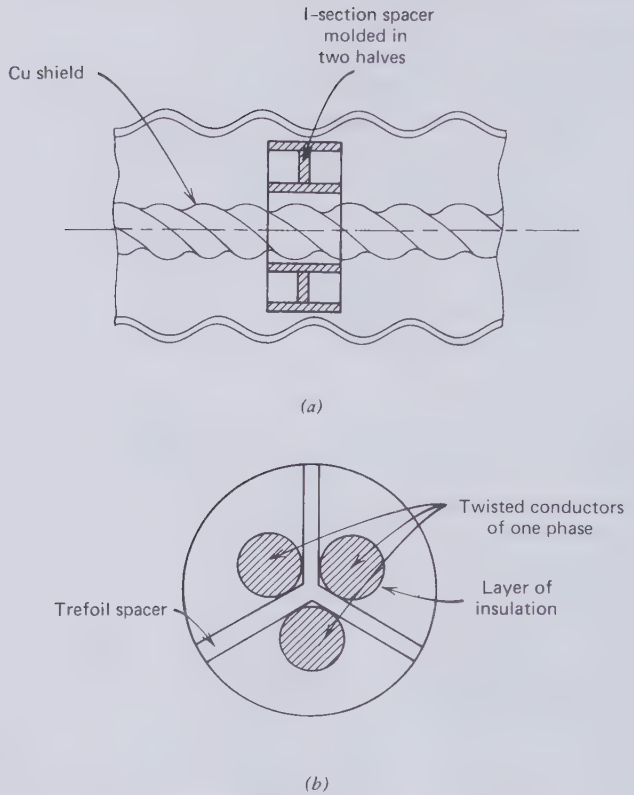

Figure 3.83 Currently preferred spacers for flexible SF_6 insulated cables. (a) U.S. spacer. (b) British spacer.

diameter of approximately 12 in. for operation in the 230–345 kV range. In Britain it is believed that the flexible gas insulated cable will have to be solidly bonded on both ends to cause the flow of heavy sheath circulating currents that are needed to suppress lateral electromechanical forces on the conductors, particularly when fault currents flow.

Rigid Three-Conductor Cables

Doepken made a case for putting all three conductors into the same gas-filled enclosure and foregoing phase isolation [3.70]. Such systems are in use in Europe but have not yet been installed in the United States. The three-conductor construction combats two economical disadvantages of isolated phase systems, namely the large quantity of aluminum in the enclosure pipes and the requirement for exceptionally wide trenches. According to Doepken a 230-kV three-conductor cable would have an overall diameter of

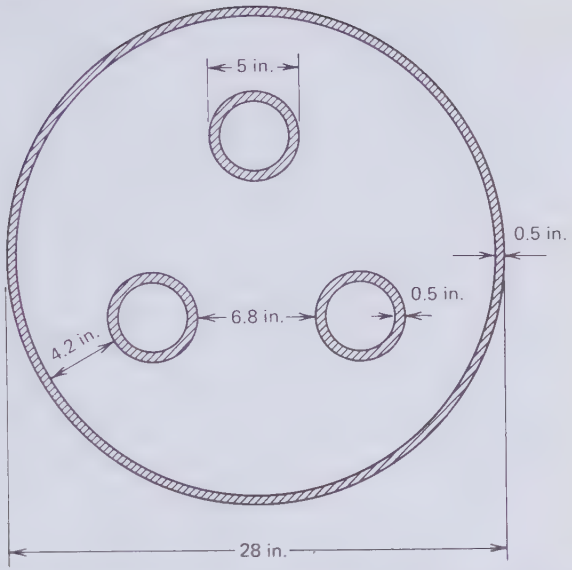

Figure 3.84 Dimensions of three-conductor SF_6 insulated 345 kV, 2020 A cable proposed by Doepken [3.70]. (By permission of the Institute of Electrical and Electronics Engineers).

18.6 in. Limiting the temperature rise of the enclosure above ambient to 35°C, the ampacity of this cable would only be 5 percent less than an isolated phase system with three 12-in.-diam pipes.

Figure 3.84 gives the dimensions of a 345-kV three-conductor cable, which has also been proposed by Doepken [3.70]. This would have an ampacity of 2020 A and a BIL of 1175 kV. The most convenient spacers for this type of cable are substantial posts holding individual conductors to the enclosure wall with freedom for differential thermal expansion between conductors and enclosure. Post-type spacers avoid bridging the high-voltage gap between phases with solid insulation material, which avoids insulator flashover in these highly stressed regions. This also has advantages with respect to dielectric losses.

Installation

Because of the relatively weak shell of large-diameter gas insulated cables it is advisable to bury them deeper than steel pipe-type cable and take additional precautions when they are buried under traffic bearing streets. This adds to the civil engineering cost. Furthermore, even if the isolated phase gas cables are touching each other, the axial spacing would be equal or greater than that required for self-contained flexible cable installations. To keep the thermal proximity factor low in order not to waste the good

heat transfer in the gas insulation, it is common practice to leave a soil space from 6 to 12 in. between pipes. This leads to very wide trenches and more civil engineering costs.

Dangers emanating from cable overheating are soil dry-out and excessive thermomechanical forces. These factors are not as critical in gas insulated cables as the thermal instability of oil-paper insulation or heat deformation in solid dielectrics. Gas cables can tolerate higher soil thermal resistivities, but at present most of the directly buried installations appear to rely on thermal sand of a resistivity of 90 thermal-$\Omega \cdot$cm.

Like all other naturally cooled cables, gas cables have the highest ampacity when surrounded by freely convecting air. A number of the existing SF_6 insulated transmission lines have in fact been located above ground for this reason and also to save the high cost of trenching. The heat dissipation from a pipe surface in air is plotted in Fig. 3.49 on page 365. It is best not to expose the pipes directly to sunlight as this would give rise to considerable increases in enclosure temperature. Figure 3.85(c) illustrates a shaded above-ground installation. The sheet metal enclosure must be well ventilated along its length so that cool outside air can continuously replace the warm air next to the cables. A similar effect can be achieved, although at greater expense, with the covered trench of Fig. 3.85(b). This has the advantage of providing more protection against external damage and vandalism. The lowest-ampacity but least-vulnerable installation is direct burial with a slab cover to prevent dig-ins, as shown in Fig. 3.85(a).

The major technical problem of installing rigid SF_6 insulated transmission lines are the numerous field welds in the three enclosure pipes. Cleanliness and immediate leak testing are most important. The cable sections are shipped with fitted end caps and filled with dry air or nitrogen above atmospheric pressure to prevent contamination and moisture pick-up. It is advisable to maintain modest dry-gas pressure in the pipes during welding operations. A certain amount of moisture will inevitably reach the high-voltage insulation space. Most of it can be removed by evacuating the line before filling it with SF_6 gas.

Aluminum pipeline welding is an established technology. In its most efficient form it is carried out in mobile above-ground enclosures with automatic pipe welding equipment. The most positive test of weld integrity is a vacuum check with a helium mass spectrometer. An adaptation of this technique to pipe welds is sketched in Fig. 3.86. An external clamp-on shell is used for quick evacuation with a high-capacity pump. A small amount of helium gas has to be introduced into the pipe from the nearest end of the welded enclosure.

Following the installation of a gas-tight section of the transmission line it should be evacuated and held at the lowest possible pressure attainable for a day or two with pumps operating at both ends. This will cause the bulk of

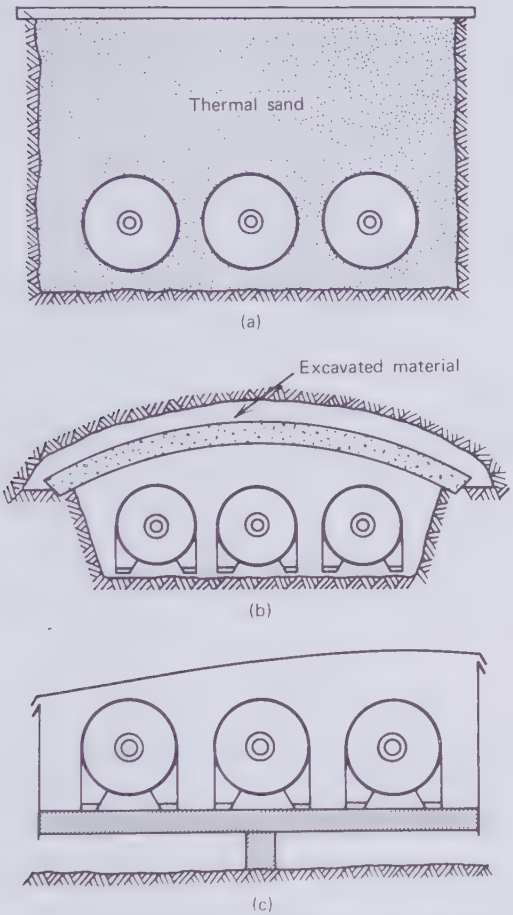

Figure 3.85 Basic modes of installing isolated phase gas insulated cables [3.63]. (a) Normal underground installation. (b) Covered trench installation. (c) Shaded above ground installation. (By permission of the Institute of Electrical and Electronics Engineers).

the moisture to evaporate and premanently leave the pipe. The line is then filled with SF_6 gas to the required pressure and a pressure drop test should be carried out to confirm the absence of significant leaks. The final operation is electrical testing with low-energy power supplies that cannot harm the line should particle-induced breakdown occur. During these tests a number of conducting particles will migrate to the field-free particle traps and this 'conditions' the cable for its transmission duty.

It is considered essential to provide gas insulated cables with continuous gas monitoring instrumentation that ensures adequate pressure and low moisture content. A small leakage rate can be made good by automatic gas

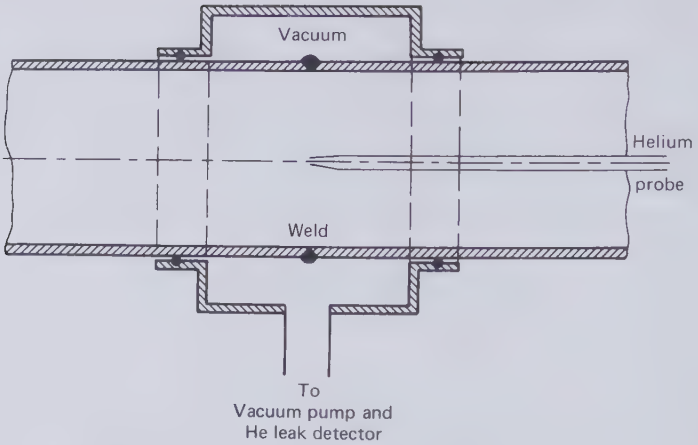

Figure 3.86 Clamp-on vacuum leak detection in pipeline welds.

injection from a pressure cylinder. When the moisture content exceeds a predetermined level, say 300 ppm, the gas has to be circulated through a drying apparatus. This can be carried out without interrupting power transmission.

Ampacity

The enclosure temperature rather than the conductor temperature limits the transmission capability of the naturally cooled gas insulated cable. This is the result of good heat transfer through the gas insulation and a small temperature drop between conductor and pipe. The enclosure temperature has to be limited so that it will not dry out the soil and increase its thermal resistivity. Fixing the maximum permissible pipe temperature T_p is a matter of judgement. The literature on this subject mentions temperatures ranging from 60 to 75°C.

Explicit ampacity equations can only be derived when the radial temperature drops are proportional to heat flux, as in thermal conduction. Heat transfer across the gas space is accomplished by radiation and convection, which makes it necessary to determine the ampacity by successive approximations. Conduction is the dominant mode of heat transfer from the pipe outward. The simple thermal circuit of Fig. 3.87 may be used for this part of the heat flow path. It results in the temperature drop equation

$$T_p - T_a = (P_c + P_p)(R_j + kR_e) \tag{3.127}$$

where T_p and T_a are the pipe and ambient temperatures, P_c and P_p the heat sources in the conductor and the pipe, which are both proportional to the

square of the conductor current. The jacket and soil thermal resistances of unit length of pipe are denoted by R_j and R_e and k is the thermal proximity factor. Equation (3.127) recognizes the fact that the dielectric loss is negligible. Since $P_c + P_p = I^2(R_{ac} + R_p')$, the ampacity equation becomes

$$I^2 = \frac{T_p - T_a}{(R_{ac} + R_p')(R_j + kR_e)} \tag{3.128}$$

R_{ac} is a function of conductor temperature. As this is not known at this stage (3.128) cannot be solved explicitly.

Fukuda [3.71] and Doepken [3.72] have discussed the heat transfer across a horizontal annular gas gap. First we consider radiation. If r_p and r_c are the radii of the radiating pipe and conductor surfaces, ξ_p and ξ_c the emissivities of the two cylindrical surfaces, the Stefan-Boltzmann law for a coaxial line is

$$W_r = 5.67 \times 10^{-12} \times 2\pi r_c \xi' \left(T_c^4 - T_p^4\right) = \quad \text{W/cm} \tag{3.129}$$

In this equation the temperatures have to be expressed in °K and r_c in centimeter. For diffuse reflection the effective emissivity ξ' is

$$\xi' = \frac{\xi_c \xi_p}{\xi_p + (r_c/r_p)(1 - \xi_p)\xi_c} \tag{3.130}$$

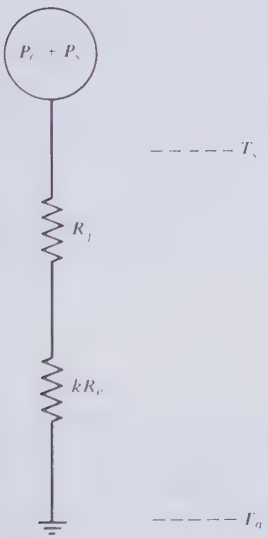

Figure 3.87 Thermal circuit of naturally cooled isolated-phase gas insulated cable.

The emissivity of a metal depends on its electrical conductivity. The higher the conductivity, the lower is the emissivity. Clean aluminum surfaces with very thin oxide coatings therefore have quite low emissivities of the order of 0.1 at room temperature [3.73]. The oxide layer is thinnest on the purest metal. Assuming that the conductors are made of EC aluminum and the enclosure pipes of some high-strength aluminum alloy it is recommended to use the following values $\xi_c = 0.3$, $\xi_p = 0.8$.

The convective heat transfer depends on the gas density and therefore pressure and temperature. For an SF_6 insulated transmission line that has been filled to 50 psi at 20°C, which is typical for isolated phase systems, Doepkens [3.72] recommends the following formula for convection

$$W_c = \frac{3.75 \times 10^{-3} (T_c - T_p)^{1.2} (r_p - r_c)^{0.6}}{\ln(r_p / r_c)} \quad \text{W/cm} \tag{3.131}$$

Now the conductor loss which must be transferred by convection and radiation to the pipe may from (3.127) be expressed as

$$P_c = W_r + W_c = \frac{T_p - T_a}{R_j + kR_e} - I^2 R_p' \quad \text{W/cm} \tag{3.132}$$

All the parameters on the right-hand side of (3.132), except I, are known from the cable design specification. Hence P_c is known as a function of I. From the sum of (3.129) and (3.131) P_c is also known as a function of the conductor and pipe temperatures. For any fixed pipe temperature T_p, the current I in (3.132) is associated with a certain conductor temperature limit. R_{ac} may then be computed for this limit and substituted into (3.128) to obtain the first approximation to the cable ampacity. This ampacity may subsequently be used to obtain a more accurate estimate of the conductor temperature and hence to find an improved value of R_{ac}, which, when substituted into (3.128) gives the second approximation to the cable ampacity, and so on. The method will be better understood with the help of the following example.

EXAMPLE

1. 1000-ft-long, 230-kV isolated phase circuit solidly bonded at both ends.
2. Depth of burial of cable axis below ground level $D = 42$ in., axial spacing of phases $S = 20$ in.; soil thermal resistivity 80 thermal-Ω·cm; ambient temperature 20°C.
3. Conductor tube: 61.8% IACS aluminum; outside radius $r_c = 2$ in. $= 5.08$ cm; inside radius $r_i = 1.5$ in. $= 3.81$ cm.

4. Enclosure pipe: 61.0% IACS aluminum alloy; inside radius $r_p = 6$ in. = 15.24 cm; wall thickness 0.25 in., $T_p = 60°C$.
5. Somastic corrosion jacket: 0.5 in. thick; 100 thermal-$\Omega \cdot$cm.

JACKET THERMAL RESISTANCE R_j. From (2.80)

$$R_j = \frac{100}{2\pi} \ln \frac{13.5}{12.5} = 1.22 \quad \text{thermal-}\Omega \quad \text{(per cm)}$$

SOIL THERMAL RESISTANCE R_e. From (3.8)

$$R_e = \frac{80}{2\pi} \ln \frac{84 - 13.5/2}{13.5/2} = 31.0 \quad \text{thermal-}\Omega \quad \text{(per cm)}$$

THERMAL PROXIMITY FACTOR k. From (3.15)

$$k = 1 + \frac{\ln\left[(84^2 + 20^2)/20^2\right]}{\ln(168/13.5)} = 2.16$$

EQUIVALENT RESISTANCE OF ENCLOSURE PIPE R_p'. We ignore any possible nonuniformity in the current distribution over the pipe wall and take R_p to be equal to the dc resistance at 60°C. From Fig. 1.71 the resistivity of the pipe material at 60°C is $3.3 \times 10^{-6}\ \Omega \cdot$cm. Therefore

$$R_p = \frac{3.3 \times 10^{-6}}{\pi(15.88^2 - 15.24^2)} = 5.27 \times 10^{-8} \quad \Omega/\text{cm}$$

Circuit length $L = 1000$ ft $= 30{,}480$ cm

From (1.94) the mutual inductance between conductor and pipe is

$$M_{c,p} = 2 \times 30{,}480 \left[-1 + \ln(2 \times 30{,}480) - \ln\left(\frac{15.875 - 15.24}{2} \right) \right]$$

$$= 443 \times 10^3 \text{ cm}$$

$$= 0.443 \text{ mH}$$

From (1.104)

$$LR_p' = \frac{(2 \times 60 \times 0.443 \times 10^{-3})^2 \times 30{,}480 \times 5.27 \times 10^{-8}}{(30480 \times 5.27 \times 10^{-8})^2 + (2 \times 60 \times 0.443 \times 10^{-3})^2} \quad \Omega$$

$$= 1.61 \times 10^{-3} \quad \Omega$$

Therefore $R_p' = 5.27 \times 10^{-8}$ Ω/cm. This proves that for a large tube of high electrical conductivity the equivalent resistance R_p' is equal to the actual resistance R_p and then, from (1.103), the conductor and pipe form a 1:1 current transformer.

HEAT TRANSFER ACROSS GAS GAP ($W_r + W_c$). Take the recommended emissivities for EC aluminum and oxidized aluminum alloy, that is, $\xi_c = 0.3$; $\xi_p = 0.8$. The effective emissivity from (3.130) then is

$$\xi' = \frac{0.3 \times 0.8}{0.8 + (5.08/15.24)(1-0.8) \times 0.3} = 0.29$$

The radiation heat transfer from (3.129) is

$$W_r = 5.67 \times 10^{-12} \times 2\pi \times 5.08 \times 0.29 (T_c^4 - 333^4)$$

$$= 5.25 \times 10^{-11} (T_c^4 - 1.23 \times 10^{10}) \quad \text{W/cm}$$

and the convective heat transfer from (3.131) is

$$W_c = \frac{3.75 \times 10^{-3} (T_c - 60)^{1.2} (15.24 - 5.08)^{0.6}}{\ln(15.24/5.08)}$$

$$= 1.37 \times 10^{-2} (T_c - 60)^{1.2} \quad \text{W/cm}$$

The sum of radiation and convection heat fluxes is plotted on Fig. 3.88 for conductor temperatures from 60 to 100°C. It should be noted that heat conduction through the spacers is neglected.

AMPACITY I. From (3.132)

$$P_c = W_r + W_c = \frac{60 - 20}{(1.22 + 2.16 \times 31.0)} - 5.27 \times 10^{-8} I^2$$

$$= 0.587 - 5.27 \times 10^{-8} I^2 \quad \text{W/cm}$$

Therefore $W_r + W_c$ must be less than 0.587 W/cm and from Fig. 3.88 this results in a limiting conductor temperature of 77.5°C. At this temperature the resistivity of the conductor material from Fig. 1.71 is 3.4×10^{-6} Ω·cm. To determine the skin effect from Fig. 1.18 we need to know the dc resistance of a 1000 ft length of conductor. This is

$$R_{dc} = 3.4 \times 10^{-6} \frac{1000 \times 12 \times 2.54}{\pi (5.08^2 - 3.81^2)} = 2.92 \times 10^{-3} \quad \Omega$$

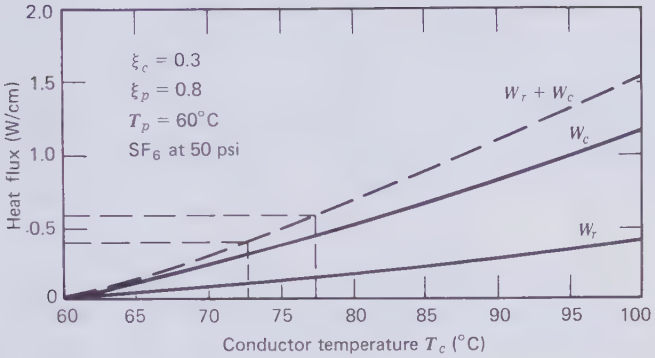

Figure 3.88 Heat transfer across the gas gap between a 4 in. diam conductor and a 12-in. i.d. enclosure at 60°C.

Therefore $\sqrt{f/R_{dc}} = (60/2.92\times10^{-3})^{1/2} = 143$. Also t/d (defined on Fig. 1.18) $= 0.5/4 = 0.125$. With these coordinates Fig. 1.18 indicates $R_{ac}/R_{dc} = 1.1$. Hence the upper limit of the conductor ac resistance is

$$R_{ac} = \frac{1.1\times3.4\times10^{-6}}{\pi(5.08^2-3.81^2)} = 10.5\times10^{-8} \quad \Omega/\text{cm (first approx.)}$$

For a first approximation to the ampacity substitute this value of R_{ac} into (3.128).

$$I^2 = \frac{60-20}{(10.5\times10^{-8}+5.27\times10^{-8})(1.22+2.16\times31.0)}$$

$$I = 1929 \text{ A} \quad \text{(first approx.)}$$

A better approximation to the ampacity may be obtained by computing the conductor loss with the first approximation, that is,

$$P_c = W_r + W_c = I^2R_{ac} = 1929^2\times10.5\times10^{-8} = 0.391 \quad \text{W/cm}$$

On Fig. 3.88 this indicates a conductor temperature of only 72.7°C. The corresponding resistivity from Fig. 1.71 is 3.33 $\Omega\cdot$cm. It results in a revised 1000-ft dc resistance of

$$R_{dc} = 2.92\times10^{-3}\left(\frac{3.33}{3.4}\right) = 2.86\times10^{-3} \quad \Omega$$

and hence

$$\sqrt{f/R_{dc}} = \left(\frac{60}{2.86\times10^{-3}}\right)^{1/2} = 145$$

This is too near to 143 to change the skin effect ratio obtained with the first approximation. Hence the second approximation of the conductor ac resistance becomes

$$R_{ac} = \frac{1.1\times3.33\times10^{-6}}{\pi(5.08^2-3.81^2)} = 10.3\times10^{-8} \quad \Omega/\text{cm}$$

Substituting this value into (3.128) gives the second ampacity approximation

$$I^2 = \frac{(60-20)}{(10.3\times10^{-8}+5.27\times10^{-8})(1.22+2.16\times31.0)}$$

$$I = 1941 \text{ A} \quad \text{(second approx.)}$$

Further approximations may be derived in the same manner until the ampacity increase becomes insignificant.

Flexible isolated phase cables should be treated in the same way, but the three-conductor cable poses a number of new and difficult problems. From the discussion in Section 1.15 it will be realized that no analytical expressions exist for the conductor ac resistance and the pipe circulating current loss of three-conductor cables. However, these parameters may be determined with good accuracy by the finite element method explained in Section 1.15 or by measurements on full or reduced scale transmission lines.

When neither computer solutions of the finite element model or experimental measurements are available, a number of expedients may be employed to arrive at an approximate ampacity of the three-conductor cable of unknown error limits. For example the conductor ac-dc resistance ratio may be computed by simply adding the skin effect to the proximity effect and ignoring the fact that the current distribution over the conductor cross section also depends on the pipe currents. The magnetic field surrounding the bundle of three-phase conductors is smaller than that surrounding an isolated phase conductor. Hence the pipe circulating currents may be expected to be smaller than the conductor currents. In the example of Fig. 1.42 they were found to be approximately half of the conductor currents. In the absence of any better information it could be assumed that this is the ratio of pipe to conductor currents in all three-conductor cables with aluminum enclosures.

Further simplifying assumptions have to be made about the heat transport through the gas insulation. As a crude model we might consider an imaginary cylindrical heat dissipation surface of radius r_c' as indicated in Fig. 3.89. This is an envelope of the three conductors and should be considered to consist of the same material as the conductors from which the Joule loss of the three conductors emanates uniformly around the periphery. This very approximate method of estimating the three-conductor cable ampacity will be further illustrated in the following example.

EXAMPLE

1. 345 kV three-conductor cable of the dimensions shown in Fig. 3.84.
2. Burial depth $D=50$ in. Soil thermal resistivity 90 thermal-$\Omega\cdot$cm. Ambient temperature 25°C.
3. Conductor material: 61.8% IACS aluminum of $\xi_c=0.3$. Enclosure material: 61% IACS aluminum of $\xi_p=0.8$, $T_p=60$°C.
4. Somastic corrosion jacket 0.5 inch thick, 100 thermal-$\Omega\cdot$cm.

JACKET THERMAL RESISTANCE R_j. From (2.80)

$$R_j=\frac{100}{2\pi}\ln\frac{29}{28}=0.56 \quad \text{thermal-}\Omega \quad \text{(per cm)}$$

SOIL THERMAL RESISTANCE R_e. From (3.8)

$$R_e=\frac{90}{2\pi}\ln\frac{100-14}{14}=26.0 \quad \text{thermal-}\Omega \quad \text{(per cm)}$$

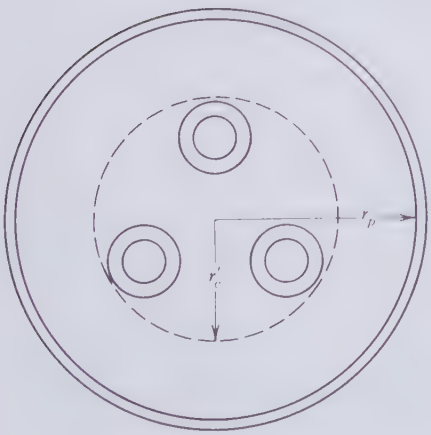

Figure 3.89 Imaginary cylindrical heat dissipation surface of radius r_c' in three-conductor gas insulated cable.

ENCLOSURE LOSS P_p AND EQUIVALENT RESISTANCE R_p'. If R_p is the dc resistance per unit length of the pipe, one-third of the pipe wall, or $3R_p$, has to carry the circulating current associated with one phase. The phase circulating current is assumed to be $I/2$. The Joule heat generated in the pipe is then given by

$$P_p = 3\left[\left(\frac{I}{2}\right)^2 \times 3R_p\right] = \left(\frac{9}{4}\right) I^2 R_p = 3I^2(0.75R_p)$$

At 60°C the resistivity of the pipe material from Fig. 1.71 is 3.3×10^{-6} Ω·cm. Hence

$$R_p = \frac{3.3\times10^{-6}}{\pi(14^2 - 13.5^2)\times 2.54^2} = 1.18\times10^{-8} \quad \Omega/\text{cm}$$

$$R_p' = 0.75R_p = 0.89\times10^{-8} \quad \Omega/\text{cm} \quad P_p = 3I^2R'_p$$

HEAT TRANSFER ACROSS GAS GAP $(W_r + W_c)$.

$$r_c' = 9.3 \text{ in.} = 23.6 \text{ cm}; \quad r_p = 13.5 \text{ in.} = 34.3 \text{ cm};$$

From (3.130)

$$\xi' = \frac{0.3\times0.8}{0.8 + (23.6/34.3)(1-0.8)\times0.3} = 0.29$$

The radiation heat transfer from (3.129) is

$$W_r = 5.67\times10^{-12}\times2\pi\times23.6\times0.29(T_c^4 - 333^4) \quad \text{W/cm}$$

$$= 2.44\times10^{-10}(T_c^4 - 1.23\times10^{10}) \quad \text{W/cm}$$

and the convection heat transfer from (3.131) is

$$W_c = \frac{3.75\times10^{-3}(T_c - 60)^{1.2}(34.3 - 23.6)^{0.6}}{\ln(34.3/23.6)}$$

$$= 0.0416(T_c - 60)^{1.2}$$

The combined radiation and convection heat transfer is plotted on Fig. 3.90 for conductor temperatures from 60 to 100°C. Heat conduction through the spacers is considered to be negligible.

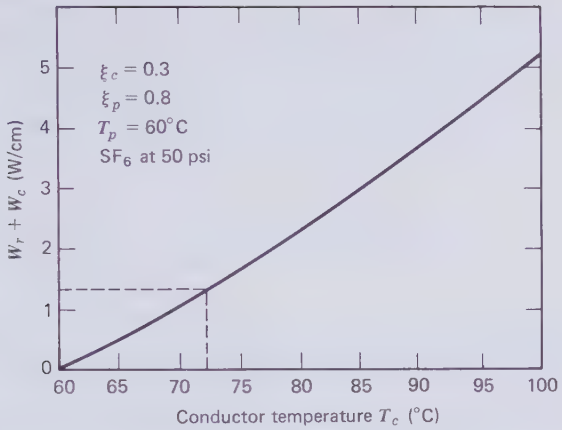

Figure 3.90 Heat transfer across gas gap in three-conductor cable example.

AMPACITY I. When adapted for three conductors, (3.132) becomes

$$W_r + W_c = 3P_g = \frac{T_p - T_a}{R_j + R_e} - 3I^2R_p' = 1.32 - 2.67 \times 10^{-8} I^2 \quad \text{W/cm}$$

Therefore $W_r + W_c$ must be less than 1.32 W/cm and from Fig. 3.90 this results in a limiting conductor temperature of 72.2°C. At this temperature the resistivity of the conductor material from Fig. 1.71 is 3.33×10^{-6} Ω·cm. To determine the skin effect from Fig. 1.18 we need to know the dc resistance of 1000 ft of the conductor

$$R_{dc} = \frac{3.33 \times 10^{-6} \times 1000 \times 12 \times 2.54}{\pi(6.35^2 - 5.08^2)} = 2.23 \times 10^{-3} \quad \Omega$$

Therefore

$$\sqrt{f/R_{dc}} = \left(\frac{60}{2.33 \times 10^{-3}}\right)^{1/2} = 164$$

Also

$$t/d \quad \text{(defined on Fig. 1.18)} = \frac{0.5}{5} = 0.1$$

With these coordinates Fig. 1.18 indicates a 10% skin effect. For reading the proximity effect off Fig. 1.24 we require the dc resistance of one foot of

conductor which is 2.23×10^{-6} Ω. Hence

$$\sqrt{f/R_{dc}} = \left(\frac{60}{2.23\times10^{-6}}\right)^{1/2} = 5187$$

Also

$$\frac{s}{d} \quad \text{(defined in Fig. 1.24)} = 11.8/5 = 2.36$$

With these coordinates Fig. 1.24 indicates an 8 percent proximity effect. Therefore $R_{ac}/R_{dc} = 1.18$. Hence the upper limit of the conductor ac resistance is

$$R_{ac} = \frac{1.18\times2.23\times10^{-6}}{12\times2.54} = 8.63\times10^{-8} \quad \Omega/\text{cm}$$

Using (3.128), the ampacity equation for the three-conductor cable is

$$I^2 = \frac{(T_c - T_a)}{3(R_{ac}+R'_p)(R_j+R_e)}$$

$$= \frac{(60-25)}{3(8.63\times10^{-8}+0.89\times10^{-8})(0.56+26.0)}$$

$$I = 2148 \text{ A}$$

A second approximation is not justified because of the ad hoc assumptions made regarding ac losses and heat transfer between conductors and the pipe.

Daily Cycle Rating

Gas insulated cables are high-ampacity cables. A further lift in ampacity due to cyclic load fluctuations has been less important for this new category of cables than for the conventional oil-paper insulated lines.

Section 3.2 explains how the cyclic soil resistance factor β depends on the soil thermal time constant τ_s. When this time constant is large, the β multiplier of the soil thermal resistance becomes small implying that the soil is then less of a restriction of the current-carrying capability of the cable. The graph of the cyclic soil resistance factor of Fig. 3.20 on page 306 is limited to thermal time constants up to 15 hours which is appropriate for small diameter self-contained cables. This time constant depends on the volume of soil involved in the thermal cycling and increases with depth of

burial, cable spacing and diameter. No measurements of the thermal time constants of gas insulated installations have been published, but it is confidently expected that they are of at least of the order of 1 or 2 days.

Equation (3.31) defines the cyclic soil resistance factor by

$$\beta = \alpha + \frac{1-\alpha}{\sqrt{1+\omega\tau_u}} \tag{3.133}$$

where ω is the radian frequency of the daily cycle given by (3.32) as $\pi/12$ rad/hr; α is the Joule loss factor defined by (1.212). When τ_u is of the order of days the second term of (3.133) becomes small compared to α. Hence to a first approximation the soil resistance factor of a gas insulated cable may be equated to the Joule loss factor. To see how much greater this will make the daily cycle rating than the continuous cable ampacity consider the numerical example previously analyzed of a 230-kV isolated phase, solidly bonded circuit. The ampacity of this circuit was found to be 1941 A. For a typical 0.6 loss factor, the daily cycle peak current would go up to 2491 A, or 28 percent above the continuous ampacity.

Forced Cooling

Forcibly cooling gas insulated cables is not an important issue because of the high ampacity attainable with natural cooling. Doepken [3.70] has made a convincing case that if the necessity of forced cooling arises it should be applied externally to the enclosure pipe. The gas space is a good thermal transmitter of heat and little is therefore gained by conductor cooling that would require fluid-tight conductor joints. Gas circulation and external gas cooling is not an attractive proposition on account of the low specific heat of SF_6 or any other gas.

Fault Current Rating

Gas insulated cables have substantial metallic enclosures. Certainly in the isolated phase designs and probably also in the three-conductor cable, the current density is highest in the conductor. So far as thermal limitations are concerned, therefore, (3.54) on page 322 applied to the conductor will determine the fault current rating. In general this will be high because of the relatively large amount of metal contained in the conductors of gas insulated cables.

Electromagnetic forces are not a serious problem in isolated phase systems as each conductor is shielded from the others by equal and opposite

circulating currents in the enclosure pipes. Should these pipes be cross-bonded to prevent the flow of circulating current, then equations (3.46) to (3.52) may be employed to calculate the lateral forces that must be supported by the dielectric spacers while fault conditions persist.

For a discussion of interconductor forces in the three-conductor cable reference should be made to the text accompanying Fig. 1.51 on page 96.

Critical Length

Equation (3.57) on page 323 shows that the critical length of a three-phase circuit is proportional to the ampacity and inversely proportional to the capacitance per unit length of the cable. On both counts the gas insulated cable is superior to others insulated with oil-paper or solid polyethylene. The dielectric constant of the gas may be taken as unity. Therefore charging current limitations are not expected to be a factor with gas cables unless extremely long lengths should one day be required. Even at 800 kV the critical length of an isolated phase installation is of the order of 200 miles [3.62].

DC Application

No gas insulated dc cables have been contemplated at the time of writing. Should a need for them be found, no particular difficulties are expected to arise in the development of single and two-conductor gas insulated dc cables.

Underwater Installation

Underwater installations of gas insulated cables have been proposed but not employed. It will be recalled that pipe-type cables were rejected for the Long Island Sound crossing because it was considered uncertain that water could be kept out of most of the cable if a pipe was accidentally ruptured. The same objection applies to gas insulated cables. Another point to be borne in mind is that gas insulated cables, as known today, are buoyant in water and have to be weighted down to sink to the bottom and be held there.

Economics

Extensive cost data on isolated phase, solidly bonded, rigid SF_6 insulated underground transmission lines has been published by the Electric Power Research Institute (EPRI) in 1975 [3.62]. Firm prices of gas cables, including field handling and welding, from this report have been multiplied by the

1.07 percent inflation factor to bring them up to the 1976 level. They are listed on Table 3.16 under "cable cost." The 1976 civil engineering charges have been computed with the following unit costs, which broadly reflect EPRI recommended figures for average suburban conditions.

Trench excavation and backfill	$\$40/yd^3$
Thermal sand fill	$\$32.10/yd^3$
Concrete slab cover (2 in. thick)	$\$48.20/yd^3$
Road surfacing	$\$20/yd^2$

The trench widths for cables of various voltages is given in [3.62]. In calculating the civil engineering cost shown in Table 3.16 it has been assumed that trenches are cut in soft soil and the cables are laid in a bed of

Table 3.16 Transmission Cost Calculations in 1976 for Isolated Phase, Rigid, Gas-Insulated Tables
$E = \$0.0255/kWh$; CLF = 0.75; $u = 1$; $\alpha = 0.62$

Line Voltage	kV	138	230	345	500
Basic Insulation Level	kV	650	900	900	1300
Enclosure O.D.	in.	9	12	14	18
Enclosure Thickness	in.	0.25	0.25	0.25	0.25
Conductor Area	$in.^2$	4	4	6	10
Ampacity	A	1600	1700	2100	2400
Capability	MVA	380	680	1250	2080
Trench Width	in.	62	72	78	90
1976 Aluminum Pipes	$/mi	181,422	236,138	325,374	515,807
SF_6 Gas	$/mi	21,120	42,240	58,080	95,040
Corrosion Protection	$/mi	84,744	169,488	197,736	254,232
1976 Cable Cost*	$/mi	1,898,266	2,259,840	2,547,970	3,141,178
Civil Engineering	$/mi	281,000	355,000	406,000	512,000
1976 YJL†	$/mi	58,288	56,556	64,863	65,334
1976 UG TC‡	$/MVA.mo.yr	1343	884	540	393
OH TC**	$/MVA.mi.yr.	380	182	111	83
1976 UG/OH Ratio		3.53	4.86	4.86	4.73

*Includes field handling and welding.
†Yearly cost of Joule losses (conductors and pipes).
‡Underground transmission cost.
**Overhead transmission cost from Table 3.10.

thermal sand. The cables are protected against accidental dig ins by 2 in thick concrete slabs laid on top of the sand and covering the full width of the trench. The upper portion of the trench is backfilled with previously excavated soil and the road surface is reinstated.

Yearly costs of Joule losses per circuit mile (YJC) comprise the conductor and pipe circulating current loss at 75 percent cable load factor ($a = 0.62$) with the daily current peak being equal to the ampacity ($u = 1$). As before the 1976 cost of electricity has been taken as $k = \$0.02$ / kWh [3.31]. Sections 3.2 and 3.3 should be consulted for an explanation of the method of deriving transmission costs.

Table 3.16 also breaks out the price of the aluminum conductor and enclosure pipes at which they could be purchased from an extrusion plant in 1976. Other cost items that are shown separately concern the anticorrosion jacket and the SF_6 gas.

All the foregoing data has been used to compute the 1976 transmission cost with (3.62) on page 340. The dielectric loss in gas insulated cables is very small and has been ignored. In addition to the 1976 transmission cost attainable with 138, 230, 345, and 500 kV isolated phase cables, Table 3.16 also lists the underground to overhead (UG / OH) transmission cost ratio using the economic information on overhead lines from Table 3.10 on page 392.

On Fig. 3.91 the UG / OH transmission cost ratios of the gas insulated cables are compared with those of self contained and pipe type oil paper insulated cables in corresponding voltage classes. It is evident that on the basis of the EPRI cost information [3.62] isolated phase gas insulated cables are not competitive with conventional underground transmission lines. Short transmission links, of the order of 1000 ft long, are dominated by the cost of terminations and then gas insulated lines become competitive with pipe type cables. Table 3.16 and Fig. 3.91 refer to underground lines which are at least several miles long.

With respect to the present generation of 138- to 500-kV gas insulated cables, the cost of the losses, civil engineering, aluminum pipes, SF_6 gas and corrosion protection jacket contribute about as much to the transmission cost as the complete oil-paper insulated cables. What on Fig. 3.91 has been labeled "remainder" is the cost of trimming and capping the aluminum pipes, fabricating and installing spacers, producing and welding in position plug-in conductor joints, factory and field welding of the enclosure pipes, pipe handling, and shipping. According to the EPRI data these operations are very expensive and they account for half of the installed cost of the underground line.

For example a single 60 ft length of one phase of a 345 kV cable has to be associated with a "remainder" cost of $7450 in 1976 dollars. This length

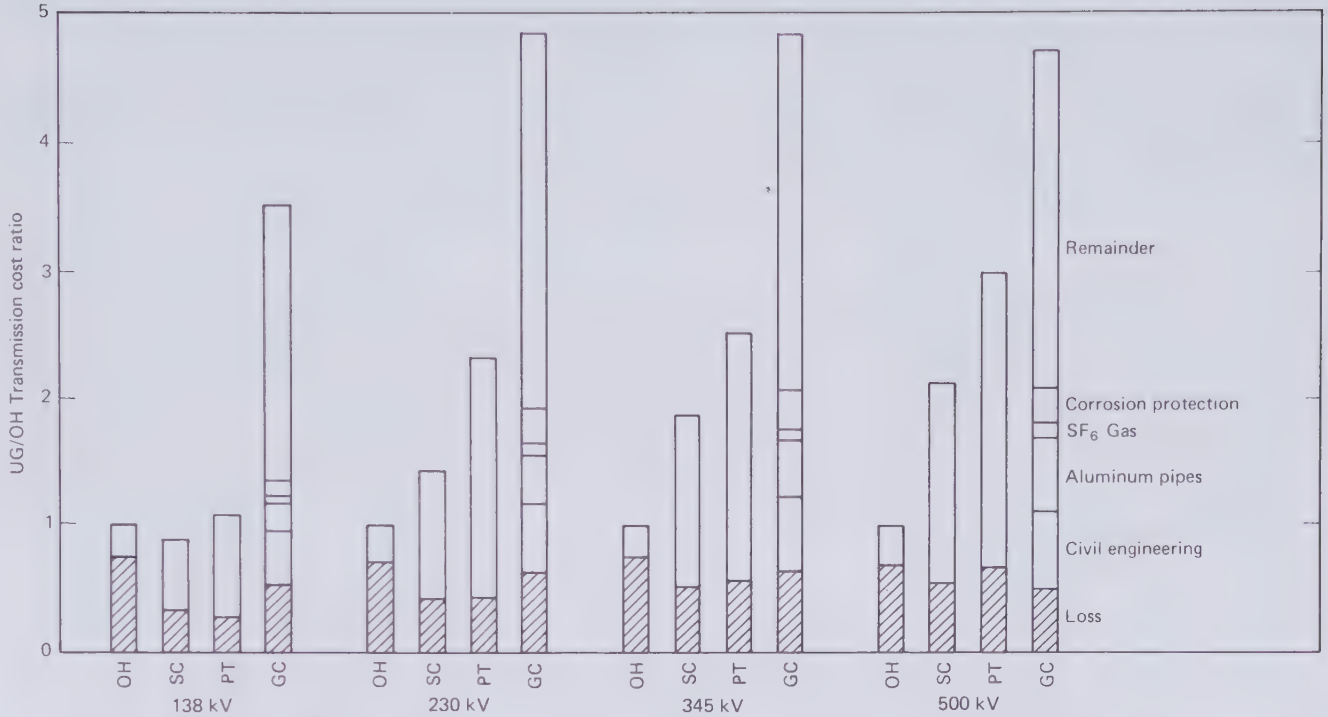

Figure 3.91 UG/OH transmission cost ratios of gas insulated, isolated phase, rigid, noncrossbonded cables compared with oil-paper insulated cables ($u = 1.0$, CLF $= 0.75$, $\alpha = 0.62$). OH—overhead line; SC—self-contained cable; PT—pipe-type cable; GC—gas insulated cable.

weighs just over 1000 lb and would typically contain four spacers, two halves of one conductor joint, and two returnable shipping end-caps. So large a sum cannot be explained by inefficient manufacturing procedures, but must contain a sizeable research and development recovery component. In the long run, therefore, mass-production would reduce the price of these cables considerably.

Cross-bonding of the enclosure pipes has the potential of reducing the cost of the Joule losses by approximately 30 percent. It would not make much difference to the transmission cost ratios but bring the losses of 138- to 345-kV gas insulated cables more in line with paper insulated cables.

It seems that isolated-phase rigid gas insulated cables have little chance of competing with self-contained oil-paper insulated cables. At the highest voltages they have some chance of rivalling pipe-type cables. These poor economic prospects of isolated-phase rigid SF_6 insulated cables explain why efforts are being made to develop more cost-effective, flexible, and three-conductor rigid cables.

3.7 THE PROSPECT OF RESISTIVE AND SUPERCONDUCTING CRYOCABLES

Early Research

Ever since the discovery of superconductivity in 1911, some electrical engineers have no doubt been dreaming about power lines capable of transmitting very large currents with no loss and at such low voltages that little insulation is required. The first to put these hopes in a more concrete written form appears to have been McFee [3.74] of Syracuse University. At about the time McFee published his heraldic papers, the city with the most concealed power lines under its surface, London, experienced a series of cable failures due to the drying out of soil. Transmission engineers began to talk seriously about forced cooling of cables and making underground circuits independent of their thermal environment. Cryocables seemed to satisfy this need better than the more conventional methods of cable cooling near ambient temperature. Besides, cryocables promised to increase trench power density by permitting the installation of several circuits in close proximity, which is normally impossible because of mutual heating. The higher trench power density promised savings in civil engineering operations, which would have to pay for the refrigeration equipment.

Experimental and theoretical studies of superconducting cables were started almost simultaneously by Klaudy [3.75] at the University of Gratz, Austria, and by Rogers [3.76] in the BICC Research Laboratories in London. In the United States the challenge was soon taken up by the Union

Carbide Corporation [3.77] and the General Electric Company [3.78]. By 1970 cryocable research was in progress in all major industrial countries.

In the wake of enthusiasm for superconducting cables it was only natural to find thought being given to cryocables with normal conductors using copper, aluminum, and beryllium. If the cryogenic temperature range is understood to extend from 0 to 100°K (−273°C to −173°C) only a few cooling fluids are at our disposal. They consist of the major constituents of air (nitrogen and oxygen), the nobel gases (argon, neon, and helium), the two highly flammable gases of methane (liquid natural gas or LNG), and hydrogen. Practical superconductors require operating temperatures from 0 to 15°K, which can only be achieved with helium cooling. All other gases solidify so close to absolute zero on the temperature scale.

One of the safest, cheapest, and most plentiful cryogens is liquid nitrogen (LN_2) which is now the preferred coolant for all cryocables that do not employ superconductors. Liquid argon and neon are as safe as LN_2 but distinctly more expensive. Liquid oxygen, methane, and hydrogen create fire hazards. Otherwise, as has been shown by the General Electric Company [3.78], hydrogen has much to recommend itself. The boiling point and heat capacity of liquid oxygen are not far removed from the corresponding liquid nitrogen parameters and little would be gained by using the dangerous liquid oxygen or liquid air in preference to LN_2. A group of investigators at the Massachusetts Institute of Technology [3.79] studied the combination of cryocable operation with LNG transportation. This is technically feasible and has obvious economic advantages when a need exists for transmitting electricity and natural gas along the same route, as between a city harbor and a peripheral generating plant.

LN_2 cooling has been proposed for copper, aluminum, and beryllium conductors. The concensus of opinion appears to be that little or nothing is gained in the LN_2 temperature range by choosing costly copper over less expensive aluminum conductors. From 65 to 100°K both metals have approximately the same resistivity, as may be seen in Fig. 1.70 on page 135, particularly when it is realized that aluminum is easier to purify then copper. Figure 1.70 also illustrates the clear cut resistivity advantage of beryllium in the LN_2 temperature range. Pure beryllium will be less brittle than the material now commercially available. Should this expectation be borne out in practice, then beryllium with its high-yield strength, small thermal expansion (see Table 1.11), and light weight would make an ideal cryocable conductor. What has prevented any serious experimenting with beryllium tubes is the high cost of refining this metal. The properties of beryllium are more fully discussed in Section 1.23.

In the latter half of the 1970's cryocable research has concentrated on helium-cooled superconducting cables and nitrogen-cooled aluminum cables.

Three different electrical insulation systems have been investigated. They are as follows:

1. Vacuum insulation with solid dielectric support insulators.
2. Liquid cryogen insulation with solid dielectric support insulators.
3. Liquid cryogen impregnated tape insulation.

What would be the Advantages of Cryocables?

The various answers that have been given to the question what are the advantages of cryocables are confusing. To begin with the reduction or elimination of Joule heating losses was a major stimulant for work on superconducting lines. In 1973 the Department of Energy claims that cryogenic cooling is essential for achieving exceptionally high circuit capabilities of 5000 to 9000 MVA, and that circuits of this size will be required in the foreseeable future. A third group believes that certain cryocables in the 500 to 2000 MVA range can be made competitive with overhead lines in suburban areas.

All the research on cryocables in the United States is presently sponsored by the Department of Energy. Its forerunner, the Energy Research and Development Administration, expressed the following views in 1976 [380]:

"Commercial application of superconducting transmission is still some years away, however, because tests to date show that the engineering tradeoffs are subtle, the requirements for extremely high, demonstrated reliability are formidable, and it may be that only the need to deliver very large amounts of electrical energy will justify the expense and complexity involved. Furthermore, it turns out that the greatest advantage of superconductivity does not rest on its reduction in losses at all, but on its ability to increase transmission capability."

In spite of the pessimism expressed by the Department of Energy, the conservation of energy through the elimination of losses has been the driving force behind research on superconducting cables and may be its only justification. Unfortunately a number of loss mechanisms operative in superconducting cables were initially overlooked or not fully appreciated and they have seriously impeded progress. For example ac losses in type II superconducting materials, which are due to magnetic hysteresis as explained in Section 1.7, have spoiled the hope for loss free current transfer. When the superconductor is a helically wound tape, the magnetic field may stray behind it into the copper or aluminum backing material and induce punishing eddy current losses in the low temperature normal metal. There are also dielectric losses to be considered. They may be quite small when the electrical insulation is vacuum or a cryogenic liquid, but they are not negligible in taped insulation.

All cryocables introduce a new kind of loss not encountered in conventional cables. This is heat leaking from the environment into the cold space, whence it has to be removed with refrigerators at a considerable expense of driving energy. The heat leak will be highest at the cable terminations where a substantial metallic conductor will at one end be immersed in liquid cryogen and at the other is in contact with the warm environment. More heat finds its way into the cryogenic coolant through pipe flow losses, the inefficiency of pumps and heat conduction from pump motors along the drive shafts to the impellers of the cryogen.

The energy loss components are magnified by the heat pump performance, which, more than any other fact, governs the total energy wastage associated with the operation of cryocables. At best the refrigerator performance is limited by the laws of thermodynamics and in particular the Carnot coefficient of performance

$$\eta_c = \frac{T_h - T_c}{T_c} \tag{3.134}$$

T_c is the cold temperature at which the coolant leaves the refrigerator and T_h is the hot temperature, both in degrees Kelvin, at which heat is rejected to the atomosphere or another heat sink. Typical figures for a helium cooled system would be $T_h = 300°K$; $T_c = 4°K$; and therefore $\eta_c = 74$. This means that for every kilowatt-hour of heat generated or leaking into the helium stream, at the very least another 74 kWh of driving energy have to be expended in the compressors of the refrigeration plant. In practice the performance coefficient is much worse and the best ever mentioned for a superconducting cable system is 150 kWh/kWh [3.81].

The great improvement of refrigerator performance at higher temperatures is one of the reasons why some investigators believe that liquid-nitrogen-cooled cables will be more economical than superconducting cables. At 64°K, just above the freezing point of nitrogen, (3.134) indicates a Carnot refrigerator performance coefficient of 3.69. A value of seven has been achieved in practice with Stirling-cycle machinery. This is a 20-fold improvement over liquid-helium refrigeration.

Of all cryogenically cooled transmission lines so far proposed, only LN_2 cryocables can make use of purely evaporative cooling. This is the result of the low cost and safety of nitrogen. It would make it possible to shut down refrigerators without interrupting power transmission and avoid the duplication of plant, which would otherwise be required to satisfy the high standards of reliability set by the electricity supply industry. The latent heat in stored LN_2 may not only be used as a reserve for refrigerator outage, but it can provide a means for boosting the line transmission capability in an

emergency situation to prevent the blackout of large areas. This is a unique advantage being offered by liquid-nitrogen-cooled lines for as long as it is economical to truck the cryogen to tanks installed at the ends of the transmission line.

Yet another and perhaps the most powerful incentive for developing cryocables has been the possibility of achieving cost equality with the majority of overhead lines in suburbs and towns on the fringe of metropolitan areas. This would require three-phase circuits in the 300 to 2000 MVA capability range. It is not an unrealistic goal when it is realized that land purchases for overhead right-of-ways in these areas require an expenditure roughly equivalent to the installed cost of refrigeration plant. A cable system that can directly compete with overhead lines must of course be simple to construct, simple to install, and be made of low-cost materials. The only candidate in this category is the vacuum insulated, liquid-nitrogen-cooled cable that consists of a collection of four extruded and welded together aluminum tubes with liquid nitrogen flowing through the conductor pipes. The vacuum space between the conductors and the enclosure pipe provides at one and the same time the electrical and the thermal insulation. Like SF_6 insulated transmission lines, such cables can be fabricated in ordinary metal workshops without the large and specialized plant required for oil-paper insulated cables. But unlike SF_6 insulated cables, this particular cryocable will require only a reasonable amount of aluminum and quite narrow trenches without special backfill.

Time will tell which, if any, of these advantages of cryocables can be translated to reality; whether it be the large circuit capability, energy conservation, load boosting with latent heat cooling, or straightforward competitiveness with medium sized overhead lines.

Vacuum Insulated, Liquid-Nitrogen-Cooled (VI-LN2) Cryocable

As far as it has gone, the development of the VI-LN2 cryocable has been directed by the author, first in the BICC Research Laboratories in London, then within the Simplex Wire and Cable Company, and more recently under the auspices of the Massachusetts Institute of Technology, the Vacuum Barrier Corporation, the Interpace Corporation, and the Underground Power Corporation. The primary object of this project is to produce underground power transmission lines which are competitive with typical suburban overhead transmission lines.

In a 1971 study [2.8] initiated by the U.S. Department of the Interior and the Edison Electric Institute it was found that for circuit capabilities in the range from 300 to 2000 MVA, the VI-LN2 cryocable promised to be more economical than all other resitive and superconducing cryocables. This study

did not consider the economic consequences of circuit duplication for standby electricity supply reliability, which is the norm rather than the exception. For a firm rating (one circuit out of use) of, say, 500 MVA all cable systems—except the VI-LN2 cryocable—require the installation of 2×500 MVA circuits. Refrigeration boosting by the expediency of evaporating LN_2 from storage tanks at refrigeration stations and exhausting the warm nitrogen to the atmosphere permits the cryocable capability to be doubled for extended periods of emergency operation. A double circuit with a firm rating of 500 MVA may therefore be constructed with what would normally be 2×250 MVA VI-LN2 cryocable circuits. Using the 1971 transmission cost figures published in [2.8], but taking this advantage of the VI-LN2 cryocable into account, the results of Fig. 3.92 have been obtained. Hence in 1971 it appeared quite feasible to make VI-LN2 cryocables as economical as suburban overhead lines. Since then the cost of energy losses has increased much more rapidly than the cost of labor and materials. This has affected the economics of the VI-LN2 cryocable more adversely than that of soil-cooled ambient temperature cables.

Milestones in the development of the VI-LN2 cryocable have been the successful field trial in 1975 of a 138-kV prototype termination [3.85] and, in 1976, the demonstration of 400 MW/phase power transmission through a short laboratory loop [3.84]. At the time of writing, in 1979, this is still 10 times more transmitted power than has previously been achieved with either resistive or superconducting cryocable samples.

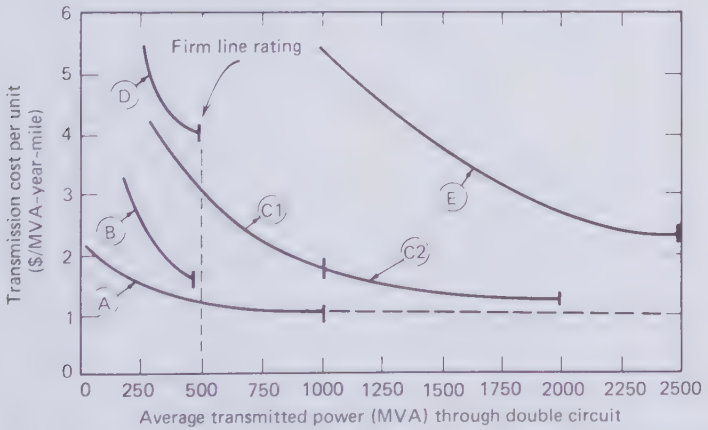

Figure 3.92 1971 Transmission cost with 230 kV double-circuits of indicated 'firm line ratings'. (A) Suburban overhead line. (B) Directly buried sodium cable. (C1 and C2) VI-LN2 cryocable. (D) Naturally cooled pipe-type cable. (E) Lower bound of superconducting and SF_6 insulated cables [3.83]. (By permission of the Institute of Electrical and Electronics Engineers).

A recent design of the VI-LN2 cryocable is illustrated in Fig. 3.93. It is based on three bare, extruded, sector-shaped EC aluminum tubes that contain pressurized and flowing liquid nitrogen. The conductor temperature is allowed to float with cable load and position along the coolant stream. Controls ensure that the refrigerator is not allowed to bring it below 65°K to prevent freeze-up. The conductor wall thickness determines the maximum allowable pressure and nonboiling coolant temperature. For substantial conductor cross-sections the maximum temperature at the coolant outlet can lie as high as 130°K. Spacers located at 6- to 10-ft intervals hold the conductor tubes in position inside an aluminum alloy enclosure pipe with external corrosion protection. This pipe may run 30 to 40°C above ambient temperature to dissipate the enclosure Joule heat to ground. In other forms of cryocable this heat has to be extracted with refrigerators that magnify the energy drain. The VI-LN2 cryocable is seen to be similar in construction to the SF_6 insulated three-phase cable but more compact.

The space between the LN_2 cooled conductors and the enclosure pipe is evacuated. Experience has shown that after a 100°C bake-out and the surface clean-up resulting from high-voltage conditioning, final low-temperature vacuum pressures from 10^{-7} to 10^{-9} torr are readily achievable. It was found advisable to leave the aluminum surfaces in the "as-extruded" condition and keep the vacuum system free of organic materials. The virtual absence of gas ensures excellent thermal and electrical insuation of the conductors. Large ion pumps at the terminations and small appendix ion pumps at approximately 1-mile spacing sustain the vacuum against a small amount of continuing outgassing. The appendix ion pumps make use of permanent magnets and the internal electric field, which avoids the need for an external power supply.

The conductor spacers incorporate porcelain post insulators, which on one end are attached to a strong stainless steel ring and on the other to conductor support rings. To control electron field emission at the highest voltages, probably from 345 kV up, metallic phase dividers may be provided in overlapping sections extending over the whole length of the cable or just for a short distance on either side of the spacer. The conductor support rings must allow a limited amount of axial motion of the aluminum tubes during cool-down and subsequent warm-up cycles. Individual cable sections may be of the order of 60 ft in length and each length has to be provided with a telescopic contraction joint, sealed vacuum and pressure tight and permitting approximately 2.5-in. axial travel. In the proposed design of Fig. 3.93 the sealing element is an internal stainless steel bellows.

Three-phase ac VI-LN2 cryocables may be terminated in a trifurcating box and three attached potheads with high-voltage connectors in ambient

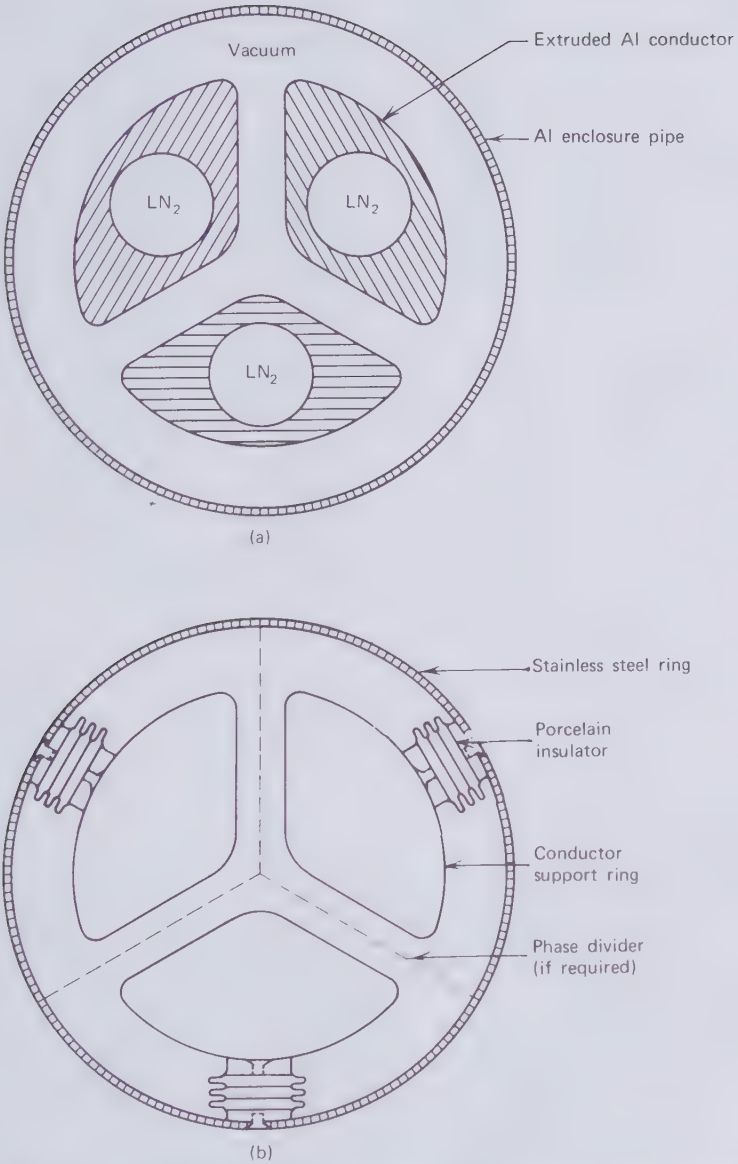

Figure 3.93 Components of VI-LN2 cryocable system. (a) VI-LN2 cryocable. (b) Spacer. (c) Termination. (d) Contraction joint.

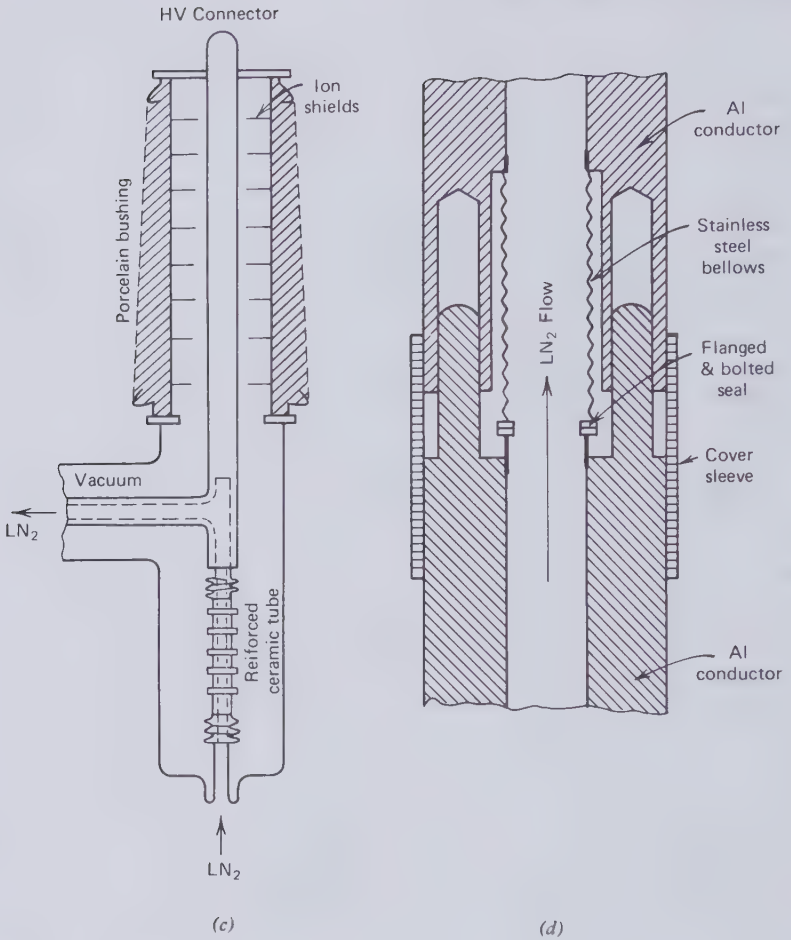

Figure 3.93 *Continued.*

air. An individual pothead can be as simple as the termination of a compressed gas insulated cable (see Fig. 3.82), except that a cryogen feed tube of dielectric material has to be provided, as indicated in Fig. 3.93. When liquid nitrogen is supplied at elevated pressure, this feed tube should be made of high-strength alumina and may have to be reinforced externally by shrink-on stainless steel or titanium rings. The electrical performance of high-voltage vacuum insulation has been discussed in Section 2.6.

Factory assembled and capped cable sections would have to be thoroughly tested before shipping to the installation site. In accordance with good pipeline practice, the best way of field jointing such a cable system would appear to be inside a van or other portable enclosure that is equipped with

welding and vacuum leak checking equipment. In the design of Fig. 3.93 each conductor length has to be joined to the next one by means of bolted and metal gasketed stainless steel flanges. It should be noted that the conductor assembly with the spacer can slide axially inside the enclosure pipe. To ensure vacuum integrity, each conductor joint must be leak tested, with a clam shell enclosure and a sensitive helium mass spectrometer. The outer pipe is most conveniently jointed by welding, and the seam also has to be carefully leak tested with a helium mass spectrometer and an external clam shell. Having jointed a sufficient length of the aluminum pipeline it should be found flexible enough for lowering into a narrow trench for direct burial. Two or more circuits may be installed in the same trench in close proximity. Elbows for bends in the transmission line would have to be prefabricated in the factory for insertion into the line with overlapping sleeves.

The typical VI-LN2 cryocable system is envisaged to consist of two circuits in the same trench. This permits coolant flow in opposite directions in the two sets of conductors. The refrigeration plants may be located at any or several points along the coolant loop. The average length of newly installed suburban transmission links is less than 10 miles and could be served with one or two cooling plants at the substations where the transmission link is terminated. The maximum length of a cooling module is a design variable determined largely by the mechanical strength of the conductor tubes and the internal pressure that they can safely withstand.

When one of the two circuits is damaged, it will no longer be available as a coolant return path. Most forced cooled cable systems have to be provided with an external coolant return pipe to deal with this contingency. Even for oil cooling, this pipe is a very costly item, and it becomes particularly expensive when the coolant is liquid nitrogen or helium. The VI-LN2 cryocable does not require an external coolant return pipe because, after operating some valves, the coolant may be returned through one of the three surviving conductor tubes. This is made possible by the vacuum insulation, which thermally isolates the conductors from each other. It would not be difficult to provide one conductor tube per three-phase circuit with a larger bore to balance the coolant streams, but this seems hardly necessary as the return flow can be switched, at intervals of a few hours, from one conductor to another to restore a certain degree of thermal balance. This mode of temperature control is further aided by the thermal inertia of the VI-LN2 cryocable system as a whole, which is large compared with the heat input.

The cooling plant required for a liquid-nitrogen-cooled cable is similar to that found in a small air liquefaction plant [3.86] without the oxygen separation and handling facilities. It is customary for such plants to run unattended with maintenance periods scheduled at yearly intervals.

The major criticism that has been voiced against the VI-LN2 cryocable is a doubt about its long-term vacuum integrity. This can only be resolved with a field trial of a sufficient length of cable. It was found relatively easy to devise methods of manufacture, transportation, and installation of a field trial termination [3.83] which proved completely vacuum tight during 8000 hours of testing in spite of 196 separate weld seams, eight metal gasket seals, two metal-to-ceramic bonds, and one elastomeric O-ring. The Vacuum Barrier Corporation has placed some 25 miles of vacuum insulated cryogenic transfer lines in service and experienced hardly any trouble with vacuum integrity of their welded thin-wall pipelines over a period of 10 years.

Liquid-Nitrogen-Cooled Cryocables with Tape Insulation

The motivation for the development of tape insulated cryocables has been the desire to depart as little as possible from the manufacturing and installation technology of oil-paper insulated cables. Therefore, given the use of similar materials, any savings achieved with this type of cryocable have to come from economies of scale (large transmission capability per circuit) and energy conservation. No claims have been made that liquid nitrogen cooled, tape-insulated cables can compete with oil-paper insulated cables at less than 2000 MVA, and there is little hope that they could ever become competitive with overhead lines.

The preferred conductor material is aluminum. Hollow-core as well as filled-core stranded conductors have been proposed. Considering the difficulties that continue to persist in the calculation and measurement of the ac resistance of stranded conductors, there exist uncertainties about the efficiency of these conductors. The 10-fold increase in the aluminum conductivity due to the low temperature will have the same effect on the ac-dc resistance ratio as a 10-fold increase of the energizing frequency. Therefore ac-dc resistance ratios of two and more may arise unless great care is taken by using insulated wires of small diameter and near perfect transposition over the conductor cross section. The efficient performance of stranded aluminum conductors at liquid nitrogen temperatures has not yet been demonstrated by experiment.

Polymer as well as paper tapes are candidate materials for the liquid-nitrogen-impregnated high-voltage insulation. The General Electric Company currently prefers Kraft paper, notwithstanding the relatively high dielectric loss indicated in Fig. 2.52 on page 270. If paper has an advantage, it is likely to reside in its mechanical properties, which are of importance in the tape application process, cable bending, and also during thermal expansion and contraction.

The stranded and tape insulated cable cores have to stretch 0.4 percent during cool-down. This must result in dimensional adjustments, tension in the conductors and relative motion between tape layers. It has yet to be shown that long length of this type of cable can safely survive thermal cycling between ambient and liquid-nitrogen temperatures without the provision of contraction loops. The high-voltage insulation should also be a good heat conductor to prevent the formation of vapor bubbles within the dielectric which could readily ionize and lead to breakdown of the insulation. Since most of the coolant is necessarily located outside the cable core, both Joule heat from the conductor and dielectric heat have to be transmitted through the high-voltage insulation. Liquid-nitrogen-impregnated paper insulation is reported to have a thermal resistivity of 650 thermal-$\Omega \cdot$ cm as compared with a figure of 500 for conventional oil-paper insulation.

To prove that the electrical insulation functions reliably—and for other reasons too—the cable should carry maximum current while it is being voltage tested. In other words the performance of the cable can only be established by transmitting power. Hitachi Cable Ltd. [3.87] demonstrated the transmission of 1000 A at 38 kV (single-phase), or 38 MVA, through a liquid-nitrogen-cooled cable sample with tape insulation. This experiment was performed in 1971 and has not been improved upon during the past 8 years.

The LN_2 impregnant and coolant has to be contained in an enclosure pipe that is strong enough to withstand reasonably high pumping pressure. If it is to contain the three cores of an ac circuit, this pipe has to be of quite large diameter. A stainless steel pipe can perform this function but it will carry the large induced currents examined in Section 1.15. This may result in as much if not more Joule heat than is being generated in the conductors. The pipe loss energy flows directly to the liquid nitrogen whence it has to be extracted with refrigerators that multiply the energy loss by a factor of seven.

These energy losses persuaded the General Electric Company to investigate the use of fiberglass-reinforced resin pipes for the containment of pressurized LN_2. Their findings were positive and nonmetallic coolant pipes are a feature of the latest GE cryocable design shown in Fig. 3.94. A metal pipe could carry the capacitive charging current on the grounded side of the dielectric. In the absence of such a pipe, a fourth (drain) conductor had to be included in the liquid-nitrogen stream.

Nitrogen gas readily diffuses through synthetic materials. Therefore the space outside the fiberglass pipe could not easily be maintained evacuated for thermal insulation purposes. This led GE to propose the bulky foam insulation surrounding the cable of Fig. 3.94. The foam, in turn, has to be protected against moisture ingress as this would spoil its thermal resistance.

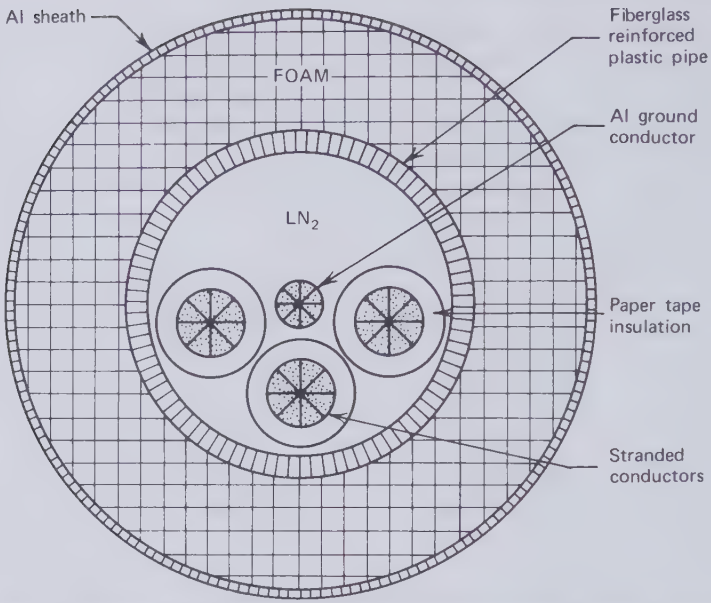

Figure 3.94 GE design of LN_2 cooled paper-tape insulated cryocable. Coolant return pipe not shown [3.31].

No other material but metal forms an effective moisture barrier. Hence the foam insulation is enclosed by a thin aluminum sheath. Compared with a stainless steel pressure pipe, the advantages of the aluminum sheath are (1) that it need not be strong, and (2) that the Joule heat generated within it will flow to the surrounding soil and not to the cryogen.

As explained earlier, a cable of the form shown in Fig. 3.94 would have to be accompanied by a separate liquid-nitrogen return flow pipe. If this return pipe is also foam insulated it would have to be of the order of 20 in. overall diameter.

A significant variation in the design of liquid-nitrogen-cooled and tape insulated cryocables has been proposed by The Furukawa Electric Company of Japan [3.88]. In this a layer of thermal insulation is inserted between the liquid-nitrogen-cooled conductor and the electrical insulation. The latter may then operate at or near ambient temperature and could consist of oil-impregnated paper tapes. For ac transmission lines this procedure would result in three self-contained cable cores of probably quite large diameter.

Vacuum Insulated Superconducting Cables

In the case of superconducting cables too, great incentives exist for solving the twin problems of thermal and electrical insulation with a single vacuum

space, which would inevitably save a great amount of costly materials. This approach presents a particularly hard challenge to the inventor because success depends more on how the cable components are arranged than on the choice of materials. The two vacuum insulated superconducting cable concepts of Fig. 3.95 illustrate this point.

Diagram (a) shows one of the first cryocable designs ever published [3.89]. It was created in the BICC Laboratories in England and comprises no less than 17 separate metal tubes in addition to many layers of aluminum foil superinsulation. Nine of the tubes are arranged coaxially. In the most recent design (b) the number of tubular components has been reduced to seven, which alleviates the difficulties of supporting and jointing the internal structure.

Design (a) is based on an ingenious method of phase-splitting. A superconducting ac three-phase circuit consists in the normal way of six superconducting tubes arranged in three coaxial pairs. The nature of superconductivity is such that each member of a pair is compelled to carry current in direct phase opposition to the other member of the pair. Instead of relying on six superconducting tubes, design (a) employs just four. The middle phase is split in two layers, each half forming a go-and-return single phase circuit with the superconducting tube nearest to it. When adding the phasor currents in the two halves of the middle conductor it will be found that the sum is equal to the phase current of the three-phase circuit and also has the correct phase angle in relation to the other two currents.

The normal metal backing of each superconductor must be in direct contact with flowing liquid or supercritical helium to ensure effective heat transfer and thermal stability of the superconductors. Metal spacers may be inserted in the helium annuluses of design (a) because no voltage should exist between the two walls confining one helium stream. The outermost helium-containing pipe would be made entirely of normal metal. The vacuum space surrounding it provides electrical insulation from the grounded heat shield.

Both concepts (a) and (b) belong to a class of superconducting cables that employ two different coolants, commonly liquid nitrogen and liquid helium. LN_2 cooling is applied to an intermediate heat shield that intercepts most of the heat inleak from the environment. The nitrogen stream then removes this large fraction of the heat leakage at a refrigeration penalty, which is small compared to what it would be if this heat reached the helium stream. It should be noted that the heat shield of (a) consists of two halves, which are thermally isolated from each other so that counterflow nitrogen cooling may be applied to it.

Research in the past decade has revealed that extruded aluminum surfaces have sufficiently good thermal emissivities to make the use of

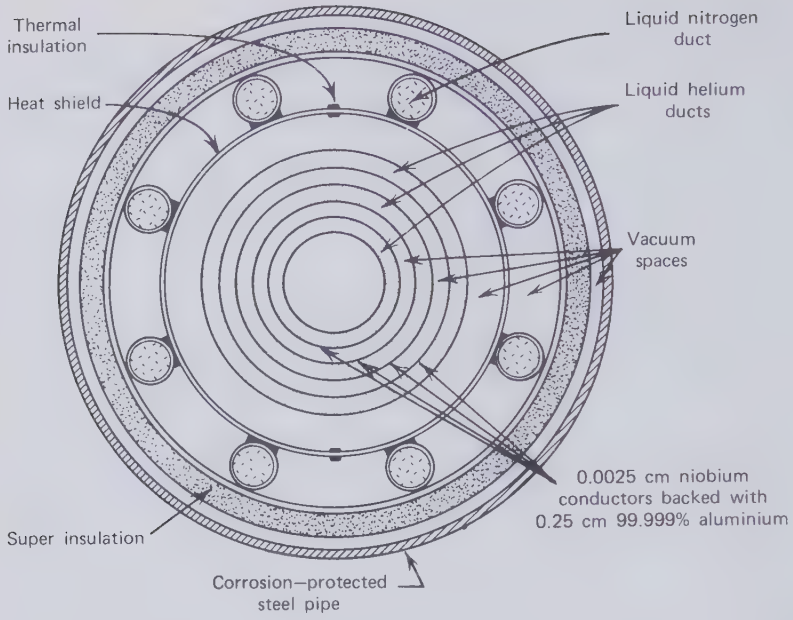

(a)

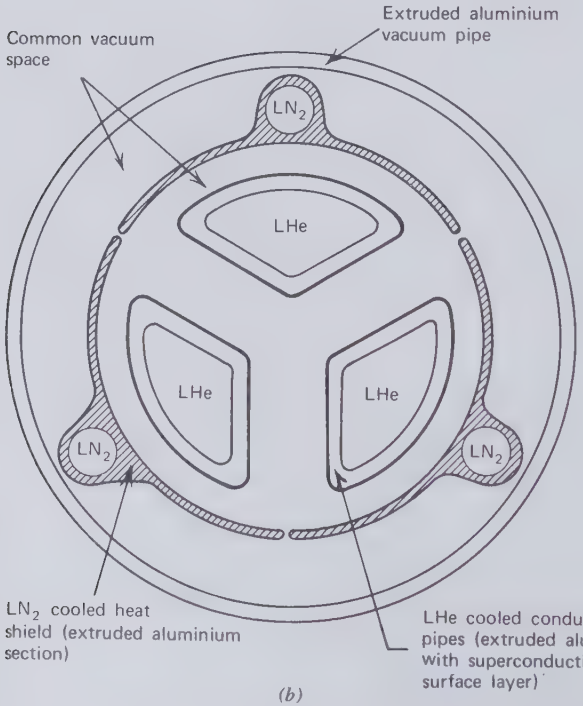

(b)

Figure 3.95 Two concepts of vacuum insulated superconducting cryocables. (a) Early design [3.89]. (By permission of Electrical Review). (b) Recent design [3.90].

additional multilayer superinsulation between ambient and a nitrogen cooled surface uneconomical. For this reason, design (b) employs an outer aluminum enclosure, instead of steel, and does not contain superinsulation.

Concept (b) depends on only three superconducting tubes. This is made possible by the vacuum insulation, which avoids the need for bringing normal metal, other than that enclosed by the superconducting tubes, in direct contact with the helium coolant. Some eddy current loss in the heat shield is acceptable because of the lower refrigeration penalty in the liquid-nitrogen stream. Almost all the shielding loss of (b) occurs in the aluminum enclosure pipe, which operates at ambient temperature and dissipates its heat to the surrounding soil. The three heat-shield segments have to be electrically isolated from each other, and the grounded enclosure pipe to prevent the flow of induced circulating currents.

Helium-Insulated Superconducting Cables

Another way of constructing cryocables is to use the cryogenic coolant as the high-voltage insulation. All cryogenic fluids are good dielectrics and pure compressed helium in the 4 to 10°K temperature range is a particularly good insulation of high breakdown strength because of the short mean free path of the electrons in the dense medium and the exceptionally high ionization potential (see Table 1.16) of the helium atom. Contaminating particles in the form of ice of impurity gases, air leaks, and refrigerator oil may, however, degrade the insulation properties of liquid and supercritical helium.

At ambient temperature and comparable pressure the breakdown strength of helium is only a fraction of that of air. This is explained by the small size of the helium atom and the consequent long mean free path of electrons, which outweighs the high ionization potential of this noble gas. Therefore, hot-spots along a helium-cooled power cable would almost inevitably lead to breakdown of the helium insulation.

The small size of the helium atom also makes it difficult to contain this fluid effectively in dielectric tubes. Therefore all the helium pipes that have been proposed for use in superconducting cables are metal pipes. If these conducting pipes are placed in the ac magnetic field of a normal three-core cable they would be subject to the flow of circulating currents and feed their Joule heat directly to the helium stream. To avoid this large energy loss in liquid helium insulated superconducting cable designs, it has been deemed necessary to shield each of the three phase conductors with a coaxial superconducting pipe. A typical design based on three pairs of coaxial superconducting tubes is shown in Fig. 3.96. This has been proposed by the Union Carbide Corporation and employs nominally pure niobium superconducting tubes backed with copper tubes.

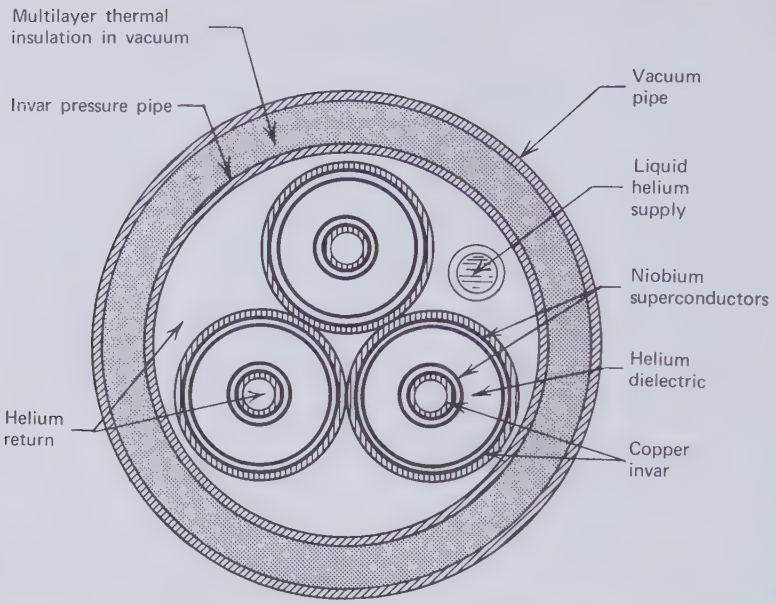

Figure 3.96 Superconducting cable with helium insulation proposed by the Union Carbide Corporation [3.31].

An interesting variation of the Union Carbide cable design is the way in which it deals with thermal contraction. Instead of providing sliding joints, which in a design of this complexity would introduce great assembly difficulties, this cable is assumed to be made of essentially invariable length conductors by making all cold pipes of Invar (low thermal expansion nickel-iron alloy) and metallically bonding the weak superconducting niobium and copper layers to the strong Invar foundation pipes. This implies the existence of permanent tensile strain in the superconducting and copper layers during cable operation. The pressure pipe that contains the pumped helium and the two pipes, which constitute the liquid helium supply line must also be made of Invar. Hence, in addition to six superconducting tubes with copper backing, this cable contains nine Invar pipes plus a large outer vacuum enclosure of aluminum or stainless steel.

Tape Insulated Superconducting Cables

If they were found to operate without detriment to energy losses, cryocables with helium impregnated polymer tape insulation and flexible stranded superconductors would have the advantage of not requiring Invar pipes or

sliding contraction joints in the three conductors of a three-phase ac circuit. Since tape insulation requires helium impregnation, there remains the need for coaxial superconducting shields and a pressure pipe to contain the pumped helium, just as in a system that is insulated by the fluid alone as in Fig. 3.96. The Invar pipe may of course be replaced by a stainless steel pipe with reinforced bellows.

The flexible superconducting core construction shown in Fig. 3.97 is that proposed by the Brookhaven National Laboratory [3.91]. Flat strip conductor strands have to be laid up—and possibly keyed together—to form a smooth cylindrical layer on either side of the tape-wound electrical insulation. The lay angles of the conductor strips may be so chosen that the conductor tube diameter shrinks on cool-down without significant axial contraction. This would also help to close the butt gaps between the conductor strands.

It has been suggested [3.91] that each elemental conductor strip should consist of either fairly pure copper or aluminum with a thin superconducting layer bonded to the side of the strip that faces the electrical insulation. The preferred superconducting material of the Brookhaven National Laboratory is niobium-tin ($Nb\ Sn_3$), a brittle material that has to be heat treated in position on the backing metal. $Nb\ Sn_3$ can sustain higher critical currents than other niobium alloys or niobium itself and also functions at a few degrees higher temperature, which is advantageous from the point of view of refrigerator efficiency.

The cylindrical superconducting surfaces on the stranded conductors are unlikely to exclude all magnetic flux from the underlying normal metal and

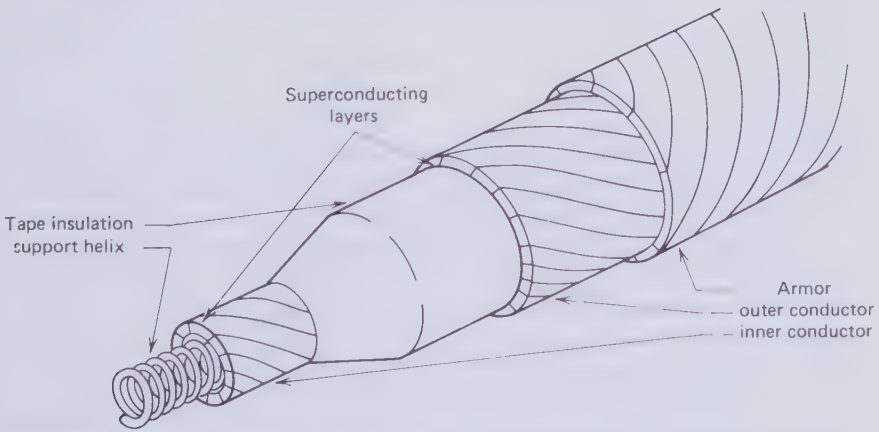

Figure 3.97 Flexible coaxial superconducting cable core structure proposed by the Brookhaven National Laboratory [3.91].

this might produce a certain amount of Joule heating that has to be absorbed by the helium coolant. Narrow butt gaps between the conductor strands through which magnetic flux leakage may occur are indeed necessary for helium penetration to the electrical insulation.

There exists yet another difficulty with this type of power conductor. The supercurrent is very likely to follow the path of individual conductor strands. This sets up a solenoidal magnetic vector potential inside and outside the superconducting layers regardless of the flux-tightness of the layers. As it is an alternating vector potential it will generate circumferential electric fields in the backing metal and metallic enclosures. The Joule losses caused by this mechanism could be severe.

Indeed loss measurements carried out on a stranded coaxial superconductor revealed large resistive losses [3.92]. They were attributed to circumferential currents induced in the helium pressure pipe. However, the method of loss measurement could not distinguish between Joule heating in the helium pipe and the normal metal in contact with the superconductor.

The cryogenic envelop of a tape insulated superconducting cable need not differ from one surrounding a fluid helium insulated system. An ingenious new feature of the Brookhaven superconducting cable is the use of one coolant stream as an expansion stage of the refrigerator, permitting heat exchange with the opposite direction stream. This eliminates the need for thermal isolation between the two coolant streams.

Terminating high-voltage superconducting power transmission lines has proved to be a particularly challenging task. It has probably been the deciding factor why, in 1979, and after a world-wide research and development effort worth on the order of $50 million, superconducting power transmission at even modest voltages has not yet been demonstrated in the laboratory.

Prospects

Owing to the mechanical complexity of superconducting cables and the quantity of exotic materials that they require, the only incentive for their development is to make them more efficient power transmitters than conventional underground cables of which the self-contained oil-paper insulated is the most effective and greatly more efficient than overhead lines. At the present time it is by no means clear that superconducting cables can attain this goal without becoming unduly expensive to manufacture and install.

There is less uncertainty about the technical viability and loss economy of liquid-nitrogen-cooled cables with aluminum conductors. However even the sponsors of the tape insulated LN_2 cooled system are pessimistic about the economic merits of this cable.

Of the various cryocables so far proposed, only the vacuum insulated, liquid-nitrogen-cooled version is claimed to be significantly more economical than self-contained oil-paper insulated cables. Furthermore it remains the only cryocable with proven transmission capability. Vacuum integrity and long-term reliability of the high-voltage insulation have to be determined by field trials involving reasonable lengths of this underground power transmission line.

REFERENCES

1.1. P. Burnier, P. Lanienceau; "Physical foundations of interest in cryomachines," *Rev. Gen. Ectricite*, Vol. 74, pp. 533–550, 1965.

1.2. *Nobel Lectures in Physics*, Elsevier Publishing Co., 1967, pp. 306–336.

1.3. F. B. Silsbee; "A note on electrical conduction in metals at low temperatures," *J. Wash. Acad. Sci.*, Vol. 6, pp. 597–602, 1916.

1.4. W. Meissner, R. Ochsenfeld; "A new effect at the onset of superconductivity," *Naturwissensch.*, Vol. 21, pp. 787–788, 1933.

1.5. F. London and H. London, "The electromagnetic equations of the supraconductor," *Proc. Roy. Soc.* (*Lond.*), Vol. 149, pp. 71–88, 1935.

1.6. A. B. Pippard, "The surface impedance of superconductors and normal metals at high frequencies," *Proc. Roy. Soc.* (*Lond.*), Vol. A191, pp. 370–384, 1947.

1.7. E. Maxwell; "Isotope effect in the superconductivity of mercury," *Phys. Rev.*, Vol. 78, p. 477, 1950.

1.8. P. W. Anderson, B. T. Mathias; "Superconductivity," *Science*, Vol. 144, pp. 373–381, 1964.

1.9. R. Reich, L. Renucci; "Influence de l'intensité du courant sur la transition état normal —état supraconducteur pour des étain de differentes puretés," *C. R. Acad. Sci. Paris*, Vol. 260, pp. 1178–1181, 1965.

1.10. Lord Raleigh; "On the selfinduction and resistance of straight conductors," *Phil. Mag.*, Vol. 21, pp. 381–394, 1886.

1.11. S. Butterworth; "Eddy-current losses in cylindrical conductors with special applications to the alternating current resistances of short coils," *Phil. Trans. Roy. Soc.* (*Lond.*), Vol. 222, pp. 57–100, 1921.

1.12. J. D. Cockcroft; "Skin effect in rectangular conductors at high frequencies," *Proc. Roy. Soc.* (*Lond.*), Vol. 122A, pp. 533–542, 1929.

1.13. H. B. Dwight: *Electrical Coils and Conductors*, McGraw Hill, 1945.

1.14. A. H. M. Arnold; "The alternating current resistance of non-magnetic conductors," H.M.S.O. London, 1946.

1.15. J. C. Maxwell; *A Treatise on Electricity and Magnetism*, Vol. 2, Oxford University Press, 1873.

1.16. A. Sommerfeld; *Electrodynamics*, Academic Press, 1952.

1.17. P. Graneau; "A re-examination of the relationship between self and mutual inductance," *J. Electron. Contr.*, Vol. 12, pp. 125–132, 1962.

1.18. W. R. Smythe; *Static and Dynamic electricity*, McGraw Hill, 1950.

1.19. J. H. Neher, M. H. McGrath; "The calculation of the temperature rise and load capability of cable systems," *AIEE Trans.*, Vol. 76, Pt. 3, pp. 752–772, 1957.

1.20. H. Goldenberg; "Some approximations to Arnold's formulae for skin and proximity effect factors for circular or shaped conductors," Electrical Research Association (England) Report F/T 203, 1961.

1.21. H. B. Dwight; "Skin effect and proximity effect in tubular conductors," *AIEE Trans.*, Vol. 41, pp. 189–198, 1922.

1.22. P. Silvester; "AC resistance and reactance of isolated rectangular conductors," *IEEE Trans.*, Vol. PAS-86, pp. 770–774, 1967.

1.23. P. Silvester; "The accurate calculation of skin effect in conductors of complicated shape," *IEEE Trans.*, Vol. PAS-87, pp. 735–742, 1968.

1.24. P. Graneau, "Alternating and transient conduction currents in straight conductors of any cross-section," *Int. J. Electron.*, Vol. 19, pp. 41–59, 1965.

1.25. P. Graneau; "Computation of losses and inter-conductor forces in low temperature ac power circuits," *Int. J. Electron.*, Vol. 22, pp. 1–18, 1967.

1.26. P. Silvester; "Modal network theory of skin effect in flat conductors," *Proc. IEEE*, Vol. 54, pp. 1147–1151, 1966.

1.27. P. Hlawiczka; *Matrix Algebra for Electronic Engineers*, New York Hayden Book Co., 1965.

1.28. A. M. H. Arnold; "Proximity effect in solid and hollow round conductors," *J. IEE, Vol. 88, pp.* 349–59, 1941.

1.29. H. B. Dwight; *Electrical Conductors and Coils*, McGraw-Hill, 1954, pp. 225–226.

1.30. F. E. Neumann; "Die mathematischen Gesetze der inducirten elektrischen Stroeme," Berliner Akademie der Wissenschaften, 1845.

1.31. F. E. Neumann; "Ueber ein allgemeines Princip der mathematischen Theorie inducirter elektrischer Stroeme," Berliner Akademie der Wissenschaften, 1847.

1.32. Pender, Del Mar; *Electrical Engineer's Handbook (Electric Power)*, Wiley 3rd Ed., 1946, pp. 14–45.

1.33. *Transmission and Distribution*, Westinghouse Reference Book, 1950, p. 71.

1.34. C. C. Barnes; *Power Cables*, Chapmann and Hall, 2nd ed., 1966.

1.35. A. Conangla, H. F. White; "Isolated phase bus enclosure loss factors," IEEE Paper No. 68 TP 19-PWR, 1968.

1.36. A. B. Niemoller; "Isolated phase bus enclosure currents," IEEE Paper No. 68 TP 89-PWR, 1968.

1.37. E. C. Elgar, R. H. Rehder, N. Swerdlow; "Measured losses in isolated phase bus and comparison with calculated values," IEEE Paper No. 68 TP 90-PWR, 1968.

1.38. S. B. Afshartous, P. Graneau; "Current distribution in the LN2 cryocable," *Cryogenics*, Vol. 10, pp. 402–405, 1970.

1.39. L. G. Kelly; *Handbook of Numerical Methods and Applications*, Addison-Wesley, 1967, Chapter 9.

1.40. A. Ralston, H. S. Wilf (Eds.); *Mathematical Methods for Digital Computers*, Wiley, Vols. I and II, 1964, 1967.

1.41. A. E. Kennelly, F. A. Laws, P. H. Pierce; "Experimental researches on skin effect in conductors," *Proc. IEE*, Vol. 34, pp. 1749–1814, 1915.

1.42. A. E. Kennely, H. A. Affel; "Skin effect resistance measurements of conductors," *Proc. Inst. Radio Eng. (N.Y.)*, Vol. 4, pp. 523–80, 1916.

1.43. A. H. M. Arnold; "Eddy-current losses in single-conductor paper-insulated lead-covered unarmored cables of a single-phase system," *J. IEE*, Vol. 89, pp. 636–45, 1942.

1.44. E. H. Ball, G. Maschio; "The ac resistance of segmental conductors as used in power cables," *IEEE Trans.*, Vol. PAS-87, pp. 1143–1148, 1968.

1.45. F. Castelli, L. Maciotta-Rolandin, P. Riner; "A new method for measuring ac resistance of large cable conductors," *IEEE Trans.*, Vol. PAS-96, pp. 414–422, 1977.

1.46. J. A. Pulsford (Ed.); *Underground Systems Reference Book*, Edison Electric Institute, 1957.

1.47. R. J. Wiseman; "AC resistance of large size conductors in steel pipe or conduit," *AIEE Trans.*, Vol. 67, pp. 1745–1758, 1948.

1.48. L. Meyerhoff, G. S. Eager; "AC resistance of segmental cables in steel pipe," *AIEE Trans.*, Vol. 68, pp. 816–834, 1949.

1.49. E. B. Forsyth et. al.; "Flexible superconducting power cables," *IEEE Trans.*, Vol. PAS-92, pp. 494–504, 1973.

1.50. P. Silvester; *Modern Electromagnetic Fields*, Prentice-Hall, 1968.

1.51. P. Graneau; "The measurement of electrical conductivity in metals research," *Materials Res.*, Vol. 1, pp. 17–25, 1962.

1.52. "Ultrapure aluminum produced," Technical News from U.S. Dept. of Commerce—National Bureau of Standards, STR-3874, 1969.

1.53. C. L. Carlson; "Aluminum versus copper for electrical conductors," *Insulation / Circuits*, Vol. 70, pp. 29–31, 1971.

1.54. G. K. White, S. B. Woods; "Electrical and thermal resistivity of the transition elements at low temperatures," *Trans. Roy. Soc. (Lond.)*, Vol. A251, pp. 273–302, 1959.

1.55. F. Pawlek, D. Rogalla; "The electrical resistivity of silver, copper, aluminum and zinc as a function of purity in the range 4–298°K," *Cryogenics*, Vol. 6, pp. 14–20, 1966.

1.56. R. Reich, V. Q. Kinh, J. Bonmarin; "Study of the resistivity of samples of beryllium of different purities as a function of temperature and the determination of the Debye temperature of the metal," *Compt. Rend.*, Vol. 256, pp. 5558–5561, 1963.

1.57. O. J. Foust; *Sodium-NaK Engineering Handbook, Vol. I, Sodium Chemistry and Physical Properties*, Gordon and Breach, 1972.

1.58. H. E. Green,; "Aluminum in the electrical industry," *Electron. Power*, Nov. 1, 1973, pp. 473–5.

1.59. P. V. Hunter, J. Temple Hazell; *Development of Power Cables*, George Newnes (Lond.), 1956.

1.60. L. E. Humphrey, R. C. Hess, G. I. Addis; "Insulated sodium conductors," *IEEE Trans.*, Vol. PAS-86, pp. 876–883, 1967.

1.61. J. A. Sinclair; "Sodium electrical conductor," Swiss Patent No. 25, 203, 1901.

1.62. J. S. Dugdale, D. Gugan; "The effect of pressure on the electrical resistance of lithium, sodium and potassium at low temperatures," *Proc. Roy. Soc. (Lond.)*, Vol. A270, pp. 186–211, 1962.

1.63. *Encyclopedia of Chemical Technology*, Vol. 18, Wiley, 2nd ed., 1969.

1.64. P. Graneau; "Thermal failure of high voltage solid dielectric cables," IEEE Paper No. A 76 037-2, 1976.

1.65. R. Reich; "Etude des propriétés électriques et supraconductrices de métaux de différentes puretés," Thesis, Faculty of Sciences of the University of Paris, 1965.

1.66. B. Broniewski, P. Burnier, and E. Carbonell; "Utilisation en électrotechnique des métaux purs aux basses températures," Revue Générale de l'Ectricité, Vol. 74, pp. 529–647, 1965.

1.67. E. N. Simons; *Guide to Uncommon Metals*, Hart Publishing Co., 1967.

1.68. D. R. Edwards; "Superconducting ac power cables," *Electr. Electron. Tech. Eng.*, March 1968.

1.69. R. W. Meyerhoff; "The fault recovery performance of a helium-insulated rigid ac superconducting cable," *IEEE Trans.*, Vol. PAS-94, pp. 1734–1741, 1975.

1.70. P. Graneau; "Trial of cryocable terminal completed," *Electr. World*, Vol. 185, No. 11, pp. 36–38, 1976.

1.71. M. Rechowicz, *Electric Power at Low Temperatures*, Clarendon Press, 1975.

1.72. "U.S.-U.S.S.R. superconducting power transmission cooperation," U.S. Energy Research and Development Administration Report ERDA-76-116, 1976.

1.73. V. L. Newhouse; *Applied Superconductivity*, Wiley, 1964.

1.74. "28th Annual electrical industry forecast," *Electr. World*, Vol. 188, No. 6, Sept. 15, 1977.

1.75. H. Cotton; *Electrical Technology*, Pitman, 1950.

2.1. "Prevention of power failures," Vol. II. A report to the Federal Power Commission, 1967.

2.2. "Prevention of power failures," Vol. I, A report to the President by the Federal Power Commission, 1967.

2.3. A. Hauspurg; "Keynote address—Underground transmission systems," IEEE Conference on Research for the Electric Power Industry, Washington, Dec. 1972.

2.4. R. W. Burrell, F. S. Young; "EEI-manufacturers 500/550 kV cable research project. Waltz Mill testing facility," *IEEE Trans.*, Vol. PAS-90, pp. 180–190, 1971.

2.5. C. A. Arkell, D. F. Johnson, J. J. Ray; "525 kV selfcontained oil-filled cable systems for Grand Coulee Third Power Plant. Design proving tests," IEEE Paper No. T 73-493-4, 1973.

2.6. "UG/underwater cables can handle up to 1100 kV," Electrical World, April 1, 1974, p. 130.

2.7. "Underground power transmission," A Report to the Federal Power Commission by the Commission's Advisory Committee on Underground Transmission, 1966.

2.8. "Underground power transmission," A study for the Electric Research Council by Arthur D. Little, Inc., Edison Electric Institute, New York, 1971.

2.9. C. Adamson; "Direct-current power transmission," *Power Eng.*, Vol. 65, p. 76, 1961.

2.10. H. W. Beaty; "12th Annual T & D construction survey," *Electr. World*, Vol. 188, Aug. 15, 1977, pp. 43–50.

2.11. J. S. Townsend; *Electricity in Gases*, Oxford University Press, 1915.

2.12. F. H. Sanders; "Measurement of the Townsend Coefficients by Collision," *Phys. Rev.*, Vol. 41, p. 667–677, 1932 and Vol. 44, p. 1020–1024, 1933.

2.13. T. W. Dakin, D. Berg; "Theory of gas breakdown," *Progr. Dielectrics* (J. B. Birks, J. Hart, Eds), Vol. 4, pp. 153–98, 1962.

2.14. J. D. Cobine, *Gaseous Conductors*, Dover Publications, 1958.

2.15. R. Geballe, M. A. Harrison; "Negative Ion Formation in Oxygen," *Phys. Rev.*, Vol. 85, p. 372, 1952.

2.16. M. J. Mulcahy, P. Bolin, F. Tse, W. R. Bell; "A review of insulation breakdown and switching in gas insulation," *Insulation/Circuits*, Aug. 1970, pp. 55–61.

2.17. H. Raether, "Uber den Aufbau der Gasentladungen," *Zeit. Phys.*, Vol. 117, pp. 375–398 and 524–542, 1941.

2.18. L. B. Loeb, J. M. Meek; *The mechanism of the Electric Spark*, Stanford University Press, 1942.

2.19. J. M. Meek, J. D. Craggs; *Electrical Breakdown of Gases*, Oxford University Press, 1953.

2.20. P. Graneau; "Corona onset between coaxial electrodes," Thesis, University of Nottingham, 1955.

2.21. G. C. Lichtenberg; *Novi. Comment. Goett.*, Vol. 8, p. 168, 1777.

2.22. F. H. Merrill, A. von Hippel; "The atomphysical interpretation of Lichtenberg figures and their application to the study of gas discharge phenomena," *J. Appl. Phys.*, Vol. 10, pp. 873–87, 1939.

2.23. M. Toepler; "Ueber die physikalischen Grundgesetze der in der Isolatorentechnik auftretenden Gleiterscheinungen," *Arch. Elektrotech.*, Vol. 10, pp. 157–185, 1921.

2.24. P. Graneau; "Lichtenberg figures produced by high-voltage discharges in vacuum," IEEE Transactions, Vol. EI-8, pp. 87–91, 1973.

2.25. R. Gomer; *Field Emission and Field Ionization*, Harvard University Press, 1961.

2.26. T. Kelsey; "Measurement of prebreakdown current and X-ray emission in vacuum," *J. Phys. D*, Vol. 5, pp. 569–574, 1972.

2.27. P. Graneau, D. B. Montgomery; "High power vacuum insulated LN2 cryocable loop," 1975 Annual Report on the Conference on Electrical Insulation and Dielectric Phenomena, National Research Council and the National Academy of Science.

2.28. P. Graneau, D. B. Montgomery; "Insulator flashover mechanism in vacuum insulated cryocables," *J. Vacuum Sci. Technol.*, Vol. 13, pp. 1081–1087, 1976.

2.29. I. Brodie; "Studies of field emission and electrical breakdown between extended nickel surfaces in vacuum," *J. Appl. Phys.*, Vol. 35, pp. 2324–32, 1964.

2.30. H. W. Graybill, J. A. Williams; "Underground power transmission with isolated-phase gas-insulated conductors," *IEEE Trans.*, Vol. PAS-89, p. 17, 1970.

2.31. A. Diessner, J. G. Trump; "Free conducting particles in coaxial compressed-gas-insulated systems," *IEEE Trans.*, Vol. PAS-89, pp. 1970–1978, 1970.

2.32. J. C. Cronin, E. R. Perry; "Optimization of insulators for gas insulated systems," *IEEE Trans.*, Vol. PAS-92, pp. 558–564, 1973.

2.33. A. Pedersen; "The effect of surface roughness on breakdown in SF_6," *IEEE Trans.*, Vol. PAS-94, pp. 1749–1754, 1975.

2.34. C. M. Cooke; "Ionization, electrode surfaces and discharges in SF6," *IEEE Trans.*, Vol. PAS-94, pp. 1518–1522, 1975.

2.35. E. B. Gaenger, A. A. Leibold; "The influence of foreign particles on dielectric strength in SF6 installations," IEEE Publication No. A. 76 152-9, 1976.

2.36. C. M. Cooke, R. E. Wootton, A. H. Cookson; "Influence of particles on ac and dc electrical performance of gas insulated systems at extra-high-voltage," *IEEE Trans.*, Vol. PAS-96, pp. 768–777, 1977.

2.37. A. H. Cookson, O. Farish, G. M. L. Sommerman; "Effect of conducting particles on ac corona and breakdown in compressed SF6," *IEEE Trans.*, Vol. PAS-91, p. 1329, 1972.

2.38. G. D. Theophilus, R. G. van Heeswijk, K. D. Srivastava; "Comparative investigations of dc and 60 Hz prebreakdown behavior of vacuum insulation," *IEEE Trans.*, Vol. PAS-94, pp. 1859–1867, 1975.

2.39. J. C. Trump; "Insulation strength of high-pressure gases and of vacuum," *Dielectric Materials and Applications* (A. R. von Hippel, Ed.), MIT Press, 1954.

2.40. T. J. Lewis; *Progress in Dielectrics* (J. B. Birks, J. H. Schulman Eds.), Wiley, 1959.

2.41. I. Adamczewski; *Ionization, Conductivity and Breakdown in Dielectric Liquids*, Taylor and Francis, London, 1969.

2.42. Z. Krasucki, H. F. Church, C. G. Garton; British Electrical Research Association Report 107–598, 1960.

2.43. A. H. Sharbaugh, P. K. Watson; *Conduction and Breakdown in Liquid Dielectrics, Progress in Dielectrics*, Vol. 4 (J. B. Birks, J. Hart, Eds) Academic Press, 1962.

2.44. C. G. Garton, Z. Krasucki; *Proc. Roy. Soc.* (*Lond.*), Vol. A280, p. 211, 1964.

2.45. Z. Krasucki; "Breakdown of Liquid Dielectrics," *Proc. Roy. Soc.* (*Lond.*), Vol. A294, pp. 393–404, 1966.

2.46. Z. Krasucki; "High-field conduction in liquid dielectrics," Proceedings of the International Colloquium on Phenomena of Conduction in Dielectric Liquids, Grenoble, France, 1968.

2.47. J. J. O'Dwyer; *The Theory of Electrical Conduction and Breakdown in Solid Dielectrics*, Clarendon Press, Oxford, 1973.

2.48. K. H. Stark, C. G. Garton; "Electric strength of irradiated polythene," *Nature*, Vol. 176, pp. 1225–1226, 1955.

2.49. P. P. Budenstein; "Dielectric Breakdown in Solids," Technical Report RG-75-25, U.S. Army Missile Command, Redstone Arsenal, Alabama, 1974.

2.50. V. Fock; *Arch. Elektrotech.*, Vol. 19, p. 71, 1927.

2.51. P. H. Moon, *IEE Trans.*, Vol. 50, p. 1008, 1931.

2.52. S. Whitehead; *Dielectric Breakdown of Solids*, Oxford Press, 1951.

2.53. S. M. Sze; "Current Transport and Maximum Dielectric Strength of Silicon Nitride Films," *J. Appl. Phys.*, Vol. 38, p. 2951, 1967.

2.54. N. Klein; *IEEE Trans.*, Vol. ED-13, p. 788, 1966.

2.55. J. R. Hanscombe; "High Temperature Electrical Breakdown in Sodium Chloride," *Austr. J. Phys.*, Vol. 15, p. 504, 1962.

2.56. S. Chou, H. Brooks; "Theory of Thermal Breakdown of Sodium Chloride," *J. Appl. Phys.*, Vol. 41, p. 4451, 1970.

2.57. L. Inge, N. Semenoff, A. Walther; *Zeit. Phys.*, Vol. 64, p. 273, 1925.

2.58. A. W. Stannet, D. H. Schroff; "Temperature Coefficient of Resistivity of Polythene and Oil-Impregnated Paper," *Nature*, Vol. 179, p. 94, 1957.

2.59. L. G. Brazier; "The breakdown of cables by thermal instability," *IEE J.*, Vol. 77, p. 104, 1935.

2.60. D. M. Robinson, *Dielectric Phenomena in High Voltage Cables*, Chapman and Hall, London, 1936.

2.61. R. S. Burington; *Handbook of Mathematical Tables and Formulas*, McGraw-Hill, 1973.

2.62. K. H. Stark, C. G. Garton; "Electric strength of irradiated polythene," *Nature*, Vol. 176, pp. 1225–1226, 1955.

2.63. J. Block, D. G. LeGrand; "High field electromechanical effects in dielectrics under pulsed stress," 1968 Annual Report: Conference on Electrical Insulation and Dielectric Phenomena, National Academy of Sciences, Washington.

2.64. N. Parkman, G. F. Goldspink, W. G. Lawson; "Effect of pressure and constraint on the apparent electric strength of polythene," *Electron. Lett.*, Vol. 1, pp. 98–100, 1965.

2.65. K. Yahagi, S. Mita; "Effect of elongation on dielectric strength in polyethylene," *IEE Proc.* 1975 Conference on Dielectric Materials, Measurements and Applications, Cambridge University.

2.66. R. P. Mott; "Status of 138 kV solid dielectric cables being evaluated at Waltz Mill," IEEE Paper No. C 75 007-0, 1975.

2.67. P. Graneau; "Thermal failure of high voltage solid dielectric cables," IEEE Paper No. A 76 037-2, 1976.

2.68. A. Renfrew; *Polythene*, Interscience, 1960.

2.69. W. G. Lawson; "Effects of temperature and techniques of measurement on the intrinsic electric strength of polyethylene," *Proc. IEE*, Vol. 113, pp. 197–202, 1966.

2.70. R. Cooper, C. T. Elliott; "Formative processes in the dielectric breakdown of potassium bromide," *Brit. J. Phys.*, Vol. 17, pp. 481–488, 1968.

2.71. D. W. Kitchin, O. S. Pratt; "Treeing in polyethylene as a prelude to breakdown," *IEE Trans.*, Vol. 77, pp. 180–186, 1958.

2.72. W. Vahlstrom; "Investigation of insulation deterioration in 15 kV and 22 kV polyethylene cables removed from service," *IEEE Trans.*, Vol. PAS-91, pp. 1023–1035, 1972.

2.73. R. M. Eichhorn; "Effect of moisture on needle testing of polyethylene," 1973 Annual Report: Conference on Electrical Insulation and Dielectric Phenomena, National Academy of Sciences (Washington), pp. 289–298.

2.74. J. Sletback, A. Botne; "A study of inception and growth of water trees and electrochemical trees in PE and XLPE insulation," IEEE Conference Record 1976 International Symposium on Electrical Insulation, pp. 228–231.

2.75. T. Tanaka, T. Fukuda; "Residual strain and water trees in XLPE and PE cables," 1974 Annual Report Conference on Electrical Insulation and Dielectric Phenomena, National Academy of Sciences (Washington).

2.76. C. Katz, B. S. Bernstein; "Electrochemical treeing at contaminants in polyethylene and crosslinked polyethylene insulation," 1973 Annual Report: Conference on Electrical Insulation and Dielectric Phenomena, National Academy of Sciences (Washington).

2.77. G. H. Hunt, M. J. Koulopoulos, P. H. Ware; "Dielectric strength and voltage life of polyethylene," *IEE Trans.*, Vol. PAS-77, pp. 25–28, 1958.

2.78. N. D. Kenney, M. J. Koulopoulos; "115 kV and 138 kV polyethylene insulated cable installations and cable evaluation data," 1968 CIGRE, Paper No. 21-07.

2.79. G. Bahder, C. Katz; "Treeing effects in PE and XLPE insulation," 1972 Annual Report: Conference on Electrical Insulation and Dielectric Phenomena, National Academy of Sciences (Washington), pp. 190–199.

2.80. D. W. Kitchen, O. S. Pratt; "An accelerated screening test for polyethylene high-voltage insulation," *IEEE Trans.*, Vol. PAS-81, pp. 112–119, 1962.

2.81. A. C. Ashcraft, R. M. Eichhorn, R. G. Shaw; "Laboratory studies of treeing in solid dielectrics and voltage stabilization of polyethylene," IEEE Conference Record: 1976 International Symposium on Electrical Insulation, pp. 213–218.

2.82. R. C. Lever, B. T. Mackenzie, N. Singh; "Influence of inorganic fillers on the voltage endurance of solid dielectric power cables," IEEE Paper No. T 73 125-2, 1973.

2.83. R. Cooper, D. W. Auckland; "The breakdown of composite insulation," 1972 Annual Report: Conference on Electrical Insulation and Dielectric Phenomena, National Academy of Sciences (Washington), pp. 151–6.

2.84. M. Ieda, M. Nawata; "DC treeing breakdown associated with space charge formation in

polyethylene," IEEE Conference Record: 1976 International Symposium on Electrical Insulation, pp. 201–204.

2.85. H. Wagner; "The influence of superstructures on the electrical breakdown of partially crystalline polymers," 1974 Annual Report: Conference on Electrical Insulation and Dielectric Phenomena, National Academy of Sciences (Washington), pp. 62–70.

2.86. F. Noto, N. Yoshimura; "Voltage and frequency dependence of tree growth in polyethylene," 1974 Annual Report: Conference on Electrical Insulation and Dielectric Phenomena, National Academy of Sciences (Washington), pp. 207–217.

2.87. L. Cranberg; "The initiation of electrical breakdown in vacuum," *J. Appl. Phys.*, Vol. 23, pp. 518–522, 1952.

2.88. M. M. Menon, K. D. Srivastava; "Electrostatic detection of large microparticles (>10 μm) in a high voltage vacuum insulated apparatus," *IEEE Trans.*, Vol. EI-9, pp. 142–50, 1974.

2.89. P. A. Chatterton, M. M. Menon, K. D. Srivastava; "Processes involved in the triggering of vacuum breakdown by low-velocity microparticles," *J. Appl. Phys.*, Vol. 43, pp. 4536–4542, 1972.

2.90. G. D. Theophilus, R. G. van Heeswijk, K. D. Srivastava; "Comparative investigations of dc and 60 Hz pre-breakdown behavior of vacuum insulation," *IEEE Trans.*, Vol. PAS-94, pp. 1859–1867, 1975.

2.91. D. Alpert, D. A. Lee, E. M. Lyman, H. E. Tomaschke; "Initiation of electrical breakdown in ultrahigh vacuum," *J. Vacuum Sci. Technol.*, Vol. 1, pp. 35–50, 1964.

2.92. P. Graneau, L. B. Thompson, M. O. Hoenig; "High power transmission test of short VI-LN2 cryocable," IEEE Conference Record: 1976 Underground T and D Conference, pp. 424–430.

2.93. E. L. Garwin, E. W. Hoyt, M. Rabinowitz, J. Jurow; "Electron-induced desorption of gases from aluminum," *Proceedings of the 4th International Vacuum Congress*, pp. 131–136, 1968.

2.94. B. Juettner, H. Wolff, B. Altrichter; "Stability of field electron emission and vacuum breakdown. Investigation with field emission microscopy and Auger electron spectroscopy," *Phys. Stat. Sol.*, Vol. (a)27, pp. 403–12, 1975.

2.95. "Development and field trial of 138 kV LN2 cryocable. Stage 1: Single-phase termination," Electric Power Research Institute Report EPRI 7813-1, 1976.

2.96. J. D. Cross, P. A. Chatterton; "The microstructure of condensed H_2O films when exposed to fields and breakdown in vacuum," *J. Phys.* D, Vol. 5, pp. 2064–2067, 1972.

2.97. L. C. Van Atta, R. J. Van de Graaf, H. A. Barton; "A New Design for a High-Voltage Discharge Tube," *Phys. Rev.*, Vol. 43, pp. 158–159, 1933.

2.98. J. G. Trump, R. J. van de Graaf; "The insulation of high voltages in vacuum," *J. Appl. Phys.*, Vol. 18, pp. 327–332, 1947.

2.99. B. P. Singh, P. A. Chatterton; "A computer simulation of microdischarge development," Proceedings of the 6th International Symposium on Discharges and Electrical Insulation in Vacuum, Swansea, pp. 55–60, 1974.

2.100. P. A. Redhead, J. P. Hobson, E. V. Kornelsen; *The Physical Basis of Ultrahigh Vacuum*, Chapman and Hall, 1968.

2.101. S. Dushman, J. M. Lafferty; *Scientific Foundations of Vacuum Technique*, Wiley, 1966.

2.102. P. Graneau, D. B. Montgomery; "Insulator flashover mechanism in vacuum insulated cryocables," *J. Vacuum Sci. Technol.*, Vol. 13, pp. 1081–1087, 1976.

2.103. P. Graneau, L. B. Thompson; "Design and testing of a 138 kV prototype termination for

a vacuum insulated LN2 cryocable," IEEE Conference Record: 1976 Underground T and D Conference, pp. 431–436.

2.104. P. Graneau, J. Jeanmonod; "Voltage surge performance of vacuum insulated cryocable," *IEEE Trans.*, Vol. EI-6, pp. 39–47, 1971.

2.105. P. Graneau, H. M. Schneider; "Vacuum insulation for cryocables and its resistance to discharges," *IEEE Trans.*, Vol. EI-9, pp. 63–68, 1974.

2.106. C. H. DeToureil, K. D. Srivastava, U. J. Woelke; "Experimental observations of surface charging of high voltage insulators for vacuum apparatus," *IEEE Trans.*, Vol. EI-7, pp. 176–179, 1972.

2.107. C. H. DeTourreil, K. D. Srivastava; "Mechanism of surface charging of high voltage insulators in vacuum," *IEEE Trans.*, Vol. EI-8, pp. 17–21, 1973.

2.108. J. P. Shannon, S. F. Philp, J. G. Trump; "Insulation of high voltage across solid insulators in vacuum," *J. Vacuum Sci. Technol.*, Vol. 2, pp. 234–239, 1965.

2.109. "Progress in the application of vacuum insulation to cryocables," National Science Foundation Report No. NSF-RANN-C670, 1974.

2.110. A. R. von Hippel; *Dielectric Materials and Application*, MIT Press, 1954.

2.111. E. O. Forster; "Effect of molecular structure on dielectric properties of polymers: I Thermoplastics," 1973 Annual Report: Conference on Electrical Insulation and Dielectric Phenomena, National Academy of Sciences (Washington), pp. 447–455.

2.112. R. Tobazeon, E. Gartner; "On the behavior of ions at insulator/liquid interfaces and its consequence for the losses in impregnated insulation," 1974 Annual Report: Conference on Electrical Insulation and Dielectric Phenomena, National Academy of Sciences (Washington), pp. 404–408.

2.113. H. A. Pohl; "Polymers with dielectric constants above 100:nomadic polymerization," 1972 Annual Report: Conference on Electrical Insulation and Dielectric Phenomena, National Academy of Sciences (Washington), pp. 381–388.

2.114. O. F. Mosotti; *Mem. Math. Fis. Modena*, [II], Vol. 24, p. 49, 1850.

2.115. N. E. Hill, W. E. Vaughan, A. H. Price, M. Davies; *Dielectric Properties and Molecular Behavior*, Van Nostrand, London, 1969.

2.116. K. N. Mathes; "Dielectric properties of cryogenic liquids," *IEEE Trans.*, Vol. EI-2, pp. 24–32, 1967.

2.117. R. N. Allan, E. Kuffel; "Dielectric losses in solids at cryogenic temperatures," *Proc. IEE*, Vol. 115, pp. 432–440, 1968.

2.118. M. J. Jefferies, S. H. Minnich, B. C. Belanger; "High voltage testing of high-capacity liquid nitrogen cooled cable," *IEEE Trans.*, Vol. PAS-92, pp. 514–518, 1973.

2.119. E. Gartner, R. Tobazeon; "On the behavior of liquid/solid insulations at very low frequency," IEEE Conference Record: 1976 International Symposium on Electrical Insulation, pp. 69–71.

2.120. E. B. Forsyth, G. A. Mulligan, J. W. Beck, J. A. Williams; "The technical and economic feasibility of superconducting power transmission: A case study," *IEEE Trans.*, Vol. PAS-94, pp. 161–169, 1975.

2.121. K. Matsuura, H. Kubo, T. Miyazaki; "Development of polypropylene laminated paper insulated EHV power cables," IEEE Conference Record: 1976 Underground T and D Conference, pp. 322–329.

2.122. Z. Iwata, H. Shii, M. Kinoshita, H. Hirukawa, E. Kawai; "New modified polyethylene paper for EHV cable insulation," *IEEE Trans.* Vol. PAS-96, pp. 1573–1582, 1977.

2.123. B. Fallou, M. Bobo; "Electrical properties of insulating materials at cryogenic tempera-

tures," 1973 Annual Report: Conference on Electrical Insulation and Dielectric Phenomena, National Academy of Sciences (Washington), pp. 514–523.

2.124. V. V. Daniel; *Dielectric Relaxation*, Academic Press, 1967.

2.125. G. Bogner; "Research at Siemens Laboratories on large scale applications of superconductivity," 1975 International Conference on the Technical Applications of Superconductivity held in the USSR.

2.126. S. J. Rigby, B. M. Weedy; "Liquid nitrogen impregnated tape insulation for cryoresistive cable," *IEEE Trans.*, Vol. EI-10, pp. 1–8, 1975.

2.127. W. R. Smythe; *Static and Dynamic Electricity*, McGraw-Hill, 1950.

2.128. I. A. Cermak, P. Silvester; "Solution of 2-dimensional field problems by boundary relaxation," *Proc. IEE, Vol.* 115, *pp.* 1341–1348, 1968.

3.1. G. J. Crowdes; "Polyethylene promises improved HV cables," *Electr. World*, March 11, 1963.

3.2. H. Brackelmann, W. Rasquin; "Conductor cooled high power cable with stainless steel cooling pipe," *Elektrotech. Zeit.*-A, Vol. 97, pp. 148–152, 1976.

3.3. L. Deschamps, A. Lacoste, A. M. Schwab; "Prospects of development in France of electric power transmission by insulated EHV cables," IEEE Publication 76-CH-1119-7-PWR, pp. 459–465, 1976.

3.4. F. J. Miranda, P. Gazzana Priaroggia; "Recent advances in selfcontained oil-filled cable systems," *Electr. Power*, Feb. 1977, pp. 136–140.

3.5. F. J. Miranda, P. Gazzana Priaroggia; "Selfcontained oil-filled cables. A review of progress," *Proc. IÊE*, Vol. 123, pp. 229–238, 1976.

3.6. J. D. Endacott; "EHV underground cable technology: present and future," *Electron. Power*, Vol. 21, pp. 20–25, 1975.

3.7. F. H. Buller, J. H. Neher; "The thermal resistance between cables and a surrounding pipe or duct wall," *IEEE Trans.*, Vol. 72, pp. 1260–1275, 1953.

3.8. P. Ralston, G. H. West; "The artificial cooling by water of underground cables," CIGRE 1960, Paper No. 215.

3.9. H. N. Cox; "Assisted cooling of transmission cables," *Electr. Rev.*, Dec. 8, 1967, pp. 2–5.

3.10. C. C. Barnes, et. al.; "Power ratings of 275 kV and 400 kV cables in the British transmission system," CIGRE 1966, Paper No. 207.

3.11. H. K. Beale et. al.; "The application of intensive cooling techniques to oil-filled cables and accessories for heavy duty transmission circuits," CIGRE 1968, Paper No. 21-09.

3.12. J. D. Endacott et. al.; "Thermal design parameters used for high capacity EHV cable circuits in Great Britain," CIGRE 1970, Paper No. 21-03.

3.13. B. M. Weedy; *Electric Power Systems*, Wiley, London, 1972.

3.14. J. A. Hitchcock, M. J. Thewell; "The cooling of underground EHV transmission cables," *IEEE Trans.*, Vol. PAS-87, pp. 129–134, 1968.

3.15. H. W. Holdup, E. Occhini, D. J. Skipper; "Thermo-mechanical behavior of large conductor cables," IEEE Paper No. 31 TP 67-478, 1967.

3.16. C. A. Arkel et al. "The development and application of forced cooling techniques to EHV cable systems in the U.K.," CIGRE 1976, Paper No. 21-02.

3.17. Genereaux; *Chem. Metallurg. Eng.*, Vol. 44, p. 241, 1937.

3.18. C. Kittel; *Introduction to Solid State Physics*, John Wiley, 1971.

3.19. P. Gazzana-Priaroggia, G. Maschio; "Continuous long length ac and dc submarine HV

power cables: The present state of the art," *IEEE Trans.*, Vol. PAS-92, pp. 1744–1751, 1973.

3.20. P. Gazzana-Priaroggia, J. H. Piscioneri, S. W. Margolin; "The Long Island Sound submarine cable interconnection," *IEEE Spectrum*, Vol. 8, pp. 63–71, 1971.

3.21. I. Eyraud, L. R. Horne; "The 300 kV direct current submarine cables transmission between British Columbia mainland and Vancouver Island," CIGRE 1970, Paper No. 21-07.

3.22. "Underwater cable fault due to thermal runaway," Electrical World, May 1, 1971, pp. 52–53.

3.23. E. P. C. Watson, E. J. Brooks, C. H. Gosling; "Canals as cable routes," *Proc. IEE*, Vol. 14, pp. 510–518, 1967.

3.24. B. O. N. Hansson; "A submarine cable for 100 kV dc power transmission," *AIEE Trans.*, Vol. 78, pp. 599–605, 1954.

3.25. A. L. Williams, E. L. Davey, J. N. Gibson; "The 250 kV submarine power cable interconnection between the North and South Islands of New Zealand," *IEE Proc.*, January 1966, pp. 121–33.

3.26. H. K. Beale, P. R. Howard, A. W. Stannett; "Gas-filled lapped polyethylene as a cable dielectric," IEEE Paper No. 31 CP 67-514, 1967.

3.27. H. K. Beale; "The realities of underground cables," *Electron. Power*, May 1973, pp. 163–65.

3.28. A. W. Stannett, J. A. M. Gibbons; "Case history of the development of the design concepts for a novel cable," *Electron. Power*, May 1976, pp. 299–303.

3.29. D. R. Edwards, D. R. G. Melville; "An assessment of the potential of EHV polypropylene/paper laminate insulated selfcontained oil-filled cables," IEEE Conference Record: 1974 Underground Transmission and Distribution Conference, Dallas, Texas, pp. 529–35.

3.30. Z. Iwata, H. Shii, M. Kinoshita, H. Hirukawa, E. Kawai; "New modified polyethylene paper proposed for UHV cable insulation," *IEEE Trans.*, Vol. PAS-96, pp. 1573–1582, 1977.

3.31. "Evaluation of the economical and technological viability of various underground transmission systems for long feeds to urban load areas," U.S. Department of Energy Report HCP/T-2055/1, 1977.

3.32. C. C. Barnes, P. M. Hollingsworth, R. S. Orchard; "Progress with underground transmission cable engineering in Great Britain," *IEEE Trans.*, Vol. PAS-86, pp. 93–105, 1967.

3.33. L. A. Kilar, J. S. Engelhardt; "Ultimate power capabilities of HPOF pipe-type cable systems," *IEEE Trans.*, Vol. PAS-92, pp. 780–789, 1973.

3.34. G. Bahder, A. F. Corry, R. B. Blodgett, E. E. McIlveen, A. L. McKean; "550 kV high pressure oil-filled pipe cable development in the U.S.A.," 1976 CIGRE, Paper No. 21-11.

3.35. R. B. Blodgett, J. Sasso; "Glass-reinforced epoxy-resin pipe for pipe-type cable," *IEEE Trans.*, Vol. PAS-86, pp. 1037–1041, 1967.

3.36. C. T. Hatcher, R. W. Gilette, R. W. Burrell; "345 kV underground transmission on the Consolidated Edison Company of New York system," *IEEE Trans.*, Vol. PAS-85, pp. 353–374, 1966.

3.37. R. W. Gillette, F. M. Hull; "Pipe-type cable installation techniques," *AIEE Trans.*, June 1954, pp. 587–599, 1954.

3.38. F. E. Kulman; "Corrosion control of underground power cables in New York," *AIEE Trans.*, August 1954, pp. 745–760, 1954.

3.39. E. D. Eich; "EEI-Manufacturers 500/550 kV cable research project. Cable B—High pressure oil paper pipe type," *IEEE Trans.*, Vol. PAS-90, pp. 212–223, 1971.

3.40. J. Notaro, D. J. Webster; "Thermal analysis of forced cooled cables," *IEEE Trans.*, Vol. PAS-90, pp. 1225–1231, 1971.

3.41. J. L. Williams, A. Zanona, R. J. Nease; "Forced-cooling tests on a 138 kV pipe cable circuit," *IEEE Trans.*, Vol. PAS-90, pp. 1246–1255, 1971.

3.42. R. Slutz, L. R. Glicksman, W. M. Rohsenow, M. Buckweitz; "Measurement of fluid flow resistance for forced cooled underground transmission lines," *IEEE Trans.*, Vol. PAS-94, pp. 1831–1834, 1975.

3.43. R. S. Abdulhadi, J. C. Chato; "Combined natural and forced convection cooling of underground electric cables," *IEEE Trans.*, Vol. PAS-96, pp. 1–8, 1977.

3.44. F. Bender, D. Purnhagen; "Evaluation of cooling equipment for forced cooled cables," IEEE Conference Record: 1972 Underground T and D Conference, pp. 227–235.

3.45. T. H. Roughley, J. T. Corbett, G. L. Winkler, G. S. Eager, S. E. Turner; "Design and installation of a 138 kV high-pressure, gas-filled pipe cable utilizing segmental aluminum conductors," *IEEE Trans.*, Vol. PAS-93, pp. 658–68, 1974.

3.46. O. Mattison, S. Wretemark; "Synthetic insulated cables," 1976 CIGRE, Paper No. 21-09.

3.47. M. A. Charoy, R. F. Jocteur; "Very high tension cables with extruded polyethylene insulation," *IEEE Trans.*, Vol. PAS-90, pp. 777–784, 1971.

3.48. F. M. McAvoy, E. E. McIlveen; "Development and installation of 138 kV cable for tests at EEI Waltz Mill Station: Cable 26," *IEEE Trans.*, Vol. PAS-91, pp. 1464–1469, 1972.

3.49. P. Metra, A. Lombardi; "Discussion on the behavior of extruded cables in water," IEEE Conference Record: 1976 Underground T & D Conference, pp. 346–352.

3.50. R. M. Eichhorn; "Measurement of water vapor transmission through polyethylene electrical insulation," *Polymer Eng. Sci.*, Vol. 10, pp. 32–37, 1970.

3.51. J. P. Lozes; "Special report on development and installation of 138 kV cable systems for tests at EEI Waltz Mill Station," *IEEE Trans.*, Vol. PAS-91, pp. 1420–1426, 1972.

3.52. G. Bahder, A. L. McKean, J. C. Carroll; "Development and installation of 138 kV cable system for tests at EEI Waltz Mill station: Cable 21," *IEEE Trans.*, Vol. PAS-91, pp. 1427–1433, 1972.

3.53. G. S. Eager, D. A. Silver; "Development and installation of 138 kV cable for test at EEI Waltz Mill station: Cable 22," *IEEE Trans.*, Vol. PAS-91, pp. 1434–1442, 1972.

3.54. H. C. Anderson, M. A. Rutherford, E. B. Cox; "Development and installation of 138 kV cable systems for tests at EEI Waltz Mill station: Cable 23," *IEEE Trans.*, Vol. PAS-91, pp. 1443–1447, 1972.

3.55. L. D. Blais; "Development and installation of 138 kV cable for tests at EEI Waltz Mill station: Cable 24," *IEEE Trans.*, Vol. PAS-91, pp. 1448–1456, 1972.

3.56. R. R. Howard, J. G. Valdes; "Design and development of 138 kV solid dielectric cable for tests at Waltz Mill station," *IEEE Trans.*, Vol. PAS-91, pp. 1457–1463, 1972.

3.57. D. W. Kitchen, O. S. Pratt; "Jointing polyethylene insulated submarine cables," *IEEE Trans.*, Vol. PAS-78, 1959.

3.58. W. Rasquin; "Limits of power transmission with internally water cooled high voltage cables," *ETZ-A*, Vol. 95, pp. 65–68, 1974.

3.59. A. Lacoste, A. Royere, J. Lepers, P. Benard; "Experimental construction prospects for the use of 225 kV-600 MVA links using polyethylene insulated cables with forced external water cooling," 1974 CIGRE, Paper No. 21–12.

3.60. R. D. Naybour; "The influence of water on the electric strength of an ethylene-propylene insulation," *IEEE Trans.*, Vol. EI-13, pp. 59–64, 1978.

3.61. P. Graneau; "Solid dielectric cables for underwater power transmission," IEEE Publication 72 COH 660-1 OCC, pp. 427–30, 1972.

3.62. "Guide to the use of gas cable systems," Report of the Electric Power Research Institute, September 1975.

3.63. "Optimized design for gas cable systems," Report of the Electric Power Research Institute, September 1975.

3.64. T. E. Chenoweth, F. A. Yeoman, A. H. Cookson; "Epoxy casting composition for UHV service in compressed SF_6 insulated equipment," IEEE Publication No. 77 CH 1273-2-EI.

3.65. E. F. Geary, L. A. Kilar; "Single SF_6 line carries generator output," *Electr. World*, October 15, 1975, pp. 61–63.

3.66. B. F. Hampton; "A flexible compressed gas insulated cable," IEE Conference Publication 44, pp. 61–64, 1968.

3.67. T. F. Brandt, P. C. Netzel, J. Z, Ponder; "Progress in insulator development for flexible gas insulated transmission systems," IEEE Publication No. 77 CH 1273-2-EI, pp. 331–335, 1977.

3.68. B. F. Hampton, D. N. Browning, R. M. Mayers; "Flexible SF_6 cables," *IEE Proc.*, Vol. 123, pp. 159–164, 1976.

3.69. R. Samm; "Flexible gas cables," *EPRI J.*, Vol. 3, p. 59, 1978.

3.70. H. C. Doepken; "Compressed gas insulated cables with increased ampacity and reduced cost," IEEE Conference Record: 1974 Underground T and D Conference, pp. 536–540.

3.71. S. Fukuda; "Ampacity of direct buried EHV cables insulated with SF_6 gas," *IEEE Trans.*, Vol. Pas-89, pp. 486–490, 1970.

3.72. H. C. Doepken; "Calculated heat transfer characteristics of air and SF_6," *IEEE Trans.*, Vol. PAS-89, pp. 1979–1985, 1970.

3.73. R. B. Scott; *Cryogenic Engineering*, Van Nostrand, 1959.

3.74. R. McFee; "Applications of superconductivity to the generation and distribution of electric power," *Electr. Eng.*, Vol. 81, pp. 122–129, 1962.

3.75. P. Klaudy; "Elektrische Energieversorgungs- und Ubertragungseinrichtungen mit tiefst gekuhlten Leitern," *Elektrotech. Maschinenbau*, Vol. 82, pp. 275–281, 1965.

3.76. E. C. Rogers, D. R. Edwards; "Design for a 750 MVA superconducting power cable," *Electr. Rev.*, Sept. 1967, pp. 2–5.

3.77. W. F. Gauster, D. C. Freemann, H. M. Long; "Applications of superconductivity to the improvement of electrical energy economics," World Power Conference, Lausanne, Switzerland, Paper No. 56, 1964.

3.78. S. Neal; "Cryogenic transmission in the power industry of the future," *Proceedings of the American Power Conference*, Vol. 30, pp. 1210–1217, 1968.

3.79. P. M. O'Farrell, E. G. Cravalho, W. M. Toscano; "Thermal performance of an LNG cooled power transmission line," 1974 International Cryogenic Engineering Conference, Kyoto, Japan.

3.80. "Superconducting transmission of electric power," U.S. Energy Research and Develop-

ment Administration, Office of the Assistant Administrator for Conservation, 1976.

3.81. J. W. Dean, H. L. Laquer; "Conceptual design of a dc superconducting power transmission line," IEEE Conference Record 76 CH1119-7-PWR, pp. 417–423, 1976.

3.82. P. Graneau, H. C. Parish, J. L. Smith; "Refrigeration requirements of the LN_2 cryocable," *Trans. ASME*, Vol. 93, Series B, pp. 1161–1165, 1971.

3.83. P. Graneau, L. B. Thompson; "Design and testing of a 138 kV prototype termination for vacuum insulated LN2 cryocable," IEEE Conference Record 76 CH 1119-7-PWR, pp. 431–436, Underground T and D Conference 1976.

3.84. P. Graneau, L. B. Thompson, M. O. Hoenig; "High power transmission tests of short VI-LN2 cryocable loop," IEEE Conference Record 76 CH 1119-7-PWR, pp. 424–430, Underground T and D Conference 1976.

3.85. P. Graneau; "Trial of cryocable terminal completed," Electrical World, June 1, 1976, pp. 36–38.

3.86. P. Graneau, H. C. Parish, J. L. Smith; "Refrigeration requirements of the LN2 cryocable," *ASME Trans.*, Vol. 93, Series B, No. 4, pp. 1161–1165, 1971.

3.87. H. Nagano, M. Fukasawa, K. Sigiyama; "Field tests of liquid nitrogen cooled cryogenic power cable," Internal Report of Hitachi Ltd., 1972.

3.88. Z. Iwata, N. Ichiyanagi, E. Kawai; "Cryogenic cable insulated with oil impregnated paper," IEEE Paper No. F 77 186-0, 1977.

3.89. E. C. Rogers, D. R. Edwards; "Design for a 750 MVA superconducting power cable," *Electr. Rev.*, pp. 2–5, Sept. 8, 1967.

3.90. "Vacuum insulated ac superconducting cables," U.S. Patent No. 3,947,622, 1976.

3.91. E. B. Forsyth; "Underground power transmission by superconducting cable," Brookhaven National Laboratory Report BNL 50325, March 1972.

3.92. K. G. Lewis, J. Sutton, C. W. Bibby, C. N. Carter, J. A. Noe; "Current tests on a flexible superconducting core for a 2 GVA ac cable," Cryogenics, March 1978, pp. 143–51.

AUTHOR INDEX

Adamczewski, I., 195, 198
Adamson, C., 329
Addis, G. I., 136, 283
Affel, H. A., 98
Afshartous, S. B., 79
Allan, R. N., 267
Alpert, D., 248
Altrichter, B., 249
Anderson, H. C., 413
Arnold, A. H. M., 36, 48, 98, 100
Ashcraft, A. C., 241, 404
Auckland, D. W., 242

Bahder, G., 240, 347, 413
Ball, E. H., 98, 102
Bardeen, J., 26
Barnes, C. C., 54, 278, 307, 337
Barton, H. A., 251
Beale, H. K., 335
Beaty, H. W., 162
Beck, J. W., 268
Belanger, B. C., 268
Bell, W. R., 174
Benard, P., 423
Bender, F., 378, 380
Berg, D., 169
Bernstein, B. S., 239
Bibby, C. W., 486
Blais, L. D., 413
Block, J., 222, 232
Blodgett, R. B., 347, 350
Bobo, M., 270
Bogner, G., 272
Bolin, P., 174
Bonmarin, J., 135
Botne, A., 239
Brackelmann, H., 281, 319
Brandt, T. F., 447
Brazier, L. G., 208, 214, 216
Brodie, I., 189
Broniewski, B., 142, 144
Brooks, E. J., 335
Brooks, H., 206
Browning, D. N., 447
Buckweitz, M., 373, 375
Budenstein, P. P., 201, 234, 239
Buller, F. H., 300
Burnier, P., 14, 142, 144
Burrell, R. W., 159, 350
Butterworth, S., 36

Carbonell, E., 142, 144
Carroll, J. C., 413
Carter, C. N., 486
Castelli, F., 102, 106
Cermak, I. A., 275
Charoy, M. A., 402
Chatterton, P. A., 250, 252
Chou, S., 206
Church, H. F., 197
Cockcroft, J. D., 36
Conangla, A., 57
Cooke, C. M., 189, 190
Cookson, A. H., 190
Cooper, L. N., 26
Cooper, R., 234, 242
Corbett, J. T., 401
Corry, A. F., 347
Cox, E. B., 413
Cox, H. N., 308, 310
Cranberg, L., 246
Cravalho, E. G., 469
Cronin, J. C., 190
Cross, J. D., 250

Crowdes, G. J., 282

Dakin, T. W., 169
Daniel, V. V., 272
Davies, M., 265
Deschamps, L., 282, 401
DeTourreil, C. H., 255
Diesner, A., 190
Doepken, H. C., 448, 453, 463
Dugdale, J. S., 139
Dushman, S., 253
Dwight, H. B., 36, 38, 48

Eager, G. S., 106, 413
Edwards, D. R., 146, 336, 468, 482
Eich, E. D., 349
Eichhorn, R. M., 238, 241, 408
Elgar, E. C., 57
Elliott, C. T., 234
Endacott, J. D., 293, 323, 329, 404
Engelhardt, J. S., 348
Eyraud, I., 333

Fallou, B., 270
Farrish, O., 190
Fock, V., 202
Forster, E. O., 266, 270
Forsyth, E. B., 113, 268, 391
Foust, O. J., 135, 139
Freemann, D. C., 469
Fukuda, S., 453
Fukuda, T., 239

Gaenger, E. B., 190
Gartner, E., 267
Garton, C. G., 197, 201, 221, 225, 231
Garwin, E. L., 249
Gauster, W. F., 469
Gazzana-Priaroggia, P., 271, 285, 288, 329, 331, 346
Geary, E. F., 445
Geballe, R., 172
Gibbons, J. A. M., 336
Gilette, R. W., 350
Glicksman, L. R., 373, 375
Goldspink, G. F., 222, 232
Gomer, R., 187
Gosling, C. H., 335
Graybill, H. W., 190
Gugan, D., 139

Hampton, B. F., 447
Hanscombe, J. R., 202
Hansson, B. O. N., 332
Harrison, M. A., 172
Hatcher, C. T., 350
Hauspurg, A., 158
Heeswijk, R. G. van, 190
Hess, R. C., 136, 283
Hill, N. E., 265
Hippel, A. von, 184, 260
Hirukawa, H., 269, 336
Hitchcock, J. A., 309
Hlawiczka, P., 45
Hobson, J. P., 253
Hoenig, M. O., 249, 473
Hollingsworth, P. M., 337
Horne, L. R., 333
Howard, P. R., 335
Howard, R. R., 413
Hoyt, E. W., 249
Hull, F. M., 350
Humphrey, L. E., 136, 283
Hunt, G. H., 239
Hunter, P. V., 159, 160, 276, 278, 405

Ieda, M., 242
Inge, L., 206
Iwata, Z., 269, 336

Jeanmonod, J., 254
Jeffries, M. J., 268
Jocteur, R. F., 402
Juettner, B., 249
Jurow, J., 249

Kamerlingh-Onnes, H., 19, 28
Katz, C., 239
Kawai, E., 269, 336
Kelsey, T., 189
Kennelly, A. E., 50, 98
Kenney, N. D., 239, 404
Kilar, L. A., 348, 445
Kinh, V. Q., 135
Kinoshita, M., 269, 336
Kitchen, D. W., 238, 241, 243
Kittel, C., 29
Klaudy, P., 468
Klein, N., 202
Kornelsen, E. V., 253
Koulopoulos, M. J., 239, 404

Krasucki, Z., 197
Kubo, H., 268, 271
Kuffel, E., 267
Kulman, F. E., 350

Lacoste, A., 282, 401, 423
Lafferty, J. M., 253
Lanienceau, P., 14
Laws, F. A., 50, 98
Lawson, W. G., 222, 232
Lee, D. A., 248
LeGrand, D. G., 222, 232
Leibold, A. A., 190
Lepers, J., 423
Lever, R. C., 242
Lewis, K. G., 486
Lewis, T. J., 195
Lichtenberg, G. C., 183
Loeb, L. B., 175
Lombardi, A., 406
London, F., 23, 25
London, H., 23, 25
Long, H. M., 469
Lozes, J. P., 413
Lyman, E. M., 248

McAvoy, F. M., 405
McFee, R., 468
McGrath, M. H., 38, 54, 301, 356, 359, 366
McIlveen, E. E., 347, 405
McKean, A. L., 347, 413
Mackenzie, B. T., 242
Maciotta-Rolandin, L., 102, 106
Margolin, S. W., 332, 346
Maschio, G., 98, 102, 331
Masotti, O. F., 262, 264
Mathes, K. N., 265
Matsuura, K., 268, 271
Mattison, O., 401, 404
Maxwell, E., 25
Maxwell, J. C., 33, 53, 113
Mayers, R. M., 447
Meaden, G. T., 9
Meek, J. M., 175
Meissner, W., 22
Melville, D. R. G., 336
Merrill, F. H., 184
Metra, P., 406
Meyerhoff, L., 106
Meyerhoff, R. W., 146, 148
Minnich, S. H., 268
Miranda, F. J., 271, 285, 288, 329
Mita, S., 222
Miyazaki, T., 268, 271
Montgomery, D. B., 189, 253, 257
Moon, P. H., 202
Mott, R. P., 223, 282
Mulcahy, M. J., 174
Mulligan, G. A., 268

Nawata, M., 242
Neal, S., 469
Nease, R. J., 372
Neher, J. H., 38, 54, 300, 356, 359, 366
Netzel, P. C., 447
Neumann, F. E., 90
Newhouse, V. L., 21, 147
Niemoller, A. B., 57
Notaro, J., 358, 372
Noto, F., 244

Ochsenfeld, R., 22
O'Dwyer, J. J., 201, 220, 237
O'Farrell, P. M., 469
Orchard, R. S., 337

Parish, H. C., 477
Parkman, N., 222, 232
Pawlek, F., 135
Pedersen, A., 189
Pender, Del M., 54
Perry, E. R., 190
Philp, S. F., 255
Pierce, P. H., 50, 98
Pippard, A. B., 19, 25, 27
Piscioneri, J. H., 332, 346
Ponder, J. Z., 447
Pratt, O. S., 238, 241, 243
Price, A. H., 265
Pulsford, J. A., 106, 123
Purnhagen, D., 378, 380

Rabinowitz, M., 249
Raether, H., 175
Ralston, P., 307
Rasquin, W., 281, 319, 423
Rayleigh, Lord, 36
Rechowicz, M., 146, 148
Redhead, P. A., 253

Rehder, R. H., 57
Reich, R., 30, 135, 142
Renfrew, A., 226
Renucci, L., 30
Rigby, S. J., 272
Riner, P., 106
Robinson, D. M., 208, 278
Rogalla, D., 135
Rogers, E. C., 468, 482
Rohsenow, W. M., 373, 375
Roughley, T. H., 401
Royere, A., 423
Rutherford, M. A., 413

Samm, R., 447
Sanders, F. H., 169
Sasso, J., 350
Schneider, H. M., 254
Schrieffer, J. R., 26
Schroff, D. H., 208
Schwab, A. M., 401
Semenoff, N., 206
Shannon, J. P., 255
Sharbaugh, A. H., 198
Shaw, R. G., 241, 404
Shii, H., 269, 336
Shoenberg, D., 24
Silsbee, F. B., 22
Silver, D. A., 413
Silvester, P., 42, 46, 47, 114, 275
Sinclair, J. A., 136
Singh, B. P., 252
Singh, N., 242
Sletback, J., 239
Slutz, R., 373, 375
Smith, J. L., 477
Smythe, W. R., 274
Sommerfeld, A., 34, 51
Sommerman, G. M. L., 190
Srivastava, K. D., 190, 255
Stannet, A. W., 208, 335
Stark, K. H., 201, 221, 225, 231
Sutton, J., 486
Swerdlow, N., 57

Sze, S. M., 202

Tanaka, T., 239
Temple-Hazell, J., 159, 276, 278, 405
Theophilus, G. D., 190
Thewell, M. J., 309
Thompson, L. B., 249, 253, 473, 478
Tobazeon, R., 267
Toepler, M., 185
Tomaschke, H. E., 249
Toscano, W. M., 469
Townsend, J. S., 168
Trump, J. G., 190, 193, 251, 255

Vahlstrom, W., 243
Valdes, J. G., 413
Van Atta, L. C., 251
Van de Graaf, R. J., 251
Vaughan, W. E., 265

Wagner, H., 243
Walther, A., 206
Watson, E. P. C., 335
Watson, P. K., 198
Webster, D. J., 358, 372
Weedy, B. M., 272
West, G. H., 307
White, G. K., 135
White, H. F., 57
Whitehead, S., 202
Williams, J. A., 190, 268
Williams, J. L., 372
Wiseman, R. J., 106
Wolff, H., 249
Woods, S. B., 135
Wooton, R. E., 190
Wretemark, S., 401, 404

Yahagi, K., 222
Yoshimura, N., 244
Young, F. S., 159

Zanona, A., 372

SUBJECT INDEX

AC current distribution, 32
  go-and-return conductor, 42
  non-circular conductor, 47
  three-core cable, 84
AC-DC resistance ratio, 33
  finite element analysis, 45
  isolated rectangular conductor, 46
  measurements, 102
AC loss, measurements, 102
  electrostatic shields, 112, 361, 386, 388, 419
  measurement circuits, 103
Adamczewski's breakdown criterion, 196
Air breakdown, 173, 193
Aluminum, 130
  Debye temperature, 10
  density, 322
  economic figure of merit, 150
  emissivity, 454
  ideal resistivity, 10
  Kohler diagram, 14
  low-temperature resistivity, 11
  measured low-temperature resistivity, 135
  mechanical properties, 132
  ore deposits, 131
  price (1976), 438
  production, 130
  purification, 132
  resistivity, 134, 141
  skin depth, 42
  solid dielectric cables, 436
  specific heat, 322
  steel-cored conductors, 133
  thermal expansion, 139
  work function, 188
  yield stress, 133
Aluminum pipes
  field welding, 450
  gas-insulated cables, 441
Ampacity
  comparison, naturally and forced cooled circuits, 317
    naturally and forced cooled pipe cables, 387
  equation, forced cooled pipe cables, 370, 382
    forced cooled selfcontained cables, 316
    internally cooled selfcontained cables, 319
    naturally cooled gas-cables, 453
      pipe cables, 360
      selfcontained cables, 299
  gas-insulated cables, 452
  pipe-type cables, 349, 355, 364
  pipe-type cables in air, 363, 365
  selfcontained cables, 293
  solid dielectric cables, 417
  water-cooled solid dielectric cables, 425
Annealing, 5
Annual capital charge, 337
Arc current, 258
Armor, underwater cables, 330, 432
Atmospheric heat sink, 294

Basic insulation level (BIL), 285
Beryllium, 141, 469
  Debye temperature, 10
  electrical conductivity, 143
  French research, 142
  ideal resistivity, 10
  Kohler diagram, 14
  low-temperature resistivity, 11
  magnetoresistance, 142

measured low-temperature resistivity, 135
ore resources, 145
specific gravity, 144
thermal expansion, 144
toxidity, 145
work function, 188
yield strength, 144
zone refined, 142
Bloch-Grueneisen, approximations, 8
equation, 7
Brazier's thermal instability diagram, 216
Breakdown channels in liquid, 197

Cable load factor, 153
Cable oils, 288
friction factor, 373
Reynold's number, 374
specific heat, 372
viscosity, 374
Cable sheathing, 288
Capacitance
coaxial cables, 210, 264, 272, 323
three-conductor cables, 274
CBS-theory, 25
Charging current, 210, 323
Chemical, bond disruption, 235, 245
chain reaction, 235
trees, 239
Circulating currents
flexible gas-insulated cables, 448
grounded pipe, 59
internal, 87
isolated phase gas-insulated cables, 445
Conducting particles, 190
breakdown due to, 191
in gas-insulated cables, 444
in liquids, 199
Conductor, Conci, 284, 348
conductance per dollar, 151
economics, 148
fabrication, 149
figure of merit, 148
joint, in gas-insulated cables, 442
in vacuum-insulated cables, 476
loss as function of voltage, 162
Milliken, 284
sizes, 101
temperature limit, 294, 357, 403
Continuous current rating, 300
Convection heat transfer, 302
Cook Inlet cable, 424, 431
Cook Strait cable, 167, 281, 335
Coolant temperature, 312
Copper, 125
Debye temperature, 10
density, 322
economic figure of merit, 150
ideal resistivity, 10
International Annealed Copper Standard (IACS), 126
Kohler diagram, 14
low-temperature resistivity, 11
measured low-temperature resistivity, 135
ore deposits, 125
price (1976), 438
production, 125
properties, 125
purity, 6
resistance ratio, 6, 134
resistivity graph, 141
skin depth, 42
solid dielectric cables, 436
specific heat, 322
thermal expansion, 139
work function, 188
Corona discharges, 199
Corrosion protection, 289
Cranberg's clump hypothesis, 246
Critical length, 323, 389, 426, 464
Crossbonding
in the field, 291
gas-insulated cables, 468
three-phase circuits, 63
water-cooled cables, 311
worked example, 65
Crosslinked polyethylene
breakdown, 224
dielectric strength, 221
modulus of elasticity, 221
Swedish 123-145 kV cables, 404
treeing, 238
voltage-stabilized, 241
Cryocables, 468
advantages, 470
dielectric constant of tape insulation, 268
evaporative cooling, 471
heat leak loss, 471
helium-insulated, superconducting, 483

prospects, 486
resistive, 468
superconducting, 468, 480
tape-insulated, LN_2-cooled, 478
superconducting, 484
vacuum-insulated, LN_2-cooled, 80, 245, 472
superconducting, 480
Current distribution in non-circular conductors, 42
Cyclic soil resistance factor, 306

Daily cycle rating, 303, 366, 462
DC cables
comparison with ac cables, 330
gas-insulated, 464
pipe-type, 389
selfcontained, 328
solid dielectric, 431
Debye temperature, 7, 10
Dielectric breakdown
gases, 167
Lichtenberg mechanism, 183
streamer mechanism, 174
Townsend mechanism, 168
liquids, 192
electronic, 194
foreign particles, 199
vapor bubble, 197
solids, 200
electromechanical, 201, 221
gas channel, 201, 221
hydrostatic pressure, 222
intrinsic, 193, 237
mechanical stress, 222
purely electrical, 201
temperature, 217
thermal expansion, 224
treeing, 238
Dielectric coatings on conductors, 250
Dielectric constant, 212, 262
Dielectric heating, oil-paper, 209
polyethylene, 217
Dielectric loss, 269
coaxial cables, 210
formula, 212
loss factor, 207, 265
low temperature, 270
power factor, 207, 270
solid dielectric cables, 418, 421
value of, 166
Dielectric particles, 190
in liquids, 199
Differential thermal expansion, 224, 312
gas-insulated cables, 443
polyethylene tape insulation, 336
three-conductor gas-insulated cables, 449
Drain wires
eddy current resistance, 420
equivalent resistance, 419
Swedish 123-145 kV cables, 404

Economics
gas-insulated cables, 464
pipe-type cables, 391
selfcontained cables, 336
solid dielectric cables, 433
Eddy currents
paths in single-core cables, 76
pipe surrounding single conductor, 59
sheath loss in single-core cables, 75
worked example, 77
Eigenvalue, matrix, 44
problem, 45
Electrical conductivity, 2, 11
dielectrics, 202, 208
Kelvin bridge measurement, 126
non-contact measurement, 126
Electrical stress, 287
Electricity cost, 337, 391
Electrodynamics of linear conductors, 31
Electromagnetic torque, 79, 96
Electromechanical forces
asymmetrical conductors, 94
conductors and metallic pipes, 90
fault currents, 320, 388
flexible gas-insulated cables, 448
go-and-return circuit, 91
numerical example, 97
pair of filaments, 36, 91
three-conductor cable, 95
Electron
band structure, 14
Cooper pair, 26
drift velocity, 3
mean free path, 3, 11, 28
spin, 15
wave representation, 6, 15
Electronegative gases, 172
breakdown strength, 174

Electronic breakdown of liquids, 194
Electrostatic pressure, 225
  collapse of dielectric, 229
  and transverse strain, 233
Energy losses
  forced-cooled pipe-type cables, 382
  oil-paper insulated cables, 400
  overhead lines, 400
  selfcontained cables, 345
  value of, 343
England-France cables, 281, 332
Ethylene propylene rubber
  dielectric constant, 266
  solid dielectric cables, 405
  tapes for splicing, 413

Fault current rating
  gas-insulated cables, 463
  pipe-type cables, 386
  selfcontained cables, 319
  solid dielectric cables, 426
Fermi-Dirac distribution of electron energies, 17
Fermi-gas of free electrons, 18
  -level, 187
  -surface, 14, 19
Ferranti tubular main, 160, 276
Fiber bridges, 200
Fiber-glass pipes, 350, 479
Field emission, 186, 194
  electron beam, 189
  electron potential diagram, 187
  enhancement factor, 189
  Fowler-Nordheim equation, 188
  gas breakdown, 189
  tunneling, 183
  into vacuum, 247
Filament model, 32, 42, 81
Finite element method
  induced currents, 59
  non-circular conductors, 42
  proximity effect, 49
  three-conductor cables, 79
Flexible solid dielectrics, 200
Forced-cooled cables, 281
  economics, 397
  gas-insulated, 463
  pipe-type, 368, 397
  reciprocating oil flow, 378
  selfcontained, 307
  solid dielectric, 423
Free electron model, 1, 16

Garton effect, 271
Gas-assisted paper insulation, 167
Gas-insulated cables, 283, 441
  ampacity, 452
  critical length, 464
  daily cycle rating, 462
  dc application, 464
  economics, 464
  fault current rating, 463
  forced cooling, 463
  installation, 449
  isolated phase, flexible, 447
    rigid, 441
  shipping length, 442
  three-conductor, 448
  underwater installation, 464
Geometric mean distance (GMD), 32, 53, 117
  circular wire, 114
  definition, 53
  round tube, 62
  7-strand conductor, 118
  stranded conductors, 119
  various conductor and pipe arrangements, 55
Gothland cable, 328, 332

Heat flow
  through coaxial dielectric, 210, 294
  through oil, 358, 372
  from pipe-type cables, 357
Heat transfer through gas, 453, 456, 459, 461
Helium
  density of liquid, 266
  dielectric constant of liquid, 266
  ionization energy, 169
  liquefaction, 19
  liquid cooling, 469
Hole conduction, 201, 237
Hunter-Brazier cable, 280
Hydrogen
  density of liquid, 266
  dielectric constant of liquid, 266
  liquid cooling, 469
  reactions, 235

Impedance matrix, 43
Impulse breakdown, 219, 245
Inflation factor, 154, 337, 391
Installation
  gas-insulated cables, 449
  pipe-type cables, 350
  selfcontained cables, 289
  solid dielectric cables, 415
Installed cost, 337
Insulation oil
  breakdown of hydrocarbons, 196
  C-C bond, 195
  dielectric strength, 193
  electron mean free path, 196
Insulation shields, 288, 402, 404
Insulator flashover, 183
  effect of profile, 185, 255
  in gas, 443
  in vacuum, 253
Ion exchange mechanism, 250
Ionization energies, 169
Ion shields, 254

Joule heating, 20, 33, 41
  fault current, 322
  solid dielectrics, 207
  superconducting cables, 486
  three-conductor cables, 88
Joule losses
  aluminum pipe enclosure, 460
  bus enclosures, 57, 454
  cable pipe, 356
  cable sheath, 71
    conductivity dependence, 72
    radius dependence, 74
    thickness dependence, 73
  conductor economics, 156
  insulation shield, 356
  pipe-type cables, 107
  three-conductor cables, 88
  U.S. power grid, 150

Kelvin's law, 152
  cost minimum, 153, 162, 439
Kingsnorth-London dc cable, 282
Klydonograph, 183
Kohler diagram, 13

Lake Champlain cable, 335
Lattice
  defects, 5
  periodic potential, 6, 18
  strain, 5
  vibrations, 6
Lead
  Debye temperature, 10
  ideal resistivity, 10
  sheath, 329
Lewis' breakdown criterion, 195
Lichtenberg discharges, 183
  dipole interaction, 185
  produced in vacuum, 186, 259
  and treeing in solids, 238, 241
Load cycle, daily, 304
  insulation failure, 224
London, equation, 23
  skin depth of superconductors, 24, 28
  theory of superconductors, 23
Long Island Sound cable, 332, 346
Longitudinally induced emf's, 334
Loss factor, 154

Magnetic hysteresis losses
  empirical formula, 111
  pipe-type cables, 107
  rotating field, 109
  Steinmetz formula, 108
Magnetoresistance, 11
  of Beryllium, 136
Massotti model, 262
Mathiessen's rule, 5
Maxwell-Boltzmann electron energy distribution, 16
Meissner effect, 22
Metal
  electrolysis, 152
  lattice, 1
  monovalent, 1
  specific heat, 4
  vapor arc, 257
Milliken conductor, 100
Molecular velocity, 250, 252
Monolayer of molecules, 253
Mutual inductance
  conductor and pipe, 50, 55
  flux linkage definition, 56
  formula in cable literature, 54
  matrix, 43, 82
  parallel conductors, 50
  two filaments, 33

Neumann's formula, 33, 51, 100, 115
  mutual potential, 90
Niobium, 22, 145, 483
  critical field, 21
  melting point, 147
  ore resources, 147
  superconducting alloys, 145
  thermal conductivity, 147
  work function, 188
Niobium-Germanium, 146
Niobium-Tin, 146, 485
Niobium-Titanium, 146
Niobium-Zirconium, 146
Nitrogen
  breakdown strength, 173
  density of liquid, 266
  dielectric constant of liquid, 266
  dielectric strength of liquid, 193
  ionization energy, 169
  liquid cooling, 469
Non-magnetic pipes, 107

Ohm's law, 3
Oil-paper insulated cables, 276, 284, 347
  Bennett's first pipe cable, 278
  gas pressure assisted, 278, 401
  mass-impregnated, 279, 329
  oil cooling, 317
  oil pressurization plant, 355
  oil tanks, 293
  pipe-type, 347
  pre-impregnated, 279
  reactive compensation, 325
  selfcontained, 284
Oil-paper insulation
  ac dielectric strength, 286
  basic insulation level (BIL), 286
  cable oils, 288, 372
  dielectric constant, 267
  dielectric heating, 216, 271
  Emanueli's invention, 278
  power factor characteristics, 209, 271
  thermal instability, 208
Overhead transmission
  capitalized transmission cost (1977), 165
  data of typical U.S. lines, 164
  transmission cost data, 392
  transmission cost graph, 342

Paper, dielectric constant, 267
  loss/stress characteristic, 272
Paschen's law, 171
  minimum, 252
Permittivity, 265
Pipe-type cables, 347
  ac strength, 349
  ampacity, 349, 355, 382, 387
  cooling plant, 378
  core pulling, 352
  daily cycle rating, 366
  dc transmission capability, 390
  description, 347
  economics, 391
  fault currents, 386
  forced cooling, 368
  impulse strength, 349
  installation, 350
  pipe welding, 351
  pressure drop, 373, 382
  pumping power, 383
  range, 348
Polarization, 259
Polyethylene
  amorphous phase, 243
  amount in solid dielectric cables, 436
  antioxidant, 241
  density, 267
  dielectric constant, 267
  dielectric heating, 217
  dielectric strength, 193
  effective ac conductivity, 208
  fillers, 242
  film insulation, 269
  insulation failures, 201
  loss/stress characteristic, 272
  modulus of elasticity, 221, 227
  power factor, 267, 269
  price (1976), 438
  stress/strain curve, 227
  thermal expansion, 139
  thermomechanical breakdown, 224
  treeing, 238
  voltage life, 241
  voltage stabilized, 241
Polypropylene laminated paper, 336
  ac strength, 269
  density, 269
  dielectric constant, 268
  impulse strength, 269
  loss/stress characteristic, 272

loss/temperature characteristic, 271
power factor, 269, 271
Pressure drop, 373, 383
Proximity effect
flat strip conductors, 49
go-and-return circuit, 47
isolated conductors, 36
non-circular conductors, 49
solid round conductors, 49
three-conductor cable, 85
tubular round conductors, 50
Pumping power, 383

Radiation heat transfer, 302
Reactive compensation, 325
oil-paper cables, 325, 389
solid dielectric cables, 428
Refrigeration power, 380, 385
Reliability
New York blackout (1977), 158
North-East blackout (1965), 158
service, 157
transmission plant, 157
Residency time, 198
Resistance, electrical, 5
low-temperature, of mercury, 20
ratio, 6, 10
residual, 5, 20
Resistivity, bulk, 12
electrical, 5
ideal, 5, 10
ratio, 10
residual, 5
unisotropy, 19

Sardinia cable, 328
Segmental conductors, ac resistance, 98, 356
Milliken, 284
Selfcontained oil-paper cables, 284
ampacity, 324
cost data, 339
critical length, 324
elements of, 284
installation, 289
reactive compensation, 325
transmission cost, 341
underwater installation, 329
Self-inductance, 35, 112
finite element analysis, 46
GMD, 34
isolated rectangular conductors, 47
Neumann's formula, 116
parallel wire line, 55, 114
pipe-type cables, 124
three-conductor cable, 88
Sheath (pipe) resistance, 70, 362
Shield resistance, 112, 361, 386, 419
Shunt reactors, 328
Silsbee hypothesis, 22, 26
Silver, Debye temperature, 10
ideal resistivity, 10
work function, 188
Skid wires, 350
Skin effect, 31
round tubes, 38
skin depth, 40
solid round conductors, 36
three-conductor cable, 84
Sodium, 136
amount in solid dielectric cables, 436
Debye temperature, 10
economic figure of merit, 150
first commercial conductors, 136
ideal resistivity, 10
Kohler diagram, 14
low temperature resistivity, 11, 135
melting point, 140
price, 138, 438
production, 138
raw material, 137
reaction with water vapor, 408
reactivity, 137
resistivity formula, 139
separation, 136
skin depth, 42
specific gravity, 140
thermal expansion, 139
work function, 188
Sodium cables, 283, 406
economics, 434
hydroxide layer, 408
Lima, Ohio, cable, 406
low-voltage installations, 411
MIT load cycle testing, 411
230/345 kV cable of the future, 412
users, 137
Solid dielectric cables, 282, 401
ampacity, 417, 425, 429
capacitance, 429

comparison of material properties, 407
critical length, 426
crosslinked polyethylene, 405
daily cycle rating, 423
economics, 433
EPR cables, 405
fault current rating, 426
forced cooling, 423
French 225 kV cable, 402
installation, 415
Puerto Rico 138 kV cable, 404
sodium cables, 406
splices, 412
Swedish 123-145 kV cables, 404
terminations, 415
voltage-stabilized polyethylene, 404
Space charge, breakdown, 235
tree initiation, 242
Spacers
gas-insulated cables, flexible, 447
rigid, 442
vacuum-insulated cables, 475
Splices, cable insulation, 158
cooling, 309
failures, 405
gas-insulated cables, 159
molded, 414
overhead conductor, 158
pipe-type cables, 352, 354
selfcontained cables, 290
slip-on, 415
solid dielectric cables, 412
Steel armor wire, 108
Steel pipes, 350
Stop joints, 291, 293, 354
Stranded conductors, ac performance, 97
concentrically, 99
GMD, 117
Milliken (segmental), 100
self-inductance, 124
spirality effect, 98
Streamers, 174
approximate onset criterion, 180
filamentary nature, 175
on insulators in vacuum, 253
Meek's theory, 175
onset in air, 183
onset criterion, 179
positive and negative, 175
Sulfur hexafluoride, breakdown strength, 173, 193
dielectric constant, 265
gas monitoring, 451
ionization energy, 169
pressure in cables, 447
Sulfur trees, 239
Superconducting transmission lines, 480
feasibility, 145
R&D programs, 146
Superconductivity, cause, 25
coherence, 25, 28
critical fields, 30
critical temperatures, 23, 30
diamagnetism, 22
energy gap, 26
isotope effect, 25, 28
Meissner effect, 22, 28
persistent current, 25
second order phase transformation, 24
surface loss, 148
two-fluid model, 25
type I, 19, 146
type II, 28, 146
Superconductors, ac losses, 30
critical fields, 21, 147
eddy current losses in backing, 148
electronic specific heat, 27
heat capacity, 25
high-frequency resistance, 26
magnetic hysteresis, 29
thermal stabilization, 147
transition temperatures, 147
type I, 146
type II, 146
Supercurrent, distribution, 22
penetration depth, 23
Surge impedance, 113
Synthetic tape insulation, 335, 391

Temperature drop across insulation, 212
Terminations, gas-insulated cables, 445
selfcontained cables, 292
solid dielectric cables, 415
vacuum-insulated cables, 476
Thermal breakdown of solid dielectrics, 202
impulse, 219
sodium chloride slab, 206
Thermal conductivity
gas-polyethylene-tape combination, 336

LN_2-impregnated paper, 479
silt, 334
soil, 294
solid dielectrics, 202
Thermal image method, 296
Thermal proximity factor, 296
Thermal resistance, air space, 30
coaxial layer, 212
solid dielectric cables, 421
Thermal resistivity, oil-paper, 212, 299
plastic jacket, 299
Thermal sand, 350
Thermal stability of solid dielectrics, 203
Thermal time constant, 301, 306, 462
Thermomechanical forces, 311
Townsend electron avalanches, 168
α-mechanism, 195
attachment coefficient, 172
diagram, 177
first ionization coefficient, 168, 170
length, 180
third ionization coefficient, 170
Townsend sparking criterion, 171, 173
Transformer, invention, 160
oil, 266
Transmission cost, equations, 340, 433
forced cooled pipe-type cables, 399
gas-insulated cables, 465, 467
general principles, 336
graphs, 341
naturally cooled pipe-type cables, 392
overhead lines, 392
selfcontained cables, 341
solid dielectric cables, 465, 467
vacuum-insulated LN_2-cryocables, 473
Tree channels (branches), in amorphous polyethylene, 243
classification, 240
cross-section, 238
Treeing, and electron transport, 234
from free surfaces, 243
and gas-channel breakdown, 236, 239
inhibitors, 241, 245, 404
Kitchen and Pratt hypothesis, 238
in polymers, 238
Trichel pulses, 174

UG/OH transmission cost ratios, cryocables, 472
forced cooled selfcontained cables, 346
gas-insulated cables, 466
naturally cooled pipe-type cables, 393
naturally cooled selfcontained cables, 342
solid dielectric cables, 439
Underwater cables, armor, 331
embedment, 432
gas-insulated, 464
manufacture, 331
pipe-type, 390
repairing, 335, 432
along rivers and canals, 335
sea return conductor, 332
selfcontained, 329
solid dielectric, 424, 431
spacing, 332

Vacuum breakdown, 245
arc current, 258
clump hypothesis, 246
high-voltage conditioning, 247
ion exchange mechanism, 250
microdischargers, 248
Vacuum-insulated LN_2-cryocable, 472
Vancouver Island cables, 281, 332
Vapor bubble breakdown, 197
Vector potential, 57
Voltage drop, 112
Voltage(s), ladder, 161
life curves for polyethylene, 241
stabilizers, 241, 245, 404
for transmission, 160

Waltz Mill, 138 kV EPR-cable testing, 405
500 kV pipe-type cable testing, 159, 349
138 kV solid dielectric cable testing, 223, 282, 402, 405
tests of flexible gas-insulated cables, 447
Water, dielectric constant, 266
in dielectric liquids, 199
ionization energy, 169
Water cooling, arrangements, 308
plant, 310
solid dielectric cables, 423
Wiedemann-Franz law, 1, 204
Work function, 168

621.31923 60478
G756
GRANEAU
AUTHOR
Underground power trans-
TITLE
mission

621.31923 60478
G756
GRANEAU
Underground power transmission